

Development of Self-Consistent Field
Theory Models for Predicting the Structure
and Properties of Inhomogeneous Polymer
Systems: Applications to the Description of
Nanocomposite Materials

Constantinos J. Revelas



ΕΘΝΙΚΟ ΜΕΤΣΟΒΙΟ ΠΟΛΥΤΕΧΝΕΙΟ
ΣΧΟΛΗ ΧΗΜΙΚΩΝ ΜΗΧΑΝΙΚΩΝ

**Ανάπτυξη Προτύπων Βασισμένων στη Θεωρία Αυτο-
Συνεπούς Πεδίου για την Πρόρρηση της Δομής και των
Ιδιοτήτων μη Ομογενών Συστημάτων Πολυμερών:
Εφαρμογή στην Περιγραφή Νανοσύνθετων Υλικών**

**Development of Self-Consistent Field Theory Models for the
Prediction of Structure and Properties of Inhomogeneous
Polymer Systems: Application to the Description of
Nanocomposite Materials**

Κωνσταντίνος Ι. Ρέβελας
Constantinos J. Revelas

Διδακτορική Διατριβή υποβληθείσα στην Σχολή Χημικών Μηχανικών του
Εθνικού Μετσόβιου Πολυτεχνείου για την απόκτηση του τίτλου του Διδάκτορος
του Εθνικού Μετσόβιου Πολυτεχνείου

Αθήνα, Απρίλιος 2023

Thesis examination committee:

1. **Professor Doros Theodorou** (supervisor)
School of Chemical Engineering
National Technical University of Athens
2. **Professor Andreas Boudouvis**
School of Chemical Engineering
Rector of the National Technical University of Athens
3. **Professor Nikolaos Papagiannakos**
School of Chemical Engineering
National Technical University of Athens
4. **Professor Friederike Schmid**
Johannes Gutenberg-Universität Mainz, Germany
5. **Professor Constantinos Charitidis**
School of Chemical Engineering
National Technical University of Athens
6. **Professor Vlasis Mavrantzas**
Professor of Chemical Engineering
University of Patras and ETH Zürich
7. **Assistant Professor Mihalis Kavousanakis**
School of Chemical Engineering
National Technical University of Athens

«Η έγκριση της διδακτορικής διατριβής από την Ανώτατη Σχολή Χημικών Μηχανικών του Ε. Μ. Πολυτεχνείου δεν υποδηλώνει αποδοχή των γνώμων του συγγραφέα. (Ν. 5343-1932. Άρθρο 202)»

*The Dissertation is dedicated to my wife Catherine,
and our “daughter” Sandy.*

CONTENTS

CONTENTS	VII
PREFACE	XI
SUMMARY	XIV
ΠΕΡΙΛΗΨΗ	XVII
LIST OF FIGURES	XX
LIST OF TABLES	XXV
NOMENCLATURE	XXVII
Symbols	xxvii
Latin symbols.....	xxvii
Greek Symbols.....	xxix
Abbreviations.....	xxxix
1. INTRODUCTION	1
1.1. Polymer brushes and grafted nanoparticles	2
1.2. Motivation	4
1.3. Aim of the thesis.....	5
1.4. Outline of the thesis.....	6
2. THEORETICAL AND NUMERICAL BACKGROUND	7
2.1. Polymer physics	7
2.1.1. Gaussian chain model – Bonded interactions	7
2.1.2. Edwards diffusion equation	8
2.1.3. Physical interpretation of the field, w'	9
2.1.4. Nonbonded polymer interactions.....	13
2.1.4.1. Helfand EoS	14
2.1.4.2. Sanchez-Lacombe EoS.....	14
2.1.4.3. Compressibility considerations	17
2.1.5. Solid/polymer interactions.....	19

Contents

2.1.5.1.	Hamaker Sphere-sphere	20
2.1.5.2.	Hamaker Sphere-planar surface	21
2.1.5.3.	Hamaker Planar-planar surface	21
2.1.5.4.	Square well and ramp potential	21
2.1.5.5.	Hamaker-like integration of arbitrary pair-wise potentials	23
2.1.5.6.	Tabulated potentials	26
2.2.	Thermodynamic description of polymer interfaces	28
2.2.1.	Systems involving polymer melt	28
2.2.2.	Systems in vacuum	29
2.2.3.	Macroscopic Work Functions	30
2.3.	Finite Differences	31
2.3.1.	Semi-implicit Time-stepping	31
2.3.2.	Implicit time-stepping	32
2.3.3.	Boundary conditions in 1D matrices	33
2.3.3.1.	Dirichlet-Dirichlet system	34
2.3.3.2.	Neumann-Neumann system	34
2.3.4.	Solving the linear system of equations	35
2.4.	Finite Element Method	36
2.4.1.	Steady-state analysis	38
2.4.2.	Transient analysis	39
2.4.3.	Integration via Gauss-quadrature	41
3.	RUSSEL	44
3.1.	Description	44
3.2.	Code Flow	48
3.3.	Commercial software vs RuSseL	50
3.4.	Calculated properties	51
3.4.1.	Total and partial segment density profiles	51
3.4.2.	Brush thickness	53
3.4.3.	Profiles of individual chain segments	54
3.4.4.	Adsorbed vs free chain segments	57
3.4.5.	Chains per area profiles	62
3.4.6.	Profiles of individual grafted chains	63
3.5.	Chain discretization	64
3.5.1.	Different discretization for matrix and grafted chains	64
3.5.2.	Uniform vs nonuniform discretization	64
3.5.3.	Hybrid chain contour discretization	66
3.6.	Convergence and Initial Conditions of Grafted Chains	67
3.6.1.	1D calculations	68
3.6.2.	3D calculations	70

3.6.2.1.	Numerical Estimation of the Delta Function on the Grafting Points.....	71
3.7.	Benchmarks of RuSseL3D	73
3.7.1.	Spatial Discretization.....	73
3.7.2.	Contour Discretization.....	75
3.7.3.	Field Mixing Fraction.....	75
3.7.4.	Renormalization of Configurational Entropy of Grafted Chains	76
3.7.5.	Parallelization and Scalability	78
3.8.	Grafting Point Distributions	81
3.9.	3D Periodic Boundary Conditions.....	83
3.9.1.	Spherical Nanoparticles in Polymer Matrix.....	84
3.9.2.	Spherical Nanoparticles in Vacuum	91
4.	SINGLE NANOPARTICLE CALCULATIONS	97
4.1.	Bare surfaces exposed to melt	99
4.1.1.	Background.....	99
4.1.2.	Structure	99
4.1.3.	Thermodynamics	103
4.1.4.	Concluding remarks.....	107
4.2.	Grafted nanoparticle inside a polymer matrix	108
4.2.1.	Background.....	108
4.2.2.	Validation against FOMC.....	108
4.2.3.	Radial density profiles from the SL EoS: exploration of R_s , σ_g , M_g parameter space.....	110
4.2.4.	Density profiles of adsorbed polymer segments	113
4.2.5.	Chains per area density profiles.....	114
4.2.6.	Chain end segregation at the interface	117
4.2.7.	Scaling of grafted polymer layers.....	118
4.2.8.	Thermodynamics	125
4.2.9.	Contributions to chain stretching.....	127
4.2.10.	Concluding remarks	130
4.3.	Grafted nanoparticle in contact with vacuum. Solvation free energy of a nanoparticle	132
4.3.1.	Background.....	132
4.3.2.	Description of the model	134
4.3.3.	Structure	135
4.3.4.	Thermodynamics and solvation free energy	140
4.3.4.1.	Contribution of individual free energy terms	145
4.3.4.2.	Effect of varying the length of matrix chains	148
4.3.5.	Model for estimation of partition coefficients	150
4.3.6.	Concluding remarks.....	153
5.	THREE DIMENSIONAL CALCULATIONS AND COMPARISON WITH 1D	157

Contents

5.1.	Background	157
5.2.	Spatial discretization	161
5.3.	Calculation Details	163
5.4.	Assessment of the Smearing Approximation: 1D- versus 3D-SCFT	165
5.4.1.	Smearred segment density profiles	165
5.4.2.	Brush thickness.....	167
5.4.3.	Thermodynamics	169
5.4.4.	Equidistributed Grafted Nanoparticles: 3D Spatial Distributions.....	171
5.5.	Irregular Grafting Point Distributions: Structure and Thermodynamics	173
5.6.	Concluding remarks	180
6.	CALCULATIONS INVOLVING TWO PARTICLES/SURFACES	181
6.1.	Background	181
6.2.	Planar surfaces.....	182
6.2.1.	Vacuum/Melt and Solid/Melt Interphases	185
6.2.2.	Grafted/Vacuum (GV) and Grafted/Melt (GM) interfaces	187
6.2.3.	Polystyrene melt capped between two bare silica surfaces (SMS)	193
6.2.4.	Interacting grafted surfaces in melt (GMG).....	198
6.2.5.	Interacting grafted surfaces in vacuum (GVG).....	208
6.2.6.	Concluding remarks.....	212
6.3.	Spherical Surfaces	215
6.3.1.	Background.....	215
6.3.2.	PMF between two grafted silica nanoparticles	216
6.3.3.	Concluding Remarks	226
7.	SCIENTIFIC AND METHODOLOGICAL ADVANCES.....	227
	APPENDICES	229
	REFERENCES	259
	CURRICULUM VITAE	271

PREFACE

Enrolling for a PhD studentship is one of the most important decisions that one has to make in one's life. This holds no matter whether one wishes to follow an academic path or a career in industry. When I came back to Greece from Belgium, after an unsuccessful pursuit of a research project that would have demanded an investment of time, money and mental stamina on my part for a period of at least 4 years, I was at a crossroads of my life on both professional and personal levels. I was determined to do a PhD, but I did not have any clue about who/what would be a suitable advisor, research group, or project for me. Beyond anything else, I wanted to be sure that I would spend the following years of my life learning a lot of new things that would enrich my arsenal of knowledge for my subsequent entry to the job market. In other words, I wanted to ensure my proper training as a future researcher. All of a sudden, I came to realize that maybe the best option would be to address one of the Professors who taught me in my undergraduate studies and inspired me with their spirit, knowledge and experience in the first place. After some thought, I sent an e-mail to Prof. Theodorou and expressed my intention to become a member of his group and undertake my PhD studies under his mentorship. This email is probably the most important message I have sent up to now. I had first met Prof. Theodorou in the first year of my undergraduate studies, where I was impressed by his professionalism, way of thinking, teaching and interacting with the class. What impressed me the most, however, was his kindness and his willingness to help the students when they had a difficult time with his assignments. A few years later, he offered me the opportunity to become a member of his group and honored me with an extremely challenging subject. He supported me with patience and persistence from my first to my very last day of my PhD. He kept believing in me at times when I did not believe in my own self and I felt sure that I would not make it eventually. For all these reasons, I want to thank him and I very much hope that my PhD will only be the start of our collaboration.

Contents

Next, I want to thank Dr. Aristotelis Sgouros with whom I have spent countless hours of research, coding, and learning. Without him, this PhD would be poorer. It is not only the amount of time that he invested for the projects of the PhD, but also the knowledge, way of thinking and problem-solving skills that he transferred to me. I want to thank him for being my friend together with Ioanna, and for making this journey so much more fun than it would have been if I were just working alone. They made me feel blessed, because the last five years of my life were not just work, but also joy and beautiful moments that I will remember when I am old. In the same spirit, I also want to thank Dr. Apostolos Lakkas, since it was his hard work, insight and perseverance which constituted the basis upon which my research was built. He was the first one who started hitting one “wall” after another in this difficult subject, before I was even ready to start performing calculations. He was the one whom I first turned to when I was completely lost; thanks to him, my introduction to the subject was smoother. Furthermore, I wish to thank the senior members of the group, Dr. Stefanos Annogiannakis, Dr. Georgios Vogiatzis, Dr. Grigorios Megariotis and Dr. Nikolaos Romanos for welcoming me in the CoMSE family and offering me a warm and pleasant work environment during these years.

I also wish to express my gratitude to the most important person in my life, my wife, Catherine, who endured with patience and understanding my bad mood and who was always there to listen, help and advise me. In her I have found the ideal partner, the one who will help me evolve and prosper, congratulating me when I succeed, and aiding me to recover when difficulties arise. It would be a serious omission on my part not to mention our beautiful dog Sandy, which was constantly keeping me company all the days that I worked from home, sitting beside me and falling asleep with the sound of the keyboard. Although I feel gratitude for the home I returned to when getting back from work, I also feel sorry about a recent loss in my family. In the middle of my PhD I lost my grandfather. After the loss of my father, he was the man that I envisaged as my role model. I feel the need to thank both of them for all the lessons they taught me and for the sacrifices they made. This PhD is a result of wise choices they made many years ago. I will work to make them proud as if they were beside me in every step. Partly, my thesis is dedicated to their memory.

This PhD would be completely unfeasible without financial support, given the amount of time that I had to sacrifice so that I could learn, research, produce results, debug, start all over from the beginning a handful of times, write productive code and scripts, and at the same time write papers to output my research to the community. I want to express my deep gratitude to Dr. Grigorios Megariotis for including me in the ELIDEK project that he prepared and supervised

with Prof. Theodorou. I want to thank the Special Account of Research Funding of the National Technical University of Athens for honoring me with a personal fellowship. Special thanks to the National Supercomputing Infrastructure, ARIS, represented by Dr. Dimitrios Dellis, for the computational resources he granted me for developing, testing and producing results.

Closing this prologue, I would like to give my own humble advice to any PhD student (or not) who happens to read the present thesis. When doing a PhD, one has to rely mostly on his patience, endurance and will to learn from failure. If someone asked me what is the most important lesson that I learned during my PhD, that would be the way to manage failure and turn it into an advantage. What is success anyway? Would we be successful if anything we tried happened to be correct in the first place, be it an experiment, a paper, a research proposal, a computation, a code, you name it.. No. My definition of success is the ability of never giving up. I like to envision success as an ascending ladder whose steps are situations of “failure”; without the steps, you stay at the same level forever: *“The only difference between the master and the student is that the master has failed more times than the student has even tried.”*

SUMMARY

Polymer *Self-Consistent Field Theory* (SCFT) is an established theoretical tool, broadly used by modelers in academic and industrial environments to obtain quantitative predictions on the equilibrium behavior of inhomogeneous polymer systems such as polymer blends, copolymer melts, gas-polymer and solid/polymer interfaces. This fact has made SCFT one of the most commonly invoked frameworks when someone needs to address polymer systems at length scales inaccessible to particle-based methodologies. Furthermore, the growing interest in the design of nanocomposite materials involving interfaces of polymer melts with inorganic fillers and the need for fast calculations to predict or even manipulate the nanoscale self-assembly properties of composite materials have also been driving forces for the development of rigorous theoretical models to investigate how these materials will respond under various conditions.

When conducting SCFT calculations, the primary task is to solve the *Edwards* diffusion equation. This is a “reaction and diffusion” partial differential equation (PDE) with contour length playing the role of time, whose solution is a *restricted partition function*, i.e., a quantity proportional to the probability density that a segment which finds itself at a specific contour length from the start of a chain, will occupy a certain position in space. In the context of this PhD, the numerical solution of the PDE is performed via a custom-made in-house code named *RuSseL*. The one-dimensional version of the code applies a *Finite-Differences* (FD) scheme, while the three-dimensional version is based on the *Finite Element Method* (FEM) and can be applied in systems of arbitrary geometry.

The first system we addressed was a single polystyrene-grafted silica nanoparticle embedded in polystyrene melt at infinite dilution. The density profiles of matrix and grafted chains, along with additional structural characteristics such as the *chain shape*, profiles of *middle/end* segments and *adsorbed/free* segments were derived for various particle radii, lengths of grafted chains and grafting densities. We have estimated the thickness of the brush across the whole range of parameters and compared our results with experimental findings and scaling laws

reported in the literature. The free energy of the system was also derived for the same parameters. Having studied the behavior of the grafted particle inside homopolymer melts, we went a step further and investigated the structural and thermodynamic properties of a system comprising the same particle in contact with vacuum. The difference in the free energy of the two systems (in presence and absence of polymer melt) allowed us to estimate the *solvation Gibbs free energy* as a function of the grafting density, intensity of solid/polymer interactions, particle size, and lengths of grafted and matrix chains.

Next, we implemented our SCFT model in a system of two opposing polystyrene-grafted silica plates to derive the *potential of mean force* (PMF); i.e., the free energy of the system as a function of the plate-to-plate distance. This system is mathematically equivalent to one containing two grafted particles of extremely large particle radius. The PMF was derived as a function of the length of grafted chains, grafting density and intensity of solid/polymer interactions. In addition, we allowed the two plates to be grafted with different numbers and/or lengths of grafted chains, in order to investigate the impact of grafting asymmetries on the PMF and therefore stability of the nanocomposite system. Such asymmetries are expected to occur when these systems are prepared experimentally. In all cases, we also calculated the PMF between the two brushes in the absence of melt chains by applying a *canonical ensemble* formulation.

All these calculations can be also performed in three-dimensions using the FEM version of *RuSseL*. This 3D implementation avoids any smearing of the grafting points, normal or parallel to the solid surfaces. We undertook detailed benchmarks on a system of a single nanoparticle immersed in polymer melt and performed a direct comparison between 1D- and 3D-SCFT calculations over a broad range parameters in order to assess the validity of the smearing approximation in terms of both chain structure and system thermodynamics.

Moreover, in 3D we are able to impose a variety of irregular grafting distributions on the solid surfaces. We have shown that different grafting distributions result in variations in brush thickness and free energy relative to the case of equidistant grafting, which is the most usual assumption when performing such calculations. Adding the grafting distributions to the degrees of freedom involved in the computational design of polymer-grafted nanoparticle systems takes us closer to experimental practice and to nanocomposites with tailor-made self-assembly properties. In this spirit, we have also determined the PMF between two spherical polystyrene-grafted silica nanoparticles in polystyrene matrix for various grafting distributions.

Finally, in order to have the ability to run 3D-SCFT calculations on multi-nanoparticle systems in presence or absence of polymer matrix, we have added in *RuSseL* the functionality of imposing *periodic boundary conditions* on the box edges, when the solution of the *Edwards* diffusion equation takes place. The user can now insert any number of grafted nanoparticles inside the periodic box, arranged in a crystalline or amorphous structure, and run SCFT calculations, as one would do in a particle-based simulation.

ΠΕΡΙΛΗΨΗ

Η Θεωρία Αυτο-Συνεπούς Πεδίου έχει εδραιωθεί πλέον ως ένα ευρέως διαδεδομένο υπολογιστικό εργαλείο για την ποσοτική πρόβλεψη της συμπεριφοράς ανομοιογενών πολυμερικών συστημάτων, όταν αυτά τελούν υπό θερμοδυναμική ισορροπία. Ως εκ τούτου εφαρμόζεται ολοένα και περισσότερο για την περιγραφή νανοσύνθετων υλικών, π.χ., συστήματα όπου ανόργανα σωματίδια διασπείρονται σε πολυμερικές μήτρες προκειμένου να βελτιωθούν οι ιδιότητες του υλικού.

Το μοντέλο που χρησιμοποιούμε διέπεται από τη μερική διαφορική εξίσωση *Edwards*, της οποίας η λύση είναι η δεσμευμένη πυκνότητα πιθανότητας να βρεθεί ένα συγκεκριμένο τμήμα πολυμερικής αλυσίδας σε ένα σημείο μέσα στο χωρίο επίλυσης. Για την επίλυση της εξίσωσης αυτής, καθώς και την όλη εφαρμογή του θεωρητικού μας μοντέλου, αναπτύχθηκε ένας πρωτότυπος κώδικας, ο οποίος φέρει την ονομασία *RuSseL*. Ο κώδικας αυτός επικαλείται τη μέθοδο των *πεπερασμένων διαφορών* για την επίλυση της εξίσωσης *Edwards* σε μία διάσταση, και αντίστοιχα την μέθοδο των *πεπερασμένων στοιχείων* για επίλυσή της σε τριδιάστατα χωρία αυθαίρετης γεωμετρίας.

Είναι αρκετά διαδεδομένη πρακτική η χημική πρόσδεση πολυμερικών αλυσίδων στην επιφάνεια ανόργανων νανοσωματιδίων, προκειμένου να επιτευχθεί ομοιόμορφη διασπορά τους εντός του πολυμερικού τήγματος. Το πρώτο σύστημα που μελετήθηκε στα πλαίσια της παρούσας διατριβής ήταν αυτό ενός νανοσωματιδίου πυριτίας εμβαπτισμένου σε μήτρα πολυστυρενίου και φέροντος στην επιφάνειά του χημικά προσδεδεμένες αλυσίδες πολυστυρενίου. Τόσο οι δομικές όσο και οι θερμοδυναμικές ιδιότητες του συστήματος μελετήθηκαν σε ένα ευρύ φάσμα τιμών ακτίνας σωματιδίου, πυκνότητας και μήκους προσδεδεμένων αλυσίδων.

Εν συνεχεία, έχοντας αναλύσει την συμπεριφορά ενός σωματιδίου εντός πολυμερικού τήγματος, προχωρήσαμε στη διερεύνηση των δομικών ιδιοτήτων των χημικά προσδεδεμένων αλυσίδων, όταν το σωματίδιο είναι εκτεθειμένο στο κενό. Το σύστημα αυτό μπορεί να θεωρηθεί

ισοδύναμο ενός συστήματος όπου οι προσδεδεμένες αλυσίδες βρίσκονται σε ισορροπία με έναν *κακό διαλύτη*. Αναπτύσσοντας έναν αυστηρό μαθηματικό φορμαλισμό, ο οποίος βασίστηκε στη θεωρία περί διαλύτωσης του *Ben-Naim*, υπολογίσαμε την *ελεύθερη ενέργεια διαλύτωσης* ενός νανοσωματιδίου πυριτίας, όταν αυτό μεταφέρεται από το κενό σε ένα πολυμερικό τήγμα. Διαπιστώσαμε ότι οι χημικά προσδεδεμένες αλυσίδες παίζουν σημαντικό ρόλο στον καθορισμό της *ελεύθερης ενέργειας διαλύτωσης*, τόσο λόγω ενθαλπικών όσο και λόγω εντροπικών παραγόντων.

Κατόπιν, η μεθοδολογία μας εφαρμόστηκε σε σύστημα δύο ημιάπειρων επίπεδων πλακών πυριτίας, ανάμεσα στις οποίες βρίσκεται είτε πολυμερικό τήγμα πολυστυρενίου είτε κενό. Οι δύο πλάκες φέρουν χημικά προσδεδεμένες αλυσίδες πολυστυρενίου, ενώ επιτρέπουμε στις πλάκες να φέρουν διαφορετικό αριθμό αλυσίδων ή/και αλυσίδες διαφορετικού μήκους. Μελετώντας εκτενώς τη θερμοδυναμική του συστήματος υπό ένα πλήθος σχεδιαστικών βαθμών ελευθερίας, προχωρήσαμε στην εξαγωγή ενός διαγράμματος φάσεων το οποίο υποδεικνύει τις περιοχές σταθερότητας του συστήματος (το σύστημα θεωρείται σταθερό όταν οι δύο πλάκες δεν μπορούν να πλησιάσουν η μία την άλλη περισσότερο από μία ελάχιστη απόσταση).

Όλοι οι προαναφερθέντες υπολογισμοί μπορούν πλέον να πραγματοποιηθούν με μεγαλύτερη λεπτομέρεια σε τρεις διαστάσεις, όπου αξιοποιείται η μέθοδος των *πεπερασμένων στοιχείων*. Πραγματοποιήσαμε μια ενδελεχή σύγκριση μεταξύ του μονοδιάστατου και του τριδιάστατου μοντέλου ως προς την ποσοτική πρόβλεψη των δομικών και θερμοδυναμικών ιδιοτήτων ενός σωματιδίου πυριτίας με χημικά προσδεδεμένες αλυσίδες πολυστυρενίου που βρίσκεται εντός πολυμερικής μήτρας πολυστυρενίου. Επιπροσθέτως, εκμεταλλευόμενοι τις δυνατότητες του τρισδιάστατου μοντέλου, ερευνήσαμε τον τρόπο με τον οποίο επηρεάζεται η ελεύθερη ενέργεια του συστήματος και η δομή των προσδεδεμένων αλυσίδων, όταν αυτές είναι μη ομοιόμορφα κατανεμημένες στην επιφάνεια του σωματιδίου. Εξ άλλου, αναπτύξαμε τη δυνατότητα επίλυσης της θεωρίας αυτο-συνεπούς πεδίου σε τρεις διαστάσεις μέσα σε χωρία χαρακτηριζόμενα από περιοδικές οριακές συνθήκες. Η δυνατότητα αυτή επιτρέπει τον υπολογισμό της δομής και της ελεύθερης ενέργειας συστημάτων πολλών νανοσωματιδίων διεσπαρμένων μέσα σε συνεχείς πολυμερικές φάσεις σε κρυσταλλικές ή άμορφες διατάξεις. Ανοίγει, έτσι, το δρόμο για τον προσδιορισμό της θερμοδυναμικά ευσταθέστερης διάταξης για δεδομένες μοριακές παραμέτρους σχεδιασμού (χημική σύσταση, μέγεθος και κλάσμα όγκου νανοσωματιδίων, πυκνότητα πρόσδεσης αλυσίδων στην επιφάνειά τους, χημική σύσταση και μοριακά βάρη προσδεδεμένων και ελεύθερων αλυσίδων).

Περίληψη

Τέλος, παρουσιάζουμε αποτελέσματα που αφορούν στο *δυναμικό μέσης δυνάμεως* που αναπτύσσεται μεταξύ δύο σφαιρικών νανοσωματιδίων πυριτίας, τα οποία φέρουν προσδεμένες αλυσίδες πολυστυρενίου και βρίσκονται σε μήτρα πολυστυρενίου. Το *δυναμικό μέσης δυνάμεως* ισούται με τη μεταβολή της ελεύθερης ενέργειας του συστήματος των δύο νανοσωματιδίων καθώς μεταβάλλεται η μεταξύ τους απόσταση. Το δυναμικό αυτό υπολογίστηκε για τρεις διαφορετικούς λόγους μηκών ελεύθερων/προσδεμένων αλυσίδων και για τρεις διαφορετικούς σχετικούς προσανατολισμούς των σωματιδίων, οι οποίοι αλλάζουν με την κατανομή με την οποία εμφυτεύονται οι αλυσίδες στις επιφάνειες τους.

LIST OF FIGURES

Figure 2.1 Comparison of numerical and analytical solutions of the <i>Edwards</i> diffusion equation against <i>Brownian</i> dynamics simulation.	10
Figure 2.2 Spatial configuration of the chain <i>propagator</i> , q , evaluated at contour $N = 10$ for different values of the field, w'	12
Figure 2.3 Spatial integral, Q , of chain <i>propagator</i> , q , for different values of the field, w'	12
Figure 2.4 Free energy density and field as functions of segment density.....	16
Figure 2.5 Effect of compressibility on density profiles and <i>adhesion tension</i>	18
Figure 2.6 Interaction energy $u_s(h)$ between a PS monomer unit and a planar SiO_2 substrate as calculated from the <i>Hamaker</i> potential at $T = 500$ K.	20
Figure 2.7 Density profiles of polyethylene in contact with solid interfaces of different affinity.....	22
Figure 2.8 A point (P) at distance $r = \mathbf{r}_P - \mathbf{r}_O $ from a sphere of radius R_s centered at O	24
Figure 2.9 Evaluations of u_{CSW} using eq 2.34 for $C_{\text{SW}} = -37.5 \cdot 10^6 \text{ J/m}^3$, $\sigma_{\text{SW}} = 1.28 \text{ nm}$, and $T = 500 \text{ K}$	26
Figure 2.10 Demonstration of tabulated solid/polymer potentials and resulting density profiles.	27
Figure 3.1 <i>RuSseL</i> input file: specifying polymer parameters. The.....	45
Figure 3.2 <i>RuSseL</i> input file: specifying solid parameters.	46
Figure 3.3 <i>RuSseL</i> input file: specifying file convergence parameters.....	47
Figure 3.4 Flow diagram of <i>RuSseL3D</i>	49
Figure 3.5 Density profiles of matrix and grafted chains in a polyethylene film.	50
Figure 3.6 Density profiles of matrix and grafted chains in various kinds of planar interfaces.	52
Figure 3.7 Density profiles of matrix and grafted chains in various kinds of spherical interfaces.....	53
Figure 3.8 Total and partial reduced segment density profile of a perfectly wetted SiO_2/PS GMV system.	53
Figure 3.9 End/middle density profiles of grafted and matrix chains in a perfectly wetted SiO_2/PS interface.....	55
Figure 3.10 Contour plots of the reduced density of segments belonging to (a) grafted and (b) matrix chains.....	57

List of Figures

Figure 3.11 Schematic representation of the <i>adsorbed</i> states of a chain.	59
Figure 3.12 Density profiles of chain segments belonging to different <i>adsorbed</i> states.	60
Figure 3.13 Chains/area profile in a perfectly wetted GMV SiO ₂ /PS system.	63
Figure 3.14. Contour discretization benchmarks: uniform vs nonuniform discretization.	65
Figure 3.15 <i>Hybrid</i> chain contour discretization scheme as implemented in the three-dimensional version of <i>RuSseL</i>	67
Figure 3.16 Schematic illustration of a grafted nanoparticle inside polymer melt.	69
Figure 3.17 Spatial discretization benchmarks: free energy terms as functions of element size.	74
Figure 3.18 Spatial discretization benchmarks: total free energy as a function of element size.	74
Figure 3.19 Contour discretization benchmarks: total free energy as a function of the contour step.	75
Figure 3.20 Field mixing/update benchmarks performed in the three dimensional version of <i>RuSseL</i>	76
Figure 3.21 Variation of free energy with increasing distance of the grafting point from the <i>Dirichlet</i> wall.	77
Figure 3.22 <i>RuSseL</i> parallelization benchmark with <i>OpenMP</i> and <i>MPI</i> protocol.	79
Figure 3.23 Demonstration of irregular grafting distributions on a spherical surface.	82
Figure 3.24 Illustration of periodic boundary conditions in two dimensions.	84
Figure 3.25 Periodic systems of multiple grafted nanoparticles embedded in polystyrene matrix.	85
Figure 3.26 A symmetric triangular mesh on the opposite faces of a cubic domain.	86
Figure 3.27 <i>Neumann</i> vs <i>periodic</i> boundary conditions.	88
Figure 3.28 Demonstration of different nanoparticle configurations.	89
Figure 3.29 3D density profile of matrix chains for different particle configurations.	90
Figure 3.30 3D density profile of grafted chains for different particle configurations.	90
Figure 3.31 Three-dimensional density profile of grafted chain segments in contact with vacuum or melt.	92
Figure 3.32 One-dimensional density profile of grafted chain segments in contact with vacuum or melt.	92
Figure 3.33 Free energy, in mJ/m ² , of a silica NP grafted with one polystyrene chain.	94
Figure 3.34 Three-dimensional density profiles of polystyrene chains grafted on the surfaces of silica particles arranged in a cubic lattice and exposed to vacuum.	96
Figure 4.1 Demonstration of the kinds of interfacial systems that are addressed in this chapter.	100
Figure 4.2 Density profiles for different particle radii and solid wetting degree.	101
Figure 4.3 <i>Adhesion tension</i> as function of the wetting degree and particle radius.	104
Figure 4.4 Macroscopic work functions with varying wetting degree and particle radius.	106
Figure 4.5 Comparison of SCFT with FOMC in deriving density profiles of grafted chains.	109
Figure 4.6 Density profiles as functions of molecular weight, grafting density and particle radius.	110
Figure 4.7 Total density profile as function of molecular weight, grafting density and particle radius. .	112

Figure 4.8 Adsorbed and free segment density profiles as functions of molecular weight, grafting density and particle radius.....	114
Figure 4.9 Chains per area profiles for various molecular weights, grafting densities and particle radii.	116
Figure 4.10 Chain-end density profiles for different molecular weights, grafting densities and particle radii.....	118
Figure 4.11 Daoud and Cotton scaling law for brush thickness.....	121
Figure 4.12 Brush thickness scaling law for different particle radii.....	122
Figure 4.13 Optimized n exponents of the power-law in eq 4.11 for set grafting density, σ_g , and NP radius, R_S	123
Figure 4.14 Optimized scaling exponents for the prediction of brush thickness scaling.....	124
Figure 4.15 Total free energy and individual terms as functions of molecular weight, grafting density and particle radius.	126
Figure 4.16 Conformational entropy of grafted chains for different molecular weight, grafting density and particle radius.....	129
Figure 4.17 Density profiles of grafted chains in contact with melt and vacuum.	135
Figure 4.18 Density profiles of chains exposed to vacuum and grafted on spherical particles.	137
Figure 4.19 Maximum density of grafted chains exposed to vacuum for various wetting degrees.....	139
Figure 4.20 Solvation free energy in a planar SiO ₂ /PS system.....	141
Figure 4.21 Solvation free energy of spherical SiO ₂ nanoparticles of various radii.	143
Figure 4.22 Solvation free energy terms as functions of the amount of grafted material.	146
Figure 4.23 Solvation free energy of a SiO ₂ particle for different matrix/grafted length ratios.	149
Figure 4.24 Schematic illustration of regimes I-IV, in terms of the amount of grafted material $\sigma_{g,seg}$ and chain crowding.	150
Figure 5.1 Meshing illustration of a NP with $R_S = 4$ nm inside a box with dimensions $45 \times 45 \times 45$ nm ³	162
Figure 5.2 Density profiles of grafted chains obtained with 1D- and 3D- SCFT calculations.....	165
Figure 5.3 Total segment density profiles obtained with 1D- and 3D- SCFT calculations.....	166
Figure 5.4 Contour plot of the density and self-consistent field near a spherical nanoparticle.	167
Figure 5.5 Comparison of 1D- (transparent markers) and 3D-SCFT (solid markers) calculations in predicting the brush thickness.	168
Figure 5.6 Comparison of 1D- (dotted lines) and 3D-SCFT (solid lines) calculations in predicting the total free energy.	169
Figure 5.7 3D density profiles of chains equidistantly grafted on spherical NPs of various radii.....	171
Figure 5.8 3D density profiles of chains irregularly grafted on spherical NPs of various radii.	173

List of Figures

Figure 5.9 Assessment of <i>smearing approximation</i> when chains are irregularly grafted on a spherical NP.	175
Figure 5.10 3D density profiles of individual chains grafted on a spherical NP.	176
Figure 5.11 Brush thickness and free energy evaluation for various grafting distributions.	177
Figure 5.12 Free energy components in a system of polystyrene chains grafted according to various distributions on the surface of a silica NP embedded in polystyrene melt.	179
Figure 6.1 Demonstration of two opposing grafted surfaces.	184
Figure 6.2 Free energy of interfaces with different wetting degree.	185
Figure 6.3 Wetting functions of silica/PS interfaces.	186
Figure 6.4 Reduced density profiles of polystyrene brushes exposed to polymer melt or vacuum.	187
Figure 6.5 Thickness of polymer brushes exposed to polymer melt or vacuum.	189
Figure 6.6 Thickness of brushes grafted on surfaces of different wetting degree.	191
Figure 6.7 Free energy of polymer brushes exposed to polymer melt or vacuum.	192
Figure 6.8 <i>Potential of mean force</i> , in mJ/m^2 , for the system of approaching bare silica surfaces in a melt (SMS).	195
Figure 6.9 <i>Potential of mean force</i> , in mJ/m^2 , for the system of approaching bare silica surfaces (SMS) starting with zero field.	196
Figure 6.10 <i>Potential of mean force</i> in a symmetric system of approaching grafted silica surfaces in contact with melt.	201
Figure 6.11 Reduced density distributions corresponding to the PMF^{GMG} panels in Figure 6.10.	201
Figure 6.12 Free energy partial contributions to the <i>potential of mean force</i> , in mJ/m^2 , of two approaching symmetrically grafted surfaces in contact with melt.	202
Figure 6.13 <i>Potential of mean force</i> between two approaching asymmetrically grafted silica surfaces in contact with melt.	203
Figure 6.14 <i>Potential of mean force</i> between two approaching asymmetrically grafted silica surfaces in contact with melt (case 2).	204
Figure 6.15 <i>Potential of mean force</i> between two approaching asymmetrically grafted silica surfaces in contact with melt (case 3).	205
Figure 6.16 <i>Potential of mean force</i> between two approaching asymmetrically grafted silica surfaces in contact with melt (case 4).	207
Figure 6.17 <i>Potential of mean force</i> between two approaching grafted silica surfaces in melt for different wetting degrees.	208
Figure 6.18 <i>Potential of mean force</i> between two opposing grafted surfaces exposed to vacuum (GVG).	209
Figure 6.19 Reduced segment density distributions corresponding to the PMF^{GVG} panels in Figure 6.18.	210

Figure 6.20 Free energy partial contributions to the <i>potential of mean force</i> of two approaching grafted surfaces exposed to vacuum.	211
Figure 6.21 Well-depth of PMF^{GMG} as a function of all design degrees of freedom of the interfacial systems of two plates.	215
Figure 6.22 Meshing illustration of two NPs with $R_S = 2$ nm inside a box with dimensions $30 \times 22 \times 22$ nm ³	217
Figure 6.23 VMD representation of distributions of grafting points for PMF calculation between two spherical particles.	219
Figure 6.24 Three-dimensional density profiles of polystyrene chains grafted on the surfaces of two silica NPs.	220
Figure 6.25 <i>Potential of mean force</i> between two silica NPs equidistantly grafted with polystyrene chains.	222
Figure 6.26 <i>Potential of mean force</i> between two silica NPs non-equidistantly grafted with polystyrene chains.	222
Figure 6.27 <i>Hamaker</i> interaction between two bare silica NPs with radius $R_S = 2$ nm.	223
Figure 6.28 <i>Potential of mean force</i> between two grafted silica NPs embedded in polystyrene matrix.	225

LIST OF TABLES

Table 2-1. Bulk densities and compressibilities from the SL EoS, and optimized compressibilities for the HFD, HFD/SGT EoS.....	18
Table 2-2 Wetting degree of planar solid surfaces for length of matrix chains equal to $N_m = 768$ at $T = 500$ K.	31
Table 3-1 Reduced densities, <i>partition functions</i> , and constraints for evaluating each state and sub-state regarding <i>adsorbed</i> and <i>free</i> chain segments.....	61
Table 3-2. Scaling of <i>Edwards</i> solution time in a spatial mesh of 88529 nodes.	80
Table 3-3 Scaling of <i>Edwards</i> solution time in a spatial mesh of 249084 nodes.	80
Table 3-4 Free energy per nanoparticle surface in the bcc and cubic nanoparticle configuration.....	91
Table 3-5 Free energy in mJ/m^2 of a silica NP grafted with one polystyrene chain.	93
Table 3-6 Free energy in $\text{mJ}/\text{segment}$ of a silica NP grafted with one polystyrene chain and exposed to vacuum.	95
Table 3-7 Free energy in $\text{mJ}/\text{segment}$ of a silica NP grafted with one polystyrene chain and embedded in polystyrene matrix.	95
Table 4-1 Explanation of symbols for the different interfacial systems and free energy contributions examined in this chapter.	98
Table 4-2 Parameters of 1D-SCFT calculations.	99
Table 4-3 Fitting coefficient for eq 4.27.	140
Table 5-1 Parameters of 3D-SCFT calculations.	164
Table 6-1 Interfacial energies and wetting functions for $N_m = 384$ in units of mJ/m^2	187
Table 6-2. Parameters for distributing grafting points on the surface of two spherical NPs.	218
Table 6-3 <i>Potential of mean force</i> between silica NPs embedded in polystyrene matrix of length $N_m = 24$ skeletal bonds.	223
Table 6-4 <i>Potential of mean force</i> between silica NPs embedded in polystyrene matrix of length $N_m = 96$ skeletal bonds.	224

Table 6-5 *Potential of mean force* between silica NPs embedded in polystyrene matrix of length $N_m =$
384 skeletal bonds.224

NOMENCLATURE

Symbols

Latin symbols

A_{bulk}	Free energy of a system of isolated end-pinned and unperturbed chains in bulk polymer melt
b_k	Kuhn length, [nm]
C_∞	Chain stiffness/characteristic ratio
d	Standard deviation of Gaussian pulse, [nm]
D	Great-circle distance (arc length) between two points on a spherical surface, [nm]
$f(\rho)$	Excess Helmholtz energy density, [mJ/m ³]
f_{mix}	Field relaxation parameter/mixing fraction
h	Segment-surface distance, [nm]
h_{ads}	Distance from solid surface where segments are considered to be adsorbed, [nm]
h_{g,i_g}	Distance of grafting point i_g from the Dirichlet wall, [nm]
$\langle h_g^2 \rangle^{1/2}$	Root mean square thickness of the polymer brush, [nm]
h_{HS}	Thickness of hard-sphere wall, [nm]
h_{M}	Thickness of fine-mesh region, [nm]
$h_{\text{ref},q=0}$	Reference grafting point distance from the Dirichlet wall, [nm]
i	The imaginary unit
i_g	Grafted chain index
k_{B}	Boltzmann constant, [J/K]
$l_{\text{C-C}}$	carbon-carbon bond length, [nm]

Nomenclature

M_{monomer}	Molar mass per skeletal carbon, [g/mol]
N	Variable spanning the contour of a polymer chain, [skeletal bonds]
N_A	Avogadro's number, [mol ⁻¹]
n_g	Number of chains grafted on solid surfaces, [chains]
n_{ch}	Number of chains per area at a certain distance from a solid surface, [chains/nm ²]
$n_{\text{ch}}^{\text{ref}}$	Number of chains per area concerning reference chains, which obey the <i>Gaussian</i> chain model and have infinite length, [chains/nm ²]
n_m	Mean number of matrix chains in a certain region
N_g	Number of skeletal carbon-carbon bonds constituting a grafted chain
N_m	Number of skeletal carbon-carbon bonds constituting a matrix chain
N_{SW}	Switching contour point for hybrid chain discretization
\mathbf{p}	Grafting point coordinates on the surface of a nanoparticle
$P(\mathbf{p})$	Insertion probability of candidate grafting point
$q_g(\mathbf{r}, N)$	Restricted partition function of a grafted chain
q_{g, i_g}	Propagator of grafted chain with index i_g
$q_m(\mathbf{r}, N)$	Restricted partition function of a matrix chain
Q_g	Partition function of grafted chains, [nm ⁻³]
Q_m	Partition function of matrix chains, [nm ⁻³]
r	Distance between segment and center of nanoparticle, [nm]
\mathbf{r}	Position coordinates in the three-dimensional space
\mathbf{r}_{gi}	Grafting point coordinates
$R_{G,g}$	Unperturbed radius of gyration of grafted chains, [nm]
$R_{G,m}$	Unperturbed radius of gyration of matrix chains, [nm]
R_S	Spherical nanoparticle radius, [nm]
$\partial\mathcal{R}_{\text{edge}}$	Periodic boundaries of the three dimensional domain
$\partial\mathcal{R}_S$	Dirichlet boundaries representing solid or gas surfaces
S_S	Nanoparticle surface area, [nm ²]
T	Temperature, [K]

u_G	Harmonic potential for bonded interactions along a Gaussian chain, [J] or $[k_B T]$
$u_{\text{Hamaker,A}}$	Attractive term of Hamaker potential, [J] or $[k_B T]$
$u_{\text{Hamaker,R}}$	Repulsive term of Hamaker potential, [J] or $[k_B T]$
u_{HS}	Hard-sphere potential, [J] or $[k_B T]$
$u_S(\mathbf{r})$	Potential energy per segment exerted by the solid surfaces, [J] or $[k_B T]$
V	Volume of the simulation domain, $[\text{nm}^3]$
$V_{\text{max,coarse}}$	Max element volume in the coarse-mesh region, $[\text{\AA}^3]$
$V_{\text{max,fine}}$	Max element volume in the fine-mesh region, $[\text{\AA}^3]$
$V_{\text{min,coarse}}$	Min element volume in the coarse-mesh region, $[\text{\AA}^3]$
$V_{\text{min,fine}}$	Min element volume in the fine-mesh region, $[\text{\AA}^3]$
W_A	Work of adhesion, [J] or $[k_B T]$
W_C	Work of cohesion, [J] or $[k_B T]$
W_I	Work of immersion, [J] or $[k_B T]$
W_S	Work of spreading, [J] or $[k_B T]$
$w(\mathbf{r})$	Chemical potential field per segment, [J] or $[k_B T]$
$w'(\mathbf{r})$	Self-consistent field per segment, equal to $iw(\mathbf{r})+u_S(\mathbf{r})$, [J] or $[k_B T]$
$w'_{\text{bulk}}(\mathbf{r})$	Value of the field in the bulk polymer region, [J] or $[k_B T]$
$w'_{\text{ifc}}(\mathbf{r})$	$w'(\mathbf{r}) - w'_{\text{bulk}}(\mathbf{r})$, [J] or $[k_B T]$

Greek Symbols

A_{PS}	Polystyrene Hamaker constant, [J] or $[k_B T]$
A_{SiO_2}	Silica Hamaker constant, [J] or $[k_B T]$
γ	Chain geometric factor $\sin(\theta/2)$ with θ being the angle between two successive skeletal bonds
γ_a^{sys}	System free energy with respect to a reference system, [mJ], where <i>sys</i> is a variable denoting the kind of the system, e.g., SM, SG, SGV (see Abbreviations); <i>a</i> denotes the kind of energy term, e.g., coh, field, m, g, s.
δr	Bin thickness for partitioning of the 3D domain, [nm]
$\Delta\gamma^{\text{tol}}$	Free energy tolerance, $[\text{mJ}/\text{m}^2]$

Nomenclature

ΔE_a^{sys}	System free energy with respect to a reference system, [mJ], where <i>sys</i> is a variable denoting the kind of the system, e.g., SM, SG, SGV (see Abbreviations); <i>a</i> denotes the kind of energy term, e.g., coh, field, m, g, s; <i>E</i> denotes the thermodynamic potential, e.g., Ω , <i>A</i> , <i>G</i> , <i>U</i> , <i>H</i> .
ΔN	Chain contour step, [skeletal bonds]
$\varepsilon_g^{\text{tol}}$	Relative grafting density tolerance
E_a^{sys}	System free energy, [mJ], where <i>sys</i> is a variable denoting the kind of the system, e.g., SM, SG, SGV (see Abbreviations); <i>a</i> denotes the kind of energy term, e.g., coh, field, m, g, s; <i>E</i> denotes the thermodynamic potential, e.g., Ω , <i>A</i> , <i>G</i> , <i>U</i> , <i>H</i> .
θ	Azimuthal angle, [rad]
κ_T	Isothermal compressibility of the polymer melt at temperature <i>T</i> , [Pa ⁻¹]
$\rho_g(\mathbf{r})$	Segment density profile of grafted chain segments, [segments/m ³]
$\rho_m(\mathbf{r})$	Segment density profile of matrix chain segments, [segments/m ³]
$\rho_{\text{mass,bulk}}$	Mass density of the bulk polymer melt, [kg/m ³]
$\rho_{\text{seg,bulk}}$	Molar segment density in the bulk polymer melt, [segments/m ³]
σ_g	Grafting density, [chains nm ⁻²]
$\sigma_{g,\text{seg}}$	Segmental grafting density, [skeletal carbons nm ⁻²]
$\sigma^{\alpha\beta}$	Interfacial free energy per interface area in a heterogeneous system involving phases α , β , [mJ/m ²]
σ_{PS}	Polystyrene monomer effective diameter, [nm]
σ_{SiO_2}	Silica effective diameter, [nm]
φ	Inclination angle, [rad]
$\varphi(\mathbf{r})$	Total reduced segment density profile of polymer segments
$\varphi_g(\mathbf{r})$	Reduced segment density profile of grafted chain segments
$\varphi_{g,\text{end}}(\mathbf{r})$	Reduced segment density profile of end segments of grafted chains
$\varphi_{g,\text{middle}}(\mathbf{r})$	Reduced segment density profile of middle segments of grafted chains
$\varphi_{g,\text{start}}(\mathbf{r})$	Reduced segment density profile of first segments of grafted chains
$\varphi_m(\mathbf{r})$	Reduced segment density profile of matrix chain segments
$\varphi_m^{\text{ads}}(\mathbf{r})$	Reduced segment density profile of adsorbed matrix chain segments
$\varphi_{m,\text{end}}(\mathbf{r})$	Reduced segment density profile of end segments of matrix chains

$\varphi_m^{\text{free}}(\mathbf{r})$	Reduced segment density profile of free matrix chain segments
$\varphi_{m,\text{middle}}(\mathbf{r})$	Reduced segment density profile of middle segments of matrix chains
$\varphi_{m,\text{start}}(\mathbf{r})$	Reduced segment density profile of first segments of matrix chains

Abbreviations

BC	Boundary Conditions
BD	Brownian Dynamics
EoS	Equation of State
FD	Finite Differences
FEM	Finite Element Method
GMG	Grafted-Matrix-Grafted interfaces
GMV	Grafted-Matrix-Vacuum interfaces
GVG	Grafted-Vacuum-Grafted interfaces
HFD	Helfand
HS	Hard-sphere wall/potential
HW	High-wetting solid/polymer interface
IC	Initial Conditions
LJ	Lennard Jones
LW	Low-wetting solid/polymer interface
MC	Monte Carlo
MD	Molecular Dynamics
MV	Matrix-Vacuum interface
NP	Nanoparticle
NW	Non-wetting solid/polymer interface
PBC	Periodic Boundary Conditions
PDE	Partial Differential Equation
PGNs	Polymer-grafted nanoparticles
PNCs	Polymer nanocomposites
PW	Perfect-wetting solid/polymer interface
SCFT	Self-Consistent Field Theory
SGT	Square Gradient Theory

Nomenclature

SL	Sanchez-Lacombe
SGM	Solid-Grafted-Matrix interfaces
SGV	Solid-Grafted-Vacuum interfaces
SM	Solid-Matrix interface
SV	Solid-Vapor interface
VM	Vacuum-Matrix interface

1. INTRODUCTION

The subject of the present thesis is the application of *Self-Consistent Field Theory* (SCFT) in gas/polymer and solid/polymer interfaces.¹⁻⁵ SCFT is a strong theoretical tool for describing the thermodynamics of heterogeneous and complex polymer systems. It is quite accurate when addressing high density and large molecular weight systems (e.g., polymer melts). Another important advantage when applying a SCFT formulation is that the excess free energy of the system investigated (relative to an ideal gas of noninteracting chains) is directly derived.

Although particle-based methodologies⁶ built on the foundations of *classical statistical mechanics* (as opposed to *quantum statistical mechanics*), e.g., *Molecular Dynamics* (MD) and *Metropolis Monte-Carlo* (MC), have enjoyed remarkable growth during the last decades, supported by the fast development of computer hardware, their application is rather impractical when it comes to large length and time scales, even on the most sophisticated supercomputers.⁷

Addressing this issue, SCFT aims to reduce significantly the computational cost of calculating properties of large polymeric systems, by introducing a saddle point approximation in calculating the *partition function* of the system. Specifically, field-theory is based on replacing the integration of degrees of freedom related to the generalized coordinates of atoms or chain segments by functional integrations over a fluctuating density field, $\rho(\mathbf{r})$, and a spatially varying *chemical potential* field, $w(\mathbf{r})$, which is thermodynamically conjugate to the density field. Their introduction serves to decouple the interactions among polymer chain segments and replace them with the interaction of each chain segment with the field emanating from the rest of the chain segments⁸ and any solid surfaces present (Appendix **B**). The way that the distribution of chain conformations is affected by the field is described by a partial differential equation known as the *Edwards diffusion equation*. By virtue of a *saddle-point approximation* (Appendix **C**), the functional integral expressing the partition function is replaced by its dominant term and the fluctuating density and chemical potential fields are replaced by average position-dependent values depending on the conformational distribution of chains. Thus, one obtains a system of

partial differential, integral, and algebraic equations with respect to the conformational distribution, which have to be solved self-consistently: conformations shape the local densities of all types of segments present and the chemical potential field, while the field dictates the conformational distribution. Solution of this system of equations gives all structural and thermodynamic properties of the inhomogeneous polymer system at equilibrium.

1.1. Polymer brushes and grafted nanoparticles

Polymer brushes are important in a wide variety of applications such as nanotechnology, membranes and biomedicine.⁹⁻¹² They are also used for steric stabilization of nanoparticles (NP's) inside a polymer matrix, leading to mechanical reinforcement and an improvement of its physicochemical properties.¹³⁻¹⁶

The dispersion state of NP's inside the polymer matrix depends on solid/solid, solid/polymer interactions as well as on entropic effects. In most cases, the embedded NP's are attracted to each other via *Van der Waals* forces and agglomerate.¹⁷ A widely used methodology to overcome this spontaneous behavior is to chemically graft polymer chains on the NP surface, which may or may not be identical to those of the matrix. In such systems, the key factors influencing NP dispersion are the size and shape of the NPs, the grafted to matrix molecular weight ratio and the grafting density.¹⁸⁻²⁰ D. Trombly et al.²¹ studied the effect of solid curvature on polymer-mediated interactions among grafted NP's and demonstrated that the dependency of NP separation on the grafting density becomes weaker with increasing particle curvature.

When the matrix chains are of the same chemistry with the grafted chains, they can serve as a *good solvent* for the brush, leading to a well-dispersed set of NPs. It is more probable for the matrix chains to wet the brush, when their length is less than that one of grafted chains.^{18,22,23} The penetration of matrix chains of molecular weight greater than or equal to that of the grafted chains is accompanied by a large conformational entropy cost, thus it is thermodynamically unfavored. This phenomenon is reported in the literature as *autophobic dewetting*.^{20,23} One way to reduce the possibility for *autophobic dewetting* is to disperse smaller NPs; when grafted chains are attached to smaller particles, they enjoy more available space, therefore the penetration of matrix chains is facilitated and the associated conformational entropy cost is mitigated.^{20,21,24}

As already mentioned, another important parameter for particle dispersion is the solid surface grafting density. When the grafting density is lower than the a threshold value, the

1.1. Polymer brushes and grafted nanoparticles

particle cores are no longer screened from the grafted chains surrounding them, so they attract each other, leading to aggregation. This is known as *allophobic dewetting*. Sunday et al.²² derived experimentally a phase diagram demonstrating the regions where *autophobic* or *allophobic dewetting* and *complete wetting* occurs. Nonetheless, there is both computational^{25–28} and experimental^{18,22,29–31} evidence that there is also a higher limit of grafting density to achieve proper dispersion; higher values of grafting density prevent matrix chains from penetrating the brushes and *autophobic dewetting* is again exhibited.

SCFT has been widely used in systems of block copolymers and polymer blends.^{32–35} In the field of polymer brushes, atomistic MD simulations have been performed by Ngoro et al.,³⁶ while Meng et al.³⁷ and Kalb et al.³⁸ have performed coarse-grained MD simulations representing the polymer chains using the *Kremer-Grest* bead-spring model. Using the same model, Ethier and Hall³⁹ studied the structure and entanglements of grafted chains on isolated polymer grafted NPs.

In the context of SCFT, the incorporation of grafted chains in a solid/polymer melt interfacial system demands the solution of an additional *Edwards* diffusion equation with challenging initial conditions.⁴⁰ Remarkable efforts have been made to bypass the numerical difficulties associated with the delta function constraining the end of the grafted chains to the surface of the solid substrate. Implementing a *spectral* formulation, Chantawansri et al.⁴¹ described a method to distribute the grafting points normal to the substrate, in such a manner that a *Dirac*-delta function is approximated for both compressible and incompressible models.

Major experimental work has been conducted to understand the behavior of polymer grafted NPs and their influence on the structural, dynamical, and mechanical properties of the composite material.^{15,16,22,42–45} Experimentalists are also interested in studying the interactions between grafted NPs in the absence of a host polymer matrix.^{43,46} Furthermore, polymer grafted nanoparticles (PGNs) are quite promising for the manufacturing of membrane materials.^{47–50}

Modeling the dynamical properties of NPs and polymer chains grafted on their surface is also an area of great academic interest.^{51–56} Miller and Hore⁵⁷ performed DPD simulations to model the dynamics of the grafted corona under melt and solution conditions. They found that, with increasing confinement, the relaxation times of the grafted chains also increased. The segmental and chain dynamics in a system of high loading of grafted nanoparticles was studied with *molecular dynamics* by Lin et al.,⁵⁸ where they demonstrated that the polymer dynamics highly depends on the number of contacts between a chain segment and the surrounding NPs. A

recent review regarding the dynamics of polymer chains and NPs in nanocomposite systems has been compiled by Bailey and Winey.⁵⁹

1.2. Motivation

This project was an idea of Prof. Theodorou after many efforts together with Dr. Vogiatzis to determine the *potential of mean force* between nanoparticles using particle-based methods. They were able to describe well the structural properties of polymer brushes grafted on nanoparticles and melt chains at interfaces,²³ but it was computationally too expensive to determine changes in the free energy of multi-nanoparticle systems brought about by varying nanoparticle configurations. It soon became clear that a continuum approach would be necessary to perform such calculations in reasonable time. A long time ago, Prof. Theodorou had developed lattice-based theoretical frameworks inspired by the work of *Dill and Flory*, *Helfand*, and *Scheutzens and Fler*.⁶⁰⁻⁶⁵ Given that *Self-Consistent Field Theory* was growing fast as a tool to derive the free energy of interfaces created in polymer blends and copolymer melts,⁵ he decided to try the same methodology as a tool to describe gas/polymer and solid/polymer interfaces. At first, lattice-based models were employed and indeed SCFT proved quite accurate in predicting the *surface tension* of polymer films and the *adhesion tension* of solid/polymer interfaces, when combined with an appropriate equation of state. The next step was to formulate and develop, with Kostas Daoulas,⁶⁶ a continuum model which addressed melt/solid interfaces in one dimension, and again SCFT proved itself as a fast and accurate method, especially in relation to atomistic *molecular dynamics* simulations.² The need to address more complex systems led Prof. Theodorou to the development of a three-dimensional SCF framework based on the *Finite Elements Method* (FEM) for the solution of the *Edwards* diffusion equation. Using an open-source FEM code called *FEAP*, calculations were extremely slow. This was quite disappointing, especially if one intended to take into consideration systems where grafted chains are also present, but the advantage of SCFT to directly derive the free energy of any interfacial system was too good to quit efforts. A project was then started by Dr. Apostolos Lakkas and Prof. Theodorou, and later by myself together with Dr. Aristotelis Sgouros, to develop our own code based on FEM which we fully controlled and optimized.⁶⁷ We are now at a point where the full convergence of a large SCFT calculation needs a few days (using 3 cores per calculation), including the solution of the *Edwards* diffusion equation in the presence of grafted chains. Just

for the history, when Prof. Theodorou tried to run calculations with *FEAP*, full convergence required a few months, without grafted chains being present in the system.

1.3. Aim of the thesis

The main goal of this PhD was to develop a generic theoretical model based on *Self-Consistent Field theory* (SCFT) to describe in detail the structural and thermodynamic properties of solid/polymer interfaces. In particular, we were interested in systems where the solid interfaces are chemically grafted with polymer chains. In addition, we wished to build upon the knowledge and frameworks which invoke Fourier-spaced methodologies and develop a *real-space* based numerical implementation, based on the *Finite Element Method*, to calculate the equilibrium structure and interactions of interfacial systems involving polymer melts, solid surfaces, and grafted chains at a mesoscopic level, still maintaining a high level of predictive power. Mathematically and numerically speaking, the challenge was to model realistic (nano)composite systems involving large length scales (≤ 100 nm) within reasonable computation time. This effort became more difficult considering our need to incorporate grafted chains in our model, which are mathematically inserted in the formalism by means of *Dirac*-delta functions. The commercial software that we have initially used to solve the *Edwards* diffusion equation (the main partial differential equation (PDE) involved in our calculations) was not able to yield an accurate and stable solution when the initial conditions were assigned at specific points of the FEM mesh. Hence, another goal of this project was to build from scratch our own code to handle a finite element mesh, assemble the matrices corresponding to the *weak* formulation of our PDE, and link to an external solver for the solution of the resulting linear system of equations. Finally, the ultimate goal was to make our code as user-friendly, fast and stable as possible, so that anyone can use it for their own purposes and predict the properties of nanocomposite systems involving solid/polymer and gas/polymer interfaces.

1.4. Outline of the thesis

In Chapter 2 we develop the theoretical and numerical background that one will have to be familiar with in order to follow the rest of the thesis. In Chapter 3 we present the code that has been developed in the context of this PhD thesis to perform calculations based on *Self-Consistent Field Theory* in heterogeneous polymer systems, namely, gas/polymer and solid/polymer interfaces. In Chapter 4 we present results regarding the system of a single polystyrene-grafted silica nanoparticle embedded in polystyrene matrix. We elaborate on the structural properties and the size of the brush and on the thermodynamics of the system. Furthermore, we examine the system of the same grafted nanoparticle exposed to vacuum and derive its *solvation* free energy under various conditions. In Chapter 5 we present results obtained via the three-dimensional code on the same single grafted nanoparticle system embedded in a molten polymer matrix. We perform a thorough comparison between 1D and 3D solutions for the structural and thermodynamic properties of the system and evaluate the smearing approximation under various conditions. Moreover, we present three-dimensional profiles of grafted chains and reveal their configurations for different chain molecular weights, grafting densities, and particle radii. We also calculate the variation of the free energy of the system when the grafted chains are non-equidistantly grafted on the surface of the particle and illustrate the corresponding grafted chain configurations. In Chapter 6 we determine the *potential of mean force* between two polystyrene-grafted solid surfaces immersed in a polystyrene melt. The surfaces may be of planar or spherical geometry. In the latter, calculations were conducted in 3D, allowing us to quantify the effect of the *distribution* of grafting points on the surfaces of the nanoparticles on the resulting *potential of mean force*. Finally, in Chapter 7, we conclude the Ph.D. thesis by summarizing the key scientific and methodological advances developed in its context.

2. THEORETICAL AND NUMERICAL BACKGROUND

2.1. Polymer physics

2.1.1. Gaussian chain model – Bonded interactions

The *Gaussian*-thread model is an ideal chain model quite often used for describing the bonded interactions along a polymer chain.^{1,3,66} This model treats polymer chains as continuous, linearly elastic threads and associates each differential contour segment along the chain with a harmonic potential. Integrating over the total contour of the chain, as shown in eq 2.1, one can calculate the free energy functional governing chain configurations.

$$u_G[\mathbf{r}(N)] = \frac{N_c k_B T}{4R_{G,c}^2} \int_0^{N_c} dN \left| \frac{d\mathbf{r}(N)}{dN} \right|^2 \quad 2.1$$

The square brackets denote that u_G is a functional of the space curve $\mathbf{r}(N)$ defining the configuration of the chain with N being the variable spanning the contour of the chain and N_c being the total length of the chain, which is of kind c ($c = m$ for matrix chains and $c = g$ for grafted chains). There is some latitude in defining a segment. *Kuhn* segments may be used, in which case: $N_c / R_{G,c}^2 = 6 / b_k^2$, but chemical segments can also be used. Equation 2.1 is commonly referred to as the *Edwards Hamiltonian*. Essentially, we think of the polymer chain as a random walk of a specific number of steps, which depends on the chemical structure of the chain. The step size of this random walk is known as the *Kuhn* segment length and it is usually denoted with b_k .

2.1.2. Edwards diffusion equation

In the context of the *Gaussian* chain model, the random walk of the polymer chain segments is mathematically modeled via the *Edwards* diffusion equation 2.2. Solving this transient PDE involving the field, w' , is the first and most essential step of an SCFT calculation. For a detailed derivation of the *Edwards* equation, the reader is referred to ref 3.

$$\begin{aligned} \frac{\partial q_c(\mathbf{r}, N)}{\partial N} - \frac{R_{G,c}^2}{N_c} \nabla^2 q_c(\mathbf{r}, N) + \beta w'(\mathbf{r}) q_c(\mathbf{r}, N) &= 0 \\ \frac{\partial q_c(\mathbf{r}, N)}{\partial N} - D \nabla^2 q_c(\mathbf{r}, N) + a q_c(\mathbf{r}, N) &= 0 \end{aligned} \quad 2.2$$

where, $D = \frac{R_{G,c}^2}{N_c}$ and $a = \beta w'(\mathbf{r})$.

with N being the variable spanning the contour of the chain and \mathbf{r} denoting position in three-dimensional space. The index c is replaced by the symbol m for matrix chains and by g for grafted chains. N_c is the length of a kind c chain measured in skeletal carbon-carbon bonds and $R_{G,c}$ its radius of gyration. From the point of view of a chemical engineer, the *Edwards* equation is a diffusion and reaction equation, the contour length N playing the role of time and D being the diffusivity. The term $a q_c$ is a sink term as would result from the presence of a first-order irreversible chemical reaction in the domain. Equation 2.2 must be solved for all different kinds of chains appearing in the system, e.g., matrix or grafted on solid surfaces.

The solution, q_c , of this PDE is called the *restricted partition function* or *chain propagator*. It is proportional to the probability that the chain segment which lies at contour length N finds itself at position \mathbf{r} , no matter where the chain may have started. Furthermore, it is normalized by the corresponding probability of a chain which performs its random walk in absence of any field.

The distinction between matrix and grafted chains reveals itself through the corresponding initial conditions, which are given by eq 2.3 and 2.4, respectively. This means that matrix chains of zero length have no chance to feel the field w' ; therefore their *propagator* equals that one of a field-free chain, which as mentioned before, is the normalization reference for the *propagator*. On the other hand, the starting end of a grafted chain must be bound at a specific point of the domain, and the way to describe this in terms of probabilities is to impose non-zero probability only at the grafting points and zero everywhere else, i.e., a delta-function initial condition which spikes at the grafting points, as eq 2.4 suggests.⁴⁰

$$q_m(\mathbf{r}, 0) = 1 \quad \forall \mathbf{r} \in \{\mathcal{R} - \partial\mathcal{R}_s\} \quad 2.3$$

$$q_g(\mathbf{r}, 0) = \frac{N_g}{\rho_{\text{seg,bulk}}} \sum_{i=1}^{n_g} \frac{\delta(\mathbf{r} - \mathbf{r}_{gi})}{q_m(\mathbf{r}_{gi}, N_g)} \quad 2.4$$

On the solid surfaces, $\partial\mathcal{R}_s$, *Dirichlet* boundary conditions are imposed with zero *propagator* value. On the edges of the simulation box, one can either assign *Neumann* boundary conditions with zero *propagator* flux, or *periodic* boundary conditions; for details regarding the implementation of periodic BCs in 1D and 3D, the reader is referred to Sections 2.3.3 and 3.9, respectively. We mathematically describe the BCs in eq 2.5 below.

$$\text{BCs: } \begin{cases} q_c(\mathbf{r}, N) = 0, \forall \mathbf{r} \in \partial\mathcal{R}_s \\ \nabla q_c(\mathbf{r}, N) = 0 \text{ or } q_c: \text{periodic}, \forall \mathbf{r} \in \partial\mathcal{R}_{\text{edge}} \end{cases} \quad 2.5$$

2.1.3. Physical interpretation of the field, w'

When the field is equal to zero everywhere inside the domain, then eq 2.2 is a simple diffusion equation governing the propagation of polymer segments in space. This is mathematically equivalent to a particle performing a random *Brownian* walk. On the other hand, when the field assumes values different from zero at a point of the domain \mathbf{r} , it can be envisioned as a *drain term* that “absorbs” or a *source term* that “generates” polymer segments. When the field is positive at a certain position \mathbf{r} , it repels the polymer segments and therefore the probability of finding a segment in that position decreases with respect to the random walk case. Conversely, when the field is negative, it attracts the polymer segments, thus the probability of finding segments at \mathbf{r} increases with respect to the random walk case.

To better demonstrate the effect of the field on the solution of eq 2.2, we have first compared the numerical solution of eq 2.2, in the absence of the field w' , with a particle based *Brownian dynamics* simulation and the analytical solution given by the following eq 2.6. Equation 2.6 describes the evolution of the concentration profile during diffusion of mass initially placed at uniform concentration M within a rectangular parallelepiped extending over the region $x_L < x < x_R$, $y_L < y < y_R$, $z_L < z < z_R$. If one of the dimensions of the parallelepiped is very small relative to $\sqrt{4Dt}$, the other two being very large, the solution given by equation 2.6 is well approximated by a *Gaussian*, i.e., by the *Green's function* for unidimensional diffusion in that direction.

Chapter 2. Theoretical and Numerical Background

$$q(\mathbf{r}, t)|_{w=0} = \frac{M}{8} \left\{ \operatorname{erf} \left[\frac{x_H - x}{\sqrt{4Dt}} \right] - \operatorname{erf} \left[\frac{x_L - x}{\sqrt{4Dt}} \right] \right\} \left\{ \operatorname{erf} \left[\frac{y_H - y}{\sqrt{4Dt}} \right] - \operatorname{erf} \left[\frac{y_L - y}{\sqrt{4Dt}} \right] \right\} \left\{ \operatorname{erf} \left[\frac{z_H - z}{\sqrt{4Dt}} \right] - \operatorname{erf} \left[\frac{z_L - z}{\sqrt{4Dt}} \right] \right\} \quad 2.6$$

The results of this comparison are presented in the following Figure 2.1. Furthermore, to demonstrate the importance of contour discretization to the accuracy of the FEM solution, the comparison is performed for the case of 20 and 200 contour-discretization points for the solution of the PDE via the implementation of FEM in *RuSseL3D*. The initial conditions are $q = 0$ everywhere, except for a rectangular parallelepiped with dimensions $400 \times 400 \times 5 \text{ \AA}^3$ where the initial value of the solution is equal to unity, $q = M = 1$. The solution is tracked over a domain of size $100 \times 100 \times 100 \text{ \AA}^3$ centered at the origin. It is clear how, with increasing time (contour length), the solution propagates towards the edges of the simulation box. Furthermore, when solving with FEM, appropriate chain discretization is crucial to get accurate results.

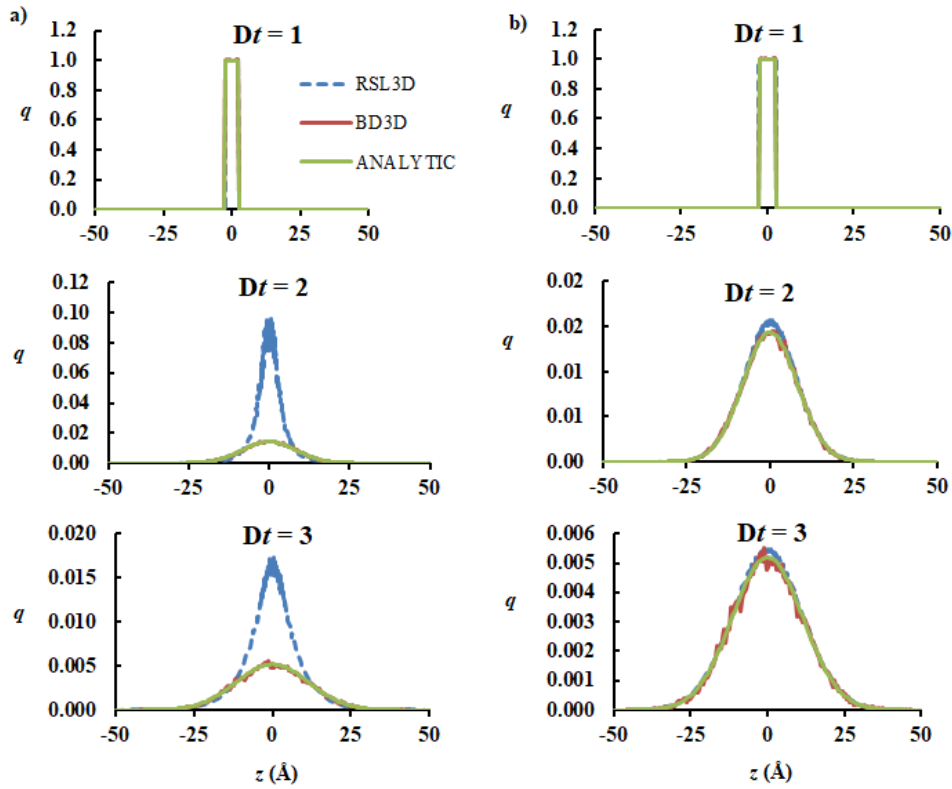


Figure 2.1 Comparison of numerical and analytical solutions of the *Edwards* diffusion equation against *Brownian* dynamics simulation. In column (a) the contour of a chain is discretized using 20 points for the numerical solution, whereas in panel (b) it is discretized using 200 points. Blue color corresponds to the FEM solution with *RuSseL*, red color corresponds to 3D *Brownian* dynamics motion and green color corresponds to the analytical solution given by equation 2.6. *Brownian* dynamics agrees with the analytical solution in all cases. The FEM solution agrees with the *Brownian* dynamics and with the analytical solution only when discretization along the contour direction (time) is adequately fine.

Now, in presence of a reaction term, w' , the analytical eq 2.6 is modified to incorporate an additional term, yielding the following eq 2.7.^{68,69} It is important to note that eq 2.7 is valid only if w' is constant in both space and time. Nonetheless, it helps understand the physics behind the reaction term of the *Edwards* equation, which would be the same, if the field was a function of \mathbf{r} , as in the case of SCFT calculations.

$$q(z, t)|_{w'=\text{const}\neq 0} = q(z, t)|_{w'=0} \cdot \exp(-w't) \quad 2.7$$

Equation 2.7 suggests that, when the field increases (which happens in SCF when the density at a certain point increases), then the exponential term suppresses the solution relative to its zero-field value. Conversely, when the field decreases, the exponential term boosts the value of the solution relative to its zero-field value. In the following Figure **2.2**, we present the evolution of the solution for different (constant in space) values of the field w' , while in Figure **2.3**, we demonstrate the spatial integral of the *propagator*, Q .

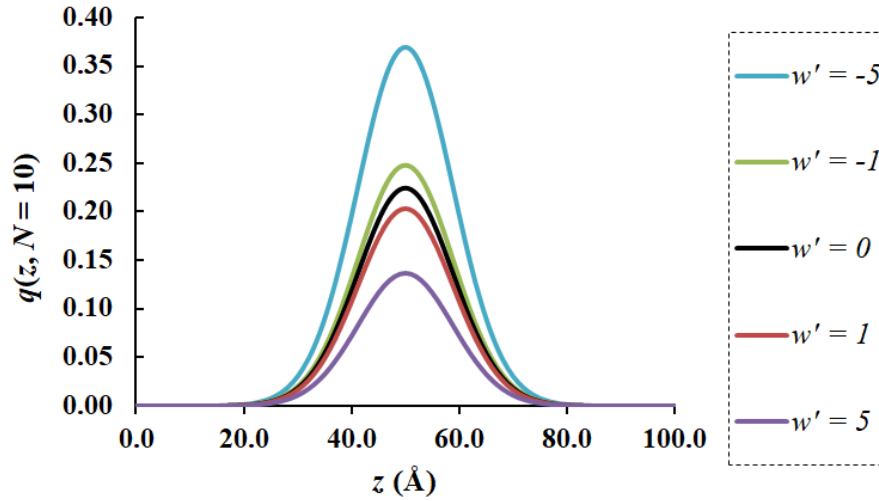


Figure 2.2 Spatial configuration of the chain *propagator*, q , evaluated at contour $N = 10$ for different values of the field, w' . The *propagator* has been calculated by solving the partial differential equation 2.2 via the analytical equation 2.7.

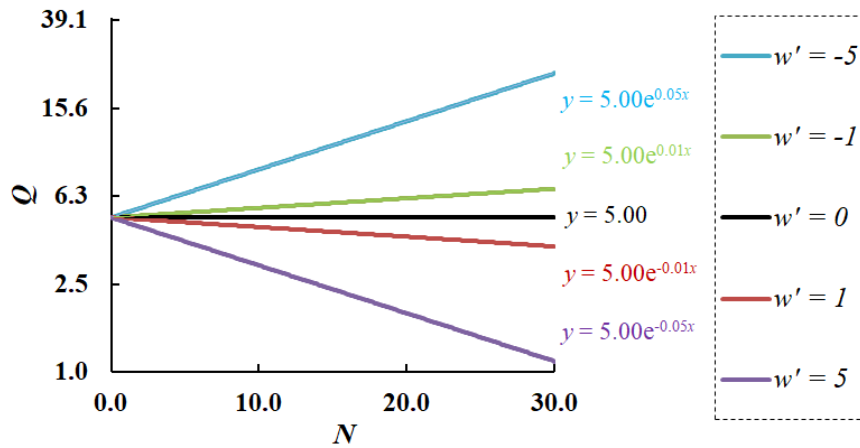


Figure 2.3 Spatial integral, Q , of chain *propagator*, q , for different values of the field, w' . Q is evaluated with respect to chain contour, N , which plays the role of time in the solution of the partial differential equation 2.2 via the analytical equation 2.7.

Looking at Figure 2.3 it becomes clear that, when the field is equal to zero, then the solution of the diffusion equation is conserved inside the domain of interest as “time” passes (i.e., as contour variable N increases), since the integral of the *propagator* remains constant (black lines in Figure 2.2 and Figure 2.3). On the contrary, when the field is negative, it leads to “production” of q with increasing N (blue and green lines in Figure 2.2 and Figure 2.3), whereas positive field values lead to “absorption” of q with increasing N (red and purple line in Figure 2.2 and Figure 2.3).

2.1.4. Nonbonded polymer interactions

In this section, we analyze the different equations of state (EoS) that can be used for the description of the nonbonded interactions between polymer chain segments. From every such equation, we derive a relationship for the free energy density as a function of the molecular density of the polymer, a relationship for the SCF, w' , as a function of the molecular density, and finally an expression for the *partition function* of the system as a function of the molecular density and the SCF, w' .

Equation 2.8 connects the field configuration, $w'(\mathbf{r})$, and the molecular segment density of the polymer. It is written in terms of the interfacial field, w'_{ifc} , referred to the value of the field in the bulk polymer region, w'_{bulk} . Subtracting w'_{bulk} from w' guarantees that the *chemical potential* field w'_{ifc} is zero in the bulk phase.

$$w'_{\text{ifc}}(\mathbf{r}) = w'(\mathbf{r}) - w'_{\text{bulk}} = \left. \frac{\partial f[\rho, \nabla \rho]}{\partial \rho} \right|_{\rho=\rho(\mathbf{r})} - \left. \frac{\partial f[\rho, \nabla \rho]}{\partial \rho} \right|_{\rho=\rho_{\text{seg,bulk}}} - \nabla \cdot \left. \frac{\partial f[\rho, \nabla \rho]}{\partial \nabla \rho} \right|_{\rho=\rho(\mathbf{r})} + u_S(\mathbf{r}) \quad 2.8$$

with $f[\rho, \nabla \rho]$ being the excess (relative to an ideal gas of chains) *Helmholtz* energy density of intermolecular interactions as a function of the local segment density and its gradient, u_S being the field exerted on a segment by any solid phases present and $\rho = \rho_m + \rho_g$ being the total segment density. The third term appearing on the right-hand side of eq 2.8 is known as the square-gradient theory (SGT) term. It is quite useful when addressing gas/polymer interfaces, since it helps in achieving quantitative agreement between *Self-Consistent Field* calculations, atomistic *molecular dynamics* simulations and experiment.² For details on the evaluation of the SGT term in spherical coordinates, the reader is referred in Appendix G.

2.1.4.1. Helfand EoS

Considering a compressible polymer melt, the *Helfand* EoS⁶⁵ penalizes deviations of the local segment density from its value in the bulk region. According to *Helfand*, the segment density variations are governed by a harmonic-type free energy density given in the following eq 2.9, and the corresponding configuration of the SCF, w' , must satisfy eq 2.8. The free energy density and its derivative are given by eqs 2.9 and 2.10, respectively. Figure 2.4a and c present evaluations of the free energy density and field terms from the HFD SL-EoS.

$$f_{\text{EoS}}^{\text{HFD}}(\rho) = \frac{1}{2\kappa_T} \left(\frac{\rho}{\rho_{\text{seg,bulk}}} - 1 \right)^2 \quad 2.9$$

$$\left. \frac{\partial f_{\text{EoS}}^{\text{HFD}}(\rho)}{\partial \rho} \right|_{\rho=\rho(\mathbf{r})} = \frac{1}{\kappa_T \rho_{\text{seg,bulk}}} \left(\frac{\rho}{\rho_{\text{seg,bulk}}} - 1 \right) \quad 2.10$$

2.1.4.2. Sanchez-Lacombe EoS

When wishing to describe the properties of a gas/polymer interfacial system, the *Helfand* model has trouble grasping the high density gradients developing there. This is because it rests on a quadratic approximation to the Helmholtz energy density for high densities, around those of the bulk liquid, which is not appropriate for the description of the low-density vapor region. A model based on an EoS that can capture vapor/liquid equilibrium would be expected to perform better. Indeed, the *Sanchez-Lacombe* (SL) EoS^{70,71} is quite accurate in reproducing the density profiles and free energies at vapor/polymer interfaces, especially when combined with a density gradient correction term.²

To invoke the SL EoS, a set of parameters are needed. The first one is the number of SL segments, r_{SL} , constituting a molecule or a polymer chain. The attractive energy between SL segments in adjacent sites is denoted by ε^* , whereas the hard core volume of a SL segment is denoted by v^* . Having introduced these quantities, we also define the characteristic SL temperature, $T^* = \varepsilon^*/(k_{\text{B}} \cdot T)$, pressure, $P^* = \varepsilon^*/v^*$, and mass density, $\rho^* = M/(r_{\text{SL}} \cdot v^* \cdot N_{\text{A}})$. The SL EoS is presented in eq 2.11.

$$\rho^2 + P + T \left[\ln(1 - \rho) + \left(1 - \frac{1}{r_{\text{SL}}} \right) \rho \right] = 0 \quad 2.11$$

where the tilde variables symbolize the reduced temperature, pressure, and density. The free energy density and its first derivative are then given by eqs 2.12 and 2.13, respectively.

$$f_{\text{EoS}}^{\text{SL}}(\rho) = P^* \left[\tilde{T} \tilde{\rho} - \tilde{\rho}^2 + \tilde{T}(1 - \tilde{\rho}) \ln(1 - \tilde{\rho}) \right] \quad 2.12$$

$$\left. \frac{\partial f_{\text{EoS}}^{\text{SL}}(\rho)}{\partial \rho} \right|_{\rho=\rho(\mathbf{r})} = k_{\text{B}} T^* \left(\frac{r_{\text{SL}}}{N_c} \right) \left\{ -2\tilde{\rho}(\mathbf{r}) - \tilde{T} \ln(1 - \tilde{\rho}(\mathbf{r})) \right\} \quad 2.13$$

Figure **2.4b** and **d** present evaluations of the free energy density and field terms from the SL-EoS. The *Sanchez-Lacombe* EoS has a firm theoretical basis in a *mean field* statistical mechanical analysis of a lattice fluid composed of chains and voids, reminiscent of *Flory-Huggins* theory with voids playing the role of solvent molecules.^{70,71}

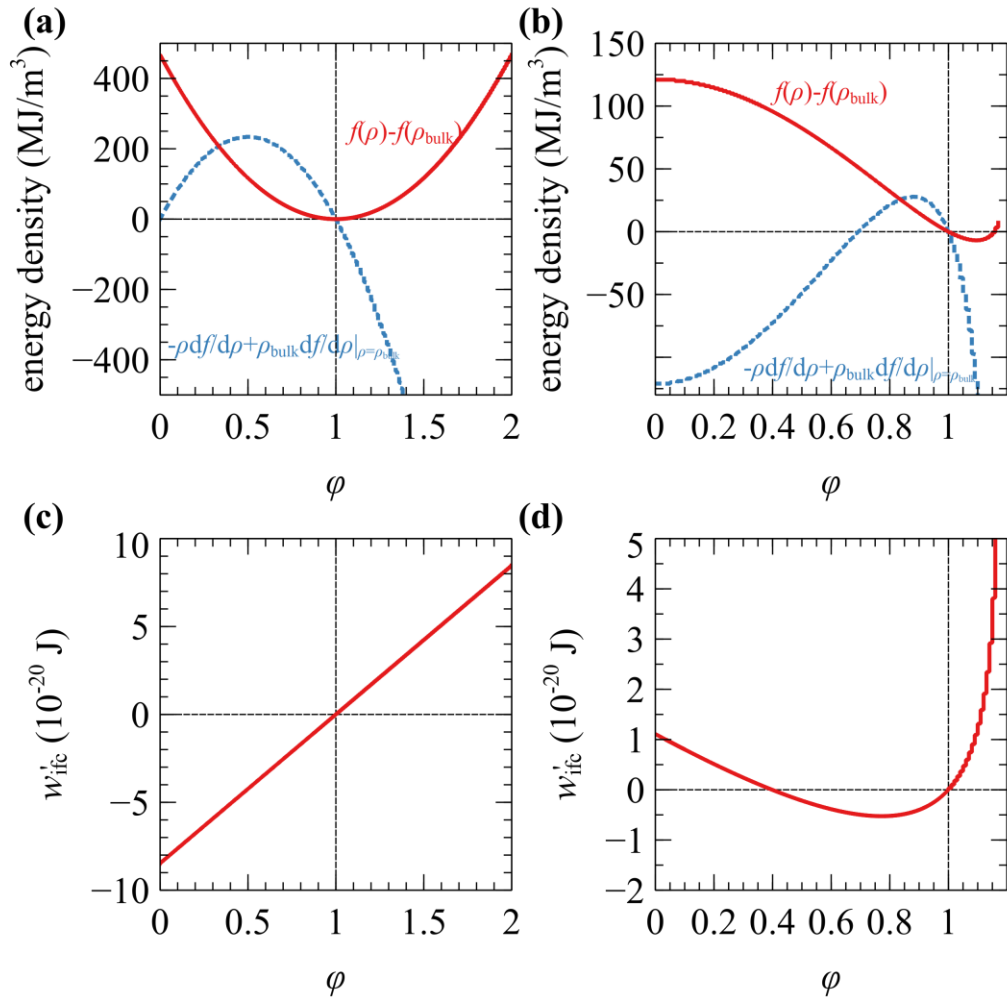


Figure 2.4 Free energy density and field as functions of segment density. Top panels depict $f(\rho) - f(\rho_{\text{seg,bulk}})$ (red line) and $-\rho df/d\rho + [\rho df/d\rho]_{\rho=\rho_{\text{seg,bulk}}}$ (dotted line) from (a) *Helfand* and (b) *Sanchez-Lacombe* free energy densities. Bottom panels depict $w'_{\text{ifc}} = w' - w'_{\text{bulk}}$ from (c) *Helfand* and (d) *Sanchez-Lacombe* free energy densities, in absence of solid/polymer interactions and gradient correction.

2.1.4.3. Compressibility considerations

As shown in eq 2.9, when using the HFD EoS, the free energy density is dictated by two free parameters; namely, the isothermal compressibility, κ_T , and the density of the bulk polymer melt, $\rho_{\text{seg,bulk}}$. A simple way to decide the values of these parameters is to either retrieve relevant experimental data or fit them in a way that reproduces the *surface tension* of the fluid. Nonetheless, setting these parameters to constant values leads to inaccurate qualitative predictions for the *surface tension* with varying chain molecular weight or temperature. For example, in Figure 2.5h, the predicted *surface tension* from HFD (with $\kappa_{T,\text{exp}} = 3.97 \text{ GPa}^{-1}$ and $\rho_{\text{mass,bulk}} = 953 \text{ g/cm}^3$) appears to be a decreasing function of chain length, whereas the opposite trend has been observed from simulations⁷² and experiments.^{73,74} The *surface tension* is indeed an increasing function of chain length, since cohesive interactions of the polymer melt are enhanced with increasing chain length.

A reasonable approach for fixing these parameters would be to set them equal to the ones predicted by the SL model for a specific chain length and temperature, using the following eq 2.14.⁷¹ Using HFD with $\kappa_{T,\text{SL}}$ (see Table 2-1), even though producing correct qualitative behavior with varying N_m and T , leads to rather high values of the *surface tension* (see squares in Figure 2.5h); the deviation becomes larger with the addition of a square-gradient term (see purple crosses in Figure 2.5h).

$$\kappa_{T,\text{SL}}^{-1} = \tilde{T}P^* \tilde{\rho}_{\text{seg,bulk}}^2 \left(\frac{1}{1 - \tilde{\rho}_{\text{seg,bulk}}} + \frac{1}{\tilde{\rho}_{\text{seg,bulk}} r_{\text{SL}} N_m} - \frac{2}{\tilde{T}} \right) \quad 2.14$$

An alternative way to determine these parameters is to fit them directly to experimental or theoretically predicted *surface tension* (from a suitable EoS such as SL-SGT) for each chain length. Table 2-1 reports the optimized isothermal compressibilities for HFD and HFD-SGT for each chain length, according to the values of *surface tension* obtained via the SL-SGT model (compare SL-SGT with HFD/ $\kappa_{T,\text{opt}}$ and HFD-SGT in Figure 2.5h). Compressibilities were optimized using the *Secant* method.

It is mentioned that, even though the reduced density profiles do not appear to be dependent on chain length, the actual density profiles do change, as indicated by the chain length-dependent $\rho_{\text{seg,bulk}}$ values in Table 2-1; it is the shape of these profiles that remains the same.

Chapter 2. Theoretical and Numerical Background

Table 2-1. Bulk densities and compressibilities from the SL EoS, and optimized compressibilities for the HFD, HFD/SGT EoS.

N_m	$\rho_{\text{mass,bulk}} \text{ (g/cm}^3\text{)}$	$\kappa_{T,\text{SL}} \text{ (GPa}^{-1}\text{)}$	$\kappa_{T,\text{HFD,opt}} \text{ (GPa}^{-1}\text{)}$	$\kappa_{T,\text{HFD/SGT,opt}} \text{ (GPa}^{-1}\text{)}$
24	0.93997	1.50804	4.56055	15.96570
48	0.94216	1.46935	4.36072	14.88736
96	0.94324	1.45060	4.26308	14.39257
192	0.94378	1.44137	4.21460	14.15635
384	0.94405	1.43679	4.18998	14.03992
768	0.94418	1.43451	4.17748	13.98211
1536	0.94425	1.43337	4.17119	13.95340

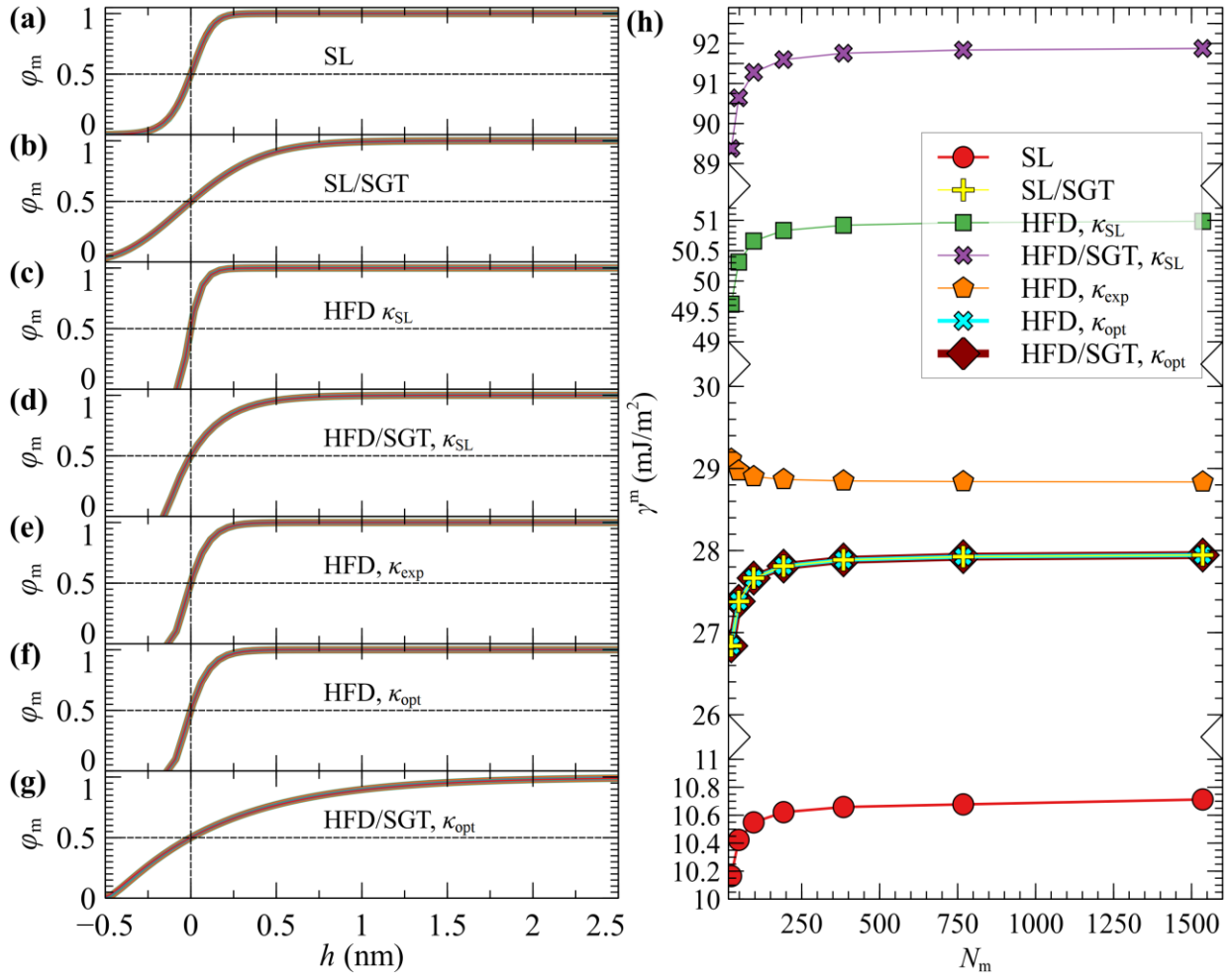


Figure 2.5 Effect of compressibility on density profiles and *adhesion tension*. (a-g) Reduced density profiles at the free surface of a melt from SL and HFD for various sets of isothermal compressibilities (Table 2-1), with and without SGT. Chain length varies from $N_m = 24$ up to 1536 skeletal bonds. The solid lines become thicker with increasing N_m , while the dashed lines are guides to the eye. (h) The *surface tension* from the corresponding profiles in (a-g).

2.1.5. Solid/polymer interactions

In the most general cases of our calculations, the solid/polymer interactions are described by the following eq 2.15.

$$u_S = u_{\text{Hamaker,A}} + u_{\text{Hamaker,R}} + u_{\text{HS}} + u_{\text{cSW}} \quad 2.15$$

The first two terms are the attractive ($u_{\text{Hamaker,A}}$) and repulsive ($u_{\text{Hamaker,R}}$) interactions as described by the *Hamaker* potential for sphere-sphere or sphere-planar surface geometries. The third term (u_{HS}) corresponds to a hard-sphere wall at distance h_{HS} from the solid surface; it is implemented as a *Dirichlet* BC that brings the *propagator*, q , to zero and prevents numerical problems that may be caused by $u_{\text{Hamaker,R}}$ blowing up at small distances.

The usual *Hamaker* constants invoked for modeling PS-SiO₂ interactions,²³ when applied to our model, yield weak adhesion indicative of superhydrophobic⁷⁵ interfaces (contact angle $\theta_c \sim 158.9^\circ$).²⁸ This is because, while the SL EoS generates realistically broad² gas/polymer density profiles, at the solid/polymer interface the free energy penalty arising due to the square gradient term (which punishes steep profiles developing in the vicinity of the solid) makes interactions less favorable.^{24,28,76}

The essence of *Hamaker* theory¹⁷ is to treat the interacting bodies as collections of homogeneously distributed infinitesimal domains interacting with a *Lennard-Jones* potential. Subsequently, integration over the volume of the bodies takes place to account for interactions amongst all possible pairs, resulting in the total potential. The *Hamaker* constant of the effective solid/polymer interaction is calculated by the geometric mean, $A_{\text{PS-SiO}_2} = \sqrt{A_{\text{PS}}A_{\text{SiO}_2}}$. Vogiatzis and Theodorou²³ employed an effective solid/polymer interaction, $A_{\text{PS-SiO}_2}^{\text{eff}} = \sqrt{A_{\text{PS}}A_{\text{SiO}_2}} - A_{\text{PS}}$, instead of $A_{\text{PS-SiO}_2}$, in order to restore the proper effective cohesive interactions at the solid/polymer interface. Herein, we opted to work with $A_{\text{PS-SiO}_2}$, since the energy of cohesion of the polymer is taken into account as part of the free energy density, $f[\rho(\mathbf{r}), \nabla\rho(\mathbf{r})]$.

Furthermore, the effective collision diameter can be calculated as being the effective diameters of solid and polymeric segment interaction sites, respectively. In each of the following cases of interacting geometries, a wall distance was used, h_{HS} , so that the maximum of the repulsive term felt by the polymer segments does not exceed $5 k_{\text{B}}T$, as shown in the following Figure 2.6.

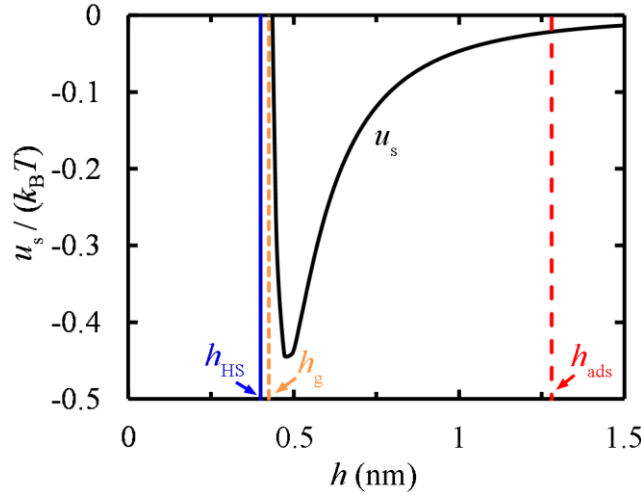


Figure 2.6 Interaction energy $u_s(h)$ between a PS monomer unit and a planar SiO₂ substrate as calculated from the *Hamaker* potential at $T = 500$ K. The blue line, $h_{\text{HS}} = 0.4$ nm, intersects the $u_s(h)$ curve at $u_s = 5 k_B T$ and depicts the distance of the hard-sphere wall from the surface employed in the calculations. The orange dashed line depicts the distance of the grafting points from the solid surface (h_g), and the red dashed line delimits the critical distance (h_{ads}), below which a matrix chain segment is considered *adsorbed* on the solid surface.

2.1.5.1. Hamaker Sphere-sphere

For the purpose of calculating the potential energy of dispersive interactions between polystyrene segments, belonging to either matrix or grafted chains, and a silica NP immersed in the polymer melt, we consider the atactic polystyrene monomers as small spheres with an

effective radius $a_1 = \sqrt[3]{\frac{3}{4\pi\rho_{\text{seg}}}}$, interacting with the spherical silica NP of radius $a_2 = R_s$. The

solid/polymer interaction potential per monomer can be split into an attractive¹⁷ and a repulsive term.⁷⁷ The two terms, u_A and u_R , respectively, are functions of the center-to-center distance, r_{12} , between two interacting spherical bodies:

$$u_A = -\frac{A_{12}}{6} \left[\frac{2a_1a_2}{r_{12}^2 - (a_1 + a_2)^2} + \frac{2a_1a_2}{r_{12}^2 - (a_1 - a_2)^2} + \ln \left(\frac{r_{12}^2 - (a_1 + a_2)^2}{r_{12}^2 - (a_1 - a_2)^2} \right) \right] \quad 2.16$$

$$u_R = \frac{A_{12}}{37800} \frac{\sigma_{\text{eff}}^6}{r_{12}} \left[\frac{r_{12}^2 - 7r_{12}(a_1 + a_2) + 6(a_1^2 + 7a_1a_2 + a_2^2)}{(r_{12} - a_1 - a_2)^7} + \frac{r_{12}^2 + 7r_{12}(a_1 + a_2) + 6(a_1^2 + 7a_1a_2 + a_2^2)}{(r_{12} + a_1 + a_2)^7} - \frac{r_{12}^2 + 7r_{12}(a_1 - a_2) + 6(a_1^2 - 7a_1a_2 + a_2^2)}{(r_{12} + a_1 - a_2)^7} - \frac{r_{12}^2 - 7r_{12}(a_1 - a_2) + 6(a_1^2 - 7a_1a_2 + a_2^2)}{(r_{12} - a_1 + a_2)^7} \right] \quad 2.17$$

where $A_{12} = A_{\text{PS-SiO}_2}$ is the *Hamaker* constant and σ_{eff} is the effective collision diameter.

2.1.5.2. Hamaker Sphere-planar surface

The attractive and the repulsive components from the interaction of a spherical NP with a semi-infinite solid terminating at a flat surface can be obtained in the context of *Hamaker* theory as follows:

$$u_A = -\frac{A_{12}}{6} \left(\frac{1}{r'} + \frac{1}{2+r'} + \ln \left(\frac{r'}{2+r'} \right) \right) \quad 2.18$$

$$u_R = \frac{A_{12}}{7560} \frac{\sigma_{\text{eff}}^6}{a_1^6} \left(\frac{8+r'}{(2+r')^7} + \frac{6-r'}{r'^7} \right) \quad 2.19$$

with $r' = d_{12} / a_1$, a_1 being the radius of the spherical NP and d_{12} being the distance between the surface of the spherical NP and the solid surface. We have $u_S = u_A + u_R$ for this case, which is shown in Figure 2.6 as a function of $h = d_{12} + a_1$.

2.1.5.3. Hamaker Planar-planar surface

Correspondingly, the attractive and repulsive terms of the *Hamaker* interaction between two semi-infinite planar surfaces (i.e., their length, L , is much higher than the distance between them, h_{SS}) is given by the following eqs 2.20 and 2.21, respectively.

$$u_A = -S_S \frac{A_{\text{SMS}}}{\pi} \frac{1}{12h_{\text{SS}}^8} \quad 2.20$$

$$u_R = S_S \frac{A_{\text{SMS}}}{\pi} \frac{\sigma_S^6}{360h_{\text{SS}}^8} \quad 2.21$$

where A_{SMS} is the polymer-mediated *Hamaker* constant between the two plates.

2.1.5.4. Square well and ramp potential

The code offers the possibility of selecting from a range of different wall potentials. In this way, the wetting degree of the interface can be altered according to the properties of the specific system that the user wishes to reproduce. The current section demonstrates evaluations with the square well and ramp potentials.

Chapter 2. Theoretical and Numerical Background

Figure 2.7 illustrates the density profiles of polyethelene (PE) melt near solid surfaces as a function of the *contact angle*, using the *Helfand* (HFD), *Sanchez-Lacombe* (SL) and SL coupled with a square-gradient correction term (SL-SGT). The solid/polymer interactions have been described via the square well ($u_{\text{square_well}}$, left) or the ramp (u_{ramp} , right) potential. The functional forms of the square well and ramp potentials are given in eqs 2.22 and 2.23, respectively.

$$u_{\text{square_well}} = v_{\text{square_well}} \quad \forall h < \sigma_{\text{square_well}} \quad 2.22$$

$$u_{\text{ramp}} = v_{\text{ramp}} \max\left(\frac{\sigma_{\text{ramp}} - h}{\sigma_{\text{ramp}}}, 0\right) \quad 2.23$$

where $v_{\text{square_well}}/v_{\text{ramp}}$ and $\sigma_{\text{square_well}}/\sigma_{\text{ramp}}$ correspond to the depth and the width of the square well/ramp potential.

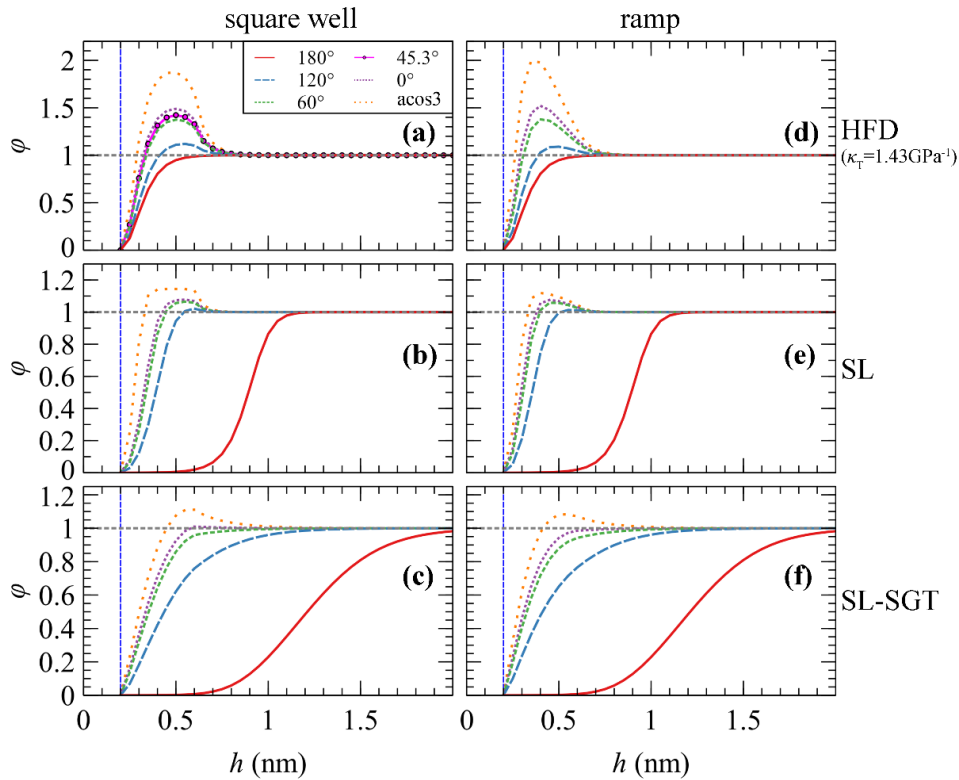


Figure 2.7 Density profiles of polyethylene in contact with solid interfaces of different affinity. *Contact angle* assumes the values, $\theta = \{180^\circ: \text{red}, 120^\circ: \text{blue}, 60^\circ: \text{green}, 45^\circ: \text{magenta}, 0^\circ: \text{violet}, \text{and } \arccos(3)^\circ: \text{orange}\}$ and density profiles are derived with (a,d) HFD, (b,e) SL and (c,f) SL-SGT equation of state in conjunction with square well (left panels) or ramp (right panels) potential. We observe that as the *contact angle* decreases, the density profile of the polymer segments near the surface is increased, suggesting an enhanced affinity of the polymer segments to the solid surface.

The range of these potentials was set to 0.65 nm and the position of the hard sphere wall is equal to $h_{\text{HS}} = 0.45 \text{ nm}$.^{66,78} For each one of the cases presented in Figure 2.7, the depth of the potential was optimized with the *Secant* optimization scheme in order to match the target

contact angles, $\theta = \arccos(-\gamma^{\text{SM}} / \gamma^{\text{VM}})$, with γ^{SM} and γ^{VM} being the interfacial free energy of the solid-matrix (SM) and vapor-matrix (VM) system, respectively. It is further noted that, for a planar interface, $\gamma^{\text{VM}} = \sigma^{\text{VM}}$ is the *surface tension*, and $\gamma^{\text{SM}} = -(\sigma^{\text{SV}} - \sigma^{\text{SM}})$ ⁷⁹ corresponds to minus the *adhesion tension*; thus, the *contact angle* can be also estimated as $\theta = \arccos[(\sigma^{\text{SV}} - \sigma^{\text{SM}}) / \sigma^{\text{VM}}]$.

In absence of solid surfaces (red lines in Figure 2.7, $\theta = 180^\circ$), the profiles exhibit a characteristic sigmoidal shape, whereas the corresponding *surface tension* becomes $\gamma^{\text{VM}} \sim 73.0, 12.0$ and 29.5 mJ/m^2 for HFD, SL and SL-SGT, respectively.^{2,78} In HFD, the isothermal compressibility was set equal to $\kappa_T = 1.43 \text{ GPa}^{-1}$,^{66,78} while the compressibility is roughly the same in the SL models (Table 2-1). The experimental *surface tension* of PE is $26.6\text{-}27.7 \text{ mJ/m}^2$,⁸⁰ whereas the corresponding atomistic profile has a span of $\sim 1 \text{ nm}$;² hence, the SL-SGT model is more suitable for describing vacuum/polymer interfaces.

With increasing intensity of solid/polymer interactions (u_s), the density profiles move closer to the solid surfaces and become more pronounced, especially when the HFD equation of state is employed. Note that the profile obtained with a square well potential for $\theta = 45.3^\circ$ is identical to the corresponding profiles in refs^{66,78}.

Another interesting observation is that, even though the compressibilities of these models are quite similar, the density profiles from SL and SL-SGT are more expanded because they allow the formation of gas phases inside the polymer melt itself. Moreover, they are less pronounced due to the existence of a logarithmic term that suppresses large fluctuations of the density above unity. In SL-SGT, the profiles are almost identical for a given *contact angle* regardless of the functional form of the potential (i.e., square well vs ramp).

2.1.5.5. Hamaker-like integration of arbitrary pair-wise potentials

Let there be a sphere with radius R_s and constant interaction site density ρ_1 . Assuming that a point-like object P lying at a distance r from the center O of the sphere interacts via a central pair-wise potential $u(r')$ with all sites in the sphere, the total interaction energy between the point and the sphere can be calculated as:

$$E_{\text{SP}}(r, R_s) = \rho_1 \int_{r-R_s}^{r+R_s} dr' S(R_s, r', r) u(r') \quad 2.24$$

where $S(R_s, r', r)$ is the area of a spherical cap of radius r' centered at P which lies inside the given sphere (Figure 2.8).

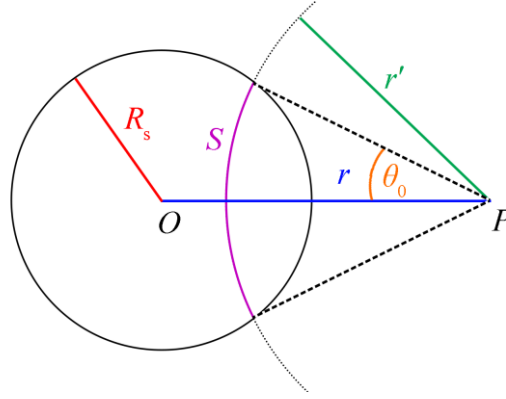


Figure 2.8 A point (P) at distance $r = |\mathbf{r}_P - \mathbf{r}_O|$ from a sphere of radius R_s centered at O .

To calculate S , we need to perform the following integration:

$$S(R_s, r', r) = \int_0^{2\pi} d\varphi \int_0^{\theta_0} d\theta r'^2 \sin \theta = -2\pi r'^2 \cos \theta_0 + 2\pi r'^2 = 2\pi r'^2 (1 - \cos \theta_0) \quad 2.25$$

From the generalized Pythagorean theorem, we can write:

$$\begin{aligned} R_s^2 &= r^2 + r'^2 - 2r'r \cos \theta_0 \\ \cos \theta_0 &= \frac{r^2 + r'^2 - R_s^2}{2r'r} \end{aligned} \quad 2.26$$

Combining eqs 2.25 and 2.26, we get:

$$S(R_s, r', r) = 2\pi r'^2 \left(1 - \frac{r^2 + r'^2 - R_s^2}{2r'r} \right) \quad 2.27$$

or

$$S(R_s, r', r) = \frac{\pi r'}{r} \left[R_s^2 - (r - r')^2 \right] \quad 2.28$$

In situations where the pair potential, $u(r)$, becomes zero beyond a cut-off distance, $r > r_c$, the upper integration bound in eq 2.24 becomes:

$$E_{\text{SP}}(r, R_s) = \rho_1 \int_{r-R_s}^{\min(r+R_s, r_c)} dr' S(R_s, r', r) u_{r' < r_c}(r') \quad 2.29$$

In the limit $R_s \rightarrow \infty$, eq 2.29 yields the interaction between a point and an infinite planar wall. Let us call the energy of this interaction $E_{\text{LP}}(R) = \lim_{R_s \rightarrow \infty} E_{\text{SP}}(R, R_s)$. To calculate E_{LP} , we work as follows: let \mathbf{r}_i be the position of the considered point at distance h from the solid planar surface. The elementary properties of the planar surface can be expressed in cylindrical

coordinates (R, z, φ) with respect to segment \mathbf{r}_i . Assuming again a constant density of interaction sites in the solid, ρ_1 , the number of segments in an elementary ring equals:

$$dN = \rho_1 2\pi R dR dz \quad 2.30$$

Subsequently, the total interaction energy is calculated as:

$$E_{\text{LP}}(h) = 2\pi\rho_1 \int_h^\infty dz \int_0^\infty dR Ru(r) \quad 2.31$$

Given that, $R = \sqrt{r^2 - z^2}$ and $\frac{dR}{dr} = \frac{1}{2} \frac{1}{\sqrt{r^2 - z^2}} \frac{d(r^2 - (z - z_i)^2)}{dr} = \frac{r}{\sqrt{r^2 - z^2}}$, eq 2.31 becomes:

$$E_{\text{LP}}(h) = 2\pi\rho_1 \int_h^\infty dz \int_z^\infty dr ru(r) \quad 2.32$$

Equation 2.32 is equivalent to eq 2.24 in the limit $R_s \rightarrow \infty$.

We developed a curvature-dependent potential by setting the pairsise potential to the square well of eq 2.33.

$$u_{\text{SW}}(r) = \begin{cases} \varepsilon_{\text{SW}}, & r \leq \sigma_{\text{SW}} \\ 0, & r > \sigma_{\text{SW}} \end{cases} \quad 2.33$$

with σ_{SW} being a cutoff distance and ε_{SW} being the well depth of the potential. The point-sphere integration of eq 2.33 yields:

$$u_{\text{cSW}} = C_{\text{SW}} \frac{1}{h + R_s} \left[g_{\text{SW}}(R_c, h) - g_{\text{SW}}(h, h) \right], h < \sigma_{\text{SW}} \quad 2.34$$

with:

$$g_{\text{SW}}(x, h) = -\frac{x^4}{4} + \frac{x^3}{3}(2h + 2R_s) - \frac{x^2}{2}(h^2 + 2hR_s) \quad 2.35$$

where $h \equiv r - R_s$ is the distance of the segment from the surface, $R_c = \min(h + 2R_s, \sigma_{\text{SW}})$,

$C_{\text{SW}} = \pi\rho_1\varepsilon_{\text{SW}}$ is a constant, and ρ_1 is the number density of interaction sites in the solid.

Regarding the point-surface interaction (or, equivalently, the limit $R_s \rightarrow \infty$):

$$\lim_{R_s \rightarrow \infty} u_{\text{cSW}} = C_{\text{SW}} \left(\frac{h^3 - \sigma_{\text{SW}}^3}{3} + \sigma_{\text{SW}}^2 (\sigma_{\text{SW}} - h) \right), h < \sigma_{\text{SW}} \quad 2.36$$

When we address systems of planar geometry, the coefficients of the force field were fitted in such a way as to reproduce the experimental work of adhesion from ref ⁸¹, corresponding to

Chapter 2. Theoretical and Numerical Background

high- and perfect-wetting degrees (see Table 2-2 and Table 4-2 of later chapter). However, such a potential does not account for the loss of solid interaction sites with increasing curvature. In other words, the solid/polymer interactions are expected to become weaker when the size of the NP decreases, since the polymer segments interact with fewer solid sites. In fact, Figure 2.9 illustrates evaluations of u_{cSW} over a broad range of R_{S} values. The solid/polymer interactions are naturally adjusted with varying curvature, whereas in the limit of $R_{\text{S}} \rightarrow \infty$ (where eqs 2.34 and 2.36) become equivalent, the functional dependence resembles the one of the ramp potential. In the limit $R_{\text{S}} \rightarrow 0$, eq 2.34 collapses to the square well potential of eq 2.33, i.e., $\lim_{R_{\text{S}} \rightarrow 0} u_{\text{cSW}} = u_{\text{SW}}$,

$$\text{for } \rho_1 = \left(\frac{4}{3} \pi R_{\text{S}}^3 \right)^{-1}$$

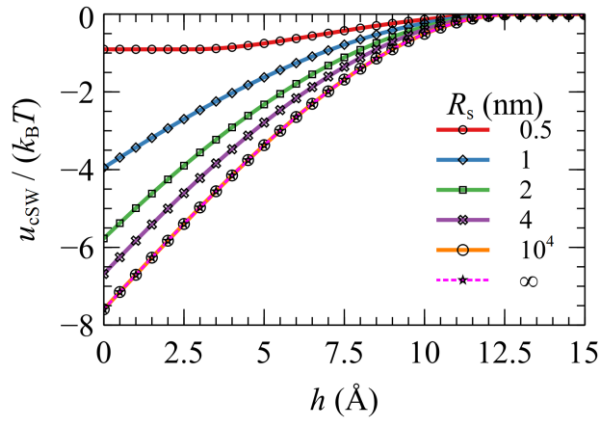


Figure 2.9 Evaluations of u_{cSW} using eq 2.34 for $C_{\text{SW}} = -37.5 \cdot 10^6 \text{ J/m}^3$, $\sigma_{\text{SW}} = 1.28 \text{ nm}$, and $T = 500 \text{ K}$. Stars depict evaluations of eq 2.36 for planar surfaces.

2.1.5.6. Tabulated potentials

Besides analytic functional forms, one can make use of tabulated potentials as well. Even though such potentials might be cumbersome to work with, they are more flexible, in the sense that, in many cases, they allow for reproduction of density profiles of arbitrary shape. For example, one can optimize the tabulated potential to reproduce a target density profile, φ_{target} , via iterative *Boltzmann inversion*, as shown in eq 2.37.

$$u_{\text{S},i}(\mathbf{r}) = u_{\text{S},i-1}(\mathbf{r}) + ak_{\text{B}}T \ln \left(\frac{\varphi_{i-1}(\mathbf{r})}{\varphi_{\text{target}}(\mathbf{r})} \right) \quad 2.37$$

with a being a relaxation parameter. This process can be envisioned as reverse engineering the self-consistent field; instead of trying to predict the density profiles for a given field, the optimizer attempts to find the field that reproduces the target density profiles.

Figure 2.10 depicts the density profile at a polyethylene-graphite interface at temperature $T = 450$ K, obtained from atomistic *molecular dynamics* simulations⁷² and the optimized density profiles obtained with *RuSseL* using the *Helfand*⁶⁵ and ideal free energy density. In the latter case, intermolecular interactions among chain segments are turned off, while chain segments interact explicitly with the solid wall. The corresponding tabulated potentials are demonstrated in Figure 2.10c.

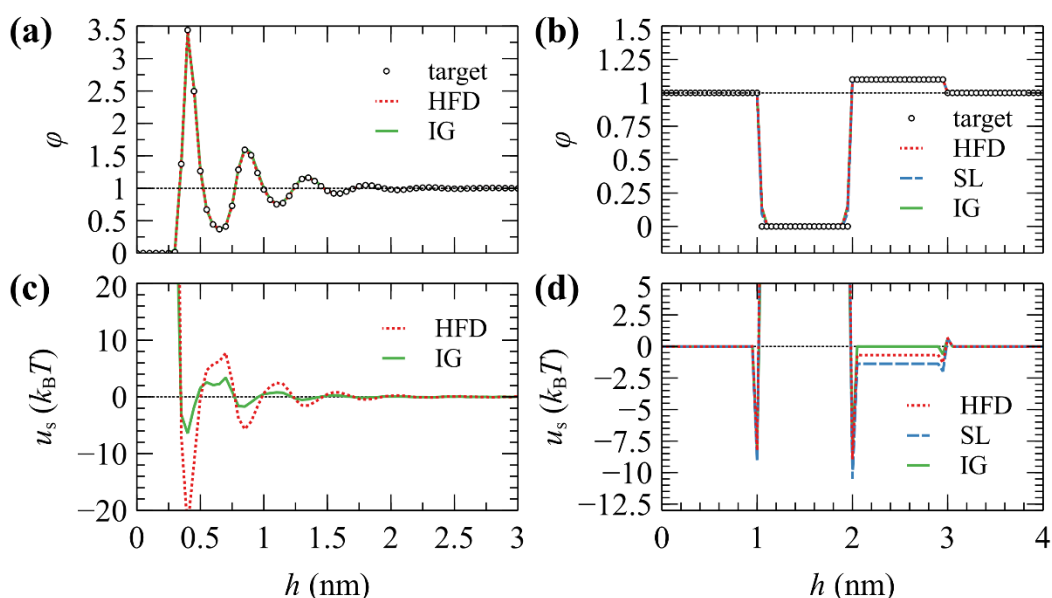


Figure 2.10 Demonstration of tabulated solid/polymer potentials and resulting density profiles. **(a,b)** Target (circles) and fitted density profiles of polyethylene segments, obtained via the *Helfand* EoS (dots), *Sanchez-Lacombe* EoS (dashes) and ideal gas of chain segments (solid lines). In **(a)**, the target profile corresponds to a profile of C_{100} /graphite interface at 450 K obtained via atomistic *molecular dynamics* simulations.⁷² In **(b)**, the target profile equals $\phi = 0$ for $h \in [1,2)$, $\phi = 1.1$ for $h \in [2,3)$, and $\phi = 1.0$ everywhere else. Panels **(c,d)** depict the tabulated potentials, $u_s(\mathbf{r})$, corresponding to profiles **(a)** and **(b)**, respectively. The horizontal dotted lines are guides to the eye.

According to Figure 2.10a, it is possible to reproduce the MD profiles exactly, given that the underlying EoS does not impose any particular constraints. For example, it is impossible to reproduce these profiles exactly when using the *Sanchez-Lacombe* EoS, since the logarithmic term does not allow the density to exceed the characteristic SL density, ρ^* . Similarly, Figure 2.10b depicts an exotic target density profile, where $\phi = 0$ for $h \in [1,2)$, $\phi = 1.1$ for $h \in [2,3)$, and $\phi = 1.0$ everywhere else. As in the previous case, the target profile has been reproduced with

HFD, SL, and IG EoS in the presence of the corresponding tabulated potentials shown in Figure 2.10d.

2.2. Thermodynamic description of polymer interfaces

2.2.1. Systems involving polymer melt

The thermodynamics of the polymer-grafted NP(s) or planar surface(s) immersed in a polymer matrix is described using the *grand canonical ensemble*, which is defined relative to a bulk phase of monodispersed matrix chains, each of length N_m , occupying a volume equal to the polymer-accessible volume of the system, and a set of n_g isolated end-pinned unperturbed chains, each of length N_g . The temperature, T , is the same between the system under investigation and the reference system (see also Appendix D). The grand potential of the system is determined as the sum of individual energetic and entropic terms as shown in the following eq 2.38.

$$\Delta\Omega^{\text{SGM}} = \Omega^{\text{SGM}} - \Omega^{\text{M}} - A^{\text{G,bulk}} = \Delta\Omega_{\text{coh}}^{\text{SGM}} + \Delta\Omega_{\text{field}}^{\text{SGM}} + \Delta\Omega_{\text{m}}^{\text{SGM}} + \Delta A_{\text{g}}^{\text{SGM}} + \Delta U_{\text{S}}^{\text{SGM}} \quad 2.38$$

where $\Delta\Omega_{\text{coh}}^{\text{SGM}}$ is the cohesive interaction component (relative to the bulk melt chains) arising due to segment-segment interactions in the polymer,

$$\Delta\Omega_{\text{coh}}^{\text{SGM}} = \int_{\mathcal{R}} d\mathbf{r} \left\{ f[\rho(r), \nabla\rho(r)] - f[\rho_{\text{seg,bulk}}, \mathbf{0}] \right\} \quad 2.39$$

$\Delta\Omega_{\text{field}}^{\text{SGM}}$ is the interaction energy between the density field and the *chemical potential* field,

$$\Delta\Omega_{\text{field}}^{\text{SGM}} = - \int_{\mathcal{R}} d\mathbf{r} \left\{ \rho(\mathbf{r})w'(\mathbf{r}) - \rho_{\text{seg,bulk}}w'_{\text{bulk}} \right\} \quad 2.40$$

$\Delta U_{\text{S}}^{\text{SGM}}$ is the contribution of the potential energy exerted from the solid to the polymer segments,

$$\Delta U_{\text{S}}^{\text{SGM}} = \int_{\mathcal{R}} d\mathbf{r} \left\{ \rho(\mathbf{r})u_{\text{S}}(\mathbf{r}) \right\} \quad 2.41$$

$\Delta\Omega_{\text{m}}^{\text{SGM}}$ describes the translational and conformational entropy (relative to the bulk melt entropy) of noninteracting matrix chains subject to a *chemical potential* $N_m\mu_m$,

$$\Delta\Omega_{\text{m}}^{\text{SGM}} = - \frac{\rho_{\text{seg,bulk}}V}{\beta N_m} \left(Q_m [w' - w'_{\text{bulk}}] - 1 \right) \quad 2.42$$

2.2. Thermodynamic description of polymer interfaces

and ΔA_g^{SGM} is associated with the conformational entropy of n_g grafted chain subject to the field $w' - w'_{\text{bulk}}$:

$$\Delta A_g^{\text{SGM}} = -\frac{1}{\beta} \sum_{i_g=1}^{n_g} \ln Q_g \left[\mathbf{r}_{g,i_g}; w' - w'_{\text{bulk}} \right] - \frac{1}{\beta} \sum_{i_g=1}^{n_g} \ln \frac{r_{\text{ref},q=0}}{r_{g,i_g,q=0}} \quad 2.43$$

The second term appearing in the right-hand side of eq 2.43 is necessary for renormalizing the free energy term with respect to the distance of the grafting points from the solid/*Dirichlet* surface. For more information, see Section 3.7.4.

$\Delta \Omega_{\text{coh}}$ is the free energy term which incorporates the cohesive interactions between polymer segments; it is a direct manifestation of the compressibility and density deviations of the polymer melt from its bulk value, due to the presence of the interface. Regarding the second term, $\Delta \Omega_{\text{field}}$, it describes the interaction between the *chemical potential* field, $w'(\mathbf{r})$, and its conjugate field, $\rho(\mathbf{r})$. Another practical way one can think of this term is the following: the field w' expresses by definition the variation of the *Gibbs* free energy of the system with respect to the amount of material, in our case polymer segments, that exists in the system. Weighting this potential/field by the density of segments, ρ , i.e., taking the product $w'(\mathbf{r}) \cdot \rho(\mathbf{r})$, and integrating over the domain of interest is a rigorous way to determine the total amount of energy associated with this *chemical potential* field.

The terms $\Delta \Omega_m$ and ΔA_g are entropic terms associated with matrix and grafted chain conformations, respectively. In Section 4.2.9, we have considered the latter term as the sum of two sub-contributions: a term which represents the contribution of grafted chains to the energy of the field and a purely entropic contribution which depends on the stretching of grafted chains relative to their unperturbed configurations.

2.2.2. Systems in vacuum

In the absence of matrix chains (i.e., systems of isolated grafted-NPs or brushes), the thermodynamics is described via the *Helmholtz* free energy of the following eq 2.44.

$$\Delta A^{\text{SGV}} = A^{\text{SGV}} - A^{\text{G,bulk}} = \Delta A_{\text{coh}}^{\text{SGV}} + \Delta A_{\text{field}}^{\text{SGV}} + \Delta A_g^{\text{SGV}} + \Delta U_S^{\text{SGV}} \quad 2.44$$

The first two terms on the right-hand side of eq 2.44 represent the cohesive (eq 2.45) and field (eq 2.46) interactions. The last two terms of eq 2.44 are again given by eqs 2.43 and 2.41 presented in the previous Section 2.2.1, with the density and field obtained for the isolated grafted-NP or brush and V replacing M in the superscript on the left-hand side.

$$\Delta A_{\text{coh}}^{\text{SGV}} = \int_{\mathcal{R}} \mathbf{dr} \{ f [\rho(r), \nabla \rho(r)] \} \quad 2.45$$

$$\Delta A_{\text{field}}^{\text{SGV}} = - \int_{\mathcal{R}} \mathbf{dr} \{ \rho(\mathbf{r}) w'(\mathbf{r}) \} \quad 2.46$$

2.2.3. Macroscopic Work Functions

To better understand the thermodynamic properties of polymer interfaces, we define four macroscopic work functions; the *work of cohesion* (W_C), *work of immersion* (W_I), *work of adhesion* (W_A), and *work of spreading* (W_S), which are calculated via the following eqs 2.47-2.50. They refer to the reversible work that must be expended to separate the interfaces and they are conceptually opposite to *Gibbs* free energies of these interfaces. Hence, spontaneity is expressed by opposite signs.⁸²

$$W_C \equiv 2\sigma^{\text{VM}} \quad 2.47$$

$$W_I \equiv \sigma^{\text{SV}} - \sigma^{\text{SM}} = \sigma_{\text{adh}}^{\text{SM}} = \sigma^{\text{VM}} \cos \theta_c \quad 2.48$$

$$W_A \equiv \sigma^{\text{SV}} - \sigma^{\text{SM}} + \sigma^{\text{VM}} = \sigma_{\text{adh}}^{\text{SM}} + \sigma^{\text{VM}} = \sigma^{\text{VM}} (\cos \theta_c + 1) \quad 2.49$$

$$W_S \equiv \sigma^{\text{SV}} - \sigma^{\text{SM}} - \sigma^{\text{VM}} = \sigma_{\text{adh}}^{\text{SM}} - \sigma^{\text{VM}} = \sigma^{\text{VM}} (\cos \theta_c - 1) \quad 2.50$$

where for planar surfaces $\sigma^{\text{VM}} = \gamma^{\text{VM}}$ is the *surface tension*, $(\sigma^{\text{SV}} - \sigma^{\text{SM}}) = -\gamma^{\text{SM}}$ is the *adhesion tension*,⁷⁹ and θ the *contact angle* of the corresponding solid-fluid-vapor interface.

W_C is the free energy per unit surface for making two polymer free surfaces and W_I is a measure of *adhesion* between a solid surface and the polymer. W_A corresponds to the reversible work per unit surface required to separate two phases in contact. W_S quantifies the spontaneity of the wetting process: positive values indicate spontaneous *spreading* across the interface (perfect wetting), while negative values indicate finite *contact angles* (partial or no wetting).

Table 2-2 describes four SiO₂-PS interfaces with different wetting degrees in planar geometries. The two rightmost columns report the expected *contact angle* (θ_c) and *work of spreading* (W_S) for each wetting degree.

Table 2-2 Wetting degree of planar solid surfaces for length of matrix chains equal to $N_m = 768$ at $T = 500$ K. The surface tension of the corresponding liquid-vacuum interface equals $\sigma^{VM} = 27.93$ mJ/m². The inequalities indicate the NW, LW, HW and PW bounds. θ_c is the contact angle and W_s is the work of spreading on the planar surface.^{28,72} The values of $C_{SW,HW}$ and $C_{SW,PW}$ are given in the calculation details reported in Table 4-2.

type	wetting	Hamaker ¹⁷	C_{SW}	θ_c (°)	W_s (mJ/m ²)
NW	nonwetting	No	0	180°	$-55.8 = -2\gamma^{VM}$
LW	low wetting	Yes	0	$180^\circ > 158.9^\circ > 90^\circ$	$-\gamma^{VM} > -54.0 > -2\gamma^{VM}$
HW	high wetting	Yes	$C_{SW,HW}$	$90^\circ > 67^\circ > 0^\circ$	$0 > -17.0 > -\gamma^{VM}$
PW	perfect wetting	Yes	$C_{SW,PW}$	Imaginary	$15.3 > 0$

2.3. Finite Differences

2.3.1. Semi-implicit Time-stepping

The code supports the solution of 1D partial differential equations with a *semi-implicit Finite Differences* scheme, also known as the *Crank-Nicholson* method.^{66,78,83,84} In this scheme, the unknown solution at a certain spatial point, q_h^N , is expressed in terms of a central differences scheme, averaged between two successive contour points, N and $N+\Delta N$, as shown in the following eq 2.51.

$$\frac{\partial^2 q}{\partial h^2} = \frac{1}{2} \frac{q_{h+1}^{N+1} - 2q_h^{N+1} + q_{h-1}^{N+1}}{\Delta h^2} + \frac{1}{2} \frac{q_{h+1}^N - 2q_h^N + q_{h-1}^N}{\Delta h^2} \quad 2.51$$

while the first derivative of the solution, q , with respect to the contour variable N is approximated via the *Finite Differences* eq 2.52, hence, the matrix form of the partial differential equation to be solved is given by eq 2.53.

$$\frac{\partial q_h}{\partial N} = \frac{q_h^{N+1} - q_h^N}{\Delta N} \quad 2.52$$

$$-Dq_{h-1}^{N+1} + \left(1 + 2D + \frac{\Delta N \beta w'_{ifc,h}}{2}\right) q_h^{N+1} - Dq_{h+1}^{N+1} = Dq_{h-1}^N + \left(1 - 2D - \frac{\Delta N \beta w'_{ifc,h}}{2}\right) q_h^N + Dq_{h+1}^N \quad 2.53$$

where the diffusion coefficient is now given by $D = \frac{R_{G,c}^2 \Delta N}{2N_c \Delta h^2}$. In matrix-vector notation, eq 2.53

can be written as presented in the following eq 2.54.

$$\left(\mathbf{I} - D\mathbf{T} + \frac{\Delta N}{2} \mathbf{W}\right) \mathbf{q}^{N+1} = \left(\mathbf{I} + D\mathbf{T} - \frac{\Delta N}{2} \mathbf{W}\right) \mathbf{q}^N \quad 2.54$$

Chapter 2. Theoretical and Numerical Background

where \mathbf{I} is the identity matrix and we have defined the matrices \mathbf{T} and \mathbf{W} via eq 2.55 and 2.56, respectively.

$$\mathbf{T} = \begin{bmatrix} -2 & 1 & & & 1 \\ 1 & -2 & 1 & & \\ & 1 & -2 & 1 & \\ & & \dots & \dots & \dots \\ & & & 1 & -2 & 1 \\ 1 & & & & 1 & -2 \end{bmatrix} \quad 2.55$$

$$\mathbf{W} = \begin{bmatrix} w(0) & & & & & \\ & w(\Delta h) & & & & \\ & & w(2\Delta h) & & & \\ & & & \dots & & \\ & & & & w(L-\Delta h) & \\ & & & & & w(L) \end{bmatrix} \quad 2.56$$

Alternatively, eq 2.54 can be written in terms of the stiffness matrix, $\mathbf{K} = \mathbf{I} - DT + \frac{\Delta N}{2} \mathbf{W}$, and the vector denoting the right-hand side, $\mathbf{R} = \left(\mathbf{I} + DT - \frac{\Delta N}{2} \mathbf{W} \right) \mathbf{q}^N$ (i.e., the solution vector at the previous contour-step weighted by $\mathbf{I} + DT - \frac{\Delta N}{2} \mathbf{W}$), as follows:

$$\mathbf{K} \mathbf{q}^{N+1} = \mathbf{R} \Rightarrow \begin{bmatrix} b_1 & c_1 & & & a_1 \\ a_2 & b_2 & c_2 & & \\ & a_3 & b_3 & c_3 & \\ & & \dots & \dots & \dots \\ & & & a_{n-1} & b_{n-1} & c_{n-1} \\ c_n & & & a_n & b_n \end{bmatrix} \begin{bmatrix} q_1^{N+1} \\ q_2^{N+1} \\ q_3^{N+1} \\ \dots \\ q_{n-1}^{N+1} \\ q_n^{N+1} \end{bmatrix} = \begin{bmatrix} R_1 \\ R_2 \\ R_3 \\ \dots \\ R_{n-1} \\ R_n \end{bmatrix} \quad 2.57$$

where $a_i = -D$, $b_i = 1 + 2D + \frac{\Delta N \beta w_{\text{ifc},h}}{2}$ and $c_i = -D$. Note that eq 2.57 has been written in the most general form, i.e., without imposing any boundary conditions; all nodes are equivalent and, as a result, the domain is periodic.

2.3.2. Implicit time-stepping

A more stable but computationally more demanding way to solve the time-dependent partial differential equation is to express the unknown solution at every spatial point, q_h^N , in terms of the next contour step, $N + \Delta N$, according to eq 2.58 presented below.

$$\frac{\partial^2 q}{\partial h^2} = \frac{1}{2} \frac{q_{h+1}^{N+1} - 2q_h^{N+1} + q_{h-1}^{N+1}}{\Delta h^2} \quad 2.58$$

In order to solve the time/contour dependent *Edwards* diffusion equation, we discretize the domain of interest into u_h intervals and the chain contour length variable into u_c intervals, where $u_h = \frac{L}{\Delta h}$ and $u_c = \frac{N_c}{\Delta N}$, respectively. The spatial and chain contour length step intervals, Δh and ΔN respectively, are chosen so that maximum accuracy and stability are obtained with minimum computational cost (see Appendix **H**).

In both discretization schemes, we end up having to solve a linear system of equations, but the *implicit* contour stepping method (also known as “backward differences”) allows for larger contour steps without reaching the numerical stability limits of the *semi-implicit* case. The first derivative of the chain *propagator*, q , is again given by eq 2.52.

Combining eqs 2.52 and 2.58, we obtain the space and chain-contour discretized form of the *Edwards* diffusion equation, as presented in eq 2.59 below.

$$-2Dq_{h-1}^{N+1} + (1 + 4D + \Delta c \beta w'_{\text{ifc},h})q_h^{N+1} - 2Dq_{h+1}^{N+1} = q_h^N \quad 2.59$$

where the diffusion coefficient is given by, $D = \frac{R_{G,c}^2 \Delta N}{2N_c \Delta h^2}$. In matrix-vector notation, eq 2.59 is written as:

$$(\mathbf{I} - 2D\mathbf{T} + \Delta N\mathbf{W})\mathbf{q}^{N+1} = \mathbf{q}^N \quad 2.60$$

where \mathbf{I} is the identity matrix, and the matrices \mathbf{T} and \mathbf{W} are those given by eqs 2.55 and 2.56, respectively. It is observed that in contrast to the *semi-implicit* scheme developed in the previous section, in the *implicit* one, the right-hand side is just the solution vector evaluated in the previous contour step. As a result, the entries of the matrix form in eq 2.57 are modified as follows: $a_i = -2D$, $b_i = 1 + 4D + \Delta N \beta w'_{\text{ifc},h}$, $c_i = -2D$ and $\mathbf{R} = \mathbf{q}^N$.

2.3.3. Boundary conditions in 1D matrices

In formulating the matrices presented above, we have not taken into consideration the boundary conditions that occur from the physics of the problem. Given the single dimensionality of the systems addressed via the *Finite Differences* version of *RuSseL*, they are mathematically represented by a line, which is bounded by one point on the left and another one on the right.

Chapter 2. Theoretical and Numerical Background

In most cases, where aperiodic systems are addressed, at least one of the bounding points needs to be assigned a *Dirichlet* boundary condition (also known as *essential* or *absorbing* boundary condition). In our case, the physical interpretation of this type of boundary condition is that the polymer melt is in contact with solid or gas surface, and thus, the polymer segments are not allowed to reach the surface.

On the other point of the domain, we can assign either a *Dirichlet* boundary condition as well, or a *Neumann* boundary condition and, therefore, specify a certain value for the derivative of the solution rather than the solution itself. If the right hand side of the domain corresponds to the position where the bulk polymer region starts and the system is considered to be symmetric, then the solution derivative is set equal to zero.

In order to better demonstrate the above analysis regarding boundary conditions in one-dimensional domains, we present the linear system of equations to be solved, in the case where *Dirichlet* or *Neumann* boundary conditions are imposed on both boundary points.

2.3.3.1. Dirichlet-Dirichlet system

In a system with *Dirichlet* boundary conditions at $i = 1$ and $i = n$, eq 2.57 becomes:

$$\begin{bmatrix} 1 & 0 & & & 0 \\ a_2 & b_2 & c_2 & & \\ & a_3 & b_3 & c_3 & \\ & & \dots & \dots & \dots \\ & & & a_{n-1} & b_{n-1} & c_{n-1} \\ 0 & & & & 0 & b_n \end{bmatrix} \begin{bmatrix} q_1 \\ q_2 \\ q_3 \\ \dots \\ q_{n-1} \\ q_n \end{bmatrix} = \begin{bmatrix} R_1^{\text{DIR}} \\ R_2 \\ R_3 \\ \dots \\ R_{n-1} \\ R_n^{\text{DIR}} \end{bmatrix} \quad 2.61$$

In practice, applying the *Dirichlet* BC to the i^{th} node of the domain entails the following substitutions: $a_i = 0$, $b_i = 1$, $c_i = 0$, and $R_i = R_i^{\text{DIR}}$ (corresponding to a fixed q_i value).

2.3.3.2. Neumann-Neumann system

If zero-derivative boundary conditions are imposed on the left ($i = 1$) and right ($i = n$) edges of the domain, then the matrix \mathbf{T} needs to be modified, which in turn, influences the final stiffness matrix and the right-hand side vector. In this case of boundary conditions, the matrix \mathbf{T} is given by eq 2.62 and 2.63, for the *semi-implicit* and the *implicit* contour stepping scheme, respectively.

$$\mathbf{T} = \begin{bmatrix} -1 & 1 & & & 0 \\ 1 & -2 & 1 & & \\ & 1 & -2 & 1 & \\ & & \dots & \dots & \dots \\ & & & 1 & -2 & 1 \\ 0 & & & & 1 & -1 \end{bmatrix} \quad 2.62$$

$$\mathbf{T} = \begin{bmatrix} -2 & 2 & & & 0 \\ 1 & -2 & 1 & & \\ & 1 & -2 & 1 & \\ & & \dots & \dots & \dots \\ & & & 1 & -2 & 1 \\ 0 & & & & 2 & -2 \end{bmatrix} \quad 2.63$$

2.3.4. Solving the linear system of equations

In the case of non-periodic systems ($a_1 = c_n = 0$), where the stiffness matrix assumes a tridiagonal form, the linear system of equations is solved with the *Thomas* algorithm.⁸⁵

As in the conventional lower-upper (LU) decomposition algorithm, the solution of the tridiagonal system comprises three essential steps: *decomposition*, *forward substitution*, and *backward substitution*, which are presented below:

$$\text{Decomposition: } \begin{cases} a_i \leftarrow \frac{a_i}{b_{i-1}} \\ b_i \leftarrow b_i - a_i c_{i-1}, \quad i = 2, \dots, n-1 \end{cases} \quad 2.64$$

$$\text{Forward Substitution: } R_i \leftarrow R_i - a_i R_{i-1}, \quad i = 2, \dots, n \quad 2.65$$

$$\text{Backward Substitution: } \begin{cases} q_n^{N+1} \leftarrow \frac{R_n}{b_n} \\ q_i^{N+1} \leftarrow \frac{R_i - c_i q_{i+1}^{N+1}}{b_i}, \quad i = n-1, \dots, 1 \end{cases} \quad 2.66$$

On the other hand, when considering periodic systems, the linear system of equations is solved with a more general (but computationally more expensive) solver, which is based on the traditional *Gauss Elimination* method with *full pivoting* functionality.⁸⁶

2.4. Finite Element Method

Usually, researchers solve the SCFT equations using (*pseudo-spectral*) methods.^{34,87–89} The main concept in these methods is to expand the solution of the differential equation as a sum of certain *basis* functions and then determine the coefficients appearing in the summation so that the differential equation is satisfied with minimum error. Those methods are most often based on *Fast Fourier Transform* solvers and offer high calculation speed and near linear scaling, $O(n \log n)$, with respect to domain discretization.⁸⁹ The main drawbacks of these methodologies is that they perform best for specific boundary conditions and become less practical when applied in complex geometries.^{32,35,88,90}

On the other hand, the *Finite Element Method* (FEM) is a widespread numerical technique for the solution of partial differential equations governing various physics and engineering problems.^{91,92} The FEM is governed by the same idea of solution expansion in terms of a number of *basis* functions. The main difference between FEM and *spectral* methods is that the first use *basis* functions that are nonzero only in small subdomains (called *elements*), whereas in *spectral* methods, they can be nonzero in the whole domain of interest. Another key advantage of the FEM is that it can be readily applied to nonlinear problems, where the coefficients appearing in the PDE are dependent on the solution itself. *Spectral* methods are most frequently used in cases of constant-coefficient PDEs.

The core concept of the FEM lies in the discretization of the domain of interest Ω into smaller subdomains, Ω_e , of certain shape, called *elements*. In other words, it approximates both the geometry and the solution of the PDE by partitioning the original geometry in a finite number of pieces. The approximation accuracy increases with finer discretization, but so does the computational cost.

The most general form of a PDE is described by the following set of equations, where the operators L and B are allowed to be functions of the solution, q (rendering the problem nonlinear as mentioned):

$$\frac{\partial q}{\partial t} + Lq = f, \text{ in } \Omega \quad 2.67$$

$$Bq = g, \text{ in } \partial\Omega \quad 2.68$$

Equations 2.67 and 2.68 constitute the *strong* form of the PDE. It is called “*strong*”, because it allows for the solution, q , to belong in an infinite space of functions. Before the problem is ready to be solved via the FEM, the *weak* or *variational* form of the PDE must be derived. In

contrast to the solution of the *strong* form, the solution corresponding to the *weak* formulation belongs to a more restricted space of functions, which must satisfy certain conditions. Namely, these functions belong to a *Hilbert* space, which are a subcategory of *Sobolev* spaces.

In practice, the *weak* form requires from the solution to have a certain degree of smoothness. Usually, the *basis* functions of the solution space are *Lagrangian* polynomials, whose order is selected by the user in order to achieve the desired accuracy. The order of these *basis* functions is also reported as the order of the elements discretizing the domain of the system. Again, accuracy increases with higher element order. Consequently, the accuracy of calculating the real solution, q , is controlled by tuning both the number and the order of elements which partition the domain, Ω .

In one-dimensional (1D) problems, the elements are just line segments, in two-dimensional (2D) problems, they can be triangles or quadrilaterals and in three-dimensional problems (3D) they can be tetrahedrals, hexahedrals, prisms or pyramids. The elements are interconnected in the nodes, where the solution of the PDE is actually computed. *Basis* functions are defined such that they are equal to one at their respective nodes and zero at all the other nodes of the mesh. At any point of the geometry which finds itself between the nodes of a finite element mesh, the solution can be determined via interpolation using again the same *basis* functions. The FEM solution, q_h , approximating the exact solution of the PDE, q , is given by the following eq 2.69, where φ^j is the symbol for the *basis* function corresponding to node j .

$$q_h = \sum_j q_j \varphi^j \tag{2.69}$$

It becomes clear that the solution q_h is a linear combination of the *basis* functions, φ^j , and q_j are the coefficients (weights) multiplying these *basis* functions which approximate q with q_h . Given that the *basis* functions are set and known, the very purpose of the FEM is to calculate the coefficients q_j of eq 2.69. Whatever may be the nature of the problem (e.g., linear or nonlinear, static or time-dependent) or the FEM variant applied, the determination of the q_j coefficients is achieved by solving a linear system of equations of the following form:

$$\mathbf{K} \mathbf{q}_h = \mathbf{b} \tag{2.70}$$

As a matter of tradition in the FEM language, \mathbf{K} is called the *stiffness* matrix, while \mathbf{b} is called the *load* vector. In the sequence of steps needed to solve a FEM problem, there is an essential step lying between the *meshing* and the *solution* of the linear system in eq 2.70. It is the

Chapter 2. Theoretical and Numerical Background

assembly of the *stiffness* matrix, \mathbf{K} , and the load vector, \mathbf{b} . In terms of computational time and memory cost, the *assembly* stage can be more demanding than the *meshing* or the *solution*.

In the FEM, we require the *weak* form of the PDE to hold for all *test* functions in a *Hilbert* function space, instead of the *strong* form to hold for every point belonging in Ω . In other words, the *weak* form relaxes the requirement of the *strong* form, where all the terms appearing in the equation must be well defined at all points, and only requires equality in an integrated sense. One of the benefits of the FEM is the possibility to appropriately select the *test* and the *basis* functions. In *Galerkin's* method, specifically, the *test* and *basis* functions belong to the same *Hilbert* and to be more specific, they are both polynomials of the same order. Usually, *test* and *basis* functions are selected to be nonzero in a very small geometrical region. This implies that the integrals appearing in the *weak* formulation are zero everywhere, except for the limited regions, where the *test* and *basis* functions overlap, since all of these integrals include products of these functions or their gradients.

The *strong* form of the *Edwards* PDE is given by eq 2.2. Regarding the boundary conditions, it is obvious that no polymer segments are allowed to occupy any space on the solid or vacuum boundaries, therefore the *propagator* on these boundaries is equal to zero: $q(\mathbf{r}, N) = 0 \forall \mathbf{r} \in \partial\Omega_{\text{solid}}$. *Neumann* boundary conditions with zero *propagator* flux or *periodic* boundary conditions can be applied on the periodic faces of the simulation box. For a thorough discussion regarding *periodic* boundary conditions on three-dimensional domains discretized via the FEM, the reader is referred to Section 3.9.

2.4.1. Steady-state analysis

To obtain the *weak* form of *Edwards*, we start by multiplying eq 2.2 with the *test* functions $\phi^i(\mathbf{r})$ and then integrate over the volume V of the domain Ω and therefore the *strong* form is replaced by i number of integral equations:

$$\begin{aligned}
 -D\nabla^2 q(\mathbf{r}) + aq(\mathbf{r}) &= 0 \\
 -D\nabla^2 q(\mathbf{r})\phi^i(\mathbf{r}) + aq(\mathbf{r})\phi^i(\mathbf{r}) &= 0 \\
 -D\int_V \nabla^2 q(\mathbf{r})\phi^i(\mathbf{r})dV + a\int_V q(\mathbf{r})\phi^i(\mathbf{r})dV &= 0 \tag{2.71} \\
 -D\left\{ \int_V \nabla \cdot [\phi^i(\mathbf{r})\nabla q(\mathbf{r})]dV - \int_V \nabla \phi^i(\mathbf{r}) \cdot \nabla q(\mathbf{r})dV \right\} + a\int_V q(\mathbf{r})\phi^i(\mathbf{r})dV &= 0 \\
 D\left\{ \int_V \nabla \phi^i(\mathbf{r}) \cdot \nabla q(\mathbf{r})dV - \int_{\partial V} \phi^i(\mathbf{r})[\nabla q(\mathbf{r}) \cdot \mathbf{n}]dV \right\} + a\int_V q(\mathbf{r})\phi^i(\mathbf{r})dV &= 0
 \end{aligned}$$

Having obtained the i number of equations that we need, we proceed by expressing the solution q as a linear combination of the *basis* functions $\varphi_j(\mathbf{r})$, as shown in the following equation 2.72, and therefore j number of unknowns occur, which are the coefficients/weights, q_j , multiplying the *basis* functions at each point of the domain. These unknown coefficients are usually called the *degrees of freedom* of the FEM analysis.

$$q = \sum_{j=1}^{numNodes} q_j \varphi^j(\mathbf{r}) \quad 2.72$$

Furthermore, when we impose *Dirichlet* boundary conditions, $q = 0$, or *Neumann* boundary conditions where the flux of the solution is equal to zero, $\nabla q = \mathbf{0}$, then the surface integral appearing in eq 2.71 is also equal to zero. Considering the removal of this boundary term and combining eqs 2.71 and 2.72, the following eq 2.73 occurs.

$$\begin{aligned} D \left\{ \int_V \nabla \varphi^i(\mathbf{r}) \cdot \nabla \left(\sum_j^{nummp} q_j \varphi^j(\mathbf{r}) \right) dV + a \int_V \varphi^i(\mathbf{r}) \left(\sum_j^{nummp} q_j \varphi^j(\mathbf{r}) \right) dV \right\} &= 0 \\ D \sum_j^{nummp} q_j \int_V \nabla \varphi^i(\mathbf{r}) \cdot \nabla \varphi^j(\mathbf{r}) dV + a \sum_j^{nummp} q_j \int_V \varphi^i(\mathbf{r}) \varphi^j(\mathbf{r}) dV &= 0 \\ \sum_j^{nummp} q_j \int_V [D \nabla \varphi^i(\mathbf{r}) \cdot \nabla \varphi^j(\mathbf{r}) + a \varphi^i(\mathbf{r}) \varphi^j(\mathbf{r})] dV &= 0 \end{aligned} \quad 2.73$$

In matrix-vector notation, eq 2.73 can be written as $\mathbf{K}\mathbf{q} = \mathbf{0}$, where the entries of the stiffness matrix, \mathbf{K} , and the solution vector, \mathbf{q} , are equal to: $K_{ij} = \int_V [D \nabla \varphi^i(\mathbf{r}) \cdot \nabla \varphi^j(\mathbf{r}) + a \varphi^i(\mathbf{r}) \varphi^j(\mathbf{r})] dV$ and $\mathbf{q} = [q_1 \quad q_2 \quad \dots \quad q_{nummp}]^T$, respectively. So, in steady-state FEM analysis, we need to solve a linear system of equations with a certain right-hand side (which in this specific case is equal to zero) and at the same time the boundary conditions must be satisfied. Initial conditions are not encountered, since time is not a parameter of the problem.

2.4.2. Transient analysis

In transient analysis, we need to include a time-dependent term, which also has to be multiplied by a *test* function, φ^i , and integrated over the domain volume, V :

$$\int_V \left(\frac{\partial q(\mathbf{r}, N)}{\partial N} \varphi^i(\mathbf{r}) \right) dV + \sum_j^{nummp} q_j(N) \int_V [D \nabla \varphi^i(\mathbf{r}) \cdot \nabla \varphi^j(\mathbf{r}) + a \varphi^i(\mathbf{r}) \varphi^j(\mathbf{r})] dV = 0 \quad 2.74$$

Chapter 2. Theoretical and Numerical Background

Again, using the expansion of the solution q in terms of the *basis* functions ϕ^j , the discretized *weak* form for every *test* function ϕ^i can be written as follows:

$$\begin{aligned}
 & \int_V \left[\frac{\partial}{\partial N} \left(\sum_{j=1}^{\text{numnp}} q_j(N) \phi^j(\mathbf{r}) \right) \phi^i(\mathbf{r}) \right] dV + \sum_j^{\text{numnp}} q_j(N) \int_V \left[D\nabla \phi^i(\mathbf{r}) \cdot \nabla \phi^j(\mathbf{r}) + a \phi^i(\mathbf{r}) \phi^j(\mathbf{r}) \right] dV = 0 \Leftrightarrow \\
 & \int_V \left[\sum_{j=1}^{\text{numnp}} \frac{\partial q_j(N)}{\partial N} \phi^j(\mathbf{r}) \phi^i(\mathbf{r}) \right] dV + \sum_j^{\text{numnp}} q_j(N) \int_V \left[D\nabla \phi^i(\mathbf{r}) \cdot \nabla \phi^j(\mathbf{r}) + a \phi^i(\mathbf{r}) \phi^j(\mathbf{r}) \right] dV = 0 \Leftrightarrow \\
 & \sum_{j=1}^{\text{numnp}} \int_V \frac{\partial q_j(N)}{\partial N} \phi^j(\mathbf{r}) \phi^i(\mathbf{r}) dV + \sum_j^{\text{numnp}} q_j(N) \int_V \left[D\nabla \phi^i(\mathbf{r}) \cdot \nabla \phi^j(\mathbf{r}) + a \phi^i(\mathbf{r}) \phi^j(\mathbf{r}) \right] dV = 0 \Leftrightarrow \\
 & \sum_{j=1}^{\text{numnp}} \frac{\partial q_j(N)}{\partial N} \int_V \phi^j(\mathbf{r}) \phi^i(\mathbf{r}) dV + \sum_j^{\text{numnp}} q_j(N) \int_V \left[D\nabla \phi^i(\mathbf{r}) \cdot \nabla \phi^j(\mathbf{r}) + a \phi^i(\mathbf{r}) \phi^j(\mathbf{r}) \right] dV = 0
 \end{aligned} \tag{2.75}$$

Notice that now—in contrast to the steady-state case—the q_j coefficients are functions of the time-variable, N , while the *basis* and *test* functions depend just on spatial coordinates. The last step is to discretize the time-derivative of the solution q_j at point j with respect to the time-variable, N . One approach would be to use FEM for the time domain as well, but this can be rather computationally expensive. Alternatively, an independent discretization of the time domain is applied using the *Finite Differences* method. In its simplest form, this can be expressed with the following difference approximation:

$$\frac{\partial q_j(N)}{\partial N} \approx \frac{q_{j,N+\Delta N} - q_{j,N}}{\Delta N} \tag{2.76}$$

Two potential *Finite Differences* approximations are possible. The first one is to express the unknown coefficients q_j in terms of $N+\Delta N$ (*implicit* method), whereas the second one is to express them in terms of N (*explicit* method). Herein, we choose to apply the first option, because it is more stable than the second one. Hence, eq 2.75 is modified as follows:

$$\begin{aligned}
 & \sum_{j=1}^{\text{numnp}} \left(\frac{q_{j,N+\Delta N} - q_{j,N}}{\Delta N} \right) \int_V \phi^i(\mathbf{r}) \phi^j(\mathbf{r}) dV + \sum_j^{\text{numnp}} q_{j,N+\Delta N} \int_V \left[D\nabla \phi^i(\mathbf{r}) \cdot \nabla \phi^j(\mathbf{r}) + a \phi^i(\mathbf{r}) \phi^j(\mathbf{r}) \right] dV = 0 \Leftrightarrow \\
 & \frac{1}{\Delta N} \sum_{j=1}^{\text{numnp}} q_{j,N+\Delta N} \int_V \phi^i(\mathbf{r}) \phi^j(\mathbf{r}) dV - \frac{1}{\Delta N} \sum_{j=1}^{\text{numnp}} q_{j,N} \int_V \phi^i(\mathbf{r}) \phi^j(\mathbf{r}) dV + \sum_j^{\text{numnp}} q_{j,N+\Delta N} \int_V \left[D\nabla \phi^i(\mathbf{r}) \cdot \nabla \phi^j(\mathbf{r}) + a \phi^i(\mathbf{r}) \phi^j(\mathbf{r}) \right] dV = 0 \Leftrightarrow \\
 & \sum_{j=1}^{\text{numnp}} q_{j,N+\Delta N} \int_V \phi^i(\mathbf{r}) \phi^j(\mathbf{r}) dV - \sum_{j=1}^{\text{numnp}} q_{j,N} \int_V \phi^i(\mathbf{r}) \phi^j(\mathbf{r}) dV + \sum_j^{\text{numnp}} q_{j,N+\Delta N} \int_V \left[\Delta N D\nabla \phi^i(\mathbf{r}) \cdot \nabla \phi^j(\mathbf{r}) + \Delta N a \phi^i(\mathbf{r}) \phi^j(\mathbf{r}) \right] dV = 0 \Leftrightarrow \\
 & \sum_{j=1}^{\text{numnp}} q_{j,N+\Delta N} \int_V \left[\phi^i(\mathbf{r}) \phi^j(\mathbf{r}) + \Delta N D\nabla \phi^i(\mathbf{r}) \cdot \nabla \phi^j(\mathbf{r}) + \Delta N a \phi^i(\mathbf{r}) \phi^j(\mathbf{r}) \right] dV = \sum_{j=1}^{\text{numnp}} q_{j,N} \int_V \phi^i(\mathbf{r}) \phi^j(\mathbf{r}) dV
 \end{aligned} \tag{2.77}$$

Or in matrix-vector notation form, eq 2.77 is written as:

$$\mathbf{A}\mathbf{q}_{N+1} = \mathbf{C}\mathbf{q}_N \quad 2.78$$

where:

$$\mathbf{q}_N = [q_{1,N} \quad q_{2,N} \quad \cdots \quad q_{numnp,N}]^T$$

$$\mathbf{q}_{N+1} = [q_{1,N+1} \quad q_{2,N+1} \quad \cdots \quad q_{numnp,N+1}]^T$$

$$C_{ij} = \int_V \varphi^i(\mathbf{r})\varphi^j(\mathbf{r})dV$$

$$K_{ij} = \int_V D\nabla\varphi^i(\mathbf{r}) \cdot \nabla\varphi^j(\mathbf{r})dV$$

$$W_{ij} = \int_V a\varphi^i(\mathbf{r})\varphi^j(\mathbf{r})dV$$

$$\mathbf{A} = \mathbf{C} + \Delta N\mathbf{K} + \Delta N\mathbf{W}$$

So, in transient FEM analysis, we need to solve a (large) linear system of equations in order to compute the solution, $q_{j,N+\Delta N}$, knowing the solution at the previous time-step, $q_{j,N}$. Besides boundary conditions, initial conditions, $q_{j,0}$ are imperative for the numerical solution of the PDE.

2.4.3. Integration via Gauss-quadrature

In this paragraph, we sketch the integration procedure which is most commonly used in the context of the FEM, namely the *Gauss Quadrature* method. In the previous section, we started from the *strong* form of the *Edwards* diffusion equation and, after some mathematical considerations, we ended up with the *weak* form of the differential equation. In order to solve the *weak* form and obtain its numerical solution, \mathbf{q} , we first need to evaluate a set of integrals and assembly the matrices \mathbf{A} and \mathbf{C} appearing in eq 2.78. In all these integrals, the integrand depends exclusively on the *basis* functions that we use to discretize the domain and the solution and their derivatives. These *basis* functions are defined in *natural coordinates*, i.e., the coordinates of the nodes of the standard element. This offers the advantage that all these integrals appearing in the *weak* formulation can be readily evaluated using a *Gauss Quadrature* numerical scheme.

Let us denote by ξ the natural coordinates of the standard element and \mathbf{r} the real coordinates in the domain of interest. For the case of first order tetrahedral elements, the vector ξ comprises four elements. Therefore, each coordinate system is defined as follows:

$$\begin{aligned} \mathbf{r} &= [x \quad y \quad z], x, y, z \in \mathcal{R} \\ \xi &= [\xi_1 \quad \xi_2 \quad \xi_3 \quad \xi_4 = 1 - \xi_1 - \xi_2 - \xi_3], \xi_1, \xi_2, \xi_3, \xi_4 \in [0, 1] \end{aligned} \quad 2.79$$

The problem is that the actual elements that are used for the discretization of the domain have not the shape of the standard elements, where the *basis* functions are defined (eq 2.80) and the *Gauss Quadrature* can be applied.

$$\begin{aligned} \varphi_1(\xi_1, \xi_2, \xi_3, \xi_4) &= \xi_1 \\ \varphi_2(\xi_1, \xi_2, \xi_3, \xi_4) &= \xi_2 \\ \varphi_3(\xi_1, \xi_2, \xi_3, \xi_4) &= \xi_3 \\ \varphi_4(\xi_1, \xi_2, \xi_3, \xi_4) &= \xi_4 \end{aligned} \quad 2.80$$

Furthermore, the nodal points constituting the actual elements are defined in *real coordinates*. In fact, the difference in shape of the domain elements from the standard element is usually quantified as the *element quality* of the mesh. When a complex geometry part is meshed with a small number of elements, they need to stretch/deform in order to capture the anomalies of the geometry and this results in poor element quality. In those cases, the number of elements (and hence nodal points) needs to be increased, so that the smaller elements are closer in shape to their standard models. Nevertheless, there will always be a deviation of the actual elements from their standard shape and the nodal points will be defined in *real* instead of *natural* coordinates.

A mechanism is therefore needed to perform a transition from real to natural coordinates and be able to perform the *Gauss Quadrature*. The mathematical operation that lets us map the *basis* functions and elements from *real* to *natural* coordinates and vice-versa, is called *isoparametric transformation* and it is defined by the following eq 2.81.

$$\mathbf{r}(\xi) = \sum_{i=1}^4 \varphi_i(\xi) \mathbf{r}^i \quad 2.81$$

and the Jacobian of the transformation in eq 2.81 (from *natural* to *real* coordinates) is defined by the matrix of eq 2.82 below.

$$\mathbf{J} = \frac{\partial \mathbf{r}}{\partial \xi} = \begin{pmatrix} \frac{\partial x}{\partial \xi_1} & \frac{\partial x}{\partial \xi_2} & \frac{\partial x}{\partial \xi_3} & \frac{\partial x}{\partial \xi_4} \\ \frac{\partial y}{\partial \xi_1} & \frac{\partial y}{\partial \xi_2} & \frac{\partial y}{\partial \xi_3} & \frac{\partial y}{\partial \xi_4} \\ \frac{\partial z}{\partial \xi_1} & \frac{\partial z}{\partial \xi_2} & \frac{\partial z}{\partial \xi_3} & \frac{\partial z}{\partial \xi_4} \end{pmatrix} \quad 2.82$$

Similarly, the solution q at a certain point of the domain in *real coordinates* can be associated with the standard element via the following eq 2.83.

$$q(\xi) = \sum_{i=1}^4 \varphi_i(\xi) q^i \quad 2.83$$

where q^i is the solution of the PDE at the nodal point i of the domain. Finally, in order to calculate the integral of q with *Gauss Quadrature*, we use the following eq 2.84.

$$Q = \int_{\mathcal{R}} q(\mathbf{r}) d\mathbf{r} = \sum_{i=1}^{numel} \int_e q(\xi) \mathbf{J} d\xi = \sum_{i=1}^{numel} \sum_{j=1}^{num_{GP}} w_{GP}(\xi_{GP}) q(\xi_{GP}) \mathbf{J} \quad 2.84$$

where $numel$ is the total number of elements used for discretizing the domain of interest, num_{GP} is the number of *Gauss* points used for integrating a quantity via *Gauss Quadrature*, w_{GP} is the weight of the *Gauss* point which finds itself in *natural coordinates* ξ_{GP} inside the current element e , and q is the value of the *propagator* (or any other integrated quantity) at *natural coordinates* ξ_{GP} .

3. RUSSEL

3.1. Description

The parameters of a theoretical calculation with *RuSseL* are set in an input file which is parsed line-by-line by a dedicated subroutine, when the runtime execution of the programs starts. The parsing subroutine searches for special *identifiers* that are related to certain variables needed for execution. In cases where an input line lacks any special identifier, it is either skipped or the variable corresponding to the identifier is assigned a default value; therefore, with few exceptions, the order of the commands in the input file does not matter. In addition, the parser has been equipped with an error handling section, which checks **(i)** whether the user has specified all imperative variables, such as the temperature, T , or the mass density of the bulk polymer, $\rho_{\text{seg.bulk}}$, **(ii)** the viability of user input regarding the specified variables, e.g., both temperature, T , and mass density, $\rho_{\text{seg.bulk}}$ must be given values that are greater than zero. If an issue is encountered while parsing the input file, the code prints a relevant error message and terminates execution. If solid surfaces are present, then the parameters of the polymer and the solid related to their interaction are also required.


```

-----POLYMER PARAMETERS-----
0.500000000D+03 # temp      [K]
0.000000000D+00 # pres      [atm]

0.953000000E+00 # mass den  [g/cm3]
0.522600000E+02 # mon mass  [g/mol]

3.970000000E-09 # isotherm compr [Pa^-1]

3.700000000E+00 # pol sigma [Angstrom]
5.840000000E+00 # pol ham   [10^-20 J]

1 # use matrix
3.840000000D+02 # chain length matrix [monomers]
0.389456247E+01 # Rg2/mon matrix   [Angstrom]

1 # use grafted
3.840000000D+02 # chain length grafted [monomers]
0.389456247E+01 # Rg2/mon grafted   [Angstrom]

```

Figure 3.1 *RuSseL* input file: specifying polymer parameters. The user specifies the temperature of the polymer melt along with other polymer related parameters such as: mass density, monomer mass and isothermal compressibility at given temperature. The length of matrix and grafted chains is also given along with the radius of gyration associated with a single monomer of the chain. In this specific example, we are running a calculation regarding polystyrene melt at 500 K.

The mass of the polymer chains and the coarse-graining degree are set by the molecular weight of the monomer unit constituting the polymer chains, m_{monomer} , whereas the radius of gyration of the chains is set indirectly based on the following relation 3.1.

$$\frac{\langle R_{g,c}^2 \rangle}{N_c} = \frac{1}{6} C_\infty l_{c-c}^2 \quad 3.1$$

with C_∞ being the characteristic ratio and l_{c-c} being the chemical bond length between consecutive polymer segments. These parameters are also defined by the user through the input file. Besides the characteristic ratio and the bond length, the user must also specify the length of the chains in terms of skeletal bonds along the backbone of the chain and the contour discretization scheme that will be used for the solution of *Edwards* (i.e., uniform, nonuniform or hybrid).

Next, the user has to specify the number of *Dirichlet* boundary faces that are present in the geometry and for each one of those, (s)he has to give the type (i.e., planar surface or spherical particle) and the id that has been assigned to the boundary during the meshing process. Furthermore, for each of these *Dirichlet* boundaries, the user must give the values of the parameters which are needed to determine the intensity of the solid/polymer interactions (Figure 3.2).

```

-----SOLID PARAMETERS-----
3.980000000E+00 # wall dist [A]
1 # num nanop
id      radius  x_center  y_center  z_center  sol sigma  sol ham
6      84.00000  0.00000  0.00000  0.00000  3.00000E+00  6.43000E+00

```

Figure 3.2 *RuSseL* input file: specifying solid parameters. User specifies the number and type of *Dirichlet* faces, i.e., planar vs spherical. In this specific example, a spherical nanoparticle is present in the system with radius 84 Å and the distance of the hard-sphere wall is set at 3.98 Å. The center of the particle is located at $(x_{\text{center}}, y_{\text{center}}, z_{\text{center}}) = (0.0, 0.0, 0.0)$ Å and its *Hamaker* parameters are equal to $\sigma_{\text{solid}} = 3.0$ Å and $A_{\text{solid}} = 6.43 \cdot 10^{-20}$ J. The spherical boundary surface representing the particle was assigned the id 6 by the mesher.

Afterwards, the FEM mesh which is used to discretize the 3D domain is imported. This mesh is externally created by the open-source mesher *GMSH*⁹³ and the code is designed to read it appropriately. There is also the possibility to read meshes created by *COMSOL* which are usually stored in a `.mpltxt` ASCII file. The mesh-file comprises the nodal coordinates, the element connectivity of the nodes and the identity of those nodes which lie in the boundaries where *Dirichlet* boundary conditions are imposed. Afterwards, we need to discretize the contour of the matrix and the grafted chains according to the contour scheme that has been selected by the user.

The cohesion of the polymer is specified by assigning an appropriate equation of state which is accompanied by necessary parameters, e.g., for *Helfand*, it is the isothermal compressibility κ_T ; for *Sanchez-Lacombe*, we need to specify the characteristic temperature (T^*), pressure (P^*) and density (ρ^*). So far, the code offers to possibility to run SCFT calculations using the *Helfand*,⁶⁵ and the *Sanchez-Lacombe*⁷³ equations of state. In addition, the free energy densities can be combined with a square gradient term to address gas/polymer interfaces more accurately.^{2,94} Nevertheless, the code has been written in a generic way, so that any other appropriate model can be inserted and used.²⁴ In general, our code is able to perform SCFT calculations for any thermoplastic polymer melt, given than an appropriate EoS and the relevant parameters are provided.

Subsequently, the user has to specify some parameters regarding the convergence of the field (Figure 3.3). Specifically, the user specifies the tolerance in the norm of the field and the energy of the system. When one of the two errors becomes lower than the corresponding tolerance, the equilibration procedure is considered to have converged. There is also the option to start a fresh calculation, where the field configuration is initialized to zero, or restart from an already existing field configuration, which is stored in binary format. In this section, the user also has to specify whether the stiffness matrix is expected to be symmetric or not, and if symmetric, if positive

definite or not. In every case considered in the context of this thesis, the stiffness matrix is symmetric and positive definite. For these definitions, the reader is referred to the reference manual of *MUMPS* or any advanced linear algebra textbook.

```
-----CONVERGENCE PARAMETERS-----
0.500000000E-00 # max error
0.001300000E-00 # fraction
1 # init field (0: zero everywhere; 1: read from file; 2: zero everywhere and -kapa at dir. BCs)
180 # init iter
181 # num iter
1 # mumps matrix (0: nonsymmetric; 1: symmetric def. pos.; 2: general symmetric)
```

Figure 3.3 *RuSseL* input file: specifying file convergence parameters. In this section, the field and energy error tolerance are specified along with the maximum number of iterations to achieve convergence. The user can also select to start a fresh calculation, where the field is initialized to zero everywhere inside the domain, or read an already existing field configuration from a binary file. Usually, the stiffness matrices occurring by the *weak* formulation of *Edwards* are symmetric and *positive definite*, but the user can also select a nonsymmetric option if not completely sure about the structure of the matrix to be fed in the solver of the linear system.

When the initialization stage is completed, the code enters the main part of the SCFT calculation, namely the field equilibration procedure. In every iteration, the stiffness matrices for the solution of *Edwards* for matrix and grafted chains are assembled according to the element connectivity. Afterwards, given the appropriate initial and boundary conditions, the *Edwards* PDE is solved using the open-source *MUMPS* solver v5.2.1.^{95,96} A useful feature of *RuSseL* is that the solution $q(\mathbf{r}, N)$ can be interpolated across the contour variable, N , of the chains. This offers the flexibility to work with different contour discretization for matrix and grafted chains for the solution of the PDE.

Afterwards, the new field configuration, $w'_{\text{new}}(\mathbf{r})$, is computed and compared to that of the previous iteration. For large chains or systems with low isothermal compressibility, κ_T , the aforementioned iterative scheme diverges, because the field becomes extremely steep along the considered interfacial region. Addressing this fact, a relaxation of the calculated field is performed by mixing it with a fraction of the field of the previous iteration, as shown in the following eq 3.2.

$$w'_{\text{mix}}(\mathbf{r}) = a_{\text{mix}} w'_{\text{new}}(\mathbf{r}) + (1 - a_{\text{mix}}) w'_{\text{old}}(\mathbf{r}) \quad 3.2$$

with a_{mix} being the relaxation parameter.

RuSseL is written in Fortran95 and there are thoughts of “translating” it in C++, which offers better feature development scalability and more friendly object-oriented features and data structures. It is written to support execution in both shared and distributed parallel systems using the broadly known *Message Passing Interface (MPI)*. Parallelization and scalability benchmarks are presented in Section 3.7.5.

3.2. Code Flow

Based on the resulting *restricted partition function*, q_c , which is obtained by solving the *Edwards* PDE 2.2, one can compute the spatial density distributions of chain segments using eq 3.3, which in turn dictates an updated configuration of the *chemical potential* field, w' , according to eq 2.8. The iterative field convergence procedure can be summarized as follows:

1. Parse the input file and set up the essential parameters of the SCFT calculation.
2. Decide what the initial configuration of the field will be: either equal to zero everywhere or imported from file, in order to continue from a specific configuration.
3. Equation 2.2 is solved for the matrix chains of length N_m , applying the initial condition of eq 2.3 and boundary conditions of eq 2.5.
4. Equation 2.2 is solved for the grafted chains of length N_g , applying the initial conditions of eq 2.4 and boundary conditions of eq 2.5. For details regarding the numerical calculation of the delta function at each grafting point, the reader is referred to Section **3.6.2.1**.
5. Determine the density profiles of matrix, ϕ_m , and grafted, ϕ_g , chain segments using eq 3.3.
6. Update the spatial configuration of the field, w' , using eq 2.8.
7. Calculate the free energy of the system using eq 2.38.
8. Repeat steps **3** to **6** until the energy difference between two successive SCF iterations has been achieved.

In Figure **3.4** below, we present the flow diagram of the three-dimensional version of *RuSseL*, which consists of two main parts: the initialization stage (yellow background, left) and the iterative stage (blue background, right).

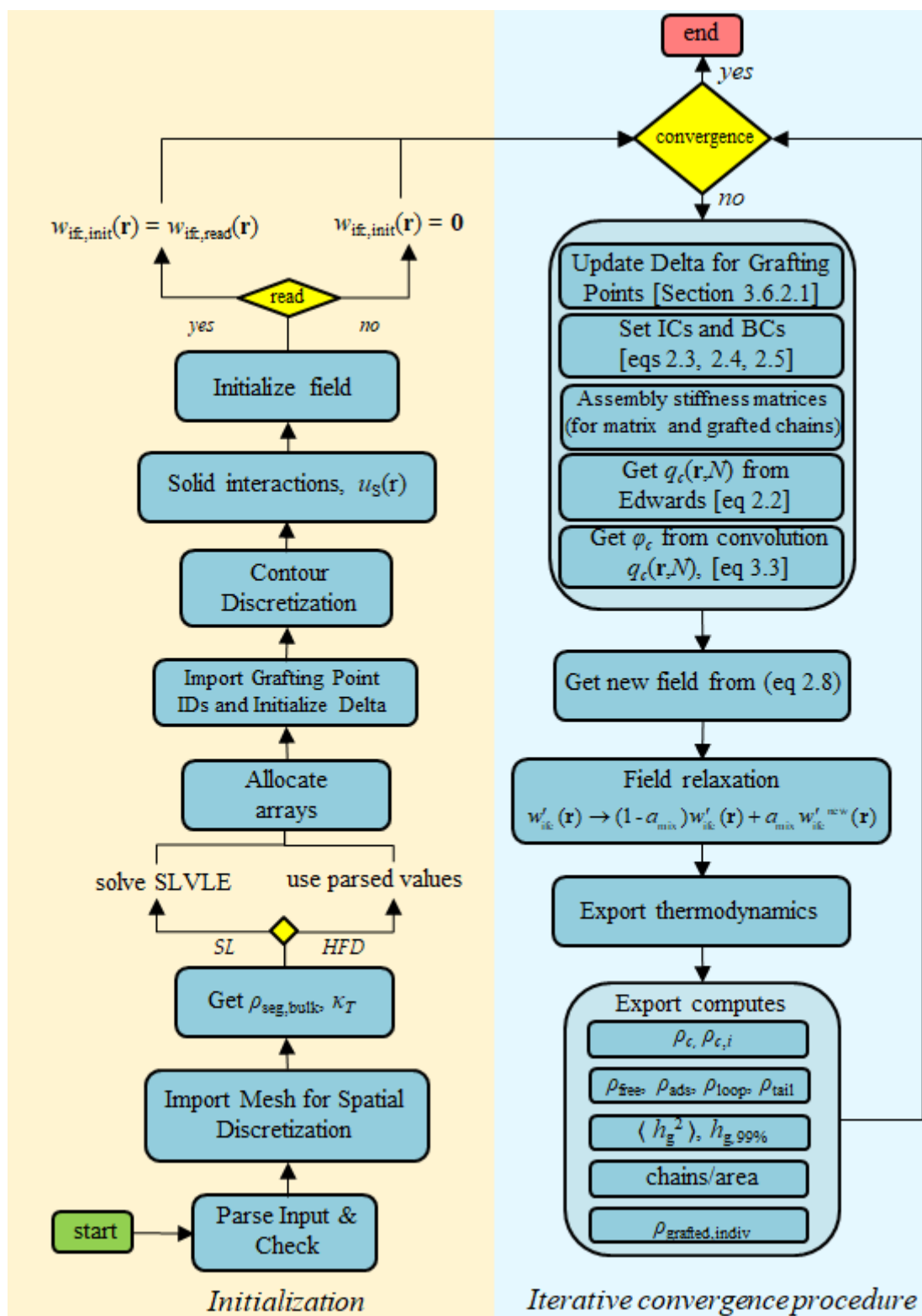


Figure 3.4 Flow diagram of RuSseL3D.

3.3. Commercial software vs RuSseL

When we first started running SCFT calculations, we addressed systems comprising exclusively matrix chains. In order to solve the *Edwards* PDE, we used the FEM as implemented by mainstream commercial software. The most challenging part when including grafted chains in the system is the initial condition of eq 2.4. Because the commercial software would not let us assign initial conditions on individual points of the mesh (which is necessary for introducing grafted chains in the SCFT mathematical model, according to eq 2.4), we opted to approximate *Dirac*-delta functions with *Gaussian* distributions of a certain standard deviation. For instance, in Figure 3.5a, we depict the density profiles of matrix and grafted chains in a molten polyethylene film sandwiched between repulsive solid walls. All chains had length equal to $N_m = N_g = 100$ skeletal bonds and the simulation temperature was equal to 450 K. The simulation box had size equal to $8 \times 80 \times 10 \text{ nm}^3$. In Figure 3.5b, we present the density profiles of polystyrene melt of $N_m = 100$ skeletal bonds at $T = 500 \text{ K}$ in a spherical geometry.

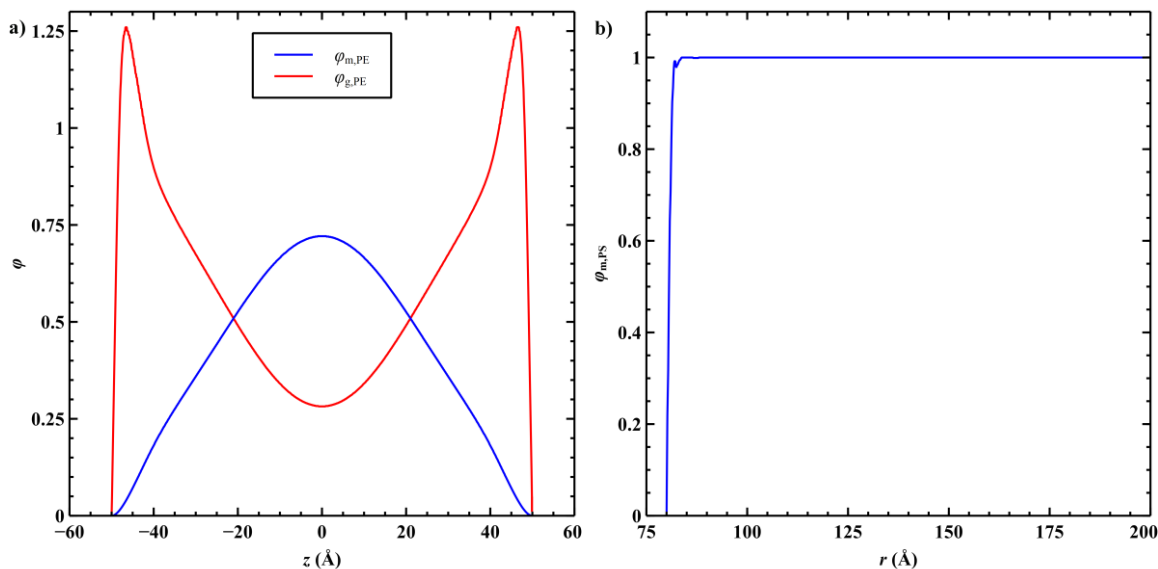


Figure 3.5 Density profiles of matrix and grafted chains in a polyethylene film. **a)** Reduced segment density profiles of grafted and matrix chains in a polyethylene film sandwiched between repulsive solid surfaces bearing terminally grafted polyethylene chains. The grafting density was equal to 0.15 nm^{-2} , corresponding to 9 grafted chains per flat surface. Temperature was equal to 450 K (isothermal compressibility, $\kappa_T = 1.43 \text{ GPa}^{-1}$) and the simulation box had size $8 \times 80 \times 10 \text{ nm}^3$. Both matrix and grafted chains had length equal to $N_m = N_g = 100$ skeletal carbon bonds. In order to obtain this solution, a spatial mesh of $\sim 5 \cdot 10^5$ mesh points and 100 chain contour points had to be used. **b)** Segment density profile of polystyrene matrix chains in contact with a spherical repulsive wall of radius equal to 8 nm. All chains had length equal to $N_m = 100$ skeletal carbon bonds and the temperature was equal to 500 K (isothermal compressibility, $\kappa_T = 1.07 \text{ GPa}^{-1}$). The simulation box had size $20 \times 20 \times 20 \text{ nm}^3$. This was the best density configuration that we were able to obtain and it required a spatial discretization of $9 \cdot 10^5$ mesh points, because of the lower isothermal compressibility of polystyrene. Polystyrene chains were also discretized with 100 contour points.

We faced some technical difficulties in solving our problem by means of commercial software. The main problem was the bad interpolation that it applied to the imported updated field configuration. As a consequence of this bad interpolation, an extremely dense mesh (roughly $9 \cdot 10^5$ mesh points) had to be used to clear out the noise in the calculated profiles, which led to a high computational cost per iteration (above 50 min for simple free-film systems).

No matter how hard we tried during the first year of this PhD thesis, we could not circumvent the interpolation performed automatically by the commercial software or assign values directly to individual points of the mesh. Another significant issue arose from the substitution of delta functions with *Gaussian* distributions. Despite the fact that the latter are infinitely differentiable, they impose a maximum grafting density that can be set in the calculation; increasing the grafting density means that we need to reduce the standard deviation of the *Gaussian* distributions so that they do not overlap. Reduction of the standard deviation of *Gaussian* pulses needs to be accompanied by a refinement of both the spatial mesh and the contour mesh of the chains, otherwise the solution of the PDE will not converge due to numerical issues.

In our code, *RuSseL*, which we control fully, we are able to set the grafting points exactly the way we wish. All solution steps are implemented in the same code, i.e., solution of *Edwards*, *propagator* convolution, and update of the field configuration based on an appropriate equation of state. This also enables us to run our field-iterative scheme without being dependent on external packages, e.g., *Matlab*, to feed the post-processed PDE solution back to the main software solving the PDE. This fact leads to considerable profit related to data I/O.

3.4. Calculated properties

3.4.1. Total and partial segment density profiles

To begin with, having obtained the propagators q_m and q_g from the solution of eq 2.2, the density profiles of matrix and grafted chain segments, $\varphi_m(\mathbf{r})$ and $\varphi_g(\mathbf{r})$, respectively, are calculated via the convolution eq 3.3. The total reduced segment density is just the sum of φ_m and φ_g . Such reduced segment density profiles are presented in the following Figure 3.6 and Figure 3.7. Having calculated the reduced profile φ , the corresponding segmental or mass density profiles can be retrieved by multiplying φ with $\rho_{\text{seg,bulk}}$ or $\rho_{\text{mass,bulk}}$ of the polymer melt, respectively.

$$\varphi_c(\mathbf{r}) = \frac{1}{N_c} \int_0^{N_c} dN q_c(\mathbf{r}, N) q_m(\mathbf{r}, N_c - N) \quad 3.3$$

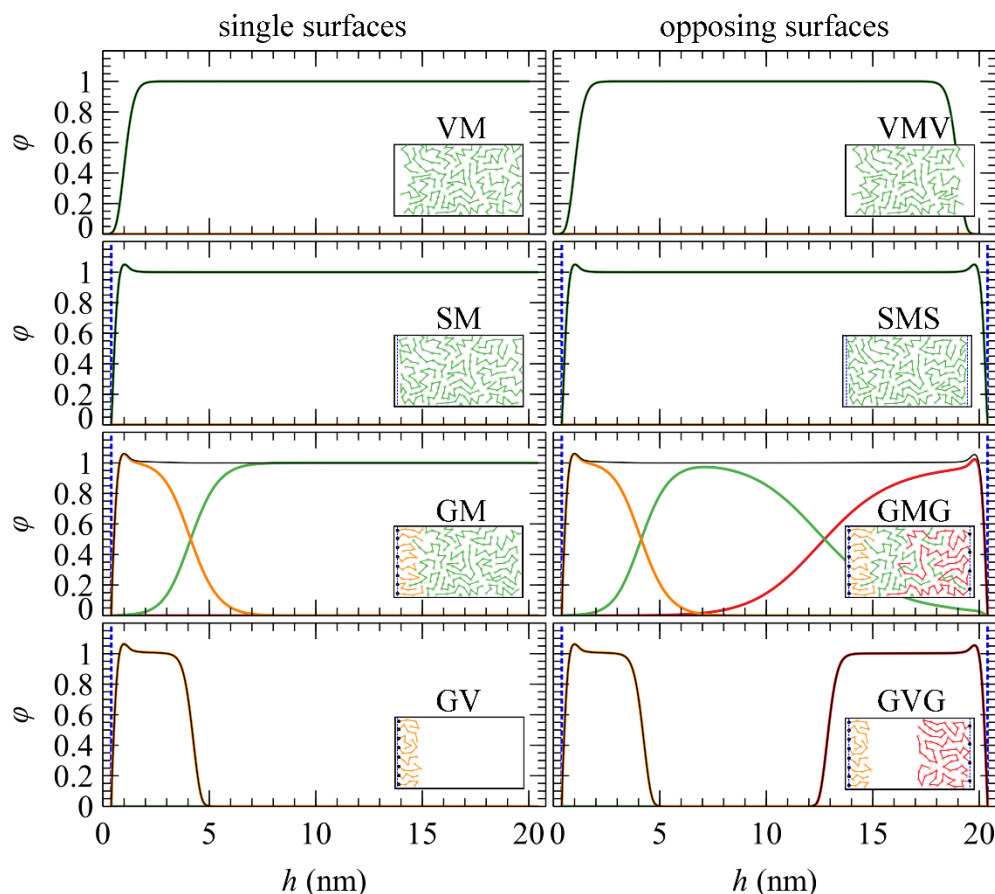


Figure 3.6 Density profiles of matrix and grafted chains in various kinds of planar interfaces. Reduced segment density profiles of matrix (m, green) and grafted (g^- : orange, g^+ : red) chains which are in contact with planar solid surfaces. The panels on the left/right correspond to single/opposing (VM/VMV) vacuum-matrix, (SM/SMS) solid-matrix, (GM/GMG) grafted-matrix, and (GV/GVG) grafted-vacuum interfaces; V: vacuum, S: solid, G: grafted, and M: matrix. The insets depict graphical representations of each system; the dots represent grafting points, and the vertical lines denote the boundaries where *Dirichlet* boundary conditions, $q_c = 0$, are imposed. The polymer-grafted surfaces (G) at the left and right boundaries exhibit grafting densities and grafted chain lengths equal to $(\sigma_g^-, N_g^-) = (0.8 \text{ nm}^{-2}, 50 \text{ skeletal bonds})$ and $(\sigma_g^+, N_g^+) = (0.4 \text{ nm}^{-2}, 200 \text{ skeletal bonds})$, respectively. The distance between the boundaries of the domain was set to $L = 20 \text{ nm}$. Matrix chains have a chain length equal to 100 skeletal bonds. Solid/polymer interactions correspond to perfectly wetting polystyrene films with the hybrid *Hamaker-ramp* potential (see Section 2.1.5) at a temperature equal to $T = 500 \text{ K}$ (for parameter values, see Table 4-2).

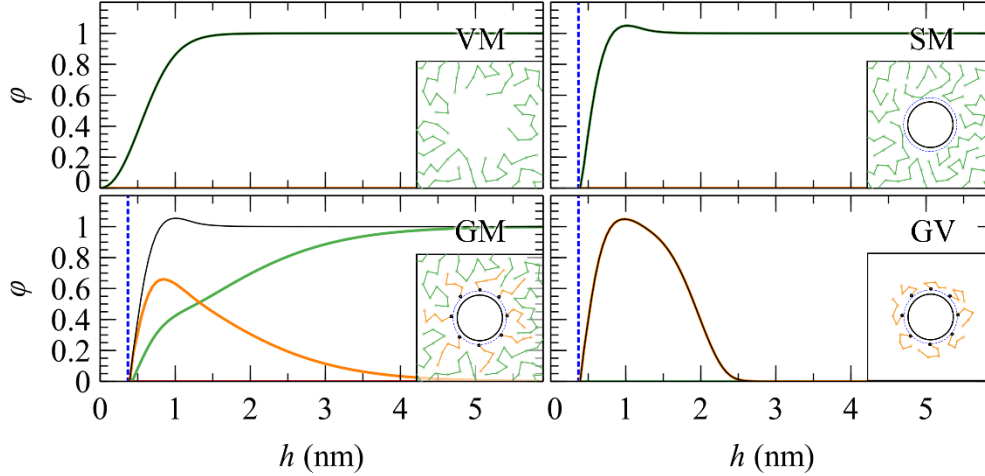


Figure 3.7 Density profiles of matrix and grafted chains in various kinds of spherical interfaces. The physical systems are (VM) spherical cavity, (SM) polymer melt/smooth nanoparticle, (GM) polymer melt/grafted nanoparticle, and (GV) a grafted nanoparticle in vacuum. In all cases, the radius of the nanoparticle/cavity is equal to 2 nm.

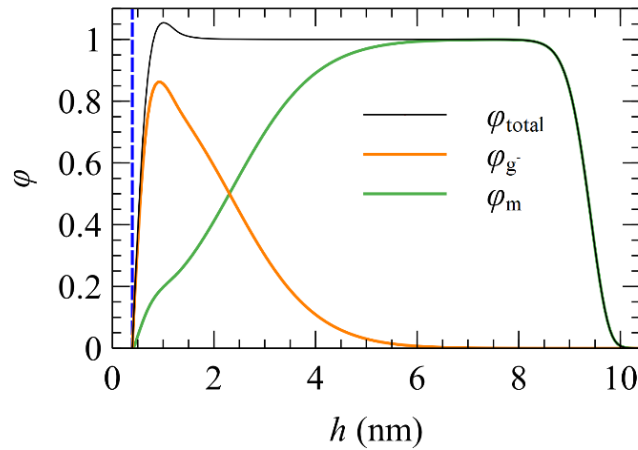


Figure 3.8 Total and partial reduced segment density profile of a perfectly wetted SiO₂/PS GMV system. For parameter values, see Table 4-2. Grafting density is $\sigma_g = 0.4 \text{ nm}^{-2}$, length of grafted chains $N_g = 50$ skeletal bonds and length of matrix chains $N_m = 100$ skeletal bonds.

3.4.2. Brush thickness

The dimensions of the grafted brush can be quantified in terms of the root mean squared brush thickness, which is calculated with eq 3.4; it is a functional of the density profile and corresponds to the rms distance of grafted chain segments from the solid surface.

$$\langle h_g^2 \rangle^{1/2} = \left[\frac{\int_{\mathcal{R}} d\mathbf{r} [h(\mathbf{r})]^2 \rho_g(\mathbf{r})}{\int_{\mathcal{R}} d\mathbf{r} \rho_g(\mathbf{r})} \right]^{1/2} \quad 3.4$$

In eq 3.4, $h(\mathbf{r})$ is the distance between a segment located at \mathbf{r} and the solid surface. Another frequently used measure for quantifying the thickness of the brush is the characteristic distance $h_{99\%}$, which is the distance between the center of the NP and a surface, $\partial\mathcal{R}_{h_{99\%}}$, parallel to the surface of the NP, which encloses 99% of grafted chain segments (eq 3.5).

$$\int_{\mathcal{R}_{99\%}} d\mathbf{r} \rho_g(\mathbf{r}) = 0.99 N_g n_g \quad 3.5$$

with $\mathcal{R}_{99\%}$ being the three-dimensional domain enclosed between $\partial\mathcal{R}_{\text{solid}}$ and $\partial\mathcal{R}_{h_{99\%}}$.

3.4.3. Profiles of individual chain segments

RuSseL allows for decomposition of the density profiles into contributions of individual chain segments, such as chain ends and middle segments.^{2,72,97} The contribution of the N^{th} segment to the corresponding density profile of the kind- c chain can be retrieved by the following eq 3.6.

$$\varphi_{c,N}(\mathbf{r}) = \frac{1}{N_c} q_c(\mathbf{r}, N) q_m(\mathbf{r}, N_c - N) \quad 3.6$$

Setting N to 1 or N_c results in the density profile of the end segments, which can be a useful measure of the tendency of chains ends to segregate at the interfaces.^{2,24,72} Setting $N = N_c/2$, on the other hand, results in the reduced density profiles of middle segments; comparisons between end and middle segment profiles provide useful information regarding the overall shape of the chains.²

Figure 3.9 depicts the segmental density profiles, $\varphi_{c,N}$, for the chain ends ($N = 1, N_c$) and middle segments ($N = N_c/2$) of grafted and matrix chains. The first segment of the grafted chains ($N = 1$) corresponds to the grafting point and features a sharp peak at $h = h_g$. The middle and the last end segment of the grafted chains exhibit continuous density profiles, and the latter spreads further towards the matrix region. The density profiles of matrix chain segments are suppressed in the vicinity of the grafted chains, since the latter reduce the available accessible space. Unlike grafted chains, the two end segments of the matrix chains are equivalent due to symmetry, hence their corresponding distributions are identical, $\varphi_{m,1} = \varphi_{m,N_m}$. The ends of the matrix chains feature more pronounced profiles near the interfaces compared to the middle segments.

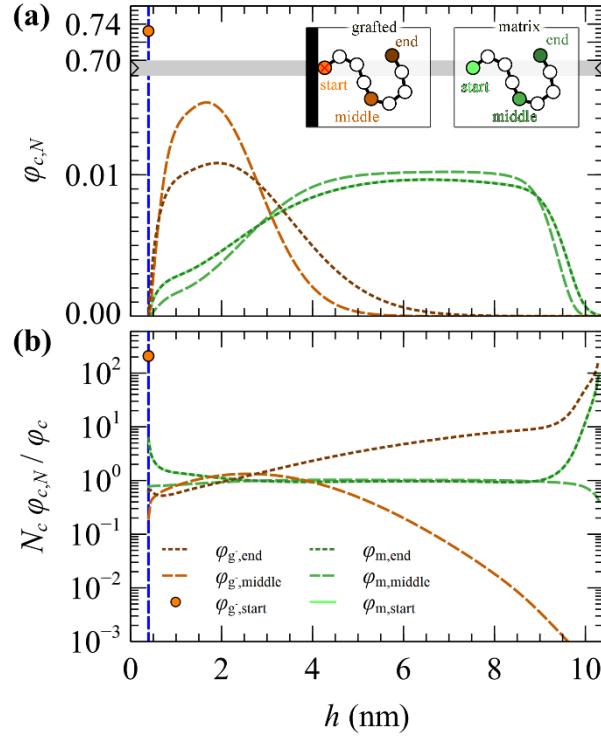


Figure 3.9 End/middle density profiles of grafted and matrix chains in a perfectly wetted SiO₂/PS interface. (a) Reduced density profiles of starting, middle and end segments of grafted and matrix chains; (b) the corresponding normalized distributions obtained via eq 3.7. Insets illustrate schematically the starting, middle and end segments of grafted and matrix chains. The profiles concern a perfectly wetted SiO₂/PS interface (for parameter values, see Table 4-2) with grafting density $\sigma_g = 0.4 \text{ nm}^{-2}$, length of grafted chains $N_g = 50$ skeletal bonds and length of matrix chains $N_m = 100$ skeletal bonds.

The tendency of chain segments to segregate at the interface(s) can be better quantified in terms of the normalized segment distribution, which is calculated via the following eq 3.7. The reduced density of the N^{th} segment of the chain is expressed relative to the total segment density of kind c chains (eq 3.7), consequently, in a bulk polymer phase, $\tilde{\varphi}_{c,N} = 1$.

$$\tilde{\varphi}_{c,N}(\mathbf{r}) = \frac{N_c \varphi_{c,N}(\mathbf{r})}{\varphi_c(\mathbf{r})} \quad 3.7$$

According to Figure 3.9b, the segment density profiles of matrix chains become $\tilde{\varphi}_{c,N} = 1$ across the bulk region. Near the solid/polymer and polymer/vacuum interfaces, the profiles of end segments of matrix chains are enhanced significantly by $\tilde{\varphi}_{m,1} \sim 6$ and $\tilde{\varphi}_{m,N_m} \sim 100$, respectively, whereas the profiles of middle segments are slightly less than the bulk value, $\tilde{\varphi}_{m,N_m/2} < 1$. The corresponding profiles for the two ends belonging to grafted chains are highly asymmetric, since $\tilde{\varphi}_{g,1} \sim 210$ and $\tilde{\varphi}_{g,N_g} \sim 0.6$ at the grafting point, while $\tilde{\varphi}_{g,1} \sim 0$ and $\tilde{\varphi}_{g,N_g} \sim 180$ at the edge of the free surface. The middle segments of grafted chains exhibit suppressed profiles

at the interfaces and over most of the region occupied by matrix chain segments. This effect regarding middle segments is much more pronounced than for matrix chains; at the polymer-vacuum interface, $\tilde{\varphi}_{g,N_g/2} \ll 1$.

Besides the end and middle segments, *RuSseL* gives the option to export the density profile of any other segment specified by the user. The contour plots presented in the following Figure **3.10** depict $\varphi_{c,N}$ and $\tilde{\varphi}_{c,N}$ for all segments belonging to grafted and matrix chains.

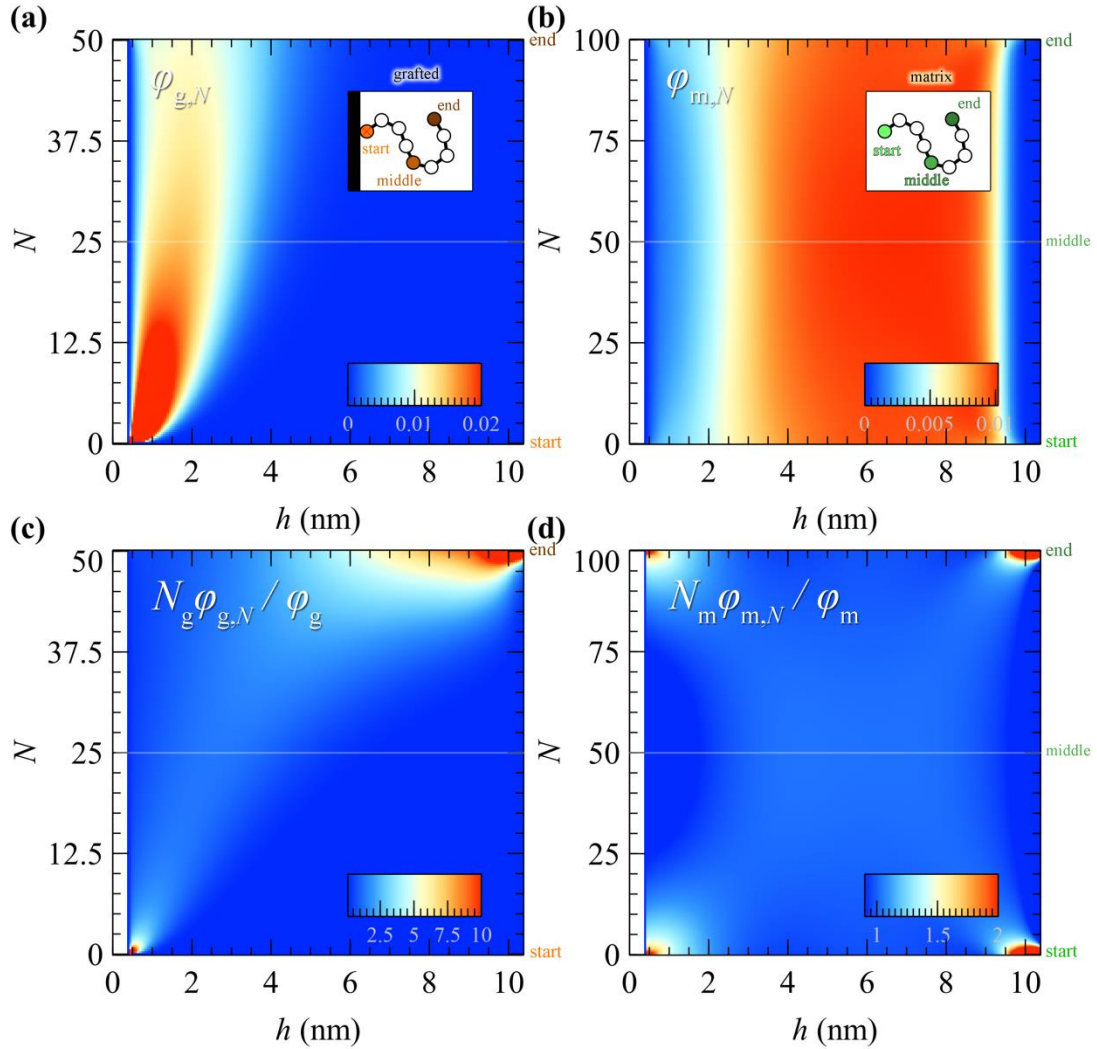


Figure 3.10 Contour plots of the reduced density of segments belonging to (a) grafted and (b) matrix chains. The ordinate indicates the index of each segment along the contour of the chain, whereas the abscissa is the distance of the segment from the left solid surface. Blue/red color corresponds to low/high values of the displayed quantity, as denoted by the color bars. The contour plots in (c) and (d) depict the corresponding normalized segmental density profiles, defined in eq 3.7. All profiles concern a perfectly wetting SiO₂/PS GMV interface (for parameter values, see Table 4-2) with grafting density $\sigma_g = 0.4 \text{ nm}^{-2}$, length of grafted chains $N_g = 50$ skeletal bonds, length of matrix chains $N_m = 100$ skeletal bonds. The horizontal line is a guide to the eye; it crosses the region corresponding to middle segments.

3.4.4. Adsorbed vs free chain segments

RuSseL offers the option to decompose the density profiles into contributions of *adsorbed* and *free* segments based on segment-surface distance criteria. Essentially, whenever a chain segment lies at a distance lower than h_{ads} from the surface, it is classified as *adsorbed* to the surface. This is purely a geometric distinction based on a critical distance from the solid surface, which is defined by the user through the input file. There are several approaches to setting the critical distance, depending on the specific application, namely:

- Solid adsorption: h_{ads} can be tuned based on the peaks of the density profile (e.g., in ref ⁹⁸, h_{ads} was set equal to 0.6 nm, which is the distance between the first two peaks of the polyethylene/graphite density profile), or based on the strength of solid/polymer interactions (e.g., in ref ²⁸, h_{ads} was set equal to 1.28 nm, where the PS/silica interactions, as described by the *Hamaker* potential, become extremely weak).

- Segregation at polymer/vacuum interfaces: in ref 2, h_{ads} was set equal to a distance where the reduced density φ reaches the value 0.5.

- Brush penetration: h_{ads} can also be set to the span of the grafted brush, $h_{\text{g},99\%}$, in order to quantify the tendency of the matrix chains to penetrate the brushes, or the tendencies of opposing brushes to penetrate each other.

Based on the distribution of *adsorbed* and *free* segments of a chain, it is possible to classify the chain into several states and sub-states, which are reported in Table 3-1.

A chain that is comprised entirely of free segments is classified as *free* (f); otherwise, in case it includes *adsorbed* segments, it is treated itself as *adsorbed* (a^{\pm}). *Adsorbed* chains can be further classified into fully (a_{full}^{\pm}) and partially *adsorbed* (a_{part}^{\pm}). Moreover, the *free* segments belonging to partially *adsorbed* chains can be classified into *free loops* ($a_{\text{loop}_f}^{\pm}$) and *free tails* ($a_{\text{tail}_f}^{\pm}$). In the same way, *adsorbed* segments belonging to *adsorbed* chains can be classified into *adsorbed loops* ($a_{\text{loop}_a}^{\pm}$) and *adsorbed tails* ($a_{\text{tail}_a}^{\pm}$). *Adsorbed* chain segments can be further characterized as *trains* or *bridges*.^{2,66,98,99} As can be imagined, grafted chains cannot be classified to be *free*, since in most cases, the grafting points are located below h_{ads} ; nevertheless, this classification procedure can unveil meaningful sub-states, such as fully and partially *adsorbed* grafted chains, as well as grafted *bridges*.

Figure 3.11 demonstrates some representative examples, whereas Figure 3.12 depicts the density profiles of the aforementioned states for a perfectly wetted SMS system (for parameter values, see Table 4-2), where the adsorption distance is set at 6 nm for both the left and the right plate, i.e., $h_{\text{ads}}^- = h_{\text{ads}}^+ = 6 \text{ nm}$.

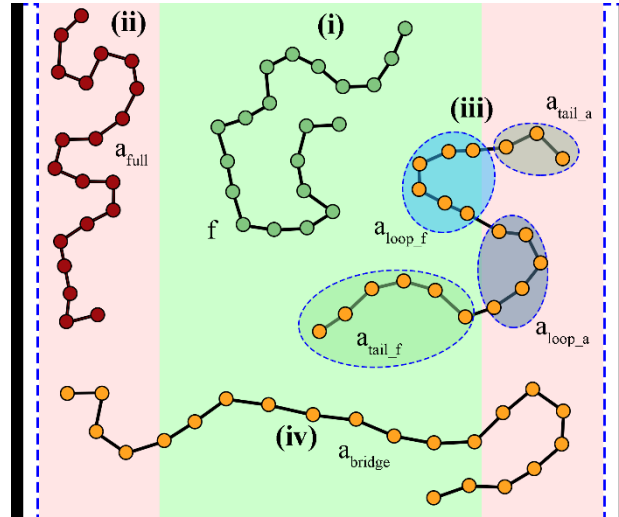


Figure 3.11 Schematic representation of the *adsorbed* states of a chain. Illustration of a (i) *free* chain, f , (ii) a fully *adsorbed* chain to the left surface, a_{full}^- , (iii) a partially *adsorbed* chain to the right surface, a_{part}^+ , which features *loops* and *tails* outside ($a_{\text{loop}_f}^+$, $a_{\text{tail}_f}^+$) and inside ($a_{\text{loop}_a}^+$, $a_{\text{tail}_a}^+$) the adsorption region, and (iv) a chain that is partially *adsorbed* on both surfaces forming a *bridge*, a_{bridge} .

The first step of the classification procedure is to calculate the *restricted partition functions* of *free* (q_c^f), fully *adsorbed* ($q_c^{\text{a}_{\text{full}}^-}$, $q_c^{\text{a}_{\text{full}}^+}$), and *non-adsorbed* ($q_c^{\text{la}^-}$, $q_c^{\text{la}^+}$) chains with respect to the left (–) and the right (+) surface; e.g., see Figure 3.12a. It is stressed that a chain which is not *adsorbed* on a specific surface is not necessarily *free*, since it might be *adsorbed* on the opposing surface.

To calculate each one of these *propagators*, the *Edwards* diffusion eq 2.2 is solved with the additional constraint that the *Dirichlet* boundary condition, $q_c(h, N) = 0$, is set to all the nodes which find themselves at distance, h , within the ranges specified at the rightmost column of Table 3-1. In other words, *Edwards* is solved in such a way that chain segments are prevented from accessing these regions of the domain. Subsequently, the density profiles corresponding to these states and sub-states are determined via convolution integrals and their relations specified in Table 3-1 below.

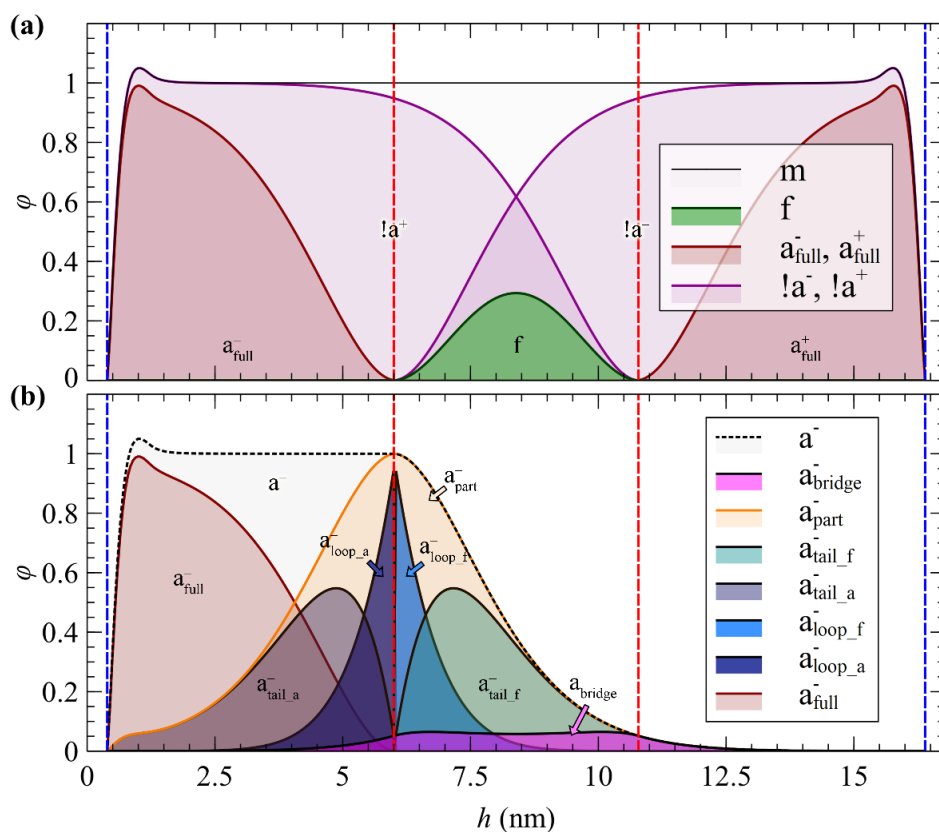


Figure 3.12 Density profiles of chain segments belonging to different *adsorbed* states. **(a)** Reduced segment density profiles of *free* (f), fully *adsorbed* (a_{full}^{\pm}), and *non-adsorbed* ($!a^{\pm}$) chains with respect to the left ($-$) and right ($+$) solid surfaces indicated by the dashed red lines. **(b)** Profiles of chains *adsorbed* on the left surface, decomposed into contributions of fully and partially *adsorbed* chains, *loops*, *tails*, and *bridges*. The profiles were obtained from a perfectly wetted SiO_2/PS SMS system (for parameter values, see Table 4-2) with grafting density, $\sigma_g = 0.4 \text{ nm}^{-2}$, length of grafted chains, $N_g = 50$ skeletal bonds, length of matrix chains, $N_m = 100$ skeletal bonds.

3.4. Calculated properties

Table 3-1 Reduced densities, *partition functions*, and constraints for evaluating each state and sub-state regarding *adsorbed* and *free* chain segments.

State	Symbol (α)	Reduced Segment Density	Restricted Part. Function	Dirichlet Nodes, $q_c(h, N) = 0$
<i>free</i>	f	$\varphi_c^f = C(q_c^f, q_c^f, N_c, h)$	q_c^f	$h \in [0, h_{\text{ads}}^-] \cup [h_{\text{ads}}^+, L]$
<i>adsorbed</i> fully	$\mathbf{a}_{\text{full}}^\pm$	$\varphi_c^{\mathbf{a}_{\text{full}}^\pm} = C(q_c^{\mathbf{a}_{\text{full}}^\pm}, q_c^{\mathbf{a}_{\text{full}}^\pm}, N_c, h)$	$q_c^{\mathbf{a}_{\text{full}}^\pm}$	$h \in [h_{\text{ads}}^-, L]$ or $h \in [0, h_{\text{ads}}^+]$
<i>not adsorbed</i>	$\mathbf{!a}^\pm$	$\varphi_c^{\mathbf{!a}^\pm} = C(q_c^{\mathbf{!a}^\pm}, q_c^{\mathbf{!a}^\pm}, N_c, h)$	$q_c^{\mathbf{!a}^\pm}$	$h \in [0, h_{\text{ads}}^-]$ or $h \in [h_{\text{ads}}^+, L]$
<i>adsorbed</i>	\mathbf{a}^\pm	$\varphi_c^{\mathbf{a}^\pm} = \varphi_c - \varphi_c^{\mathbf{!a}^\pm}$	-	-
<i>adsorbed</i> partially	$\mathbf{a}_{\text{part}}^\pm$	$\varphi_c^{\mathbf{a}_{\text{part}}^\pm} = \varphi_c^{\mathbf{a}^\pm} - \varphi_c^{\mathbf{a}_{\text{full}}^\pm}$	-	-
<i>loops</i>	$\mathbf{a}_{\text{loop}}^\pm$	$\varphi_c^{\mathbf{a}_{\text{loop}}^\pm} = C(q_c^{\mathbf{a}_{\text{loop}}^\pm}, q_c^{\mathbf{a}_{\text{loop}}^\pm}, N_c, h)$	$q_c^{\mathbf{a}_{\text{loop}}^\pm} = q_c - q_c^{\mathbf{!a}^\pm} - q_c^{\mathbf{a}_{\text{r}}^\pm}$	-
<i>tails</i> outside the <i>adsorbed</i> region	$\mathbf{a}_{\text{tail}_f}^\pm$	$\varphi_c^{\mathbf{a}_{\text{tail}_f}^\pm} = 2C(q_c^{\mathbf{a}_{\text{loop}}^\pm}, q_c^{\mathbf{!a}^\pm}, N_c, h)$	-	-
<i>tails</i> inside the <i>adsorbed</i> region	$\mathbf{a}_{\text{tail}_a}^\pm$	$\varphi_c^{\mathbf{a}_{\text{tail}_a}^\pm} = 2C(q_c^{\mathbf{a}_{\text{loop}}^\pm}, q_c^{\mathbf{a}_{\text{full}}^\pm}, N_c, h)$	-	-
<i>bridges</i>	$\mathbf{a}_{\text{bridge}}$	$\varphi_c^{\mathbf{a}_{\text{bridge}}} = \varphi_c^{\mathbf{a}^-} + \varphi_c^{\mathbf{a}^+} + \varphi_c^f - \varphi_c$	-	-

It is noted that $\mathbf{a}_{\text{loop}}^\pm$ states corresponding to *free* or *adsorbed* segments are denoted as $\mathbf{a}_{\text{loop}_f}^\pm$ and $\mathbf{a}_{\text{loop}_a}^\pm$, respectively; hence, $\mathbf{a}_{\text{loop}}^\pm = \mathbf{a}_{\text{loop}_f}^\pm + \mathbf{a}_{\text{loop}_a}^\pm$. Moreover, *free/adsorbed* states have been defined in a way so that the following relations, 3.8, 3.9, 3.10, are satisfied.

$$\varphi_c^{\mathbf{a}^\pm} = \varphi_c^{\mathbf{a}_{\text{full}}^\pm} + \varphi_c^{\mathbf{a}_{\text{part}}^\pm} \quad 3.8$$

$$\varphi_c^{\mathbf{a}_{\text{part}}^\pm} = \varphi_c^{\mathbf{a}_{\text{loop}_f}^\pm} + \varphi_c^{\mathbf{a}_{\text{loop}_a}^\pm} + \varphi_c^{\mathbf{a}_{\text{tail}_f}^\pm} + \varphi_c^{\mathbf{a}_{\text{tail}_a}^\pm} \quad 3.9$$

$$\varphi_c = \varphi_c^{\mathbf{a}^-} + \varphi_c^{\mathbf{a}^+} + \varphi_c^f - \varphi_c^{\mathbf{a}_{\text{bridge}}} \quad 3.10$$

Finally, we mention here that the profiles of the *bridges* are a measure of the overlap between the profiles of *adsorbed* chains at the opposing surfaces; thus, in situations that the separation distance of these surfaces is large enough, $\varphi_{\text{bridge}} \rightarrow 0$.

3.4.5. Chains per area profiles

In three dimensions, the chains/area can be defined as the number of chain segments which cross at least once a surface $\partial\mathcal{R}_{h_0}$ and it is a measure of chain orientation introduced in references ^{2,64,66}. A meaningful choice for $\partial\mathcal{R}_{h_0}$ would be a surface which is parallel to the surface of the solid ($\partial\mathcal{R}_{\text{solid}}$) at distance h_0 ; $\min(\|\mathbf{r}_1 - \mathbf{r}_2\|, \mathbf{r}_1 \in \partial\mathcal{R}_{h_0}, \mathbf{r}_2 \in \partial\mathcal{R}_{\text{solid}}) = h_0$. References ^{2,64,66} include a detailed explanation of the chains/area calculation in one dimension; in this thesis, we present a more general formalism in three dimensions, which is compatible with smooth surfaces of arbitrary shape. For both matrix and grafted chains, the number of chains per unit area can be determined using the following eqs 3.11 and 3.12. ^{2,24,64,66}

$$p_{\text{int},c}(h_0) = 1 - \frac{\int_{\mathcal{R}} q_{c,h_0}^{\text{shape}}(\mathbf{r}, N_c) d\mathbf{r}}{\int_{\mathcal{R}} q_c(\mathbf{r}, N_c) d\mathbf{r}} \quad 3.11$$

$$n_{\text{ch},c}(h_0) = p_{\text{int},c}(h_0) \frac{1}{S_{h_0}} \frac{1}{N_c} \int_{\mathcal{R}} \rho_c(\mathbf{r}) d\mathbf{r} \quad 3.12$$

Initially, we estimate the probability $p_{\text{int},c}(h_0)$ that a chain of kind c will intersect the surface $\partial\mathcal{R}_{h_0}$ at least once (regardless of where in \mathcal{R} it may have started) using eq 3.11. q_{c,h_0}^{shape} is the *restricted partition function* of all kind c chains (i.e., matrix or grafted) that are unable to cross the surface at distance h_0 from the interface, and it is calculated by solving the *Edwards* diffusion equation with the additional *Dirichlet* boundary condition, $q_c(\mathbf{r}, N) = 0, \forall \mathbf{r} \in \partial\mathcal{R}_{h_0}$. Moreover, S_{h_0} is the surface area of $\partial\mathcal{R}_{h_0}$, and $\int_{\mathcal{R}} \rho_c(\mathbf{r}) d\mathbf{r}$ is the total number of type- c chains. $n_{\text{ch},c}(h_0)$ corresponds to the number of type- c chains per unit area that pass (at least once) through the surface at which finds itself at distance h_0 from the solid surface. By this definition, near the grafting points, the chains/area will be equal to the grafting density, as illustrated by the dashed line in the following Figure 3.13.

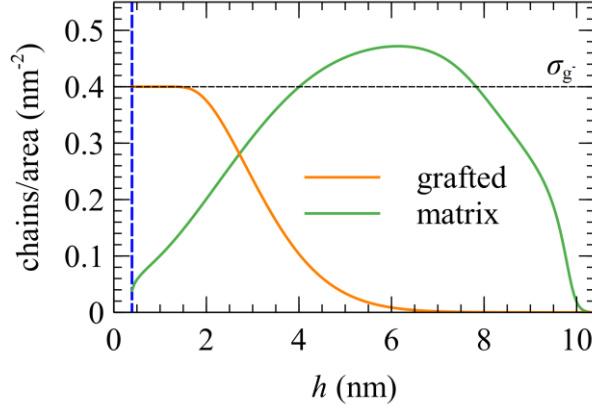


Figure 3.13 Chains/area profile in a perfectly wetted GMV SiO₂/PS system. For parameter values, see Table 4-2. Grafting density $\sigma_g = 0.4 \text{ nm}^{-2}$, length of grafted chains $N_g = 50$ skeletal carbon bonds, length of matrix chains $N_m = 100$ skeletal carbon bonds and domain length $L = 10 \text{ nm}$.

3.4.6. Profiles of individual grafted chains

In 3D, we are able to determine the density profiles of segments belonging to a specific grafted chain or group of grafted chains. This happens by evaluating the *restricted partition function* of the i_g^{th} grafted chain via the following initial condition:

$$q_{g,i_g}(\mathbf{r}, 0) = \frac{N_{g,i_g}}{\rho_{\text{seg,bulk}}} \frac{\delta(\mathbf{r} - \mathbf{r}_{g,i_g})}{q_m(\mathbf{r}_{g,i_g}, N_g)} \quad 3.13$$

In other words, after the iterations on the field have converged, we solve eq 2.2 using the initial condition value corresponding to the grafted chain of interest and all other grafted chains are assigned an initial value equal to zero so that they do not interfere in the solution. Afterwards, we substitute the resulting *propagator* in the convolution eq 3.3 and calculate the spatial distribution of segments belonging to the grafted chain i_g :

$$\varphi_{g,i_g}(\mathbf{r}) = \frac{1}{N_{g,i_g}} \int_0^{N_{g,i_g}} dN q_{g,i_g}(\mathbf{r}, N) q_m(\mathbf{r}, N_{g,i_g} - N) \quad 3.14$$

3.5. Chain discretization

3.5.1. Different discretization for matrix and grafted chains

An important step towards the acceleration of our 3D calculations is the ability to solve the *Edwards* equation for matrix chains with different contour discretization than grafted chains. The chain contour step, $d_i = n_i - n_{i-1}$, is a vital parameter for the numerical solution of the PDE. Low d_i values result in finer discretization (more steps, n_s) and thus higher accuracy and computational cost. The initial solution steps are sensitive to d_i —especially for grafted chains—whereas the latter steps are not; therefore, applying the same discretization for matrix chains is overkill. In our code, we have introduced the feature of different contour discretization for matrix and grafted chains and furthermore the corresponding *chain propagators* can be convolved in contour space through one-dimensional interpolation.

3.5.2. Uniform vs nonuniform discretization

It is essential to benchmark the solution of *Edwards* under different contour discretization schemes, especially for grafted chains which are more sensitive due to their delta initial condition (eq 2.4). At a first stage, we compare a uniform and a nonuniform discretization, where the latter is based on a *Chebyshev* expression given in the following eq 3.15.⁸⁹

$$n_i = N \left\{ 1 - \cos \left[\frac{\pi(i-1)}{2n_s} \right] \right\} \quad 3.15$$

where N is the length of the chain, i is the contour index and n_i is the contour point value. Following this formula, the chain contour step, d_i , is smaller at the initial steps and gradually increases, reducing the total number of required contour steps, n_s , to obtain accurate results.

Figure 3.14a presents the profile of the *chain propagator*, $q(\mathbf{r}, N)$, for $N = 10.5$ along the line $\{x = y = 0\}$ with the uniform (left) and nonuniform (right) scheme, while the bottom panels display the error with respect to the exact solution. The error of the uniform scheme is noticeable for $n_s \leq 64$, whilst with the nonuniform scheme the required n_s is halved. We come to the same conclusion in the case where ICs are applied at a single mesh point, as shown in Figure 3.14b. The latter case is directly related to assigning ICs for the grafted chains.

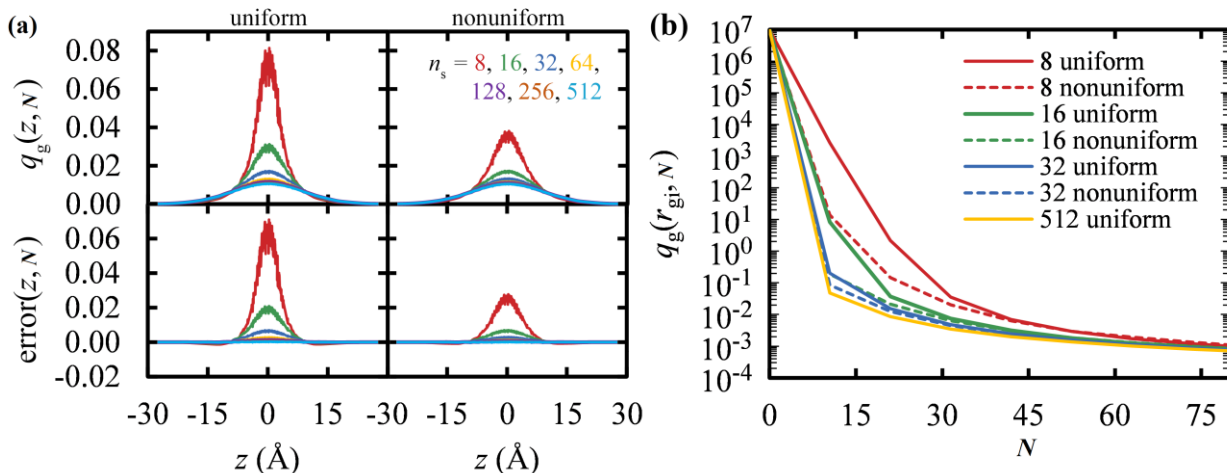


Figure 3.14. Contour discretization benchmarks: uniform vs nonuniform discretization. Effect of chain contour discretization on the solution of the *Edwards* PDE for PS chains in contact with a solid surface. **(a)** The ICs of grafted chains are imposed at points lying at $\Omega_{\text{rect}} = |x|, |y|, |z| < 2.5$. Top panels depict $q_g(z, N)$ for $N = 10.5$ and bottom panels show the error with respect to the exact solution. **(b)** $q_g(r_{g_i}, N)$ versus N where the ICs are applied at a single point of the domain.

At the next step, we wish to render the chain discretization independent of the chain length. Until a certain contour point, $N_{c, \text{sw}}$, we perform a *Chebyshev*-based contour discretization which is the same no matter the length of the chain to be discretized. The value of $N_{c, \text{sw}}$ is determined after a series of benchmarks, which are presented in Section 3.7.2. Beyond that point, the discretization is uniform, the step size is the same for any chain length and what changes is just the number of points. Mathematically, this hybrid contour discretization scheme is expressed via eq 3.16.

Applying the scheme described above, which is illustrated in Figure 3.15, we manage to maintain a fair weighting of the ends of the chains, no matter its length, while keeping an economical discretization of the rest of the chain. This allows for larger chains to be addressed and accuracy to be ensured.⁶⁷

3.5.3. Hybrid chain contour discretization

The efficiency of solving eq 2.2 can be enhanced by invoking a contour discretization which is finer near the starting end of the chain and gradually increases to a maximum value. Equation 3.16 illustrates the *hybrid* (asymmetric) discretization scheme, which is used in all calculations performed with the three-dimensional version of *RuSseL*. The chain contours are discretized nonuniformly based on a *Chebyshev* polynomial^{67,89} until a threshold contour length, $N_{c,sw}$. After that point, a uniform discretization is used.

$$N_{c,i} = \begin{cases} N_{c,sw} \left[1 - \cos \left(\pi \frac{i}{2i_{c,sw}} \right) \right], & 0 < i \leq i_{c,sw} \\ N_{c,sw} + (i - i_{c,sw}) \Delta N_{c,max}, & i_{c,sw} < i < i_{c,total} \end{cases} \quad 3.16$$

where, $N_{c,i}$ is the contour length of a kind- c chain at discretization step i ; $i_{c,sw} = N_{c,sw} / \Delta N_{c,ave}$ is the number of steps up to a switching point, $N_{c,sw} = N_{c,i_{c,sw}}$; $\Delta N_{c,ave}$ is the average contour step size for $N_{c,i} \leq N_{c,sw}$; $\Delta N_{c,max}$ is the maximum contour step; $i_{c,total} = i_{c,sw} + (N_c - N_{c,sw}) / \Delta N_{c,max}$ is the total number of contour steps.

Figure 3.15 illustrates an indicative discretization for a case with $N_c = 92.0$, $N_{c,sw} = 40.0$ and $\Delta N_{c,ave} = 1.0$. Using this *hybrid* chain discretization scheme, we manage to maintain a fair weighting of the ends of the chain no matter its length, while keeping an economical discretization for the rest of the chain. This allows for larger chains to be addressed accurately with minimal cost.⁶⁷ The efficiency of the scheme can be further enhanced by incorporating different sets of $(N_{m,sw}, \Delta N_{m,ave})$ and $(N_{g,sw}, \Delta N_{g,ave})$ for the matrix and grafted chains, respectively. It is noted that the convolution integral in eq 3.3 requires a symmetric discretization scheme (eq 3.17), which receives values from the asymmetric scheme in eq 3.16 via interpolation along the contour of the chain.

$$N_{c,i} = \frac{1}{2} N_c \left[1 - \cos \left(\pi \frac{i}{i_{c,conv}} \right) \right] \quad 3.17$$

with $i_{c,conv} = N_c / \Delta N_{c,ave}$ being the number of steps for *propagator* convolution.

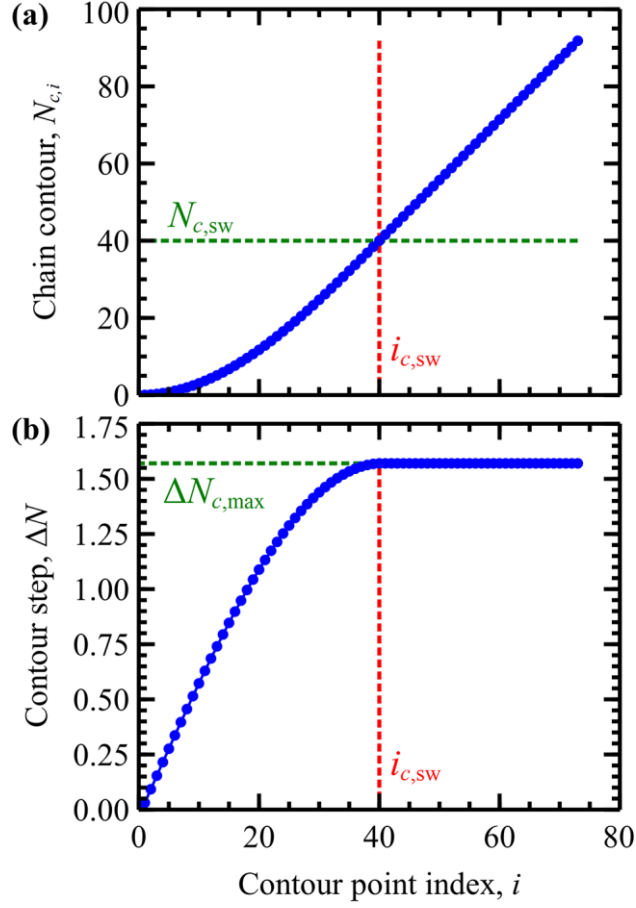


Figure 3.15 Hybrid chain contour discretization scheme as implemented in the three-dimensional version of *RuSseL*. Panel (a) depicts the chain contour and critical contour point, $N_{c,sw} = 40.0$ (green dotted line), indicating the point where the discretization switches from *Chebyshev* to uniform. Panel (b) depicts the corresponding step size employed for the solution of the *Edwards* eq 2.2 and its value, $\Delta N_{c,max}$, after the switching point.

3.6. Convergence and Initial Conditions of Grafted Chains

The initial conditions of grafted chains for the solution of *Edwards* eq 2.2 are given by eq 3.18 below.

$$q_g(\mathbf{r}, 0) = \frac{N_g}{\rho_{\text{seg,bulk}}} \sum_{i_g=1}^{n_g} \frac{\delta(\mathbf{r} - \mathbf{r}_{g,i_g})}{q_m(\mathbf{r}_{g,i_g}, N_g)} \quad 3.18$$

In eq 3.18, $\delta(\mathbf{r} - \mathbf{r}_{g,i_g})$ is the *Dirac*-delta function, firing at the grafting points and associating each grafting point with its corresponding value of the initial condition. $\rho_{\text{seg,bulk}}$ is the segment density in the bulk polymer melt. The *Dirac*-delta function triggered at the grafting points is consistent with the physical meaning of the *restricted partition function*; the probability of finding the first segment of a grafted chain i_g is nonzero only at the corresponding grafting point, \mathbf{r}_{g,i_g} , and zero everywhere else inside the domain of interest. It is noted that the *Dirichet*

boundaries make the surface $\partial\mathcal{R}_S$ inaccessible to both matrix and grafted chains; hence, the latter are grafted at a distance h_{g,i_g} from the solid surface.^{40,41,67,100}

3.6.1. 1D calculations

When invoking SFCT, there is a special difficulty associated with the mathematical description of grafted chains, whose one end is grafted to the solid surface. The chain *propagator* of these chains is subject to the *Dirac*-delta function initial condition in eq 2.4.⁴¹ Moreover, the denominator on the right-hand side of eq 2.4 is numerically challenging, since the chain *propagator* of matrix chains goes to zero close to the solid surface. A commonly used approach to address these issues is to reposition the grafting points to a surface close to the solid instead of right on top of it.^{67,88,100}

Regarding the numerical implementation of the delta function, *smearing* of the grafting points in the direction normal to the solid surface is often introduced by treating the grafting point density as a *Gaussian* distribution⁴¹ or as a rectangular function. Guided by these studies, in the 1D version of *RuSseL*, we set the location of the grafting points at the discretization nodal point which is nearest to the hard-sphere wall. In 1D systems of spherical symmetry, e.g., single grafted nanoparticle in a polymer matrix or contact with vacuum, the grafting points degenerate into a grafting “*spherical shell*” with radius slightly larger than that of the NP itself (Figure 3.16 orange arrow) and thickness Δh .

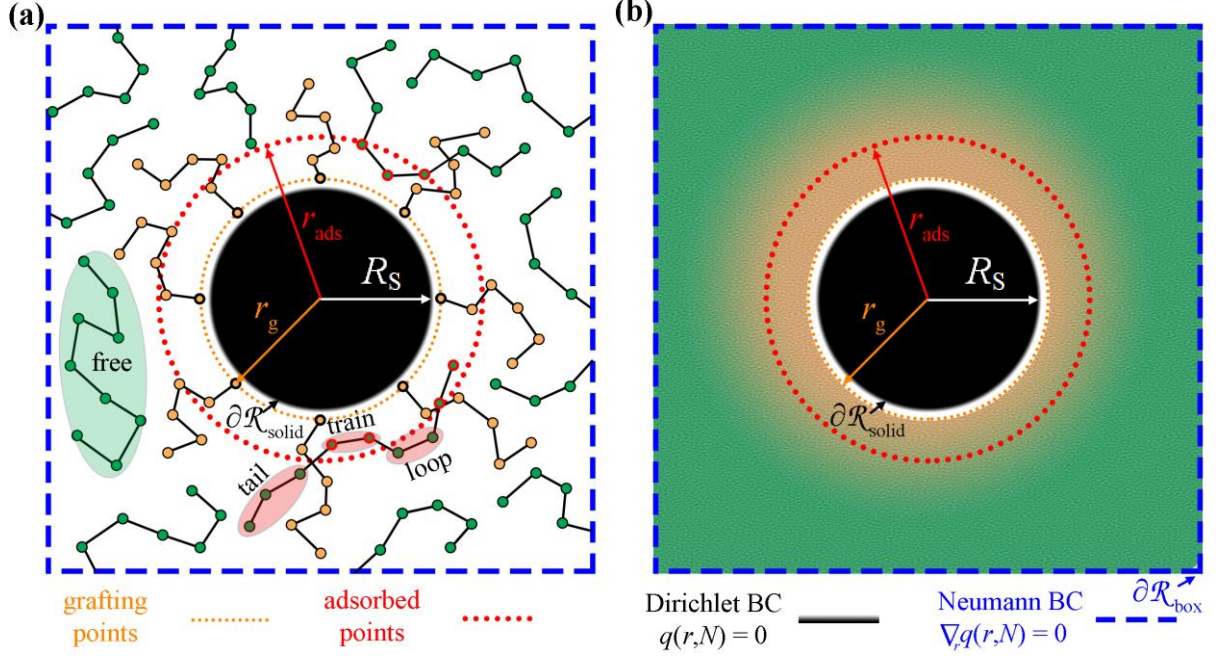


Figure 3.16 Schematic illustration of a grafted nanoparticle inside polymer melt. **(a)** A particle-based representation of a nanoparticle with polymer chains grafted at r_g (orange), embedded in a polymer matrix (green chains). **(b)** In unidimensional SCFT calculations, the chains are replaced by a density field and the grafting points are smeared normal to the radial direction. r_{ads} depicts the critical distance from the center of the NP, based on which the matrix chains are categorized as *adsorbed* (e.g., see red circles in **(a)**) or *free*.

Smearing of the grafting points means that they become delocalized throughout the surface near the solid substrate, suggesting a smoothed distribution of grafting points, which practically ignores the presence of a grafting point at a specific surface point; e.g., in Figure 3.16b the grafting points have been smeared across a spherical cell highlighted by an orange dotted circle. In doing so, eq 3.18 for the ICs of grafted chains can be written as follows:

$$q_g(h_g, 0) = \frac{S_S}{S_{h_g}} \frac{\sigma_g N_g}{\rho_{\text{seg, bulk}}} \frac{\delta(h - h_g)}{q_m(h_g, N_g)} \quad 3.19$$

where $\sigma_g = n_g/S_S$ is the grafting density, S_S is the surface area of the solid, and S_{h_g} is the surface area over which the grafting points are smeared. To make eq 3.19 applicable for both spherical and planar geometries, it has been written in terms of h and h_g , which denote segment-surface and point-surface distance, respectively. Consequently, in spherical geometries, $h \equiv r - R_S$; this relation is ill-defined in planar geometries, since $r, R_S \rightarrow \infty$. The three-dimensional delta function $\delta(\mathbf{r} - \mathbf{r}_{g, i_g})$ is approximated as $\delta(h - h_g)/S_{h_g}$ for all i_g .

For planar surfaces with area S_S , the *Edwards* eq 2.2 is evaluated across the normal direction with respect to the surface, and the differential $d\mathbf{r}$ of the spatial integration equals the volume of the layer, $d\mathbf{r} \rightarrow S_S dh$. The delta function in eq 3.19 is set to the inverse discretization step in the h direction; i.e., $\delta(h - h_g) \approx 1/\Delta h$, with Δh being the width of the intervals in which h is subdivided in the numerical solution.

On the other hand, for spherical NPs with area equal to $S_S = 4\pi R_S^2$, the *Edwards* eq 2.2 can be evaluated across a radial direction (normal to the surface) as shown in Appendix F.

3.6.2. 3D calculations

In the three-dimensional version of *RuSseL*, where the FEM numerical scheme is applied, the initial condition of the grafting points is evaluated exactly upon the desired points of the domain and the delta function is again evaluated as the inverse volume assigned to the nodal point.⁶⁷

The stability of the 3D-SCFT algorithm is accomplished by means of a successive substitution scheme, which is typically used in these calculations, and a mixing parameter which acts on the field and has to be lower than a maximum value.¹⁰¹ This maximum value is always lower than unity and depends on the length of the chains (Section 3.7.3) and the isothermal compressibility, κ_T , as shown in eqs 3.20 and 3.21 below.

$$w'_{\text{ifc}} \rightarrow a_{\text{mix}} w'_{\text{ifc,next}} + (1 - a_{\text{mix}}) w'_{\text{ifc,prev}} \quad 3.20$$

$$a_{\text{mix}} = \frac{\lambda_{\text{mix}}}{\max(N_g, N_m)} \quad 3.21$$

where λ_{mix} is proportional to κ_T .

At each iteration of the SCF algorithm, the linear system of equations arising from the discretization of the *weak* form of the *Edwards* equation is solved by the open-source direct solver *MUMPS*,^{95,96,102} which is also linked to our code. The iterative scheme is executed until the error in successive evaluations of the total free energy is lower than a set tolerance, ΔE^{tol} .

As iterations proceed, there is another source of error that needs to be controlled. Ideally, the delta function values, for the initial condition at each grafting point, are independent of the configuration of the field. In practice, however, the number of grafted chains corresponding to the current field configuration deviates slightly from that corresponding to the specified grafting density. For that reason, the number of grafted chains is restored through numerical evaluation

3.6. Convergence and Initial Conditions of Grafted Chains

of the proper value of the delta function at each one of the grafting points. This delta evaluation involves the solution of the *Edwards* equation n_g times; therefore, it is performed sparsely at certain stages of the field iteration process. In particular, the numerical evaluation of the delta function is performed if the relative error in the number of grafted chains exceeds $\varepsilon_g^{\text{tol}} = 0.5\%$. When this happens, the field equilibration procedure pauses, delta values and initial conditions at each grafting point are updated, and afterwards, field convergence proceeds with the updated grafting point initial conditions. Below we sketch the procedure of the numerical calculation of initial conditions.

3.6.2.1. Numerical Estimation of the Delta Function on the Grafting Points

To begin with, a tentative approximation of the delta function is obtained as the inverse volume assigned to the grafting point (node) of the mesh:

$$\delta_{\text{tentative}}(\mathbf{r} - \mathbf{r}_{g,i_g}) = \frac{1}{V_{i_g}} = \frac{1}{\sum_{j \in L_{\text{el},i_g}} V_{\text{el},j} / 4} \quad 3.22$$

with L_{el,i_g} being a list including all elements sharing the common point (node) i_g , and $V_{\text{el},j}$ the volume of the j^{th} element. The factor 4 is because each (tetrahedral) element has 4 nodes.

Ideally, solving the PDE 2.2 using the initial condition in eq 3.18 subject to $\delta_{\text{tentative}}$ should yield exactly n_g grafted chains; there is, however, a slight deviation from this number during field equilibration. In order to correct for this, for each grafted chain i_g , the corresponding delta function $\delta(\mathbf{r} - \mathbf{r}_{g,i_g})$ is calculated as follows:

- 1) The tentative *restricted partition function* $q_{g,i_g,\text{tentative}}$ of the i_g^{th} grafted chain is calculated by evaluating the PDE 2.2 subject to the tentative initial condition in eq 3.23 (i.e., eq 3.18 with $\delta \rightarrow \delta_{\text{tentative}}$ and $n_g = 1$).

$$q_g(\mathbf{r}_{g,i_g}, 0) = \frac{\delta_{\text{tentative}}(\mathbf{r} - \mathbf{r}_{g,i_g}) \cdot N_g \cdot 1}{q_m(\mathbf{r}_{g,i_g}, N_g) \cdot \rho_{\text{seg,bulk}}} \quad 3.23$$

with q_m being the *propagator* of matrix chains subject to a field w_{fc}' .

- 2) The tentative density field of the i_g^{th} chain is calculated via convolution:

$$\varphi_{g,i_g,\text{tentative}}(\mathbf{r}) = \frac{1}{N_{g,i_g}} \int_0^{N_{g,i_g}} dN q_{g,i_g,\text{tentative}}(\mathbf{r}, N) q_m(\mathbf{r}, N_{g,i_g} - N) \quad 3.24$$

3) The number of grafted chains (which, ideally, is 1 in this case) is calculated by integrating eq 3.24.

$$n_{g,i_g,tentative} = \frac{\rho_{seg,bulk}}{N_{g,i_g}} \int_{\mathcal{R}} d\mathbf{r} \varphi_{g,i_g,tentative}(\mathbf{r}) \quad 3.25$$

4) By taking advantage of the linear dependence of $n_{g,i_g,tentative}$ on $\delta_{tentative}(\mathbf{r} - \mathbf{r}_{g,i_g})$, the delta function value which yields exactly one grafted chain is given by eq 3.26.

$$\delta_{numerical}(\mathbf{r} - \mathbf{r}_{g,i_g}) = \frac{1}{n_{g,i_g,tentative}} \delta_{tentative}(\mathbf{r} - \mathbf{r}_{g,i_g}) \quad 3.26$$

Finally, we compute the correct value of the initial condition via eq 3.28 and solve *Edwards* once again for all grafting points, where each grafting point has its own initial condition and the *propagator* is zero everywhere else inside the domain, as suggested by eq 3.18.

$$q_g(\mathbf{r}, 0) = \sum_{i_g=1}^{n_g} q_{g,i_g}(\mathbf{r}, 0) \quad 3.27$$

where

$$q_{g,i_g}(\mathbf{r}, 0) = \frac{N_g}{\rho_{seg,bulk}} \frac{\delta_{numerical}(\mathbf{r} - \mathbf{r}_{g,i_g})}{q_m(\mathbf{r}_{g,i_g}, N_g)} \quad 3.28$$

The updated value, $\delta_{numerical}$, requires the solution of *Edwards* n_g times, but this happens rarely compared to the total number of *Edwards* solutions required for equilibration of the field. In the most intensive 3D-SCFT calculations, meaning low isothermal compressibility or high chain length and therefore steeper field in the interface, the number of iterations for field equilibration varies between 10^3 and $2 \cdot 10^3$. For each one of these iterations, the *Edwards* equation must be solved 2 times, once for matrix and once for grafted chains, giving us a number of *Edwards* equation solutions on the order of $2 \cdot 4 \cdot 10^3$. With a relative tolerance in the number of grafted chains equal to $\varepsilon_g^{tol} = 0.5\%$ (which is quite strict), delta update takes place on the order of 3 times. For the largest grafting density and particle radius that we have addressed so far, we had 644 grafted chains and therefore approximately $3 \cdot 644 = 1932$ *Edwards* equation solutions were required, so we can say that for the largest systems addressed in this work, we had roughly a 100% overhead, which is the cost of analytically treating each grafted chain on its own.

We mention, however, at this point, that calculating the initial condition of grafted chains is a trivially parallel operation, meaning that each grafted chain can be assigned to a subset of CPU processes and no communication is required whatsoever among processes working on different grafted chains, because each grafted chain must be treated as if no other grafted chains exist in the system. The total number of *Edwards* solutions is given by a relationship of the form:

$$\text{Total Edwards solutions} = 2 \cdot \text{field_iterations} + k \cdot n_g \quad 3.29$$

with k being the number of delta updates to meet the tolerance regarding the number of grafted chains.

3.7. Benchmarks of RuSseL3D

3.7.1. Spatial Discretization

In all 3D-SCFT calculations, domain discretization is mainly controlled by tuning the maximum allowed element volume, when the meshing process is executed. When decreasing the maximum element volume that the mesher is allowed to create, the discretization becomes finer and vice-versa.

Furthermore, given the steepness of the solution of the PDE near the solid surfaces, we need to ensure that a finer discretization is applied in those regions, while maintaining a coarser mesh outside that region, to prevent the number of mesh points from increasing dramatically. Hence, a second degree of freedom is introduced to control the number of mesh points. It is the width of the spherical cell which defines the subdomain where the finer meshing will be applied. In the context of the *Helfand* EoS (which is used in all 3D-SCFT calculations presented in this thesis), the steepness of the solution is detected below a distance of 0.5 nm from the solid surface; hence, the width of the spherical mesh is set equal to this distance, $h_M = 0.5$ nm. Beyond that distance, conditions resembling bulk prevail and a coarser mesh is applied. In Figure **3.17** we demonstrate the dependence of the free energy terms on the maximum element volume inside the dense-mesh region and in Figure **3.18** the corresponding total free energy.

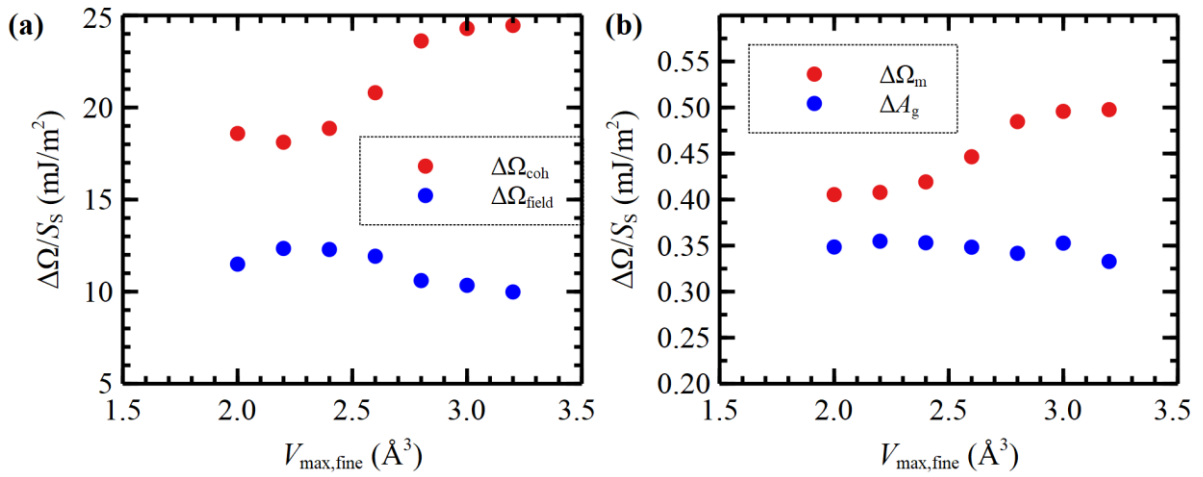


Figure 3.17 Spatial discretization benchmarks: free energy terms as functions of element size. Individual free energy terms as functions of the maximum element volume in a system of a single nanoparticle embedded in polystyrene matrix and grafted with one polystyrene chain on its surface. In panel (a), we present the dependence of the cohesive term (red color), as obtained from eq 2.39, and the term of the *chemical potential* field (blue color), as obtained from eq 2.40. In panel (b), we present the dependence of the conformational entropy of matrix chains (red color), as obtained from eq 2.42, and the conformational entropy of grafted chains (blue color), as obtained from eq 2.43.

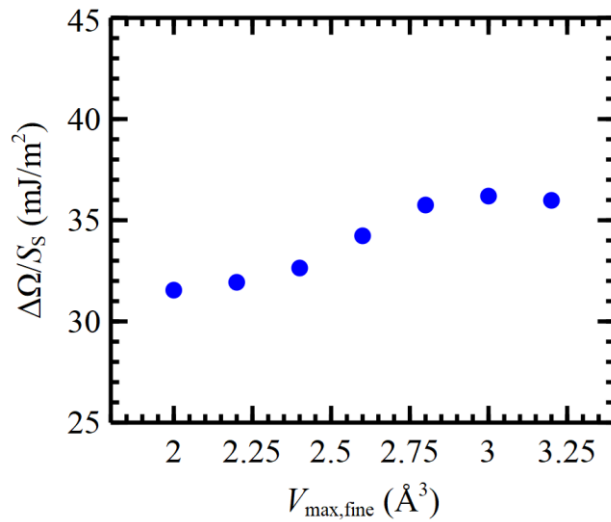


Figure 3.18 Spatial discretization benchmarks: total free energy as a function of element size. Total free energy obtained from eq 2.38 as a function of the maximum element volume in a system of a single nanoparticle embedded in polystyrene matrix and grafted with one polystyrene chain on its surface.

3.7.2. Contour Discretization

In Figure 3.19 below, we present the benchmarks of *RuSseL* with respect to the contour discretization of grafted chains, which is varied through the average contour step, ΔN_g , along a grafted chain and the contour point, N_{sw} , where the discretization switches from *Chebyshev* to uniform (see Section 3.5.3). The benchmarks concern the free energy per NP area, $\Delta\Omega/S_s$, of a system of one spherical silica NP embedded in polystyrene matrix and whose surface is grafted with polystyrene chains.

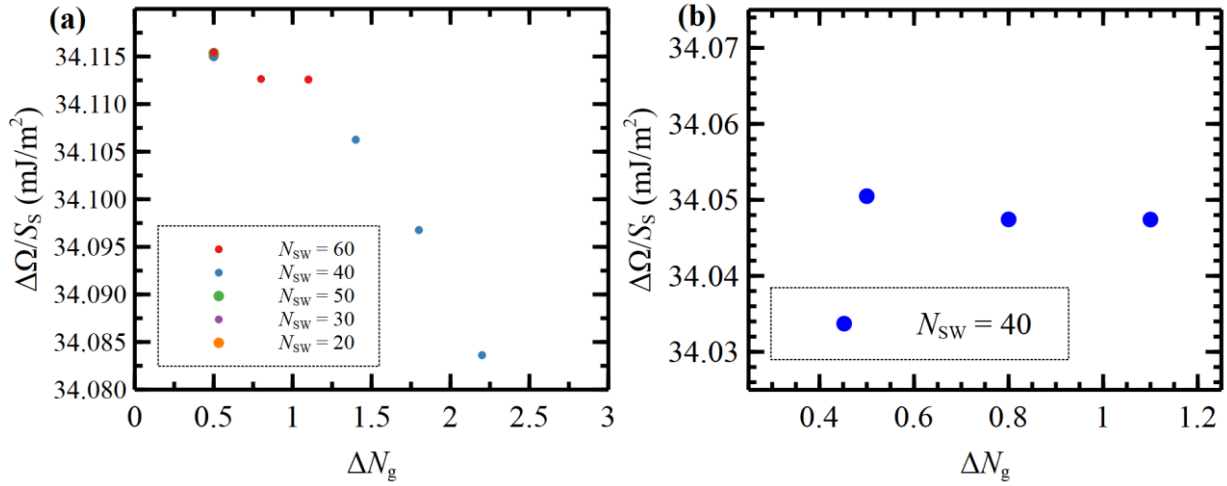


Figure 3.19 Contour discretization benchmarks: total free energy as a function of the contour step. Total free energy (eq 2.38) in a system of a single nanoparticle embedded in polystyrene matrix and grafted with one polystyrene chain on its surface, as a function of the step size, ΔN_g , used for the discretization of grafted chains with length N_g equal to (a) 60, (b) 120 skeletal carbon bonds. In case (a), we also report the effect of the switching point, N_{sw} .

3.7.3. Field Mixing Fraction

In order to ensure the convergence of the 3D-SCFT calculation leading to the equilibrated configuration of the self-consistent field, we need to multiply the updated field resulting from the solution of the *Edwards* PDE and the convolution of *chain propagators*, with a fraction value which is always lower than unity and depends on the length of the chains and the isothermal compressibility of the polymer melt.

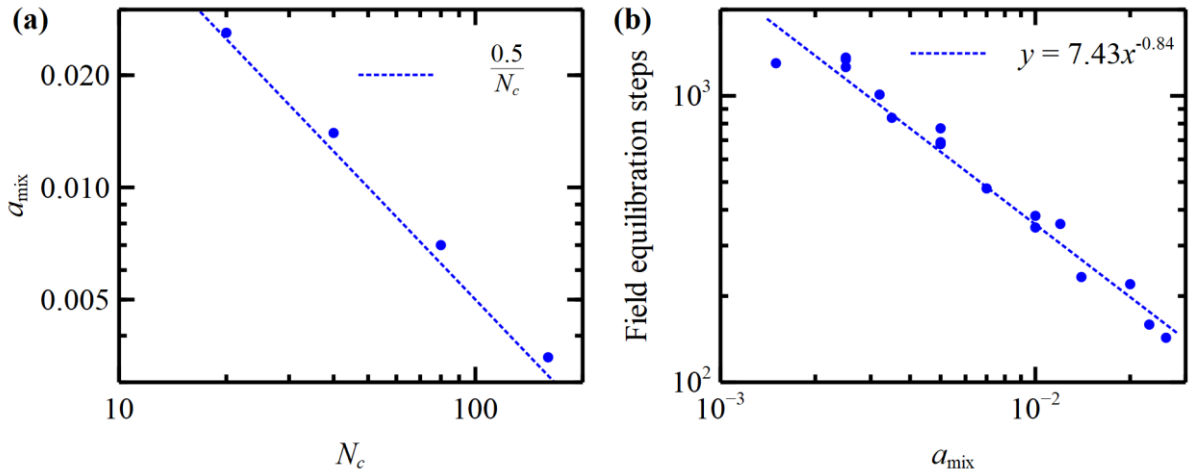


Figure 3.20 Field mixing/update benchmarks performed in the three dimensional version of *RuSseL*. **(a)** Field mixing fraction which has to be used in the field equilibration procedure, as a function of chain length measured in skeletal bonds. Both axes are presented in logarithmic scale. For a given value of chain length, N_c , if a larger fraction value is used than the one predicted by the blue line, the SCFT algorithm will most likely diverge. When both matrix and grafted chains are present in the system, the fraction must be determined with respect to the maximum chain length. **(b)** Number of SCFT algorithm steps required for field equilibration as a function of the fraction parameter. The satisfying fitting of the linear regression suggests a power-law dependence.

In Figure 3.20a, we present the dependence of the field mixing fraction, f_{mix} , on chain length. It is noted that, when both matrix and grafted chains are present in the system, then the value of the fraction has to be determined with respect to the maximum length between the two kinds of chains, otherwise the algorithm will diverge. In panel b of the same figure we present the number of steps required for field equilibration as a function of the field mixing parameter. The same benchmarks have been conducted with the one-dimensional version of *RuSseL*, where a similar trend is exhibited (see Appendix I).

3.7.4. Renormalization of Configurational Entropy of Grafted Chains

The free energy contribution associated with the configurational entropy of grafted chains is originally given by eq 3.30.

$$\Delta A_g = -\frac{1}{\beta} \sum_{i_g=1}^{n_g} \ln Q_g \left[\mathbf{r}_{g,i_g}; w' - w'_{\text{bulk}} \right] = -\frac{1}{\beta} \sum_{i_g=1}^{n_g} \ln q_m \left[\mathbf{r}_{g,i_g}; w' - w'_{\text{bulk}} \right] \quad 3.30$$

Equation 3.30 is sensitive to the distance of each one of the grafting points from the solid surface. The equality between Q_g and q_m is based on the very definition of the restricted partition function and it is further discussed in the proof presented in Appendix E. Taking advantage of the fact that the unique space-dependent variable in eq 3.30 is the *propagator* q_m , and that it

decreases linearly with distance from the surface in the region close to the *Dirichlet* boundary (see Figure 3.21a), we can normalize this entropic term with respect to a reference distance, $h_{\text{ref},q=0}$, by adding the second term appearing on the right-hand side of eq 3.31.

$$\Delta A_g = -\frac{1}{\beta} \sum_{i_g=1}^{n_g} \ln Q_g[\mathbf{r}_{g,i_g}; w' - w'_{\text{bulk}}] - \frac{1}{\beta} \sum_{i_g=1}^{n_g} \ln \frac{r_{\text{ref},q=0}}{r_{g,i_g,q=0}} \quad 3.31$$

with h_{g,i_g} denoting the distance of the grafting point i_g from the solid surface. As demonstrated in Figure 3.21b, eq 3.31 is insensitive to the distance of the grafting points from the surface. It is noted that when $h = h_{\text{ref},q=0}$ (dashed vertical line in Figure 3.21), the normalized value of the free energy of grafted chains is equal to its non-normalized value.

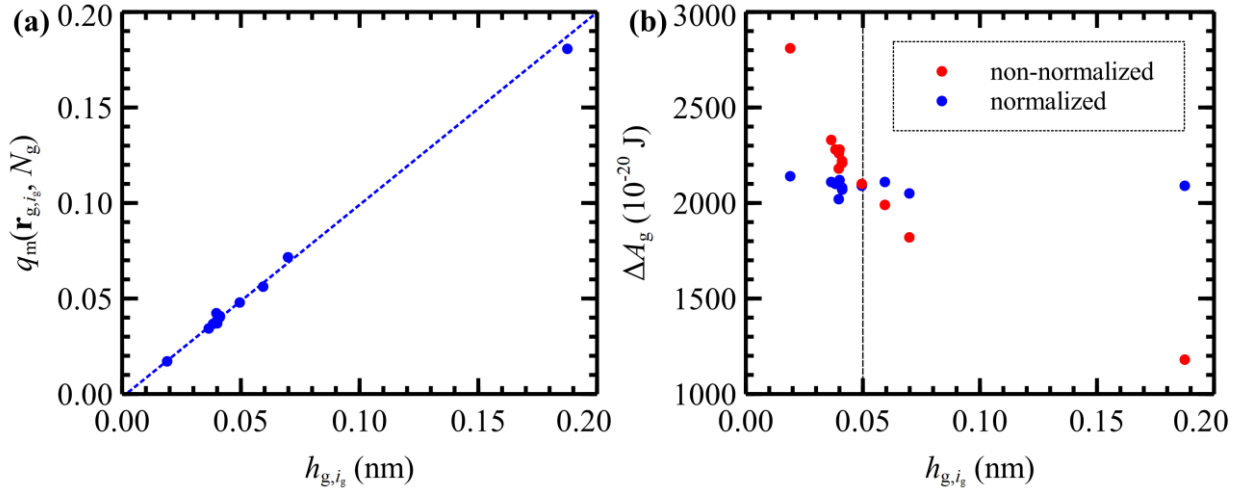


Figure 3.21 Variation of free energy with increasing distance of the grafting point from the *Dirichlet* wall. (a) *Chain propagator* of matrix chains, q_m , evaluated at the grafting points as a function of the distance of the grafting point from the solid surface. The dashed line is a guide to the eye. (b) Conformational entropy of grafted chains as a function of the distance of the grafting point from the solid surface. Red points correspond to the non-normalized conformational entropy (eq 3.30), while blue points correspond to the normalized conformational entropy (eq 3.31) for $h_{\text{ref},q=0} = 0.05$ nm (black dashed line). This benchmark was conducted in a planar system of polystyrene melt at $T = 500$ K. Chain length of matrix and grafted chains was equal to $N_m = N_g = 100$ skeletal carbon bonds. Box size was $4 \times 4 \times 5$ nm³. One polystyrene chain ($n_g = 1$) was grafted on the solid/*Dirichlet* wall.

3.7.5. Parallelization and Scalability

We have performed a series of benchmarks on the Greek national supercomputing system, ARIS, to investigate the scaling of our code with respect to the number of threads and/or processes when using the *OpenMP* or *MPI* protocols, respectively. These benchmarks are presented in the following Figure 3.22. They were performed for two different mesh sizes, i.e., one consisting of 88529 nodes (red color) and a larger one consisting of 249084 nodes. In all cases, there is a certain speedup when running on multiple cores, but the efficiency suggests a sublinear scaling. Nonetheless, it has to be noted that in all cases the speed-controlling stage is the solution of the *Edwards* equation which is performed by the opensource solver *MUMPS*. In fact, we have measured the time that the code spends to solve *Edwards* and the total amount of time that the code spends before and after calling *MUMPS* to solve the PDE. Results are reported in the following Table 3-2 (smaller mesh) and Table 3-3 (larger mesh). It is clear that the stages before PDE solution (i.e., initialization, chain contour discretization, spatial mesh import, matrix assembly) and those after the PDE solution (field update, export of structural and thermodynamic quantities) are just 3% of the overall code running duration. This is a clear indication that the scaling observed in Figure 3.22 concerns the solver itself and could perhaps be improved in later versions of the solver. Another solver might possibly be more suitable for our matrices. *MUMPS* does not offer a (close to) linear scaling for the numbers of nodes on which the benchmarks were conducted ($\sim 10^4$, $\sim 10^5$). Nonetheless, comparing the scaling of the larger to the smaller mesh, one comes to the conclusion that *MUMPS* could indeed offer a better scaling at much higher orders of matrices, i.e., $> 10^6$. For detailed instructions on the compilation of the three-dimensional version of *RuSseL* and linkage with the necessary libraries, e.g., *MUMPS*, *MPI*, the reader is referred to Appendix J.

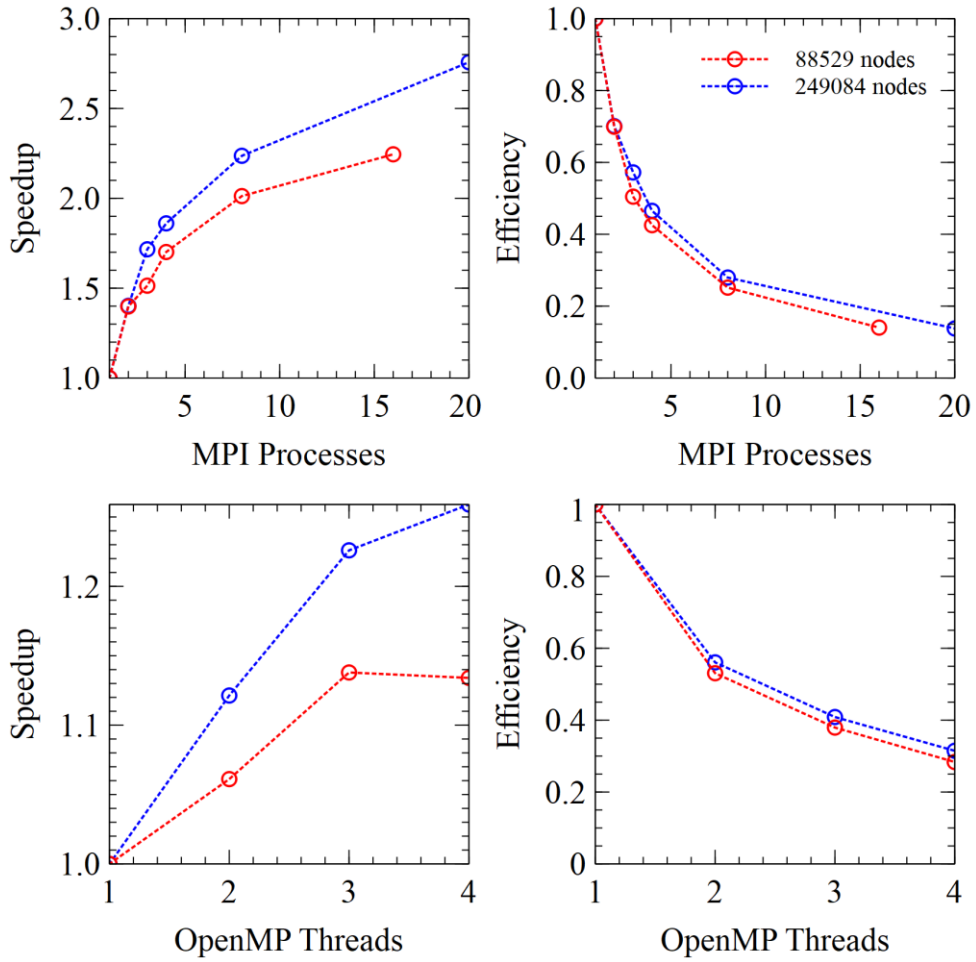


Figure 3.22 *RuSseL* parallelization benchmark with *OpenMP* and *MPI* protocol. Red color corresponds to a small spatial mesh of 88529 nodes, while blue color corresponds to a larger spatial mesh of 249084 nodes. Top panels report the speedup (left) and efficiency (right) with increasing number of *MPI* processes and one *OpenMP* thread. Bottom panels report the speedup (left panel) and efficiency (right) with increasing number of *OpenMP* threads and one *MPI* process. The broken lines are guides to the eye.

The speedup and efficiency were calculated using the following eqs 3.32 and 3.33, respectively.

$$\text{speedup} = \frac{\text{serial time per field iteration}}{\text{parallel time per field iteration}} \quad 3.32$$

$$\text{efficiency} = \frac{\text{speedup}}{\# \text{ procs/threads}} \quad 3.33$$

Table 3-2. Scaling of *Edwards* solution time in a spatial mesh of 88529 nodes.

<i>88529 nodes</i>	mpiprocs/node	threads/proc	total code time (s)	total code time per iteration (s)	non-mumps code time per iteration (s)	
SERIAL	1	1	113	113	3.0	2.7%
<i>MPI</i>	2	1	248	83	4.0	4.8%
	3	1	225	75	2.3	3.1%
	4	1	204	68	3.3	4.9%
	8	1	176	59	4.0	6.8%
	16	1	158	53	3.7	7.0%
<i>OpenMP</i>	1	1	113	113	3.0	2.7%
	1	2	324	108	4.3	4.0%
	1	3	303	101	4.3	4.3%
	1	4	302	101	3.7	3.6%

Table 3-3 Scaling of *Edwards* solution time in a spatial mesh of 249084 nodes.

<i>249084 nodes</i>	mpiprocs/node	threads/proc	total code time (s)	total code time per iteration (s)	non-mumps code time per iteration (s)	
SERIAL	1	1	861	431	10.0	2.3%
<i>MPI</i>	2	1	620	310	10.0	3.2%
	3	1	511	256	10.5	4.1%
	4	1	236	236	10.0	4.2%
	8	1	198	198	10.0	5.1%
	20	1	327	164	11.0	6.7%
<i>OpenMP</i>	1	1	861	431	10.0	2.3%
	1	2	385	385	10.0	2.6%
	1	3	353	353	10.0	2.8%
	1	4	344	344	10.0	2.9%

Looking at the tables above, we observe that communication overhead between *MPI* processes increases with the number of processes and this is reflected in the increased fraction of time spent on “non-mumps” code in relation to the total code execution time. When using *OpenMP*, on the other hand, communication time does not scale; this is reasonable since, in this protocol, threads work on shared memory.

3.8. Grafting Point Distributions

Hereafter, the coordinates of grafting points across the sphere surface will be described in spherical coordinates, (r, θ, φ) , using the convention: $r \in [0, \infty)$, distance from the origin; $\theta \in [-\pi/2, \pi/2]$, inclination angle; $\varphi \in [-\pi, \pi]$, azimuthal angle.

The NPs with equidistributed grafting points on their surface were generated using the algorithm presented in ref ¹⁰³. The algorithm produces distributions comprising almost equidistant grafting points, albeit it does not produce the exact number of grafting points (the discrepancy is however negligible). For example, Figure **3.23a** depicts the coordinates of 500 grafting points across the (θ, φ) space and Figure **3.23e** the corresponding distribution across the surface of a NP with $R_S = 8$ nm. To generate the nanoparticles with irregular grafted chain distributions on their surface, we devised a *Monte Carlo* sampling scheme comprising two stages, which are explained below.

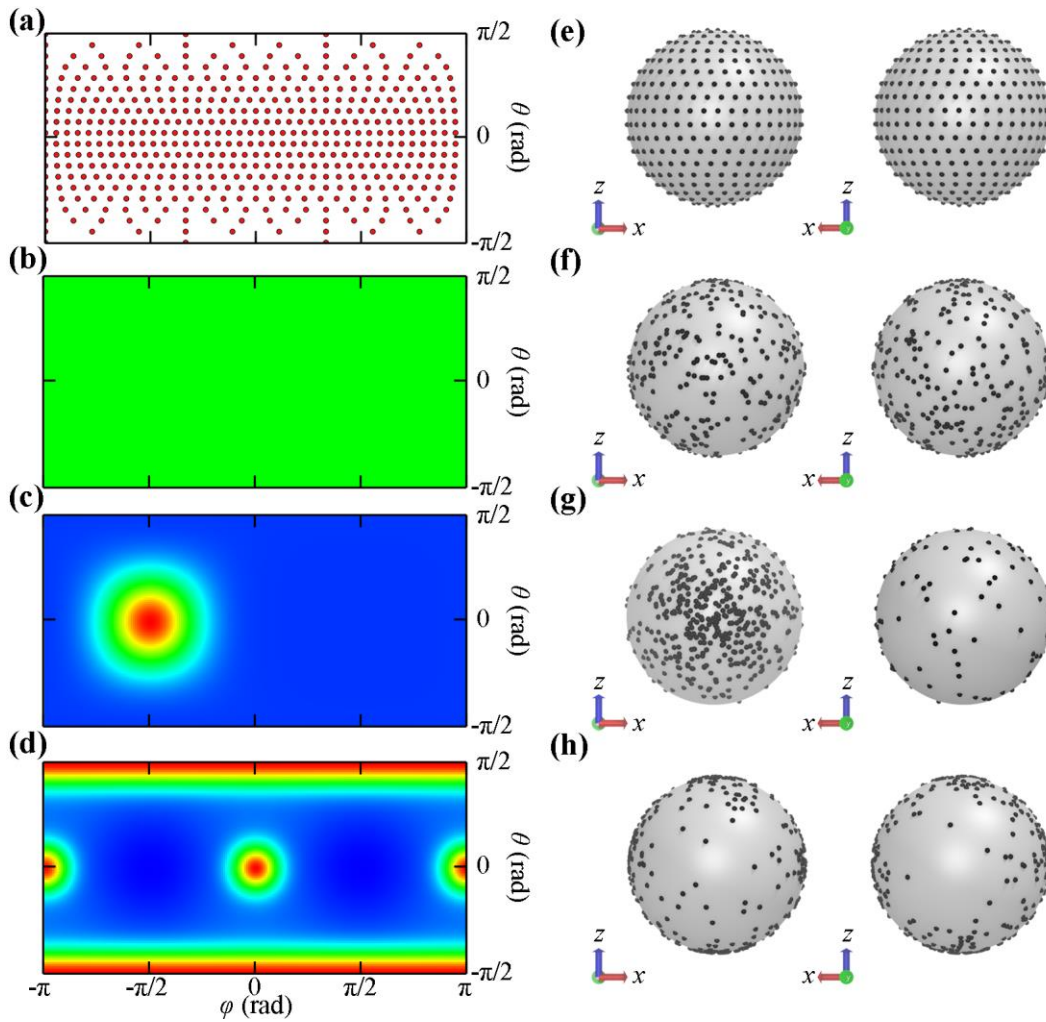


Figure 3.23 Demonstration of irregular grafting distributions on a spherical surface. **(a)** Coordinates of 500 equidistributed grafting points across the (θ, φ) space using the algorithm of ref ¹⁰³. Probability maps for **(b)** uniform and **(c,d)** biased grafting point distributions from eq 3.34; details concerning **c, d** are presented in the text. Blue, green and red color corresponds to $P = 0, 0.5$ and 1.0 , respectively. Panels **(e-h)** illustrate the front and back side of spheres with $R_S = 8$ nm (average $\sigma_g \sim 0.62$ nm²), whose grafting points are distributed according to the corresponding probability maps in panels **(a-d)**, respectively.

First, a candidate random point, \mathbf{p} , at the surface of the sphere is sampled uniformly across the surface of the sphere. The insertion of the grafting point at \mathbf{p} is accepted with a probability $P(\mathbf{p}) = P(r, \theta, \varphi)$. The process is repeated until the required number of grafted chains is achieved. The probability maps are obtained by summing *Gaussian* pulses of a homogeneous probability distribution, as shown in the following eq 3.34.

$$P(\mathbf{p}) = \min \left(1, \max \left(0, P_0 + \sum_{i=1}^{n_{\text{GP}}} P_i \exp \left(-\frac{D_i^2}{2d_i^2} \right) \right) \right) \quad 3.34$$

where $P_0 \in [0,1]$ is the background probability (acceptance probability in absence of any bias), the operator Σ sums over n_{GP} *Gaussian* pulses centered at \mathbf{p}_i , the pre-exponential factor $P_i \in [-P_0, 1-P_0]$ is the maximum acceptance probability, and d_i the standard deviation of the *Gaussian* pulse. $D(\mathbf{p}, \mathbf{p}_i) = r\omega(\mathbf{p}, \mathbf{p}_i)$, is the great-circle distance (arc-length) between points \mathbf{p} and \mathbf{p}_i ; and ω is the great-circle angle; for two points \mathbf{p}_j and \mathbf{p}_i , ω is defined as follows:

$$\omega(\mathbf{p}_j, \mathbf{p}_i) = \arccos\left(\sin \theta_j \sin \theta_i + \cos \theta_j \cos \theta_i \cos |\varphi_j - \varphi_i|\right) \quad 3.35$$

In the trivial case, $P(\mathbf{p}) = c$, with $c \in (0,1]$, the grafting points are uniformly distributed on the sphere surface. By bounding the probability P_i between $-P_0$ and $1-P_0$, the total probability is bounded between $[0, 1]$. Note that, if the *Gaussian* pulses lie too close together, their sum might exceed this bound; in this case, the insertion probability is restricted between 0 and 1 (see eq 3.34).

Figure 3.23b and Figure 3.23c,d illustrate uniform and biased probability maps, respectively, whereas panels (f-h) present indicative distributions of 500 points on the surface of a sphere with $R_S = 8$ nm. In Figure 3.23c and g, the background probability is set to $P_0 = 0.05$, and there is a single attractive biasing pole which finds itself at position $(\theta, \varphi) = (0, -\pi/2)$ with $P_i = 0.95$ and $d_i = 4$ nm. Figure 3.23d and h present a more complicated distribution, where: $P_0 = 0.2$, there are two repulsive poles at $(0, \pm\pi/2)$ with $P_i = -0.2$ and $d_i = 8$ nm, and four attractive poles at $(\pm\pi/2, 0)$, $(0, -\pi)$, $(0, 0)$ with $P_i = 0.8$ and $d_i = 2$ nm.

According to the case in Figure 3.23f for a uniform distribution, the grafting points appear much more clustered than the equidistributed case in Figure 3.23e. Emanation of grafted chains from grafting points that lie very close to each other can be unphysical due to *excluded volume* effects; the latter can be taken into account by imposing a minimum distance between the grafting points below which the candidate insertion is rejected.

3.9. 3D Periodic Boundary Conditions

The ultimate goal of developing *RuSseL* is the possibility to address multiple grafted nanoparticles inside a polymer melt. This will allow for the determination of the free energy for a specific number of NPs which may be arranged in various disordered or lattice-like

configurations, e.g., body-centered cubic (bcc) or face-centered cubic (fcc), and this way one can obtain the most stable configuration. To perform such calculations in a computationally efficient manner, we needed to add a nontrivial feature in the three-dimensional version of *RuSseL*: the ability to address systems with periodic boundary conditions (PBC).

In particle-based computational methods, e.g., *molecular dynamics*, PBCs are imposed by invoking the minimum image convention. They enable a simulation to be performed using a relatively small number of particles, in a way that the particles experience forces as if they found themselves in a bulk material. In two-dimensions, each box is surrounded by eight neighbors, whereas in three-dimensions each cubic box has 26 neighbors. The coordinates of the particles in the image boxes can be computed simply by adding or subtracting integer multiples of the box sides. Should a particle leave the box during the simulation, then it is replaced by an image particle that enters from the opposite side, as illustrated in Figure 3.24.

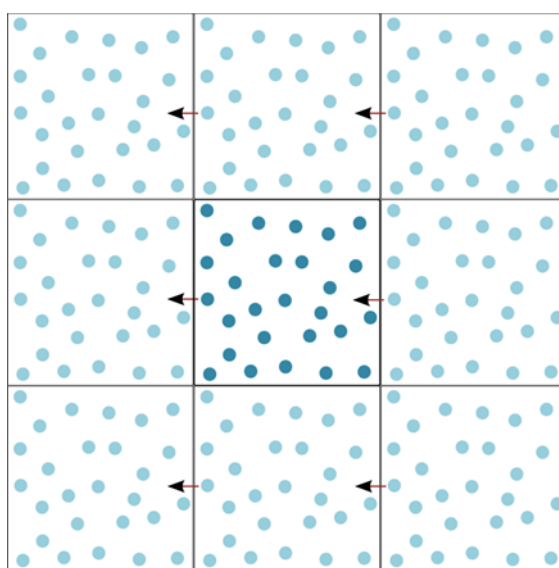


Figure 3.24 Illustration of periodic boundary conditions in two dimensions. The central box is the primary domain of the simulation and it has eight neighboring images. Should a particle leave from one face of the main box, then it re-enters the primary box from the opposite face.

3.9.1. Spherical Nanoparticles in Polymer Matrix

In a continuum methodology such as the *Finite Element Method*, we do not have access to the exact coordinates of the chain segments; we only know the probability of finding a chain segment at the mesh points of the domain. This probability is commensurate to the *restricted partition function*, q , which is the solution of the *Edwards* diffusion eq 2.2. The periodic systems that we wish to address consist of multiple polystyrene-grafted silica nanoparticles embedded inside a polystyrene matrix. In the first system shown in Figure 3.25, the NPs are arranged in a

simple cubic lattice configuration, while in the alternative system they assume body-centered cubic (bcc) configuration.

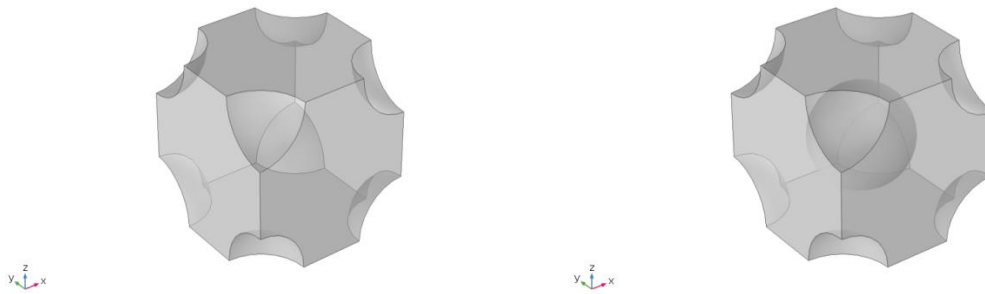


Figure 3.25 Periodic systems of multiple grafted nanoparticles embedded in polystyrene matrix. Nanoparticles are arranged in **a)** simple cubic lattice, **b)** body-centered cubic lattice (bcc). In each case, the volume accessible to polymer inside a unit cell of the structure is shown.

In order to ensure the periodicity of the system, we have to require that the solution at the points of one periodic face of the domain be exactly equal to the solution at the corresponding point on the opposing face. This requires that the opposite faces along each dimension are symmetrically meshed, otherwise an interpolation would have to be performed and this would add considerable complexity and overhead in the solution of the PDE. To ensure the symmetry of the mesh on the boundaries of the box, we first mesh one of the two faces representing each periodic dimension and then we take advantage of the “copy mesh” feature of the *GMSH* mesher,⁹³ which allows us to transfer the mesh of an already meshed face to another face of the geometry, as we demonstrate in the following Figure 3.26.

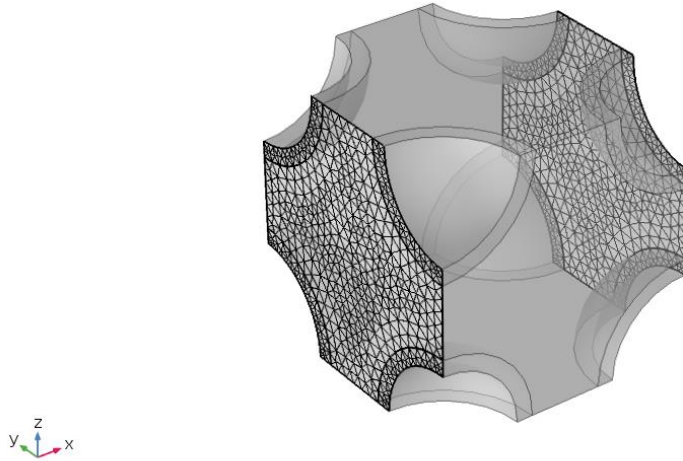


Figure 3.26 A symmetric triangular mesh on the opposite faces of a cubic domain. Demonstration of the “copy mesh” feature which allows for creation of perfectly symmetric triangular meshes on opposite faces. For clarity, we only show the symmetry of the mesh on the periodic faces normal to the x -axis.

Having established that, for a pair of opposing periodic faces, the nodes of one face have symmetric coordinates with respect to the points of the other face, we create a *hash table* or *dictionary* in our code, whose key-value pairs are the id’s of the opposing nodes. A hash table is an array-like data structure which stores data in an associative manner and therefore maps *keys* to *values*. In our case, the keys are the id’s of the nodes belonging to the source (*src*) face and the corresponding values are the id’s of the nodes belonging to the destination (*dst*) face. In other words, each node of the *src* face knows exactly its symmetric point that lies on the *dst* face. The hash table associating the periodic node pairs is built by taking advantage of the fact that the coordinates of the nodes of periodic pairs satisfy the following conditions (the origin is located at the center of the simulation box):

Periodic node pairs along the x -axis: $x_{\text{src}} = -x_{\text{dest}}, y_{\text{src}} = y_{\text{dest}}, z_{\text{src}} = z_{\text{dest}}$

Periodic node pairs along the y -axis: $x_{\text{src}} = x_{\text{dest}}, y_{\text{src}} = -y_{\text{dest}}, z_{\text{src}} = z_{\text{dest}}$

Periodic node pairs along the z -axis: $x_{\text{src}} = x_{\text{dest}}, y_{\text{src}} = y_{\text{dest}}, z_{\text{src}} = -z_{\text{dest}}$

These periodic node pairs need to be taken into account to create the corresponding rows and columns of the FEM stiffness matrix. It is stressed at this point that in our three-dimensional FEM based methodology we take advantage of the sparsity of the stiffness matrix. Instead of storing and feeding it to the *MUMPS*^{95,96} solver in its full form, we rather store the ids of the neighboring node pairs, which, by the definition of the *basis* functions, are those contributing

nonzero values to the corresponding rows and columns of the stiffness matrix. The reader is reminded that for two neighboring nodes, n_1 and n_2 , the nonzero entries of the stiffness matrix (considering of course the fact that each node is also neighbor with itself) will be:

$$\mathbf{p}_1: (n_1, n_1), \mathbf{p}_2: (n_1, n_2), \mathbf{p}_3: (n_2, n_1), \mathbf{p}_4: (n_2, n_2)$$

where we denote by p_i the id of each node-pair.

For a certain *src-dst* periodic pair, let the id of the (*src, src*) nonzero entry in the FEM stiffness matrix be denoted by p_1 , the (*src, dst*) pair by p_2 , the (*dst, src*) by p_3 and the (*dst, dst*) pair by p_4 . Let us also denote by *val*, the nonzero value of the $p_i = \text{id}(\text{row}, \text{col})$ entry of the stiffness matrix. For periodicity to be applied in the context of the *Finite Element Method*, the modifications shown in the following eqs 3.36-3.39 must be ensured for all *src-dst* periodic node pairs before the solution of the *Edwards* diffusion equation.

$$val(p_1) \leftarrow val(p_1) + val(p_2) \quad 3.36$$

$$val(p_2) \leftarrow 0.0 \quad 3.37$$

$$val(p_3) \leftarrow -1.0 \quad 3.38$$

$$val(p_4) \leftarrow +1.0 \quad 3.39$$

In order to validate that the periodicity constraint is indeed satisfied, we compare the density profiles of matrix chains (in absence of grafted chains) in a system where PBCs are applied on all faces of the simulation box and in a system where *Neumann* BCs are applied with zero *propagator* flux. In these cases, we simply address a bulk polymer system and therefore the density profile of matrix chain segments must be equal to unity everywhere inside the domain, as we demonstrate in the following Figure 3.27.

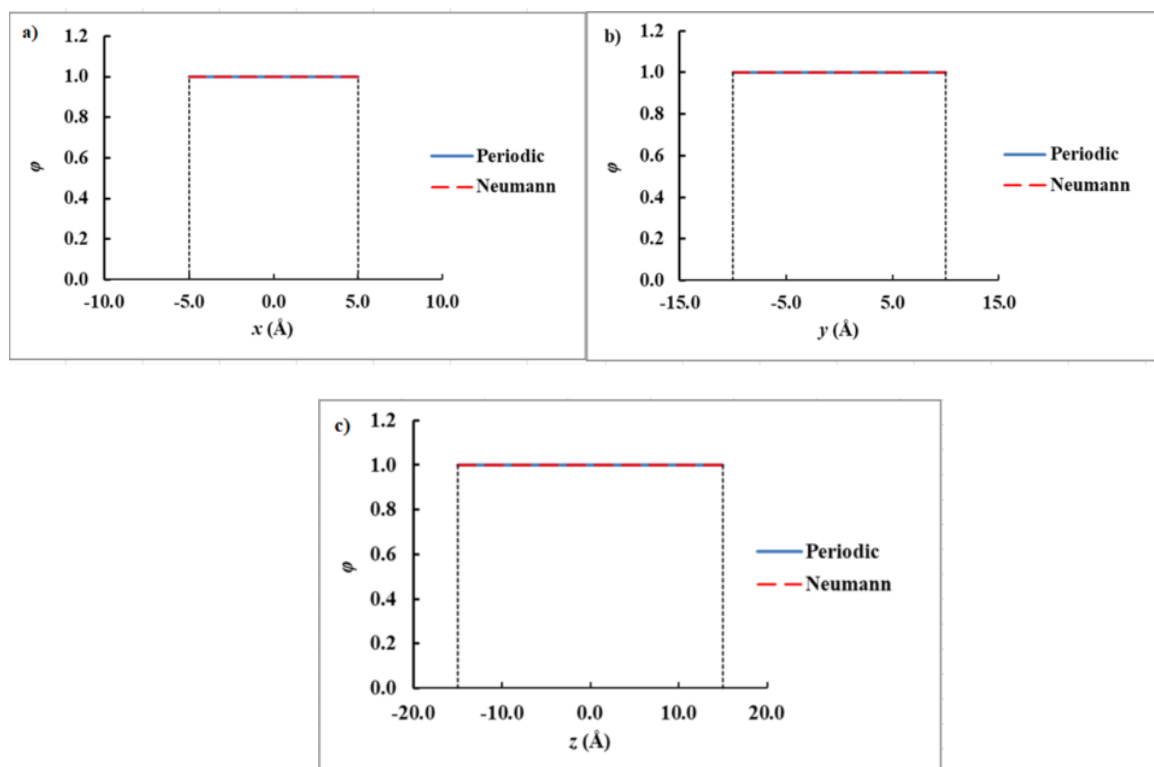


Figure 3.27 *Neumann vs periodic* boundary conditions. Reduced segment density profile of matrix chains in a bulk polystyrene melt obtained with periodic and *Neumann* boundary conditions with zero *propagator* flux. Profiles are plotted across the a) x , b) y , c) z axis to demonstrate that density assumes its bulk value everywhere, as it should. The size of the periodic box is equal to $1 \times 2 \times 3 \text{ nm}^3$.

In the following figures we present the segment density profiles of matrix and grafted chain segments in a system where the grafted nanoparticles are arranged in a **(a)** a bcc configuration and therefore each periodic cell includes 4 silica nanoparticles in polystyrene melt (illustrated in the following Figure 3.28a) and **(b)** a simple cubic-lattice configuration where each periodic cell includes 1 silica nanoparticle in polystyrene melt (illustrated in Figure 3.28b).

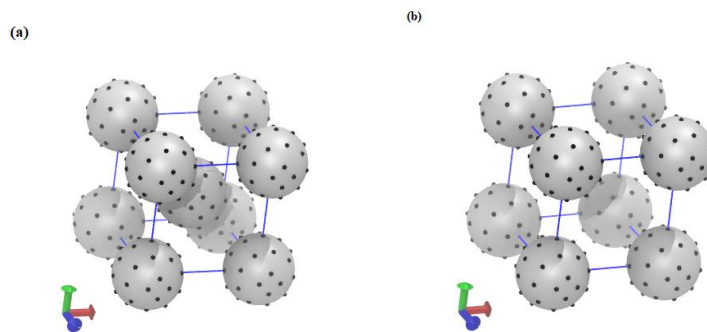


Figure 3.28 Demonstration of different nanoparticle configurations. Illustration of the **(a)** body centered cubic (bcc), **(b)** cubic configuration of polystyrene-grafted silica nanoparticles embedded inside melt of polystyrene chains. Nanoparticle radius is equal to $R_s = 2$ nm. The size of the periodic box is equal to $8 \times 8 \times 8$ nm³.

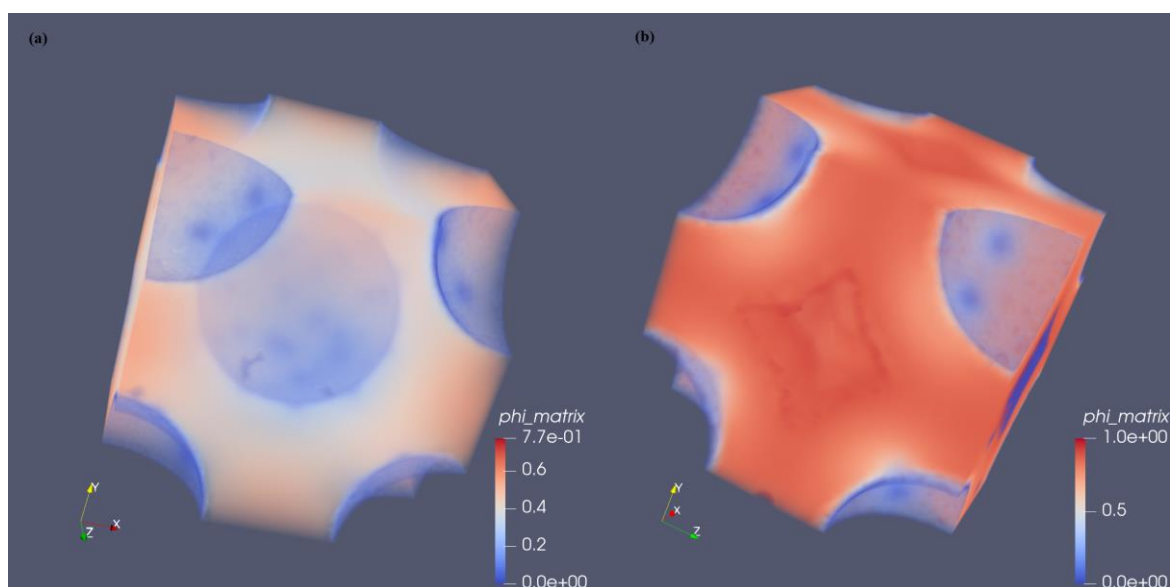


Figure 3.29 3D density profile of matrix chains for different particle configurations. (a) bcc, (b) cubic arrangement of polystyrene-grafted silica nanoparticles. The length of the matrix and grafted chains is equal to $N_m = 24$ and $N_g = 48$ skeletal carbon bonds, respectively. The grafting density is 0.5 chains/nm². The radius of the nanoparticles is $R_s = 2$ nm. The size of the periodic box is $8 \times 8 \times 8$ nm³.

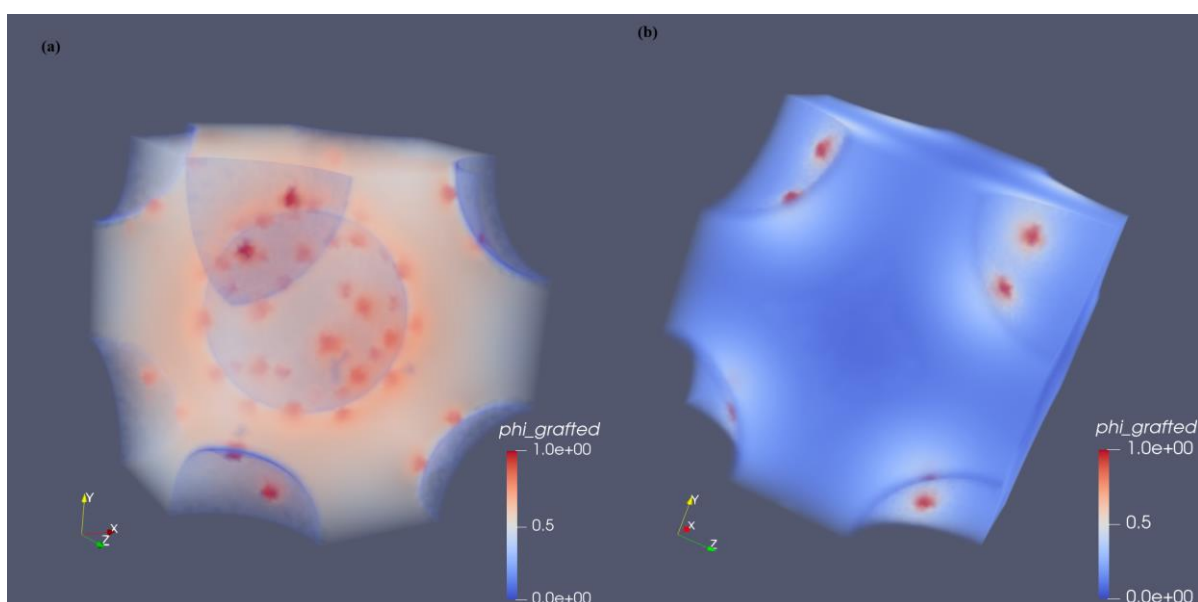


Figure 3.30 3D density profile of grafted chains for different particle configurations. (a) bcc, (b) cubic arrangement of polystyrene grafted silica nanoparticles. The length of the matrix and grafted chains is equal to $N_m = 24$ and $N_g = 48$ skeletal carbon bonds, respectively. The grafting density is 0.5 chains/nm². The radius of the nanoparticles is $R_s = 2$ nm. The size of the periodic box is $8 \times 8 \times 8$ nm³.

In the following Table 3-4, we report the free energy of the two different configurations (i.e., bcc vs cubic lattice). The free energy of the bcc lattice was found to be higher than that of the cubic lattice, which indicates that for this specific distance between the particles, the latter cannot tolerate the addition of another particle in the middle (i.e., transition from cubic to bcc).

For a lot of applications, this is good, since it means that, at equilibrium, the grafted particles do not want to form aggregates, but they rather want to stay away from each other.

Table 3-4 Free energy per nanoparticle surface in the bcc and cubic nanoparticle configuration.

Free energy per nanoparticle surface (mJ/m ²)	BCC	CUBIC
	9.38	3.99

3.9.2. Spherical Nanoparticles in Vacuum

Using the *Sanchez-Lacombe* EoS, we can also run SCFT calculations in three-dimensional domains, where the solid particles and the chains grafted on their surfaces are exposed to vacuum. Using *Helfand* to describe polymer/vacuum interfaces is not an option, since it cannot lead to field convergence when no matrix chains exist in the system. It is noted that, even in the case of the SL EoS, the explicit presence of grafting points via non-smearred delta functions is a factor that creates numerical difficulties due to the logarithmic term that is present in eqs 2.12 and 2.13, but eventually the field can converge at a fair speed.

First, we present the structure of a polystyrene-grafted silica nanoparticle in contact with vacuum and then, as a proof of concept, we demonstrate the 3D density profiles of grafted chains in a periodic system of polystyrene-grafted silica nanoparticles in vacuum and arranged in a cubic lattice, as we did in the previous section where the silica particles were embedded in polystyrene matrix. In Figure 3.31 we present the density of grafted chain segments in 3D, when one polystyrene chain is grafted on the surface of the NP and exposed to vacuum, and when the same grafted NP finds itself inside polystyrene melt. In Figure 3.32, we present the corresponding projections of the 3D density profile of a grafted chain with length $N_g = 96$ (third column of Figure 3.31), along the radial direction, i.e., a line which emanates from the surface of the NP and ends at a corner of the periodic simulation box. As we show below, this is quite useful to predict how drastically the 3D configuration of a polymer chain changes when transferred from vacuum into homopolymer melt of the same chemistry.

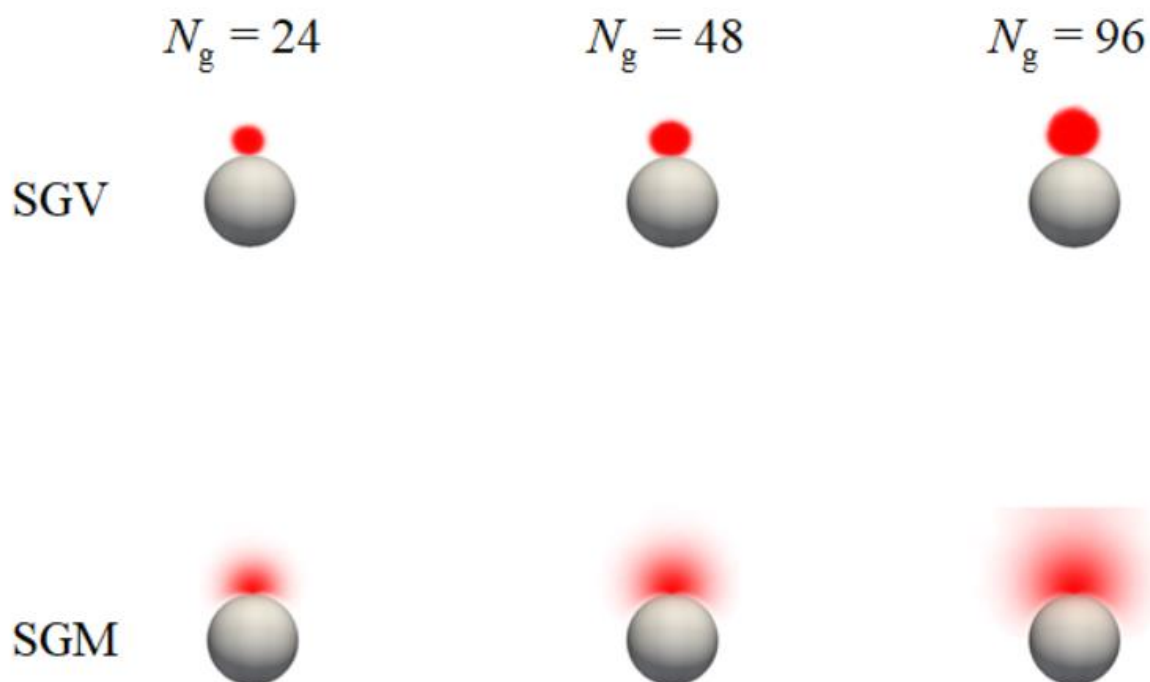


Figure 3.31 Three-dimensional density profile of grafted chain segments in contact with vacuum or melt. A single polystyrene chain is grafted on the surface of a silica NP. The length of the grafted chain assumes the values $N_g = \{24, 48, 96\}$ skeletal carbon bonds, varying from left to right. The NP is either exposed to vacuum (SGV, first row) or embedded in polystyrene matrix (SGM, second row). The radius of the NP is 2 nm. In the SGM case, the length of the matrix chains is equal to that of the grafted chains, $N_m = N_g$.

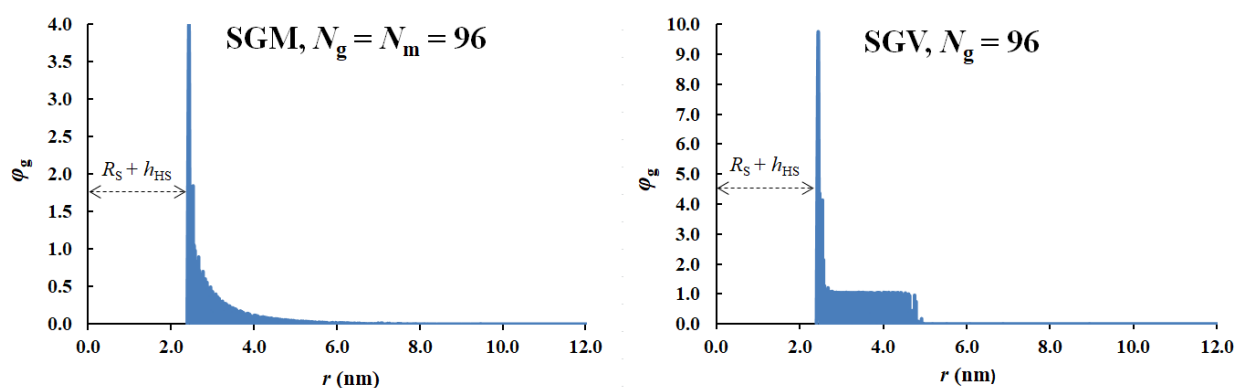


Figure 3.32 One-dimensional density profile of grafted chain segments in contact with vacuum or melt. A single polystyrene chain is grafted on the surface of a silica NP. The grafted NP is either embedded in polystyrene melt (SGM, left panel) or exposed to vacuum (SGV, right panel). The length of the grafted chain is $N_g = 96$ skeletal bonds. The radius of the NP is $R_s = 2$ nm. These profiles are projections of the corresponding three-dimensional profiles presented in Figure 3.31 (rightmost column, $N_g = 96$). The segment-depleted zone has a thickness equal to $R_s + h_{HS}$, where $h_{HS} = 0.4$ nm, is the thickness of the *Hamaker* hard-sphere wall. In the SGM case, $N_m = N_g = 96$.

Looking at Figure 3.31, we can see how different the configuration of the chain becomes when it is exposed to vacuum (equivalent to a *poor solvent*) as opposed to when it is in contact with matrix chains of the same chemistry (equivalent to a *theta solvent*). To be more specific, the

3.9. 3D Periodic Boundary Conditions

profile of grafted chain segments assumes a completely spherical shape in the SGV system, whereas in SGM chain segments seem to be more diffuse in space. This is an expected behavior, because the vacuum is considered to be a *poor solvent* for chain segments, which means that the interactions between segments and vacuum are quite unfavorable. Hence, the chain responds by minimizing the surface area that is exposed to vacuum. Chain segments do not have a reason to get closer to the solid surface either, since the *Hamaker* interactions that we have employed for these calculations are extremely weak to attract the polymer segments. As a net result, the cohesion of the polymer dominates the structure of the chain and drives the segments to get as close to each other as possible. With increasing chain length, N_g (SGV row, from left to right), the radius of the sphere increases.

On the contrary, in the SGM system, the interaction between grafted chain segments with those of the matrix is favorable, since they are chemically identical, thus the segments are thermodynamically allowed to explore more space in the three-dimensional domain. With increasing chain length (SGM row, from left to right), the grafted chain swells more towards the bulk, gradually reaching higher distances from the surface of the NP; in the case where $N_g = N_m = 96$ we can see that there are even grafted segments reaching the edge of the box. The difference in the configuration of the grafted chain is also reflected in the one-dimensional profiles of Figure 3.32, resulting from the projection of the corresponding three-dimensional profiles of Figure 3.31.

In the following Table 3-5, we report the free energy, normalized with respect to the area of the NP, as a function of chain length, N_g , for the system of single NP grafted with one polystyrene chain embedded in polystyrene matrix (solid-grafted-matrix, SGM) and for the same particle exposed to vacuum (solid-grafted-vacuum, SGV). In Figure 3.33, we present a graphical representation of the chain length dependence of the free energy of the two systems.

Table 3-5 Free energy in mJ/m^2 of a silica NP grafted with one polystyrene chain. The NP is embedded in polystyrene matrix (SGM) or exposed to vacuum (SGV). In the SGM case, the length of the matrix chains is equal to that of grafted chains, $N_m = N_g$. The radius of the particle is $R_S = 2$ nm.

N_g	SGM						SGV					
	$\Delta\Omega_{\text{coh}}/S_S$ (mJ/m^2)	$\Delta\Omega_{\text{field}}/S_S$ (mJ/m^2)	$\Delta\Omega_m/S_S$ (mJ/m^2)	$\Delta\Omega_g/S_S$ (mJ/m^2)	$\Delta\Omega/S_S$ (mJ/m^2)	$\Delta\Omega$ (10^{-17} mJ)	$\Delta A_{\text{coh}}/S_S$ (mJ/m^2)	$\Delta A_{\text{field}}/S_S$ (mJ/m^2)	$\Delta\Omega_m/S_S$ (mJ/m^2)	$\Delta A_g/S_S$ (mJ/m^2)	$\Delta A/S_S$ (mJ/m^2)	ΔA (10^{-17} mJ)
24	55.09	-42.84	1.44	0.40	14.09	70.82	-4.44	4.84	0.00	1.60	2.00	10.07
48	54.65	-41.44	0.78	0.39	14.38	72.30	-9.36	9.89	0.00	2.42	2.95	14.83
96	55.12	-41.41	0.46	0.39	14.56	73.20	-19.29	18.92	0.00	4.37	4.01	20.16

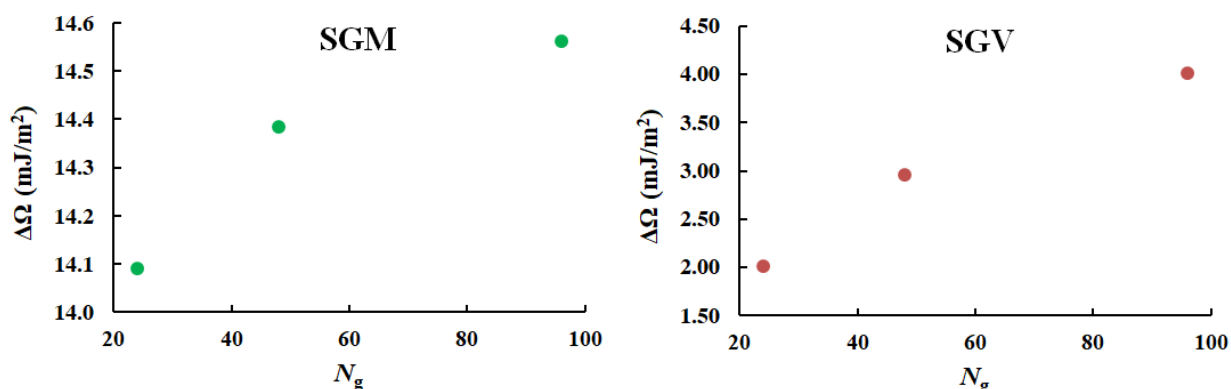


Figure 3.33 Free energy, in mJ/m^2 , of a silica NP grafted with one polystyrene chain. The NP is embedded in polystyrene matrix (SGM) or exposed to vacuum (SGV). In the SGM case, the length of the matrix chains is equal to that of grafted chains, $N_m = N_g$. The radius of the particle is $R_S = 2$ nm.

The first observation regarding the energies reported in Table 3-5 is that the free energy of the SGV system is quite lower than the energy of the corresponding SGM. At first, this seems to be unexpected, since one would argue that the cohesive interactions among polymer segments of the same chemistry would favor the incorporation of the grafted NP inside the polymer melt. Nonetheless, in this specific case, the lower energy of the SGV system can be explained by considering that we have addressed the edge case where the *Hamaker* interactions between chain segments and NP surface are extremely weak and, furthermore, only one chain is grafted on the surface of the particle.

To be more specific, since only one polymer chain is grafted on the surface of the NP, which assumes a spherical configuration in shape in SGV as explained earlier, the area of interaction between polymer and vacuum is not so large as to raise the energy of the system. At the same time, in SGM, the area of interaction between grafted chain segments and the solid surface is quite larger. The solid, however, is practically equivalent to vacuum for the polymer segments, because the attraction exerted on them is negligible. These two phenomena explain why the total energy of the SGV system is lower than that of the SGM system in this limiting case examined here. Had the solid/polymer interactions been stronger and/or more chains been grafted on the surface of the NP (which would imply that larger area in total would be exposed to vacuum in the SGV case), then the energy of SGM would indeed become lower than that of SGV.

Instead of normalizing the free energy of SGV and SGM with respect to the surface of the NP, an alternative approach would be to normalize the total energy of the system (in the SGM case we need to add the contribution of the bulk, which is mainly entropic) with respect to the

3.9. 3D Periodic Boundary Conditions

number of polymer segments in the system. In the following Table 3-6 and Table 3-7, we present the results of the approach for the SGV and SGM system, respectively.

Table 3-6 Free energy in mJ/segment of a silica NP grafted with one polystyrene chain and exposed to vacuum.

SGV					
# chains, n_g	segments per chain N_g	$\Delta A/S_S$ (mJ/m ²)	$A_{G,bulk}/S_S$ (mJ/m ²)	$A = \Delta A + A_{G,bulk}$ (10 ⁻¹⁷ mJ)	$A_{seg} = A/(n_g \cdot N_g)$ (10 ⁻¹⁷ mJ/seg)
1	24	2.00	0.0	10.07	0.42
1	48	2.95	0.0	14.83	0.31
1	96	4.01	0.0	20.16	0.21

Table 3-7 Free energy in mJ/segment of a silica NP grafted with one polystyrene chain and embedded in polystyrene matrix.

SGM					
# chains, $n_g + n_m$	segments per chain, $N_g = N_m = N$	$\Delta \Omega/S_S$ (mJ/m ²)	$\Omega_{M,bulk}/S_S$ (mJ/m ²)	$\Omega = \Delta \Omega + \Omega_{M,bulk}$ (10 ⁻¹⁷ mJ)	$\Omega_{seg} = \Omega/[(n_g+n_m) \cdot N_g]$ (10 ⁻¹⁷ mJ/seg)
1203	24	14.09	-0.81	66.75	0.0023
603	48	14.38	22.54	185.59	0.0064
302	96	14.56	70.92	429.69	0.0148

At this point, we need to remind the reader that the reference states correspond to a homogeneous system (grand potential, $\Omega_{M,bulk}$) of matrix chains of length N_m at temperature T , subject to a *chemical potential*, $\mu_M N_m$, and occupying the same polymer accessible volume as the interfacial system, and a system of a single end-pinned and unperturbed (there are no interfaces) grafted chains of length N_g (Helmholtz energy, $A_{G,bulk}$) interacting with a bulk phase of matrix chains of length N_g at temperature T . In our code, we consider that $A_{G,bulk} = 0$. Regarding the SGM system, we observe that Ω_{seg} increases considerably with increasing chain length, despite the fact that the total number of segments $N_m \cdot n_m + N_g \cdot n_g$ remains constant and, approximately, so does the quantity $\Delta \Omega/S_S$.

Regarding the SGV system, we observe that the free energy per segment decreases with increasing chain length. This can be explained by the fact that the size of the sphere which is formed in the SGV system (first row of) increases with the number of segments of the grafted chain. When the size of the sphere increases, its volume rises faster than its surface, which practically means that the number of segments of the grafted chain that form a bulk region (and therefore have zero contribution to the energy of the system) rises faster than the number of

segments in the vacuum/polymer interface. Finally, we can see that the energies per segment of the SGM system are orders of magnitude smaller than the corresponding energies in the SGV system, which underlines the large cost in free energy that is associated with exposure of polymer segments to vacuum in the SGV case.

Finally, in Figure 3.34 below we present the three-dimensional density profile of grafted chains in a cubic lattice configuration of polystyrene-grafted particles exposed to vacuum. All particles have a radius equal to $R_S = 2$ nm and periodic boundary conditions are imposed on the edges of the simulation box.

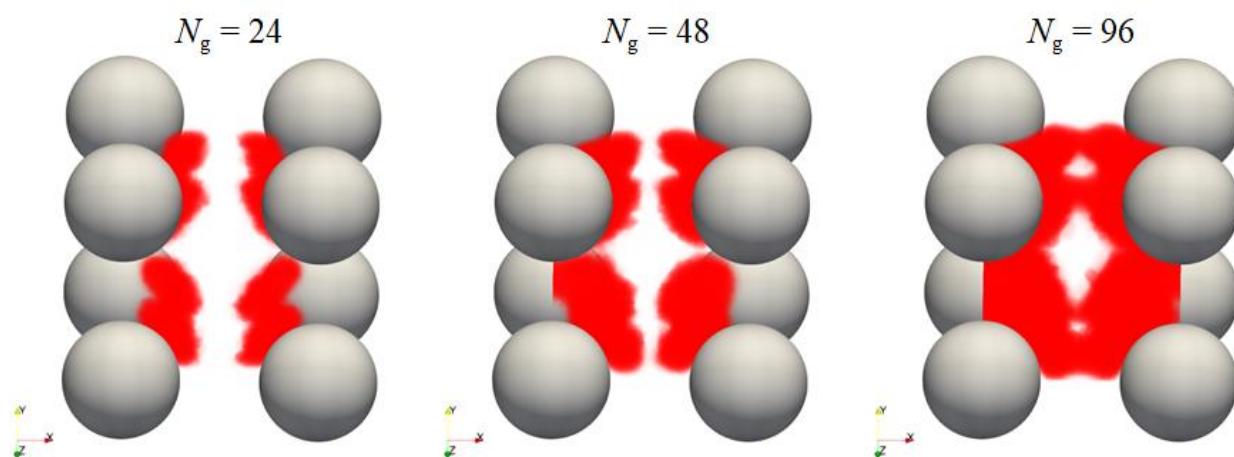


Figure 3.34 Three-dimensional density profiles of polystyrene chains grafted on the surfaces of silica particles arranged in a cubic lattice and exposed to vacuum. The length of grafted chains assumes the values $N_g = \{24, 48, 96\}$ skeletal carbon bonds and varies from left to right. The radius of all NPs is equal to $R_S = 2$ nm. The lattice parameter is 4 nm and the coordination number of the lattice is 6. Periodic boundary conditions are imposed on the edges of the simulation box, and the surface of each NP inside the box is grafted with two polystyrene chains; this corresponds to grafting density, $\sigma_g = 0.3 \text{ nm}^{-2}$.

4. SINGLE NANOPARTICLE CALCULATIONS

In this chapter, we present our findings regarding systems of a single polystyrene-grafted silica nanoparticle. The particle is either embedded in polystyrene matrix or exposed to vacuum. As a reference, we begin by analyzing the thermodynamics of a bare (i.e., non-grafted) silica particle inside polystyrene melt. To investigate the structural properties of grafted chains and their impact on the free energy of the system, we systematically vary the molecular weight of grafted chains, the grafting density, the size of the particle and the strength of solid/polymer interactions. For the convenience of the reader, we present in Table **4-1** all the different systems addressed in this chapter. Furthermore, in Table **4-2** we report the values of all parameters required for our SCFT calculations.

Chapter 4. Single Nanoparticle Calculations

Table 4-1 Explanation of symbols for the different interfacial systems and free energy contributions examined in this chapter. Energy contributions are reported using the conventions: E_a^{sys} (system energy), ΔE_a^{sys} (energy with respect to a reference system), $\Delta G_{s,a}^{*,o} = \Delta \Omega_\alpha^{SGM} - \Delta A_a^{SGV}$ (solvation free energy). With $\gamma_a^{sys} = E_a^{sys} / S_s$ we refer to the energy of the solid per unit area. The meaning superscripts (sys), subscripts (a) and symbol (E) is presented below.

Superscript (sys)	system	Physical system for each geometry type	
		spherical	planar ($R_s \rightarrow \infty$)
VM	vacuum-matrix	cavity/bubble	free matrix surface
MV	matrix-vacuum	droplet	
SM	solid-matrix	bare NP/matrix	bare solid surface/matrix
SGM	solid-grafted-matrix	grafted NP/matrix	brush/matrix
SGV	solid-grafted-vacuum	isolated grafted NP	isolated brush
M	matrix	bulk melt phase of matrix polymer chains	
A,bulk	grafted	isolated end-pinned and unperturbed chains in bulk melt	

Subscript (a)	energy component	equation
-	total energy	2.38 or 2.44
coh	cohesion	2.39 or 2.45
field	field	2.40 or 2.46
m	translational entropy of matrix chains	2.42
g	conformational entropy of grafted chains	2.43
S	solid field	2.41

Symbol (E)	thermodynamic potential
A	<i>Helmholtz</i> free energy
Ω	grand potential
G	Gibbs free energy
U	internal energy
H	enthalpy

Table 4-2 Parameters of 1D-SCFT calculations.

component	parameter	value	source
System	T	500 K	-
	$h_{\text{ref},q=0}$	0.05 nm	24
Chain stiffness	$h_{\text{g},i_{\text{g}},q=0}$	0.05 nm	24
	b_{k}	1.83 nm	23
	$l_{\text{C-C}}$	0.154 nm	-
	γ	0.829	3
	m_{monomer}	52.08 g/mol	-
<i>Hamaker</i>	h_{HS}	~0.4 nm	24
	σ_{PS}	0.37 nm	23
	σ_{SiO_2}	0.30 nm	23
	A_{PS}	$5.84 \cdot 10^{-20}$ J	23
	A_{SiO_2}	$6.43 \cdot 10^{-20}$ J	23
u_{cSW}	$C_{\text{SW,HW}}$	$-3.75 \cdot 10^{-13}$ J/m ³	Fitted to $W_{\text{A}} = 38.8$ mJ/m ² from ¹⁰⁴
	$C_{\text{SW,PW}}$	$-5.88 \cdot 10^{-13}$ J/m ³	Fitted to $W_{\text{A}} = 71.1$ mJ/m ² from ¹⁰⁴
	σ_{SW}	1.28 nm	-
<i>Sanchez-Lacombe</i>	ρ^*	1105 kg/m ³	70
	P^*	357 MPa	70
	T^*	735 K	70
Square Gradient	κ	$0.2233 \cdot 10^{-66}$ J m ⁵	2
<i>Edwards Diffusion</i>	Δh	0.05 nm	24
	ΔN	0.25	24
	$\Delta W_{\text{ifc}}^{\text{tol}}$	$10^{-6} k_{\text{B}} T$	24

4.1. Bare surfaces exposed to melt

4.1.1. Background

4.1.2. Structure

The present section investigates the thermodynamics of solid-matrix systems (SM) with varying strength of solid/polymer interactions and curvature. The strength of solid/polymer interactions in relation to the cohesion of the polymer dictates the tendency of the latter to wet the solid surface. The wetting degree can be classified as nonwetting (NW), low (LW), high (HW), and perfect wetting (PW).

Figure 4.1a illustrates a spherical cell with radius R_{S} exposed to a phase of matrix chains of length N_{m} and characterized by a *chemical potential* $\mu_{\text{m}} N_{\text{m}}$, with μ_{m} being the *chemical potential* per monomer unit of a matrix chain. In the presence or absence of solid/polymer interactions, the system corresponds to a solid/matrix (SM) or a vacuum/matrix (VM) interface, respectively. In Figure 4.1b, the solid surface has been grafted with $n_{\text{g}} = \sigma_{\text{g}} S_{\text{g}}$ chains of length equal to N_{g} , with

Chapter 4. Single Nanoparticle Calculations

σ_g and S_g being the grafting density and surface area of the sphere, respectively. This system will be symbolized with SGM. In contrast, Figure 4.1c illustrates an isolated grafted NP, meaning that the NP and the chains grafted on its surface are exposed to vacuum; this system will be denoted by SGV.

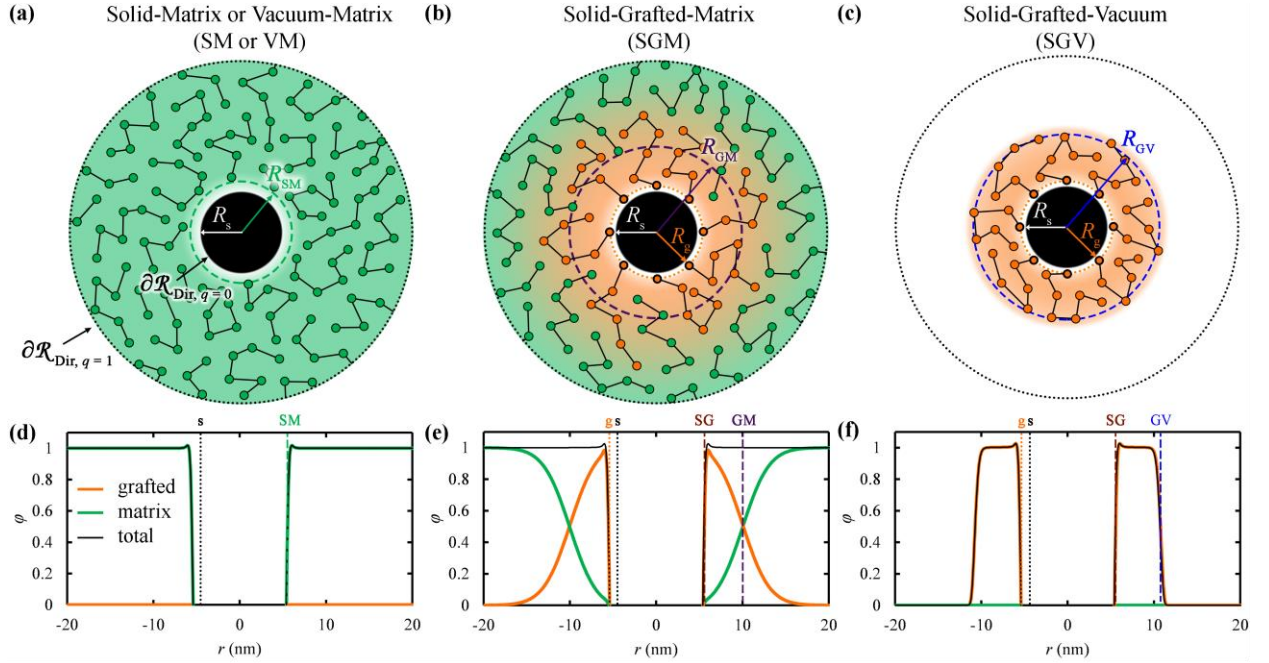


Figure 4.1 Demonstration of the kinds of interfacial systems that are addressed in this chapter. Bead spring representation of (a) bare NP-matrix (SM) or vacuum-matrix (VM), (b) grafted NP-matrix (SGM), and (c) grafted NP-vacuum (SGV) systems. The solid core of the spherical NP has radius R_s . Green/orange beads depict segments of matrix/grafted chains. The density profiles of matrix (green), grafted (orange) and total (black) segments in (d), (e) and (f) correspond to the systems in (a), (b) and (c), respectively. The dotted curves mark the position of grafting points (g, orange), and the edge of the solid sphere (s, black). The dashed curves illustrate the location of characteristic interfaces across the domain (e.g., SM, SG, GM, GV). The black dotted lines represent the boundaries on which *Dirichlet* BCs are imposed with propagator value equal to unity, corresponding to bulk conditions.

The system of Figure 4.1a is discussed in the current Section 4.1, of Figure 4.1b in Section 4.2 and that of Figure 4.1c in Section 4.3. R_i symbolizes the distance between the center of the sphere and a characteristic interface i ; e.g., $i = g, s, SG, GM$, etc. as shown in Figure 4.1. The way interfaces are drawn on the basis of the continuous density profiles obtained by SCF is explained in Section 4.3. The distance between any point \mathbf{r} and the surface of the NP along the radial direction is denoted by $h = |\mathbf{r}| - R_s = r - R_s$. Likewise, the distance between an interface i and the edge of the spherical core is defined as:

$$h_i = R_i - R_s \quad 4.1$$

and its corresponding surface area as:

$$S_i = 4\pi R_i^2 \quad 4.2$$

In addition, the number of grafted segments per NP area will be denoted as:

$$\sigma_{g,seg} = \sigma_g N_g = \frac{6}{C_\infty l_{C-C}^2} \sigma_g R_{G,g}^2 \quad 4.3$$

with C_∞ being *Flory's* characteristic ratio, l_{C-C} the length of a skeletal carbon-carbon bond along the polymer chain, and $R_{G,g}$ the unperturbed root mean squared radius of gyration of a grafted chain. It is noted here that the term $\sigma_g R_{G,g}^2$ is a common threshold value to characterize brush conformations.

Under non-wetting (NW) conditions (the reader is referred to Table 2-2 in Section 2.2.3), the polymer does not experience any forces from the solid and the interface is equivalent to a vacuum-matrix one (nonwetting). In LW, the solid/polymer interactions are described by the *Hamaker* potential¹⁷ presented in Section 2.1.5, which yields low wetting when applied in our model ($\theta_c \sim 158.9^\circ$, see Section 2.2.3). In the HW and PW systems, in addition to the *Hamaker* potential, the polymer²⁸ segments interact with the u_{csw} potential of eq 2.34 (Section 2.1.5.5), which has been fitted to yield the experimentally measured work of adhesion.⁸¹

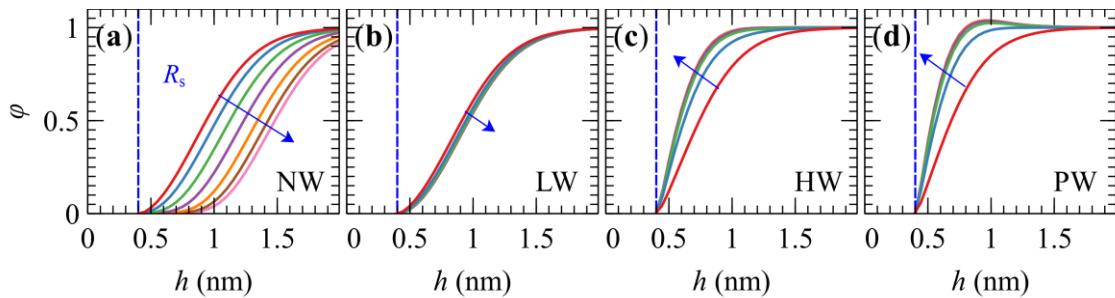


Figure 4.2 Density profiles for different particle radii and solid wetting degree. (a-d) Density profiles of NW, LW, HW and PW systems in Table 2-2 for $R_s = \{5: \text{red}, 20: \text{blue}, 80: \text{green}, 320: \text{purple}, 1280: \text{orange}, 5120: \text{brown} \text{ and } \infty: \text{pink}\}$ nm. Colors vary in the direction of blue arrows. The vertical dashed line depicts the position of the imposed hard sphere wall, $h_{HS} \sim 0.4$ nm.

The density profiles corresponding to different wetting conditions are illustrated in Figure 4.2a-d as a function of curvature. According to numerous atomistic simulations,^{36,105-107} repulsive solid/polymer interactions lead to the emergence of a depletion zone near the solid. Excluded volume repulsion at short distances from the solid is modeled here by a hard sphere

Chapter 4. Single Nanoparticle Calculations

wall, represented by the blue vertical dashed lines in Figure 4.2a-d. The profiles shift toward the bulk or the solid phase depending on the strength of solid/polymer interactions. The shift is attributed to a complex interplay between three factors: (1) tendency of the interface to minimize its surface area assuming a curved shape, (2) entropic penalty associated with chain confinement, and (3) enthalpic gain from the solid/polymer interactions (in the cases of high and perfect wetting).

Mechanism (1) can be understood as follows: Let there be two (infinitely) sharp vacuum/polymer interfaces at distance R_1 and $R_2 > R_1$ from the center of an imposed cavity with radius $R_S \leq R_1$. The area of the first interface ($S_1 = 4\pi R_1^2$) is smaller than that of the second by a factor (R_1/R_2); hence, it has a lower surface free energy and is more stable. As a result, the stable solution corresponds to $R_1 = R_S$.

Realistic polymer profiles are not infinitely sharp. In fact, as the length of the chains increases, the entropy associated with bonded interactions along the chain contributes to the smoothness of the profile. A chain segment at the edge of the film experiences a net force toward the bulk phase from its interchain neighbor segments. The net force becomes zero in a situation where a segment and its neighbors reside in the same plane, which means that the chain is oriented parallel to the edge of the film, corresponding to an improbable configuration. This entropic factor resists the collapse of the interface at R_S and pushes the chain segments toward the bulk phase (mechanism (2)). It is observed from Figure 4.2a that this mechanism prevails under nonwetting conditions and at lower curvature.

Regarding mechanism (3), the enthalpic gain from the solid/polymer interactions, in relation to the cohesive segment-segment interactions, increases with increasing R_S . Larger NPs exert stronger attraction on the polymer segments. As a result, the interface tends to shift toward the solid with increasing R_S .

The interplay between mechanisms (1) and (2) is demonstrated by the profiles of the NW system in Figure 4.2a, which is equivalent to a vacuum/matrix (nanobubble) system. Indeed, the interface shifts toward the cavity with decreasing R_S , since the tendency to minimize the surface area surpasses the entropic penalty of chain confinement.

In the LW system (Figure 4.2b), the enthalpic solid/polymer interactions (albeit weak) counterbalance the entropic penalty with increasing R_S , and as a result, the position/shape of the profiles is about constant, i.e., independent from R_S . The trend is reversed in the HW and PW systems (Figure 4.2c,d), wherein the profiles shift toward the solid with increasing R_S and

become more pronounced; it is notable that the profile of the PW system develops a peak at large R_S . We remind the reader that it is not straightforward to capture with an SCF treatment the layering effects seen in atomistic simulations; rather, smoothed density profiles are obtained in most cases. If one wishes, one can reproduce the layering effects by appropriately tuning the field exerted by the solid, e.g., via *Boltzmann* inversion (e.g., see Figure 2.10).⁷⁶

In the extreme situation of very small R_S , the profiles become about the same for all cases (NW, LW, HW, and PW) both position- and shape-wise. The solid/polymer interactions are mitigated as the NP radius decreases and it is eventually experienced as a cavity (e.g., compare Figure 4.2a-d for $R_S = 5$ nm).

4.1.3. Thermodynamics

Figure 4.3 presents the free energy per NP area ($\Delta\gamma^{\text{SM}} = \Delta\Omega^{\text{SM}} / S_S$) for each system in Table 2-2. In the limit $R_S \rightarrow \infty$, $\Delta\gamma^{\text{SM}}$ plateaus to the interfacial free energy of the planar solid/polymer interface.² The hyperbolic-like dependence at low R_S is attributed to the mismatch between the actual position of the SM interface and the edge of the sphere, based on which we have normalized the total free energy, e.g., compare R_S with R_{SM} in Figure 4.1a,d. As a result, $\Delta\gamma^{\text{SM}}$ is larger than the actual interfacial free energy by a factor $\sim (R_{\text{SM}} / R_S)^2$.

By normalizing the free energy with respect to the area of the SM interface, we can derive the *adhesion tension* of an SM as follows:

$$\sigma_{\text{adh}}^{\text{SM}} \equiv (\sigma^{\text{SV}} - \sigma^{\text{SM}}) = -\frac{\Delta\Omega^{\text{SM}}}{S_{\text{SM}}} = -\Delta\gamma^{\text{SM}} \frac{R_S^2}{R_{\text{SM}}^2} \quad 4.4$$

under the approximation that the solid is incompressible.¹⁰⁸ Similarly, the *surface tension* of the VM (or MV) interfaces can be calculated as:

$$\sigma^{\text{VM}} = \frac{\Delta\Omega^{\text{VM}}}{S_{\text{VM}}} = \Delta\gamma^{\text{VM}} \frac{R_S^2}{R_{\text{VM}}^2} \quad 4.5$$

It is noted here that in the NW case, where the solid does not exert any potential on the polymer segments ($\sigma^{\text{SV}} = 0$), the solid is experienced as a vacuum phase, and thus, $-\sigma_{\text{adh}}^{\text{SM}} = \sigma^{\text{SM}} = \sigma^{\text{VM}}$.

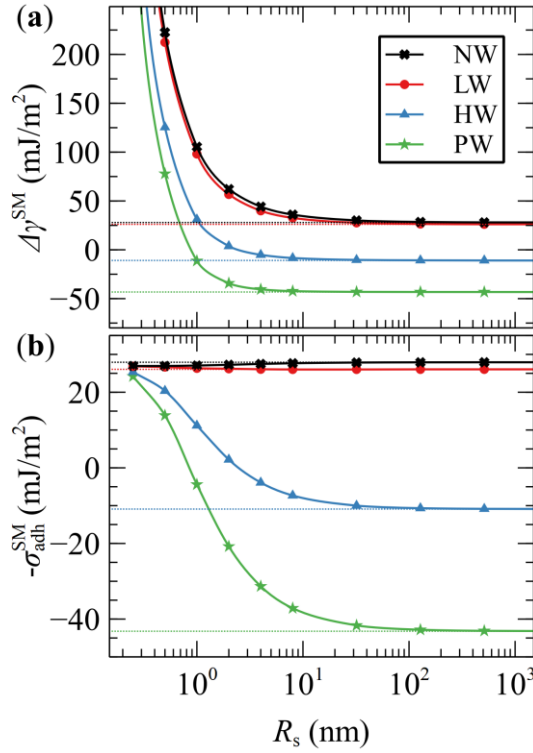


Figure 4.3 Adhesion tension as function of the wetting degree and particle radius. **(a)** Free energy per NP core area, $\Delta\gamma^{\text{SM}} = \Delta\Omega^{\text{SM}} / S_{\text{S}}$, and **(b)** negative of the adhesion tension, $-\sigma_{\text{adh}}^{\text{SM}} \equiv -(\sigma^{\text{SV}} - \sigma^{\text{SM}})$, for the aforementioned systems. The horizontal dotted lines depict the limiting values corresponding to planar solid surfaces. In all cases, the chain length of matrix chains is equal to $N_{\text{m}} = 768$ skeletal carbon bonds.

In planar geometries (large R_{S}), the position of a vacuum/liquid interface can be defined as the position $R_{0.5}$, where $\varphi(R_{0.5}) = 0.5$.^{2,72} This concept can be generalized to curved geometries in terms of the radius $R_{\alpha\beta,\text{eq}}$ of the *Gibbs equimolar dividing surface*, which, for two phases α and β in contact, satisfies the integral presented in eq 4.6 below.

$$\int_0^{\infty} r^2 [\rho(r) - \rho^{\alpha,\beta}] dr = 0 \quad 4.6$$

where

$$\rho^{\alpha,\beta} = \begin{cases} \rho^{\alpha}, & r \leq R_{\alpha\beta,\text{eq}} \\ \rho^{\beta}, & r > R_{\alpha\beta,\text{eq}} \end{cases} \quad 4.7$$

with ρ_{α} and ρ_{β} being the bulk densities of phases α and β , respectively.¹⁰⁹ Dividing the grand potential by $R_{\alpha\beta,\text{eq}}^2$ leads to “scale invariant” surface energies, whereas additional first-order corrections can be introduced in terms of the *Tolman length*.^{109,110} The curvature affects the

position of the *equimolar dividing surface* in a different manner when applied to convex (MV system, droplet) or concave (MV, cavity) interfaces. $R_{MV,eq}$ ($R_{VM,eq}$) shifts towards the gas (bulk) phase relative to $R_{0.5}$ when applied to convex (concave) interface.

Figure 4.3b illustrates $-\sigma_{adh}^{SM}$ for each system in Table 2-2 as a function of R_S . For each case, R_{SM} has been estimated based on the *Gibbs equimolar dividing surface*, applied to either VM or SM interfaces (eqs 4.6 and 4.7). For $R_S < 10$ nm, σ^{VM} becomes slightly lower than its value for the planar system (~ 28.0 mJ/m²),^{2,28} indicating that the approximation of the *Gibbs dividing surface* becomes insufficient.¹⁰⁹ For that reason, first-order corrections are introduced based on the *Tolman length*, which is equal to the distance between R_{eq} and the surface of tension and is usually on the order of few molecular diameters.^{111,112}

The LW interface exhibits similar behavior to NW across the full R_S range, because the solid/polymer interactions are weak. On the contrary, the HW and PW systems exhibit a rather rich behavior. For $R_S < 100$ nm, $-\sigma_{adh}^{SM}$ departs from its planar value, whereas at $R_S \sim 1-2$ nm, it becomes positive. The change in sign below a specific NP radius indicates that the polymer/polymer cohesive interactions become stronger than the solid/polymer ones. Finally, in the extreme case of very small NPs, the free energies converge to that of the vacuum/matrix system; this effect is also reflected by the fact that the density profiles in Figure 4.2a-d are practically identical for $R_S = 2$ nm.

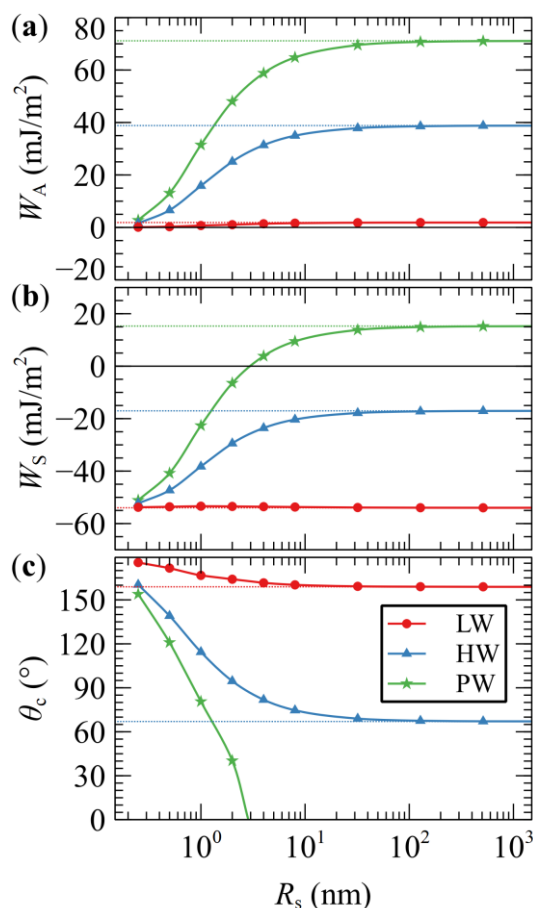


Figure 4.4 Macroscopic work functions with varying wetting degree and particle radius. **(a)** *Work of adhesion*, **(b)** *work of spreading*, and **(c)** *contact angle* of the LW, HW, and PW systems with $N_m = 768$ (384 styrene units per chain) at 500 K (see Table 2-2), as functions of the core radius R_s . The *surface tension* of a planar melt surface is equal to 27.93 mJ/m^2 . Horizontal dotted lines depict limiting cases corresponding to planar geometries and equal experimental values from ref ⁸¹.

W_C is the free energy of two free polymer surfaces and is equivalent to the evaluations in Figure 4.3b for the NW interface ($\sigma^{\text{SV}} = 0, -\sigma_{\text{adh}}^{\text{SM}} = \sigma^{\text{VM}}$). W_I is equivalent to minus the *Gibbs solvation free energy* per unit area. Since $W_I = \sigma_{\text{adh}}^{\text{SM}}$, it can be inferred from the evaluations in Figure 4.3b for the LW, HW, and PW cases. W_A is the reversible work required to separate the polymer melt from the solid surface. As shown in Figure 4.4a, it assumes its maximum value in the limit of large NPs, corresponding to the experimental HW and PW systems from ref ⁸¹, denoted by the dotted lines. With increasing R_s , it is easier to separate the polymer from the solid (W_A decreases), and in the limit $R_s \rightarrow 0$, zero work is required for the separation.

W_S describes the tendency of a melt to spread on a surface. Positive values indicate spontaneous *spreading* across the surface (imaginary *contact angle*, θ_c). Negative values indicate

partial or no *spreading* ($0 \leq \theta_c \leq 180^\circ$). W_S and the corresponding θ_c in Figure 4.4b,c suggest a rather complex behavior with respect to curvature. For example, in the most strongly interacting solid/polymer interface (PW), the polymer wets the solid spontaneously for $R_S > 3$ nm ($W_S > 0$, imaginary θ_c), whereas with decreasing R_S , the wetting tendency gradually decreases from high to low and eventually to nonwetting for very small NPs.

The aforementioned results and insights conform with findings of *molecular dynamics* simulations that report enhanced adhesion on soft surfaces with increasing NP size.^{113,114} In addition, experiments based on the *capillary rise method* applied on magnetic micropowders¹¹⁵ demonstrate that θ_c is indeed a decreasing function of R_S , as presented in Figure 4.4c.¹¹⁶

4.1.4. Concluding remarks

In this section, we examined the case of a bare NP embedded inside the polymer melt. This system serves as a reference for the limiting case where the grafting density and/or length of grafted chains is extremely small. Three mechanisms govern the position of the profile relative to the solid surface. The first mechanism is related to the size of the NP; the larger the curvature, the closer the polymer profile gets to the solid surface. The second mechanism is related with the conformational entropy of each polymer chain. With increasing chain molecular weight, chains are pushed towards the bulk polymer region. The third mechanism prevails for strong solid/polymer interactions; when these interactions are getting stronger in relation to the cohesion of the polymer itself, then the polymer segments are pulled towards the solid.

We compared the thermodynamics of the bare solid/polymer system with experimentally measured work functions and for various solid curvatures, ranging from flat surfaces to very small particles. In the spherical cases, a proper renormalization of the free energy of the system was required with respect to the area of the interface. To this end, we generalized the notion of the *Gibbs* equimolar dividing surface for spherical geometries. The main finding here was that the experimentally measurable properties of any solid/polymer interface (here it was silica-polystyrene) are deviating from those of the corresponding flat interface, when the curvature of the solid is high and the solid/polymer interactions are strong.

4.2. Grafted nanoparticle inside a polymer matrix

4.2.1. Background

We say that the matrix chains *wet* the grafted polymer brush when they are able to interpenetrate with grafted chains and therefore access the space occupied by the polymer brush. Such a situation leads to a well-dispersed set of NPs. It has been seen that, in most cases, matrix chains are able to wet the brush, when their molecular weight is less than that of the grafted chains.²² Depending on the grafting density, when matrix chains are longer than the grafted chains, it is harder for them to penetrate into the interfacial region due to the higher entropy loss they experience (*autophobic dewetting*).

Various studies employing particle-based simulation methods exist in literature addressing nanoparticles in a polymer melt^{117–119} or solution, as well as isolated NPs.^{120–122} *Dissipative Particle Dynamics* (DPD)¹²³ and *Density Functional Theory* calculations addressing systems of polymer brushes are also reported. Vogiatzis et al.²³ devised a hybrid particle-field approach called FOMC (*Fast Off-Lattice Monte Carlo*), which is a coarse-grained class of *Monte Carlo* simulations, where the nonbonded interactions are described by a *mean-field* inspired *Hamiltonian*.

4.2.2. Validation against FOMC

The following Figure 4.5 depicts the reduced radial segment density profiles of matrix and grafted chains from *Fast Off-Lattice Monte Carlo* (FOMC) simulations, SCFT/SL and SCFT/SL + SGT. Beyond a certain distance from the solid surface, our SCF model results in practically identical radial segment density profiles to those obtained by FOMC. This is true for both the *Helfand* and the *Sanchez-Lacombe Hamiltonian*.

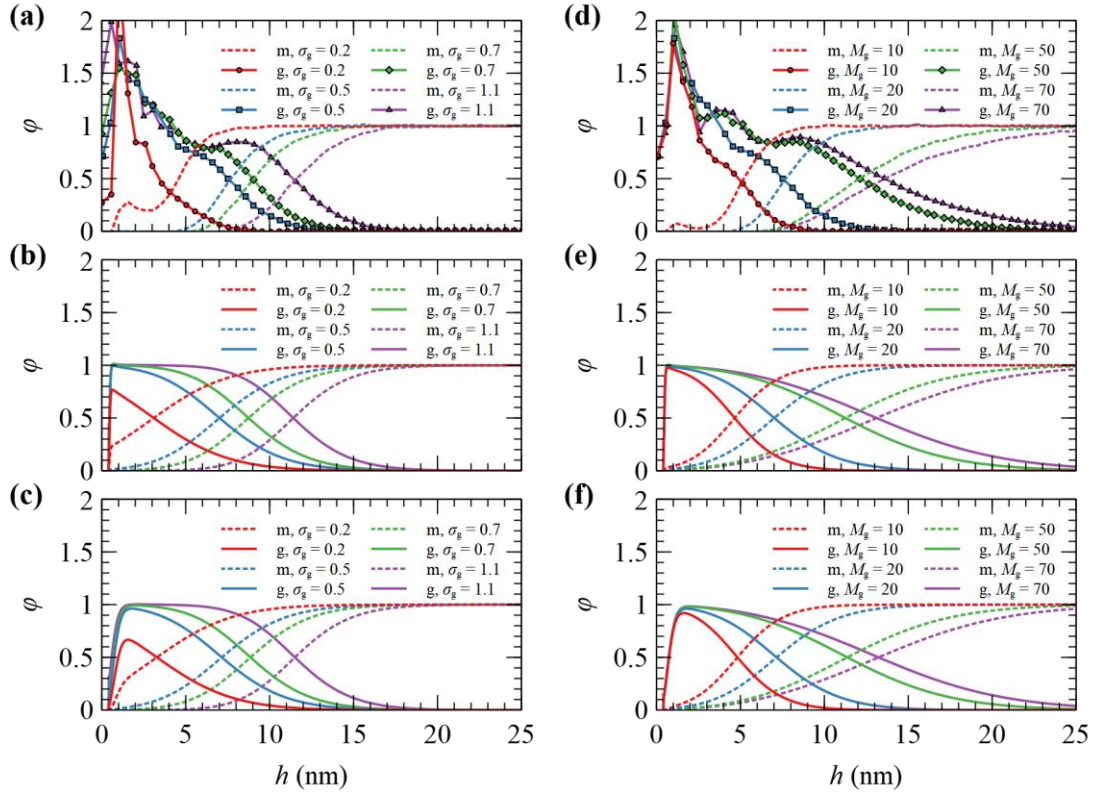


Figure 4.5 Comparison of SCFT with FOMC in deriving density profiles of grafted chains. Radial segment density distribution for matrix (m) and grafted (g) chains on a NP with $R_S = 8$ nm, from FOMC²³ (top), SCFT with HFD (middle), and SCFT with SL + SGT (bottom). In panels (a-c), $M_g = 20$ kg/mol, $M_m = 100$ kg/mol, and σ_g varies from 0.2 to 1.1 nm⁻². In panels (d-f), $\sigma_g = 0.5$ nm⁻², $M_m = 100$ kg/mol and M_g varies from 10 to 70 kg/mol.

Nevertheless, there is a discrepancy near the surface of the NP, which could be related to the fact that unidimensional SCFT cannot describe the packing of chain segments or the anchoring of grafted segment at discrete points close to the solid surface, while FOMC invokes not an atomistic, but rather a coarse-grained model. Another observation is that the SCFT/SL + SGT model provides smoother radial density profiles for grafted chain segments in comparison to FOMC or SCFT/HFD. This mainly has to do with the incorporation of the square gradient term in the description of the nonbonded interactions, which does not affect the long-ranged segment interactions, but the smoothness of the density profiles in the region near the solid surface. Furthermore, SCFT features a depletion region ranging from the solid surface up to a distance equal to $h_{HS} = 0.4$ nm (the position of the aforementioned hard-sphere wall), wherein the repulsive interactions from the *Hamaker* potential are very strong.

It is underlined at this point that the density profiles obtained via the SCFT/SL + SGT model are closer to the corresponding ones obtained from atomistic *molecular dynamics* simulations

than FOMC.^{36,105–107} If the oscillations of the atomistic density profiles are averaged out, then the smeared analogues from atomistic MD come out quite close to the density profiles of SCFT/SL + SGT in terms of the position of the peak and the width of the depletion zone near the solid surface.^{36,105–107} Interestingly, the peak of the density profiles appears to become less pronounced in atomistic simulations with increasing grafting density, presumably due to *excluded volume* effects.^{36,107}

4.2.3. Radial density profiles from the SL EoS: exploration of R_s , σ_g , M_g parameter space

Figure 4.6 presents the reduced segment density profiles of grafted and matrix chains across the (R_s, σ_g, M_g) parameter space. In all cases, grafted and matrix chains have the same molar mass, $M_m = M_g$.

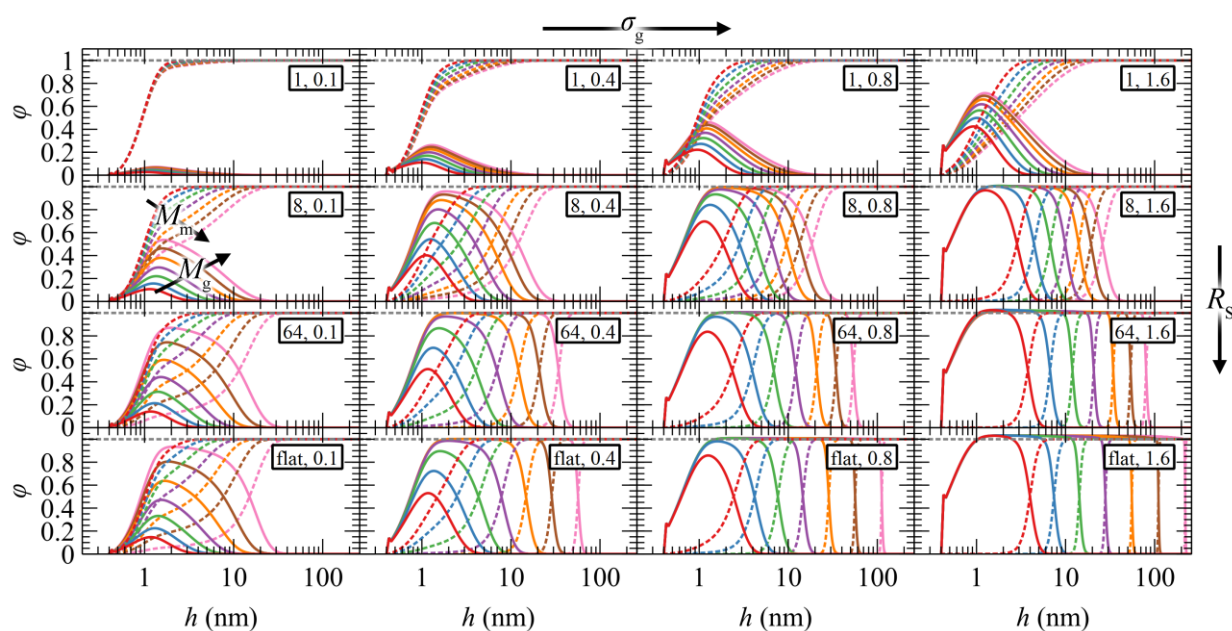


Figure 4.6 Density profiles as functions of molecular weight, grafting density and particle radius. Density profiles of grafted (solid lines) and matrix (dashed lines) chains with molar mass $M_g = \{1.25: \text{red}, 2.5: \text{blue}, 5: \text{green}, 10: \text{violet}, 20: \text{orange}, 40: \text{brown}, 80: \text{pink}\}$ kg/mol. In all cases, $M_m = M_g$. Legend in rectangles: R_s (nm), σ_g (nm^{-2}).

Overall, the density profiles of grafted chains expand with increasing σ_g , M_g , and R_s . Concerning the latter parameter, with increasing particle radius (i.e., decreasing curvature), the grafted chain segments have less available space to explore near the surface, so they experience *crowding* and extend further towards the bulk phase of the polymer. In general, the density profiles exhibit a rather rich behavior which could be classified into three distinct regimes:

4.2. Grafted nanoparticle inside a polymer matrix

(i) *Mushroom regime*. In the region of low σ_g , M_g , and R_S , the radial density profiles of the grafted chains become very suppressed and their peaks are much lower than the bulk density. That the grafted chains are short and the distance between them is relatively large implies that they cannot experience the presence of each other. In other words, the density distributions of individual chains do not overlap and therefore chains tend to form *mushroom*-like configurations.¹²⁴ This effect is expected to be more pronounced at small R_S , since chains would have more available space thanks to the increased curvature. On the other hand, matrix chains can readily penetrate the brush and reach the surface of the NP.

(ii) *Dense brush regime*. With increasing σ_g , M_g , and R_S , the density profiles become more pronounced and feature extended regions with bulk densities; e.g., see Figure 4.6 for $\sigma_g \geq 0.8 \text{ nm}^{-2}$ and $R_S \geq 64 \text{ nm}$. Towards the bulk phase, the density profiles feature a characteristic sigmoid shape² suggesting stretched brushes. The profiles of matrix and grafted chains intersect at reduced densities: $\varphi_m = \varphi_g \approx 0.5$. The presence of chemically grafted chains on the particle surface inhibits the penetration of matrix chains into the solid/polymer interfacial region and the strength of this exclusion of matrix chains increases with increasing σ_g , M_g , and R_S .

(iii) *Crowding regime*. In the case of extremely high grafting densities ($\sigma_g \geq 1.6 \text{ nm}^{-2}$) and low curvatures (e.g., $R_S \geq 64 \text{ nm}$), the *crowding* experienced by the grafted chain segments reaches a level where their densities slightly exceed the bulk density (see dashed grey line in the plots of Figure 4.6). In other words, the compressing forces imposed by the stretching of grafted chains overcome the tendency of the equation of state to maintain bulk density; hence, density exceeds this level. In this regime, matrix chains are completely unable to reach the surface of the NP, even for the shortest grafted chains ($M_g = 1.25 \text{ kg/mol}$).

In Figure 4.6 and for given grafting density, σ_g , and NP radius, R_S , the edges of the density profiles are shifted by about a constant amount along the abscissa (especially when the system is driven towards the crowding regime), whenever the molecular weight of grafted chains, M_g , is doubled; this effect becomes more pronounced with increasing R_S . Given that the density profiles are presented in semi-log plots, this observation leads to the conclusion that the edges of the profiles follow a power-law with respect to M_g , for constant σ_g and R_S . The scaling exponent of this power-law exhibits a complicated dependence on σ_g and R_S , as we demonstrate in Section 4.2.7.

In Figure 4.7, we present the total segment density profiles of polystyrene (i.e., sum of grafted and matrix chain segments), when in contact with a silica surface. Even though the total profiles are practically insensitive to M_g (except under very crowded conditions), they slightly

increase near the silica surface with increasing σ_g and deviate from unity across the brush region, under conditions of intense segment *crowding*.

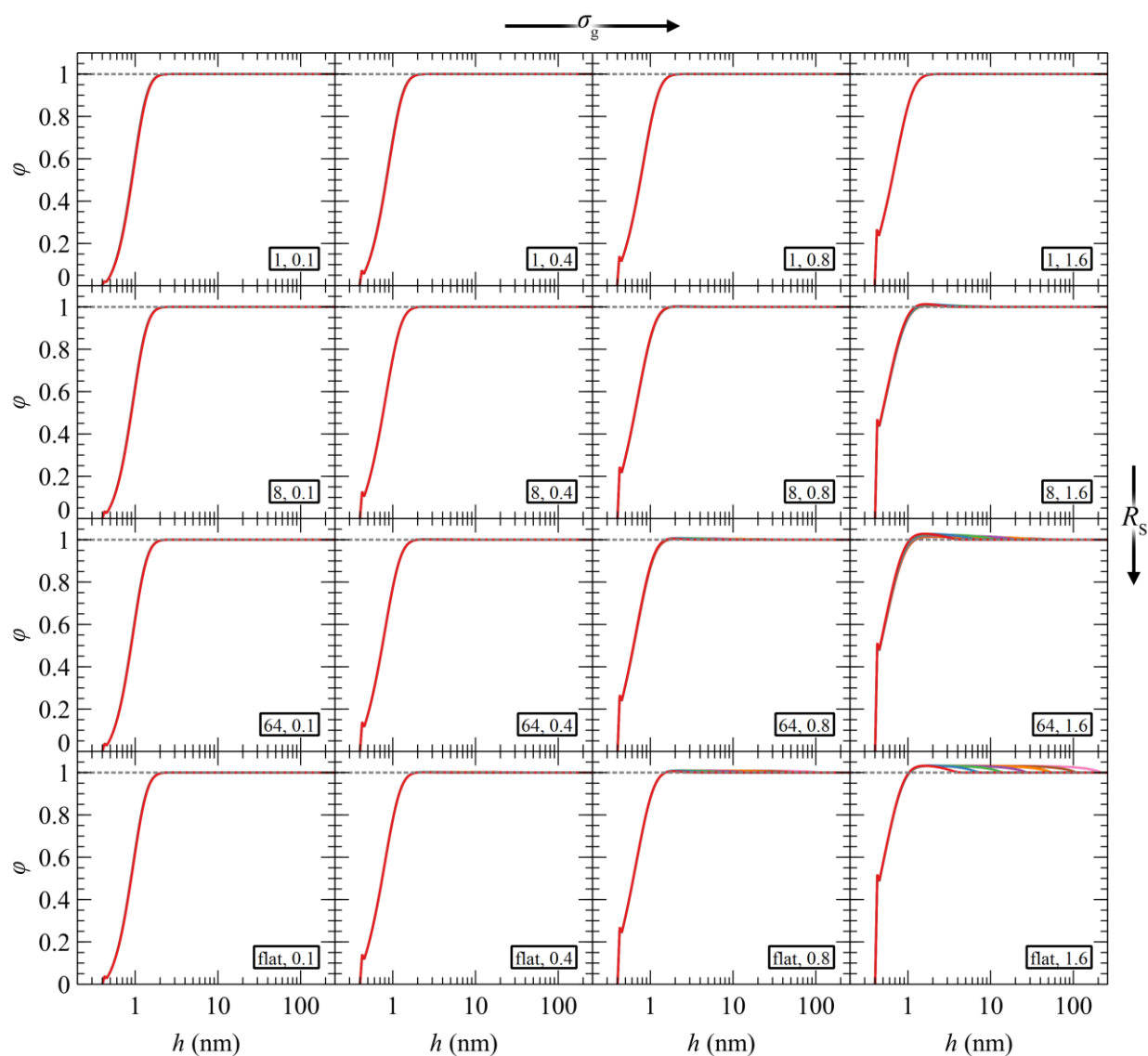


Figure 4.7 Total density profile as function of molecular weight, grafting density and particle radius. Total segment density profiles for grafted chain molar mass equal to $M_g = \{1.25: \text{red}, 2.5: \text{blue}, 5: \text{green}, 10: \text{violet}, 20: \text{orange}, 40: \text{brown}, 80: \text{pink}\}$ kg/mol. In all cases, $M_m = M_g$. Legend in rectangles: R_s (nm), σ_g (nm^{-2}). The dashed line, $\phi = 1$, is a guide to the eye. The little blip at $h = 0.44$ nm is caused by the grafting points.

4.2.4. Density profiles of adsorbed polymer segments

Chain segments cannot propagate against the solid surface. Consequently, their conformations are dictated by configurational entropy effects different from those prevailing in the bulk polymer melt. In addition, the presence of the NP (or planar surface) creates an attraction of chain segments (which belong either to matrix or grafted chains) towards the solid surface. The strength of this interaction, in relation to the cohesive interactions of the polymer, determines the wetting behavior of the polymer melt on the solid surface. Low, moderate and high energy surfaces lead to low, high (e.g., treated silica⁸¹) and perfect (e.g., untreated silica⁸¹) wetting conditions, respectively, which may affect the local configurations of grafted and matrix chains, in comparisons to configurations that would be dictated by purely entropic phenomena.

In order to investigate these effects, a distinction is made between “*adsorbed*” and “*free*” chains. By definition, grafted chains are *adsorbed*, therefore the aforementioned distinction concerns primarily the matrix chains. The value of the characteristic distance of closest approach to the NP surface, below which a matrix chain is considered to be *adsorbed*, is set at $h_{\text{ads}} = 1.28$ nm. This is the starting point of the tail of the *Hamaker* potential emanating from the solid, i.e., where the *Hamaker* potential assumes a value equal to $\sim -0.005k_{\text{B}}T$. It should be emphasized at this point that the distinction between *adsorbed* and *free* chains is not based on chain dynamics, but rather on a geometric criterion revealing the tendency/ability of matrix chain segments to penetrate the brush and experience the potential exerted by the solid surface.

The reduced density of *free* matrix chain segments can be derived from the convolution integral of eq 4.8.

$$\varphi_{\text{m}}^{\text{free}}(\mathbf{r}) = \frac{1}{N_{\text{m}}} \int_0^{N_{\text{m}}} dN q_{\text{m}}^{\text{free}}(\mathbf{r}, N) q_{\text{m}}^{\text{free}}(\mathbf{r}, N_{\text{m}} - N) \quad 4.8$$

where $q_{\text{m}}^{\text{free}}$ is the *propagator* of the *free* matrix chains, following the discussion in Section 3.4.4. Subsequently, the reduced density of segments belonging to *adsorbed* matrix chain segments is obtained as in eq 4.9 below.

$$\varphi_{\text{m}}^{\text{ads}}(\mathbf{r}) = \varphi_{\text{m}}(\mathbf{r}) - \varphi_{\text{m}}^{\text{free}}(\mathbf{r}) \quad 4.9$$

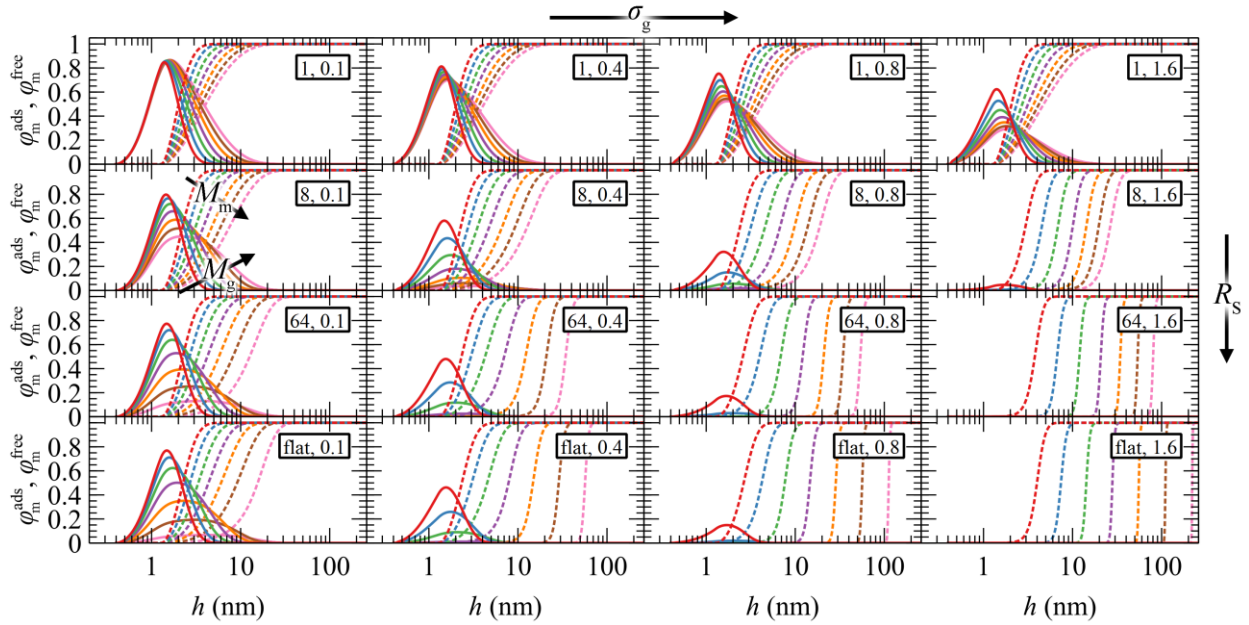


Figure 4.8 Adsorbed and free segment density profiles as functions of molecular weight, grafting density and particle radius. ϕ_m^{ads} (solid lines) and ϕ_m^{free} (dashed lines) profiles of adsorbed and free matrix chains with molar mass equal to $M_m = \{1.25: \text{red}, 2.5: \text{blue}, 5: \text{green}, 10: \text{violet}, 20: \text{orange}, 40: \text{brown}, 80: \text{pink}\}$ kg/mol. In all cases, $M_g = M_m$. Legend in rectangles: R_s (nm), σ_g (nm^{-2}).

Figure 4.8 presents the reduced density profiles of free (ϕ_m^{free}) and adsorbed (ϕ_m^{ads}) matrix chains across the (M_g, σ_g, R_s) parameter space. The profiles of segments belonging to free chains assume a value equal to unity in the bulk region, while going by definition to zero when approaching at distance equal to h_{ads} from the solid surface. According to Figure 4.8, matrix chains can easily penetrate the brush in the mushroom regime. With increasing σ_g and R_s , matrix chains experience noticeable resistance in penetrating the region occupied by grafted chains, while $\phi_m^{ads} \rightarrow 0$ upon transitioning to the crowding regime.

4.2.5. Chains per area density profiles

The mathematical definition of this structural property is given in Section 3.4.5. At this point, for the sake of comparison, we define a reference chain which obeys the Gaussian chain model and has infinite length. Given this definition, the reference chain will cross any shell-surface at least once. Hence, and since the number of grafted chains equals $n_g = \sigma_g 4\pi R_s^2$, the number of these reference chains passing through a surface separated by h from the surface of the solid per unit area of that surface is given by eq 4.10.

$$n_{\text{ch,g}}^{\text{ref}} = \frac{n_{\text{g}}}{4\pi(R_{\text{S}} + h)^2} = \sigma_{\text{g}} \left(\frac{R_{\text{S}}}{R_{\text{S}} + h} \right)^2 \quad 4.10$$

In Figure **4.9a**, we present n_{ch} for matrix and grafted chains, while Figure **4.9b** illustrates the normalized number $n_{\text{ch,g}}/\sigma_{\text{g}}$ for the grafted chains across the considered parameter space (R_{S} , σ_{g} , M_{g}). In both panels, the corresponding $n_{\text{ch,g}}^{\text{ref}}$ are represented by dotted lines. In the flat geometry case, $n_{\text{ch,g}}^{\text{ref}} = \sigma_{\text{g}}$ throughout the whole domain, while for finite curvatures, $n_{\text{ch,g}}^{\text{ref}}$ decreases with distance from the surface according to eq 4.10, and this is reasonable, since the polymer chains enjoy more available space to diffuse.

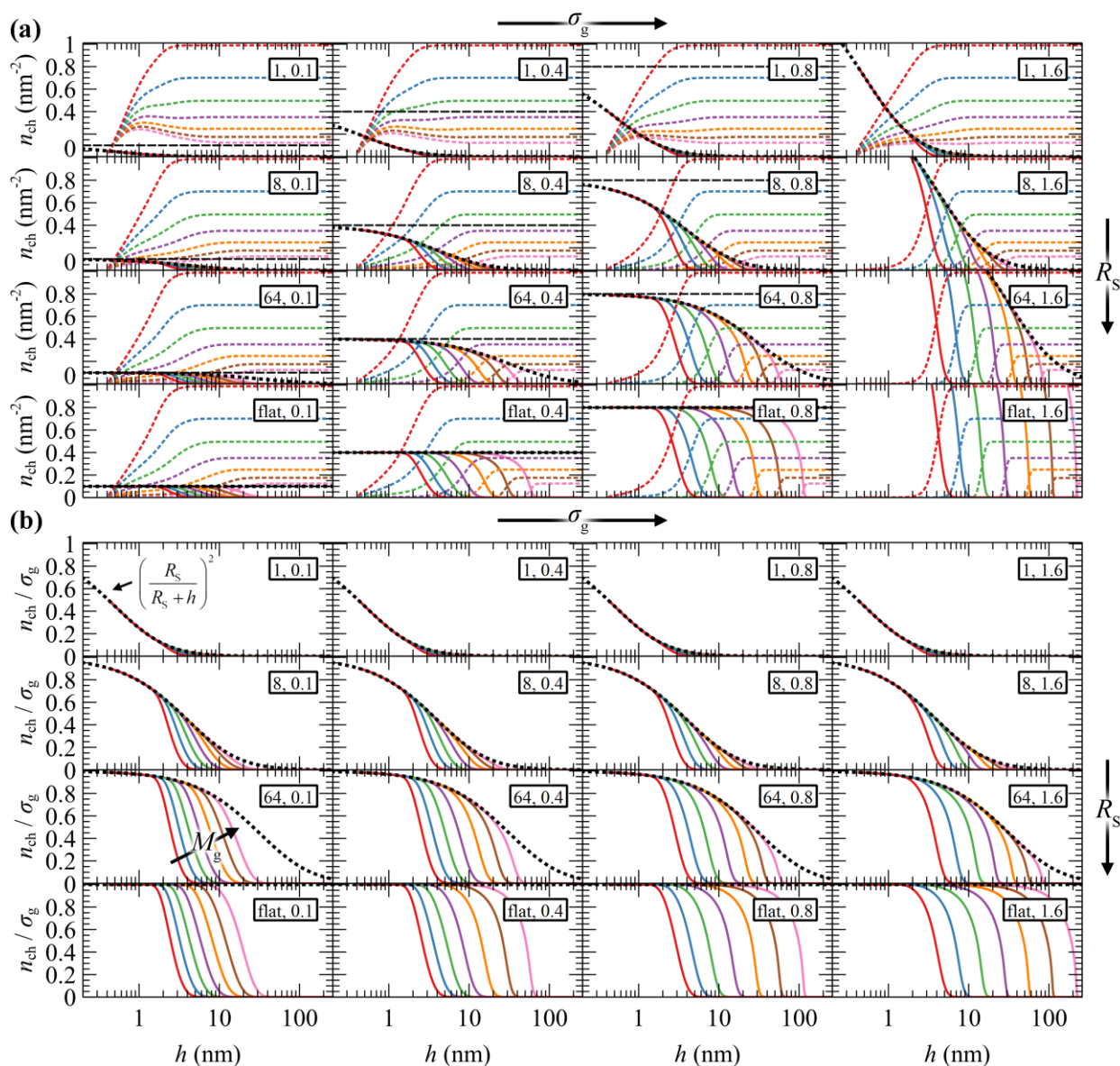


Figure 4.9 Chains per area profiles for various molecular weights, grafting densities and particle radii. Profiles of (a) n_{ch} of matrix (dashed lines) and grafted (solid lines), (b) n_{ch}/σ_g of grafted chains. Molecular weight of grafted chains is equal to $M_g = \{1.25: \text{red}, 2.5: \text{blue}, 5: \text{green}, 10: \text{violet}, 20: \text{orange}, 40: \text{brown}, 80: \text{pink}\}$ kg/mol. In all cases, $M_g = M_m$. Legend in rectangles: R_s (nm), σ_g (nm^{-2}). The dotted lines depict $n_{\text{ch,g}}^{\text{ref}}/\sigma_g$ for the reference chain from eq 4.10. The horizontal dashed lines denote the grafting density.

The behavior of the chains/area profiles with increasing grafting density or molar mass is consistent with the reduced density profiles of Figure 4.6. For low NP radius, the chains/area profiles are insensitive to grafting density, a picture that is consistent with the *mushroom* regime. Higher grafting density or molar mass leads to gradual extension of grafted chains towards the bulk region and a simultaneous exclusion of matrix chain segments from the solid/polymer

interface. For larger NPs and grafting densities, the *crowding* phenomena inside the interfacial region intensify and push the grafted chain segments further towards the bulk region.

As expected, in the planar geometry case, the number of grafted chains per area on the surface of the solid equals the grafting density throughout a broad region of the profile and starts to deviate upon approaching the region where ends terminate, where the number of grafted chains per area decreases. It is also noted that, since the hard sphere wall is located at ~ 0.4 nm from the solid surface, the maximum $n_{\text{ch,g}}$ assumed by the chains is $n_{\text{ch}} = \sigma_{\text{g}} R_{\text{NP}}^2 / (R_{\text{NP}} + h_{\text{HS}})^2$, albeit $n_{\text{ch}} = \sigma_{\text{g}}$ upon extrapolation towards $h \rightarrow 0$.

4.2.6. Chain end segregation at the interface

As already discussed in Section 3.4.3, the reduced density of the N^{th} segment, $\varphi_{c,N}$, of a chain of type c and located at \mathbf{r} can be retrieved by eq 3.6. Normalizing this quantity with the corresponding density in the bulk phase ($\varphi_{c,N}^{\text{bulk}} = 1/N_c$; since $q = 1$ in the bulk), we obtain a quantity of particular interest, which denotes the tendency of a region to attract or repel particular segments.

Figure 4.10 depicts the reduced density profiles of the end segments of grafted and matrix chains across the investigated parameter space. As expected, the density of *free ends* of grafted chains increases with increasing grafting density, σ_{g} , as well as with increasing R_{S} , since there is less space for the grafted chains to develop their conformations. With increasing grafting density, the profiles of chain ends are shifted towards the bulk region. In the *crowding* regime, where σ_{g} and R_{S} are high, chain ends are segregated far from the solid surface, suggesting that grafted chains are stretched. These profiles resemble those obtained for incompressible brushes, such as those in ref ¹²⁵, and with the more extreme case of *Alexander* model.^{126,127} In the latter case, all chain ends are by definition concentrated at the edge of the brush, h_{edge} , the position of which is denoted by the vertical dotted lines in Figure 4.10 (Appendix A).

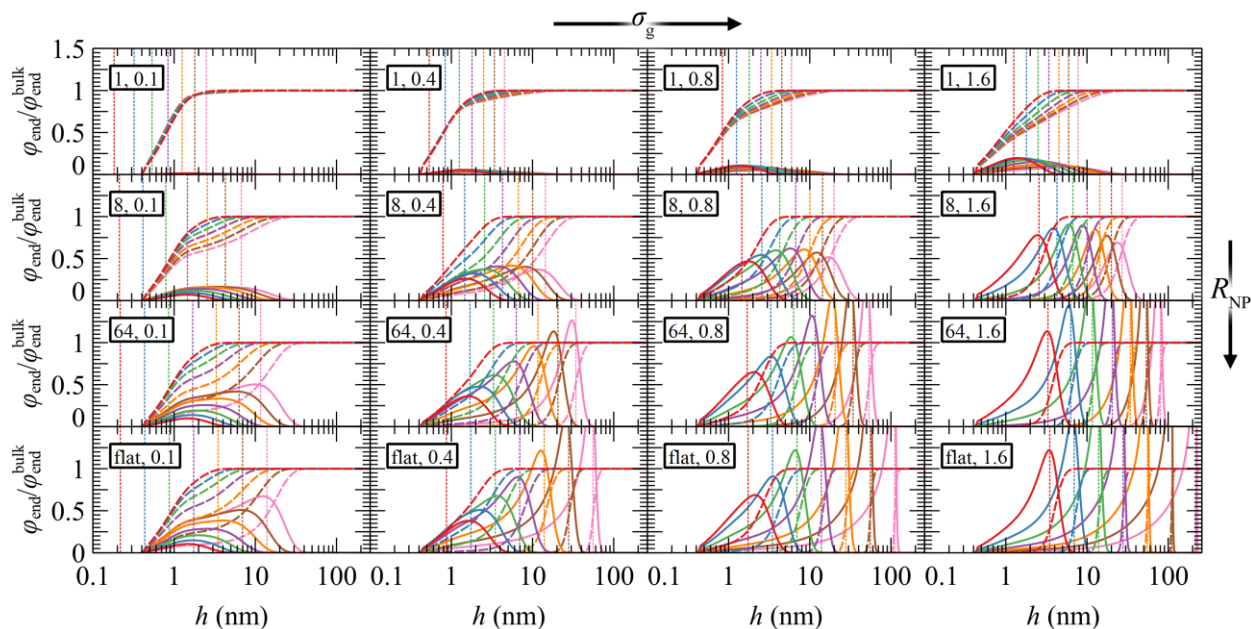


Figure 4.10 Chain-end density profiles for different molecular weights, grafting densities and particle radii. Chain-end density profiles, φ_{end} , of grafted (solid lines) and matrix (dashed lines) chains with molar mass equal to $M_g = \{1.25: \text{red}, 2.5: \text{blue}, 5: \text{green}, 10: \text{violet}, 20: \text{orange}, 40: \text{brown}, 80: \text{pink}\}$ kg/mol. Vertical dotted lines illustrate predictions for the position of chain ends from *Alexander* model for the corresponding M_g , σ_g and R_s . In all cases, $M_g = M_m$. Legend in rectangles: R_s (nm), σ_g (nm^{-2}).

In the *mushroom* regime, the chain ends from *Alexander* model are segregated much closer to the solid wall as compared to our SCFT model. This is attributed to the following factors:

(i) The *Alexander* model requires constant segment density of the grafted polymer and equal to the bulk melt; therefore, in the *mushroom* regime, where interpenetration of matrix and grafted chains becomes significant, it needs to squeeze the profiles of grafted chain segments in order to maintain the bulk density and conserve the amount of material at the same time.

(ii) The segments in our SCFT model experience an additional repulsive interaction which is modeled by a hard-sphere wall located at $h_{\text{HS}} \sim 0.4$ nm.

Clearly, the *Alexander* model with fixed density is not appropriate to describe the *mushroom* regime and, more generally, regimes where the matrix chains can penetrate the brush. Nevertheless, it is expected to perform very well under *poor solvent* conditions (e.g., polymer-vacuum interfaces), which lead to a collapsed brush across the solid surface.

4.2.7. Scaling of grafted polymer layers

Extensive research has been conducted to understand the behavior of polymer brushes in terms of their configurations near and far from the grafting surface.^{18,19,50,88,128,129} The expansion of the

4.2. Grafted nanoparticle inside a polymer matrix

grafted polymer chains exhibits a complicated behavior with respect to σ_g , M_g and R_s . In this section, an analysis is performed to elucidate the behavior of the mean brush thickness, $\langle h_g^2 \rangle^{1/2}$, when these parameters are varied. Brush thickness is directly related to the density profiles presented in Section 4.2.3 of the present thesis.¹³⁰ For details regarding the calculation of the brush thickness, the reader is referred to Section 3.4.2.

The scaling behavior of polymer brushes shows quite a similar behavior to star polymers. According to *Daoud and Cotton*,¹³¹ the radius of a star polymer (R_{star}) in a solvent exhibits a power-law dependence of the form: $R_{\text{star}} \sim N_{\text{star}}^n f_{\text{star}}^m v^k$, where N_{star} is the number of segments constituting a branch, f_{star} is the number of branches, $v = 0.5 - \chi$ is the monomer *excluded volume* parameter, χ is the *Flory-Huggins* parameter⁶⁰ and n , m , k are the corresponding scaling exponents.^{60,132,133} *Daoud and Cotton*¹³¹ classified the behavior of stars into three distinct regimes:

- (i) $N_{\text{star}} \gg f_{\text{star}}^{1/2} v^{-2}$: $R_{\text{star}} \sim N_{\text{star}}^{3/5} f_{\text{star}}^{1/5} v^{1/5} b_k$
- (ii) $f_{\text{star}}^{1/2} v^{-2} \gg N_{\text{star}} \gg f_{\text{star}}^{1/2}$: $R_{\text{star}} \sim N_{\text{star}}^{1/2} f_{\text{star}}^{1/4} b_k$
- (iii) $f_{\text{star}}^{1/2} \gg N_{\text{star}}$: $R_{\text{star}} \sim N_{\text{star}}^{1/3} f_{\text{star}}^{1/3} b_k$

with b_k being the *Kuhn length*. By substituting $f_{\text{star}} \rightarrow \sigma_g$ and $N_{\text{star}} \rightarrow M_g$, and by ignoring the influence of the core of the NP to the brush, the model by *Daoud and Cotton*¹³¹ could be applied to describe the scaling of polymer brushes via the following eq 4.11.

$$\langle h_g^2 \rangle^{1/2} = M_g^n \sigma_g^m l_g \quad 4.11$$

where l_g is a coefficient with dimensions $(\text{kg mol}^{-1})^{-n} \text{nm}^{2m+1}$.

It should be noted here that the first regime of the *Daoud & Cotton* model, $N_{\text{star}} \gg f_{\text{star}}^{1/2} v^{-2}$, cannot be addressed through our calculations, since the latter are performed in melt conditions (equivalent to *theta solvent* conditions), where the *Flory-Huggins* parameter, χ , is equal to 0.5 and therefore the quantity v^{-2} goes to infinity (*excluded volume* parameter, v , is equal to zero). Another important difference between *Daoud and Cotton's* model and ours is that, in NPs, the grafted chains emanate from different grafting points, whereas in star polymers, chains emanate from the same point. Hence, under *theta* or *good solvent* conditions and for large curvatures, grafted chains will not interact with each other and the dependence of brush height on grafting density will be weak. The situation might be different under *poor solvent* conditions, where the brushes are partially or fully collapsed (depending on how large the parameter χ is).

Figure 4.11 illustrates brush height evaluations for NPs with $R_S = 8$ nm, obtained from SCFT calculations with *RuSseL*,⁷⁶ from FOMC (blue “+”) and from small angle neutron scattering (SANS)¹³⁴ measurements (red “×”). Overall, eq 4.11 can describe accurately the scaling of PS brushes grafted on SiO₂ NPs with radius equal to 8 nm, since both $\langle h_g^2 \rangle^{1/2}$ and $\langle h_{99\%} \rangle$ appear to obey the scaling $\sim M_g^{0.5} \sigma_g^{0.25}$. It is observed that evaluations from SCFT appear shifted with respect to FOMC. This is attributed to that in FOMC, the increased density near the solid surfaces increases the weight of smaller h_g in the integration of eq 3.4; thus, it leads to decreased overall $\langle h_g^2 \rangle^{1/2}$. In addition, $\lim_{M_g \rightarrow 0} \langle h_g^2 \rangle^{1/2} \sim 0$ in *RuSseL*, since the length of grafted chains goes to zero. For the same reasons, $h_{99\%}$ points obtained with *RuSseL* lie slightly higher than FOMC and SANS values, while the minimum value of $h_{99\%}$ is equal to the radius of the NP.

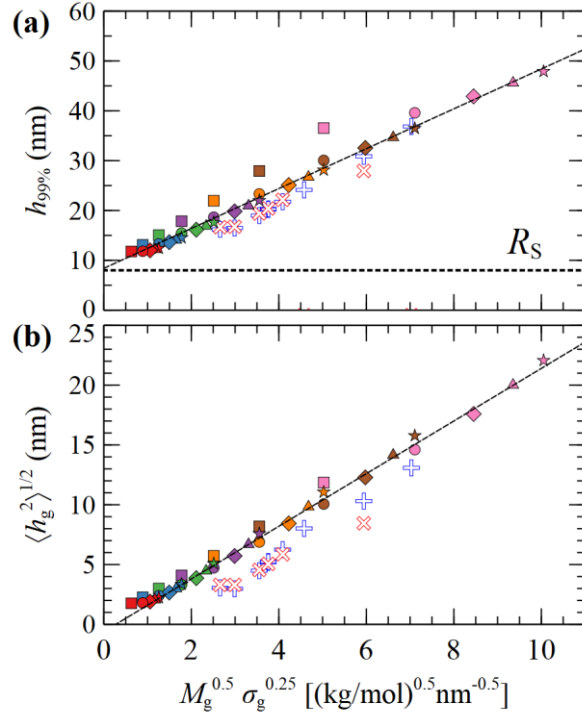


Figure 4.11 *Daoud and Cotton* scaling law for brush thickness. Evaluation of (a) $h_{99\%}$ and (b) $\langle h_g^2 \rangle^{1/2}$ as a function of $M_g^{0.5} \sigma_g^{0.25}$ for $R_S = 8$ nm, from FOMC (+),²³ SANS measurements (\times),¹³⁴ and SCFT/*RuSseL*: in the latter case, colors denote chains with molar mass $M_g = \{1.25: \text{red}, 2.5: \text{blue}, 5: \text{green}, 10: \text{violet}, 20: \text{orange}, 40: \text{brown}, 80: \text{pink}\}$ kg/mol, and shapes denote different grafting densities, $\sigma_g = \{0.1: \square, 0.4: \circ, 0.8: \diamond, 1.2: \triangle, 1.6: \star\}$ nm⁻². Dashed lines are guides to the eye.

In the following, we test the scaling laws proposed by *Daoud and Cotton* across the full parameter space explored herein. Figure 4.12 displays evaluations of $\langle h_g^2 \rangle^{1/2}$ plotted versus the quantity $M_g^{0.5} \sigma_g^{0.25}$ and for NP radius equal to 1, 4, 16 and 64 nm, as well as for flat surfaces, and for various M_g and σ_g .

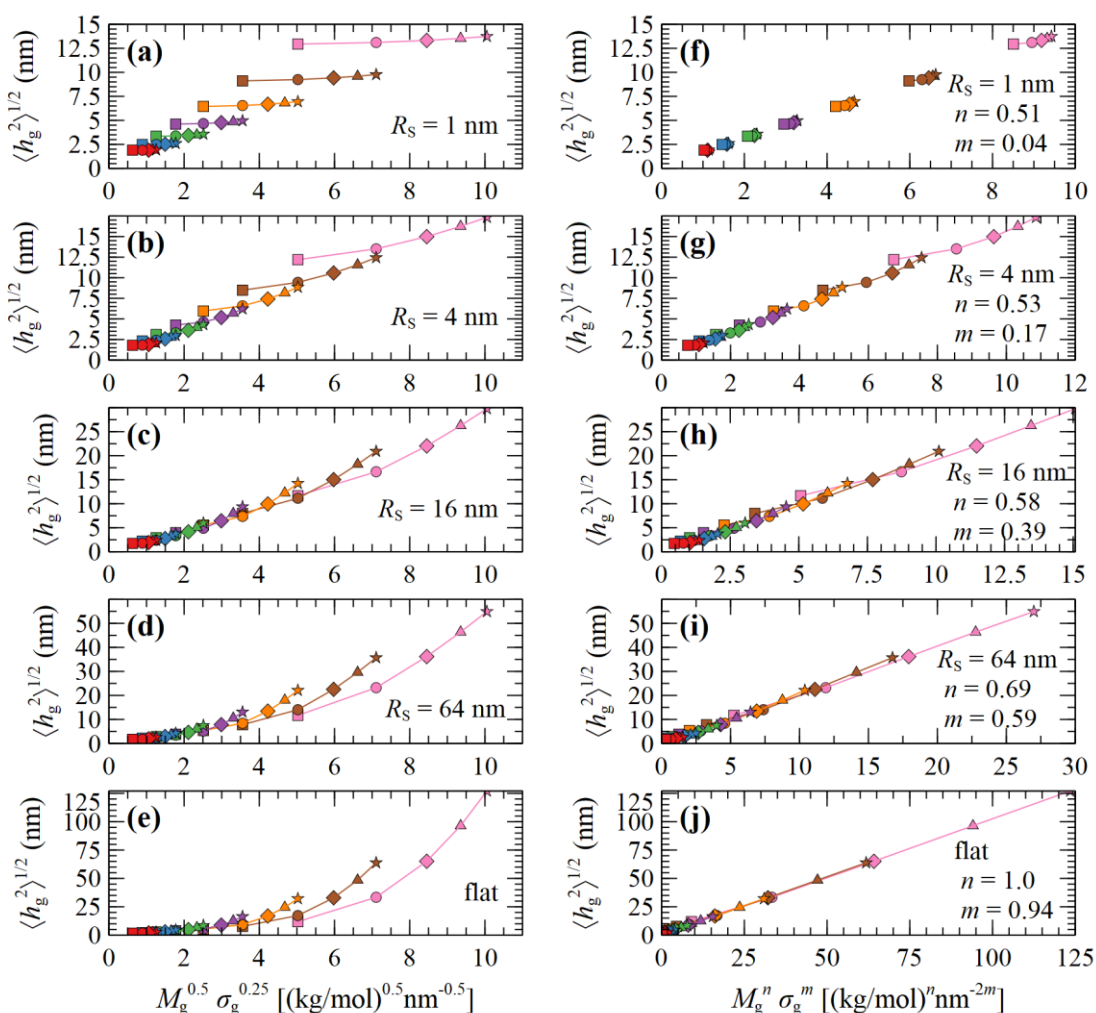


Figure 4.12 Brush thickness scaling law for different particle radii. Evaluations of the *mean brush thickness*, $\langle h_g^2 \rangle^{1/2}$, as a function of **(a-e)** $M_g^{0.5} \sigma_g^{0.25}$ proposed by *Daoud and Cotton* and **(f-j)** $M_g^n \sigma_g^m$, where n, m are the optimized exponents from Figure 4.14a. Colors denote chains with $M_g = \{1.25: \text{red}, 2.5: \text{blue}, 5: \text{green}, 10: \text{violet}, 20: \text{orange}, 40: \text{brown}, 80: \text{pink}\}$ kg/mol. Shapes denote different grafting densities, $\sigma_g = \{0.1: \square, 0.4: \circ, 0.8: \diamond, 1.2: \triangle, 1.6: \star\}$ nm⁻². In all cases, $M_g = M_m$.

An interesting behavior is manifested in these plots, which reveals three distinct regimes: **(i)** for NP with small R_s (e.g., Figure 4.12a), the curves for specific M_g (same colors) are disconnected and feature a very weak slope; **(ii)** for NPs with intermediated sizes $R_s = 4\text{-}8$ nm (e.g., Figure 4.12b), the curves for specific M_g connect with each other, suggesting that the $M_g^{0.5} \sigma_g^{0.25}$ law is fairly accurate in describing this regime;²³ **(iii)** for NPs with larger sizes $R_s > 8$ nm (e.g., Figure 4.12c,e), the curves appear disconnected as in the case of small NPs, the difference now being that the slope for each individual M_g curve appears to be stronger. This

4.2. Grafted nanoparticle inside a polymer matrix

analysis suggests that even though the $\sim M_g^{0.5} \sigma_g^{0.25}$ correlation appears to describe the scaling of the brush with reasonable accuracy for $R_S \sim 4\text{-}8$ nm, it becomes inaccurate for NPs with relatively large or small radius.

In view of these observations, one can optimize the n , m exponents for each R_S to retrieve the power-law in eq 4.11. According to Figure 4.6, for constant R_S and σ_g , the density profiles expand by a roughly constant factor when doubling M_g ; thus, it is reasonable to assume that $\langle h_g^2 \rangle^{1/2} \sim M_g^n$ with n being a function of (R_S, σ_g) . Figure 4.13 presents the optimized n exponent from fitting *RuSseL* results against the power-law $\langle h_g^2 \rangle^{1/2} \sim M_g^n$ over all R_S and σ_g .

n		σ_g (nm ⁻²)					fit
		0.1	0.4	0.8	1.2	1.6	
R_S (nm)	1	0.51	0.50	0.50	0.50	0.49	0.51
	2	0.51	0.51	0.50	0.50	0.49	0.51
	4	0.52	0.52	0.52	0.51	0.50	0.53
	8	0.53	0.55	0.54	0.53	0.52	0.55
	16	0.55	0.59	0.59	0.57	0.55	0.58
	32	0.57	0.66	0.65	0.63	0.61	0.62
	64	0.58	0.73	0.72	0.70	0.68	0.69
	128	0.60	0.79	0.79	0.77	0.75	0.76
	256	0.61	0.84	0.85	0.84	0.82	0.83
	512	0.61	0.87	0.90	0.89	0.88	0.89
	1024	0.62	0.89	0.93	0.93	0.92	0.94
	2048	0.62	0.90	0.95	0.95	0.95	0.96
	4096	0.62	0.91	0.96	0.97	0.97	0.98
	8192	0.62	0.91	0.96	0.98	0.98	0.99
	16384	0.62	0.92	0.97	0.98	0.98	0.99
flat	0.62	0.92	0.97	0.98	0.99	1.00	

Figure 4.13 Optimized n exponents of the power-law in eq 4.11 for set grafting density, σ_g , and NP radius, R_S . The rightmost column depicts the fit with eq 4.12.

Given that the 1D model employed herein might not be able to describe accurately the chain configurations at low grafting densities or molecular weights of grafted chains, due to the inevitable smearing of grafting points, we decided not to take into account the cases corresponding to values of $\sigma_g R_g^2 < 3$, and $\sigma_g = 0.1$ nm⁻² (which exclude the larger part of cases corresponding to the *mushroom* regime) when fitting the scaling exponents for the master eq 4.11.

For large σ_g , the exponent n presents a stronger dependence on R_S than σ_g ; thus, for simplicity, one could treat n as being a function of R_S exclusively. Consequently, the data for $\sigma_g > 0.1$ nm⁻² were fitted to a sigmoid function of the following form:

$$n = n_{\min} \left[\frac{1}{2} \tanh \left(n_s \ln \frac{R_s}{R_d} \right) + \frac{3}{2} n_{\max} \right] \quad 4.12$$

with $n_{\min} = 0.5$ and $n_{\max} = 1$, being the minimum and maximum values of n , $R_d = 113.7$ nm and $n_s = 0.4337$. Subsequently, with n set, one can optimize the exponent of σ_g with respect to R_s aiming at aligning the data points for a given R_s . Figure 4.12f-j displays evaluations of $\langle h_g^2 \rangle^{1/2}$ using the optimized n and m exponents presented in Figure 4.14a.

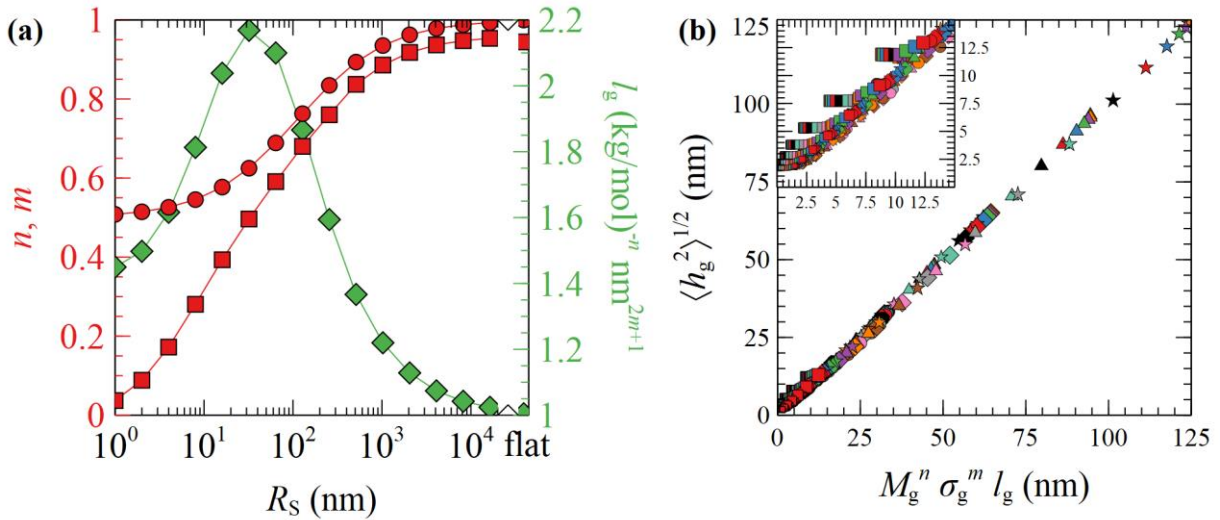


Figure 4.14 Optimized scaling exponents for the prediction of brush thickness scaling. **(a)** The optimized n (circles) and m (squares) exponents of eq 4.11 and l_g (diamonds) as functions of R_s . The rightmost data points correspond to flat surfaces. **(b)** Evaluations of eq 4.11 using the n , m and l_g parameters in **(a)**. Colors denote chains with molar mass $M_g = \{1.25: \text{red}, 2.5: \text{blue}, 5: \text{green}, 10: \text{violet}, 20: \text{orange}, 40: \text{brown}, 80: \text{pink}\}$ kg/mol. Shapes denote different grafting densities, $\sigma_g = \{0.1: \square, 0.4: \circ, 0.8: \diamond, 1.2: \triangle, 1.6: \star\}$ nm⁻². The size of the symbols increases slightly with R_s . The inset in **(b)** depicts a zoomed region of the master curve. In all cases, $M_g = M_m$.

Using these optimized n , m exponents, $\langle h_g^2 \rangle^{1/2}$ increases linearly with $M_g^n \sigma_g^m$ over the full range of examined R_s (from 1 nm to ∞). In addition, the curves in Figure 4.12 can be collapsed onto the master curve shown in Figure 4.14b, where $\langle h_g^2 \rangle^{1/2}$ is plotted against eq 4.11 with l_g being the slopes of the individual curves in Figure 4.12f-j (see green diamonds in Figure 4.14a). Overall, the data points in Figure 4.14b are in good quantitative agreement with eq 4.11, with the exception of the low M_g, σ_g regime where $\langle h_g^2 \rangle^{1/2}$ plateaus; see zoomed region in Figure 4.14b.

4.2.8. Thermodynamics

In Figure 4.15, the plots (a-e) depict individual *grand potential* terms (eqs 2.39-2.43) over the parameter space (R_S , σ_g , M_g). Regarding the cohesive interaction term per unit solid surface ($\Delta\Omega_{\text{coh}}^{\text{SGM}} / S_S$ in Figure 4.15a), it decreases steeply in the vicinity of small R_S and this is attributed to that, when high curvatures are involved (small R_S), the surface of the spherical cells where we integrate $\Delta\Omega_{\text{coh}}^{\text{SGM}}$ is larger than the surface S_S of the NP (by which we normalize all energy quantities), by a factor $(R_S + h)^2 / R_S^2$. At low grafting densities, (*mushroom* regime, circles in Figure 4.15a), $\Delta\Omega_{\text{coh}}^{\text{SGM}} / S_S$ appears to be insensitive to molecular weight, M_g , for M_g up to 80 kg/mol; i.e., all different colored lines with circular markers collapse onto the same curve in Figure 4.15a. $\Delta\Omega_{\text{coh}}^{\text{SGM}} / S_S$ deviates notably with increasing M_g and R_S . This is a consequence of ρ_g exceeding $\rho_{\text{seg,bulk}}$ due to chain *crowding* (e.g., see bottom-right panels of Figure 4.7) and this enhances the cohesion of the brush, when the SL-EoS is used. To be more specific, as shown in Figure 2.4, the minimum of $f(\rho) - f(\rho_{\text{bulk}})$ for SL is about -0.5 mJ/m^3 for reduced densities slightly larger than one; thus, accumulation of these negative values over the integration of larger and larger brushes, due to *crowding*, leads to eventual decrease of $\Delta\Omega_{\text{coh}}^{\text{SGM}} / S_S$.

Similarly, the field term ($\Delta\Omega_{\text{field}}^{\text{SGM}} / S_S$ in Figure 4.15b) presents the same qualitative behavior as $\Delta\Omega_{\text{coh}}^{\text{SGM}} / S_S$ for the exact same reasons: (i) steep initial decline due to high curvature, (ii) accumulation of negative values (see $-\rho df / d\rho + [\rho df / d\rho] \Big|_{\rho=\rho_{\text{seg,bulk}}}$ in Figure 2.4 for $\varphi > 1$) by integrating over gradually larger brushes.

Considering the solid/polymer interaction term ($\Delta U_s / S_S$), it is practically insensitive to chain molar mass; i.e., in Figure 4.15c, the energies for different chain molar masses do not exhibit noticeable variations with each other, irrespectively of the size of NP. With increasing grafting density, it is obvious that the *adhesion* between the solid and the polymer is enhanced, because of the increased density of polymer segments close to the surface, as it is depicted in the total segment density profiles presented in Figure 4.7.

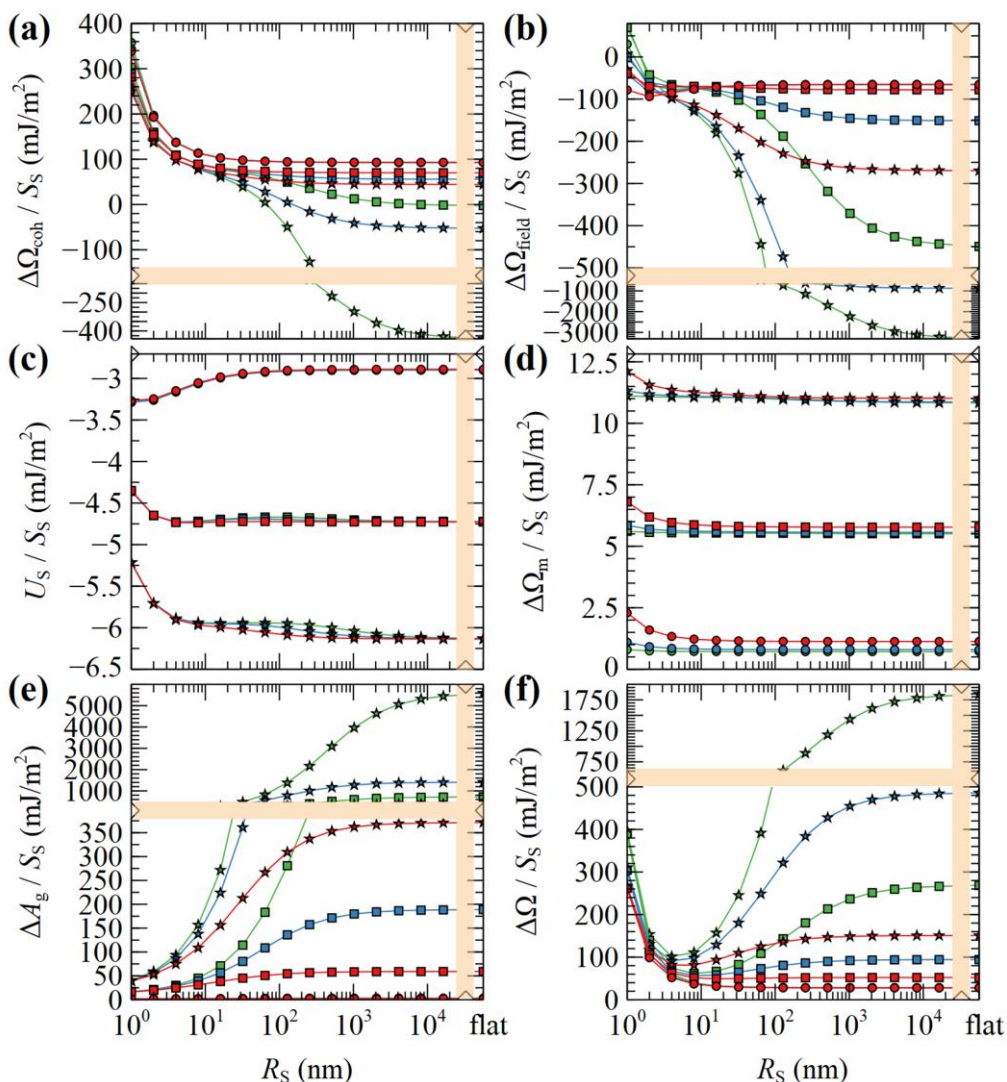


Figure 4.15 Total free energy and individual terms as functions of molecular weight, grafting density and particle radius. (a-e) Partial contributions to the grand potential per unit area from eqs 2.39-2.43. (f) Total grand potential per unit area. Colors denote chains with molar mass $M_g = \{1.25: \text{red}, 2.5: \text{blue}, 5: \text{green}, 10: \text{violet}, 20: \text{orange}, 40: \text{brown}, 80: \text{pink}\}$ kg/mol, and shapes denote different grafting densities, $\sigma_g = \{0.1: \square, 0.4: \circ, 0.8: \diamond, 1.2: \triangle, 1.6: \star\}$ nm⁻². In all cases $M_m = M_g$. Bands denote scale changes along the axes.

In all cases, the entropy term associated with the *partition function* of matrix chains ($\Delta\Omega_m^{\text{SGM}} / S_S$ in Figure 4.15d) appears to be rather weak. It shifts upwards by a constant amount with increasing grafting density, because grafted chains claim more space in the interfacial region, leaving the matrix chains with fewer available conformations.

Regarding the entropy term associated with grafted chains ($\Delta A_g^{\text{SGM}} / S_S$ in Figure 4.15e), it exhibits a rather interesting behavior: in the *mushroom* regime ($\sigma_g = 0.1$ nm⁻², circles in Figure 4.15e), $\Delta A_g^{\text{SGM}} / S_S$ appears to be flat and roughly equal to zero, indicating that for low grafting

densities there is no entropic penalty with increasing R_S associated with brush conformations. On the contrary, for larger σ_g (squares and stars), $\Delta A_g^{\text{SGM}} / S_S$ increases with R_S up to ~ 100 nm and plateaus to finite values in the limit of planar surfaces. This response is attributed to the stretching of grafted chains caused by *crowding* phenomena. A direct manifestation of this effect is presented in Figure 4.10, which depicts the segregations of grafted chain ends towards the bulk phase under crowded conditions.

The total *grand potential* from eq 2.38 is presented in Figure 4.15f. Across the *mushroom* regime ($\sigma_g = 0.1 \text{ nm}^{-2}$, circles), $\Delta \Omega_{\text{coh}}^{\text{SGM}} / S_S$ exhibits a monotonic decrease and plateaus to a value commensurate to the *surface tension* of PS for $R_S \geq 100$ nm, which is about $\gamma_{\text{PS}} \sim 25.9$ mN/m at $T = 500$ K.² It is noted that, in the limiting case $\sigma_g \rightarrow 0$ and $R_S \rightarrow \infty$, and in absence of the *Hamaker* potential, $\gamma_{\text{PS}} \equiv \Delta \Omega_{\text{coh}}^{\text{SGM}} / S_S$. With increasing σ_g , the *grand potential* features a minimum at $R_S \sim 10$ nm, after which it increases in a way suggesting the domination of the stretching term in Figure 4.15e.

4.2.9. Contributions to chain stretching

The entropy term associated with grafted chains in Figure 4.15e does not reflect the total conformational contribution to the grand potential, since the *partition function* in eq 2.43 is evaluated in presence of the field. Consequently, in the context of SCFT, the free energy associated with the conformations of grafted chains can be estimated by the following eqs 4.13 and 4.14.

$$A_{\text{conf}}^g = \Delta A_g + \Delta A_{\text{field}}^g \quad 4.13$$

with $\Delta A_{\text{field}}^g$ being the field experienced by the grafted chains:

$$\Delta A_{\text{field}}^g = - \int_{\mathcal{R}} d\mathbf{r} \left\{ \sum_{i_g=1}^{n_g} \rho_{g,i_g}(\mathbf{r}) w'_{\text{ifc}}(\mathbf{r}) \right\} \quad 4.14$$

and ρ_{g,i_g} being the segment density associated with the i_g^{th} grafted chain.

At this point, it is worth analyzing and comparing the conformation free energy of grafted chains with a rough estimate of the free energy obtained from the density profiles of the grafted chain ends. In the one-dimensional calculations employed in this chapter, grafted chain conformations are reflected random walks starting at h_g . Assuming that the system finds itself in the *dense brush* rather than the *mushroom* regime, the number of conformations of a chain such

Chapter 4. Single Nanoparticle Calculations

that the end-to-end vector projection normal to the solid surface is between h and $h + \Delta h$, can be estimated through the corresponding number in the unperturbed melt. It will be proportional to $f_{\text{end}}(h)dh$, where the probability density $f_{\text{end}}(h)$ is given by the following eq 4.15 in the context of the *Gaussian* chain model.

$$f_{\text{end}}(h) = \left(\frac{3}{2\pi \langle R_{\text{end,g}}^2 \rangle} \right)^{1/2} \exp\left(-\frac{3h^2}{2 \langle R_{\text{end,g}}^2 \rangle} \right), h > 0 \quad 4.15$$

Note that this is based on the assumption that a grafted chain will access all conformations accessible to it at given value of the end-to-end distance. In reality, as is obvious from the profiles in Figure 4.9 and Figure 4.10, grafted chains are more stretched near their grafted end (indicative of the *concentrated polymer brush* regime, as called in literature^{135,136}) and less stretched near the *free end*. Based on eq 4.15, the *Helmholtz* energy contribution, A_{chain} , of a *Gaussian* chain grafted at $\mathbf{r}_{\text{g},i_{\text{g}}}$ whose *free end* lies at point \mathbf{r} , is given by eq 4.16 within an additive constant. In eqs 4.15 and 4.16, $\langle R_{\text{end,g}}^2 \rangle$ is the mean squared end-to-end distance of an unperturbed chain of length equal to N_{g} .

$$A_{\text{chain}}(\mathbf{r}) = \frac{3k_{\text{B}}T}{2} \frac{(\mathbf{r} - \mathbf{r}_{\text{g},i_{\text{g}}})^2}{\langle R_{\text{end,g}}^2 \rangle} \quad 4.16$$

Let $\rho_{\text{g,end}} = \varphi_{\text{g,end}} \rho_{\text{seg,bulk}}$ be the local number density (segments per unit volume) of *free ends* of grafted chains; note that each grafted chain contributes one *free end*. Consecutively, integrating $\rho_{\text{g,end}}$ across the domain results the total number of grafted chains, i.e., $\int_{\mathcal{R}} \rho_{\text{g,end}}(\mathbf{r}) d\mathbf{r} = n_{\text{g}}$. The total stretching free energy of grafted chains in our system equals (within an additive constant):

$$A_{\text{stretch}}^{\text{g}} = \int_{\mathcal{R}} \rho_{\text{g,end}}(\mathbf{r}) A_{\text{chain}}(\mathbf{r}) d\mathbf{r} \quad 4.17$$

and it can be approximated across the *dense brush* regime as:

$$A_{\text{stretch}}^{\text{g}} \sim \int_{\mathcal{R}} \rho_{\text{g,end}}(h) A_{\text{chain}}(h) 4\pi (R_{\text{S}} + h)^2 dh \quad 4.18$$

in spherical and:

4.2. Grafted nanoparticle inside a polymer matrix

$$A_{\text{stretch}}^g = \int_{\mathcal{R}} \rho_{g,\text{end}}(h) A_{\text{chain}}(h) S_S dh \quad 4.19$$

in planar geometries. In the special case of *Alexander's* model, in which all chain ends are segregated at the edge of the film, $\rho_{g,\text{end}} = \sigma_g \delta(h - h_{\text{edge}})$, thus eq 4.19 can be written as follows:

$$A_{\text{stretch}}^g \sim S_S \sigma_g A_{\text{chain}}(h_{\text{edge}}) \quad 4.20$$

with h_{edge} given by eq A3 in Appendix A. In Figure 4.16, we demonstrate a comparison between the stretching energy term obtained by the *Alexander* model (lines) and our SCFT theoretical model (markers); the latter is calculated either from: (a) A_{conf}^g given by eqs 4.13 and 4.14 or (b) A_{stretch}^g given by eqs 4.17 and 4.18.

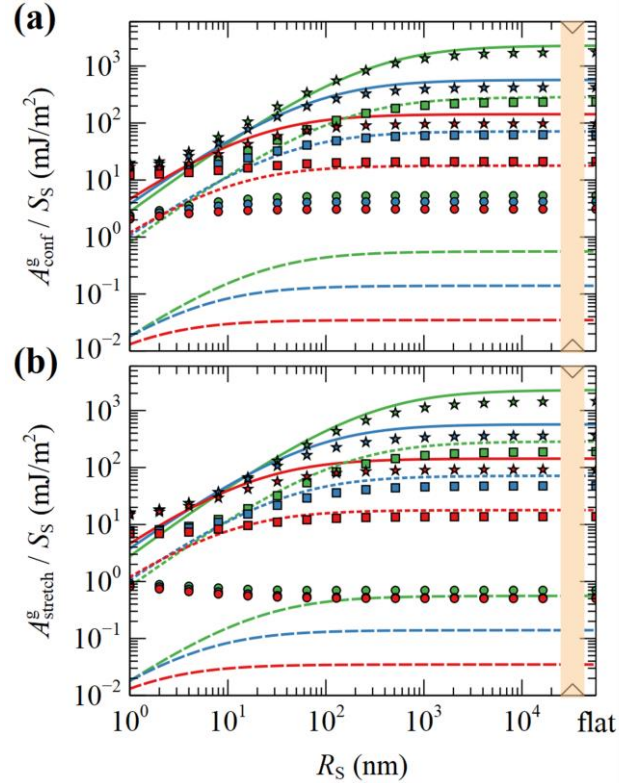


Figure 4.16 Conformational entropy of grafted chains for different molecular weight, grafting density and particle radius. Evaluations of (a) A_{conf}^g and (b) A_{stretch}^g . Markers correspond to evaluations from our SCFT theoretical model, whereas lines correspond to A_{stretch}^g from the model of *Alexander*. Colors denote chains with different molecular weight, $M_g = \{5: \text{red}, 20: \text{blue}, 80: \text{green}\}$ kg/mol. Shapes/lines denote different grafting density, $\sigma_g = \{0.1: \text{circles/dashes}, 0.8: \text{squares/dots}, 1.6: \text{stars/solid lines}\}$ nm⁻². In all cases, $M_g = M_m$. The rightmost data correspond to flat surfaces.

We mention at this point that the *Alexander* model, which we develop in Appendix A, is similar to the h_{dry} region that Midya et al.⁵⁰ report in the context of their two-layer theoretical

model for the description of nanoparticle brushes. In that work,⁵⁰ the authors state that in curved surfaces and for constant grafting density, the free energy associated with the stretching of grafted chains does not increase indefinitely with increasing length of grafted chains, but it rather saturates at a maximum value. This is well expected, since at some point the grafted chains cannot feel the presence of each other due to the curvature of the solid surface and therefore become unperturbed. It must be pointed out, however, that, in the case of planar surfaces, the grafted chains experience the presence of each other indefinitely due to steric confinement and thus A_{stretch}^g increases monotonically with N_g in this regime. Our model is consistent with this behavior: A_{conf}^g and A_{stretch}^g are about to form a plateau with increasing N_g across the small R_S regime, whereas in the limit of flat surfaces, they appear to increase indefinitely with N_g .

It is observed that for larger grafting densities, our SCFT results and *Alexander's* model are in good agreement for all chain lengths and in describing the conformational entropy of grafted chains as a function of nanoparticle radius. A large discrepancy between the two models occurs for lower grafting density; there, the totally stretched chains assumption of the *Alexander* model and the requirement to maintain bulk density everywhere result in suppressed grafted chains and thus lower A_{stretch}^g (compare the evaluations of *Alexander's* model at low grafting densities in Figure 4.10). On the contrary, in the *mushroom* regime, the profiles of grafted chains obtained with our model appear broader and this is reflected in the increased contribution to the conformation component of the free energy.

4.2.10. Concluding remarks

The conformations and size of a polymer brush grafted on a solid surface, which is immersed in a homopolymer melt of the same chemical constitution as the grafted chains, are complex and depend on a number of molecular parameters. In this section, we first explored the system of a bare and then a grafted single nanoparticle immersed in a polymer matrix, and next, we will proceed by addressing the system of the same grafted particle in contact with vacuum and derive its *solvation* free energy. In each case, a broad parameter space is explored.

Given the radial symmetry of these systems, we used the one-dimensional version of *RuSseL*,⁷⁶ where the *Edwards* diffusion equation is solved via an *implicit Finite Differences* numerical scheme. A smearing approximation is introduced to address the presence of grafting

4.2. Grafted nanoparticle inside a polymer matrix

points in this one-dimensional model. The parametrization of the system corresponds to a particular chemical constitution, i.e., silica/polystyrene), which is readily accessible experimentally.^{14,15,22,43,81,134,137,138}

The segment density distributions and conformations of grafted and matrix chains have been derived for various surface grafting densities, nanoparticle radii and molar mass of grafted chains (which was always equal to the molar mass of matrix chains). We distinguish three different regimes to categorize the behavior of the brushes: the *mushroom* regime, the *dense brush* regime and the *crowding* regime. The response of the system in each one of these regimes is quantified in terms of the chains/area profiles, the distribution of grafted and matrix chain ends, as well as the segment density profiles of *adsorbed* and *free* matrix chains. It becomes clear that, with increasing grafting density and chain molar mass, grafted chains need to stretch/swell towards the bulk region in order to adjust to their gradual conformational restriction; therefore, the penetration of matrix chain segments inside the brush is inhibited.

The dependence of the brush thickness was examined with respect to all the aforementioned parameters in order to thoroughly investigate and clarify the behavior reported in literature. The scaling law, $R_{\text{star}} \sim N_{\text{star}}^{1/2} f_{\text{star}}^{1/4} b_k$, proposed by *Daoud and Cotton* in the intermediate regime, $f_{\text{star}}^{1/2} v^{-2} \gg N_{\text{star}} \gg f_{\text{star}}^{1/2}$, is accurate over a specific range of NP radii, specifically from 4 nm to 8 nm. For larger NPs, the scaling exponents exhibit a complicated behavior and thus a more general equation must be implemented, which treats the exponents of the molecular weight, M_g , and grafting density, σ_g , as functions NP radius/curvature.

Adjusting also the pre-exponential factor of the scaling law, a master curve can be obtained, which provides a faithful description of SCFT predictions for the brush height given the molecular weight of grafted chains, grafting density and NP radius. This master curve seems to be quite accurate, especially in the region of high molecular weight and grafting density. In the *mushroom* regime, brush height exhibits a weak dependence on grafting density and NP radius and it is proportional to the square root of molecular weight. In the *crowding* regime, the brush scales linearly with grafting density and molecular weight, while the density profiles of grafted chain segments, and in general the overall behavior of brushes compares well with the *Alexander* model for incompressible brushes.

In calculating the free energy of the system, the term associated with the conformational entropy of grafted chains does not depend on NP radius for low grafting densities and molar masses (Figure 4.15e). The same plot reflects that with increasing grafting density or molar

mass, chains need to stretch and, therefore, the free energy penalty associated with chain stretching increases. This entropic contribution of grafted chains becomes dominant for high grafting densities and molar masses. The entropic term associated with matrix chains has a minor contribution to the total free energy of the system.

The stretching free energy of grafted chains has been calculated with two different ways: 1. from the configurational *partition functions* of grafted chains, 2. approximately, from the density profiles of grafted chain ends. In either case, a good agreement was observed with the *Alexander* model in the limit of large grafting densities.

4.3. Grafted nanoparticle in contact with vacuum. Solvation free energy of a nanoparticle

4.3.1. Background

Dissolving liquid molecules or nanosized particles in different liquids or gaseous solvents is important in a variety of applications, such as pharmacokinetics,^{139,140} drug development,^{141,142} design of responsive NPs for targeted drug delivery,¹⁴³ and many more. Being able to predict the distribution of a molecule or NP across multiple phases is thus critical to various chemical, materials and biomolecular engineering processes. In the field of environmental protection, researchers are concerned about the transport properties of environmental contaminants,^{144,145} and about the partitioning of organic pollutants, such as polychlorinated biphenyls (PCBs),¹⁴⁶ between the atmosphere, water, and tissues of living organisms.

The tendency of a particle (P) to distribute itself between two fluid phases formed by immiscible or partially miscible components A and B can be quantified in terms of the equilibrium *partition* (distribution) *coefficient*, $K^{A/B}$, which satisfies the following relation:

$$\Delta G_S^{*o,PA} - \Delta G_S^{*o,PB} = -RT \ln K^{A/B} \quad 4.21$$

where $\Delta G_S^{*o,Pj} = G_S^{Pj} - G_S^{PV}$ is the *Gibbs* free energy of *solvation* (also referred to as *solvation* free energy) of the particle in phase j , G_S^{Pj} is the *Gibbs* energy of the particle immersed in a homogeneous phase of type j , and G_S^{PV} is the *Gibbs* energy of the particle in vacuum. Upon reaching equilibrium (*Gibbs* energy at a minimum under prescribed temperature and pressure),¹⁴⁴ the activities, or, for very dilute systems, the concentrations of particles in each phase, C^A and C^B , are related to $K^{A/B}$ as follows:

4.3. Grafted nanoparticle in contact with vacuum. Solvation free energy of a nanoparticle

$$K^{A/B} = \frac{C^A}{C^B} = \frac{k^{B \rightarrow A}}{k^{A \rightarrow B}} \quad 4.22$$

with $k^{i \rightarrow j}$ signifying the rate constant for transfer from phase i to phase j . The *partition coefficient* was initially introduced by Hansch and Fujita to predict the distribution of various compounds between octanol and water.¹⁴⁷ Such coefficients are also used in metallurgy and as a measure of activity of agrochemicals.¹⁴⁸ In literature, there is a wealth of data regarding the *partition coefficients* of polystyrene^{149–152} and *n*-alkanes (up to C8)¹⁴⁸ in water-chloroform and octanol-water¹⁴⁸ systems.

The theoretical basis of *solvation* had been established by *Ben-Naim*,¹⁵³ whose framework introduces the notion of a *pseudo-chemical potential*, directly related to the free energy of *solvation* under constant temperature and pressure. In general, *solvation* is considered to comprise two main stages. At first, a cavity must be formed in the bulk solvent, where the solute molecule will enter the system. In the second stage, the solute molecule enters the system and starts interacting with the molecules of the solvent surrounding it. Graziano¹⁵⁴ derived the *Ben Naim pseudo-chemical potential* for a solute molecule inside a *Van der Waals* liquid solvent and in the limit of infinite dilution.

The experimental determination of *partition coefficients* for NPs and large organic molecules (e.g., C₆₀ fullerenes¹⁵⁵) is highly nontrivial due to the difficulty of the NP/A,B blend systems to reach true equilibrium. According to Praetorius et al.,¹⁴⁴ the concept of the *partition coefficient* for NPs has been misused extensively in the literature. Depending on the surface chemistry of the NPs and on the blend properties, instead of homogeneously dispersing across the blend, the NPs may tend to: (i) agglomerate and form their own phase, (ii) segregate to the liquid/liquid interface, or (iii) adsorb irreversibly to a solid surface. In such cases, the measured *partition coefficients* are not representative of thermodynamic equilibrium between the A and B phases and depend on the experimental conditions (e.g., concentration of the NPs, duration of the experiment, etc.).

The aforementioned limitations have been discussed by several researchers,^{144,155,156} whereas in many cases “apparent” *partition coefficients* are being reported.^{157–159} Regardless, it has been argued¹⁴⁴ that the applicability of such “apparent” *partition coefficients* as fate descriptors may be inappropriate for risk-assessment models. These experimental artifacts can be bypassed by physics-based calculations, capable of sampling the *partition coefficients* and the corresponding *solvation* free energies under true equilibrium conditions.

In this section, we develop a generic theoretical framework for the determination of the *solvation* free energy of bare and grafted NPs in polymers as a function of the NP/polymer degree of wetting, NP curvature, surface grafting density, and lengths of grafted and matrix chains, which are assumed to be of the same chemical constitution. To obtain the free energy of *solvation* of a NP, we perform two SCF theoretic calculations: one on a NP immersed in the polymer matrix at infinite dilution (which has been extensively investigated in the previous Section 4.2) and a second one on the isolated NP in vacuo. In the latter state, where calculations in absence of any bulk melt or solvent are required, one has to invoke compressible SCFT.

Various approaches are reported in the literature, many of which are based on lattice-fluid models, where the free-volume effects are reproduced by introducing vacancies as an additional pseudo-component.^{80,160,161} Herein, we avoid the use of a quasi-solvent of vacancies by employing the *Sanchez-Lacombe* EoS^{70,71} combined with a square gradient correction term. Using these tools, we can achieve a quantitative description of the behavior of the spherical or planar grafted polymer brush exposed to vacuum, which is analogous to bringing it in contact with a *poor solvent*.

By imposing *Dirichlet* BCs for the *restricted partition functions* of matrix and grafted chains on the NP surface^{40,162} (instead of *reflective* boundary conditions)^{41,163}, we can model realistic wetting conditions at the solid/polymer interface. In addition, the short-range potential that is employed herein (*Hamaker*-square well, cSW, see Section 2.1.5.5) takes into account the convex geometry of the NPs and deals appropriately with the loss of interaction sites with increasing curvature. As a result, we can explicitly predict the evolution of polymer affinity to the solid surface (zero, low, high and perfect wetting) with increasing curvature. We demonstrate that the behavior of the system is quite different when addressing planar and spherical interfaces^{26,28,164,165} and compare the overall behavior against theoretical^{113,114,166} and experimental^{81,116} observations.

4.3.2. Description of the model

For the convenience of the reader, a tabular description of the types of systems considered is provided in Table 4-1 (section *sys*). Each type of system was studied for different radii of the spherical shell, lengths of matrix and grafted chains, and strength of solid/polymer interactions. In the “code” denoting the system type, the left- and right-most characters refer to the

4.3. Grafted nanoparticle in contact with vacuum. Solvation free energy of a nanoparticle

(nano)phase inside the innermost spherical cell and to the outer bulk phase, respectively, while the intermediate character (if any) refers to the intermediate (nano)phase.

4.3.3. Structure

Figure 4.17 illustrates the profiles of grafted chains either in contact with vacuum (SGV systems, solid lines) or exposed to a polymer matrix (SGM systems, dashed lines) in dependence of the chain length N_g (varying colors), grafting density σ_g (left-to-right), and NP radius R_S (top to bottom). Overall, the profiles expand with increasing N_g , σ_g , and, to certain extent, with R_S .

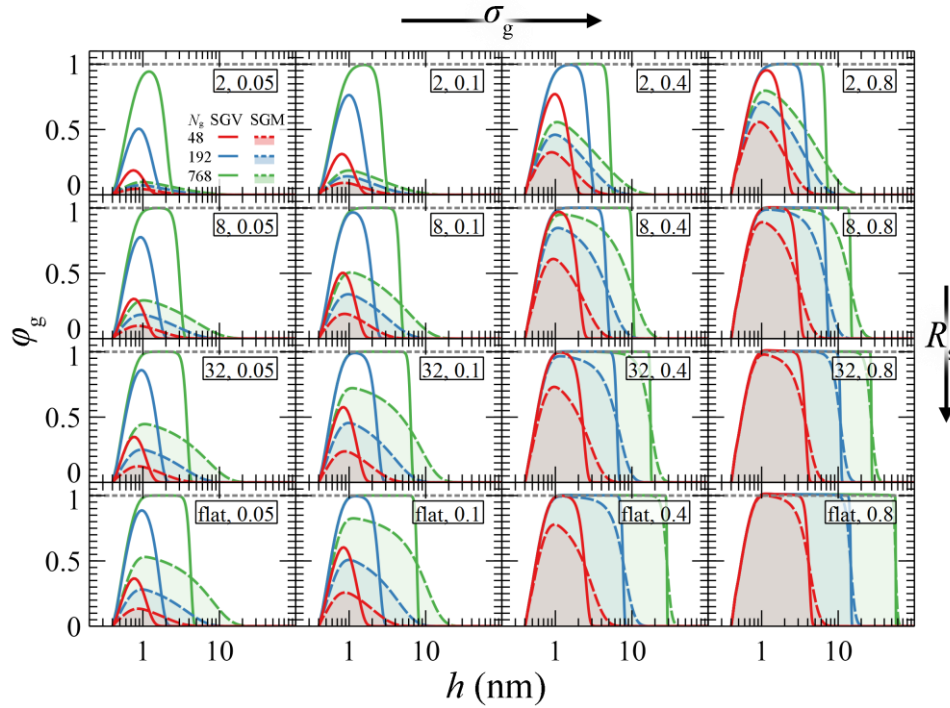


Figure 4.17 Density profiles of grafted chains in contact with melt and vacuum. Grafted chains are either isolated (solid lines) or exposed to a matrix phase of the same chemical constitution and chain length (dashed lines with fill). Results are shown in dependence of the chain length of grafted chains $N_g = \{48: \text{red}, 192: \text{blue}, 768: \text{green}\}$ skeletal bonds, grafting density $\sigma_g = \{0.05, 0.1, 0.4, 0.8\} \text{ nm}^{-2}$ (left to right) and NP radius $R_S = \{2, 8, 32, \infty\} \text{ nm}$ (top to bottom). Legends denote $[R_S, \sigma_g]$ in $[\text{nm}, \text{nm}^{-2}]$ units. All cases correspond to the high-wetting system (HW) in Table 2-2.

The shape of the brushes is qualitatively different between the SGM and SGV systems. In the presence of matrix chains, the brushes swell considerably towards the bulk polymer phase. In absence of melt, the brushes collapse towards the solid surface, since there is an energy cost associated with them being exposed to vacuum. The varying area under the profiles for the same $\sigma_{g,\text{seg}} = \sigma_g N_g$ is due to the curvature and logarithmic h -axis used; integration in spherical coordinates yields the exact same areal density of grafted segments $\sigma_{g,\text{seg}}$.

Chapter 4. Single Nanoparticle Calculations

Let us first consider some limiting cases for the SGM systems (melt/*ideal solvent conditions*). Across the *mushroom regime*¹⁶⁷ ($\sigma_g R_{G,g}^2 < 1$; leftmost panels in Figure **4.17**), grafted chains do not experience the presence of each other and exhibit the characteristic scaling of random coils, i.e., $\langle h_g^2 \rangle^{1/2} \sim N_g^{0.5}$.

For larger grafting densities and chain lengths ($\sigma_g R_{G,g}^2 > 1$, *brush regime*), the scaling depends on both N_g and σ_g . The scaling exponents (n, m) gradually increase from (0.5, 0) to (1, 1) with increasing R_S and σ_g (to a lesser extent with the latter),²⁴ and eventually, in planar geometries, the scaling becomes linear, e.g., $\langle h_g^2 \rangle^{1/2} \sim \sigma_g N_g \sim \sigma_{g,seg}$.^{24,168} The configuration of the brush (or parts of it) depends on the chain *crowding* conditions, which can be quantified in terms of the number of grafted chains passing through a surface at distance h from the NP, which can be calculated via the following eq 4.23.

$$n_{ch,g}^{ref} = \sigma_g \left[R_S / (R_S + h) \right]^2 \quad 4.23$$

Above a threshold value of $n_{ch,g}^{ref}$, the grafted chains are gradually restricted, and therefore they start stretching (*concentrated polymer brush, CPB*).^{129,135} On the other hand, for low $n_{ch,g}^{ref}$, grafted chains enjoy a lot of available space and thus exhibit the scaling of *semi-dilute polymer brushes* (SDPB: $n \sim 0.5-0.6$).^{129,135} In the case of spherical NPs, brushes can assume hybrid CPB-SDPB configurations, wherein they are *concentrated* (CPB) close to the NP surface (high $n_{ch,g}^{ref}$ at low h), and *semi-dilute* (SDPB) after exceeding a critical distance from the NP surface (low $n_{ch,g}^{ref}$ at high h).¹³⁵ For chains grafted on planar surfaces, the CPB or SDPB regime persist indefinitely, since segments lying at higher distances do not enjoy any additional space than those near the NP surface, $\lim_{R_S \rightarrow \infty} n_{ch,g}^{ref} = \sigma_g$. Our model is consistent with this behavior and this has been demonstrated in Section **4.2.9** in terms of the conformational entropy penalty of grafted chains due to stretching as a function of chain length.

The length of matrix chains, N_m , also affects the thickness of the brush; in cases where matrix chains are considerably shorter than the grafted chains, they tend to penetrate into the interfacial region and swell the brush.²⁸ For detailed information regarding the scaling of the brush/melt systems and the effects of varying the length of matrix chains, the reader is referred to Section **4.2.7**.

4.3. Grafted nanoparticle in contact with vacuum. Solvation free energy of a nanoparticle

Concerning the systems of isolated grafted NPs (SGV), where grafted chains can be considered as being in contact with a poor solvent (vacuum), polymer brushes tend to collapse in the region around the solid surface. Their shape depends exclusively on the segmental density, $\sigma_{g,seg}$. This is demonstrated in Figure 4.18, where the grafted chain profiles of equal $\sigma_{g,seg}$ are seen to collapse together, regardless of the NP curvature.

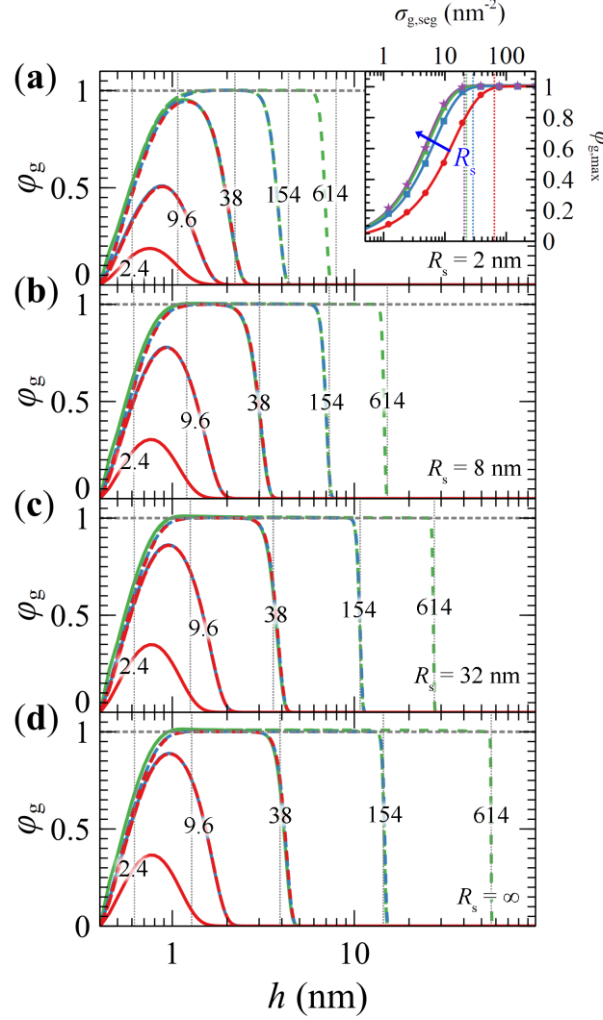


Figure 4.18 Density profiles of chains exposed to vacuum and grafted on spherical particles. Chains are grafted on high-wetting (HW, see Table 2-2) solid surfaces, exposed to vacuum (SGV) with $R_s =$ (a) 2, (b) 8, (c) 32 and (d) ∞ nm. In all cases, $N_g = \{48: \text{solid lines}, 192: \text{dotted lines}, 768: \text{dashed lines}\}$ skeletal bonds and $\sigma_g = \{0.05: \text{red}, 0.2: \text{blue}, 0.8: \text{green}\} \text{ nm}^{-2}$. The numbers on the individual curves denote the segment density per NP area, $\sigma_{g,seg}$ (in nm^{-2} units). The vertical dotted lines correspond to $h_{edge,HS}$ from eq 4.25. The inset in panel (a) depicts the maximum of the profiles in panels (a)-(d) capped at 1 (eq 4.26); R_s increases in the direction of the blue arrow. Curves in the inset are fits with eq 4.27 and vertical lines depict $\sigma_{g,seg99\%}$ from eq 4.28.

One can again discern two distinct regimes, a *dense brush* and a *mushroom* one. Here we use the term *mushroom* to describe conformations in the low $\sigma_{g,seg}$ regime, even though collapsed chains may actually look like *pancakes*¹⁶⁹ or *globules*¹⁷⁰ in the HW and PW cases, respectively. It is noted that the apparent gradual rise of the profile next to the solid in Figure 4.18 (which is

Chapter 4. Single Nanoparticle Calculations

in contrast to the very sharp drop of the density on the vacuum side) is an illusion due to logarithmic scaling of the x -axis.

For large $\sigma_{g,\text{seg}}$ values (*brush regime*), the profiles are fully developed and feature a broad bulk-like region. Their thickness can be predicted accurately by *Alexander's* model for incompressible brushes,^{126,127} which has been extended to curved surfaces.^{24,48,50} The edge of the *dense brushes* can be predicted as a function of curvature from eq 4.24.²⁴

$$h_{\text{edge}}[R_S] = \left(\frac{3\sigma_{g,\text{seg}}}{\rho_{\text{seg,bulk}}} R_S^2 + R_S^3 \right)^{1/3} - R_S \quad 4.24$$

A more general version of eq 4.24 is the following:

$$h_{\text{edge,HS}}[R_S, h_{\text{HS}}] = h_{\text{edge}}[R_S + h_{\text{HS}}] + h_{\text{HS}} \quad 4.25$$

Equation 4.25 takes into account the *excluded volume* interactions (hard sphere wall positioned at h_{HS}) and offers more accurate predictions for intermediate values of $\sigma_{g,\text{seg}}$. Indeed, as shown in Figure 4.18, at high $\sigma_{g,\text{seg}}$ and R_S , the edges of the *dense brushes* coincide with the predictions of eq 4.25. Note that, with h_{edge} known, the root mean squared *brush thickness* for this model is simply $\langle h_g^2 \rangle^{1/2} \sim h_{\text{edge}} / \sqrt{3}$.²⁴ Below a threshold $\sigma_{g,\text{seg}}$, the brushes are only partially formed (*mushroom regime*) and the aforementioned model breaks down; e.g., the vertical lines in Figure 4.18 lie below the edges of the *mushrooms*.¹⁶⁷

The *mushroom-to-brush* crossover can be quantified in terms of the evolution of the maximum segment density:

$$\varphi_{g,\text{max}} = \max(\varphi_g) \quad 4.26$$

This is illustrated in the inset of Figure 4.18a for the case of HW systems, whose enlarged version is presented in Figure 4.19, both in terms of $\sigma_{g,\text{seg}}$ and of the dimensionless quantity $\sigma_g R_{G,g}^2 = \sigma_{g,\text{seg}} R_{G,g}^2 / N_g$, which is commonly used to estimate the *mushroom-to-brush* crossover.^{24,129} The evolution of $\varphi_{g,\text{max}}$ is described accurately by the following eq 4.27.

$$\varphi_{g,\text{max}}[\sigma_{g,\text{seg}}] \sim \varphi_{\text{br}} \tanh \left[\left(\frac{\sigma_{g,\text{seg}}}{\sigma_{\text{br}}} \right)^{\beta_{\text{br}}} \right] \quad 4.27$$

where σ_{br} is a characteristic areal segmental density, β_{br} a stretching exponent, and

$\varphi_{\text{br}} = \lim_{\sigma_{g,\text{seg}} \rightarrow \infty} \varphi_{g,\text{max}}$. By setting $\varphi_{g,\text{max}} / \varphi_{\text{br}} = 0.99$ and solving eq 4.27 for $\sigma_{g,\text{seg}}$:

4.3. Grafted nanoparticle in contact with vacuum. Solvation free energy of a nanoparticle

$$\sigma_{g,\text{seg}99\%} = \sigma_{\text{br}} \tanh^{-1}(0.99)^{1/\beta_{\text{br}}} \quad 4.28$$

we can derive a characteristic areal density corresponding to the formation of the 99% of the brush. The corresponding fitting coefficients of eq 4.27, and $\sigma_{g,\text{seg}99\%}$ from eq 4.28 are reported in Table 4-3. Looking at this table, it is observed that the critical value of $\sigma_g R_{G,g}^2$ is on the order of unity and increases with decreasing particle radius. As we will discuss later, such characteristic length scales are related with the free energy of *solvation* and its evolution with the *mushroom-to-brush* crossover.

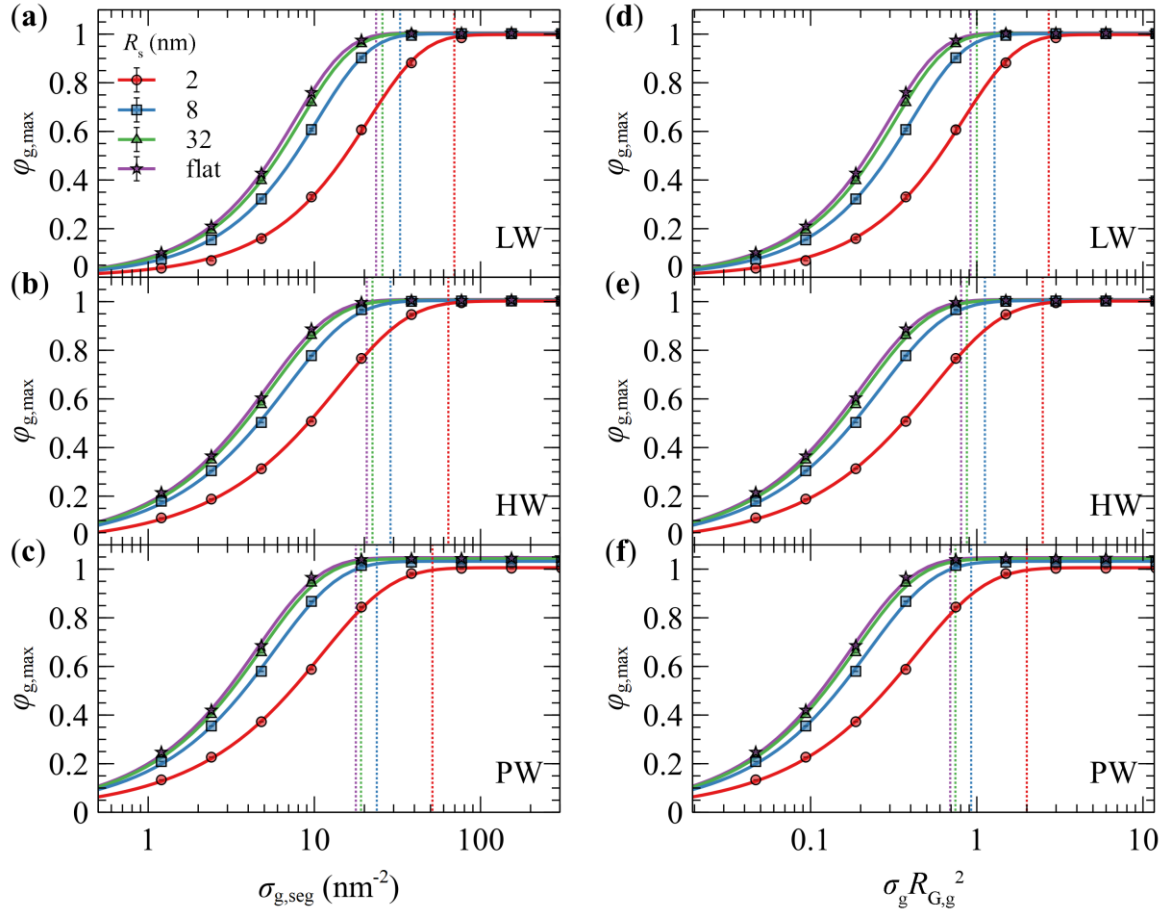


Figure 4.19 Maximum density of grafted chains exposed to vacuum for various wetting degrees. The maximum of the profiles capped at 1 of (a) low-, (b) high- and (c) perfect-wetting solid surfaces exposed to vacuum (SGV) with $R_s = \{2: \text{red circles}, 8: \text{blue squares}, 32: \text{green triangles}, \infty: \text{violet asterisks}\}$ nm. Markers depict evaluations from the SCFT calculations and lines illustrate fits with eq 4.27; the corresponding fitting coefficients are reported in Table 4-3. The vertical lines depict $\sigma_{g,\text{seg}99\%}$ from eq 4.28. Panels (d-e) depict the same data as (a-c), but with respect to the dimensionless quantity $\sigma_g R_{G,g}^2 = \sigma_{g,\text{seg}} R_{G,g}^2 / N_g$.

Table 4-3 Fitting coefficient for eq 4.27.

type	R_s (nm)	φ_{br}	σ_{br} (nm ⁻²)	β_{br}	$\sigma_{g,seg99\%}$ (nm ⁻²)	$(\sigma_g R_{G,g}^2)_{99\%}$
LW	2	0.998	27.2	1.04	69.3	2.7
	8	1.001	13.3	1.08	32.8	1.3
	32	1.003	10.6	1.10	25.7	1.0
	∞	1.005	9.7	1.10	23.5	0.9
HW	2	1.002	19.3	0.81	64.2	2.5
	8	1.004	9.3	0.86	28.8	1.1
	32	1.006	7.5	0.89	22.4	0.9
	∞	1.009	7.0	0.90	20.6	0.8
PW	2	1.006	15.4	0.81	51.2	2.0
	8	1.032	7.8	0.87	23.9	0.9
	32	1.043	6.5	0.90	19.2	0.7
	∞	1.047	6.1	0.91	17.8	0.7

4.3.4. Thermodynamics and solvation free energy

Figure 4.20a,b illustrates the free energy density per NP core area of a grafted HW planar surface exposed to polymer melt of the same chemical constitution ($\Delta\gamma^{SGM}$) and vacuum ($\Delta\gamma^{SGV}$, but with a minus sign), as a function of $\sigma_{g,seg}$, respectively. Figure 4.20c presents the sum of these quantities (eq 4.29), i.e., the free energy of *solvation* per NP area.

$$\Delta\gamma_s^{*o} = \Delta\gamma^{SGM} - \Delta\gamma^{SGV} = \Delta G_s^{*o} / S_s \quad 4.29$$

4.3. Grafted nanoparticle in contact with vacuum. Solvation free energy of a nanoparticle

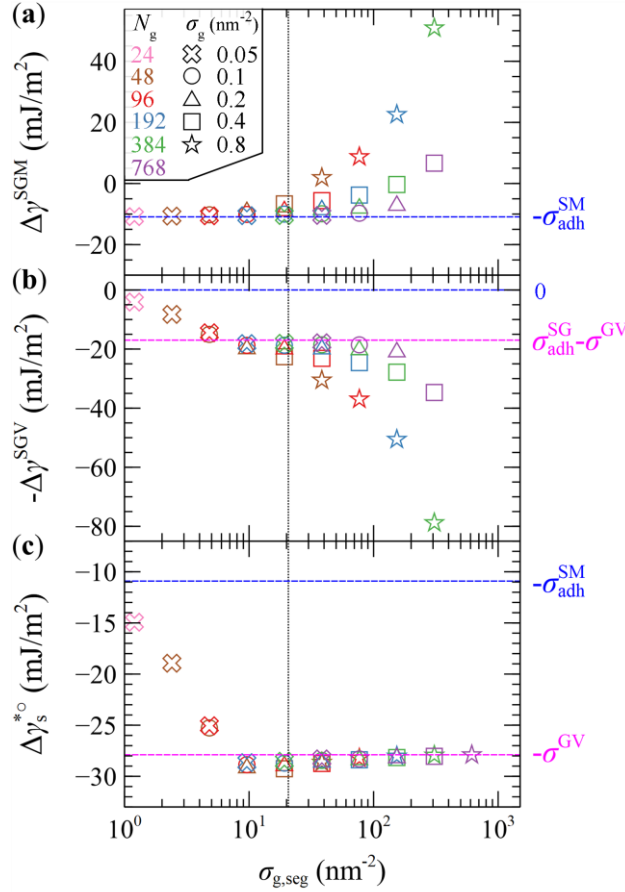


Figure 4.20 Solvation free energy in a planar SiO_2/PS system. **(a)** Free energy per solid surface area of a grafted, high-wetting NP (HW, see Table 2-2) of extremely small curvature (i.e., planar interface) embedded in a matrix phase of the same chemical constitution and chain length ($N_g = N_m$), **(b)** negative free energy per unit surface of an isolated grafted NP and **(c)** solvation free energy, per solid surface area, as functions of $\sigma_{g,\text{seg}} = \sigma_g N_g$. The values on the ordinate of panel (c) are obtained by direct summation of those in (a) and (b). The blue/magenta lines indicate limiting values for $\sigma_{g,\text{seg}} \rightarrow 0$, and for characteristic $\sigma_{g,\text{seg}}$ of fully developed brushes, respectively. The vertical line denotes $\sigma_{g,\text{seg}99\%}$ from eq 4.28, which is indicative of the *mushroom-to-brush* crossover.

For very low σ_g and N_g , the contribution of the grafted chains to the free energy in Figure 4.20a is marginal. The free energy of the SGM system tends to the negative *adhesion tension* of a corresponding SM interface, $\lim_{\substack{\sigma_{g,\text{seg}} \rightarrow 0 \\ R_s \rightarrow \infty}} \Delta\gamma^{\text{SGM}} = \lim_{R_s \rightarrow \infty} \Delta\gamma^{\text{SM}} = -\sigma_{\text{adh}}^{\text{SM}}$ (see blue curve in Figure 4.3a or b

in the planar limit). For the SGV system in Figure 4.20b, $\lim_{\sigma_{g,\text{seg}} \rightarrow 0} \Delta\gamma^{\text{SGV}} = 0$; therefore, its

contribution to the solvation free energy is zero in this limit, hence: $\lim_{\substack{\sigma_{g,\text{seg}} \rightarrow 0 \\ R_s \rightarrow \infty}} \Delta\gamma_s^{*o} = \lim_{R_s \rightarrow \infty} \Delta\gamma^{\text{SM}} = -\sigma_{\text{adh}}^{\text{SM}}$

. With increasing $\sigma_{g,\text{seg}}$ and up to a characteristic value, we notice a transition region. The free energy per unit surface of the SGM system in Figure 4.20a remains constant ($\lim_{R_s \rightarrow \infty} \Delta\gamma^{\text{SGM}} \sim -\sigma_{\text{adh}}^{\text{GM}}$

), because there is still no enthalpic gain with increasing area of the homogeneous GM interface.

Chapter 4. Single Nanoparticle Calculations

Furthermore, at low $\sigma_{g,seg}$, grafted chains have not been stretched enough for entropic penalties to start affecting the thermodynamics of the system. In contrast, the free energy per unit surface of the SGV system increases gradually from 0 up to a temporary plateau value (magenta line in Figure 4.20b). This value depends on the free energies of the inner SG and the outer GV interfaces (e.g., see Figure 4.1). At a characteristic value of $\sigma_{g,seg}$, which is indicative of the *mushroom to dense brush* crossover, $\lim_{R_s \rightarrow \infty} \Delta\gamma^{SGV} \sim \lim_{R_s \rightarrow \infty} \Delta\gamma^{SG} + \lim_{R_s \rightarrow \infty} \Delta\gamma^{GV} \sim -\sigma_{adh}^{SG} + \sigma^{GV}$.

It is noted that after the *mushroom to brush* crossover, the outer polymer/vacuum interface of a GV system can be considered equivalent to that of a MV system, since grafted and matrix chains are of the same length and chemical constitution, $\sigma^{GV} \sim \sigma^{MV}$. As a result, the contribution of σ_{adh}^{SG} to $\Delta\gamma_S^{*0}$ from SGM and SVG cancels out, and therefore $\lim_{R_s \rightarrow \infty} \Delta\gamma_S^{*0} \sim -\sigma^{GV}$. The characteristic value of $\sigma_{g,seg}$ for this behavior to emerge appears to be somewhat smaller than the characteristic length $\sigma_{g,seg99\%}$, obtained from eq 4.28 (vertical line in Figure 4.20).

For larger $\sigma_{g,seg}$, $\Delta\gamma^{SGM}$ and $\Delta\gamma^{SGV}$ deviate significantly from the aforementioned plateau values (blue/magenta lines in Figure 4.20a,b), due to chain stretching. In planar configurations, the stretching free energy increases about monotonically with N_g (at constant grafting density, σ_g), since the contours of neighboring grafted chains interact indefinitely; thus, $\Delta\gamma^{SGM}$ and $\Delta\gamma^{SGV}$ both increase indefinitely as well.^{24,50} At $\sigma_{g,seg} \sim 10 \text{ nm}^{-2}$, a weak minimum is exhibited, because the entropy penalty associated with the conformations of grafted chains in the SGV system is slightly higher than in the SGM system.

The conformational entropy effect becomes more pronounced when considering denser brushes, because the chains experience additional confinement and stretch even more. However, $\Delta\gamma_S^{*0}$ appears to be rather insensitive to chain stretching, indicating that these entropic chain stretching contributions in the SGM and SGV systems are about equal and cancel out; hence, $\lim_{R_s \rightarrow \infty} \Delta\gamma_S^{*0} \sim -\sigma^{GV}$ across this regime. This is reasonable, since the structure of densely grafted SGM is quite similar to that of SGV in terms of their segment profiles (e.g., compare profiles in the bottom panel of Figure 4.17), and so are their profiles of end-segments, which tend to segregate to the polymer/vacuum interface²⁴ in agreement with *Alexander's* model for incompressible brushes.^{126,127} Thus, the *solvation* free energy per unit surface of a very large NP well-coated with a thick layer of grafted chains becomes practically equal to minus the melt *surface tension*.

4.3. Grafted nanoparticle in contact with vacuum. Solvation free energy of a nanoparticle

Figure 4.21 presents $\Delta\gamma_s^{*o}$ and $\Delta G_s^{*o} = \Delta\gamma_s^{*o} S_s$ versus $\sigma_{g,seg}$ (left and right ordinates) for various NP sizes and surface potentials.

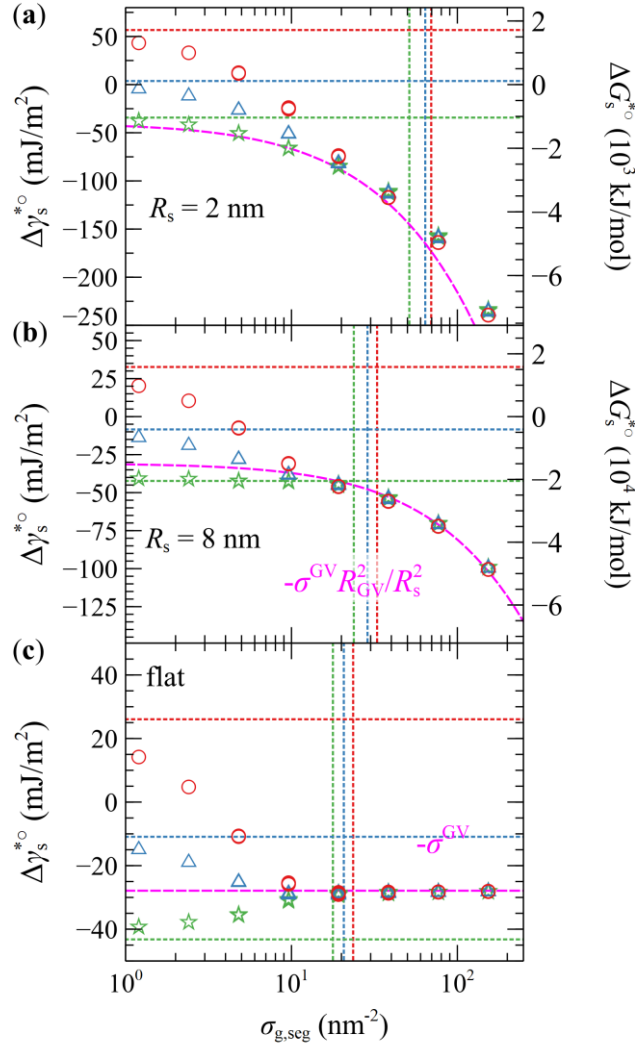


Figure 4.21 Solvation free energy of spherical SiO₂ nanoparticles of various radii. $\Delta\gamma_s^{*o}$ and ΔG_s^{*o} (left and right ordinates) versus $\sigma_{g,seg}$, for low wetting (red circles), high wetting (blue triangles), and perfect wetting (green stars) surfaces with R_s equal to (a) 2 nm, (b) 8 nm and (c) ∞ . The horizontal dotted lines depict $\Delta\gamma^{SM} = -\sigma_{adh}^{SM} R_{SM}^2 / R_s^2$ from Figure 4.3a with R_{SM} set to $h_{edge,HS}$. The vertical lines illustrate the *mushroom-to-brush* crossover, $\sigma_{g,seg}^{99\%}$ (eq 4.28). The dashed magenta lines depict predictions across the high $\sigma_{g,seg}$ regime obtained via eq 4.25, for $R_{GV} \rightarrow R_{GV,edge} = R_s + h_{edge,HS}$ (eq 4.25). In all cases, $N_m = N_g$.

Similar to the planar case, the effect of grafted chains is negligible at low $\sigma_{g,seg}$; thus, $\Delta\gamma^{SGV} \sim 0$ and $\Delta\gamma_s^{*o} \sim \Delta\gamma^{SGM} \sim \Delta\gamma^{SM}$. Indeed, as shown in Figure 4.21, $\Delta\gamma_s^{*o}$ tends to γ^{SM} with decreasing $\sigma_{g,seg}$. The value of *solvation* free energy in the limit $\sigma_{g,seg} \rightarrow 0$ is represented by the horizontal dotted lines and can be expressed in terms of the *adhesion tension* of a planar interface via eq 4.4 as follows:

$$\lim_{\sigma_{g,seg} \rightarrow 0} \Delta G_S^{*o} \sim \gamma^{SM} S_S \sim -\sigma_{adh}^{SG} S_{SM} \quad 4.30$$

where $S_{SM} = 4\pi R_{SM}^2$ and R_{SM} is the position of the inner SM interface.

With increasing $\sigma_{g,seg}$ and up to a threshold value, a characteristic transition is observed, during which the contributions of the SM and SG interfaces to ΔG_S^{*o} are gradually screening each other and the latter starts being dominated by the GV interface of the SGV system. That threshold value appears to be slightly smaller than $\sigma_{g,seg99\%}$ from eq 4.28 (vertical lines in Figure 4.21).

For large $\sigma_{g,seg}$, ΔG_S^{*o} can be reasonably approximated in terms of the *surface tension* of the GV interface via eq 4.5, as follows:

$$\Delta G_S^{*o} \sim \gamma^{SGV} S_S \sim -\sigma^{GV} S_{GV}, \quad \sigma_{g,seg} \geq \sigma_{g,seg99\%} \quad 4.31$$

with S_{GV} being the area of the outer GV interface and $\sigma_{g,seg99\%}$ a characteristic areal density indicative of the *mushroom-to-brush* crossover.

Supposing that a GV interface can be described reasonably well as an incompressible brush, its position can be approximated as $R_{GV,edge} = h_{edge,HS} + R_S$ from eqs 4.24 and 4.25. Indeed, according to Figure 4.21b,c, ΔG_S^{*o} for intermediate and large R_S is in good match with the predictions of eq 4.31 for $R_{GV} \rightarrow R_{GV,edge}$ (compare with magenta curves).

In the case of the smaller NP considered here (see Figure 4.21a), there is a slight deviation between the magenta curve and the points. Describing highly curved interfaces with simple relations such as eq 4.31 is nontrivial because there are sensitive curvature-dependent mechanisms at play. For starters, the profiles of SGM and SGV differ substantially, even for cases with large $\sigma_{g,seg}$, e.g., compare the top-right panel of Figure 4.17 with the panels below it for larger R_S . As a result, the chains stretch in a different manner and therefore entropic contributions do not exactly cancel out (this mechanism is discussed in depth in Section 4.3.4.1). In addition to this, the approximation $R_{GV} \rightarrow R_{GV,edge}$ is moderate at high curvatures. Indeed, as shown in Figure 4.18a, the actual position of the film is consistently lower than $R_{GV,edge}$ at large $\sigma_{g,seg}$.

The order of magnitude of calculated *solvation* free energies is noteworthy. ΔG_S^{*o} depends on the size of the particle being solvated. According to *Lum-Chandler-Weeks* theory of hydrophobicity¹⁶⁶ and the present findings (eq 4.31), it scales proportionally with the area of the

4.3. Grafted nanoparticle in contact with vacuum. Solvation free energy of a nanoparticle

interface. Consequently, it scales about quadratically with the effective particle radius (taking into account the thickness of a grafted brush), while in the case of a macroscopic particle bounded by a practically planar surface, it tends to infinity.

Quantitatively, the *solvation* of usual organic molecules $|\Delta G_s^{*o}|$ is in the order of decades of kJ/mol,¹⁴⁶ whereas for large particles, it may span hundreds of kJ/mol (e.g., *solvation* free energy of C₆₀ in a variety of common solvents (*j*) is in the order of $\Delta G_s^{*o,C_{60}j} = -100$ kJ/mol). Given that the average radius of C₆₀ equals $R_{C_{60}} \sim 0.35$ nm¹⁷¹ and supposing that *solvation* scales quadratically with radius, a particle with $R_S = 2$ nm and the same *solvation* free energy per particle area would have a *solvation* free energy of $\Delta G_s^{*o,C_{60}j} R_S^2 / R_{C_{60}}^2 = -3300$ kJ/mol, which is in accordance with the order of magnitude depicted in Figure 4.21a for $R_S = 2$ nm.

4.3.4.1. Contribution of individual free energy terms

The present section investigates the contribution of individual free energy terms per NP core area to the grand potential of SGM systems ($\Delta\gamma^{SGM} = \Delta\Omega^{SGM} / S_s$), *Helmholtz* free energy of SGV systems ($\Delta\gamma^{SGV} = \Delta A^{SGV} / S_s$) and *solvation free energy* ($\Delta\gamma_s^{*o} = \Delta\gamma_s^{SGM} - \Delta\gamma_s^{SGV}$) as a function of σ_g , N_g , and curvature. As a test case, Figure 4.22a-d illustrate the energy terms of grafted NPs with $R_S = 2$ nm and Figure 4.22f-i the corresponding contributions of a planar brush. The total energy of the NP and planar surface system is shown in Figure 4.22e and j, respectively.

The term $\Delta\gamma_{\text{coh+field}}^{\text{sys}} = \Delta\gamma_{\text{coh}}^{\text{sys}} + \Delta\gamma_{\text{field}}^{\text{sys}}$ is a functional of the total density profile (eqs 2.39 and 2.40) and refers to the combination of the cohesion and field terms; the latter incorporates entropic penalties as well, as explained in Section 2.2. As demonstrated in Figure 4.22a and f, there is a substantial difference in this term between the limiting cases of high and zero curvatures. For not too densely grafted NPs (low σ_g), $\Delta\gamma_{\text{coh+field}}^{SGM}$ remains approximately constant. $\Delta\gamma_{\text{coh+field}}^{SGM}$ is affected by the total segment density distribution close to the NP surface ($\rho = \rho_g + \rho_m$), which remains approximately the same with increasing $\sigma_{g,\text{seg}}$ (since $G = M$). The latter fact would not be true if $G \neq M$, since the MG interface would add to the free energy a factor $\sim S_{GM}\sigma^{GM}$.

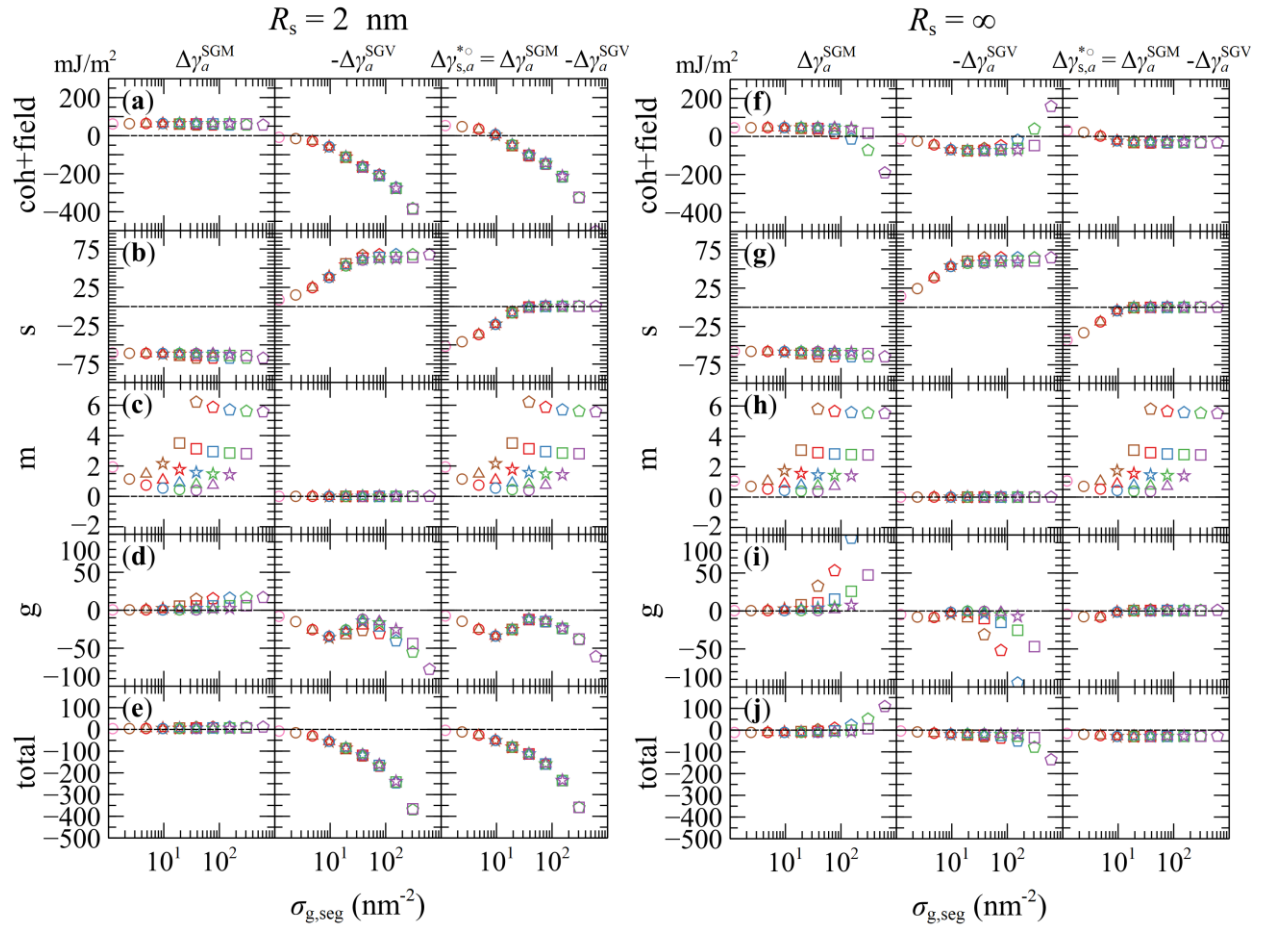


Figure 4.22 Solvation free energy terms as functions of the amount of grafted material. Individual free energy contributions to $\Delta\gamma_a^{\text{SGM}}$, $\Delta\gamma_a^{\text{SGV}}$ and $\Delta\gamma_s^{*o} = \Delta\gamma_a^{\text{SGM}} - \Delta\gamma_a^{\text{SGV}}$, as functions of the amount of grafted segments per NP core area, $\sigma_{g,\text{seg}} = \sigma_g N_g$. Panels (a–e) depict energy contributions for NPs with $R_S = 2$ nm, whereas panels (f–j) concern a planar surface ($R_S \rightarrow \infty$). Evaluations have been performed for σ_g (nm^{-2}) = 0.05 (O), 0.1 (Δ), 0.2 (\star), 0.4 (\square) and 0.8 (pentagons), $N_g = 24$ (pink), 48 (brown), 96 (red), 192 (blue), 384 (green) and 768 (violet), and $N_m = N_g$.

The difference between the two curvatures reveals itself in the SGV systems. With increasing $\sigma_{g,\text{seg}}$ two new interfaces are emerging, one close to the wall (SG) and one exposed to the vacuum phase (GV). For high curvatures, the free energy is dominated by the area of the GV interface which increases approximately quadratically with $\sigma_{g,\text{seg}}$; hence, its contribution to the free energy is on the order of $\sim -S_{\text{GV}}\sigma^{\text{GV}}$. In the planar case, on the other hand, the surface area of both the SG and GV interfaces remain the same and thus the free energy plateaus to a value that depends on both the *adhesion tension* of the SG interface and the *surface tension* of the GV interface.

4.3. Grafted nanoparticle in contact with vacuum. Solvation free energy of a nanoparticle

In addition to these considerations, for very large σ_g and low curvature (dense chain packing), the reduced density exceeds unity in the planar system ($\varphi > 1$), and $\Delta\gamma_{\text{coh+field}}^{\text{sys}}$ becomes slightly negative as shown in Figure 4.22f due to the entropic contributions of the field term (for information see Figure 2.4 of Section 2.1.4.2). In any case, the contributions of the cohesive and field terms to the free energy of the planar SGM and SGV systems are approximately equal and thus the net sum is around zero. As a result, the *solvation* free energy plateaus to the negative *surface tension*, as shown in Figure 4.22f.

The evolution of $\Delta\gamma_{\text{solid}}^{\text{sys}}$ with increasing $\sigma_{g,\text{seg}}$ is depicted in Figure 4.22b and g. In SGM systems, $\Delta\gamma_{\text{solid}}^{\text{SGM}}$ is practically constant since the area of the SG interface does not change. In SGV systems, $\Delta\gamma_{\text{solid}}^{\text{SGV}} = 0$ when $\sigma_{g,\text{seg}} = 0$ (there are no grafted chains to interact with the wall) and saturates to the same value as in the SGM system at the point where the brush has been fully formed. Consequently, for $\sigma_{g,\text{seg}} \gg \sigma_{g,\text{seg}99\%}$, the solid/polymer interactions are the same ($\Delta\gamma_{\text{solid}}^{\text{SGM}} = \Delta\gamma_{\text{solid}}^{\text{SGV}}$) and their contribution to the *solvation* free energy cancels out.

The entropic contribution from eq 2.42 (which depends exclusively on matrix chains) appears to be very similar between the high and zero curvature geometries (compare Figure 4.22c and h). In situations where $N_g \leq N_m$, these contributions are subtle; this is not the case when $N_m \ll N_g$ (see Figure 4.23 of the following Section 4.3.4.2).

The entropic contributions associated with the conformations of grafted chains are quite different between SGM ($\Delta\gamma_g^{\text{SGM}}$) and SGV ($\Delta\gamma_g^{\text{SGV}}$) systems in high curvature geometries, whereas in planar geometries they are quite similar; compare Figure 4.22d and i. In planar geometries, and for large $\sigma_{g,\text{seg}}$ —where such entropic factors become significant—the structure of the grafted chains is similar between SGM and SGV. In both cases, brush thickness can be approximated very well by that of an incompressible *Alexander* brush,^{126,127} and as a result the grafted chains experience similar stretching, whether they are in contact with melt or exposed to vacuum. Hence, this entropic contribution is counterbalanced and does not affect *solvation*.

This is not the case for high curvatures (Figure 4.22d): at very low $\sigma_{g,\text{seg}}$, all grafted chain segments tend to fully collapse towards the solid surface (to avoid interacting with vacuum), but this generates an entropic penalty. At $\sigma_{g,\text{seg}} \sim 10 \text{ nm}^{-2}$, where the brush has been partially developed (e.g., see Figure 4.18a for $R_s = 2 \text{ nm}$), we notice that entropy starts decreasing, since beyond a certain distance from the solid, segments enjoy more available space. Finally, when the

brush is fully developed, the behavior of entropy switches back to what is expected; thicker brushes are accompanied by higher entropic cost.

It is worth noting that the points of our SCFT model for the 2 nm NP in Figure 4.21 lie above the theoretical magenta line (instead of below). This happens because the position of the GV interface has been estimated in terms of the edge of an *Alexander* brush, which is a poor approximation for small NPs. It lies further than the actual position of the GV interface (Figure 4.18a; thus, the estimation from the magenta line in Figure 4.21 underestimates the *solvation* free energy.

4.3.4.2. Effect of varying the length of matrix chains

In the previous sections, we considered cases where the length of grafted chains was equal to that of the matrix chains ($N_g = N_m$). In general, polymer blends with different chain sizes, but the same chemical constitution, are considered completely miscible.¹⁷² However, in the presence of grafted chains, the ratio N_g/N_m has a profound effect on the quality of the solvent.^{24,28,48}

In situations where $N_m \geq N_g$, matrix chains cannot readily penetrate the brush, due to the manifestation of the entropic penalty of confinement discussed in Section 4.1.2 (mechanism 2). Matrix chain segments are pulled towards the polymer phase by their intramolecular neighbors. At the same time, penetration of the (larger) matrix chains into the region occupied by the grafted chains would reduce the number of available conformations of the latter. As a result, matrix chains are effectively repelled from the brush (which remains unperturbed^{23,24,28,164}) favoring the agglomeration tendency of the NPs.^{25,27,28,37}

On the other hand, when $N_m < N_g$, the matrix-grafted interactions become entropically favorable, and therefore, the penetration of matrix chains into the brush is thermodynamically promoted. In this case, grafted chains experience the melt as if it were an athermal solvent. The segregation of matrix chain segments inside the interfacial region can significantly affect the configurations of grafted chains and even lead to excessive swelling in some situations.^{24,28} The quality of the solvent is enhanced with increasing N_g/N_m , and as a result, the favorable grafted-matrix interactions resist the attraction between NPs.^{25,27,28,37}

In this paragraph, we investigate the effect of chain length ratio, N_g/N_m , on the *solvation* free energy.

4.3. Grafted nanoparticle in contact with vacuum. Solvation free energy of a nanoparticle

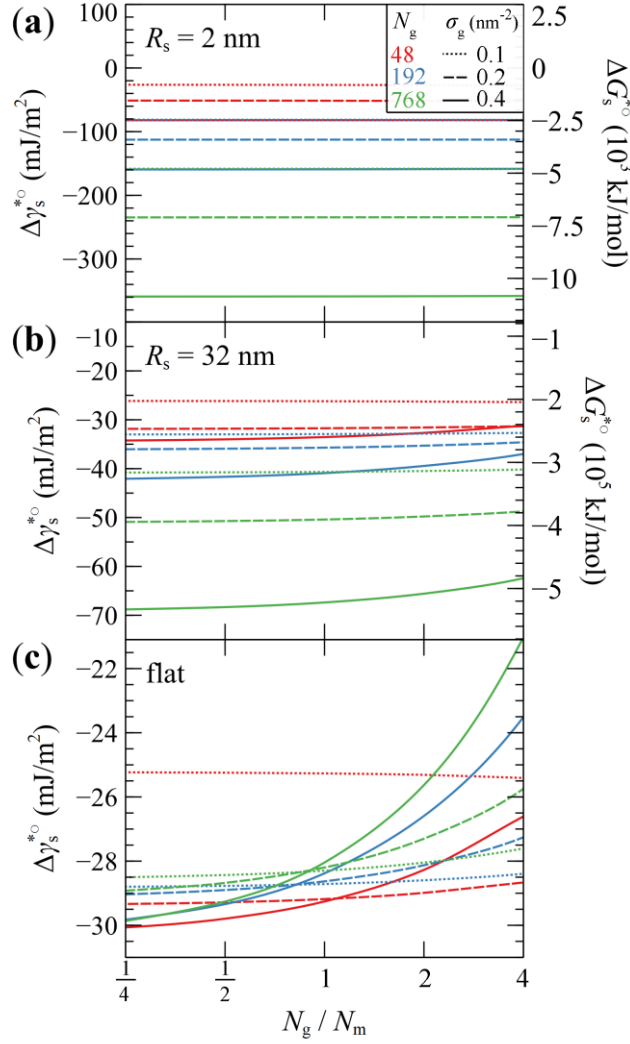


Figure 4.23 Solvation free energy of a SiO_2 particle for different matrix/grafted length ratios. $\Delta\gamma_s^*$ and ΔG_s^* (left and right ordinates) versus N_g/N_m for high wetting surfaces with R_s equal to (a) 2 nm, (b) 32 nm and (c) ∞ . The chain length of grafted chains is denoted by different colors: $N_g = \{4: \text{red}, 192: \text{blue}, 768: \text{green}\}$ and the grafting density by different line styles: $\sigma_g = \{0.1: \text{dotted}, 0.2: \text{dashed}, 0.4: \text{solid}\} \text{ nm}^{-2}$.

Figure 4.23 depicts $\Delta\gamma_s^*$ and ΔG_s^* as a function of N_g/N_m . Starting with the case of the smallest NP considered herein (Figure 4.23a), we notice that ΔG_s^* is practically insensitive to N_g/N_m . However, for larger NP sizes, ΔG_s^* increases with N_g/N_m , with this effect reaching maximum intensity in the planar geometry limit. This is attributed to both the free energy penalty arising from the stretching of the grafted chains (eq 2.43) and to the translational entropy of matrix chains (eq 2.42). Note that the length of matrix chains, N_m , appears in the denominator of eq 2.42, indicating that the brush is penetrated by more matrix chains. This effect becomes more pronounced in denser brushes or in the planar limit, where the high confinement leads to an abrupt scaling of the height of the brush with both σ_g and N_g , and the associated entropic

penalties in eqs 2.42 and 2.43 are maximized. On the contrary, this effect is mitigated at high particle curvatures, where the matrix chains can readily surround the grafted chains. It is thus proven that, apart from the interactions between NPs or the scaling of the brush,¹⁶⁵ curvature plays an essential role on *solvation free energy* as well.

4.3.5. Model for estimation of partition coefficients

The *solvation* free energy of a grafted NP depends on the comparison between the free energy of a grafted NP exposed to i) vacuum (SGV), and ii) a polymer matrix (SGM). Different behaviors

are expected for different ranges of the amount of grafted material, $\sigma_{g,seg} = \frac{6}{C_{inf} l_{c-c}^2} \sigma_g R_{G,g}^2$, and the chain crowding conditions as quantified by $n_{ch,g}^{ref}$ (eq 4.23). For starters, we will consider cases where $N_g \geq N_m$, and the brush does not experience particular swelling.

	(I) $\sigma_{g,seg} \sim 0$	(II) $\sigma_{g,seg} < \sigma_{g,seg99\%}$	(III) $\sigma_{g,seg} > \sigma_{g,seg99\%}, \text{ low } n_{ch,g}^{ref}$	(IV) $\sigma_{g,seg} > \sigma_{g,seg99\%}, \text{ high } n_{ch,g}^{ref}$
SGM				
$\Delta\Omega^{SGM}$	$-\sigma_{adh}^{SM} S_{SM}$	$-\sigma_{adh}^{SM} S_{SM} \rightarrow \sigma_{GM}^{GM} S_{GM} - \sigma_{adh}^{SG} S_{SM}$	$\sigma_{GM}^{GM} S_{GM} - \sigma_{adh}^{SG} S_{SM}$	$\sigma_{GM}^{GM} S_{GM} - \sigma_{adh}^{SG} S_{SM} + \Delta\Omega_{m+g}^{SGM}$
SGV				
$-\Delta A^{SGV}$	0	$0 \rightarrow \sigma_{adh}^{SG} S_{SM} - \sigma_{GV}^{GV} S_{GV}$	$\sigma_{adh}^{SG} S_{SM} - \sigma_{GV}^{GV} S_{GV}$	$\sigma_{adh}^{SG} S_{SM} - \sigma_{GV}^{GV} S_{GV} - \Delta\Omega_{m+g}^{SGV}$
ΔG_s^{*o}	$-\sigma_{adh}^{SM} S_{SM}$	$-\sigma_{adh}^{SM} S_{SM} \rightarrow \sigma_{GM}^{GM} S_{GM} - \sigma_{GV}^{GV} S_{GV}$	$\sigma_{GM}^{GM} S_{GM} - \sigma_{GV}^{GV} S_{GV}$	$\sigma_{GM}^{GM} S_{GM} - \sigma_{GV}^{GV} S_{GV}$

Figure 4.24 Schematic illustration of regimes I-IV, in terms of the amount of grafted material $\sigma_{g,seg}$ and chain crowding. The crowding is quantified by $n_{ch,g}^{ref}$ (eq 4.23). The bead-spring configurations of the second (fourth) row of the grid depict representative SGM (SGV) configurations. The dominant contributions to the free energy are shown below each illustration. The last row of the grid depicts the dominant terms of the *solvation* free energy (eq 4.33).

4.3. Grafted nanoparticle in contact with vacuum. Solvation free energy of a nanoparticle

Equation 4.32 illustrates a generic model for the quantitative predictions of *solvation* free energy in terms of $\Delta\Omega^{\text{SM}}$ and ΔA^{GV} :

$$\Delta G_s^{*o,\text{SGM}}(\sigma_{g,\text{seg}}, R_s) \sim \begin{cases} \Delta\Omega^{\text{SM}}, & \sigma_{g,\text{seg}} \sim 0 \\ \Delta\Omega^{\text{SM}} [1 - F(\sigma_{g,\text{seg}}, R_s)] + (\Delta\Omega^{\text{GM}} - \Delta A^{\text{GV}}) F(\sigma_{g,\text{seg}}, R_s), & 0 < \sigma_{g,\text{seg}} < \sigma_{g,\text{seg}99\%} \\ \Delta\Omega^{\text{GM}} - \Delta A^{\text{GV}}, & \sigma_{g,\text{seg}99\%} < \sigma_{g,\text{seg}} \end{cases} \quad 4.32$$

where $\sigma_{g,\text{seg}99\%} R_{G,g}^2 / N_g$ is in the order of unity for $R_s > 8$ nm (see Table 4-3). Alternatively, we can describe ΔG_s^{*o} in terms of the interfacial free energies, as shown in the following eq 4.33.

$$\Delta G_s^{*o,\text{SGM}}(\sigma_{g,\text{seg}}, R_s) \sim \begin{cases} -\sigma_{\text{adh}}^{\text{SM}} S_{\text{SM}}, & \sigma_{g,\text{seg}} \sim 0 \\ -\sigma_{\text{adh}}^{\text{SM}} S_{\text{SM}} [1 - F(\sigma_{g,\text{seg}}, R_s)] + (\sigma_{\text{GM}}^{\text{GM}} S_{\text{GM}} - \sigma_{\text{GV}}^{\text{GV}} S_{\text{GV}}) F(\sigma_{g,\text{seg}}, R_s), & 0 < \sigma_{g,\text{seg}} < \sigma_{g,\text{seg}99\%} \\ \sigma_{\text{GM}}^{\text{GM}} S_{\text{GM}} - \sigma_{\text{GV}}^{\text{GV}} S_{\text{GV}}, & \sigma_{g,\text{seg}99\%} < \sigma_{g,\text{seg}} \end{cases} \quad 4.33$$

The main parameters of this model are the *surface tension* (σ^{GV}), *adhesion tension* ($-\sigma_{\text{adh}}^{\text{SM}}$), *interfacial tension* (σ^{GM} , in case $G \neq M$) as well as the corresponding interfacial areas. The ranges of each branch are determined based on the amount of grafted polymer per unit NP area, $\sigma_{g,\text{seg}}$, and are indicative of four characteristic regimes discussed below.

Regime I: very short and sparsely grafted brushes, $\sigma_{g,\text{seg}} \sim 0$ ($\sigma_g R_{G,g}^2 < 1$); see Figure 4.24 (Regime I). The contribution of the brush is marginal and ΔG_s^{*o} depends explicitly on the *adhesion tension* as indicated by the first branch of eq 4.33.

Regime II: partially developed brushes ($\sigma_{g,\text{seg}} < \sigma_{g,\text{seg}99\%}$ or $\sigma_g R_{G,g}^2 < 1$); see Figure 4.24 (Regime II). The evolution of ΔG_s^{*o} during the formation of the brush is mainly affected by the strong enthalpic interactions arising due to the formation of the GM (in case $G \neq M$) and GV interfaces. In addition, ΔG_s^{*o} is also affected by the expansion/shrinkage of the SG/SM interface near the solid surface. In situations where the strength of the solid/grafted and solid/matrix interaction is similar, the effect of SG and SM interfaces is miniscule. In high curvature geometries (small NPs), the size of the SG/SM interface is much smaller than that of the GM and GV interfaces; hence, the effect of enthalpic and entropic contributions to ΔG_s^{*o} has been lumped in function F which has been computed above through SCFT calculations for determining the *solvation* free energy across regime II, where no limiting rules apply. In practice, F resembles a half-sigmoid function which rises more or less monotonically from 0 to 1.

Regime III: fully formed ($\sigma_{g,seg} > \sigma_{g,seg99\%}$ or $\sigma_g R_{G,g}^2 > 1$) but not too dense chain packing (low $n_{ch,g}^{ref}$, SDPB^{129,135}); see Figure 4.24 (Regime III). The SG interfaces become identical in the SGM and SGV systems; thus, the contribution of the SG interface to the ΔG_s^{*o} fully cancels out. As a result, the *solvation free energy* depends explicitly on the interplay between the enthalpic contributions of the GM and SG interfaces, as illustrated by the third branch of eq 4.33.

Regime IV: fully formed ($\sigma_{g,seg} > \sigma_{g,seg99\%}$ or $\sigma_g R_{G,g}^2 > 1$) but very dense chain packing (high $n_{ch,g}^{ref}$, CPB^{129,135}); see Figure 4.24 (Regime IV). The entropic phenomena associated with chain stretching become non-negligible. It turns out, however, that for large $\sigma_{g,seg}$, the entropy related to grafted chain conformations is not so different between SGM and SGV systems. Thus the entropic contributions in the two systems cancel out, and the *solvation free energy* is practically determined by the enthalpic interactions of the GM and GS interfaces. Similar to Regime III, the evolution of ΔG_s^{*o} can be described by the third branch of eq 4.33. For spherical particles and if the grafted chains are long enough, the brush may assume a hybrid CPB-SDPB configuration (a combination of Regimes III and IV); near the particle, the chains are oriented normal to the particle surface (CPB), whereas above a critical distance, they assume SDPB-like configurations.^{129,135}

Having presented these considerations regarding the structure of the brush near and far from the particle, we emphasize that the *solvation free energy* of the grafted particle depends strongly on the total amount of grafted polymer, $\sigma_{g,seg}$, and not so much on whether the brush assumes SDPB (Regime III), CPB (Regime IV) or hybrid CPB-SDPB configurations.^{129,135} Especially in situations where the relevant height of the brush in the SGV and SGM systems is similar (e.g., in the limit where $N_g \rightarrow \infty$), any entropic contributions to the *solvation energy* cancel out, when taking the difference of the free energy of the two systems.

The parametrization of eq 4.33 is straightforward for moderate to large NPs. The free energies of the planar SM and GV interfaces can be determined based on *surface tension* theories¹⁰⁴ and *Flory's* χ -parameter.¹⁷³ The interfacial areas close to the NP, S_{SM} and S_{SG} , are practically equal to S_s , while the surface area of the MG and GV interfaces can be estimated by brush scaling measures. S_{GV} can be determined analytically via eq 4.25, and S_{GM} can be estimated by more elaborate scaling laws from SCFT calculations²⁴ or theoretical predictions.^{131,164,167}

4.3. Grafted nanoparticle in contact with vacuum. Solvation free energy of a nanoparticle

In the limit of very small NPs, the model becomes less accurate because the boundary between the interfaces becomes fuzzier and the determination of the interface area is nontrivial. In addition, due to the mismatch of the SGM and SGV profiles, the entropic effects do not exactly cancel out and become important. To add to the above, in situations where the matrix chains are much shorter than the grafted ones ($N_m/N_g \ll 1$), entropic contributions become even more significant,²⁸ whereas these are not taken into account by the model in eq 4.33. In all these situations, calculations via SCFT-based models are particularly valuable.

Having calculated the *solvation free energy* for two different systems in terms of the chemical constitution of the matrix phase, the *partition coefficient* of a nanoparticle between two different matrices can be retrieved via eqs 4.21 and 4.33 as follows:

$$\begin{aligned}
 -RT \ln K^{M_1/M_2} &= \Delta G_s^{*o,SGM_1} - \Delta G_s^{*o,SGM_2} \\
 &\sim \begin{cases} -\sigma_{adh}^{SM_1} S_{SM_1} + \sigma_{adh}^{SM_2} S_{SM_2} & , \quad \sigma_{g,seg} \sim 0 \\ \left(-\sigma_{adh}^{SM_1} S_{SM_1} + \sigma_{adh}^{SM_2} S_{SM_2} \right) [1 - F(\sigma_{g,seg}, R_s)] + \left(\sigma_{GM_1}^{GM_1} S_{GM_1} - \sigma_{GM_2}^{GM_2} S_{GM_2} \right) F(\sigma_{g,seg}, R_s) & , \quad 0 < \sigma_{g,seg} < \sigma_{g,seg,99\%} \\ \sigma_{GM_1}^{GM_1} S_{GM_1} - \sigma_{GM_2}^{GM_2} S_{GM_2} & , \quad \sigma_{g,seg,99\%} < \sigma_{g,seg} \end{cases} \\
 &4.34
 \end{aligned}$$

Note that the terms concerning the SGV system have been canceled out. With K^{M_1/M_2} known as a function of $\sigma_{g,seg}$ and the chemical constitution of the SGM₁ and SGM₂ systems, one can potentially design the grafting for optimal *partitioning* of NPs in blends.¹⁷⁴

4.3.6. Concluding remarks

The *solvation* of a grafted NP inside a polymer matrix is a complex phenomenon whose thermodynamics depends on multiple factors. The curvature of the particle, the amount of grafted material, the lengths of matrix and grafted chains, and the affinity of the polymer segments to the particle are essential parameters to be examined when attempting such a calculation.

Calculation of the *solvation* free energy of a grafted NP requires analyzing two different systems; the grafted NP embedded in the polymer matrix (Section 4.2) and the same NP exposed to vacuum. In the latter case, the grafted polymer chains are in contact with a *poor solvent* and a compressible model is required for the nonbonded interactions in order to capture the density profiles of polymer segments around the solid surface. Furthermore, the presence of the solid is explicitly taken into account in the present work, by strictly preventing all polymer segments from reaching a zone near the solid surface, through essential *Dirichlet* BCs. This brings our

Chapter 4. Single Nanoparticle Calculations

SCF theoretical framework closer to a *molecular dynamics* representation of the solid/polymer interface.

In this section, we addressed the system of a grafted NP which is exposed to vacuum. In contrast to the system of the same NP embedded inside the polymer matrix (Section 4.2), where the grafting density, σ_g , and the length of the grafted chains, N_g , are individually affecting the profiles of grafted chain segments and the energy of the system, in the vacuum case, it is the product of the grafting density and length of grafted chains, $\sigma_{g,seg}$, that makes the difference. This product is equal to the total number of segments belonging to grafted chains divided by the area of the solid surface. Furthermore, we demonstrated how important the presence of the melt is to the configurations of grafted chains: when in melt, matrix chain segments interpenetrate the region occupied by the grafted chains, and the latter start to swell towards the bulk, since the favorable cohesive interactions with matrix chain segments (which herein were chemically identical to grafted chain segments) overcompensate the entropic cost associated with their stretching. On the contrary, when in contact with vacuum, grafted chains want to minimize their exposure to the vacuum and therefore they are pulled towards the surface of the solid or collapse upon themselves, assuming *pancake* or *globule*-like configurations at low grafting densities.

Having connected our thermodynamic framework with the *solvation* free energy as defined by *Ben-Naim*, we determined the *solvation* free energy of a polystyrene-grafted silica nanoparticle inside a polystyrene matrix, by taking the direct difference of the grand potential of the solid-grafted-matrix system and the *Helmholtz* energy of the solid-grafted-vacuum system. This calculation was performed for the whole range of solid/polymer interactions. Depending on the amount of grafted polymer and the curvature of the particle, entropic phenomena associated with the conformations of grafted chains are cancelling out or not.

It is clear that the *solvation* free energy of the grafted particle in the polymer melt is strongly negative. It is mainly the enthalpic interactions between matrix and grafted chain segments that render the melt a much more favorable environment for the grafted NP than vacuum. Entropic phenomena also contribute to the *solvation* of the particle, since the melt chains wet the grafted chains and offer them a higher number of available configurations. The role of entropy, however, becomes more pronounced only at higher curvatures. The net result of this complex interplay of a large number of parameters is that, even in the case of weak solid/polymer interactions, where a bare NP would not gain anything when transferred from vacuum into the

4.3. Grafted nanoparticle in contact with vacuum. Solvation free energy of a nanoparticle

polymer, if enough chains are grafted on its surface, then its incorporation into the matrix is thermodynamically favored (see Figure 4.21).

The theoretical calculations employed herein revealed three regions in the $\sigma_{g,seg}$ space with different behavior of the *solvation* free energy. When $\sigma_{g,seg}$ tends to zero, then the *solvation* free energy is equal to minus the *adhesion tension* between the polymer and the solid being immersed in the polymer melt times the surface area of the NP. On the other hand, when $\sigma_{g,seg}$ becomes larger than a threshold value, the behavior of *solvation* free energy is dominated by the *surface tension* of the grafted-matrix (if any) and grafted-vacuum interfaces. The SCFT calculations performed herein give a direct insight on the *solvation* free energy in the intermediate regions of the $\sigma_{g,seg}$ space, where there is not an analytic or numerical model to follow. Furthermore, the behavior in each one of these regions is quite different in the limit of infinite and very small particle radius.

Based on our calculations, we went a step further and proposed a model for the qualitative prediction of the *solvation* free energy as a function of the radius of the NP and the number of grafted segments, $\sigma_{g,seg}$ (eqs 4.32, 4.33). This model is intended to be general, i.e., cover the case of chemically dissimilar matrices M_1 and M_2 . Looking at these equations, if one knows the value of *surface tension*, σ^{GM1} and σ^{GM2} , between the grafted chains, G, and two chemically different polymer melts, M_1 and M_2 , and the *adhesion tension* of each polymer matrix to the particle surface, σ^{SM1} and σ^{SM2} , then the equation can predict quite accurately the *solvation* free energy in the limits of very low, and high amount of grafted material without having to perform SCFT calculations. The reason this is expected to perform well is because *solvation* is dominated by enthalpy across these regimes and thus one can perform direct estimations based on the surface energies and the area of G/M_1 and G/M_2 interfaces.

To test these predictions, our SCFT model will be extended in order to address polymers of different chemical constitution (e.g., different grafted and matrix chains or block copolymers). Having obtained information regarding the free energy of *solvation* of a grafted NP inside a polymer matrix which chemically different from the brush, we will be able to directly determine the equilibrium *partition coefficient* of the NP between two different polymer melts, which is quite hard to do experimentally.¹⁴⁴

According to Praetorius et al.,¹⁴⁴ knowing the *solvation* free energies and the corresponding *partition coefficient* is only one part of the problem. In addition, one needs information on other thermodynamic properties of the system; namely, the free energy of solid/liquid^{24,67,72} and liquid/liquid^{94,175-183} interfaces, and the *potential of mean force*, which is directly related to the

Chapter 4. Single Nanoparticle Calculations

aggregation tendencies of the NPs. Using this information, one can obtain a broader picture regarding the thermodynamics and evolution of a composite system. Several of the aforementioned tasks have been reported in literature in one dimension.^{24,67,72,184} In Section 6.3, we present results obtained with our three-dimensional version of *RuSseL*, regarding the *potential of mean force* between two spherical grafted NPs as a function of grafting density, chain length and spatial distribution of grafted chains across the NP surface. The SCF approach offers a convenient theoretical framework for obtaining this information^{27,28} and ultimately linking it to atomic-level structure and interactions in the context of multiscale modeling.

5. THREE DIMENSIONAL CALCULATIONS AND COMPARISON WITH 1D

5.1. Background

In this chapter, we investigate the influence of dimensionality on the computational study of polymer nanocomposites in the context of *Self-Consistent Field Theory* and using a *real-space* framework based on the *Finite Element method*. We perform calculations in a three dimensional domain to address the system of a single silica-grafted nanoparticle and compare the results against those obtained with the one-dimensional calculations, which were presented in Section 4.2.

We find that the one-dimensional representation is quite close to the three-dimensional one when it comes to predicting the thickness of the brush and its scaling with respect to grafting density, chain length and particle size. Nonetheless, differences arise when calculating the free energy of the system in the *mushroom* regime. Moreover, the three-dimensional profiles of grafted chains more realistically reproduce the spikes corresponding to the grafting points. This is caused by the inevitable smearing of the grafting points, which degenerate into a single point when using a one-dimensional representation. Furthermore, in three-dimensions, each grafted chain maintains its identity and its own configuration inside the domain. We compare the two geometric levels of description based on the free energy of a system of a single polystyrene-grafted silica nanoparticle embedded in polystyrene matrix. We demonstrate the density profile of a single grafted chain as a 3D plot inside the domain and visualize the *mushroom* and *dense brush* configurations. We also determine the variations of the free energy and the structural properties of the system as functions of the distribution of grafting points around the spherical particle.

Chapter 5. Three dimensional calculations and comparison with 1D

Theoretical frameworks and computer simulations have been very useful for guiding and verifying experimental studies and help resolve major issues of industrial interest.^{45,47,129,185,186} A variety of theoretical and simulation methodologies have been employed to address systems of polymer grafted nanoparticles, like the *Polymer-Reference Interaction Site Model* (PRISM),¹¹⁹ *Self-Consistent Field Theory* (SCFT),^{21,41,187,188} *Density Functional Theory* (DFT),^{189–193} *Molecular Dynamics* (MD),^{36,38,39,50,55,56,58,105–107,117,120,194–200} *Dissipative Particle Dynamics* (DPD),^{57,123,184,201} as well as *machine-learning* frameworks.^{202,203} In addition to these studies, multiple scaling laws regarding the height of the brush have been proposed to describe the structural behavior of grafted chains in the solid/polymer interfacial region over a broad range of experimental conditions.^{18,19,24,50,130,164}

The free energy of brushes and PGNPs exposed to polymeric bulk phases constitutes a useful tool for the prediction of stable configurations and surface properties of materials. For instance, the strength of solid/polymer and vacuum/polymer interfaces can be quantified in terms of the *adhesion tension* and *surface tension*, respectively. The *partition* of PGNPs in polymer blends in thermodynamic equilibrium can be predicted via the *solvation* free energy.¹³⁶ The agglomeration tendencies of PGNPs in a polymer matrix can be quantified in terms of the *potential of mean force* (PMF), i.e. the variation in the free energy of systems of multiple PGNPs in dependence of the configuration of their centers. The latter has been investigated thoroughly via traditional methodologies such as SCFT,^{21,25,28,163,204} MD^{37,117,165,199,205,206} and DPD.¹⁸⁴ Recently, the PMF between single-chain-grafted nanoparticles (*tadpoles*) has been derived by a *deep neural network* methodology which has been trained on a set of equilibrated trajectories obtained via MD simulations.²⁰² In the context of *machine-learning* inspired methodologies, Xuan et al.²⁰³ devised a combination of *mean-field* theory with a *deep learning* framework to accelerate the investigation of polymer phases in incompressible block copolymer systems.

The main advantage of SCFT relative to the aforementioned methods is that it allows for direct calculation of the free energy and structural features of the brushes at a relatively low computational cost. Over the years, several SCFT frameworks have been developed for incompressible,^{35,41,83,90,187,207} and compressible^{41,66,90,208} models; the latter take into account the density deviations and potential formation of cavities, at the cost of additional complexity. *Scheutjens and Fleer* were pioneers in conducting lattice-based *Self-Consistent Field* calculations,⁶² whereas Matsen and Kim started describing polymer brushes using the so-called

Strong-Stretching Theory (SST).⁸⁸ They explored the capabilities and limitations of the latter computational approach and set the foundations of the mathematical description of polymer brushes via SCFT along with Müller.⁴⁰ 3D implementations of SCFT are less common in the literature, because they imply a high computational cost. For instance, 3D-SCFT calculations have been conducted by the group of Fredrickson on block polymer systems and in arbitrary domains.^{35,90} Daoulas and Müller²⁰⁸ have devised a 3D-SCFT methodology to determine the thermodynamically favored morphology of amphiphilic molecules by discretizing the domain of interest with a finite volume scheme.

Being one-dimensional, the 1D-SCFT model exhibits limited flexibility in describing more elaborate geometries, such as pairs of interacting NPs,¹⁶⁹ dry PGNP lattices,⁵⁰ and irregular grafting distributions such as single-chain-grafted NPs,^{202,209,210} all being experimentally relevant. Moreover, the *smearing approximation* is expected to break down in the limit of very low grafting densities (*mushroom* regime),²⁴ where the grafted chains can assume intricate configurations such as *pancakes*¹⁶⁹ and *globules*.¹⁷⁰ There has been considerable effort in the past to simulate systems of nonuniform grafting of solid surfaces.^{20,211–214} Frischknecht et al.²⁰ have employed both an incompressible SCFT and a (compressible) DFT model, where they investigated the interactions between grafted nanorods (NRs) immersed in homopolymer matrix. Koski et al.^{213,214} have used a *Dynamic Mean-Field Theory* model, which is a combination of *Brownian dynamics* motion of polymer segments and a *Hamiltonian* that depends on a density field. Having direct access to segment coordinates from the solution of the BD equation in 2D, they were able to explicitly attach the grafting points on the solid surfaces according to nonuniform patterns and investigate the resulting agglomeration of the NRs.

In this section, the *Edwards* diffusion equation is solved in a three-dimensional domain by means of the *Finite Element Method*.^{35,67,92} The *strong* form of the PDE is transformed into the corresponding *weak* form (see Section 2.4) and the domain is discretized in a finite number of elements using an open source 3D meshing tool.⁹³ The FEM allows us to define a denser mesh near the solid/polymer interfaces, where the *propagator/solution* is steeper due to *Dirichlet* boundary conditions imposed on the solid boundaries, and at the same time maintain a coarser mesh in the bulk polymer region. In an effort to stay as close to the atomistic representation of the grafted chains as possible, we explicitly instruct the mesher to create points at specific coordinates, where the grafting point initial conditions will be assigned. During the equilibration of the field and the solution of the *Edwards* diffusion equation, each grafting point will assume

its own delta function value and initial condition; no smearing of grafting points takes place, normal or parallel to the solid surface.^{24,41}

We first validate the 3D-SCFT model by conducting direct comparisons with its 1D-SCFT counterpart on the same systems. The structural and thermodynamic properties of a single silica NP equidistantly grafted with polystyrene (PS) chains in a molten PS matrix are investigated over a broad parameter space, where we vary the length of grafted (N_g) and matrix (N_m) chains, grafting density (σ_g) and NP radius (R_S). We test the *smearing approximation* invoked in 1D-SCFT by probing the low N_g , σ_g range. Interestingly, the *mean-field* structural and thermodynamic properties of the 1D- and 3D-SCFT models are in reasonable agreement. Having validated the 3D-SCFT model, we turn our attention to the total and single-chain 3D spatial distributions and how they are affected by N_g , σ_g and R_S . By taking advantage of the single-chain representation of the 3D-SCFT method, we explore the effect of equidistributed and exotic irregular grafting distributions (such as single- and dual-pole, and “ring”-like) on brush structure and thermodynamics.

The majority of literature studies which are based on SCFT employ an incompressible *Hamiltonian*.^{35,41,83,90,187,207} Practically, this means that the total segment density of the system must be constant throughout the calculation. This way, one avoids the computational penalties and convergence difficulties associated with penalizing density fluctuations in a compressible model (e.g., harmonic type penalty in the case of *Helfand* EoS,⁶⁵ logarithmic term when using SL).⁷¹ Nonetheless, the incompressibility constraint comes with some drawbacks: first of all, one can monitor only entropic contributions to the total free energy of the system, since no cohesive term appears in the *Hamiltonian*. Moreover, it is not possible to combine an incompressible model with *Dirichlet* BCs, which need to be imposed on the solid surfaces to confine the polymer segments.^{1,35,90} Another system that is hard to simulate with an incompressible model is one of polymer chains which are grafted on solid surfaces in the absence of any free melt chains (see Section 4.3). For more information on such systems, the reader is referred to references 28,136.

The methodology presented in the current section combines the virtues of three-dimensional calculations, an explicit excess *Helmholtz* energy density functional describing the nonbonded interactions among polymer segments, realistic presence of a solid surface through *Dirichlet* boundary conditions, and strict mathematical representation of chains grafted on the solid surface. The goal of the 3D model developed in the context of this PhD thesis is to achieve a

representation that is as close as possible to atomistic simulations and at the same time takes advantage of the power of field-theoretic calculations. Having such a computational tool to represent one or more grafted NPs in arbitrary 3D domains can prove to be quite helpful in reproducing or designing complex systems that experimentalists are interested in, such as the ones studied in the recent work by Rungta et al.,²¹⁵ where chains of two different molecular weights were grafted on the surface of silica colloidal particles via controlled radical polymerization.

5.2. Spatial discretization

The FEM allows us to define a denser mesh near the solid/polymer interfaces, where the *propagator*/solution is steeper due to the *Dirichlet* BCs imposed on the solid boundaries, and at the same time maintain a coarser mesh in the bulk polymer region above a threshold distance, h_M , as shown in Figure 5.1 below. The density of nodal points in each region (fine/coarse) is controlled via the maximum element size, $V_{\max, \text{fine/coarse}}$ and the minimum element size, $V_{\min, \text{fine/coarse}}$.

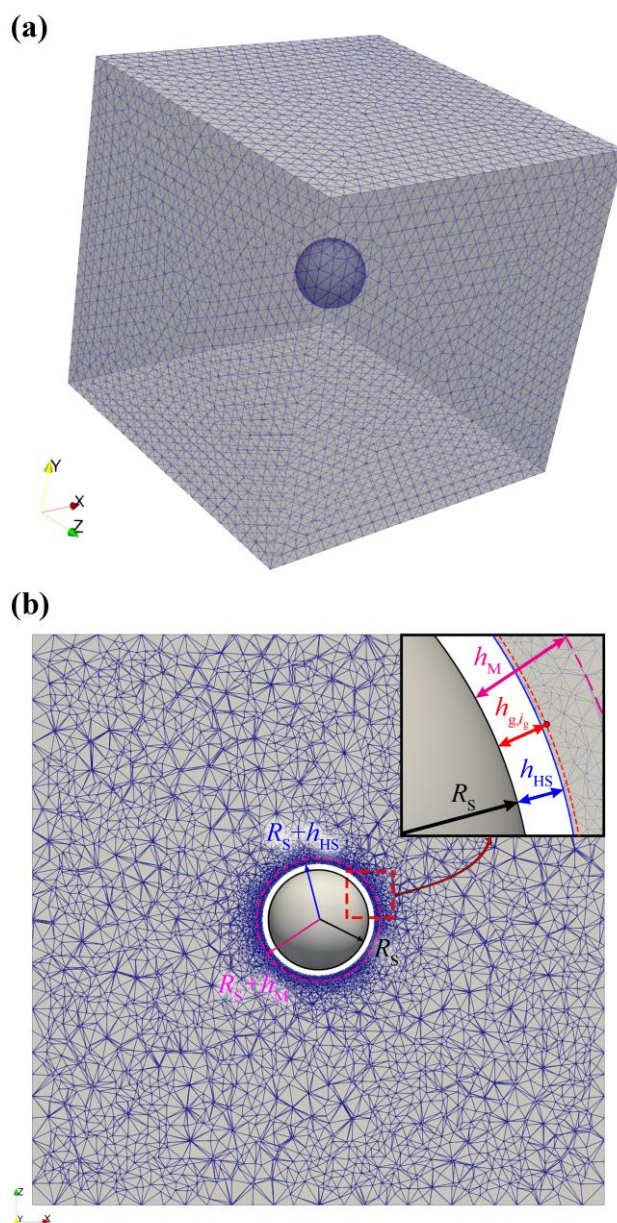


Figure 5.1 Meshing illustration of a NP with $R_s = 4$ nm inside a box with dimensions $45 \times 45 \times 45$ nm³. **(a)** A perspective view showing the mesh at the *periodic* and *Dirichlet* (solid) boundaries. **(b)** A *xz*-slice passing through the center of the NP (created with the “Slice” operation of *Paraview* software^{216,217}). The inset provides with an enlarged view of the solid/polymer interface.

5.3. Calculation Details

The radius of the NP assumes the values $R_s = \{1, 2, 4, 8\}$ nm. The length of grafted chains is equal to $N_g = \{24, 48, 96, 192, 384\}$ skeletal bonds. The length of matrix chains is always equal to that of the grafted chains, i.e., $N_m = N_g$.

The dimensions of the box in all directions are large enough ($L \geq 9 R_{G,g}$, after excluding the volume occupied by the NP) to ensure that the solution of PDE 2.2 is not influenced by finite size effects. As already mentioned in the previous section, the mesh is denser near the surface of the particle and coarser in the bulk box region (see Figure 5.1). In the dense region, which has a width $h_M = 0.5$ nm, the minimum element volume is $V_{\min, \text{fine}} = 1.0 \text{ \AA}^3$ and the maximum element volume is $V_{\max, \text{fine}} = 2.4 \text{ \AA}^3$. These values were selected according to the mesh benchmarks presented in Section 3.7.1. In the coarse mesh region, the minimum element volume is $V_{\min, \text{coarse}} = 2.4 \text{ \AA}^3$ and the maximum element volume is $V_{\max, \text{coarse}} = 20 \text{ \AA}^3$. These values are also reported in Table 5-1.

Regarding the chain contour discretization, we used the hybrid scheme that we presented in Section 3.5.3. According to the relative benchmarks presented in Section 3.7.2, and in order to keep the computational cost at the minimum level, we decided the following: for both grafted and matrix chains, the switching contour point is set at $N_{m, \text{SW}} = N_{g, \text{SW}} = 40.0$. The average contour step size for matrix and grafted chains is $\Delta N_{m, \text{ave}} = 1.0$ and $\Delta N_{g, \text{ave}} = 0.8$, respectively. For the convenience of the reader, all parameters of the 3D-SCFT calculations of this chapter are presented in the following Table 5-1.

Chapter 5. Three dimensional calculations and comparison with 1D

Table 5-1 Parameters of 3D-SCFT calculations.

component	parameter	value	description	source
System	T	500 K	temperature	-
Grafting points	$h_{\text{ref},q=0}$	0.44 nm	Reference g-point-HS wall distance	-
	$h_{\text{g},i_{\text{g}}}$	0.44 nm	g-point-HS wall distance	-
Chain characteristics	b_{k}	1.83 nm	<i>Kuhn length</i>	23
	$l_{\text{C-C}}$	0.154 nm	Backbone carbon bond length	-
	γ	0.829	Geometric factor	3
	M_{monomer}	52.08 g/mol	Segment molar mass (1/2 repeat unit)	-
<i>Helfand</i> EoS	$\rho_{\text{mass,bulk}}$	953 kg/m ³	mass density @500K	23
	κ_T	3.97 GPa ⁻¹	isothermal compressibility @500K	28,67
Solid/polymer interactions	h_{HS}	0.4 nm	Hard sphere wall	24
	σ_{PS}	0.37 nm	PS effective diameter	23
	σ_{SiO_2}	0.30 nm	SiO ₂ effective diameter	23
	A_{PS}	5.84 · 10 ⁻²⁰ J	PS <i>Hamaker</i> constant	23
	A_{SiO_2}	6.43 · 10 ⁻²⁰ J	SiO ₂ <i>Hamaker</i> constant	23
Mesh discretization	h_{M}	0.5 nm	Width of dense mesh region	-
	$V_{\text{min,fine}}$	1.0 Å ³	Min element volume in dense region	-
	$V_{\text{max,fine}}$	2.4 Å ³	Max element volume in dense region	Section 3.7.1
	$V_{\text{min,coarse}}$	2.4 Å ³	Min element volume in coarse region	-
	$V_{\text{max,coarse}}$	20.0 Å ³	Max element volume in coarse region	-
Contour discretization	$N_{\text{m,sw}}$	40.0	Switching point of matrix chains	Section 3.7.2
	$\Delta N_{\text{m,ave}}$	1.0 (edw), 0.4 (conv)	Average step size for matrix chains for the PDE (edw) and convolution (conv)	Section 3.7.2
	$N_{\text{g,sw}}$	40.0	Switching point of grafted chains	Section 3.7.2
	$\Delta N_{\text{g,ave}}$	0.8 (edw), 0.4 (conv)	Average step size for grafted chains for the PDE (edw) and convolution (conv)	Section 3.7.2
Convergence	λ_{mix}	0.5	Field mixing fraction	Section 3.7.3
	$\Delta E^{\text{tol}}/S_{\text{S}}$	10 ⁻⁶ (mJ/m ²)	Free energy tolerance	-
	$\varepsilon_{\text{g}}^{\text{tol}}$	0.5%	Grafting density tolerance	-

5.4. Assessment of the Smearing Approximation: 1D- versus 3D-SCFT

All calculations described in the current section are conducted with the three-dimensional version of *RuSseL* in a system of a single silica NP with equidistantly grafted polystyrene chains on its surface. The system is the same as the one addressed in Section 4.2, where a one-dimensional formulation has been employed, taking advantage of the spherical symmetry of the problem after smearing over all polar and azimuthal angles at each radial distance. We study the same system here with 3D-SCFT, aiming to reveal the similarities and differences between the two levels of geometry, when employing SCFT calculations on solid/polymer interfaces.

5.4.1. Smearred segment density profiles

Besides the size of the brush (which we elaborate on in Section 4.2.7), it is useful to determine first the density profile of polymer segments belonging to grafted polymer chains around the solid surface and towards the bulk polymer melt. In Figure 5.2 below, we present the density of grafted polystyrene segments for different values of the particle radius, R_S , grafting density, σ_g , and length of grafted chains, N_g . In all cases, the length of matrix chains is equal to that of grafted chains, $N_m = N_g$.

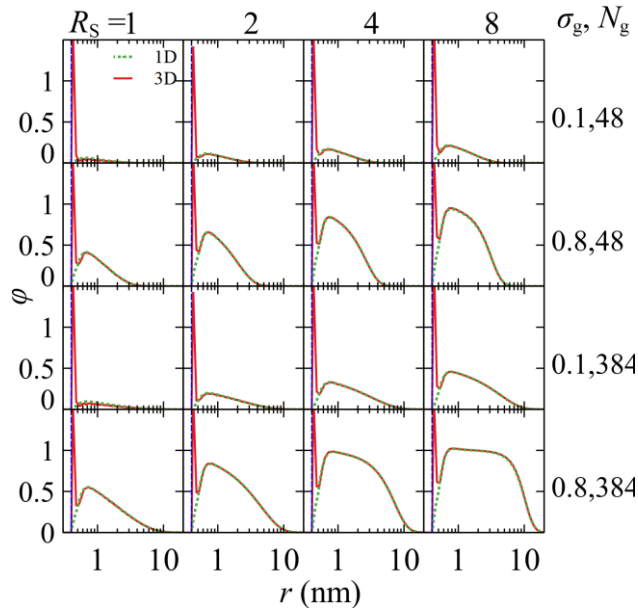


Figure 5.2 Density profiles of grafted chains obtained with 1D- and 3D- SCFT calculations. Comparison of 1D-SCFT (dotted green lines) and 3D-SCFT (solid red lines) smeared density profiles of grafted polystyrene chains. r -axis is presented in logarithmic scale. The NP size increases from left to right as $R_S = \{1, 2, 4, 8\}$ nm. The $(\sigma_g/\text{nm}^{-2}, N_g)$ combination varies from top to bottom as $(0.1, 48)$, $(0.8, 48)$, $(0.1, 384)$ and $(0.8, 384)$. In all cases, grafted chains are equidistantly distributed and $N_m = N_g$. Regarding the smearing in 3D, bin thickness is $\delta r = 0.05$ nm (eq 5.1).

In order to perform a transition from the density field evaluated at the points of the three-dimensional mesh to a 1D profile representation, we perform a partitioning of the 3D domain in spherical cells with thickness δr , and the average density is calculated according to eq 5.1 below.

$$\varphi_c(r) = \frac{\sum_{i \in \text{nodes}, r-\delta r/2 < r_i < r+\delta r/2} \varphi_{c,i} V_i}{\sum_{i \in \text{nodes}, r-\delta r/2 < r_i < r+\delta r/2} V_i} \quad 5.1$$

Figure 5.2 presents the smeared density profile of grafted polystyrene segments (φ_g) for different particle radii, R_s , grafting densities, σ_g , and grafted chain length N_g ; keeping $N_g = N_m$. For clarity, the abscissa (radial distance axis) is presented in logarithmic scale. Overall, the density profiles obtained via 1D- and 3D-SCFT calculations are in excellent agreement. There is, however, a substantial difference at low r . In 3D-SCFT, the density profiles reproduce exactly the density cusp on the grafting point that one expects to see when grafting polymer chains on a surface. This cusp does not exist in the profiles derived by 1D-SCFT, since the grafting points are completely smeared parallel to the solid surface; hence the cusp is replaced by a small increase in the density profile. The total segment density profile (i.e., sum of the profiles of grafted and matrix chains) is presented in the following Figure 5.3.

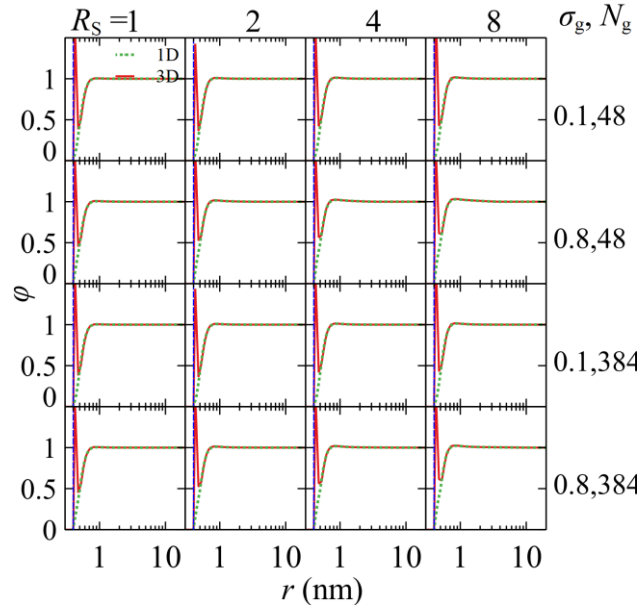


Figure 5.3 Total segment density profiles obtained with 1D- and 3D- SCFT calculations. Comparison of 1D-SCFT (dotted green lines) and 3D-SCFT (solid red lines) smeared total density profiles of grafted and matrix polystyrene chains. r -axis is presented in logarithmic scale. The size of the NP is varied from left to right panels, assuming values $R_s = \{1, 2, 4, 8\}$ nm. The $(\sigma_g/\text{nm}^{-2}, N_g)$ combination varies from top to bottom as (0.1, 48), (0.8, 48), (0.1, 384) and (0.8, 384). In all cases, the grafted chains are equidistantly distributed and $N_m = N_g$. Regarding the smearing in 3D, bin thickness is $\delta r = 0.05$ nm (eq 5.1).

5.4. Assessment of the Smearing Approximation: 1D- versus 3D-SCFT

As was demonstrated in Section 4.2.3, the shape of the density profile at the solid interface depends on several factors, such as the interplay between the *surface* and *adhesion tension*, the manifestation of entropic penalties due to confinement and curvature. In the current model, the cohesive interactions are much stronger than the adhesive ones, attracting the polymer film further towards the bulk phase.⁵³ Radially averaging the density across the (high) density region at the grafting point and intermediate (low) density region between the grafting points, results in the generation of a density drop, right after the grafting point. This effect is observed in both the grafted (Figure 5.2) and total (Figure 5.3) smeared density profiles, and it is reminiscent of the *excluded volume* effects reported in atomistic simulations.^{56,194,218}

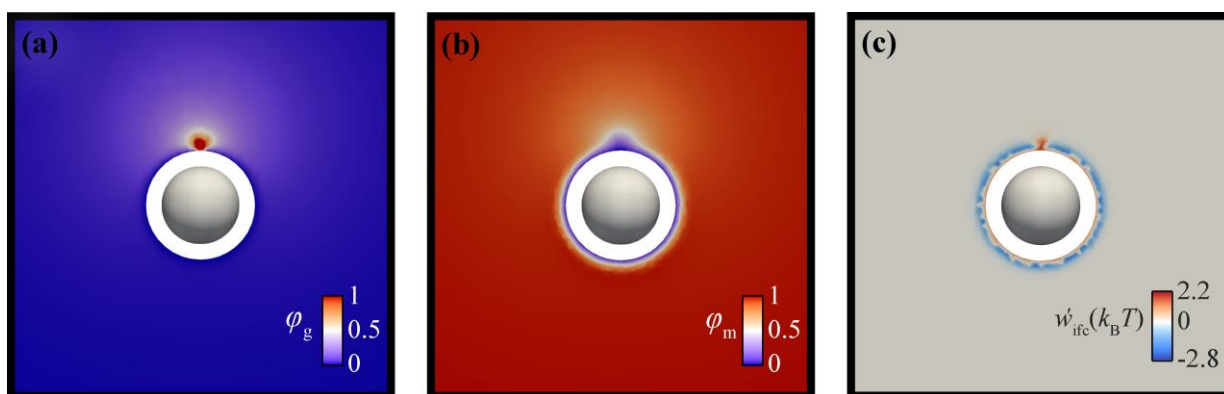


Figure 5.4 Contour plot of the density and self-consistent field near a spherical nanoparticle. Contour plot of the segment density of (a) grafted, and (b) matrix chains, and (c) self-consistent field, evaluated on a planar cross-section of the three-dimensional domain, which contains the grafting point. High/moderate/low density regions are indicated by red/white/blue color. The size of the particle is $R_S = 1$ nm and one single polystyrene chain is grafted on its surface with length $N_g = N_m = 384$ skeletal bonds (corresponding to the left-most column, third row of Figure 5.2).

Aiming to provide the reader with a more informative illustration of the density profile of grafted chain segments, we present in Figure 5.4 a contour plot of the density profile, which is depicted on a plane parallel to a pair of parallel box faces and passing through the sphere center and the grafting point on the particle surface. Furthermore, we show the same contour plot for the density profile of matrix chain segments (panel b) and the self-consistent field, w'_{ifc} (panel c).

5.4.2. Brush thickness

In Section 4.2.7, we demonstrated that the scaling of the brush with respect to chain length and grafting density is subject to a scaling law of the following form:

$$\langle h_g^2 \rangle^{1/2} \sim N_g^n \sigma_g^m \quad 5.2$$

where the scaling exponents m and n are functions of R_S . In Figure 5.5 below, instead of plotting the brush thickness with respect to the product $N_g^n \sigma_g^m$, we opted to render this quantity dimensionless by multiplying with $(R_g^2/N_g)^m$.

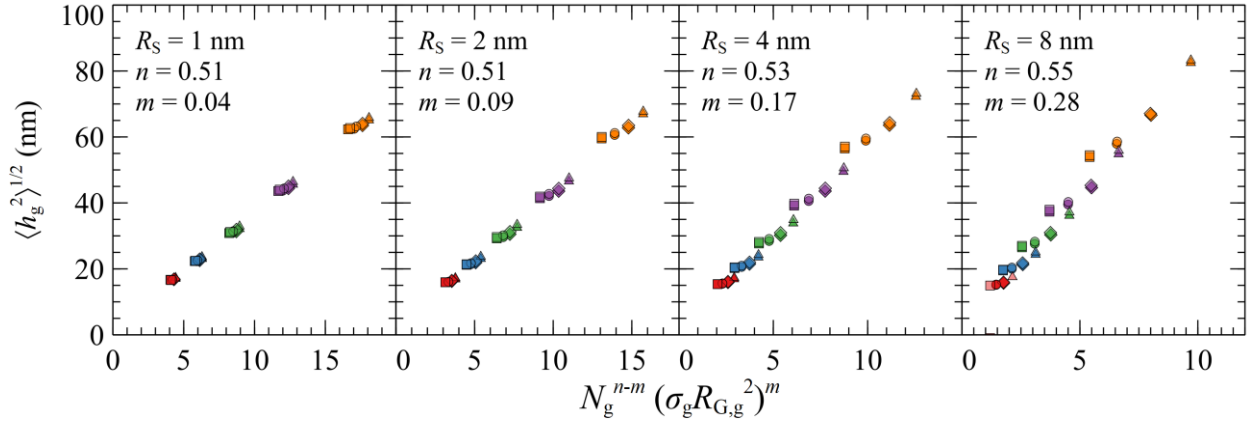


Figure 5.5 Comparison of 1D- (transparent markers) and 3D-SCFT (solid markers) calculations in predicting the brush thickness. The latter is calculated via eq 3.4. The scaling exponents n, m appearing in the x -axis are retrieved from Section 4.2.7. The NP size increases from left to right as $R_S = \{1, 2, 4, 8\}$ nm. The length of grafted chains is denoted by different colors; $N_g = \{24: \text{red}, 48: \text{blue}, 96: \text{green}, 192: \text{purple}, 384: \text{orange}\}$ skeletal bonds. Grafting density is denoted by different shapes; $\sigma_g = \{0.1: \text{square}, 0.2: \text{circle}, 0.4: \text{diamond}, 0.8: \text{triangle}\} \text{ nm}^{-2}$. In all cases, the grafted chains are equidistantly distributed and $N_m = N_g$.

Figure 5.5 illustrates the mean brush thickness (varying R_S, σ_g and N_g) against $N_g^{n-m} (\sigma_g R_{G,g}^2)^m$. Evaluations with 1D-SCFT/3D-SCFT are represented by transparent/solid markers. It becomes clear that, despite the *smearing approximation*, the 1D model gives identical results with the 3D one, for the whole range of examined parameters. It is also observed that both models reveal a deviation from the suggested scaling when the parameters of the system correspond to the *mushroom* regime (i.e., squares and circles in Figure 5.5), meaning that this scaling law cannot reproduce the scaling of the brush in this regime; this is in accordance with the findings in Section 4.2.7.

5.4.3. Thermodynamics

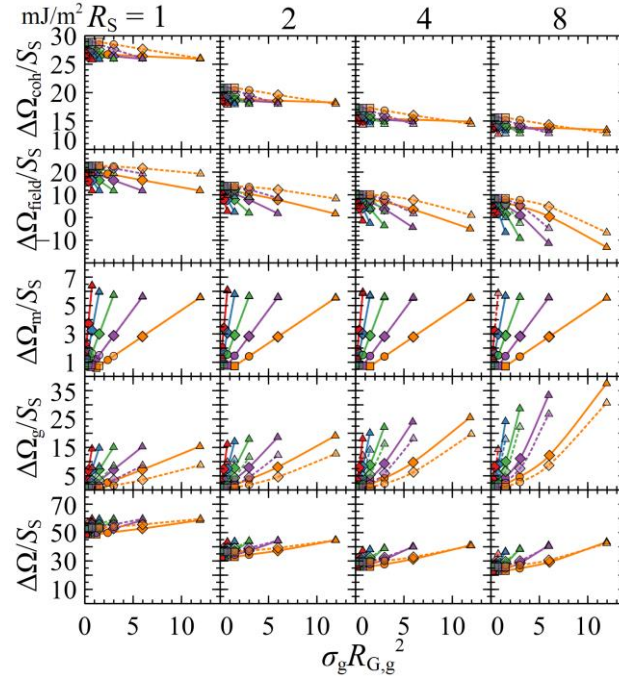


Figure 5.6 Comparison of 1D- (dotted lines) and 3D-SCFT (solid lines) calculations in predicting the total free energy. Individual free energy components are also evaluated in a system of a single polystyrene-grafted silica NP embedded in polystyrene matrix. The NP size increases from left to right as $R_S = \{1, 2, 4, 8\}$ nm. The length of grafted chains is denoted by different colors; $N_g = \{24: \text{red}, 48: \text{blue}, 96: \text{green}, 192: \text{purple}, 384: \text{orange}\}$ skeletal bonds. Grafting density is denoted by different shapes; $\sigma_g = \{0.1: \text{square}, 0.2: \text{circle}, 0.4: \text{diamond}, 0.8: \text{triangle}\}$ nm^{-2} . In all cases, the grafted chains are equidistantly distributed and $N_m = N_g$.

Figure 5.6 compares 1D- and 3D-SCFT models in predicting the dependence of the total (eq 2.38) and individual free energy components (eqs 2.39-2.43) per NP area, for the same values of R_S , σ_g and N_g where the structural properties of the brush were determined and assessed.

We observe that the cohesive and field terms are quantitatively different between 1D and 3D, the main difference being their sensitivity to the grafting density (different symbols). In 3D, Ω_{coh} and Ω_{field} are calculated based on the spatial integration of $f(\rho(\mathbf{r}))$ and its derivative (see eqs 2.39 and 2.40), whereas in 1D, they are functions of the smeared density profile $f(\rho(r))$.

Regarding the cohesive term (first row of Figure 5.6), it is simply an integration of the excess *Helmholtz* energy density of the system (eq 2.39), which is determined in this section using a *Helfand Hamiltonian* (eq 2.9). Consequently, this free energy term drops as the density at the interface gets closer to the one in the bulk. In both models, as the grafting density increases, the total segment density increases towards the bulk values, with this effect being more pronounced in the 1D case (see Figure 4.7 and Figure 5.3). Hence, it is reasonable that

there is a slightly steeper drop of the cohesive term with increasing grafting density in the 1D than in the 3D case.

The field term (second row of Figure 5.6) depends on the density derivative of the free energy (eqs 2.8 and 2.40). The 3D model is more sensitive than its 1D counterpart since the delta functions impose a steep density field close to the grafting points and, as the grafting density increases, more of these grafting points exist near the solid surface.

The conformational entropy of matrix chains, $\Delta\Omega_m$ (eq 2.42), is an increasing (decreasing) function of σ_g (N_g) and is practically identical in both models; i.e., see third row of panels in Figure 5.6.

Regarding the conformational entropy of grafted chains $\Delta\Omega_g$ (eq 2.43), it increases with σ_g and to a lesser extent with N_g (same symbols different colors), indicating that the chains are being stretched; see fourth row of Figure 5.6.²⁴ This effect becomes more pronounced with increasing R_S (decreasing curvature), because chains experience more confinement. However, the slope corresponding to 3D-SCFT is consistently higher than the one obtained by 1D-SCFT. The smearing approximation invoked in 1D-SCFT entails that the grafting points are delocalized in the tangential direction relative to the NP. The model understands the stretching only as a variation of the distance between a projection of the *free chain end* and the *grafted end*. On the other hand, in 3D, the grafting points are fixed as would be the case in reality, and it is more costly for the chain to assume configurations that stretch it tangentially with respect to the grafting point.

As a general conclusion, the total free energy of the system is qualitatively similar between the two models, whereas the quantitative differences between the two levels of geometry are mitigated with increasing particle radius. This is expected, since the *mushroom* regime is more difficult to prevail at lower solid curvatures.

5.4.4. Equidistributed Grafted Nanoparticles: 3D Spatial Distributions

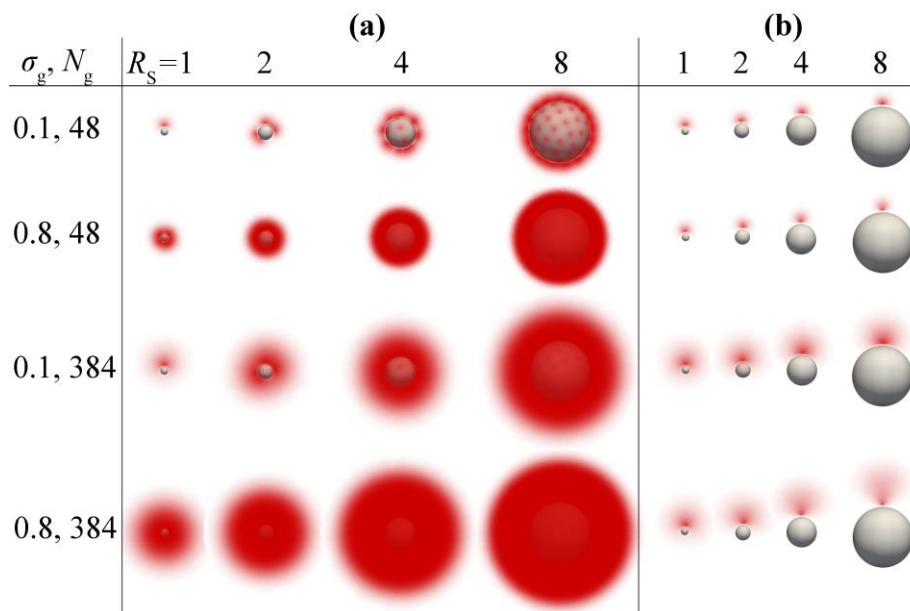


Figure 5.7 3D density profiles of chains equidistantly grafted on spherical NPs of various radii. **(a)** Spatial distributions of polystyrene chains equidistantly grafted on the surface of a silica NP embedded in polystyrene matrix. **(b)** Spatial distributions of individual polystyrene chains on the surface of a silica NP. The size of the NP is varied from left to right panels assuming values $R_S = \{1, 2, 4, 8\}$ nm. The $(\sigma_g/\text{nm}^{-2}, N_g)$ combination varies from top to bottom as $(0.1, 48)$, $(0.8, 48)$, $(0.1, 384)$ and $(0.8, 384)$. Denser color corresponds to higher values of density and vice-versa. For clarity, the NP core is overlaid with 10% opacity. Calculation parameters can be found in Table 5-1. In all cases, $N_m = N_g$.

Going a step further in the 3D description of this system, we present in Figure 5.7a the spatial distribution of all grafted chain segments inside the simulated domain, as a function of R_S for two extreme cases of grafting density and chain length considered here. Denser color corresponds to higher segment density and vice-versa. We could manipulate color opacity at higher density values to demonstrate the grafting points, but we considered best to present the system as it would look like in a particle based simulation.

It becomes clear how the size of the brush increases with chain length and grafting density. The positions of the grafting points are clearly visible in cases of short and sparsely grafted chains which do not interpenetrate each other (*mushroom* regime), whereas, when NPs are more densely grafted, the density cloud becomes so dense that the grafting points disappear inside this cloud; e.g., compare $(\sigma_g/\text{nm}^{-2}, N_g) = (0.1, 48)$ with $(0.8, 48)$ in Figure 5.7a. Increasing R_S results in significant swelling, since the chains have less available space and stretch further towards the bulk phase.

It is possible to isolate specific chains out of the total number of chains grafted on the surface of the NP and see how the corresponding segment density behaves. After the iterative

scheme is terminated and the field is equilibrated, in order to derive the density profile of segments emanating from a specific grafted chain, i_g , we need to solve the *Edwards* eq 2.2 using the initial condition value corresponding to this specific chain (eq 3.18); all other grafted chains are assigned an initial value equal to zero, so that they do not interfere in the solution. Solving the *Edwards* equation under these conditions results in the individual grafted *chain propagator*, q_{g,i_g} , which can be convolved (see eqs 3.13 and 3.14) with respect to the contour variable, N , and give the desired density profile.

In Figure **5.7b**, we present the evolution of the spatial distributions of segments belonging to individual grafted chains emanating from the surface of the particle. The configurations are affected by bonded interactions, interactions with the low affinity wall,^{76,136} nonbonded interactions with matrix chain segments, but also nonbonded interactions with the rest of grafted chains existing in the system which are deliberately not illustrated.

This kind of isolated representation of the density segments belonging to a single grafted chain is serving very well as a visualization of the shape of individual chains. In situations with long chains and small NPs, the cloud of polymer segments completely surrounds the NP surface; e.g., inspect cases with $N_g = 384$ and $R_S = 1$ nm in Figure **5.7b**. Increasing the R_S reduces the available space and the chains extend towards the bulk polymer region rather than surrounding the solid surface. Another observation made on the basis of Figure **5.7b** is that the effect of grafting density on the shape assumed by grafted chains (keeping the chain length constant) becomes stronger for larger particle size. Furthermore, it seems that, for all particle sizes, increasing the chain length (keeping constant grafting density) mainly affects the height of the brush rather than its shape.

5.5. Irregular Grafting Point Distributions: Structure and Thermodynamics

In this section, we demonstrate a definite advantage of 3D-SCFT relative to its 1D counterpart, which is the determination of brush thickness and free energy of the system with varying distribution of grafting points around the solid surface. In our calculations, we opted to keep the radius of the particle ($R_S = 4$ nm) and number of grafted chains ($n_g = 80$) constant and vary the chain length in addition to the distribution of grafting points.

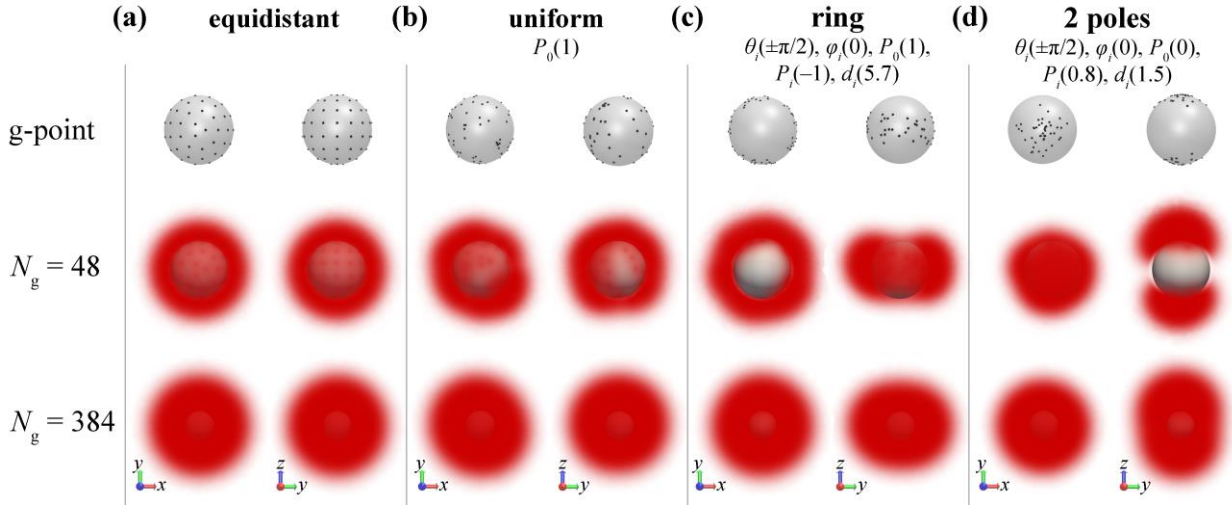


Figure 5.8 3D density profiles of chains irregularly grafted on spherical NPs of various radii. Spatial distributions of polystyrene chains (a) equidistantly, and (b, c, d) irregularly grafted on the surface of a silica NP embedded in polystyrene matrix. For each grafted chain distribution, we present the density profiles for two chain lengths; $N_g = \{48, 384\}$. The row “g-point” illustrates the positions of the grafting points on a sphere with radius $R_S + h_{HS}$. The parameter values of the biased distributions (eq 3.34) are presented in parentheses in the heading of each panel. Denser color corresponds to higher values of density and vice-versa. For clarity, the NP core is overlaid with 10% opacity. Calculation parameters can be found in Table 5-1. In all cases, $R_S = 4$ nm, $n_g = 80$ and $N_m = N_g$.

In Figure 5.8, we present the density cloud of grafted segments in three-dimensional space for different grafting distributions, namely uniform (random) distributions (panel b), a “ring”-like distribution (panel c) and a pair of grafting point-rich poles (panel d). For reference, we also present, in panel a, the density cloud corresponding to the equidistant distribution of grafting points for the same system parameters. In the non-equidistant cases, we also report the set of parameters used to sample the grafting points according to the corresponding probability map from eq 3.34. We suggest that the reader revisit Section 3.8 for details regarding the generation of grafting points.

To better understand how the cloud of grafted chain segments evolves for different distributions and values of chain length, we illustrate it in two different NP orientations. In most cases, it is difficult to detect the position of grafting points visually, so we also provide a *VMD*

representation of the NP and the grafting points for each distribution (“g-point” row of Figure 5.8).

It is clear that the grafted segment cloud may become distorted in the uniform case with respect to the equidistant case, leading to the formation of segment-rich and segment-depleted regions inside the domain (e.g., compare Figure 5.8a with Figure 5.8b). The distortion of the overall segment cloud becomes significant in cases with primarily equatorial and primarily bipolar grafting. In particular, Figure 5.8c illustrates a case with two repulsive *Gaussian* pulses applied to the poles of the NP, resulting to a ring-like configuration. Figure 5.8d depicts the opposite scenario with attractive *Gaussian* pulses applied to the poles of the NP, resulting in a dual-pole PGNP. It appears that the overall shape of the density cloud becomes more homogeneous with increasing chain length, since chains are given the opportunity to explore the segment depleted regions, especially in cases of high particle curvature. Varying the grafting point distributions is expected to alter dramatically the self-assembly properties of these systems.

According to the following Figure 5.9, with increasing segregation of the grafting points, the smeared density profiles are suppressed near and enhanced far from the interface, relative to the equidistant case, indicating that the brushes become more swollen on average. The corresponding density profiles occurring from equidistant grafting are practically identical between 3D-SCFT and 1D-SCFT (see Figure 5.2); thus, we conclude that the smearing approximation becomes less accurate with increasing segregation of the grafting points on the solid surface.

5.5. Irregular Grafting Point Distributions: Structure and Thermodynamics

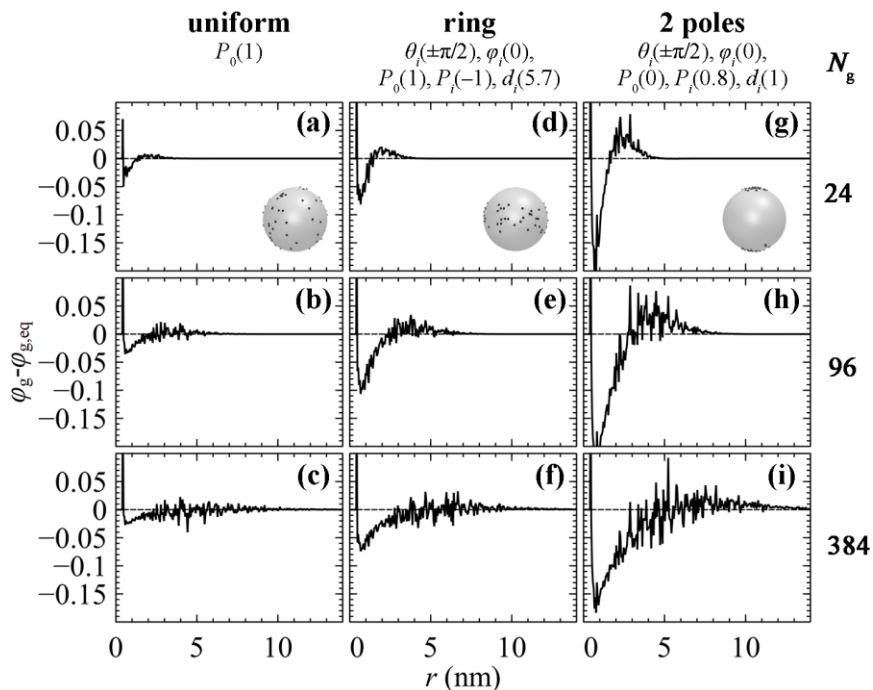


Figure 5.9 Assessment of *smearing approximation* when chains are irregularly grafted on a spherical NP. Difference of the smeared density profiles of (a-c) uniform, (d-f) ring and (g-i) dual pole grafted schemes from the smeared density profiles of equidistantly grafted NPs, for the same particle radius, R_S , number of grafted chains, n_g , and length of grafted and matrix chains, $N_g = N_m$. N_g equals 24, 96 and 384 skeletal bonds from top to bottom panels. The insets in the top panels illustrate the distribution of grafting points in each case. The parameter values of the biased distributions (eq 3.34) are presented in parentheses in the heading of each panel. Calculation parameters can be found in Table 5-1. In all cases, $R_S = 4$ nm, $n_g = 80$, and $N_m = N_g$.

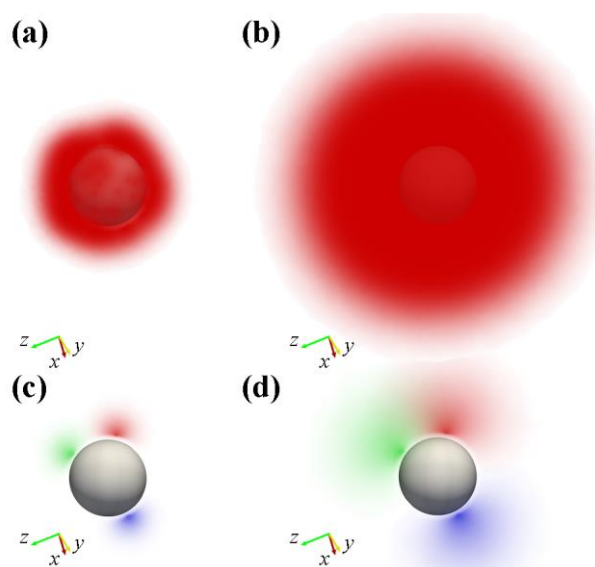


Figure 5.10 3D density profiles of individual chains grafted on a spherical NP. Spatial distributions of polystyrene chains of (a, b) all and (c, d) three individual polystyrene chains (depicted by red, blue and green color) uniformly grafted on the surface of a silica NP embedded in polystyrene matrix; i.e., same configuration as in Figure 5.8b. The length of grafted chains is equal to (a, c) 48, (b, d) 384 backbone carbon atoms. Denser color corresponds to higher values of density and vice-versa. In (a, b), the NP core is overlaid with 10% opacity. Calculation parameters can be found in Table 5-1. In all cases, $R_S = 4$ nm, $n_g = 80$ and $N_m = N_g$.

In Figure 5.10, we have isolated three random grafted chains of the uniform distribution case shown in Figure 5.8b to visualize the density profile and the interactions between segments of two different chains which happen to lie closer to each other, so that their profiles overlap in space (see green and red cloud for high chain length case in Figure 5.10). On the contrary, the cloud of the blue chain segments suggests that it is far from the green and red chains, so that it does not interact with them. Nonetheless, it can still interact with another subset of the grafted chains which are deliberately not illustrated.

5.5. Irregular Grafting Point Distributions: Structure and Thermodynamics

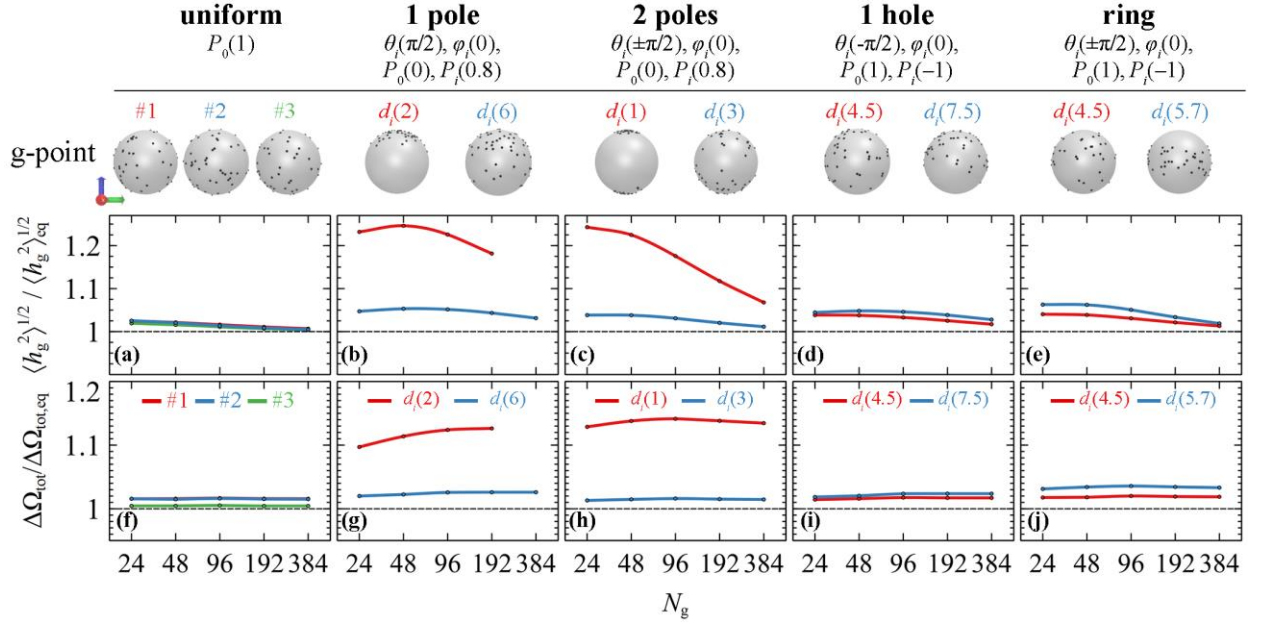


Figure 5.11 Brush thickness and free energy evaluation for various grafting distributions. **(a-e)** Mean brush thickness and **(f-j)** free energy in a system of polystyrene chains grafted according to various distributions on the surface of a silica NP embedded in polystyrene melt. Both the mean brush thickness and the free energy are normalized with respect to those obtained for the case of equidistant chain grafting with $R_S = 4$ nm, $n_g = 80$ and $N_m = N_g$. In each panel, the distribution of grafting points corresponds to the image presented in the first row of the figure. The individual free energy components are illustrated in Figure 5.12. Calculation parameters can be found in Table 5-1.

In Figure 5.11, we present how the total free energy of the system is affected from the distribution of grafted chains on the solid surface and as a function of chain length, N_g . In the first column, we present free energy variations with respect to three different samplings of grafting points from a uniform probability distribution. The free energy variation is minor and can serve as a metric for the deviation in the free energy with respect to the exact positions of the grafting points.

In the remaining columns of Figure 5.11, we illustrate the evolution of the free energy with respect to chain length for four different distribution cases: (i) one attractive pole, (ii) two attractive poles which result in a grafting point-deprived zone around the equator of the NP, (iii) one repulsive pole and (iv) a ring-like configuration with two repulsive poles which result in a grafting point-rich zone around the equator of the NP. In each of these cases, we also vary the intensity of attraction or repulsion of grafting points, which is practically controlled by the standard deviation d_i used in the generation of grafting points via eq 3.34. Moreover, in all cases, the free energy of the system is normalized with respect to the corresponding free energy of the same system (in terms of R_S , n_g , and N_g) with equidistantly placed grafting points.

With these considerations, it is clear that the free energy of the system is always higher when the chains are not regularly grafted on its surface. Both the thickness of the brush and the free energy of the system increase when the distribution compels the grafted chains to get closer to each other. When the center of the *Gaussian* distribution of grafting points is attractive in nature, it is easier for the grafting point generation algorithm to bring the chains closer to each other, and this has a clear impact on increasing the free energy of the system compared to the cases of repulsive centers (compare panels **g**, **h** with **i**, **j**). An interesting behavior of the brush thickness is observed in panels **b** and **c**; beyond a certain value of the chain length, the thickness of the brush starts decreasing. This is explained by the fact that, given the crowding of grafting points, only longer grafted chains are given the opportunity to explore more space, which in turn is offered by the curvature of the particle. In other words, as the length of the chains increases, the cloud of segments becomes more uniform and tends to that of the equidistant grafting case. In Figure 5.12 below, we present the dependence of all free energy terms on the distribution of grafting points and chain length.

5.5. Irregular Grafting Point Distributions: Structure and Thermodynamics

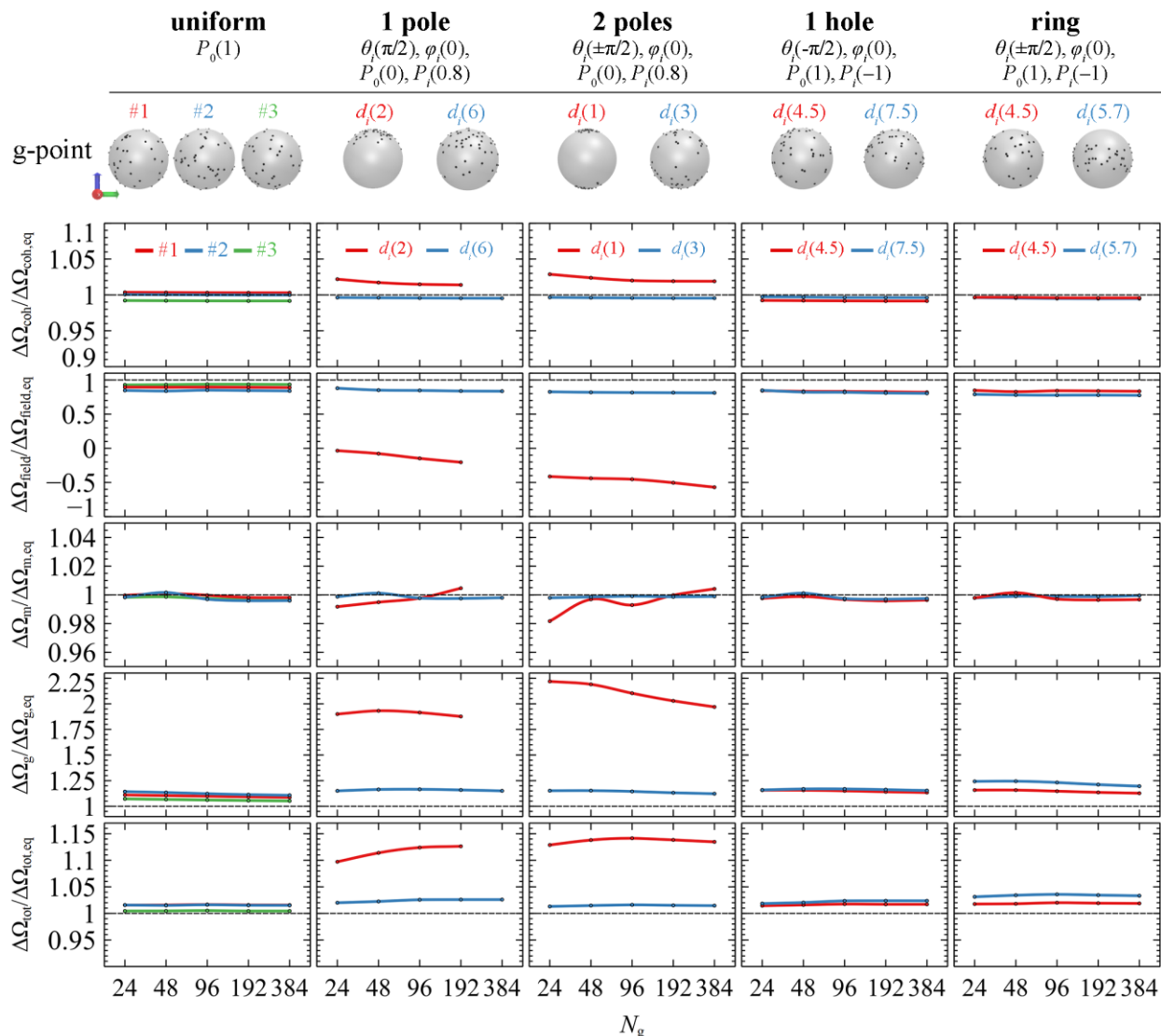


Figure 5.12 Free energy components in a system of polystyrene chains grafted according to various distributions on the surface of a silica NP embedded in polystyrene melt. All components are normalized with respect to those obtained for the case of equidistant chain grafting with $R_s = 4$ nm, $n_g = 80$ and $N_m = N_g$. In each panel, the distribution of grafting points corresponds to the image presented in the “g-point” row above. Calculation parameters can be found in Table 5-1.

It is mentioned here that in all calculations of this chapter, there is the freedom for two grafted chains to emanate from the exact same point on the surface of the NP. This effect does not cause convergence issues in the SCF algorithm, nor does it generate significant uncertainties in the values reported herein. There is, however, an option to use the grafting point generation algorithm presented in Section 3.8, while at the same time imposing a minimum distance between the grafting points. This restriction affords more chemical realism and can prove to be quite useful when the free energy differences are expected to be comparable to the error of the

algorithm, e.g., in the case of two grafted NPs moving relative to each other, whose *potential of mean force* needs to be calculated.

5.6. Concluding remarks

In this chapter, we directly compare the usually implemented 1D-SCFT models against a fully three-dimensional SCFT model solved by the *Finite Element Method*. We demonstrate that, when addressing a single equidistantly grafted nanoparticle, the two models give identical results as regards the smeared density profiles, the size of the brush, and the free energy term associated with the conformational entropy of matrix chains. Nevertheless, even in this simplest of cases, there is a slight deviation between the two models when calculating the total free energy of the system, especially when the combination of grafting density, chain length and particle radius brings the system into the *mushroom* regime.

Taking advantage of the 3D-SCFT framework, we have also addressed systems where the grafted chains are non-equidistantly grafted on the surface of the NP. It is obvious that such a system cannot be addressed by 1D (or even 2D) models, where smearing of the grafting points takes place parallel to the surface of the particle. As we show, when the grafting point distribution brings grafted chains closer to each other, then the free energy of the system increases slightly with respect to the equidistant case, as a consequence of the entropic cost associated with stretching of chains grafted close to each other.

Furthermore, the distribution of configurations of each individual chain can be quite different depending on the distribution of grafting points, since neighboring grafted chains influence its conformation. To the best of our knowledge, this is the first time that the structure of an individual grafted chain around the grafting surface is mapped in the context of a field-theoretic formulation. Nonuniform distributions of grafting points can lead to pronounced deviations of the grafted segment from sphericity, as exemplified by cases of grafting primarily around the two poles or primarily in the vicinity of the equator.

6. CALCULATIONS INVOLVING TWO PARTICLES/SURFACES

6.1. Background

Grafting polymer chains on solid surfaces is a standard procedure for the steric stabilization of nanocomposite systems.^{19,186,219} Various methods for the experimental synthesis of such systems are reported in the literature.^{220–222} Understanding the behavior of grafted polymer brushes requires a thorough investigation of the thermodynamics of the systems under different conditions. In the case of two or more nanoparticles embedded inside a polymer melt, the challenge is to keep them in a well-dispersed state by overcoming their tendency to form aggregates. When inorganic particles are bare, the attractive *Van der Waals* forces¹⁷ drive them to come closer to each other. One of the possible ways to get around this behavior is to graft polymer chains on the surface of the particles. Achieving a proper dispersion of nanoparticles inside the polymer melt is associated with a considerable enhancement of its properties.^{14,15,42–44}

Major computational research has been conducted on systems comprising a single grafted nanoparticle embedded in a solvent or homopolymer matrix, using theoretical formulations^{204,223} or atomistic simulations.^{23,36,38,192,224} Moreover, considerable work has addressed the behavior of grafted and matrix chains in systems comprising multiple grafted solid surfaces.^{10–12,21,25,26,37,118,206,225} Munao et al.²⁰⁶ demonstrated the effect of a third nanoparticle, when inserted in a system of two interacting grafted silica nanoparticles, while Martin et al.¹¹⁸ investigated the effect of polydispersity of grafted chains on the structural properties of the nanocomposite system.

Materials consisting entirely of matrix-free grafted plates or *hairy nanoparticles* (also referred to as “*particle solids*”, exhibit interesting mechanical and optical properties, while they behave as tough glasses when assembling in specific configurations.^{46,226–228} Barnett and Kumar^{120,229} have published several works, where they report the use of such materials in the design of membranes for separation processes. In their recent work, Biltchak et al.⁴⁸ studied the effect of addition of matrix chains to a neat grafted nanoparticle-based membrane on its selectivity in separations of gases of different molecular size. Mydia et al.⁵⁰ developed a two-layer theoretical model to describe the configurations of the grafted chains in the vicinity of the

grafted nanoparticles and at intermediate distances between them and they compared their model with atomistic *molecular dynamics* simulations.

6.2. Planar surfaces

In this section, we present a SCFT analysis to examine the structural and thermodynamic properties of polystyrene (PS) melt confined between two silica plates, either grafted or bare, as well as of the same plates in absence of any melt. In fact, as discussed in Section 4.3, when no matrix chains exist between the two grafted surfaces, or they exist but their molecular weight is significantly larger than that of the grafted chains, the latter behave as if they were in contact with a *poor solvent*. Following *Flory's* theory, when matrix chains are chemically identical to the grafted chains and their molecular weight is similar to that of the grafted chains, then the system is analogous to one wherein the grafted chains are embedded inside a *theta solvent*. Finally, when matrix chains are much shorter than the grafted chains, the latter are starting to swell towards the bulk polymer region as if they were in contact with a *good solvent*.

Herein, we derive the *potential of mean force* between the plates by varying the distance between them. Studying the thermodynamics in such planar geometry is quite important in the field of biomembranes and other biological applications.^{230,231} One could consider this planar geometry study as the equivalent of investigating the *potential of mean force* between spherical particles, whose radius is large enough, in comparison to chain dimensions, for their curvature to be negligible.

The problem of polymer chains grafted on planar surfaces has been addressed in the past by several studies.^{40,88,163,187} By removing the incompressibility assumption and imposing *Dirichlet* boundary conditions at the solid surfaces, we make a step forward towards the investigation of systems with realistic interfacial free energies. Furthermore, we explicitly describe the solid/polymer and solid/solid interactions via the *Hamaker* potential, and we explore their influence on the resulting PMF. Without these considerations, we would not be able to apply our methodology in systems comprising exclusively grafted chains, i.e. systems in absence of matrix chains, since the incompressibility condition requires that the total segment density profile be uniform across the entire domain of interest.⁸⁸ Furthermore, such approaches, when applied in three dimensions, allow for the investigation of systems of complex geometry, where the use of *Fourier* based methodologies is not recommended, since no symmetry appears and no *periodic* boundary conditions can be implemented.³⁵

In the majority of computational works, it is assumed that the plates have the same grafting density and molecular weight as the grafted chains.^{40,88,163,187} In reality, it is rather hard for experimentalists to prepare such a perfectly symmetric system. Herein, we increase the degrees of freedom of the system by allowing the grafted chains on each plate to have different molecular weights, whereas each plate may also have its own grafting density. The goal is to reveal the influence of these kinds of asymmetries on the PMF between the two grafted plates when varying the distance between them, and to propose a scaling law that accounts for all these design aspects.

We build our thermodynamic reference system by deriving the free energy of a single bare or grafted silica plate, either isolated or in contact with polystyrene matrix chains. Next, we calculate the PMF of a system which contains exclusively matrix chains. The melt is assumed to be at equilibrium with a bulk phase melt at all times and it is gradually squeezed by reducing the distance between the two silica surfaces. Having established the thermodynamics of the reference systems, we demonstrate results regarding the structure and PMF in a system of two grafted silica plates over a large parameter space, involving the molecular weight of matrix, the molecular weight of grafted chains on each plate and the grafting density of each plate. Understanding the behavior of matrix and grafted chains in this planar geometry is a stepping stone towards the corresponding spherical case, i.e., two or more polystyrene grafted silica nanoparticles embedded in polystyrene melt.

The following Figure **6.1** illustrates a mesoscopic bead-spring representation of the system under investigation.

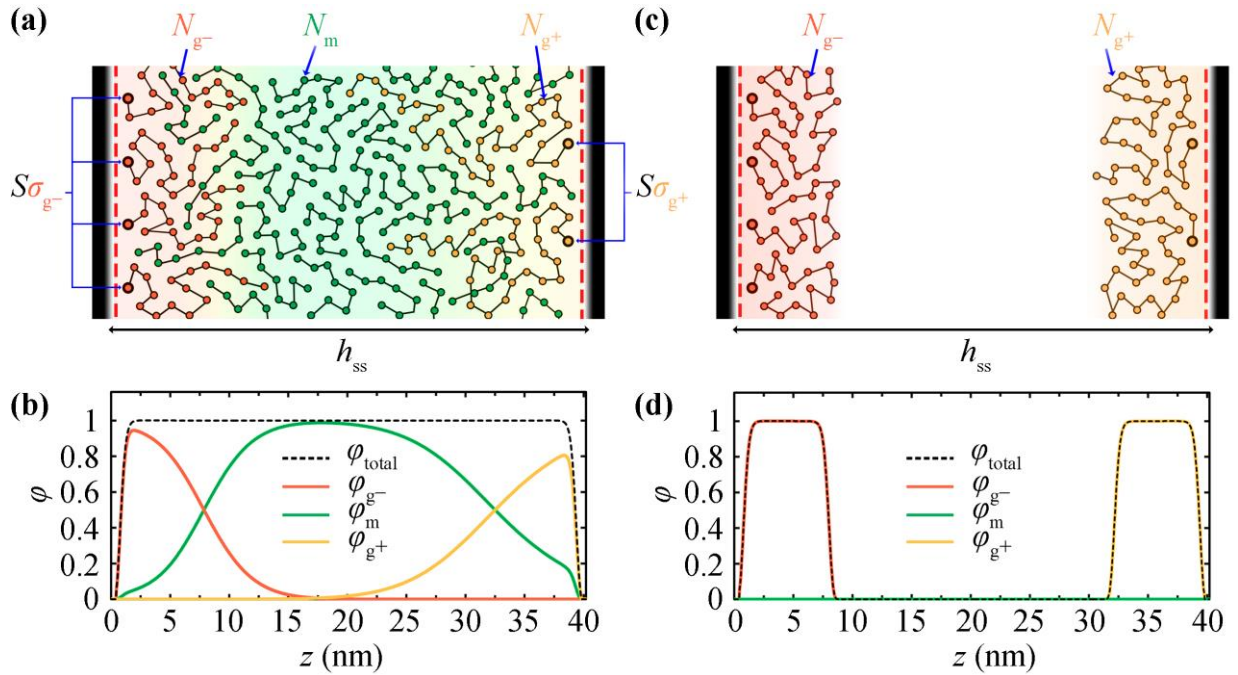


Figure 6.1 Demonstration of two opposing grafted surfaces. (a) Bead-spring representation of two opposing grafted silica walls embedded in melt (GMG system) comprising matrix chains of length N_m . The silica wall on the left (right) is grafted with $\sigma_g^- S_s$ ($\sigma_g^+ S_s$) grafted chains of length N_{g^-} (N_{g^+}). (c) The same system as (a), but in absence of matrix chains (GVG system). Additionally, the corresponding reduced density profiles from the opposing grafted silica walls in the (b) presence and (d) absence of matrix chains are shown.

Two opposing silica plates at distance h_{SS} are grafted with PS chains, while matrix chains may or may not occupy the space between the grafted plates. Hereafter, the matrix chains are denoted by m, the chains grafted on the left silica plate are denoted by g^- , and the chains grafted on the right silica plate are denoted by g^+ . When polymer melt exists between the two plates, it comprises a total number of n_m monodispersed chains of length equal to N_m skeletal bonds. The melt, when present, is at equilibrium with a bulk polymer phase at chain length equal to N_m of temperature T and pressure P . The left/right surfaces are grafted with n_g^-/n_g^+ chains of length N_{g^-}/N_{g^+} skeletal bonds, whereas the corresponding grafting density equals $\sigma_{g^\pm} = N_{g^\pm} / S_s$ with S_s denoting the area of each surface. As mentioned before, the grafting density and molecular weight of grafted chains are allowed to vary between the two plates. It is apparent from the density profiles in Figure 6.1b,d, corresponding to systems with (Figure 6.1a) and without (Figure 6.1c) matrix chains, that, in the former case, the extension of each brush towards the opposing plate is favored.

6.2.1. Vacuum/Melt and Solid/Melt Interphases

Figure 6.2 presents the free energy of VM (*surface tension*) and SM (minus *adhesion tension*) interphases as a function of chain length. In Figure 6.1, the free energies have been evaluated with the HFD EoS. In Figure 6.2b, the SL-SGT model is considered with the original *Hamaker* potential corresponding to low wetting conditions (LW), and with the addition of the ramp potential, which has been adjusted to reproduce the work of adhesion of PS melts in contact with treated (high wetting, HW) and untreated (perfect wetting, PW) silica.⁸¹ For more information regarding the intensity of solid/polymer interactions, the reader is referred to Section 2.1.5, Table 2-2 and Table 4-2.

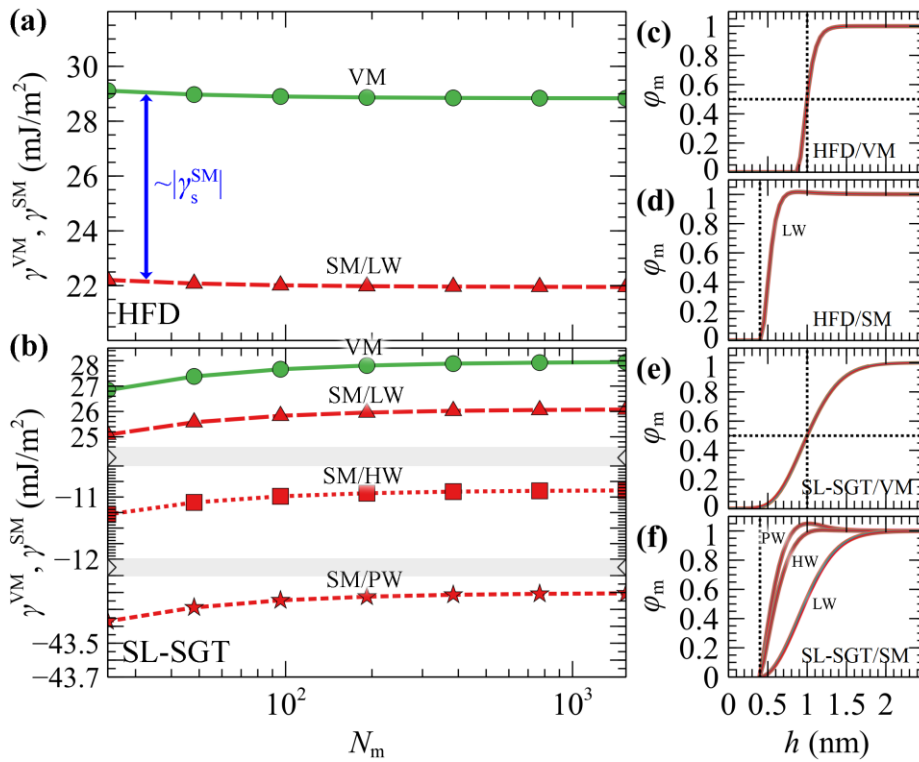


Figure 6.2 Free energy of interfaces with different wetting degree. The free energy of vacuum/melt (VM, circles) and bare solid/melt (SM) with low wetting (LW, triangles), high wetting (HW, squares) and perfect wetting (PW, stars), as a function of chain length using (a) *Helfand* (HFD) EoS, (b) *Sanchez-Lacombe* EoS combined with a square-gradient term (SL-SGT). Bands denote scale changes along the axes. The right panels depict the corresponding reduced segment density profiles of VM and SM interphases with HFD (c,d) and SL-SGT (e,f) for $N_m = \{24, 48, 96, 192, 384, 768 \text{ and } 1536\}$ skeletal bonds. Even though the thickness of the lines increases with increasing N_m , the density profiles practically coincide for all chain lengths; thus, the reader has to zoom considerably to notice any deviations. The dotted lines in (c-f) are guides to the eye.

In interphases with low wetting, the free energies are qualitatively similar for VM and SM; they differ by about γ_s^{SM} across the chain molar mass range explored herein (with γ_s^{SM} being the free energy component associated with solid/polymer interactions). This is attributed to the fact that the density profiles for these cases are very similar (e.g., compare Figure 6.2c with Figure

6.2d, and Figure 6.2e with the LW curve in Figure 6.2f); thus any differences in the free energies can be attributed to the silica/polystyrene *Hamaker* interactions. Increasing the strength of the ramp potential enhances the solid/polymer interactions as indicated by the more negative free energies in Figure 6.2b, and the more pronounced peaks exhibited by the density profiles of Figure 6.2f.

The free energy from SL in Figure 6.2b appears to be an increasing function of chain length, and this behavior is anticipated, since the cohesion of the polymer increases with increasing chain length.^{72–74} In contrast, HFD (Figure 6.2a) exhibits the opposite trend and this is attributed to that all evaluations have been performed using a constant isothermal compressibility for the polymer melt. In Section 2.1.4, we demonstrate that tuning the HFD compressibilities (with and without employing the square-gradient term) based on the predictions of SL, or even fitting them directly to the experimental measurements of *surface tension*, allows restoring the proper chain length dependence in the thermodynamic behavior of the system.

To better quantify the thermodynamics of these films, we use again the four macroscopic *wetting functions* introduced in Section 2.2.3, namely, the *work of cohesion* (W_C), the *work of adhesion* (W_A), the *work of spreading* (W_S) and the *work of immersion* (W_I) defined by eqs 2.47–2.50, respectively.

In Table 6-1, we report the wetting functions and *contact angles* of the PS/SiO₂ interphases studied here for $N_m = 384$; they remain practically the same with increasing chain length, as shown in Figure 6.3.

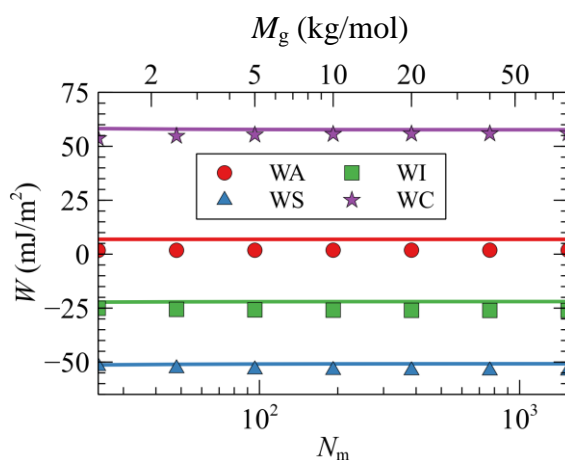


Figure 6.3 Wetting functions of silica/PS interfaces. Calculations were performed with the SL-SGT (markers) and HFD (lines) EoS in absence of the ramp potential (low wetting). The wetting functions are the following: *work of adhesion* (red/circles), *work of spreading* (blue/triangles), *work of immersion* (green/squares), and *work of cohesion* (violet/stars).

We remind the reader that the *work of adhesion*, W_A , corresponds to the reversible work required to separate two phases in contact. It is noted that, in the absence of the ramp potential, W_A is significantly lower than in the HW and PW cases, where v_{ramp} has been fitted to experimentally reported values of W_A . The *work of spreading*, W_S , quantifies the spontaneity of the wetting process: positive values indicate spontaneous *spreading* across the interface (perfect wetting), while negative values indicate finite *contact angles* (partial or no wetting). In the LW and HW interfaces, W_S remains negative across the full molar mass regime investigated here, indicating that the corresponding solid-fluid-vapor interface will form finite *contact angles*. The PW interface, on the other hand, exhibits positive W_S ; thus, PS will spread spontaneously on the silica surface.

Table 6-1 Interfacial energies and wetting functions for $N_m = 384$ in units of mJ/m^2 .

EoS	Wetting	γ^{VM}	γ^{SM}	$\sigma^{\text{SV}} - \sigma^{\text{SM}}$	W_A	W_S	W_I	W_C	θ ($^\circ$)
HFD	low (LW)	28.85	21.97	-21.97	6.88	-50.81	-21.97	57.70	139.6
SL-SGT	low (LW)	27.89	26.02	-26.02	1.86	-53.91	-26.02	55.77	158.9
SL-SGT	high (HW)	27.89	-10.91	10.91	38.8 ⁸¹	-16.97	10.91	55.77	67.0
SL-SGT	perfect (PW)	27.89	-43.21	43.21	71.1 ⁸¹	15.33	43.21	55.77	-

6.2.2. Grafted/Vacuum (GV) and Grafted/Melt (GM) interfaces

Figure 6.4, depicts the reduced density profiles of PS grafted chains in (a) GV and (b) GM systems in absence of the ramp potential (low wetting) as a function of σ_g and N_g .

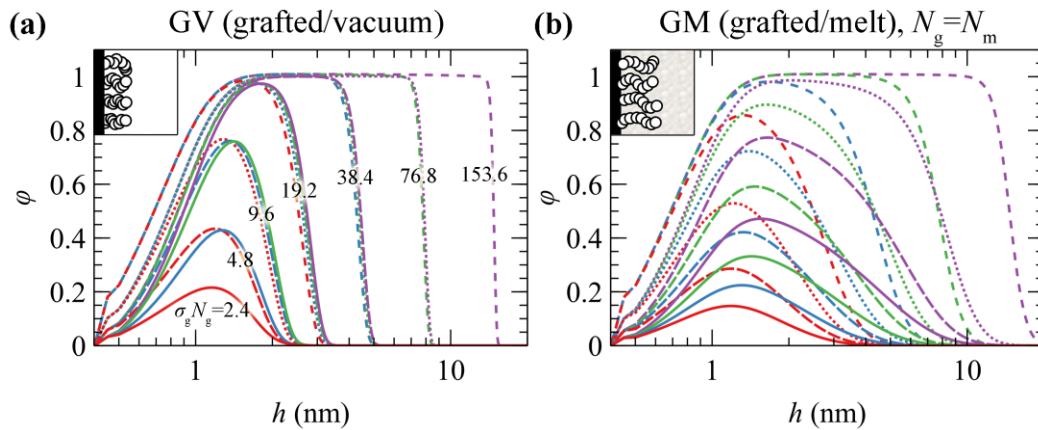


Figure 6.4 Reduced density profiles of polystyrene brushes exposed to polymer melt or vacuum. Calculations were performed with SL-SGT EoS in absence of the ramp potential in (a) grafted/vacuum (GV) and (b) grafted/melt (GM) systems for chain length of grafted chains equal to $N_g = \{24: \text{red}, 48: \text{blue}, 96: \text{green}, 192: \text{violet}\}$ skeletal bonds and grafting density, $\sigma_g = \{0.1: \text{solid lines}, 0.2: \text{dashes}, 0.4: \text{dots}, 0.8: \text{short dashes}\}$ chains/ nm^2 . The numbers in (a) correspond to the values of the product $\sigma_{g,\text{seg}}$ in nm^{-2} units.

The behavior of grafted chains in this planar geometry can be classified into three distinct regimes depending on the combinations of σ_g and N_g . We remind the reader at this point that

$\sigma_{g,seg} = \sigma_g N_g = \frac{6}{C_\infty l_{C-C}^2} \sigma_g R_{G,g}^2$) and the number of chains per area is given by eq 4.10, thus in

planar geometries, it is equivalent to the grafting density σ_g .

1. *Mushroom regime* ($\sigma_{g,seg} \sim 0$ or $\sigma_g R_{G,g}^2 < 1$, short and sparsely grafted brushes). The density of the profiles is less than the bulk density and chains assume random-coil configurations.²³² Increasing σ_g or N_g has a minor effect on the thickness of the profiles but rather makes them more pronounced.

2. *Dense brush regime* ($\sigma_{g,seg} > \sigma_{g,seg99\%}$ or $\sigma_g R_{G,g}^2 > 1$, low $n_{ch,g}^{ref}$, fully formed brush but not too dense chain packing). The brushes become stretched^{24,232} and feature extended regions with bulk density. The thickness of the profiles depends strongly on both σ_g and N_g , reaching the limiting case behavior $\sim \sigma_g^{-1} N_g^{-1}$, i.e., the dimensions of the brushes become proportional to their mass.

3. *Crowding regime* ($\sigma_{g,seg} > \sigma_{g,seg99\%}$ or $\sigma_g R_{G,g}^2 > 1$, high $n_{ch,g}^{ref}$, very dense chain packing). In this regime, the *crowding* of the chains becomes so intense that the density of the grafted chains surpasses slightly the bulk one, as we have already demonstrated in Figure 2.4. This happens because the entropic penalty due to stretching overcomes the enthalpic penalty due to deviations from the bulk density.

There are, however, noticeable differences between the two systems. In GV, the thickness of the density profiles becomes commensurate to the number of the grafted PS segments, $\sigma_{g,seg}$, as already presented in Figure 4.18 of the present thesis for the system of a single spherical particle. Moreover, the density profiles in Figure 6.4a collapse together for constant $\sigma_{g,seg}$ values, i.e., for constant amount of grafted material. In GV, the tails of the profiles feature a sigmoid region on the order of 1 nm at the polymer/vacuum interface^{2,72}, whereas in GM they are much more expanded towards the bulk region.^{23,24} Finally, in both GV and GM, the profiles become slightly more pronounced with increasing σ_g in the vicinity of the grafting points (~ 0.4 nm). The dimensions of the brush are again quantified in terms of the root mean squared brush thickness (eq 3.4) and the height of the surface which encloses 99% of grafted chain segments (eq 3.5).

Figure 6.5a,b illustrates evaluations of $\langle h_g^2 \rangle^{1/2}$ and $h_{99\%}$ against the scaling law $\sim \sigma_g^{-1} N_g^{-1}$ in GV (left column) and GM with the matrix chains either being equal in length to the grafted chains ($N_m = N_g$; central column), or varying between 24 and 1536 skeletal bonds (right column). Figure 6.5c depicts the ratio $h_{99\%} / \langle h_g^2 \rangle^{1/2}$ which can be thought of as a measure of the

shape of the profile. A striking difference between the two systems is that, in the first one, the measures of the brush thickness collapse to a single master curve across the full regime. This is because in GV, the shape of the collapsed films is a function of the mass of the film ($\sim\sigma_g N_g$) and does not depend on the individual factors (σ_g, N_g); see Figure 6.4a.

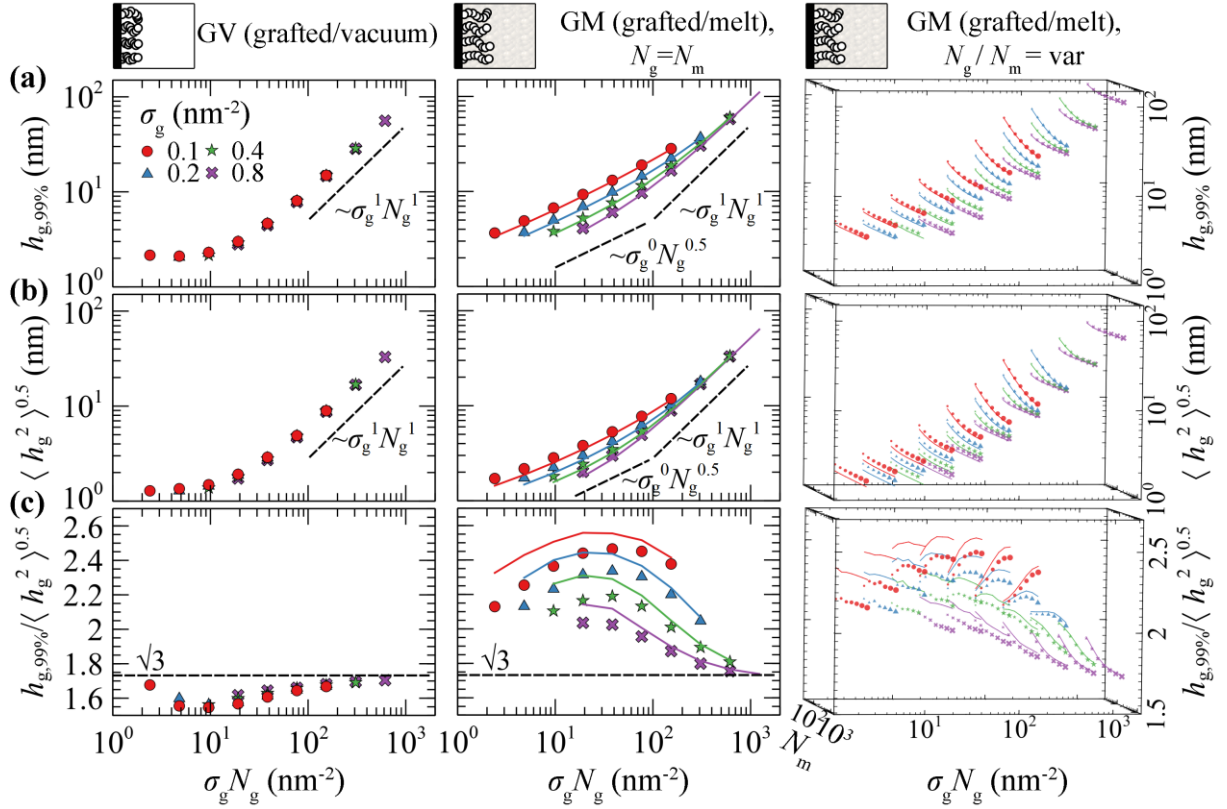


Figure 6.5 Thickness of polymer brushes exposed to polymer melt or vacuum. (a) $h_{99\%}$, (b) $\langle h_g^2 \rangle^{1/2}$ and (c) their ratio $h_{99\%} / \langle h_g^2 \rangle^{1/2}$ versus the scaling $\sigma_g N_g$ using the SL-SGT (markers) and HFD (solid lines) EoS. The panels on the left column correspond to the GV system. The panels in the central column regard the GM system where $N_m = N_g$. The rightmost column depicts results for the GM system as well, but with N_m varying from 24 to 1536 skeletal bonds. Different colors and symbols denote different values of the surface grafting density: $\sigma_g = \{0.1: \text{red circles}, 0.2: \text{blue triangles}, 0.4: \text{green stars}, 0.8: \text{violet crosses}\} \text{ nm}^{-2}$. The length of grafted chains, N_g , increases implicitly in each panel from left to right, according to the scaling law expression presented in the labels of the x -axis. In the rightmost column, the size of the symbols increases with the length of matrix chains. All cases have been evaluated in absence of the ramp potential (low wetting).

Across the *mushroom* regime, the brush thickness is practically independent of σ_g . The thickness in vacuum is independent of N_g as well, indicating collapse of the sparsely grafted chains on the surface. In the case where melt chains are present, the thickness exhibits a random walk-like N_g -dependence, and scales approximately as $\sim N_g^{0.5}$. The shape of the brushes, as quantified by the ratio $h_{99\%} / \langle h_g^2 \rangle^{1/2}$, is quite sensitive to the grafting density in presence of

matrix chains. In GV, the brush ratio decreases with respect to the predictions from *Alexander's* model^{126,127} for incompressible brushes, whilst the opposite trend is exhibited in the GM system.

Across the *dense brush* regime, the brush dimensions depend strongly on both σ_g and N_g . For very large σ_g and N_g the brush thickness scales as $\sim \sigma_{g,seg}$, no matter the solvent conditions (vacuum or melt). This means that the dimensions of the brushes become proportional to their mass and the ratio $h_{99\%} / \langle h_g^2 \rangle^{1/2}$ approaches the limiting value of $\sqrt{3}$ predicted by *Alexander's* model.^{126,127}

Regarding the effect of matrix chains on the scaling of the brushes, it appears that, as long as $N_g \leq N_m$, the brush dimensions are practically independent of N_m . For $N_m \ll N_g$, on the other hand, the brushes expand with decreasing N_m due to the fact that the matrix chains can readily penetrate the brushes, thus the latter swell towards the bulk region. A similar behavior has been recently observed by Bilchak et al.⁴⁸ Therefore, modulating N_m allows for the tuning of solvent conditions, from *theta solvent* ($N_m = N_g$) up to *good solvent* ($N_m < N_g$) conditions. Regarding the ratio $h_{99\%} / \langle h_g^2 \rangle^{1/2}$, it features a complicated behavior with varying N_m , where it decreases/increases for low/high σ_g .

It seems that, regardless of the choice of the free energy density equation [e.g., compare lines (HFD) with markers (SL-SGT) in Figure 6.5] or the strength of the solid/polymer interactions (see Figure 6.6), the structural features and the scaling behaviors of GM systems are quantitatively very similar. In addition, the shortcoming of using HFD with constant isothermal compressibility, κ_T , does not have a practical effect on the structural properties of grafted chains and on the *potential of mean force* of the system, as will be shown below.

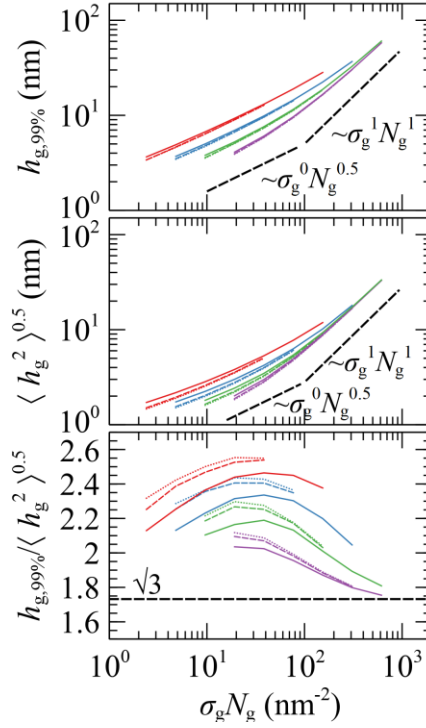


Figure 6.6 Thickness of brushes grafted on surfaces of different wetting degree. (a) $h_{99\%}$, (b) $\langle h_g^2 \rangle^{1/2}$, and (c) their ratio $h_{99\%} / \langle h_g^2 \rangle^{1/2}$ compared to the scaling law $\sigma_g^1 N_g^1$ in GM systems where the length of grafted chains is equal to that of matrix chains, $N_g = N_m$. Different line styles denote interfaces with low (solid lines), high (dashed lines) and perfect (dots) wetting. Different colors denote different grafting density, $\sigma_g = \{0.1: \text{red}, 0.2: \text{blue}, 0.4: \text{green}, 0.8: \text{violet}\} \text{ nm}^{-2}$.

Figure 6.7 illustrates the total grand potential per unit area of grafted/vacuum (γ^{GV}) and grafted/melt (γ^{GM}) interfaces as a function of N_g and σ_g , as well as the partial contributions from the solid/polymer interactions (γ_s), and the entropy of matrix (γ_m) and grafted chains (γ_g). Some key remarks regarding the evaluation of each term with SL-SGT are summarized below.

- γ_s is purely of enthalpic origin and thus it is a functional of the total density profiles. It becomes more attractive with increasing σ_g , since the profiles become more pronounced in the vicinity of the solid (e.g., see Figure 6.4). In GV, γ_s^{GV} decreases with increasing N_g , since increasing N_g means higher amount of material near the solid surface. In GM, γ_s^{GM} is independent of N_g , since the total density profiles are also invariant to N_g , e.g., compare profiles in Figure 6.2c-f for different chain lengths.
- γ_m describes the entropic contribution of the matrix chains. Looking at the GM panels, it decreases precipitously with increasing N_g/N_m , since the grafted chains occupy more space in the vicinity of the interface, leaving the matrix chains with fewer available conformations.

Note that, by keeping N_g fixed, γ_m scales with N_m about as $\gamma_m \sim N_m^{-1}$; which is consistent with eq 2.42. In GV systems, this term is of course zero, since there are no matrix chains at all.

- γ_g quantifies the entropic contribution of the grafted chains and it is an indicator of the stretching of the brush. It increases monotonically with increasing N_g and σ_g , since the grafted chains expand and stretch further towards the bulk region. In addition, γ_g^{GM} increases with decreasing N_m , since the grafted chain-melt interactions are enhanced and, as a result, the brushes swell as shown in Figure 6.5b,c (rightmost column).
- γ is the total free energy of the interfacial systems per unit area. It increases with increasing molecular weight of grafted chains and appears to be dominated by the conformational entropy of grafted chains, γ_g .

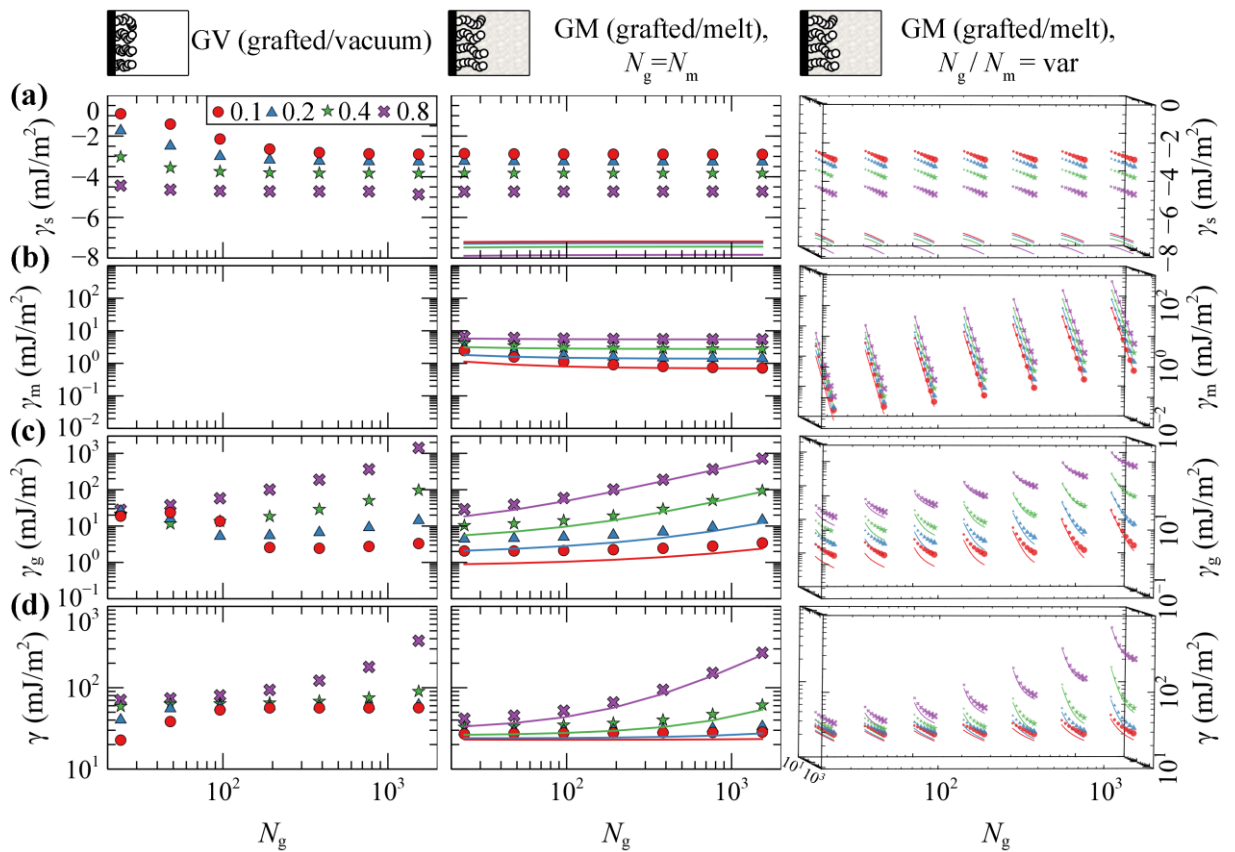


Figure 6.7 Free energy of polymer brushes exposed to polymer melt or vacuum. Partial contributions to the grand potential (a) γ_s , (b) γ_m , (c) γ_g and (d) total grand potential, γ , per unit area, using the SL-SGT (markers) and HFD (solid lines) EoS. The panels on the left column correspond to the GV system. The panels in the central column depict results regarding the GM system, for $N_g = N_m$. The rightmost column depicts results for the GM system as well, but with N_m varying from 24 up to 1536 segments. Different colors and symbols correspond to different values of the surface grafting density: $\sigma_g = \{0.1: \text{red circles}, 0.2: \text{blue triangles}, 0.4: \text{green stars}, 0.8: \text{violet crosses}\}$ chains/nm². The chain length of grafted chains, N_g , increases implicitly in each panel from left to right, according to the scaling law expression presented in the labels of the x-axis. In the rightmost column, the size of the symbols increases with the chain length of matrix chains. All cases have been evaluated in absence of the ramp potential.

Overall, the evaluations of the free energy terms with HFD are in good qualitative agreement with SL-SGT. Furthermore, it appears that γ_S^{GM} evaluated with HFD is more negative than when the SL-SGT EoS is used, because the density profiles lie closer to the silica surface in the former model (e.g., compare Figure 6.2d,f). In their recent work concerning neat grafted nanoparticles, Mydia et al.⁵⁰ report that, for constant grafting density, the stretching energy does not increase monotonically with the chain length. This behavior is attributed to the curved space around the nanoparticles, since, at some point, the grafted chains do not experience the presence of each other and become unperturbed. For planar surfaces, however, the threshold chain length becomes infinitely large, since no curvature is involved and the chains will always experience the presence of each other, considering that the dimensionless quantity $\sigma_g R_g^2$ is above a threshold value as well.²⁴

6.2.3. Polystyrene melt capped between two bare silica surfaces (SMS)

In this paragraph, we study the *potential of mean force* (PMF) between two approaching *bare* silica surfaces. This means that only matrix chains are present in the system. This situation corresponds to the limiting case of extremely low grafting densities, where *allopobic dewetting* occurs and the enthalpic interactions between the two solid surfaces prevail. The matrix chains are gradually restricted in terms of available conformations as the distance between the two plates decreases. For these calculations, the PMF^{SMS} is expressed with respect to the free energies of the single SM interfaces for the same chain length, as shown in the following eq 6.1. In other words, the reference system is that of the same plates being at infinite distance from each other.

$$\text{PMF}^{\text{SMS}} = \gamma^{\text{SMS}} - \gamma_\infty^{\text{SMS}} = \gamma^{\text{SMS}} - \lim_{h_{ss} \rightarrow \infty} \gamma^{\text{SMS}} = \gamma^{\text{SMS}} - 2\gamma^{\text{SM}} \quad 6.1$$

with γ^{SM} being the free energy of a SM interface in presence of matrix chains of length N_m , depicted in Figure 6.2a,b. Note that, with PMF^{SMS} known, the *disjoining pressure* can be calculated as:

$$\Pi(h_{ss}) = - \left(\frac{\partial \gamma^{\text{SMS}}}{\partial h_{ss}} \right)_{\mu, T} \quad 6.2$$

Due to numerical issues that arise when employing the SL EoS, the initial configuration of the field can affect the outcome of the converged solution. To investigate this effect, we performed our calculations using two different compression methods:

1. In the first method, the calculations were performed in a decremental fashion, in which the initial configuration of the field was set to the field corresponding to the converged calculation

for a slightly larger domain: $\mathbf{w}'_{\text{ifc,init}}(h_{\text{ss}}) = \mathbf{w}'_{\text{ifc,final}}(h_{\text{ss}} + \Delta h)$

2. In the calculations corresponding to the second method, the initial configuration of the field was set to zero across the domain: $\mathbf{w}'_{\text{ifc,init}} = \mathbf{0}$

Using the first method, it is easier to derive a solution which corresponds to a stable configuration. The second method, on the other hand, can provide a measure of the stability of the films in terms of their tendency to collapse and their sensitivity to fluctuations about equilibrium (e.g., their response during the formation of a cavity).

Figure 6.8 illustrates evaluations of PMF^{SMS} with HFD (a), and with SL-SGT under low (b, LW), high (c, HW) and perfect (d, PW) wetting situations, using the first method for decremental compression. The same results obtained via the second method are presented in Figure 6.9.

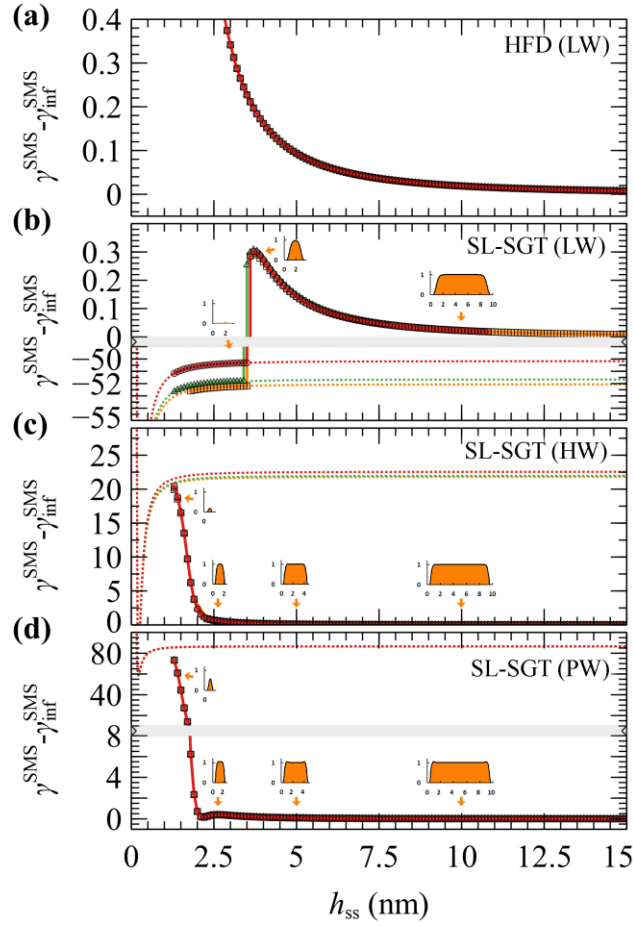


Figure 6.8 Potential of mean force, in mJ/m^2 , for the system of approaching bare silica surfaces in a melt (SMS). Calculations were performed with (a) HFD, (b) SL-SGT (LW), (c) SL-SGT (HW) and (d) SL-SGT (PW), for $N_m = \{24: \text{red}, 96: \text{green}, 384: \text{orange}\}$ skeletal bonds. The calculations were performed in a decremental fashion, in which $\mathbf{w}'_{\text{fc,init}}(h_{\text{ss}}) = \mathbf{w}'_{\text{fc,final}}(h_{\text{ss}} + \Delta h)$, with a compression rate equal to $-0.1 \text{ nm/evaluation}$. The inset graphs in (b-d) depicts snapshots of the density profiles at plate-plate distances denoted by the arrows, for $N_m = 384$. Bands denote scale changes along the axes. The dashed lines display the Hamaker potential contribution to the solid/solid interaction, shifted by twice the solid/polymer adhesion tension.

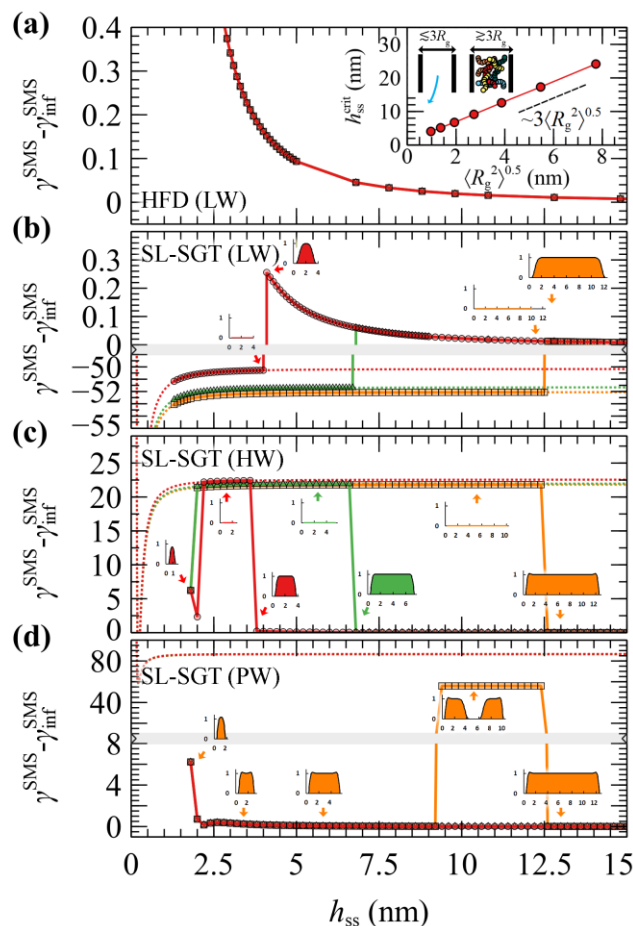


Figure 6.9 Potential of mean force, in mJ/m^2 , for the system of approaching bare silica surfaces (SMS) starting with zero field. Calculations were performed with (a) HFD, (b) SL-SGT (LW), (c) SL-SGT (HW) and (d) SL-SGT (PW), for $N_m = \{24: \text{red}, 96: \text{green}, \text{and } 384: \text{orange}\}$. The initial configuration of the field was set to $\mathbf{w}'_{ifc,init} = \mathbf{0}$. The inset in panel (a) depicts the critical plate-plate distance for the matrix chains to evacuate the system, against their radius of gyration. The schematic of the inset depicts the film situation for h_{ss} larger and lower than $\sim 3R_g$. The inset graphs in (b-d) depict snapshots of the density profiles at plate-plate distances denoted by the arrows and their fill corresponds to the color of the corresponding chain length. Bands denote scale changes along the axes. The dashed lines display the *Hamaker* potential contribution to the solid/solid interactions, shifted by twice the solid/polymer *adhesion tension*.

In the case of HFD, regardless of the compression approach, PMF^{SMS} increases with decreasing plate-plate distance, suggesting the manifestation of a repulsive force that resists the attractive interactions between the surfaces. These repulsive forces are dominated by the loss of solid/polymer interactions; with decreasing h_{ss} , the mass of the film decreases and there are fewer interaction sites. The sign of these forces depends on an interplay between the strength of the solid/polymer and solid/solid interactions. If the latter become much stronger than the former, the solid/solid forces will dominate and PMF^{SMS} will become attractive. The steadily

increasing forces in this case can be, however, a misleading result, because HFD does not account for the gaseous phases which may arise during the process.

According to evaluations with SL-SGT under low wetting (LW) conditions (Figure 6.8b), the functional dependence of PMF^{SMS} is quite similar to that of HFD. However, below a critical plate-plate distance, $h_{\text{ss}}^{\text{crit}}$, PMF^{SMS} decreases abruptly, indicating a phase transition. At these distances, it is impossible for SCF to maintain a metastable film; hence, a cavity is formed and the calculation converges to the more stable solution, $\boldsymbol{\phi} = \mathbf{0}$. The films remain stable above $h_{\text{ss}}^{\text{crit}}$ (on the order of 3.5 nm), regardless of N_{m} (Figure 6.8b).

Upon departure of the melt from the gap between the plates, the only contribution to the free energy is due to plate-plate interactions which are described here by means of the *Hamaker* potential; therefore, leading to the eventual contact of the adjacent solid surfaces. Note that for LW surfaces, $\text{PMF}^{\text{SMS}}(\boldsymbol{\phi} = \mathbf{0}) = \gamma_{\text{ss}}^{\text{SMS}} - \gamma_{\infty}^{\text{SMS}}$ (depicted by dashed lines in Figure 6.8b) is negative, indicating that the solid/polymer interactions are really weak for the LW films and these films are actually metastable with respect to cavitation across the entire range of thicknesses.

A similar picture has been reported by past simulations from a variable-density lattice based SCF model.²³³ In that model, the interactions in flat geometries become insignificant for h_{ss} slightly larger or equal than $4\langle R_{\text{g}}^2 \rangle^{0.5}$, whereas the maximum recorded force per radius before cavitation in a crossed cylinder geometry was on the order of ~ 0.01 mN/m when considering high energy surfaces and 0.1 mN/m for low energy surfaces.

With enhanced solid/polymer interactions, the stability of the capped polymer films is reinforced considerably. According to the more reliable solution scheme where the domain length is adjusted decrementally, the HW and PW films remain stable throughout the full h_{ss} range examined here, always converging to the stable, polymer-filled equilibrium solution of the problem (see Figure 6.8c,d). In contrast to LW films, the PMF^{SMS} of the HW and PW ones increases steadily for h_{ss} less than 2.5 nm, whereas in the limit of low h_{ss} , the density decreases significantly due to entropy confinement. A significant free energy barrier of approximately $-\gamma_{\infty}^{\text{SMS}}$, on the order of 20 mN/m in the HW case and 80 mN/m in the PW case, has to be overcome for the polymer to be expelled completely and the solids to come in direct contact at $\text{PMF}^{\text{SMS}}(\boldsymbol{\phi} = \mathbf{0}) = \gamma_{\text{ss}}^{\text{SMS}} - \gamma_{\text{inf}}^{\text{SMS}}$.

There is, however, a striking difference between the HW and PW films. The HW films can be considered as metastable with respect to cavitation, since, after crossing a barrier of $\sim -\gamma_{\text{inf}}^{\text{SMS}}$

with decreasing h_{ss} , they can be trapped in the global minimum of attractive *Hamaker* interactions between the bare solids (see minima of the dashed lines in Figure 6.8c), as in the case of the LW film. The PW film, on the other hand, is indeed stable down to thicknesses of ca. 1.5 nm, since the minimum of the *Hamaker* potential lies way higher (~ 60 mJ/m²) than the plateau PMF^{SMS} value at large h_{ss} .

6.2.4. Interacting grafted surfaces in melt (GMG)

The current section presents evaluations of the *potential of mean force* of approaching grafted surfaces. To facilitate comparisons across the wide parameter space considered for these calculations, the PMF^{GMG} will be expressed in terms of the reduced surface-surface distance which is defined by the following eq 6.3.

$$h_{ss} = \frac{2h_{ss}}{\langle h_{g^-}^2 \rangle^{0.5} + \langle h_{g^+}^2 \rangle^{0.5}} \quad 6.3$$

with $\langle h_{g^-}^2 \rangle^{0.5}$ and $\langle h_{g^+}^2 \rangle^{0.5}$ being the root mean squared brush thickness of the single grafted surfaces (infinite surface-surface distance) at the same temperature and in the presence of matrix chains of length N_m (brush thickness from Figure 6.5). A similar normalization can be obtained by dividing h_{ss} with $\langle R_g^2 \rangle^{0.5}$, since $\langle R_g^2 \rangle^{0.5} \sim N_g$ and $N_g \sim \langle h_g^2 \rangle^{0.5}$ across the *dense brush* regime. Nevertheless, normalizing the plate-plate distance as shown in eq 6.3 is a more natural approach for making such comparisons, because it allows evaluating the tendencies of the brushes to interpenetrate. Furthermore, $\langle h_g^2 \rangle^{0.5}$ takes account of the chain perturbations when varying the melt conditions that are less sensitive to the particular equation of state in the nonbonded free energy density model.

As in the SMS systems, PMF^{GMG} will be expressed relative to the free energy of the G⁻M and G⁺M systems in the presence of matrix chains of length N_m (see Figure 6.7) as presented in eq 6.4 below. In other words, PMF^{GMG} is expressed with respect to the free energy of the systems at infinite plate-plate separation. Regarding the segment-solid interactions, LW conditions are employed throughout this section, unless otherwise stated.

$$\text{PMF}^{\text{GMG}} = \gamma^{\text{GMG}} - \gamma_{\infty}^{\text{GMG}} = \gamma^{\text{GMG}} - \lim_{h_{ss} \rightarrow \infty} \gamma^{\text{GMG}} = \gamma^{\text{GMG}} - \gamma^{\text{G}^- \text{M}} - \gamma^{\text{G}^+ \text{M}} \quad 6.4$$

At first, we present the PMF^{GMG} for the simplest case where the opposing surfaces are grafted symmetrically with respect to σ_g and N_g for varying N_m/N_g . Figure 6.10 illustrates PMF^{GMG} as a function of the plate-plate distance, h_{ss} , whereas Figure 6.11 depicts the corresponding density distribution across the examined parameter space for $N_m = N_g$.

According to Figure 6.10, the brushes start experiencing the presence of each other at distances in the order of 4-5 \tilde{h}_{ss} , while, for larger \tilde{h}_{ss} , $\text{PMF}^{\text{GMG}} \approx 0$. At lower separation distances, the brushes interact strongly with each other and PMF^{GMG} increases. In systems with low σ_g (*mushroom* regime), the brushes are relatively soft and thus the PMF increases at lower \tilde{h}_{ss} . In dense systems, on the other hand, the brushes are more compact and as a result the PMF increases abruptly at larger \tilde{h}_{ss} , on the order of 3-3.5 (see bottom right panel of Figure 6.10. This regime coheres with the predictions of the *Alexander* model for incompressible brushes,^{126,127} where, regardless of N_g and σ_g , the predicted separation distance of two *Alexander* brushes in contact is $\tilde{h}_{\text{ss,min}} = 2\sqrt{3} \sim 3.4$. This is proved by considering that, in planar surfaces, the edge of a brush with chain length N_g and grafting density σ_g is:

$$h_{\text{edge,g}} = \frac{\sigma_g N_g}{\rho_{\text{seg,bulk}}} \quad 6.5$$

thus, the separation distance between two *Alexander* brushes (grafted with σ_{g^-} , N_{g^-} and σ_{g^+} , N_{g^+}) in contact is calculated as follows:

$$h_{\text{ss,min}} = h_{\text{edge,g}^-} + h_{\text{edge,g}^+} = \frac{\sigma_{g^-} N_{g^-} + \sigma_{g^+} N_{g^+}}{\rho_{\text{seg,bulk}}} \quad 6.6$$

The root mean squared brush thickness of an *Alexander* brush is equal to:²⁴

$$\langle h_g^2 \rangle^{1/2} = \frac{h_{\text{edge,g}}}{\sqrt{3}} \quad 6.7$$

hence, in terms of reduced units, the plate-to-plate distance, $h_{\text{ss,min}}$, becomes:

$$\tilde{h}_{\text{ss,min}} = 2 \frac{h_{\text{edge,g}^-} + h_{\text{edge,g}^+}}{\langle h_{g^-}^2 \rangle^{1/2} + \langle h_{g^+}^2 \rangle^{1/2}} = 2 \frac{h_{\text{edge,g}^-} + h_{\text{edge,g}^+}}{\frac{h_{\text{edge,g}^-}}{\sqrt{3}} + \frac{h_{\text{edge,g}^+}}{\sqrt{3}}} = 2\sqrt{3} \quad 6.8$$

Regarding the effect of varying the chain length of matrix chains on PMF^{GMG} , for $N_m/N_g \leq 1$, PMF^{GMG} becomes strictly repulsive, with the exception of the case for densely grafted and long

grafted chains, $\sigma_g = 0.4 \text{ nm}^{-2}$, $N_g = 768$. Increasing N_m/N_g leads to the manifestation of attractive interactions as indicated by the formation of a minimum in PMF^{GMG} (autophobic dewetting). These interactions become slightly stronger with increasing N_g , and even stronger with increasing σ_g . The enhancement of the attractive interactions with increasing grafting density has been also observed in several theoretical²⁵⁻²⁷ and experimental studies.^{18,22,29-31}

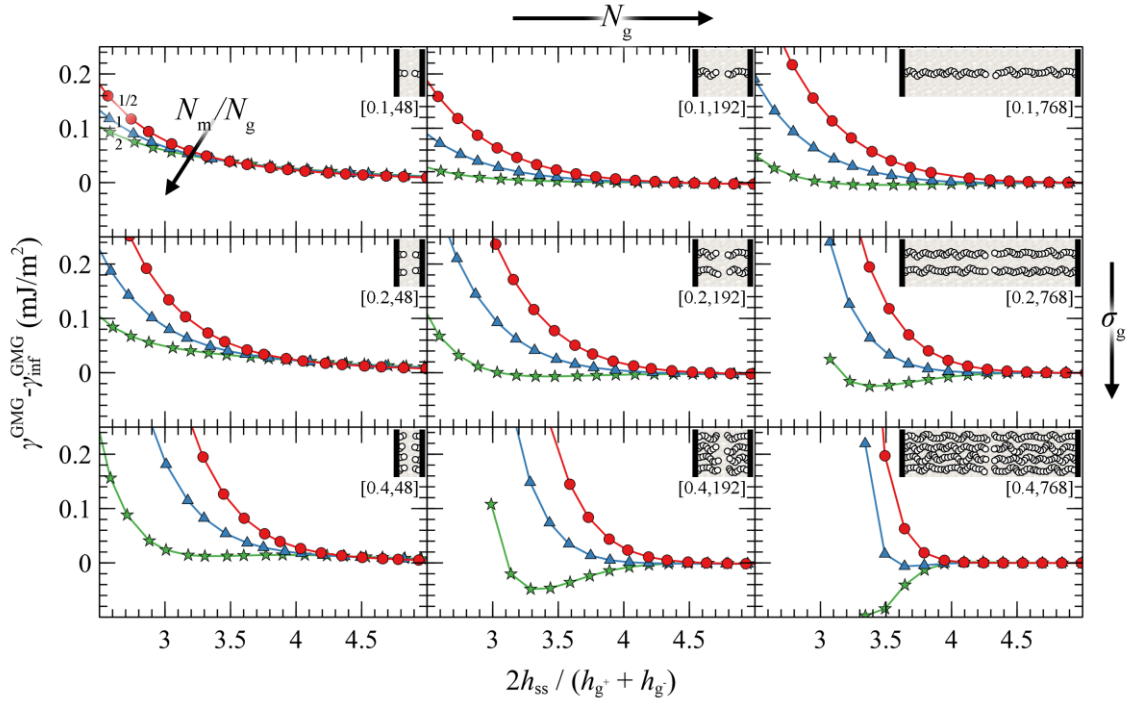


Figure 6.10 Potential of mean force in a symmetric system of approaching grafted silica surfaces in contact with melt. Calculations were performed with the SL EoS. Colors correspond to different matrix-to-grafted chain length ratios, $N_m/N_g = \{0.5: \text{red}, 1: \text{blue}, 2: \text{green}\}$ skeletal bonds. The labels in brackets denote σ_g (nm^{-2}) and N_g (skeletal bonds). Lines are guides to the eye.

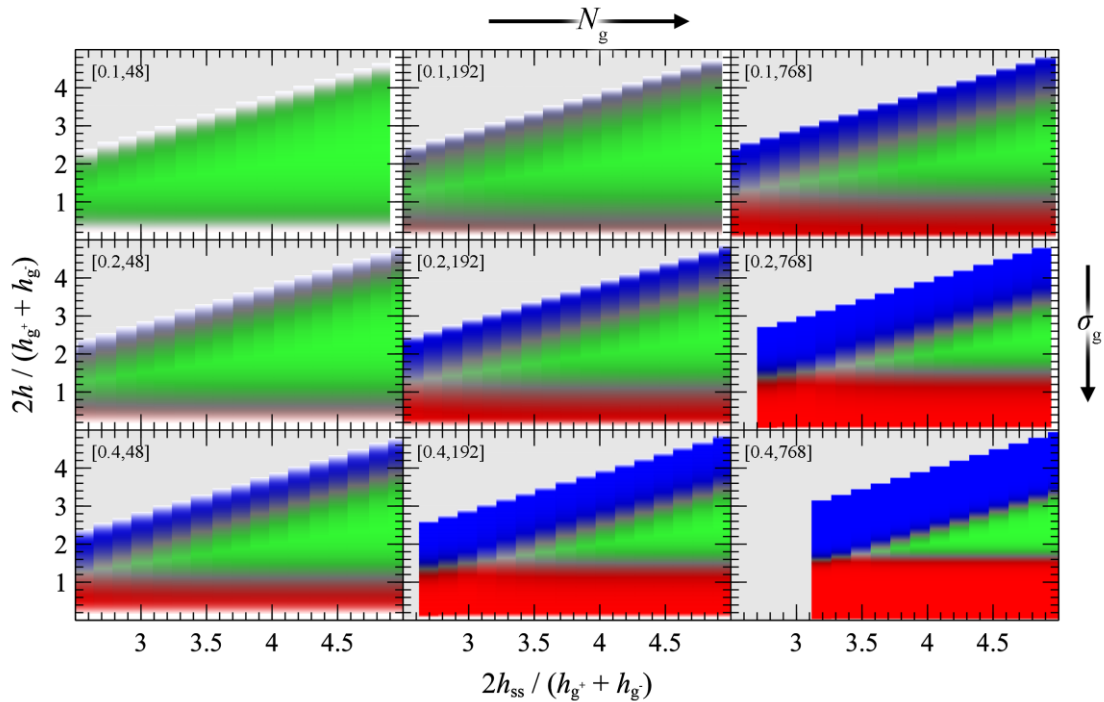


Figure 6.11 Reduced density distributions corresponding to the PMF^{GMG} panels in Figure 6.10. Profiles are derived as functions of the plate-plate distance (abscissa) and the distance from the left wall (ordinate) in reduced units. Red/green/blue colors correspond to regions with high density ($\phi_c = 1$) of $c = g/m/g^+$ chains, respectively. Grey denotes regions which lie outside the modeled domain or have not been evaluated at all. Labels in brackets denote σ_g (nm^{-2}) and N_g (skeletal bonds).

Figure 6.12 illustrates the contribution of individual free energy terms to PMF^{GMG} for a case with $\sigma_g = 0.2 \text{ nm}^{-2}$ and $N_g = 192$ skeletal bonds. It appears that the attractive part of PMF^{GMG} is dominated by the entropic contribution of the grafted chains, γ_g^{GMG} , shown in panel Figure 6.12c. In addition, the terms responsible for the cohesive and the *chemical potential*-density field interactions change due to minor variations in the mean density profile and exhibit an opposite trend to that of γ_g^{GMG} , albeit weaker. That PMF^{GMG} becomes more repulsive when $N_m < N_g$ is attributed to the matrix chains being able to penetrate the space occupied by the brush, compelling the grafted chains of the two surfaces to expand in space until they interact with each other, thus keeping the two surfaces separated. In other words, the solvent conditions improve with decreasing N_m/N_g ; hence, the brushes prefer to interact with the solvent molecules than with each other.

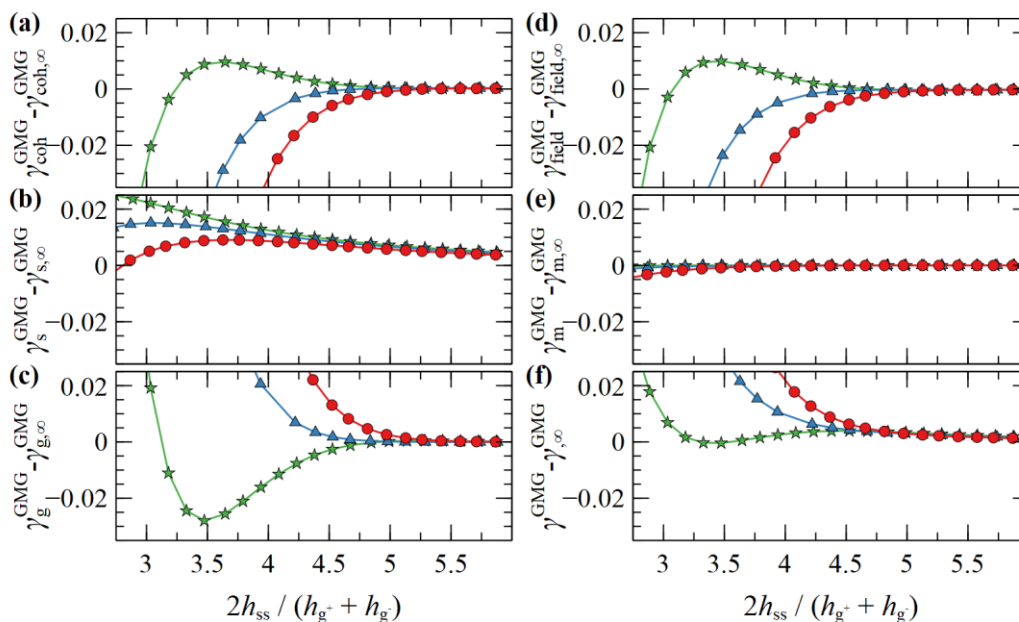


Figure 6.12 Free energy partial contributions to the *potential of mean force*, in mJ/m^2 , of two approaching symmetrically grafted surfaces in contact with melt. Grafting density, $\sigma_g = 0.2 \text{ nm}^{-2}$, length of grafted chains, $N_g = 192$, matrix-to-grafted length ratio, $N_m/N_g = \{0.5: \text{circles}, 1: \text{triangles}, 2: \text{stars}\}$. (a) cohesive interactions, (b) solid/polymer interactions, (c) entropic contribution from grafted chain conformations, (d) density-field interactions, (e) entropic contribution of matrix chains and (f) total grand potential.

In general, the evolution of the energy term associated with solid/polymer interactions, γ_s^{GMG} , with decreasing plate-plate distance, depends on an interplay between two processes: (i) the thinner the film becomes, the fewer polymer segments can interact with the solid, thus

leading to increased γ_s^{GMG} (less attractive). (ii) the brushes can become slightly denser with decreasing \tilde{h}_{ss} , hence leading to decreased γ_s^{GMG} (more attractive). Indeed, for $N_m > N_g$, γ_s^{GMG} is dominated by the first process, since it increases monotonically with decreasing \tilde{h}_{ss} . However, for $N_m < N_g$, it features an interesting behavior where it initially increases with decreasing \tilde{h}_{ss} , while for $\tilde{h}_{\text{ss}} < 3.8$ it decreases, indicating that the second process dominates.

Let us now investigate the effect of asymmetry of the opposing grafted surfaces in terms of the relative chain lengths and grafting densities. In particular, Figure 6.13 illustrates evaluations of PMF^{GMG} for constant chain length and grafting density at the lower face ($N_{g^-} = 96$, $\sigma_{g^-} = 0.2 \text{ nm}^{-2}$) and varying N_{g^+}/N_{g^-} , N_m/N_{g^-} and $\sigma_{g^+}/\sigma_{g^-}$. Similarly, Figure 6.14 and Figure 6.15 depict the same evaluations, but for four times larger N_{g^-} and for two times larger σ_{g^-} , respectively.

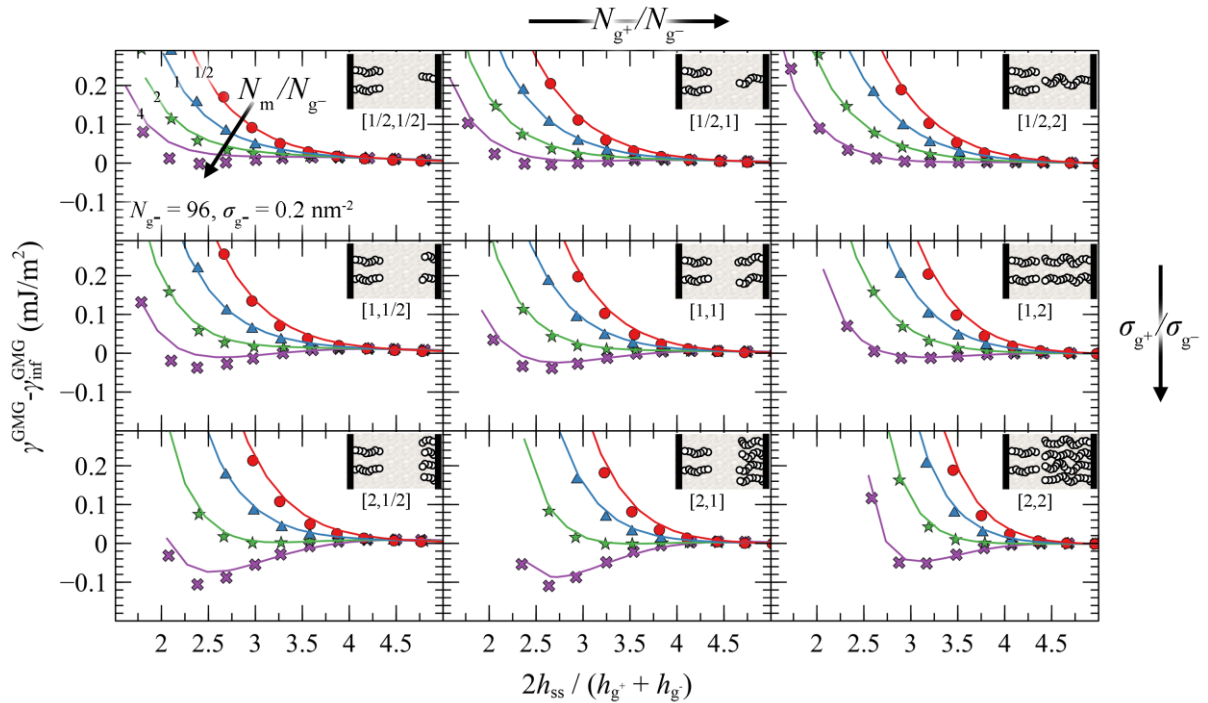


Figure 6.13 Potential of mean force between two approaching asymmetrically grafted silica surfaces in contact with melt. $\sigma_{g^-} = 0.2 \text{ nm}^{-2}$ and $N_{g^-} = 96$ skeletal bonds. Colors correspond to evaluations for $N_m/N_{g^-} = \{0.5, 1, 2, 4\}$, and the labels in brackets denote the ratios $\sigma_{g^+}/\sigma_{g^-}$ and N_{g^+}/N_{g^-} . Lines and markers correspond to evaluations with the HFD and SL EoS, respectively. Inset cartoons: each bead denotes a segment of 24 PS skeletal bonds.

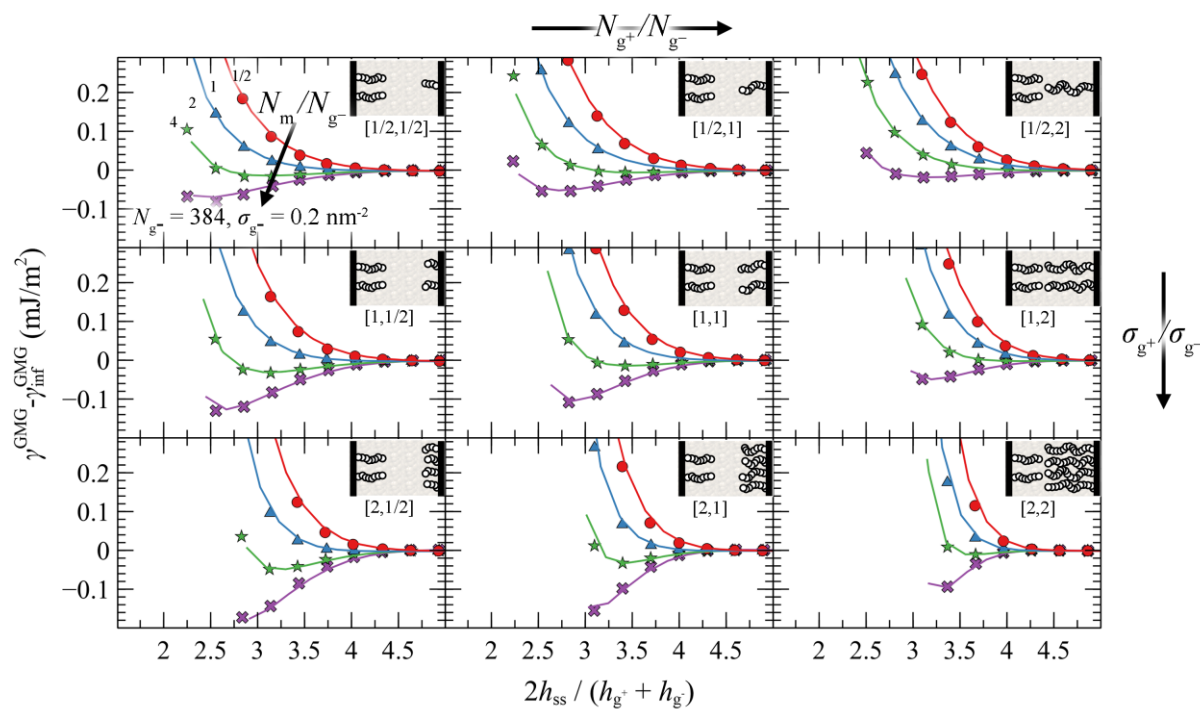


Figure 6.14 Potential of mean force between two approaching asymmetrically grafted silica surfaces in contact with melt (case 2). $\sigma_{\text{g}^-} = 0.2 \text{ nm}^{-2}$ and $N_{\text{g}^-} = 384$ skeletal bonds. Colors correspond to evaluations for $N_{\text{m}} / N_{\text{g}^-} = \{0.5: \text{red}, 1: \text{blue}, 2: \text{green}, 4: \text{purple}\}$, and the labels in brackets denote the ratios $\sigma_{\text{g}^+} / \sigma_{\text{g}^-}$ and $N_{\text{g}^+} / N_{\text{g}^-}$. Lines and markers correspond to evaluations with the HFD and SL EoS, respectively. Inset cartoons: each bead denotes a segment of 96 PS skeletal bonds.

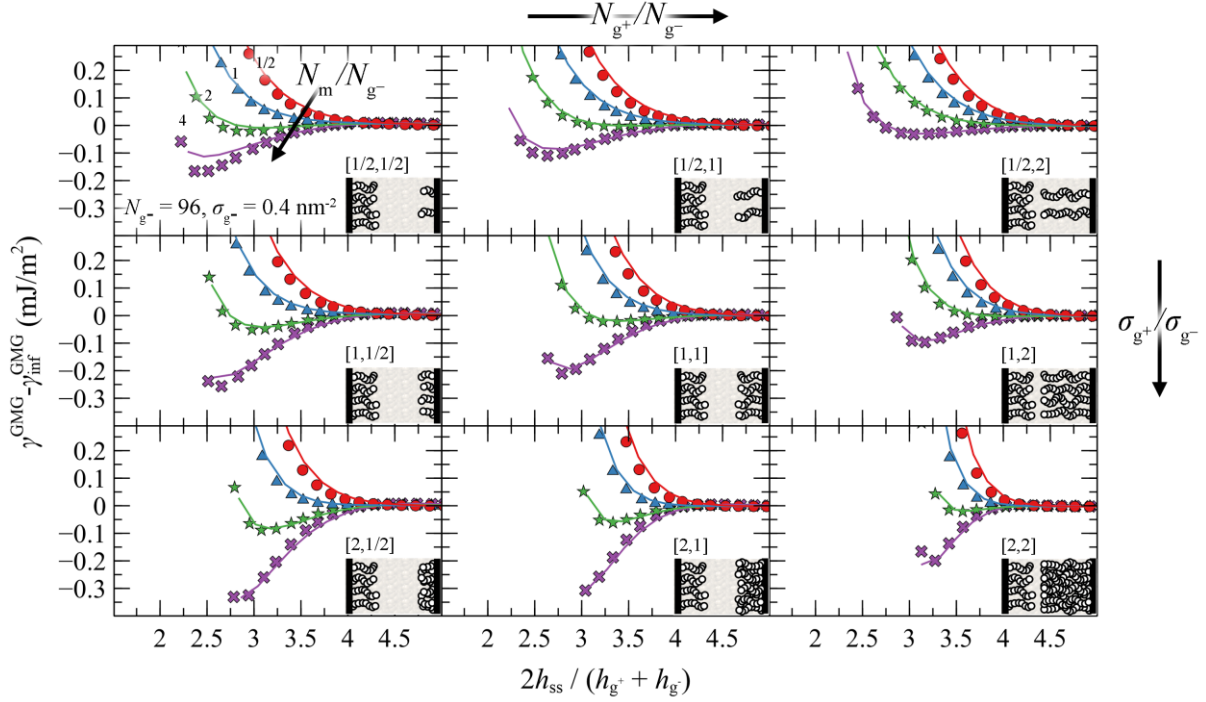


Figure 6.15 Potential of mean force between two approaching asymmetrically grafted silica surfaces in contact with melt (case 3). $\sigma_{\text{g}^-} = 0.4 \text{ nm}^{-2}$ and $N_{\text{g}^-} = 96$ skeletal bonds. Colors correspond to evaluations for $N_{\text{m}} / N_{\text{g}^-} = \{0.5: \text{red}, 1: \text{blue}, 2: \text{green}, 4: \text{purple}\}$, and the labels in brackets denote the ratios $\sigma_{\text{g}^+} / \sigma_{\text{g}^-}$ and $N_{\text{g}^+} / N_{\text{g}^-}$. Lines and markers correspond to evaluations with the HFD and SL EoS, respectively. Inset cartoons: each bead denotes a segment of 24 PS skeletal bonds.

Irrespective of the degree of asymmetry, adjacent brushes experience the presence of each other at distances \tilde{h}_{ss} commensurate with 4 to 5, similarly to the symmetric case in Figure 6.10. By keeping σ_{g^-} and N_{g^-} constant and the ratio $N_{\text{m}} / N_{\text{g}^-}$ fixed at different values (same colors), and varying σ_{g^+} and N_{g^+} , some general trends are emerging: the attractive interactions between the surface become stronger with increasing $\sigma_{\text{g}^+} / \sigma_{\text{g}^-}$ ratios (from top to bottom panels) and with decreasing $N_{\text{g}^+} / N_{\text{g}^-}$ (from right to left panels).

That PMF^{GMG} becomes more attractive with increasing $\sigma_{\text{g}^+} / \sigma_{\text{g}^-}$ is to be expected: upon increasing σ_{g^+} the mean grafting density increases as well, thus PMF^{GMG} becomes more attractive, as in the case of symmetric surfaces in Figure 6.10. However, that the interactions become more attractive with decreasing has to be reconciled with the findings reported in Figure 6.10 for symmetrically grafted surfaces. To interpret this effect, one should take into account

that during these evaluations, the ratio N_m / N_{g^-} was fixed, whereas varying σ_{g^+} and N_{g^+} can have direct implications to the effective ratio of N_m with respect to the average size of grafted chains.

Let $N_{\bar{g}}$ be the average chain length of grafted chains in the two surfaces, estimated as the weighted average of grafted chain length with respect to the grafting densities:

$$N_{\bar{g}} = \frac{\sigma_{g^-} N_{g^-} + \sigma_{g^+} N_{g^+}}{\sigma_{g^-} + \sigma_{g^+}} \quad 6.9$$

$N_m / N_{\bar{g}}$ is a measure of the length of matrix chains in relation to that of grafted chains. Based on eq 6.9, it is evident that, upon decreasing N_{g^+} / N_{g^-} at constant N_{g^-} and $\sigma_{g^+} / \sigma_{g^-}$, $N_{\bar{g}}$ decreases as well and thus the effective ratio $N_m / N_{\bar{g}}$ increases. Increasing the size of matrix chains was shown to enhance the attractive interactions in Figure 6.10, and therefore the results shown in Figure 6.13 are consistent with this trend.

An alternative way to interpret and isolate the effect of asymmetry is to vary the ratios $\sigma_{g^+} / \sigma_{g^-}$ and N_{g^+} / N_{g^-} , while keeping constant the effective ratio $N_m / N_{\bar{g}}$ based on eq 6.9. Figure 6.16 demonstrates the results of this process, wherein the top left panel depicts the reference symmetric case ($\sigma_g = 0.2 \text{ nm}^{-2}$, $N_g = 96$), and the asymmetry with respect to σ_g (N_g) increases from top-to-bottom (left-to-right). As we can see in this figure, varying $\sigma_{g^+} / \sigma_{g^-}$ or N_{g^+} / N_{g^-} individually has a minor effect on PMF^{GMG} . This finding is important, because it shows that minor deviations in σ_g and N_g do not affect the resulting PMF^{GMG} provided that $N_m / N_{\bar{g}}$ remains constant. On the other hand, PMF^{GMG} can become very attractive in extreme cases of asymmetry, where both the asymmetry in σ_g and N_g increases (e.g., see bottom right panel in Figure 6.16), and this is mainly attributed to the increased average grafting density.

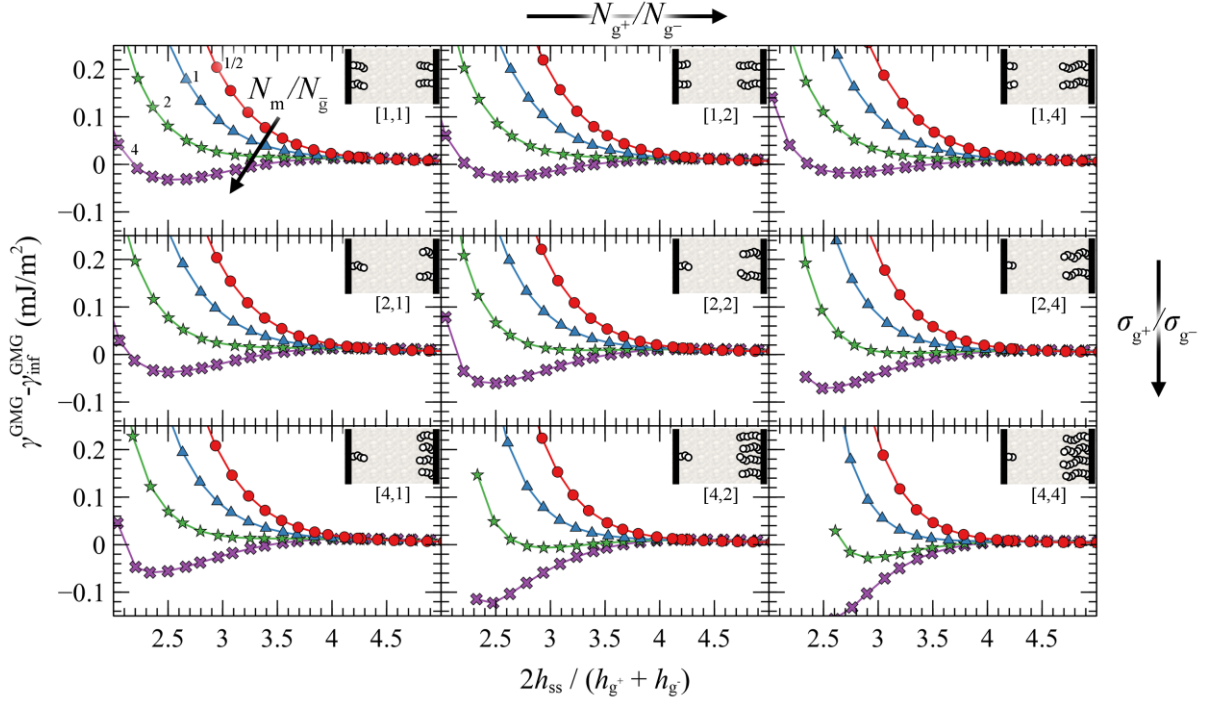


Figure 6.16 Potential of mean force between two approaching asymmetrically grafted silica surfaces in contact with melt (case 4). Colors correspond to evaluations for $N_{\text{m}}/N_{\text{g}} = \{0.5: \text{red}, 1: \text{blue}, 4: \text{purple}\}$, whereas the small legends in brackets below the insets denote the ratios $\sigma_{\text{g}^+}/\sigma_{\text{g}^-}$ and $N_{\text{g}^+}/N_{\text{g}^-}$, respectively. The top left panel corresponds to the reference symmetric case with $\sigma_{\text{g}}^{\text{ref}} = \sigma_{\text{g}^-} = \sigma_{\text{g}^+} = 0.2 \text{ nm}^{-2}$ and $N_{\text{g}}^{\text{ref}} = N_{\text{g}^-} = N_{\text{g}^+} = 96$. The actual $\sigma_{\text{g}^{\pm}}$ and $N_{\text{g}^{\pm}}$ for each case can be retrieved as follows: $\sigma_{\text{g}^{\pm}} = \sigma_{\text{g}}^{\text{ref}} m^{\pm 1/2}$ and $N_{\text{g}^{\pm}} = N_{\text{g}}^{\text{ref}} n^{\pm 1/2}$, with $[m, n] = [\sigma_{\text{g}^+}/\sigma_{\text{g}^-}, N_{\text{g}^+}/N_{\text{g}^-}]$ being the numbers at the legends under the insets. It should be noted that inset schematics belonging to panels other than the corner ones are only approximate; in these cases, $\sigma_{\text{g}^{\pm}}$ and $N_{\text{g}^{\pm}}$ are scaled by a factor of $\pm\sqrt{2}$.

Figure 6.17 presents the PMF^{GMG} for symmetric systems as a function of the energy of the solid surface, i.e., the strength of solid/polymer interactions. It seems that, regardless of σ_{g} , N_{g} and the ratio $N_{\text{m}}/N_{\text{g}}$, the affinity of the polymer chain segments to the solid (wetting degree) has a minor effect on the PMG^{GMG} . In each case, the PMF becomes less pronounced for higher wetting degree, albeit the effect is minor.

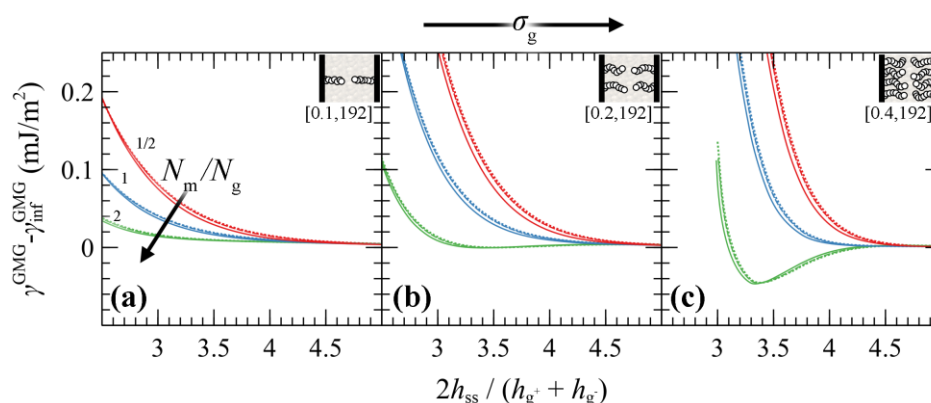


Figure 6.17 Potential of mean force between two approaching grafted silica surfaces in melt for different wetting degrees. Calculations were performed with SL EoS for σ_{g} equal to (a) 0.1, (b) 0.2 and (c) 0.4 nm⁻² and $N_{\text{g}} = 192$. Colors correspond to evaluations for $N_{\text{m}}/N_{\text{g}} = \{0.5: \text{red}, 1: \text{blue}, 2: \text{green}\}$, whereas different line styles denote interfaces with low (solid lines), high (dashed lines) and perfect (dots) wetting.

6.2.5. Interacting grafted surfaces in vacuum (GVG)

This paragraph presents evaluation of the potential of mean force between approaching grafted surfaces separated by vacuum, denoted by PMF^{GVG} . Figure 6.18 presents evaluations of PMF^{GVG} with the chain length of grafted chains, N_{g} , varying from 24 to 768 skeletal bonds and the grafting density, σ_{g} , varying from 0.1 to 0.4 nm⁻². Low wetting (LW) conditions have been used for solid/polymer interactions.

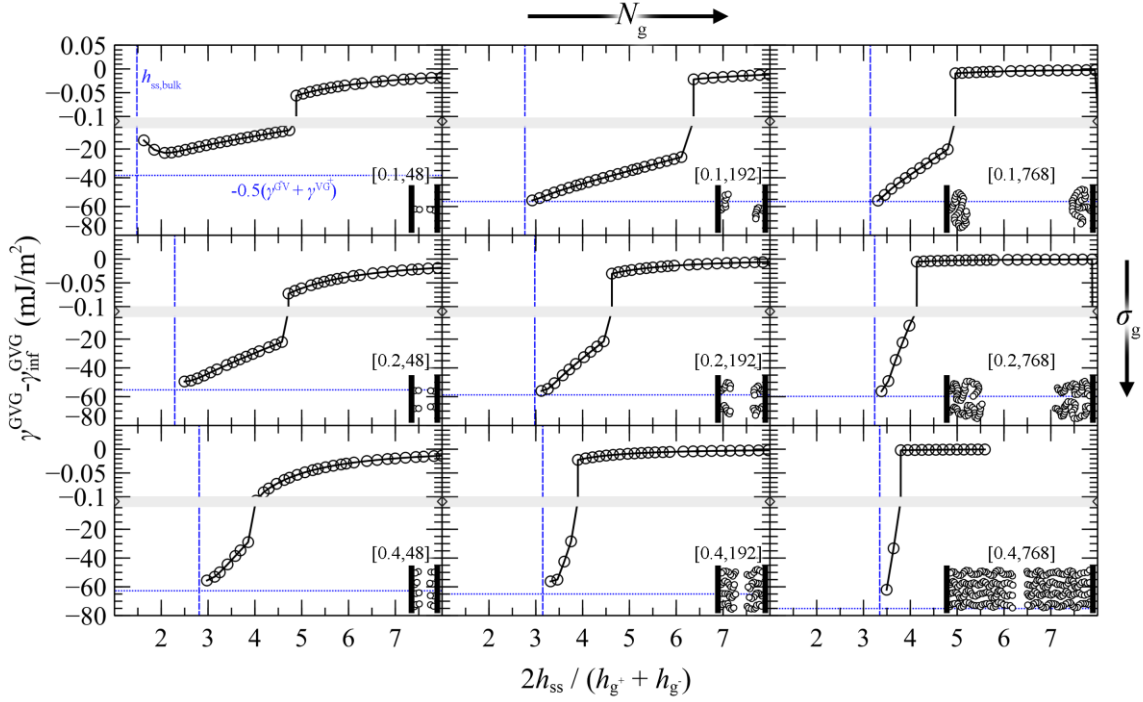


Figure 6.18 Potential of mean force between two opposing grafted surfaces exposed to vacuum (GVG). Calculations were performed with the SL-SGT EoS. Values of σ_g (in nm^{-2}) and N_g are indicated inside the brackets. Horizontal blue lines mark minus the average surface free energy of the individual grafted films. Vertical blue lines mark the thickness h_{ss} , that would correspond to the total mass of grafted polymer at bulk density. Insets: each bead denotes a segment of 24 PS skeletal bonds. Bands denote scale changes along the axes.

Looking at Figure 6.18 above, the evolution of PMF^{GVG} with decreasing plate-plate distance can be classified in three distinct regimes described below. Chain configurations across these regimes are illustrated in the inset of Figure 6.20.

1. For large separation distances, the opposing polymer brushes interact weakly with each other and the dominant contribution to PMF^{GVG} is that of solid/polymer and solid/solid *Hamaker* interactions (e.g., compare with the dotted lines in Figure 6.8b,d).
2. Below a critical plate-plate distance, PMF^{GVG} decreases abruptly, indicating the manifestation of a phase transition, where the opposing brushes interpenetrate each other and form a single film in the central region of the system. In addition, low density regions are formed in the vicinity of the solid surfaces, indicating that the brushes have been stretched significantly towards the bulk region that has formed.
3. Decreasing the plate-plate separation further makes the brushes more compact. The low-density regions next to the solid plates become suppressed, until the free energy becomes commensurate to minus the mean surface free energy of isolated brushes, $-0.5(\gamma^{\text{GV}} + \gamma^{\text{VG}})$.

Further squeezing of the brushes leads to increased reduced densities above unity, as indicated by the vertical dashed lines in Figure 6.18.

Figure 6.19 illustrates the segment density profiles corresponding to the PMF^{GVG} calculations of Figure 6.18.

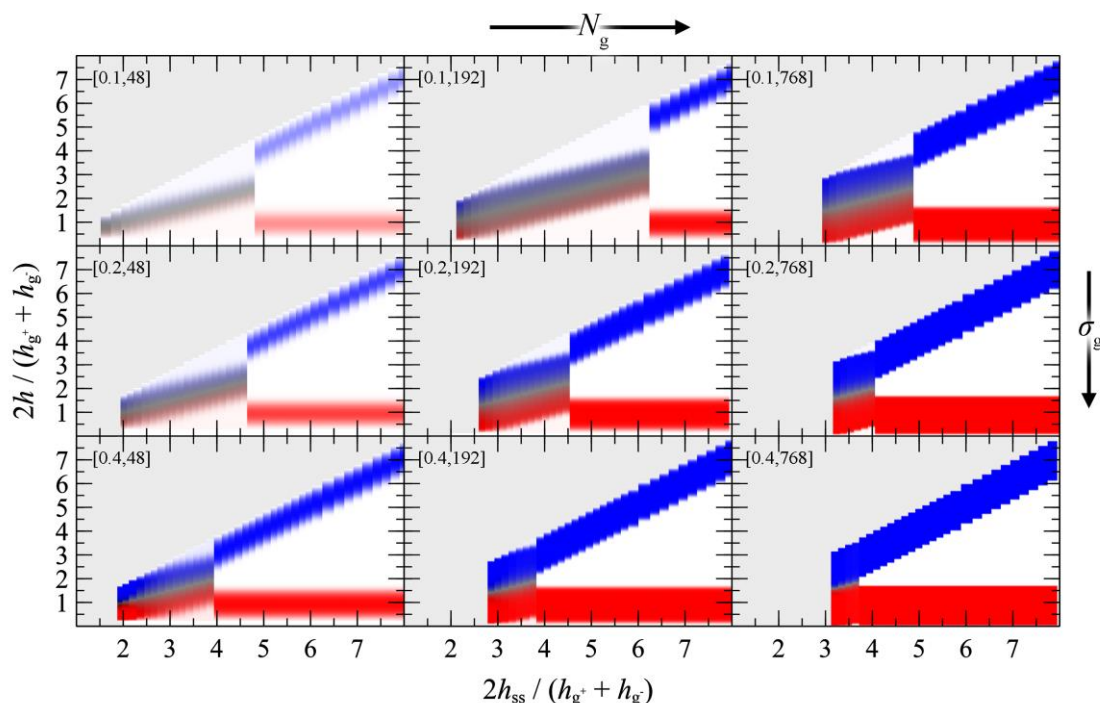


Figure 6.19 Reduced segment density distributions corresponding to the PMF^{GVG} panels in Figure 6.18. The profiles were derived as functions of the plate-plate distance (abscissa) and the distance from the left wall (ordinate) in reduced units. Red/blue colors correspond to regions with high density ($\varphi_c = 1$) of $c = g^-, g^+$ chains. White corresponds to vacuum. Grey denotes regions which lie outside the modeled domain or have not been evaluated at all. Labels in brackets denote σ_g (in nm^{-2}) and N_g .

A more detailed picture can be unveiled by inspecting the evolution of individual contributions to the energy terms, which are shown in Figure 6.20 below.

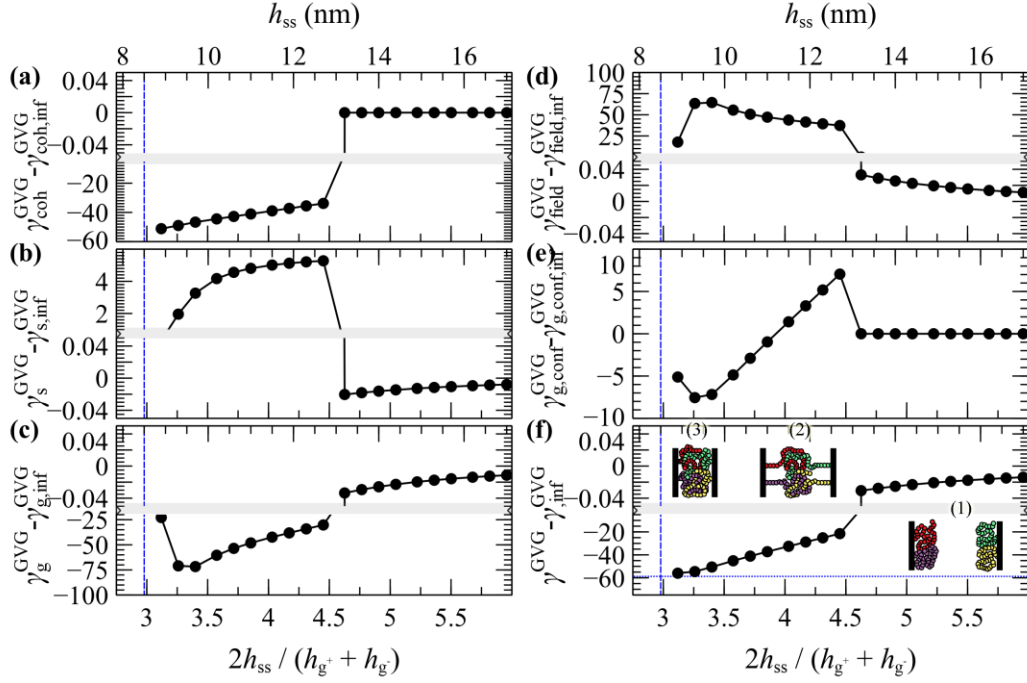


Figure 6.20 Free energy partial contributions to the *potential of mean force* of two approaching grafted surfaces exposed to vacuum. Grafting density, $\sigma_g = 0.2 \text{ nm}^{-2}$ and length of grafted chains, $N_g = 192$ skeletal bonds. **(a)** cohesive interactions, **(b)** solid/polymer interactions, **(c)** entropic contribution from grafted chains, **(d)** density-field interactions, **(e)** stretching contribution from grafted chains, **(f)** total grand potential. The vertical lines denote plate-plate distances where the reduced density exceeds unity. The horizontal dotted line in **(f)** depicts $-0.5(\gamma^{G^v} + \gamma^{G^+})$. The insets in **(f)** depict grafted chain configurations across the 1st, 2nd and 3rd regime. Bands denote scale changes along the axes.

The thermodynamics of the merger seems to be dominated by cohesive interactions among chain segments. According to Figure 6.20a, below some critical distance, the abrupt drop of the cohesive term ($\gamma_{\text{coh}}^{\text{GVG}}$) indicates the enthalpic gain upon film merging. At the same time, the more positive solid/polymer interactions in Figure 6.20b (γ_s^{GVG}) indicate the enthalpic penalty due to the departure of a large portion of the brushes from the solid surfaces.

The term associated with the entropy of the grafted chains (γ_g^{GVG}) in Figure 6.20c is of particular interest. At a first glance, it does not quite reflect the entropic penalty due to the stretching of grafted chains. However, this can be attributed to that γ_g^{GVG} itself does not reflect the total conformational contribution to the grand potential, since it is evaluated in presence of the field.²⁴ The conformational component of the grafted chains can be retrieved as follows:²⁴

$$\gamma_{g,\text{conf}}^{\text{GVG}} = \gamma_g^{\text{GVG}} + \gamma_{g,\text{field}}^{\text{GVG}} \quad 6.10$$

with $\gamma_{g,\text{field}}^{\text{GVG}}$ being the field experienced by the grafted chains:

$$\gamma_{\text{g,field}}^{\text{GVG}} S_{\text{solid}} = - \int_{\mathcal{R}} d\mathbf{r} \left\{ \left(\rho_{\text{g}^-}(\mathbf{r}) + \rho_{\text{g}^+}(\mathbf{r}) \right) w'_{\text{ifc}}(\mathbf{r}) \right\} \quad 6.11$$

Indeed, as indicated in Figure 6.20e, the conformational entropy of the grafted chains increases abruptly below a critical distance (entropic penalty due to stretching) and then decreases with decreasing \tilde{h}_{ss} , as the film becomes more compact and the grafted chains become less stretched. In summary, the manifestation of the phase transition depends on an interplay among three dominant factors:

- An enthalpic gain due to the lower surface area of the merged brushes, which increases with increasing *surface tension*, i.e., higher energy cost of grafted chain segments being exposed to vacuum.
- An enthalpic loss due to detachment of the grafted film from the solid surfaces that depends on the strength of solid/polymer interactions.
- A conformational penalty associated with chain stretching.

As far as the equilibrium plate-to-plate distance (after the merger) is concerned, for low $\sigma_{\text{g,seg}}$ products, this is on the order of $1.5 \tilde{h}_{\text{ss}}$, or $0.75 (h_{\text{g}^+} + h_{\text{g}^-})$. This means that the two silica plates come considerably closer to each other than the sum of the individual root-mean-squared brush thickness, since the brushes lie in the *mushroom* regime and can readily interpenetrate each other. On the other hand, for the case of high $\sigma_{\text{g,seg}}$, the brushes are more compact, and hence, one could make meaningful predictions using *Alexander's* model for incompressible brushes (Appendix A).^{126,127} Indeed, the denser brushes investigated here become compact ($\rho > \rho_{\text{seg,bulk}}$) at separation distances on the order of $\tilde{h}_{\text{ss}} \sim 2\sqrt{3} \sim 3.4$, e.g., compare with the vertical line in the bottom-right panel of Figure 6.18.

Overall, the effect of asymmetry on the equilibrium distance is expected to be minor. Indeed, according to Figure 6.18, brushes with equal $\sigma_{\text{g,seg}}$ become compact at similar distances. For example, compare the case $(\sigma_{\text{g}}, N_{\text{g}}) = (0.4 \text{ nm}^{-2}, 48)$ with $(0.1 \text{ nm}^{-2}, 192)$ and the case $(0.4 \text{ nm}^{-2}, 192)$ with $(0.1 \text{ nm}^{-2}, 768)$.

6.2.6. Concluding remarks

All of the above results regarding the *potential of mean force* between two planar surfaces (or equivalently of particles with radius large in relation to the chain dimensions) imply some design rules that one can be guided by when addressing such nanostructured systems.

As mentioned earlier, addressing the system of bare solid surfaces can give us an insight on what happens in the limit of very low grafting density. At moderate distances, the behavior of the PMF depends on an interplay between the strength of the solid/polymer, polymer/polymer and solid/solid interactions, as quantified by the *wetting/spreading* phenomena taking place at a single solid/polymer interface.

For *low wetting conditions* ($\theta > 90^\circ$), the PMF becomes weakly repulsive from distances on the order of 3.5-10 nm, but the polymer film is metastable with respect to the chains evacuating the gap and the solid surfaces snapping into direct contact with each other. The spontaneous manifestation of cavities can lead to eventual collapse of the surfaces, leading to agglomeration. This is a manifestation of the allophobic dewetting phenomenon observed in the low wetting condition examined here. On the contrary, for *high* ($\theta < 90^\circ$) and *perfect* (imaginary θ) *wetting conditions*, the PMF is practically zero at large distances and starts rising steeply below ca. 2 nm. A free energy barrier on the order of 20-80 mJ/m² has to be overcome for the solid surfaces to come into direct contact. The system is stabilized in terms of the solid surfaces sticking to each other, and is trapped in a potential whose depth is on the order of ca. 20 mJ/m² with respect to a melt-free system, e.g., with respect to the dotted lines shown in Figure 6.8. Matrix chains adhering to the solid surfaces resist compression and screen the solid/solid attractive interactions, as if they were grafted. The PMF between bare solid surfaces does not depend strongly on the length of matrix chains; therefore, varying the molecular weight of matrix chains does not have a significant effect on the stability of the system.

In the case of low wetting, the presence of grafted chains is imperative for the solid surfaces to be stabilized. In particular, when the grafted chain lengths and grafting densities are sufficiently high (see Figure 6.17), the grafted chains effectively screen the solid/solid interactions, preventing the two plates from approaching each other at a distance where they would experience the full depth of the plate-plate distance. In many cases, the PMF can become strictly repulsive, but a prerequisite for this is that the grafted chains be longer than those of the matrix. The longer the grafted chains in comparison to the matrix chains, the steeper the repulsive PMF that develops and the longer the range over which it manifests itself. Short matrix chains are able to penetrate the brush of long grafted chains and swell it, increasing the range of the repulsive interaction. In this case, the most important design rule that has to be met, as already reported in experimental studies,^{18,22,29-31} is that the grafted chains need to be longer than the matrix chains, $N_m/N_g \leq 1$. On the other hand, when the matrix chains start becoming larger than the grafted, then immediately an attractive well is exhibited in the PMF (*autophobic*

dewetting); solvent conditions become worse for the grafted chains. Moreover, this behavior is intensified at high surface grafting densities. In these cases, the density of grafted chain segments near the interface is so high, that matrix chains are not able to penetrate into the region occupied by the grafted chains, even if matrix chains have lower molecular weight. Thus, the use of excessive grafting densities is to be avoided for the purpose of steric stabilization, even if $N_g > N_m$.

For the asymmetric cases, where the grafting density or the molecular weight of grafted chains differs on each silica plate, it seems that the introduction of asymmetries does not give rise to a minimum in the PMF, as long as deviations from the symmetric case are small, and the effective ratio $N_m / N_{\bar{g}}$ (see eq 6.9) is kept constant. Individually, adjusting the asymmetry on the grafting density or on the molecular weight of grafted chains does not alter significantly the PMF, with the former having a stronger influence. This implies that, when experimentalists are trying to achieve the dispersion of two slabs (or large grafted particles) inside a polymer melt, there is some room for deviation from symmetry, especially as regards the molecular weight of grafted chains. Nonetheless, when there are large discrepancies between both the grafting densities and the molecular weight ratios, then the system will eventually exhibit an attractive well. Again, this phenomenon is more pronounced when the molecular weight of matrix chains increases.

The characteristics of the well-depth of PMF^{GMG} reflect the “softness” of the brush as well as the associated tendency to penetrate into each other.²⁵ Wrapping together all the parameters which influence the attractive well of the PMF^{GMG} between the two plates, one can generate empirical design rules regarding the prediction of stable configurations of opposing plates (membranes or fine particles) as a function of the mean grafting density, the chain length of grafted chains and the chain length of matrix chains.

According to Hasegawa et al.,²⁶ PMF is expected to become repulsive for $\sigma_g \leq b_k^{-2} N_{k,\bar{g}}^{-1/2}$, with $N_{k,c} = N_c C_{\infty} l_{c-c}^2 / b_k^2$ being the number of Kuhn segments that comprise a chain. In addition, as has been demonstrated in Section 6.2.4 of the present thesis, PMF^{GMG} becomes more attractive when the length of matrix chains increases with respect to the effective length of grafted chains, $N_m / N_{\bar{g}}$ (or $N_{k,m} / N_{k,\bar{g}}$ in Kuhn units). Note that the effective ratio, $N_m / N_{\bar{g}}$, takes account of the asymmetry in both the grafting density and the chain length in the two plates. Putting all these together, it would be instructive to present the depth of the attractive well as a function of

the dimensionless quantity $\sigma_{\bar{g}} b_k^2 N_{k,\bar{g}}^{1/2} [N_{k,m} / N_{k,\bar{g}}]$, or $\sigma_{\bar{g}} b_k^2 N_{k,\bar{g}}^{-1/2} N_{k,m}$ for simplicity. Such comparisons are shown in the master plot of Figure 6.21 below, against all the data gathered here for both the symmetric and asymmetric surfaces.

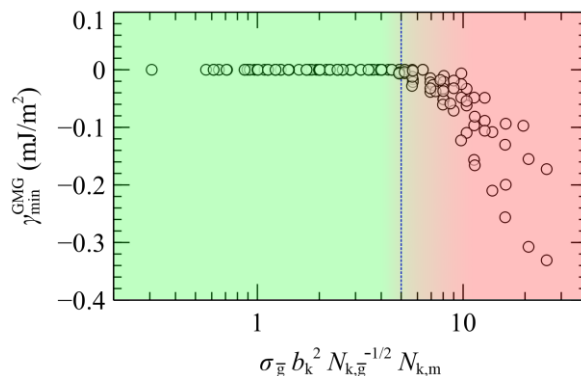


Figure 6.21 Well-depth of PMF^{GMG} as a function of all design degrees of freedom of the interfacial systems of two plates. The degrees of freedom are combined in the dimensionless quantity: $\sigma_{\bar{g}} b_k^2 N_{k,\bar{g}}^{-1/2} N_{k,m}$. Green/red shades illustrate regime with repulsive/attractive interactions between the opposing plates. The vertical dashed line is a guide to the eye.

According to Figure 6.21 presented above, the attractive interactions become negligible for $\sigma_{\bar{g}} b_k^2 N_{k,\bar{g}}^{-1/2} N_{k,m} < 5$, therefore for such combinations, the surfaces are expected to stabilize. For larger values, on the other hand, in most cases the plates tend to stick to each other (*aggregation*). Furthermore, we must take into account that in the limit of very small average grafting density, the system will be led towards the case of bare solid plates in contact with vacuum, thus the melt is expected to evacuate the gap and the plates will spontaneously come in contact to each other, According to our calculations, the polystyrene melt remains stable even for low grafting densities, on the order of 0.1 nm^{-2} ($\sim 0.33 b_k^{-2}$), thus for these systems, the region of stability could be traced along the range $0.33 \leq \sigma_{\bar{g}} b_k^2 \leq 5 N_{k,\bar{g}}^{1/2} N_{k,m}^{-1}$. Our findings conform with experimental studies concerning systems of the same^{22,30,31} or similar^{18,29,30} chemical constitution and with theoretical investigations,^{5,25,26} whilst accounting for the effect of asymmetry as well.

6.3. Spherical Surfaces

6.3.1. Background

The ability to efficiently disperse inorganic NPs inside polymer matrices is essential for the design and manufacturing of well-behaving nanocomposite materials.^{7,135,186,234} The mechanical and viscoelastic properties of polymeric materials are enhanced when hosting well dispersed

nano-sized particles.^{42,196,235–237} There is plenty of experimental studies where the structural, dynamic and mechanical properties of PGNs are investigated.^{14–16,42–44,81,138} Furthermore, it is of high interest to the academic community and industrial practice to investigate the properties of PGNs when they are isolated from any polymer melt or solvent.^{43,199,226,227,238} The latter systems are particularly important for the design of state-of-the-art separation membranes.^{47,50,120,229}

The interactions between two particles which are embedded in polymer melt or a solvent are strongly dependent on the NP size.^{21,24} Spherical NPs with small radius are easier to disperse, because their shape and increased curvature offer more space to the grafted chains to adopt a variety of conformations; hence the NPs are prevented from collapsing together.^{204,239} Martin et al.¹⁹⁵ have performed a detailed investigation of the PGN interactions in the case of dissimilar chemistry between grafted and matrix chains, giving insights on the role of enthalpic interactions on the *potential of mean force* and stabilization of the system. Ghanbari et al.²⁴⁰ have studied the dependence of the dynamics of matrix and grafted chains on the grafting density and molecular weight of matrix chains via coarse-grained *molecular dynamics* simulations.

6.3.2. PMF between two grafted silica nanoparticles

For the case of two interacting silica NPs in polymer melt, the geometry and discretization of the considered domain is presented in Figure 6.22. The two NPs have the same radius, $R_S = 2$ nm, which is kept constant in all PMF calculations. As shown by the orientation of axes in Figure 6.22, the surface-to-surface distance, h_{SS} , between the two particles is varied along the x -axis.

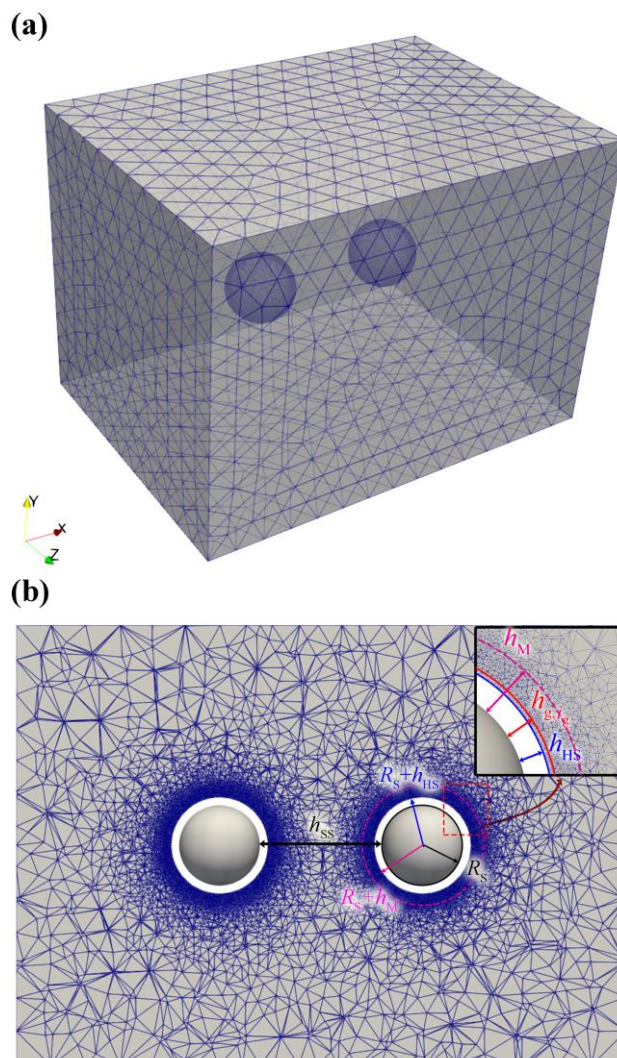


Figure 6.22 Meshing illustration of two NPs with $R_s = 2$ nm inside a box with dimensions $30 \times 22 \times 22$ nm³. **(a)** Perspective view showing the mesh at the periodic (edge) and *Dirichlet* (solid) boundaries. **(b)** An xy -slice passing through the centers of the NPs (created with the Slice operation of the Paraview software). For the calculation of the PMF, the distance between the two NPs is varied along the x -axis. The inset depicts an enlarged view of the solid/polymer interface; the solid red line corresponds to the distance of grafting points from the solid surface, while the dotted magenta line corresponds to the thickness of the fine-mesh region.

The grafting distributions we have addressed are illustrated in Figure 6.23 below and they correspond to: equidistant grafting with density $\sigma_g = 0.8$ nm⁻² corresponding to 40 grafted chains per NP (“E40-E40”), equidistant grafting with density $\sigma_g = 0.3$ nm⁻² corresponding to 15 grafted chains per NP (“E15-E15”), and nonequidistantly grafted chains where the relative orientation of grafting of the two NPs is: parallel to each other and parallel to the x -axis (“H15-H15”, for parameters of grafting see third row of Table 6-2), parallel to each other and perpendicular to the x -axis (“V15-V15”, for parameters of grafting see fourth row of Table 6-2) and perpendicular to each other (“H15-V15”, for parameters of grafting see fifth row of Table 6-2).

Table 6-2. Parameters for distributing grafting points on the surface of two spherical NPs. Two equidistant and three non-equidistant cases are examined: equidistant grafting with density 0.8 nm^{-2} (E40-E40), equidistant grafting with density 0.3 nm^{-2} (E15-E15), horizontal parallel orientation (H15-H15), vertical parallel orientation (V15-V15) and perpendicular orientation (H15-V15). The radius of the two NPs is $R_S = 2 \text{ nm}$.

Distribution (Particle radius, $R_S = 2$ nm)	NP ₁		NP ₂	
	Pole ₁ (θ, φ)	Pole ₂ (θ, φ)	Pole ₁ (θ, φ)	Pole ₂ (θ, φ)
E40-E40	Algorithm of ref 103 for generation of 40 grafting points on the surface of each NP			
E15-E15	Algorithm of ref 103 for generation of 15 grafting points on the surface of each NP			
H15-H15	(0.0, 0.0)	(π , 0.0)	(0.0, 0.0)	(π , 0.0)
V15-V15	($+\pi/2$, 0.0)	($-\pi/2$, 0.0)	($+\pi/2$, 0.0)	($-\pi/2$, 0.0)
H15-V15	(0.0, 0.0)	(π , 0.0)	($+\pi/2$, 0.0)	($-\pi/2$, 0.0)

In the equidistant grafting cases, E40-E40 and E15-E15, we have implemented the algorithm of ref ¹⁰³ to generate 40 and 15 chains per NP, respectively. In Figure 6.24, we present the density profiles of grafted chain segments in the three-dimensional space for surface-to-surface distance equal to $h_{SS} = \{2.20, 6.12, 12.09\}$ nm and for all different grafting orientations of the NPs. In this figure, the length of matrix chains is equal to that of grafted chains, $N_m = N_g = 96$ skeletal carbon bonds.

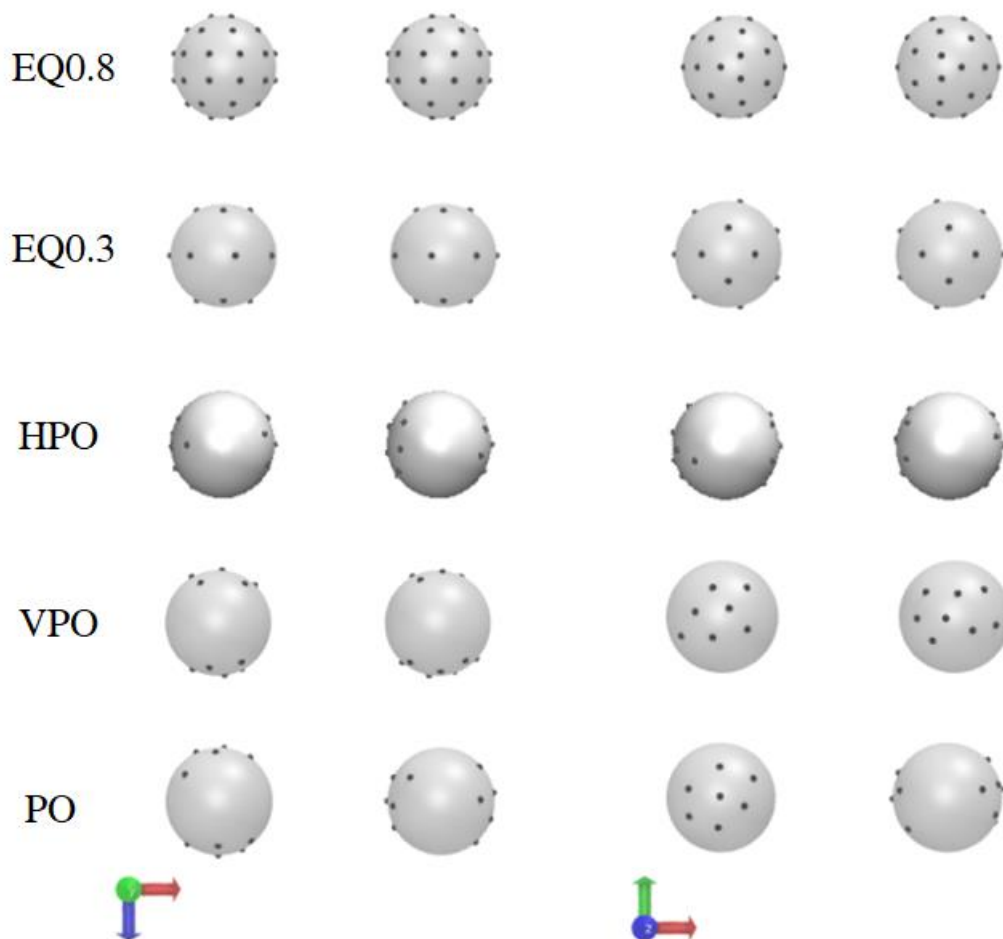


Figure 6.23 VMD representation of distributions of grafting points for PMF calculation between two spherical particles. Two equidistant and three non-equidistant cases are examined: equidistant grafting with density 0.8 nm^{-2} (E40-E40), equidistant grafting with density 0.3 nm^{-2} (E15-E15), horizontal parallel orientation (H15-H15), vertical parallel orientation (V15-V15) and perpendicular orientation (H15-V15). The radius of the two NPs is $R_S = 2 \text{ nm}$.

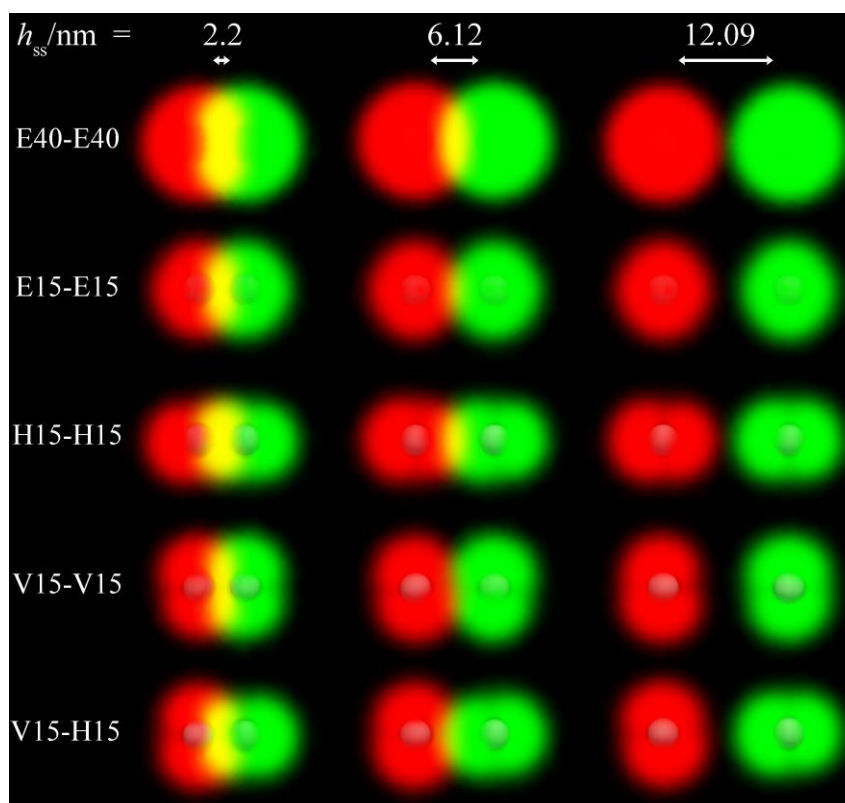


Figure 6.24 Three-dimensional density profiles of polystyrene chains grafted on the surfaces of two silica NPs. The brush of the left NP is plotted with red color, while that one of the right NP is plotted with green color. Five different grafting cases are considered: equidistant grafting with 40 grafted chains per NP (E40-E40), equidistant grafting with 15 grafted chains per NP (E15-E15), and three non-equidistant cases with 15 grafted chains per NP: H15-H15, V15-V15 and H15-V15).

In Figure 6.25 and Figure 6.26, we plot the PMF between for equidistant and non-equidistant grafting, respectively, and for varying matrix-to-grafted chain length ratio. On the x -axis, we vary the surface-to-surface NP distance, which assumes the values $h_{SS} = \{2.20, 2.80, 3.46, 4.12, 4.80, 5.46, 6.12, 12.09, 12.76, 13.42, 14.08\}$ nm. In the last four distances, the brushes of the two NPs do not interact with each other (e.g., see the third column of Figure 6.24, so the average free energy density of the system in these distances is equivalent to the energy of the particles when they are at infinite distance from each other. All energies are expressed with reference to the free energy of the two grafted particles at infinite distance. On the y -axis, we report this (relative) free energy in kJ/mol. In Table 6-3, Table 6-4 and Table 6-5, we report the values of the PMF for different values of the N_m/N_g ratio and varying the grafting distribution. These data are also illustrated in the master plot of Figure 6.28. In all cases, we have taken into account the *Hamaker* interaction between the silica-silica surfaces, which in the distances of interest is negligible compared to the PMF of the system. Nonetheless, it is interesting to observe that the

grafted chains prevent the particles from getting closer than 2.2 nm, where they could potentially collapse easier due to the well of the silica-silica interaction. One could certainly argue that this *Hamaker* potential concerns bare particles and therefore if they were grafted (as in our case), the entropic factors associated with grafted chains would counterbalance this attraction of the particles. This is totally reasonable, nonetheless, the logic behind our calculations and distance sampling is that, if the particles are not even allowed (due to the presence of grafted chains) to come at distance where their *Hamaker* attraction would be a factor promoting destabilization, then there is absolutely no way that the thermodynamics will allow them to coagulate. The *Hamaker* potential between two bare silica particles with $R_S = 2$ nm is depicted in the following Figure 6.27. The absolute values of the potential for surface-to-surface distances larger than 2.2 nm (which is the minimum distance for PMF calculations with SCFT, see dashed line in Figure 6.27) are lower than 0.2 kJ/mol.

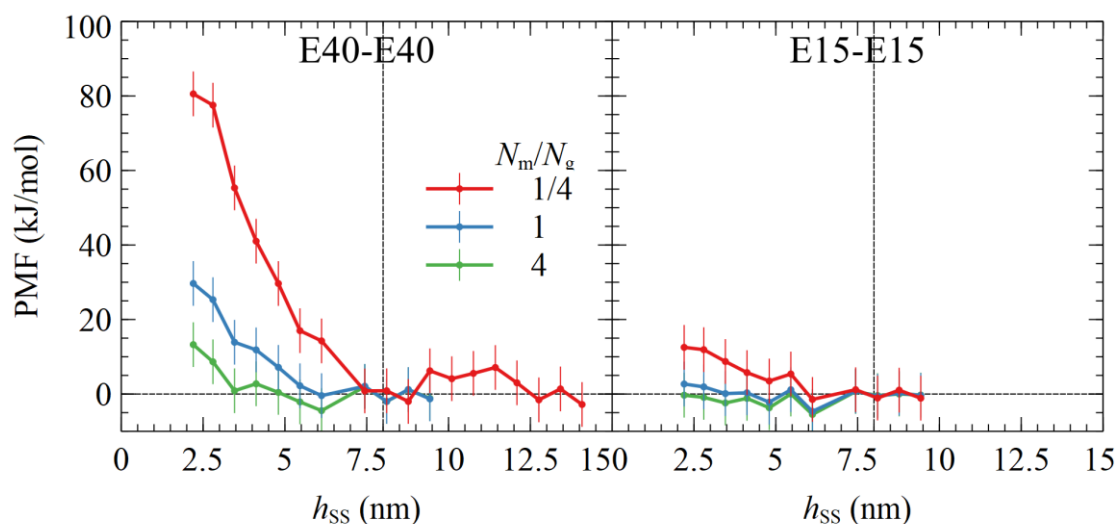


Figure 6.25 Potential of mean force between two silica NPs equidistantly grafted with polystyrene chains. The two NPs are embedded in a matrix of polystyrene chains and the matrix to grafted chain length ratio assumes the values $N_m/N_g = \{0.25: \text{red}, 1.0: \text{blue}, 4.0: \text{green}\}$. The x -axis represents the surface-to-surface distance between the two NPs. In the left panel, each NP is grafted with 40 polystyrene chains, while in the right panel, each NP is grafted with 15 polystyrene chains. The radius of the particles is equal to $R_S = 2$ nm.

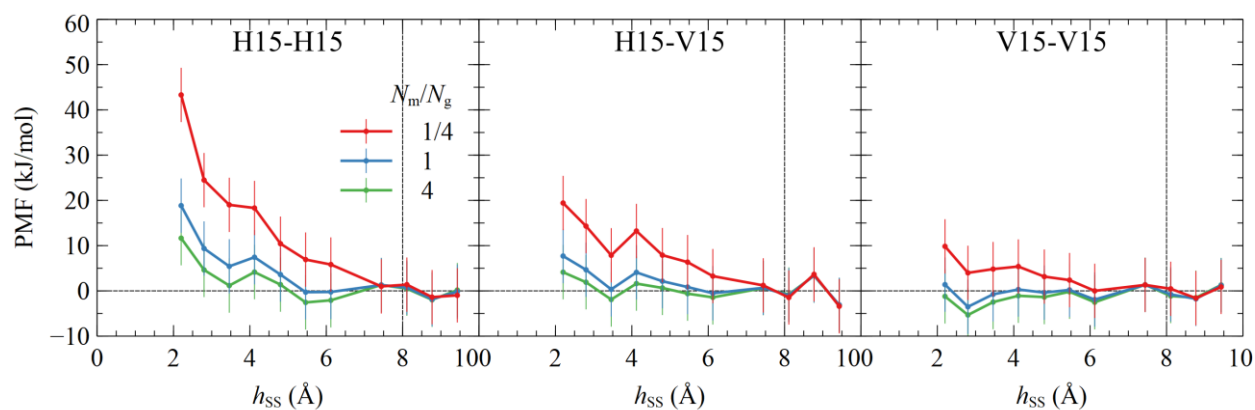


Figure 6.26 Potential of mean force between two silica NPs non-equidistantly grafted with polystyrene chains. The two NPs are embedded in a matrix of polystyrene chains and the matrix to grafted chain length ratio assumes the values $N_m/N_g = \{0.25: \text{red}, 1.0: \text{blue}, 4.0: \text{green}\}$. The x -axis represents the surface-to-surface distance between the two NPs. In the left/middle/right panel, the two NPs are grafted according to H15-H15, H15-V15 and V15-V15 orientations, respectively (see Table 6-2 and Figure 6.23). The radius of the particles is equal to $R_S = 2$ nm.

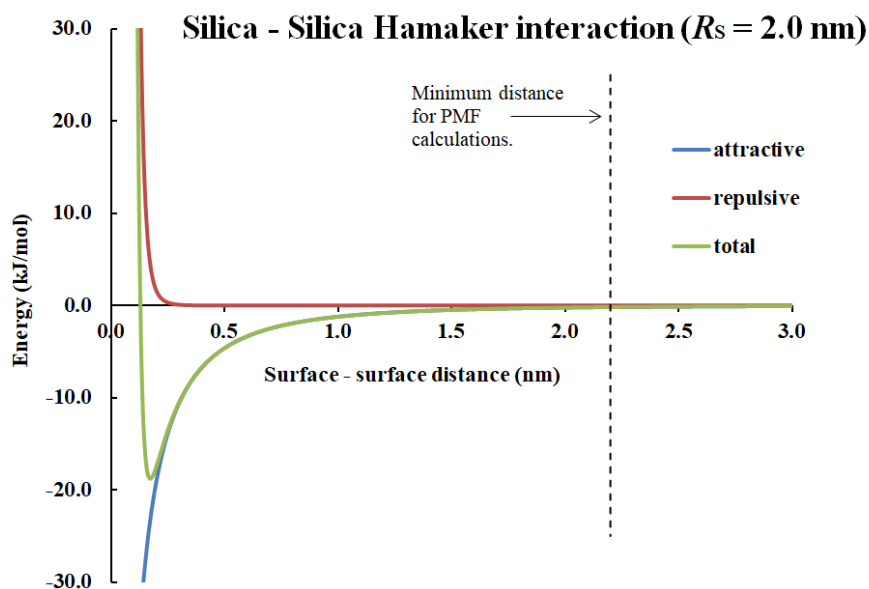


Figure 6.27 Hamaker interaction between two bare silica NPs with radius $R_S = 2$ nm. Blue color corresponds to the attractive term, red color to the repulsive term, and the final potential is depicted with green color. The depth of this potential is equal to -18.7 kJ/mol and the width of the potential is approximately 1.5 nm (after this distance the potential assumes absolute values lower than 0.2 kJ/mol).

Table 6-3 Potential of mean force between silica NPs embedded in polystyrene matrix of length $N_m = 24$ skeletal bonds. The radius of the NPs is equal to $R_S = 2$ nm and the length of grafted chains is equal to $N_g = 96$ skeletal bonds. The PMF is reported for all grafting distributions that we have investigated. The values of the present table are plotted in the left panel of Figure 6.28.

	h_{ss} (nm)	E40-E40 (kJ/mol)	E15-E15 (kJ/mol)	H15-H15 (kJ/mol)	V15-V15 (kJ/mol)	H15-V15 (kJ/mol)
$N_m = 24$	2.20	80.56	12.53	43.30	9.83	19.42
	2.80	77.53	11.90	24.48	3.98	14.31
	3.46	55.33	8.73	19.01	4.81	7.86
	4.12	41.02	5.75	18.31	5.38	13.23
	4.80	29.66	3.49	10.43	3.15	7.90
	5.46	17.00	5.38	6.91	2.38	6.35
	6.12	14.26	-1.45	5.82	0.00	3.26
	12.09	3.01	1.16	0.99	1.31	1.21
	12.76	-1.57	-1.08	1.38	0.45	-1.46
	13.42	1.37	1.04	-1.38	-1.61	3.65
	14.08	-2.81	-1.12	-0.99	0.87	-3.40

Chapter 6. Calculations involving two particles/surfaces

Table 6-4 *Potential of mean force* between silica NPs embedded in polystyrene matrix of length $N_m = 96$ skeletal bonds. The radius of the NPs is equal to $R_s = 2$ nm and the length of grafted chains is equal to $N_g = 96$ skeletal bonds. The PMF is reported for all grafting distributions that we have investigated. The values of the present table are plotted in the middle panel of Figure 6.28.

$N_m = 96$	h_{ss} (nm)	E40-E40 (kJ/mol)	E15-E15 (kJ/mol)	H15-H15 (kJ/mol)	V15-V15 (kJ/mol)	H15-V15 (kJ/mol)
	2.20	29.67	2.69	18.84	1.38	7.70
2.80	25.32	1.92	9.36	-3.52	4.67	
3.46	13.89	0.12	5.42	-0.76	0.33	
4.12	11.85	0.33	7.43	0.30	4.09	
4.80	7.16	-2.20	3.60	-0.39	2.13	
5.46	2.22	1.14	-0.30	0.21	0.84	
6.12	-0.43	-4.66	-0.24	-1.92	-0.53	
12.09	2.08	0.75	1.29	1.32	0.67	
12.76	-1.99	-0.59	0.73	-0.78	-0.98	
13.42	1.21	0.21	-1.85	-1.77	3.39	
14.08	-1.30	-0.37	-0.17	1.22	-3.08	

Table 6-5 *Potential of mean force* between silica NPs embedded in polystyrene matrix of length $N_m = 384$ skeletal bonds. The radius of the NPs is equal to $R_s = 2$ nm and the length of grafted chains is equal to $N_g = 96$ skeletal bonds. The PMF is reported for all grafting distributions that we have investigated. The values of the present table are plotted in the right panel of Figure 6.28.

$N_m = 384$	h_{ss} (nm)	E40-E40 (kJ/mol)	E15-E15 (kJ/mol)	H15-H15 (kJ/mol)	V15-V15 (kJ/mol)	H15-V15 (kJ/mol)
	2.20	13.25	-0.32	11.64	-1.21	4.13
2.80	8.65	-0.90	4.63	-5.33	1.91	
3.46	0.88	-2.40	1.17	-2.48	-1.91	
4.12	2.74	-1.16	4.15	-1.08	1.61	
4.80	0.43	-3.69	1.38	-1.37	0.65	
5.46	-2.11	0.00	-2.56	-0.20	-0.61	
6.12	-4.46	-5.49	-2.08	-2.52	-1.44	
12.09	1.99	0.67	1.31	1.35	0.61	
12.76	-2.00	-0.41	0.49	-1.14	-0.81	
13.42	1.15	0.01	-1.97	-1.51	3.36	
14.08	-1.14	-0.26	0.17	1.30	-3.17	

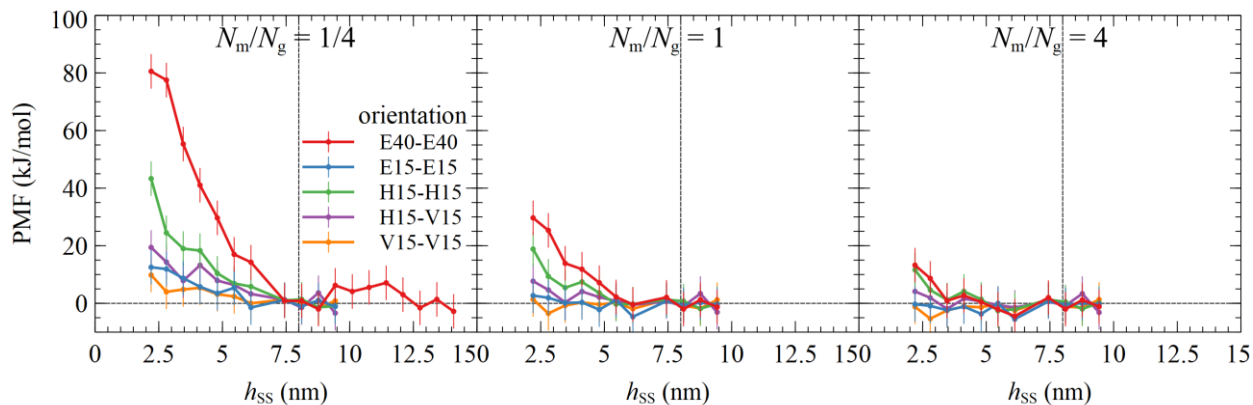


Figure 6.28 Potential of mean force between two grafted silica NPs embedded in polystyrene matrix. The matrix to grafted chain length ratio assumes the values $N_m/N_g = \{0.25: \text{left panel (Table 6-3)}, 1.0: \text{middle panel (Table 6-4)}, 4.0: \text{right panel (Table 6-5)}\}$. In each panel, we vary the grafting orientation on the surfaces of the two NPs: {E40-E40: red, E15-E15: blue, H15-H15: green, H15-V15: purple, V15-V15: yellow}. The x -axis represents the surface-to-surface distance between the two NPs. The radius of the particles is equal to $R_S = 2$ nm.

Looking at Figure 6.25 and Figure 6.26, we observe that when $N_m < N_g$, the PMF increases with decreasing surface-to-surface NP distance. This is totally expected, since the smaller matrix chains can interpenetrate into the brushes and swell them towards the bulk, increasing the conformational cost associated with their conformations. The error in the estimated free energy is a consequence of the randomness of the mesh of elements that is used for the solution of *Edwards* in each case, which is directly related to the delta function and initial condition assigned in the *propagator* of each grafting chain.

We can qualitatively compare our plot with the black line of Figure 5 of ref 206 and see the satisfying agreement between the two plots. It would not be of essence to quantitatively compare the two plots, because in the case of Munao et al.,²⁰⁶ a hybrid particle-field methodology is implemented and furthermore, there are some differences in the parametrization of the system. For example, the description bonded and nonbonded interactions, and therefore the compressibility of the polymer, between the two models may be quite different which is directly related to density deviations and their impact on the energy of the system.

In Figure 6.28, we can clearly see the impact of the matrix-to-grafted chain length ratio (increasing from left panel to the right) on the stability of the system. When the length of matrix chains becomes equal to that of grafted chains (middle panel), then only the E40-E40 and H15-H15 distributions are able to maintain the stability of the system. Furthermore, when $N_m = 4N_g$, having 15 chains grafted per particle in H15-H15 distribution (green line), becomes equivalent to having 40 chains equidistantly distributed on each particle (red line).

6.3.3. Concluding Remarks

In this last chapter of the thesis, we have presented thorough calculations regarding the interactions of two spherical silica nanoparticles which are grafted with polystyrene chains and they are embedded inside polystyrene melt. These calculations are quite valuable because they provide with information on how the particles tend to behave under conditions of thermodynamic equilibrium.

Since the two particles are quite small, having a radius equal to 2 nm, these calculations can be considered as the opposite end of the extreme case where the particles are infinitely large, i.e., solid planar surfaces (Section 6.2). To investigate this system, we had to perform three-dimensional calculations where the distance of the two particles is varied and the energy of the system at each distance is measured resulting in the so-called *potential of mean force*. The entropy of grafted chains when the two particles get closer to each other decreases, since there is less available space and therefore the number of available conformations also decreases. This results in a free energy rise which prevents the system from coagulating.

We have derived the *potential of mean of mean force* of the system and the ability of grafted chains to stabilize the nanocomposite system, for different matrix-to-grafted chain length and most importantly, for different distribution of the grafting points on the surfaces of the two particles. We found that, when the relative grafting orientation results in extreme *crowding* of grafted chain segments, then the free energy rises more than the case of equidistant grafting. In other words, keeping all other parameters of the system constant, including the number of grafted chains, the grafting distribution plays a decisive role in the dispersion of the particles. This is a rather novel finding, especially in the context of a field-based method, since it proves that experimentalists can indeed tune the dispersion of chains on the solid surfaces to alter its equilibrium tendencies.

7. SCIENTIFIC AND METHODOLOGICAL ADVANCES

The current section summarizes all the methodological advances and computational tools developed by the author and collaborators.

- We have compiled a thorough and generalized *Self-Consistent Field Theory* mathematical formulation for addressing gas/polymer and solid/polymer interfaces, where the latter involve chains grafted on the solid surface.
- We have developed a *Self-Consistent Field*-based thermodynamic formulation for calculating the *solvation* free energy of a grafted particle inside a polymer matrix. This formalism serves as the basis for quantitative and fast calculation of the *solvation* free energy and the free energy of transferring one or more nanoparticles between different melt or solvent environments. Moreover, to more accurately perform these calculations, we have devised a curvature-dependent *Hamaker* potential to address solid/polymer interactions. This potential takes into account the loss of interacting sites when the radius of the particle decreases.
- Regarding the *potential of mean force* between two opposing solid surfaces, the solid/polymer and solid/solid interactions are described by means of a *Hamaker* potential in conjunction with a ramp potential. We built thermodynamic reference by examining the free energy of single surfaces, either bare or grafted, under various wetting conditions in terms of the corresponding *contact angles* and macroscopic *wetting functions* (i.e., *work of cohesion*, *adhesion*, *spreading* and *immersion*). Subsequently, the *potential of mean force* between bare and grafted plates is derived. These calculations provide us with design rules for the steric stabilization of (fine) grafted particles under various conditions.
- We devised a numerical scheme which is based on the broadly used *Finite Element Method* and combines the virtues of three-dimensional calculations, an explicit *Helmholtz* energy

Chapter 7. Scientific and Methodological Advances

density functional describing the nonbonded interactions among polymer segments and strict mathematical representation of chains grafted on solid surfaces.

- The three-dimensional code offers the possibility to model grafted polymer chains on the solid surfaces according to irregular grafting distributions. For this purpose, we have written a python script which performs a *Monte Carlo* sampling on the surface of the particle and grafts polymer chains according to a certain probability distribution. The same script also handles the generation of equidistant grafting points.
- At a post-processing level, our code gives the ability to calculate the density profiles of segments belonging to individual grafted chains and illustrate it in 3D plots.
- Since we wanted our code to address systems of more than two nanoparticles, we have also developed the feature of periodic boundary conditions in the solution of the *Edwards* diffusion equation by the *Finite Element Method*. This type of boundary conditions requires an association between the nodes of the element which find themselves in opposing faces of the periodic box, so that proper modification of the stiffness matrix can be applied. Furthermore, a lot of refactoring was necessary for the code to execute these additional steps with minimum overhead.
- Using the aforementioned feature of periodic boundary conditions and the mathematical and numerical formalism developed in the context of this thesis, one can perform SCFT based theoretical calculations with multiple polymer-grafted nanoparticles (of any shape) which may be embedded in polymer melt or exposed to vacuum (i.e., particle solids).

APPENDICES

Appendix A Brush Height of Constant Density: Alexander Model

It is instructive to compare the brush height predictions of SCFT with the predictions of a simpler brush model such as that of incompressible *Alexander* brushes. Let hedge be the edge of a brush comprising n_g grafted chains of length N_g , emanating from a NP with radius, R_S , such as the one shown in Figure **A.1a**.

For simplicity let us assume that the segment density is constant and equal to $\rho_{\text{seg,bulk}}$ across the region occupied by the brush of grafted chains, $[R_S, R_S + h_{\text{edge}}]$, which are terminated at hedge; Figure **A.1c** presents the corresponding density profile for this model. Consequently, the volume occupied by the brush can be calculated as the number of the brush segments in this region, divided by its segment density, as show in the following eq A1.

$$V = \frac{n_g N_g}{\rho_{\text{seg,bulk}}} = \frac{\sigma_g 4\pi R_S^2 N_g}{\rho_{\text{seg,bulk}}} \quad \text{A1}$$

where $\sigma_g = N_g / (4\pi R_S^2)$ is the grafting density. Alternatively, the volume of a brush of constant density that terminates at distance h_{edge} can be calculated via eq A2.

$$V = \frac{4}{3} \pi \left[(R_S + h_{\text{edge}})^3 - R_S^3 \right] \quad \text{A2}$$

Combining eqs A1 and A2 and solving with respect to h_{edge} , we get the following expression:

$$h_{\text{edge}} = \left(\frac{3\sigma_g N_g}{\rho_{\text{seg,bulk}}} R_S^2 + R_S^3 \right)^{\frac{1}{3}} - R_S \quad \text{A3}$$

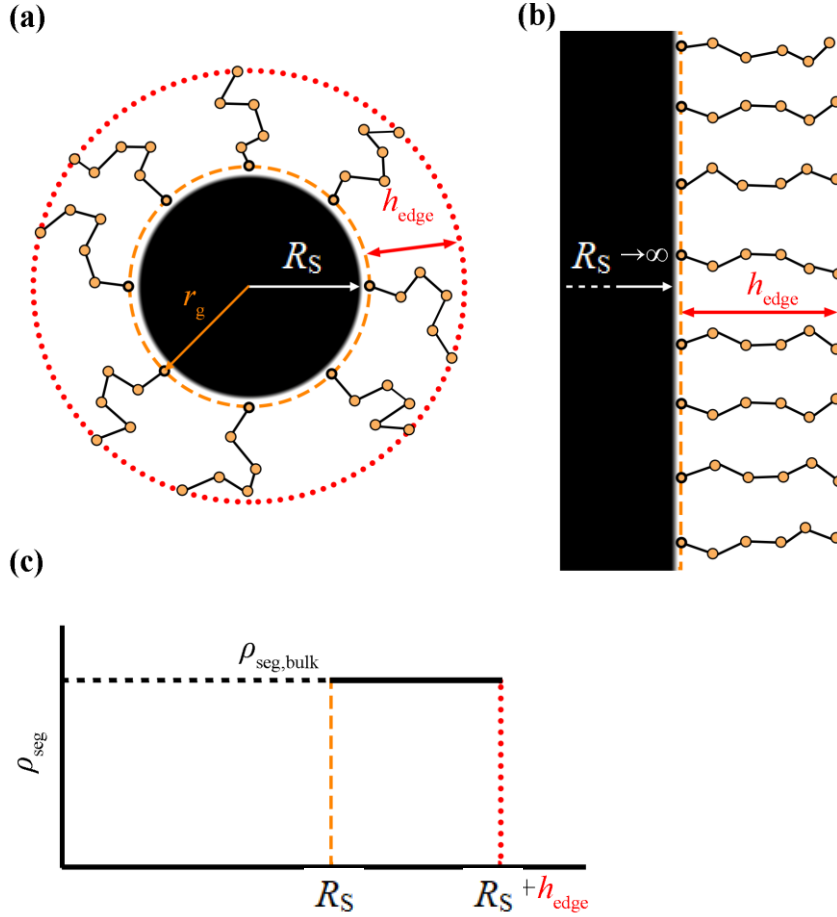


Figure A.1 (a) A nanoparticle with grafted chains forming a brush of height h_{edge} . (b) In the limit $R_S \rightarrow \infty$, the surface of the NP becomes flat. (c) The segment density profile of a brush with constant segmental density, $\rho_{\text{seg,bulk}}$.

With h_{edge} known and given that the density profiles are uniform, $h_{99\%}$ can be calculated as follows:

$$h_{99\%} = 0.99h_{\text{edge}} + R_S \quad \text{A4}$$

Similarly, the mean brush thickness $\langle h_g^2 \rangle^{1/2}$ can be obtained by eq A5.

$$\begin{aligned} \langle h_g^2 \rangle^{1/2} &= \left(\frac{\int_0^{h_{\text{edge}}} h^2 \rho(h) dh}{\int_0^{h_{\text{edge}}} \rho(h) dh} \right)^{1/2} = \left(\frac{1}{h_{\text{edge}}} \int_0^{h_{\text{edge}}} h^2 dh \right)^{1/2} = \frac{h_{\text{edge}}}{\sqrt{3}} \\ &= \frac{1}{\sqrt{3}} \left(\frac{3\sigma_g N_g}{\rho_{\text{seg,bulk}}} R_S^2 + R_S^3 \right)^{1/3} - \frac{R_S}{\sqrt{3}} \end{aligned} \quad \text{A5}$$

In the limit of very large NPs (flat surfaces), $\langle h_g^2 \rangle^{1/2}$ becomes:

$$\lim_{R_{\text{NP}} \rightarrow \infty} \langle h_g^2 \rangle^{1/2} = \frac{\sigma_g N_g}{\sqrt{3} \rho_{\text{seg,bulk}}} = \frac{1}{\sqrt{3}} \lim_{R_{\text{NP}} \rightarrow \infty} h_{\text{edge}} \quad \text{A6}$$

Thus, for this model, appears to be proportional to σ_g and N_g in the limit of large NPs/flat surfaces (i.e., see Figure **A.1b**).

The thermodynamics of these brushes can be described by a total free energy given by the following eq A7:

$$A_{\text{total}} = A_{\text{coh}} + A_{\text{stretch}} \quad \text{A7}$$

where A_{coh} is the contribution from the cohesive interactions described by the free energy density (i.e., $A_{\text{coh}} \equiv \Omega_{\text{coh}}$ from eq 2.39), while A_{stretch} is the entropic contribution from the stretched grafted chains. Given that the grafted chains are terminated at the edge of the brush, and assuming that they can be described as *Gaussian strings*, the contribution of the brushes to the free energy due to stretching can be approximated by the following eq A8.

$$A_{\text{stretch}} = S_{\text{solid}} \sigma_g \frac{3k_B T}{2 \langle R_{\text{end,g}}^2 \rangle} h_{\text{edge}}^2 \quad \text{A8}$$

Combining eqs A3 and A8, the stretching free energy per unit area as a function of R_S is given by eq A9.

$$\frac{A_{\text{stretch}}}{S_S} = \sigma_g \frac{3k_B T}{2 \langle R_{\text{end,g}}^2 \rangle} \left[\left(\frac{3\sigma_g N_g}{\rho_{\text{seg,bulk}}} R_S^2 + R_S^3 \right)^{\frac{1}{3}} - R_S \right]^2 \quad \text{A9}$$

Appendix B Grand canonical partition function and Hamiltonian

We consider a polymer melt within an arbitrarily shaped three-dimensional region \mathcal{R} of volume V at temperature T . The region \mathcal{R} is not necessarily convex. It is partly bounded by one or multiple solid surfaces, which exert an external potential $u_s(\mathbf{r})$ per polymer segment at each position $\mathbf{r} \in \mathcal{R}$. The boundary of the domain \mathcal{R} will be referred to as $\partial\mathcal{R}$. Part of $\partial\mathcal{R}$ may be defined by solid surfaces, while the rest of $\partial\mathcal{R}$ will be characterized by zero-flux *Neumann* boundary conditions.

The polymer consists of matrix chains of length N_m skeletal bonds each. In addition, there are chains terminally grafted on the solid surfaces, the length of each grafted chain being N_g segments. Both matrix and grafted chains are assumed to be monodisperse, but matrix chains can have different chain length from grafted chains. In the context of the present work, matrix and grafted chains are of the same chemical composition; hence the potential energy field per segment, $u_s(\mathbf{r})$, is applicable to both.

We use the symbols n_m and n_g to denote the numbers of matrix and grafted chains, respectively. The number n_g will be fixed. The number n_m is free to fluctuate, subject to the condition that the matrix chains in the interfacial region are in equilibrium with a bulk polymer phase at temperature T , whose density, in segments per unit volume, is $\rho_{\text{seg,bulk}}$. Of course, $\rho_{\text{seg,bulk}}$ can be determined from the temperature T and the pressure P of the bulk polymer phase through an appropriate equation of state. From the same equation of state one can determine the *chemical potential* μ_m per chain segment in the bulk polymer.

In general, the mean segment density of polymer in the considered interfacial region, $\bar{\rho}_{\text{seg}} = \frac{n_m N_m + n_g N_g}{V}$, will be different from $\rho_{\text{seg,bulk}}$. The interfacial region and the bulk one will be at equilibrium; the *chemical potential* μ_m of matrix chain segments in \mathcal{R} is the same as in a bulk phase of matrix chains.

The unperturbed mean square radii of gyration of matrix and grafted chains will be denoted as $\langle R_{G,g}^2 \rangle$ and $\langle R_{G,m}^2 \rangle$, respectively. The grafting points (starts of the grafted chains) will be denoted by \mathbf{r}_{g,i_g} , $i_g=1, 2, \dots, n_g$. They all lie on solid surfaces which belong to $\partial\mathcal{R}$. In practice, the grafting point is located at a finite distance from the solid surface. Technically speaking, it is not possible to attach the end of the chain exactly on the surface, because this

would result in a conflict between the grafted chains initial condition and the *Dirichlet* boundary conditions imposed on the solid boundaries.

The matrix chains in the interfacial region of volume V at temperature T and *chemical potential* $\mu_m N_m$ follow the probability distribution of the *grand canonical ensemble*. Treating all chains as *Gaussian* strings and describing the nonbonded interactions by an equation of state in conjunction with a gradient term, $f[\hat{\rho}(\mathbf{r}), \nabla \hat{\rho}(\mathbf{r})]$, we can write the *grand partition function* for the polymer contained in \mathcal{R} as:

$$\Xi = \sum_{n_m=0}^{\infty} \frac{1}{n_m!} \exp[\beta \mu_m N_m n_m] \mathcal{A}_m^{n_m} \mathcal{A}_g^{n_g} \int \prod_{i_m=1}^{n_m} \mathcal{D}\mathbf{R}_{i_m}(\cdot) \mathcal{P}_m[\mathbf{R}_{i_m}(\cdot)] \prod_{i_g=1}^{n_g} \mathcal{D}\mathbf{R}_{i_g}(\cdot) \mathcal{P}'_g[\mathbf{R}_{i_g}(\cdot)] \exp\left\{-\beta \int (f[\hat{\rho}(\mathbf{r}), \nabla \hat{\rho}(\mathbf{r})] + u_s(\mathbf{r}) \hat{\rho}(\mathbf{r})) d\mathbf{r}\right\} \quad \text{B1}$$

where $\beta = 1/(k_B T)$, $\int \mathcal{D}\mathbf{R}_{i_m}(\cdot)$ symbolizes a functional integral over all paths $\mathbf{R}_{i_m}(N)$, $0 \leq N \leq N_m$, of a matrix chain i_m ($1 \leq i_m \leq n_m$) and $\int \mathcal{D}\mathbf{R}_{i_g}(\cdot)$ symbolizes a functional integral over all paths $\mathbf{R}_{i_g}(N)$, $0 \leq N \leq N_g$, of a grafted chain i_g ($1 \leq i_g \leq n_g$). $\mathcal{A}_m, \mathcal{A}_g$ are normalizing factors per matrix and per grafted chain, respectively, appearing in the path integral formulation. They must be the same between the interfacial system and the bulk polymer and render the *grand partition function*, Ξ , dimensionless.

The functional $f[\hat{\rho}(\mathbf{r}), \nabla \hat{\rho}(\mathbf{r})]$ is the *Helmholtz* energy density (*Helmholtz* energy per unit volume) describing the nonbonded interactions between polymer segments, obtainable from an appropriate equation of state. Herein we identify f with an excess *Helmholtz* energy, i.e., the *Helmholtz* energy of a real polymer fluid consisting of a certain number of chains in a given volume minus the *Helmholtz* energy of an equal number of noninteracting (ideal gas) chains occupying the same volume. $u_s(\mathbf{r})$ is the total potential energy exerted by the solid on a polymer segment as a function of the position \mathbf{r} of that segment.

In the absence of a field, the probability density distribution (statistical weight) of a matrix chain conformation/path, $\mathbf{R}_{i_m}(N)$, and the corresponding one of a grafted chain, $\mathbf{R}_{i_g}(N)$, are given by eqs B2 and B3, respectively, in the context of the *Gaussian* chain model.

$$\mathcal{P}_m[\mathbf{R}_{i_m}(\cdot)] = \exp\left[-\frac{1}{4R_{G,m}^2} \int_0^{N_m} \left(\frac{d\mathbf{R}_{i_m}}{dN}\right)^2 dN\right] \quad \text{B2}$$

$$\mathcal{P}'_g[\mathbf{R}_{i_g}(\cdot)] = \exp\left[-\frac{1}{4R_{G,g}^2} \int_0^{N_g} \left(\frac{d\mathbf{R}_{i_g}}{dN}\right)^2 dN\right] \delta[\mathbf{R}_{i_g}(0) - \mathbf{r}_{g,i_g}] = \mathcal{P}_g[\mathbf{R}_{i_g}(\cdot)] \delta[\mathbf{R}_{i_g}(0) - \mathbf{r}_{g,i_g}] \quad \text{B3}$$

The reduced segment density operators $\hat{\phi}_m(\mathbf{r})$, $\hat{\phi}_g(\mathbf{r})$ are defined as shown in eqs B4 and B5 respectively.

$$\hat{\phi}_m(\mathbf{r}) \equiv \frac{\hat{\rho}_m(\mathbf{r})}{\rho_{\text{seg,bulk}}} = \frac{\sum_{i_m=1}^{n_m} \int_0^{N_m} \delta(\mathbf{r} - \mathbf{R}_{i_m}(N)) dN}{\rho_{\text{seg,bulk}}} \quad \text{B4}$$

$$\hat{\phi}_g(\mathbf{r}) \equiv \frac{\hat{\rho}_g(\mathbf{r})}{\rho_{\text{seg,bulk}}} = \frac{\sum_{i_g=1}^{n_g} \int_0^{N_g} \delta(\mathbf{r} - \mathbf{R}_{i_g}(N)) dN}{\rho_{\text{seg,bulk}}} \quad \text{B5}$$

and we set the total reduced segment density operator as $\hat{\phi}(\mathbf{r}) = \hat{\phi}_m(\mathbf{r}) + \hat{\phi}_g(\mathbf{r})$. Next, we wish to re-express the *Boltzmann* factor on the right-hand side of eq B1 in terms of a density field, $\rho(\mathbf{r})$, and a *chemical potential* field, $w(\mathbf{r})$. To begin with, this term can be written as presented in the following eq B6.⁵

$$\exp\left\{-\beta \int (f[\hat{\rho}(\mathbf{r}), \nabla \hat{\rho}(\mathbf{r})] + u_s(\mathbf{r}) \hat{\rho}(\mathbf{r})) d\mathbf{r}\right\} = \int \mathcal{D}\rho(\mathbf{r}) \delta[\rho(\mathbf{r}) - \hat{\rho}(\mathbf{r})] \exp\left\{-\beta \int (f[\rho(\mathbf{r}), \nabla \rho(\mathbf{r})] + u_s(\mathbf{r}) \rho(\mathbf{r})) d\mathbf{r}\right\} \quad \text{B6}$$

Next, we write the *Dirac-delta* functional as the inverse Fourier transform of eq B7, which involves the two aforementioned fields.

$$\delta[\rho(\mathbf{r}) - \hat{\rho}(\mathbf{r})] = C \int \mathcal{D}[\beta w(\mathbf{r})] \exp\left\{i \int d\mathbf{r} \beta w(\mathbf{r}) [\rho(\mathbf{r}) - \hat{\rho}(\mathbf{r})]\right\} \quad \text{B7}$$

with C being a normalization constant.⁸⁰

Combining eqs B6 and B7, the following expression is obtained for the *Boltzmann* factor of the *grand partition function* of the system.

$$\begin{aligned} & \exp\left\{-\beta \int (f[\hat{\rho}(\mathbf{r}), \nabla \hat{\rho}(\mathbf{r})] + u_s(\mathbf{r}) \hat{\rho}(\mathbf{r})) d\mathbf{r}\right\} = \\ & = C \int \mathcal{D}\rho(\mathbf{r}) \int \mathcal{D}[\beta w(\mathbf{r})] \exp\left\{i \int d\mathbf{r} \beta w(\mathbf{r}) [\rho(\mathbf{r}) - \hat{\rho}(\mathbf{r})]\right\} \exp\left\{-\beta \int (f[\rho(\mathbf{r}), \nabla \rho(\mathbf{r})] + u_s(\mathbf{r}) \rho(\mathbf{r})) d\mathbf{r}\right\} \end{aligned} \quad \text{B8}$$

Within the functional integral of the right-hand side of eq B8, there is a term incorporating the density operator, $\hat{\rho}(\mathbf{r})$, which is the sum of $\hat{\rho}_m(\mathbf{r})$ and $\hat{\rho}_g(\mathbf{r})$. Introducing the

definitions for these operators, eqs B4 and B5 respectively, that term can be written as in the following eq B9.

$$\begin{aligned}
 \exp\left(-i\int d\mathbf{r}\beta w(\mathbf{r})\hat{\rho}(\mathbf{r})\right) &= \exp\left[-i\int d\mathbf{r}\beta w(\mathbf{r})\left(\sum_{i_m=1}^{n_m}\int_0^{N_m}\delta(\mathbf{r}-\mathbf{R}_{i_m}(N))dN + \sum_{i_g=1}^{n_g}\int_0^{N_g}\delta(\mathbf{r}-\mathbf{R}_{i_g}(N))dN\right)\right] \\
 &= \exp\left[-\sum_{i_m=1}^{n_m}\int d\mathbf{r}\int_0^{N_m}dN\delta(\mathbf{r}-\mathbf{R}_{i_m}(N))i\beta w(\mathbf{r})\right]\cdot\exp\left[-\sum_{i_g=1}^{n_g}\int d\mathbf{r}\int_0^{N_g}dN\delta(\mathbf{r}-\mathbf{R}_{i_g}(N))i\beta w(\mathbf{r})\right] \\
 &= \prod_{i_m=1}^{n_m}\exp\left(-\int d\mathbf{r}\int_0^{N_m}dN\delta(\mathbf{r}-\mathbf{R}_{i_m}(N))i\beta w(\mathbf{r})\right)\cdot\prod_{i_g=1}^{n_g}\exp\left(-\int d\mathbf{r}\int_0^{N_g}dN\delta(\mathbf{r}-\mathbf{R}_{i_g}(N))i\beta w(\mathbf{r})\right) \\
 &= \prod_{i_m=1}^{n_m}\exp\left(-i\beta\int_0^{N_m}dNw(\mathbf{R}_{i_m}(N))\right)\cdot\prod_{i_g=1}^{n_g}\exp\left(-i\beta\int_0^{N_g}dNw(\mathbf{R}_{i_g}(N))\right)
 \end{aligned}$$

B9

Combining eqs B1, B8 and B9 the following equation is obtained for the *grand partition function*.

$$\begin{aligned}
\Xi &= C \sum_{n_m=0}^{\infty} \frac{1}{n_m!} \exp[\beta\mu_m N_m n_m] \mathcal{A}_m^{n_m} \mathcal{A}_g^{n_g} \int \prod_{i_m=1}^{n_m} \mathcal{D}\mathbf{R}_{i_m}(\cdot) \mathcal{P}_m[\mathbf{R}_{i_m}(\cdot)] \\
&\quad \times \prod_{i_g=1}^{n_g} \mathcal{D}\mathbf{R}_{i_g}(\cdot) \mathcal{P}'_g[\mathbf{R}_{i_g}(\cdot)] \int \mathcal{D}\rho(\mathbf{r}) \int \mathcal{D}[\beta w(\mathbf{r})] \exp\left\{i \int d\mathbf{r} \beta w(\mathbf{r}) [\rho(\mathbf{r}) - \hat{\rho}(\mathbf{r})]\right\} \\
&\quad \times \exp\left\{-\beta \int (f[\rho(\mathbf{r}), \nabla\rho(\mathbf{r})] + u_s(\mathbf{r})\rho(\mathbf{r})) d\mathbf{r}\right\} \\
&= C \sum_{n_m=0}^{\infty} \frac{1}{n_m!} \exp[\beta\mu_m N_m n_m] \mathcal{A}_m^{n_m} \mathcal{A}_g^{n_g} \\
&\quad \times \int \mathcal{D}\rho(\mathbf{r}) \int \mathcal{D}[\beta w(\mathbf{r})] \exp\left\{i \int d\mathbf{r} \beta w(\mathbf{r}) \rho(\mathbf{r})\right\} \exp\left\{-\beta \int (f[\rho(\mathbf{r}), \nabla\rho(\mathbf{r})] + u_s(\mathbf{r})\rho(\mathbf{r})) d\mathbf{r}\right\} \\
&\quad \times \int \prod_{i_m=1}^{n_m} \mathcal{D}\mathbf{R}_{i_m}(\cdot) \mathcal{P}_m[\mathbf{R}_{i_m}(\cdot)] \prod_{i_m=1}^{n_m} \exp\left(-i\beta \int_0^{N_m} dN w(\mathbf{R}_{i_m}(N))\right) \\
&\quad \times \prod_{i_g=1}^{n_g} \mathcal{D}\mathbf{R}_{i_g}(\cdot) \mathcal{P}'_g[\mathbf{R}_{i_g}(\cdot)] \prod_{i_g=1}^{n_g} \exp\left(-i\beta \int_0^{N_g} dN w(\mathbf{R}_{i_g}(N))\right) \\
&= C \sum_{n_m=0}^{\infty} \frac{1}{n_m!} \exp[\beta\mu_m N_m n_m] \mathcal{A}_m^{n_m} \mathcal{A}_g^{n_g} \\
&\quad \times \int \mathcal{D}\rho(\mathbf{r}) \int \mathcal{D}[\beta w(\mathbf{r})] \exp\left\{i \int d\mathbf{r} \beta w(\mathbf{r}) \rho(\mathbf{r})\right\} \exp\left\{-\beta \int (f[\rho(\mathbf{r}), \nabla\rho(\mathbf{r})] + u_s(\mathbf{r})\rho(\mathbf{r})) d\mathbf{r}\right\} \\
&\quad \times \prod_{i_m=1}^{n_m} \int \mathcal{D}\mathbf{R}_{i_m}(\cdot) \mathcal{P}_m[\mathbf{R}_{i_m}(\cdot)] \prod_{i_m=1}^{n_m} \exp\left(-i\beta \int_0^{N_m} dN w(\mathbf{R}_{i_m}(N))\right) \\
&\quad \times \prod_{i_g=1}^{n_g} \int \mathcal{D}\mathbf{R}_{i_g}(\cdot) \mathcal{P}'_g[\mathbf{R}_{i_g}(\cdot)] \delta[\mathbf{R}_{i_g}(0) - \mathbf{r}_{g,i_g}] \prod_{i_g=1}^{n_g} \exp\left(-i\beta \int_0^{N_g} dN w(\mathbf{R}_{i_g}(N))\right)
\end{aligned}$$

B10

The next step is to define the single chain *partition functions* (or functionals to be technically accurate) of a matrix and a grafted chain, $Q_m[iw(\mathbf{r})]$ and $Q_g[\mathbf{r}_{g,i_g}; iw(\mathbf{r})]$ respectively, in the field $iw(\mathbf{r})$ by the following eqs B11 and B12.

$$Q_m[iw(\mathbf{r})] = \frac{\int \mathcal{D}\mathbf{R}_{i_m}(\cdot) \mathcal{P}_m[\mathbf{R}_{i_m}(\cdot)] \exp\left[-i\beta \int_0^{N_m} dN w(\mathbf{R}_{i_m}(N))\right]}{\int \mathcal{D}\mathbf{R}_{i_m}(\cdot) \mathcal{P}_m[\mathbf{R}_{i_m}(\cdot)]} \quad \text{B11}$$

$$Q_g[\mathbf{r}_{g,i_g}; iw(\mathbf{r})] = \frac{\int \mathcal{D}\mathbf{R}_{i_g}(\cdot) \mathcal{P}'_g[\mathbf{R}_{i_g}(\cdot)] \delta[\mathbf{R}_{i_g}(0) - \mathbf{r}_{g,i_g}] \exp\left[-i\beta \int_0^{N_g} dN w(\mathbf{R}_{i_g}(N))\right]}{\int \mathcal{D}\mathbf{R}_{i_g}(\cdot) \mathcal{P}'_g[\mathbf{R}_{i_g}(\cdot)] \delta[\mathbf{R}_{i_g}(0) - \mathbf{r}_{g,i_g}]} \quad \text{B12}$$

where, $\int \mathcal{D}\mathbf{R}_{i_m}(\cdot) \mathcal{P}_m[\mathbf{R}_{i_m}(\cdot)] = Z_{m,\text{free}} V$ is the configurational integral of a field-free matrix chain and $\int \mathcal{D}\mathbf{R}_{i_g}(\cdot) \mathcal{P}_g[\mathbf{R}_{i_g}(\cdot)] \delta[\mathbf{R}_{i_g}(0) - \mathbf{r}_{g,i_g}] = Z_{g,\text{free}}$ is the configuration integral of a field-free grafted chain. $Q_m[iw(\mathbf{r})]$ is the *configurational integral* or *partition function* of a single matrix chain of length N_m , whose segments are subject to the field $iw(\mathbf{r})$, relative to the corresponding *partition function* of a field-free chain (i.e., *Gaussian* string performing a *random-walk*) and is dimensionless by definition. In like manner, $Q_g[\mathbf{r}_{g,i_g}; iw(\mathbf{r})]$ is the *partition function* of a grafted chain of length N_g , which starts at \mathbf{r}_{g,i_g} and whose segments are subject to the field $iw(\mathbf{r})$, relative to the *partition function* of a field-free chain of the same length starting at \mathbf{r}_{g,i_g} . It is dimensionless as well.

Combining eqs B10, B11 and B12 the *grand partition function* becomes:

$$\begin{aligned}
 \Xi &= C \sum_{n_m=0}^{\infty} \frac{1}{n_m!} \exp[\beta \mu_m N_m n_m] \mathcal{A}_m^{n_m} \mathcal{A}_g^{n_g} \\
 &\times \int \mathcal{D}\rho(\mathbf{r}) \int \mathcal{D}[\beta w(\mathbf{r})] \exp\left\{i \int d\mathbf{r} \beta w(\mathbf{r}) \rho(\mathbf{r})\right\} \exp\left\{-\beta \int (f[\rho(\mathbf{r}), \nabla \rho(\mathbf{r})] + u_s(\mathbf{r}) \rho(\mathbf{r})) d\mathbf{r}\right\} \\
 &\times (Z_{m,\text{free}} V)^{n_m} (Q_m[iw(\mathbf{r})])^{n_m} Z_{g,\text{free}}^{n_g} \left(\prod_{i_g=1}^{n_g} Q_g[\mathbf{r}_{g,i_g}; iw(\mathbf{r})] \right) \\
 &= C \int \mathcal{D}\rho(\mathbf{r}) \int \mathcal{D}[\beta w(\mathbf{r})] \exp\left\{i \int d\mathbf{r} \beta w(\mathbf{r}) \rho(\mathbf{r})\right\} \exp\left\{-\beta \int (f[\rho(\mathbf{r}), \nabla \rho(\mathbf{r})] + u_s(\mathbf{r}) \rho(\mathbf{r})) d\mathbf{r}\right\} \\
 &\times \sum_{n_m=0}^{\infty} \frac{1}{n_m!} \exp[\beta \mu_m N_m n_m] (\mathcal{A}_m Z_{m,\text{free}} V)^{n_m} (Q_m[iw(\mathbf{r})])^{n_m} (\mathcal{A}_g Z_{g,\text{free}})^{n_g} (Q_g[iw(\mathbf{r})])^{n_g} \\
 &= C \int \mathcal{D}\rho(\mathbf{r}) \int \mathcal{D}[\beta w(\mathbf{r})] \exp\left(\int d\mathbf{r} \beta \{iw(\mathbf{r}) \rho(\mathbf{r}) - f[\rho(\mathbf{r}), \nabla \rho(\mathbf{r})] - u_s(\mathbf{r}) \rho(\mathbf{r})\}\right) \\
 &\times \exp\left\{\exp[\beta \mu_m N_m] \mathcal{A}_m Z_{m,\text{free}} V Q_m[iw(\mathbf{r})]\right\} \prod_{i_g=1}^{n_g} (\mathcal{A}_g Z_{g,\text{free}} Q_g[\mathbf{r}_{g,i_g}; iw(\mathbf{r})])
 \end{aligned} \tag{B13}$$

We set the *grand partition function* to be equal to:

$$\Xi = C \int \mathcal{D}[\rho(\mathbf{r})] \int \mathcal{D}[\beta w(\mathbf{r})] \exp(-\beta H[\rho(\mathbf{r}), \nabla \rho(\mathbf{r}), w(\mathbf{r})]) \tag{B14}$$

where the *Hamiltonian* of the system, H , is a functional of the segment density, $\rho(\mathbf{r})$, of its spatial gradient, and of the *chemical potential* field, $w(\mathbf{r})$. Finally, using eqs B13 and B14, the general form of the *Hamiltonian* is given by eq B15.

$$\begin{aligned}
 H[\rho(\mathbf{r}), \nabla \rho(\mathbf{r}), w(\mathbf{r})] &= \int d\mathbf{r} \{-iw(\mathbf{r}) \rho(\mathbf{r}) + f[\rho(\mathbf{r}), \nabla \rho(\mathbf{r})] + u_s(\mathbf{r}) \rho(\mathbf{r})\} \\
 &- \frac{1}{\beta} \exp(\beta \mu_m N_m) \mathcal{A}_m Z_{m,\text{free}} V Q_m[iw(\mathbf{r})] - \frac{1}{\beta} \sum_{j=1}^{n_g} \ln(\mathcal{A}_g Z_{g,\text{free}} Q_g[\mathbf{r}_{g,i_g}; iw(\mathbf{r})])
 \end{aligned} \tag{B15}$$

Appendix C Saddle point approximation

In the context of *Self-Consistent Field Theory*, we need to replace the functional integral of eq B15 with its dominant term, i.e., the density and field configurations which have the highest probability and thus the maximum contribution to the *Hamiltonian* of the system. In order to determine those configurations, we need to perform a so-called saddle-point approximation, i.e., find the stationary point of the *Hamiltonian* functional with respect to $\rho(\mathbf{r})$ and $w(\mathbf{r})$. To this end, we first set the functional derivative of the *Hamiltonian* with respect to $w(\mathbf{r})$ equal to zero, as shown in eq C1.

$$\frac{\delta H}{\delta w} = 0 \Leftrightarrow -i\rho(\mathbf{r}) - \frac{1}{\beta} \exp(\beta\mu_m) \mathcal{A}_m Z_{m,\text{free}} V \frac{\delta Q_m[iw(\mathbf{r})]}{\delta w} - \frac{1}{\beta} \sum_{i_g=1}^{n_g} \frac{\delta \ln Q_g[\mathbf{r}_{g,i_g}; iw(\mathbf{r})]}{\delta w} = 0 \quad \text{C1}$$

Following eq B11, we write:

$$\begin{aligned} \frac{\delta Q_m[iw(\mathbf{r})]}{\delta w} &= \frac{\int \mathcal{D}\mathbf{R}_{i_m}(\cdot) \mathcal{P}_m[\mathbf{R}_{i_m}(\cdot)] \left(-i\beta \int_0^{N_m} dN \delta(\mathbf{r} - \mathbf{R}_{i_m}(N)) \right) \exp \left[-\int d\mathbf{r} \int_0^{N_m} dN \delta(\mathbf{r} - \mathbf{R}_{i_m}(N)) i\beta w(\mathbf{r}) \right]}{\int \mathcal{D}\mathbf{R}_{i_m}(\cdot) \mathcal{P}_m[\mathbf{R}_{i_m}(\cdot)]} \\ &= -\beta i Q_m[iw(\mathbf{r})] \frac{\int \mathcal{D}\mathbf{R}_{i_m}(\cdot) \mathcal{P}_m[\mathbf{R}_{i_m}(\cdot)] \left(\int_0^{N_m} dN \delta(\mathbf{r} - \mathbf{R}_{i_m}(N)) \right) \exp \left[-\int d\mathbf{r} \int_0^{N_m} dN \delta(\mathbf{r} - \mathbf{R}_{i_m}(N)) i\beta w(\mathbf{r}) \right]}{\int \mathcal{D}\mathbf{R}_{i_m}(\cdot) \mathcal{P}_m[\mathbf{R}_{i_m}(\cdot)] \exp \left[-\int d\mathbf{r} \int_0^{N_m} dN \delta(\mathbf{r} - \mathbf{R}_{i_m}(N)) i\beta w(\mathbf{r}) \right]} \\ &= -\beta i Q_m[iw(\mathbf{r})] \left\langle \int_0^{N_m} dN \delta(\mathbf{r} - \mathbf{R}_{i_m}(N)) \right\rangle \\ &= -\frac{\beta i \rho_{\text{seg,bulk}} Q_m[iw(\mathbf{r})]}{\bar{n}_m} \left\langle \frac{\sum_{i_m=1}^{\bar{n}_m} \int_0^{N_m} dN \delta(\mathbf{r} - \mathbf{R}_{i_m}(N))}{\rho_{\text{seg,bulk}}} \right\rangle = -\frac{\beta i \rho_{\text{seg,bulk}} Q_m[iw(\mathbf{r})]}{\bar{n}_m} \langle \hat{\phi}_m(\mathbf{r}) \rangle = -\frac{\beta i \rho_{\text{seg,bulk}} Q_m[iw(\mathbf{r})]}{\bar{n}_m} \varphi_m(\mathbf{r}) \end{aligned} \quad \text{C2}$$

Likewise, following equation B12, we can write:

$$\begin{aligned}
 \frac{\delta \ln Q_g[\mathbf{r}_{g,i_g}; iw(\mathbf{r})]}{\delta w} &= \frac{1}{Q_g[\mathbf{r}_{g,i_g}; iw(\mathbf{r})]} \frac{\delta Q_g[\mathbf{r}_{g,i_g}; iw(\mathbf{r})]}{\delta w} \\
 &= \frac{1}{Q_g[\mathbf{r}_{g,i_g}; iw(\mathbf{r})]} \frac{\int \mathcal{D}\mathbf{R}_{i_g}(\cdot) \mathcal{P}_{i_g}[\mathbf{R}_{i_g}(\cdot)] \left(-i\beta \int_0^{N_g} dN \delta(\mathbf{r} - \mathbf{R}_{i_g}(N)) \right) \exp \left[-\int_0^{N_g} d\mathbf{r} \int_0^{N_g} dN \delta(\mathbf{r} - \mathbf{R}_{i_g}(N)) i\beta w(\mathbf{r}) \right]}{\int \mathcal{D}\mathbf{R}_{i_g}(\cdot) \mathcal{P}_{i_g}[\mathbf{R}_{i_g}(\cdot)]} \\
 &= -\beta i \frac{\int \mathcal{D}\mathbf{R}_{i_g}(\cdot) \mathcal{P}_{i_g}[\mathbf{R}_{i_g}(\cdot)] \left(\int_0^{N_g} dN \delta(\mathbf{r} - \mathbf{R}_{i_g}(N)) \right) \exp \left[-\int_0^{N_g} d\mathbf{r} \int_0^{N_g} dN \delta(\mathbf{r} - \mathbf{R}_{i_g}(N)) i\beta w(\mathbf{r}) \right]}{\int \mathcal{D}\mathbf{R}_{i_g}(\cdot) \mathcal{P}_{i_g}[\mathbf{R}_{i_g}(\cdot)] \exp \left[-\int_0^{N_g} d\mathbf{r} \int_0^{N_g} dN \delta(\mathbf{r} - \mathbf{R}_{i_g}(N)) i\beta w(\mathbf{r}) \right]} \\
 &= -\beta i \left\langle \int_0^{N_g} dN \delta(\mathbf{r} - \mathbf{R}_{i_g}(N)) \right\rangle
 \end{aligned} \tag{C3}$$

and thus

$$\sum_{i_g=1}^{n_g} \frac{\delta \ln Q_g[\mathbf{r}_{g,i_g}; iw(\mathbf{r})]}{\delta w} = -\beta i \rho_{\text{seg,bulk}} \left\langle \frac{\sum_{i=1}^{n_g} \int_0^{N_g} dN \delta(\mathbf{r} - \mathbf{R}_{i_g}(N))}{\rho_{\text{seg,bulk}}} \right\rangle = -\beta i \rho_{\text{seg,bulk}} \langle \hat{\phi}_g(\mathbf{r}) \rangle = -\beta i \rho_{\text{seg,bulk}} \phi_g(\mathbf{r}) \tag{C4}$$

Combining eqs C1, C2 and C4, the following eq C5 is obtained for the density field, $\rho(\mathbf{r})$.

$$\rho(\mathbf{r}) = \exp(\beta \mu_m) \mathcal{A}_m Z_{m,\text{free}} V \frac{Q_m[iw(\mathbf{r})]}{\bar{n}_m} \rho_{\text{seg,bulk}} \phi_m(\mathbf{r}) + \rho_{\text{seg,bulk}} \phi_g(\mathbf{r}) \tag{C5}$$

The saddle point approximation requires that the functional derivative of the *Hamiltonian* with respect to the density field, $\rho(\mathbf{r})$, be also equal to zero:

$$\begin{aligned}
 \frac{\delta H}{\delta \rho(\mathbf{r})} = 0 &\Leftrightarrow -iw(\mathbf{r}) + u_s(\mathbf{r}) + \left[\frac{\partial f}{\partial \rho} - \nabla \cdot \frac{\partial f}{\partial \nabla \rho} \right]_{\rho=\rho(\mathbf{r})} = 0 \\
 &\Leftrightarrow w(\mathbf{r}) = -i \left(\left[\frac{\partial f}{\partial \rho} - \nabla \cdot \frac{\partial f}{\partial \nabla \rho} \right]_{\rho=\rho(\mathbf{r})} + u_s(\mathbf{r}) \right)
 \end{aligned} \tag{C6}$$

After the saddle point approximation, the *Hamiltonian* of the system, from eq B15, is given by eq C7.

$$\begin{aligned}
 \bar{H} &= \int d\mathbf{r} \left\{ f[\rho(\mathbf{r}), \nabla \rho(\mathbf{r})] - \rho(\mathbf{r}) \frac{\partial f}{\partial \rho} \Big|_{\rho=\rho(\mathbf{r})} + \rho(\mathbf{r}) \nabla \cdot \frac{\partial f}{\partial \nabla \rho} \Big|_{\rho=\rho(\mathbf{r})} \right\} \\
 &\quad - \frac{1}{\beta} \exp(\beta \mu_m) \mathcal{A}_m Z_{m,\text{free}} V Q_m[iw(\mathbf{r})] - \frac{1}{\beta} \sum_{i_g=1}^{n_g} \ln \left(\mathcal{A}_g Z_{g,\text{free}} Q_g[\mathbf{r}_{g,i_g}; iw(\mathbf{r})] \right)
 \end{aligned} \tag{C7}$$

Appendix D Free energy terms

According to the saddle point approximation considerations which were developed in the previous section, the grand potential of our interfacial polymer system, occupying volume V at temperature T and chain *chemical potential* $\mu_m N_m$ is given by eq D1.

$$\Omega(\mu_m, n_g, V, T) = -\frac{1}{\beta} \ln \Xi = -\frac{1}{\beta} \ln \left[\exp(-\beta \bar{H}) \right] = \bar{H} \quad \text{D1}$$

Any multiplicative factor arising in Ξ upon introduction of the saddle point approximation contributes an additive constant to Ω , which will cancel upon referring Ω to an equal amount of polymer in the bulk. Ω is an extensive—system size-dependent—thermodynamic property. It is convenient to express the system thermodynamics with reference to a bulk phase of matrix chains occupying volume V at temperature T and *chemical potential* $\mu_m N_m$, a set of n_g isolated end-pinned unperturbed chains of length N_g at temperature T , and an isolated bare nanoparticle, as described below.

The grand potential of an amount of bulk polymer occupying volume V at temperature T and *chemical potential* $N_m \mu_m$ is:

$$\Omega_{\text{bulk}}(\mu_m, V, T) = -\frac{1}{\beta} \ln \Xi_{\text{bulk}} = \bar{H}_{\text{bulk}} \quad \text{D2}$$

with \bar{H}_{bulk} being the effective *Hamiltonian* of eq C6 applied to bulk polymer:

$$\bar{H}_{\text{bulk}} = \int \mathbf{dr} \left\{ f[\rho, 0] - \rho \frac{\partial f}{\partial \rho} \right\} \Bigg|_{\rho=\rho_{\text{seg,bulk}}} - \frac{1}{\beta} \exp(\beta \mu_m) \mathcal{A}_m Z_{m,\text{free}} V Q_m[iw_{\text{bulk}}] \quad \text{D3}$$

Note that, for all forms of the local free energy density f considered here, $\frac{\partial f}{\partial \nabla \rho} = \mathbf{0}$ in the bulk polymer phase.

Application of eq C5 for the density to the bulk polymer gives:

$$\rho_{\text{seg,bulk}} = \exp(\beta \mu_m) \mathcal{A}_m Z_{m,\text{free}} V \frac{Q_m[iw_{\text{bulk}}]}{n_{m,\text{bulk}}} \rho_{\text{seg,bulk}} \Leftrightarrow \exp(\beta \mu_m) \mathcal{A}_m Z_{m,\text{free}} V Q_m[iw_{\text{bulk}}] = \frac{\rho_{\text{seg,bulk}} V}{N_m} \quad \text{D4}$$

Combining eqs D3 and D4,

$$\bar{H}_{\text{bulk}} = \int d\mathbf{r} \left\{ f[\rho, 0] - \rho \frac{\partial f}{\partial \rho} \right\} \Bigg|_{\rho=\rho_{\text{seg,bulk}}} - \frac{\rho_{\text{seg,bulk}} V}{\beta N_m} \quad \text{D5}$$

In the bulk melt, the self-consistent field from eq C6 becomes:

$$w_{\text{bulk}} = -i \frac{\partial f}{\partial \rho} \Bigg|_{\rho=\rho_{\text{seg,bulk}}} \quad \text{D6}$$

and thus the matrix chain *partition function* from eq B11 takes the form

$$Q_m [iw_{\text{bulk}}] = \exp \left(-\beta N_m \frac{\partial f}{\partial \rho} \Bigg|_{\rho=\rho_{\text{seg,bulk}}} \right) \quad \text{D7}$$

On the other hand, for a set of isolated end-pinned unperturbed chains of length N_g at temperature T , which are identical in length and chemical composition to our grafted chains, the total *Helmholtz* energy in the context of our model is given by eq D8.

$$A_g^{\text{isol}}(T, n_g) = -\frac{1}{\beta} \sum_{i_g=1}^{n_g} \ln \left(\mathcal{A}_g Z_{g,\text{free}} Q_g [\mathbf{r}_{g,i_g}; iw_{\text{bulk}}] \right) \quad \text{D8}$$

Subtracting eqs D5 and D8 from eq C7:

$$\begin{aligned} \Delta\Omega &= \Omega(\mu, V, T) - \Omega_{\text{bulk}}(\mu, V, T) - A_g^{\text{isol}}(T, n_g) \\ &= \int d\mathbf{r} \left\{ f[\rho(\mathbf{r}), \nabla\rho(\mathbf{r})] - \rho(\mathbf{r}) \frac{\partial f}{\partial \rho} \Bigg|_{\rho=\rho(\mathbf{r})} + \rho(\mathbf{r}) \nabla \cdot \frac{\partial f}{\partial \nabla\rho} \Bigg|_{\rho=\rho(\mathbf{r})} \right\} \\ &\quad - \int d\mathbf{r} \left\{ f[\rho, \mathbf{0}] - \rho \frac{\partial f}{\partial \rho} \right\} \Bigg|_{\rho=\rho_{\text{seg,bulk}}} \\ &\quad + \frac{\rho_{\text{seg,bulk}} V}{\beta N_m} (1 - Q_m [w'(\mathbf{r}) - w'_{\text{bulk}}]) \\ &\quad - \frac{1}{\beta} \sum_{i_g=1}^{n_g} \ln Q_g [\mathbf{r}_{g,i_g}; w'(\mathbf{r}) - w'_{\text{bulk}}] \end{aligned} \quad \text{D9}$$

In eq D9, we have made the following substitution:

$$iw(\mathbf{r}) = w'(\mathbf{r}), \text{ a real field.} \quad \text{D10}$$

The second integral in eq D9, referring to a homogeneous bulk phase of matrix chains, can be performed immediately, yielding a factor of V times the integrand.

Appendices

By expressing eq C6 in terms of the real field from eq D10, $\partial f / \partial \rho = w'(\mathbf{r}) + \nabla \cdot \partial f / \partial \nabla \rho - u_s(\mathbf{r})$, and by substituting it to eq D9, the latter can be expressed as follows:

$$\begin{aligned}
 \Delta\Omega = & \int d\mathbf{r} \left\{ f[\rho(\mathbf{r}), \nabla\rho(\mathbf{r})] - f[\rho_{\text{seg,bulk}}, \mathbf{0}] \right\} \\
 & - \int d\mathbf{r} \left\{ \rho(\mathbf{r})w'(\mathbf{r}) - \rho_{\text{seg,bulk}}w'_{\text{bulk}} \right\} \\
 & + \int d\mathbf{r} \left\{ \rho(\mathbf{r})u_s(\mathbf{r}) \right\} \\
 & + \frac{\rho_{\text{seg,bulk}}V}{\beta N_m} \left(1 - Q_m[w'(\mathbf{r}) - w'_{\text{bulk}}] \right) \\
 & - \frac{1}{\beta} \sum_{i_g=1}^{n_g} \ln Q_g[\mathbf{r}_{g,i_g}; w'(\mathbf{r}) - w'_{\text{bulk}}]
 \end{aligned} \tag{D11}$$

wherein the *first term* is the contribution of the cohesive interactions, the *second term* is the interaction energy between the density field and the *chemical potential* field, the third term describes the polymer-solid interactions, the *fourth term* describes the translational and conformational entropy (relative to the bulk melt) of the matrix chains, and the *fifth term* is associated with the conformational entropy of the n_g grafted chains subject to the field w' .

Appendix E Derivation of Segment Balance Equations

To deal with the grafted and the matrix chains in the presence of the field w' , we introduce the *propagator* $G(\mathbf{r}_{\text{start}}, \mathbf{r}, s)$ following *Edwards*²⁴¹:

$$G(\mathbf{r}_{\text{start}}, \mathbf{r}, N) = \frac{\int_{\mathbf{R}(0)=\mathbf{r}_{\text{start}}}^{\mathbf{R}(N)=\mathbf{r}} \mathcal{D}[\mathbf{R}(\cdot)] \mathcal{P}[\mathbf{R}(\cdot)] \exp\left\{-\beta \int_0^N dN' w'(\mathbf{R}(N'))\right\}}{\int d\mathbf{r} \int_{\mathbf{R}(0)=\mathbf{r}_{\text{start}}}^{\mathbf{R}(N)=\mathbf{r}} \mathcal{D}[\mathbf{R}(\cdot)] \mathcal{P}[\mathbf{R}(\cdot)]} \quad \text{E1}$$

$G(\mathbf{r}_{\text{start}}, \mathbf{r}, N)$ has dimensions of inverse volume. It is proportional to the conditional probability that a chain, which has started at $\mathbf{r}_{\text{start}}$ and is subject to the field $w'(\mathbf{r})$ on its segments, finds itself at position \mathbf{r} at contour length N , as depicted in Fig. S1. The denominator in eq E1 is a *partition function* for a field-free chain, represented as a *Gaussian string*, which has started at $\mathbf{r}_{\text{start}}$ and may end anywhere in the system. The denominator is independent of $\mathbf{r}_{\text{start}}$ and \mathbf{r} ; it depends only on N .

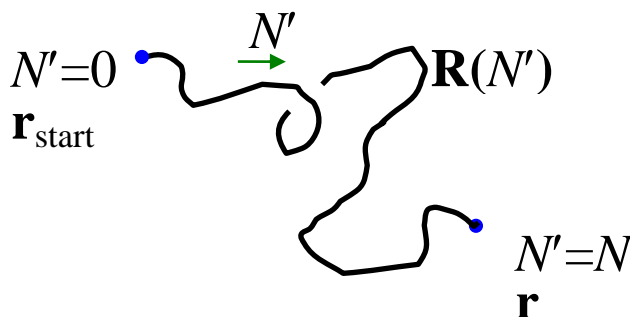


Figure S1. Schematic representation of a *Gaussian string* starting at $N' = 0$ and ending at $N' = N$.

We also define the *restricted partition function* of a matrix chain in the presence of the field $w'(\mathbf{r})$ by the following eq E2.

$$q_m(\mathbf{r}, N) = \int_V d\mathbf{r}_{\text{start}} G(\mathbf{r}_{\text{start}}, \mathbf{r}, N) \quad \text{E2}$$

This quantity is dimensionless and proportional to the probability that the segment at contour length N of a matrix chain subject to the field finds itself at position \mathbf{r} , regardless of where in the system the particular matrix chain may have started. It is reduced by the corresponding probability of a field-free chain. Thus, it equals unity for a field-free chain. The *partition*

Appendices

function of a matrix chain, Q_m , is related to the corresponding restricted one by the equation:

$$Q_m[w'(\mathbf{r})] = \frac{1}{V} \int_V d\mathbf{r} q_m(\mathbf{r}, N_m). \text{ It is also dimensionless and normalized such that it would be}$$

unity for a field-free chain in volume V .

The *partition function*, Q_g , of a chain which is grafted at \mathbf{r}_g , relative to a field-free chain of equal length, is given by eq E3.

$$Q_g[\mathbf{r}_g; w'(\mathbf{r})] = \int_V d\mathbf{r} G(\mathbf{r}_g, \mathbf{r}, N_g) \quad \text{E3}$$

But, by definition, $G(\mathbf{r}_g, \mathbf{r}, N_g) = G(\mathbf{r}, \mathbf{r}_g, N_g)$, so:

$$Q_g[\mathbf{r}_g; w'(\mathbf{r})] = \int_V d\mathbf{r} G(\mathbf{r}, \mathbf{r}_g, N_g) = q_m(\mathbf{r}_g, N_g) \quad \text{E4}$$

Following eq E1, the *propagator* of a grafted chain, whose grafted end lies at coordinates \mathbf{r}_g , can be written as:

$$\begin{aligned} G(\mathbf{r}_g, \mathbf{r}, N) &= \frac{\int \mathcal{D}[\mathbf{R}'(\cdot)] \mathcal{P}[\mathbf{R}'(\cdot)] \delta(\mathbf{R}'(0) - \mathbf{r}_g) \delta(\mathbf{R}'(N) - \mathbf{r}) \exp\left\{-\beta \int_0^N dN' w'(\mathbf{R}'(N'))\right\}}{\int \mathcal{D}[\mathbf{R}'(\cdot)] \mathcal{P}[\mathbf{R}'(\cdot)] \delta(\mathbf{R}'(0) - \mathbf{r}_g)} \\ &= \frac{\int \mathcal{D}[\mathbf{R}'(\cdot)] \mathcal{P}[\mathbf{R}'(\cdot)] \delta(\mathbf{R}'(0) - \mathbf{r}_g) \delta(\mathbf{R}'(N) - \mathbf{r}) \exp\left\{-\beta \int_0^N dN' w'(\mathbf{R}'(N'))\right\}}{\frac{1}{V} \int \mathcal{D}[\mathbf{R}'(\cdot)] \mathcal{P}[\mathbf{R}'(\cdot)]} \end{aligned} \quad \text{E5}$$

So far, we denote by $\mathbf{R}'(\cdot)$ the curve in three-dimensional space, which is followed by a *Gaussian* thread of length N . At this point, we introduce the symbol $\mathbf{R}''(\cdot)$, which represents the curve in three-dimensional space, which is followed by a *Gaussian* thread of length $N_g - N$. Using these definitions and combining eqs E1 and E2, the *restricted partition function* of a matrix chain can be written as follows.

$$q_m(\mathbf{r}, N_g - N) = \frac{\int d\mathbf{r}_{\text{start}} \int \mathcal{D}[\mathbf{R}''(\cdot)] \mathcal{P}[\mathbf{R}''(\cdot)] \delta(\mathbf{R}''(0) - \mathbf{r}_{\text{start}}) \delta(\mathbf{R}''(N_g - N) - \mathbf{r}) \exp\left\{-\beta \int_0^{N_g - N} dN' w'(\mathbf{R}''(N'))\right\}}{\frac{1}{V} \int \mathcal{D}[\mathbf{R}''(\cdot)] \mathcal{P}[\mathbf{R}''(\cdot)]} \quad \text{E6}$$

Next, we consider the product $G(\mathbf{r}_g, \mathbf{r}, N) q_m(\mathbf{r}, N_g - N)$. By eqs E5 and E6, the numerator of this product will be equal to the following expression.

$$\begin{aligned}
 numer &= \int \mathcal{D}[\mathbf{R}'(\cdot)] \mathcal{P}[\mathbf{R}'(\cdot)] \delta(\mathbf{R}'(0) - \mathbf{r}_g) \delta(\mathbf{R}'(N) - \mathbf{r}) \exp \left\{ -\beta \int_0^N dN' w'(\mathbf{R}'(N')) \right\} \\
 &\times \int_V d\mathbf{r}_{\text{start}} \int \mathcal{D}[\mathbf{R}''(\cdot)] \mathcal{P}[\mathbf{R}''(\cdot)] \delta(\mathbf{R}''(0) - \mathbf{r}_{\text{start}}) \delta(\mathbf{R}''(N_g - N) - \mathbf{r}) \exp \left\{ -\beta \int_0^{N_g - N} dN' w'(\mathbf{R}''(N')) \right\}
 \end{aligned} \tag{E7}$$

Changing the integration variable from N' to $N_g - N'$ in the second line, eq E7 is modified to:

$$\begin{aligned}
 numer &= \int \mathcal{D}[\mathbf{R}'(\cdot)] \mathcal{P}[\mathbf{R}'(\cdot)] \delta(\mathbf{R}'(0) - \mathbf{r}_g) \delta(\mathbf{R}'(N) - \mathbf{r}) \exp \left\{ -\beta \int_0^N dN' w'[\mathbf{R}'(N')] \right\} \\
 &\times \int_V d^3 r_{\text{start}} \int \mathcal{D}[\mathbf{R}''(\cdot)] \mathcal{P}[\mathbf{R}''(\cdot)] \delta(\mathbf{R}''(N_g) - \mathbf{r}_{\text{start}}) \delta(\mathbf{R}''(N) - \mathbf{r}) \exp \left\{ -\beta \int_N^{N_g} dN' w'[\mathbf{R}''(N')] \right\} \\
 &= \frac{1}{V} \int \mathcal{D}[\mathbf{R}(\cdot)] \mathcal{P}[\mathbf{R}(\cdot)] \delta(\mathbf{R}(0) - \mathbf{r}_g) \delta(\mathbf{R}(N) - \mathbf{r}) \exp \left\{ -\beta \int_0^{N_g} dN' w'[\mathbf{R}(N')] \right\}
 \end{aligned} \tag{E8}$$

where now the functional integration is performed over all paths $\mathbf{R}(\cdot)$ of an N_g segment-long (grafted) chain.

On the other hand, the denominator of the product $G(\mathbf{r}_g, \mathbf{r}, N) q_m(\mathbf{r}, N_g - N)$ becomes:

$$denom = \frac{1}{V^2} \int \mathcal{D}[\mathbf{R}'(\cdot)] \mathcal{P}[\mathbf{R}'(\cdot)] \int \mathcal{D}[\mathbf{R}''(\cdot)] \mathcal{P}[\mathbf{R}''(\cdot)] = \frac{1}{V^2} \int \mathcal{D}[\mathbf{R}(\cdot)] \mathcal{P}[\mathbf{R}(\cdot)] \tag{E9}$$

Dividing eq E8 with E9, we obtain:

$$G(\mathbf{r}_g, \mathbf{r}, N) q_m(\mathbf{r}, N_g - N) = \frac{\int \mathcal{D}[\mathbf{R}(\cdot)] \mathcal{P}[\mathbf{R}(\cdot)] \delta(\mathbf{R}(0) - \mathbf{r}_g) \delta(\mathbf{R}(N) - \mathbf{r}) \exp \left\{ -\beta \int_0^{N_g} dN' w'[\mathbf{R}(N')] \right\}}{\frac{1}{V} \int \mathcal{D}[\mathbf{R}(\cdot)] \mathcal{P}[\mathbf{R}(\cdot)]}$$

E10

Combining eqs E3 and E5, we can write the following eq E11 for the *partition function* of a grafted chain.

$$\begin{aligned}
 Q_g[\mathbf{r}_g; w'(\mathbf{r})] &= \frac{\int d^3 r_{\text{end}} \int \mathcal{D}[\mathbf{R}(\cdot)] \mathcal{P}[\mathbf{R}(\cdot)] \delta(\mathbf{R}(0) - \mathbf{r}_g) \delta(\mathbf{R}(N_g) - \mathbf{r}_{\text{end}}) \exp \left\{ -\beta \int_0^{N_g} dN' w'(\mathbf{R}(N')) \right\}}{\frac{1}{V} \int \mathcal{D}[\mathbf{R}(\cdot)] \mathcal{P}[\mathbf{R}(\cdot)]} \\
 &= \frac{\int \mathcal{D}[\mathbf{R}(\cdot)] \mathcal{P}[\mathbf{R}(\cdot)] \delta(\mathbf{R}(0) - \mathbf{r}_g) \exp \left\{ -\beta \int_0^{N_g} dN' w'(\mathbf{R}(N')) \right\}}{\frac{1}{V} \int \mathcal{D}[\mathbf{R}(\cdot)] \mathcal{P}[\mathbf{R}(\cdot)]}
 \end{aligned} \tag{E11}$$

Dividing eq E10 with E11, we obtain the following expression:

$$\begin{aligned}
 \frac{1}{Q_g[\mathbf{r}_g; w'(\mathbf{r})]} \int_0^{N_g} dN G(\mathbf{r}_g, \mathbf{r}, N) q_m(\mathbf{r}, N_g - N) \\
 &= \frac{\int_0^{N_g} dN \int \mathcal{D}[\mathbf{R}(\cdot)] \mathcal{P}[\mathbf{R}(\cdot)] \delta(\mathbf{R}(0) - \mathbf{r}_g) \delta(\mathbf{R}(N) - \mathbf{r}) \exp \left\{ -\beta \int_0^{N_g} dN' w'(\mathbf{R}(N')) \right\}}{\int \mathcal{D}[\mathbf{R}(\cdot)] \mathcal{P}[\mathbf{R}(\cdot)] \delta(\mathbf{R}(0) - \mathbf{r}_g) \exp \left\{ -\beta \int_0^{N_g} dN' w'(\mathbf{R}(N')) \right\}} \\
 &= \frac{\int \mathcal{D}[\mathbf{R}(\cdot)] \mathcal{P}[\mathbf{R}(\cdot)] \delta(\mathbf{R}(0) - \mathbf{r}_g) \int_0^{N_g} dN' \delta(\mathbf{R}(N') - \mathbf{r}) \exp \left\{ -\beta \int_0^{N_g} dN' w'(\mathbf{R}(N')) \right\}}{\int \mathcal{D}[\mathbf{R}(\cdot)] \mathcal{P}[\mathbf{R}(\cdot)] \delta(\mathbf{R}(0) - \mathbf{r}_g) \exp \left\{ -\beta \int_0^{N_g} dN' w'(\mathbf{R}(N')) \right\}} \\
 &= \left\langle \int_0^{N_g} dN' \delta(\mathbf{R}(N') - \mathbf{r}) \right\rangle_{\substack{\mathbf{R}(0) = \mathbf{r}_g \\ \text{Field } w'}}
 \end{aligned} \tag{E12}$$

Using the definition eq B5, we can write:

$$\frac{1}{Q_g[\mathbf{r}_g; w'(\mathbf{r})]} \int_0^{N_g} dN' G(\mathbf{r}_g, \mathbf{r}, N') q_m(\mathbf{r}, N_g - N') = \rho_{\text{seg, bulk}} \left\langle \hat{\phi}_g(\mathbf{r}) \right\rangle_{\substack{\mathbf{R}(0) = \mathbf{r}_g \\ \text{Field } w'}} = \rho_{\text{seg, bulk}} \varphi_g(\mathbf{r}) = \rho_g(\mathbf{r})$$

E13

where $\varphi_g(\mathbf{r})$ is the reduced density and $\rho_g(\mathbf{r})$ the segment density contributed by the considered grafted chain, at position \mathbf{r} .

Taking into account eq E4, which relates the *partition function* of a grafted chain to the *restricted partition function* of a matrix chain, we rewrite eq E13 for a specific grafted chain, i_g , as:

$$\varphi_{i_g}(\mathbf{r}) = \frac{1}{\rho_{\text{seg,bulk}} q_m(\mathbf{r}_{i_g}, N_g)} \int_0^{N_g} dN' G(\mathbf{r}_{i_g}, \mathbf{r}, N') q_m(\mathbf{r}, N_g - N') \quad \text{E14}$$

The total reduced density due to all grafted chains will be:

$$\begin{aligned} \varphi_g(\mathbf{r}) &= \sum_{i_g=1}^{n_g} \varphi_{i_g}(\mathbf{r}) = \frac{1}{\rho_{\text{seg,bulk}}} \sum_{i_g=1}^{n_g} \frac{1}{q_m(\mathbf{r}_{i_g}, N_g)} \int_0^{N_g} dN' G(\mathbf{r}_{i_g}, \mathbf{r}, N') q_m(\mathbf{r}, N_g - N') = \\ &= \int_0^{N_g} dN' \left\{ \sum_{i_g=1}^{n_g} \frac{1}{\rho_{\text{seg,bulk}} q_m(\mathbf{r}_{i_g}, N_g)} G(\mathbf{r}_{i_g}, \mathbf{r}, N') \right\} q_m(\mathbf{r}, N_g - N') \end{aligned} \quad \text{E15}$$

Let us set

$$q_g(\mathbf{r}, N) = \sum_{i_g=1}^{n_g} \frac{N_g}{\rho_{\text{seg,bulk}} q_m(\mathbf{r}_{i_g}, N_g)} G(\mathbf{r}_{i_g}, \mathbf{r}, N) \quad \text{E16}$$

With this definition,

$$\varphi_g(\mathbf{r}) = \frac{1}{N_g} \int_0^{N_g} dN q_g(\mathbf{r}, N) q_m(\mathbf{r}, N_g - N) \quad \text{E17}$$

Appendix F Solution of Edwards in 1D spherical coordinates

In spherical polar coordinates the Laplacian is written as follows:

$$\nabla^2 u = \frac{\partial^2 u}{\partial x^2} + \frac{\partial^2 u}{\partial y^2} + \frac{\partial^2 u}{\partial z^2} = \frac{1}{r} \frac{\partial^2 (ru)}{\partial r^2} + \frac{1}{r^2 \sin \theta} \frac{\partial}{\partial \theta} \left(\sin \theta \frac{\partial u}{\partial \theta} \right) + \frac{1}{r^2 \sin^2 \theta} \frac{\partial^2 u}{\partial \phi^2} \quad \text{F1}$$

In the planar surface case, $u = u(z, t)$, $\frac{\partial^2 u}{\partial x^2} = 0$ and $\frac{\partial^2 u}{\partial y^2} = 0$ with z being the direction normal to the surface. Therefore, the *Edwards* diffusion equation in *Cartesian* coordinates assumes the one-dimensional form:

$$\frac{\partial u(z, t)}{\partial t} - D \frac{\partial^2 u(z, t)}{\partial z^2} + au(z, t) = 0 \quad \text{F2}$$

with t corresponding to the contour length along a chain, u being a *restricted partition function* (*propagator*), D determined by the conformational stiffness, and a by the self-consistent field (compare eq 1 in main text).

In the case of a spherical nanoparticle with uniformly smeared grafting points on its surface, there is spherical symmetry. There is no dependence on the polar and azimuthal angles, $u = u(r, t)$ and the Edwards diffusion equation in spherical polar coordinates simplifies to:

$$\begin{aligned} \frac{\partial u}{\partial t} - D \left[\frac{1}{r} \frac{\partial^2 (ru)}{\partial r^2} \right] + au = 0 \quad \text{or} \\ \frac{\partial (ru)}{\partial t} - D \frac{\partial^2 (ru)}{\partial r^2} + a(ru) = 0 \end{aligned} \quad \text{F3}$$

If we set

$$\psi(r, t) = ru(r, t) \quad \text{F4}$$

eq F3 becomes

$$\frac{\partial \psi(r, t)}{\partial t} - D \frac{\partial^2 \psi(r, t)}{\partial r^2} + a\psi(r, t) = 0 \quad \text{F5}$$

Appendix G Derivation of the density gradient term from the square gradient and the Laplacian

The general expression of the gradient term of the free energy in three dimensions is the following:

$$\Omega_{\text{SGT}} = \kappa \int_{\mathbb{R}^3} [\nabla \rho(\mathbf{r})]^2 \, d\mathbf{r} \quad \text{G1}$$

with $\rho(\mathbf{r})$ being the local segment density and κ the influence parameter. The corresponding free energy function used in our calculations is

$$f[\rho(\mathbf{r}), \nabla \rho(\mathbf{r})] = f[\rho(\mathbf{r}), \mathbf{0}] + f_{\text{SGT}}(\nabla \rho(\mathbf{r})) = f[\rho(\mathbf{r}), \mathbf{0}] + \kappa [\nabla \rho(\mathbf{r})]^2 \quad \text{G2}$$

with $f[\rho(\mathbf{r}), \mathbf{0}]$ being the *Helmholtz* energy density of a homogeneous polymer fluid of segment density $\rho(\mathbf{r})$ at the considered temperature, calculated from an equation of state. In many cases, the gradient term E_{SGT} can be calculated instead from the *Laplacian* of the density, as will be shown below.

In planar geometries one can take advantage of the homogeneity along the planar (x, y) directions (i.e., cylindrical symmetry). Since $\partial \rho / \partial x = \partial \rho / \partial y = 0$, the gradient term can be written as follows:

$$\Omega_{\text{SGT}} / S = \kappa \int_{\mathbb{R}^1} \left(\frac{d\rho}{dh} \right)^2 \, dh \quad \text{G3}$$

with h being the segment-surface distance and S the considered surface area. Alternatively, the gradient term can be written in terms of the Laplacian as follows:

$$\Omega_{\text{SGT}} / S = \kappa \int_0^L \frac{d\rho}{dh} \frac{d\rho}{dh} \, dh = \kappa \left[\frac{d\rho}{dh} \rho \right]_0^L - \kappa \int_0^L \frac{d^2 \rho}{dh^2} \rho \, dh \quad \text{G4}$$

Either $\rho = 0$ at the *Dirichlet* boundaries ($q = 0$) or $d\rho/dz=0$ at the *Neumann* boundaries ($dq/dz=0$); thus, eq G4 becomes:

$$\Omega_{\text{SGT}} / S = -\kappa \int_0^L \frac{d^2 \rho}{dh^2} \rho \, dh \quad \text{G5}$$

Appendices

In systems with spherical homogeneity with respect to the center of the nanoparticle one can express eq G1 as follows:

$$\Omega_{\text{SGT}} = \kappa \int_0^R \left(\frac{d\rho}{dr} \right)^2 4\pi r^2 dr \quad \text{G6}$$

with r being the distance between the center of the spherical nanoparticle and the polymer segment. The gradient term can be written in terms of the Laplacian as follows:

$$\begin{aligned} \Omega_{\text{SGT}} &= \kappa \int_0^R \frac{d\rho}{dr} \frac{d\rho}{dr} 4\pi r^2 dr = \kappa \left[\frac{d\rho}{dr} \int_0^r \left(\frac{d\rho}{dr'} 4\pi r'^2 \right) dr' \right]_0^R - \kappa \int_0^R \frac{d^2\rho}{dr^2} \int_0^r \left(\frac{d\rho}{dr'} 4\pi r'^2 dr' \right) dr \\ &= -\kappa \int_0^R \frac{d^2\rho}{dr^2} \int_0^r \left(\frac{d\rho}{dr'} 4\pi r'^2 dr' \right) dr \end{aligned} \quad \text{G7}$$

However,

$$4\pi \int_0^r \frac{d\rho}{dr'} r'^2 dr' = 4\pi \left[\rho(r') r'^2 \right]_0^r - 8\pi \int_0^r \rho(r') r' dr' = -8\pi \int_0^r \rho(r') r' dr'$$

Thus, eq G7 becomes:

$$\Omega_{\text{SGT}} = 8\pi\kappa \int_0^R \frac{d^2\rho}{dr^2} \int_0^r \rho(r') r' dr' dr \quad \text{G8}$$

Appendix H Space and contour discretization benchmarks in RuSseL1D

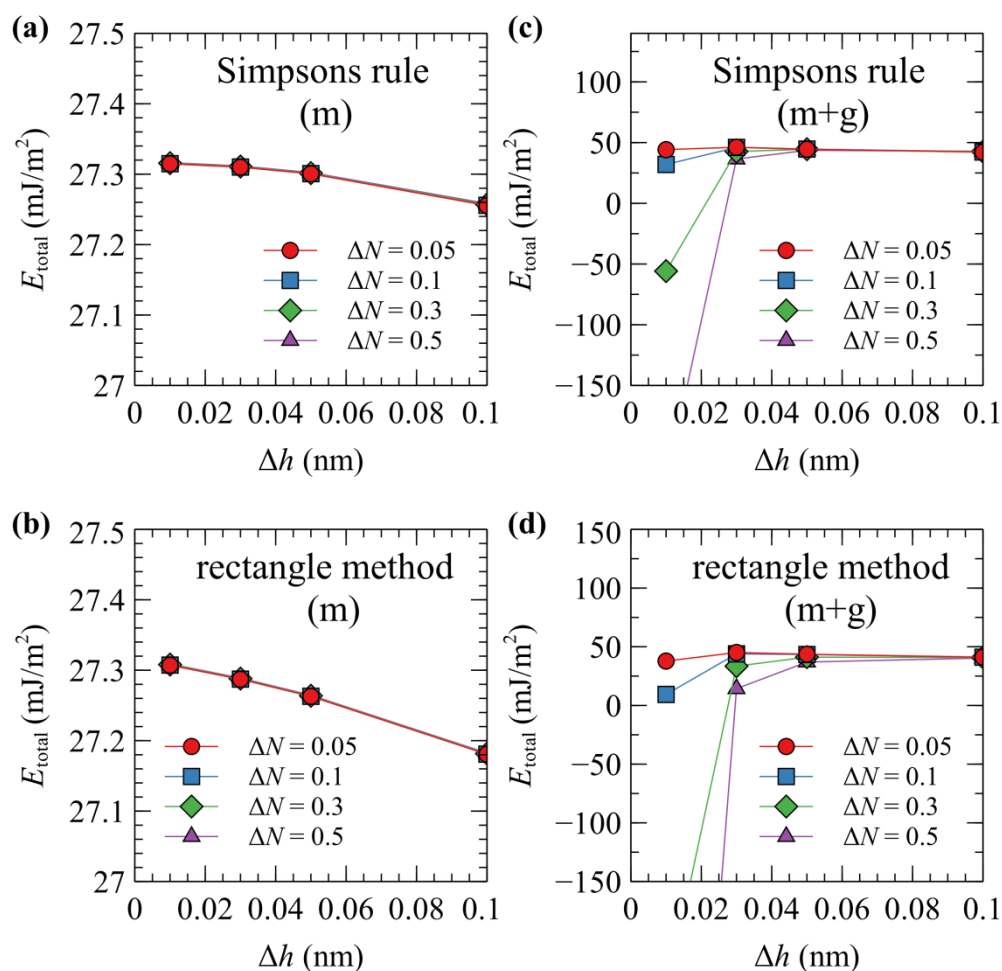


Figure H.1 Evaluations of the grand potential from systems with matrix (m) (a, b) and with matrix and grafted (m+g) (c, d), for various degrees of spatial (Δh) and chain contour (ΔN) discretization and integration methods. (a), (c) and (b), (d) panels correspond to evaluations of the convolution integrals with the Simpson and rectangle integration methods, respectively. These evaluations were performed in planar geometries, for molecular weights of grafted and matrix chains $M_g = M_m = 5.2$ kg/mol, grafting density $\sigma_g = 0.5$ nm⁻² (when grafted chains are present) and in absence of any solid/polymer interactions.

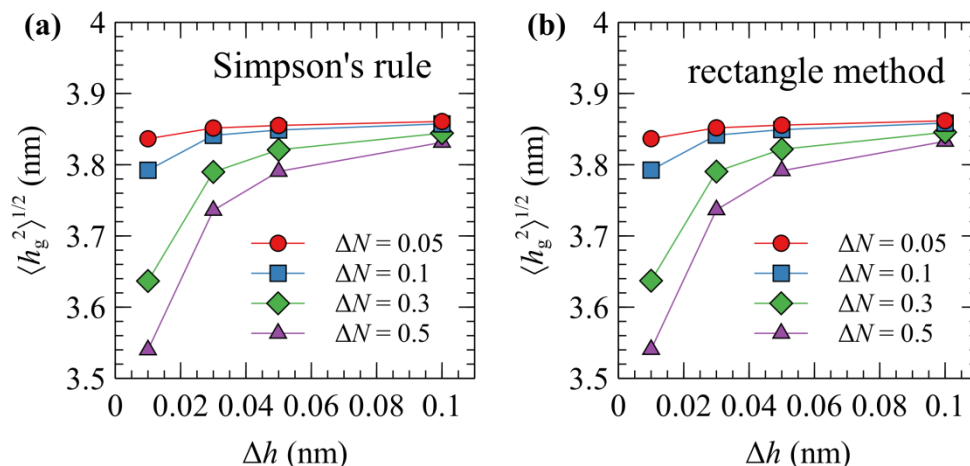


Figure H.2 Evaluations of the mean brush thickness for various degrees of spatial and chain-contour discretizations. (a) and (b) panels correspond to evaluations of the convolution integrals with the Simpson and rectangle integration methods, respectively. These evaluations were performed in planar geometries, for molecular weights of grafted and matrix chains $M_g = M_m = 5.2$ kg/mol, grafting density $\sigma_g = 0.5$ nm⁻² (when grafted chains are present) and in absence of any solid/polymer interactions.

Figure H.1 and Figure H.2 illustrate a sensitivity analysis of the grand potential and the mean brush thickness on the degree of spatial (Δh) and chain-contour discretization using either the Simpson or the rectangle integration method for the evaluation of convolution integrals. Overall, Simpson's rule has slightly better performance in terms of accuracy than the rectangle method. It is noteworthy that in presence of grafted chains, the solution becomes more sensitive to ΔN with decreasing Δh . This can be attributed to that smaller Δh values lead to sharper delta functions, $\Delta(h) \sim \Delta h^{-1}$; hence, much smaller ΔN steps are required.

An advantage of the rectangle method is that it results in slightly more accurate prediction of the grafting density via the segment balance equation; in detail, the error with the Simpson and the rectangle method is in the order of $\sim 10^{-4}$ and $\sim 10^{-5}$, respectively. In addition, it offers the possibility to compute the gradient energy term via both the square gradient and the Laplacian of the segment density (see Appendix G above). This probably has to do with that Simpson's rule does not weight all the points evenly; e.g., in Simpson's $\frac{3}{4}$ rule, the weights on the first and last point is $\frac{3}{4}$, while the weight of the remaining points alternates between $\frac{4}{3}$ and $\frac{2}{3}$.

Appendix I Field mixing fraction benchmarks in RuSseL1D

Figure I.1a and c presents the number of steps to achieve field convergence as a function of the field mixing fraction (f_{mix}). The number of steps for convergence is inversely proportional to f_{mix} . Figure I.1b and d depict the optimum values of a_{mix} as a function of the molar mass of the grafted chains. Slightly larger a_{mix} value than those depicted in Figure I.1 (right) can critically affect the stability of the iterative scheme. According to our tests, three different situations may arise for large a_{mix} values and in the context of the *Sanchez-Lacombe* equation of state: (i) the field equilibration procedure diverges, (ii) $\Delta w_{\text{ifc}}^{\text{max}}$ oscillates indefinitely around a value that is larger than the accepted tolerance, $\Delta w_{\text{ifc}}^{\text{tol}}$, (see Figure I.2b) or (iii) the field converges to an unphysical solution (e.g., the matrix chains or part of them become extinct, as shown in Figure I.2c).

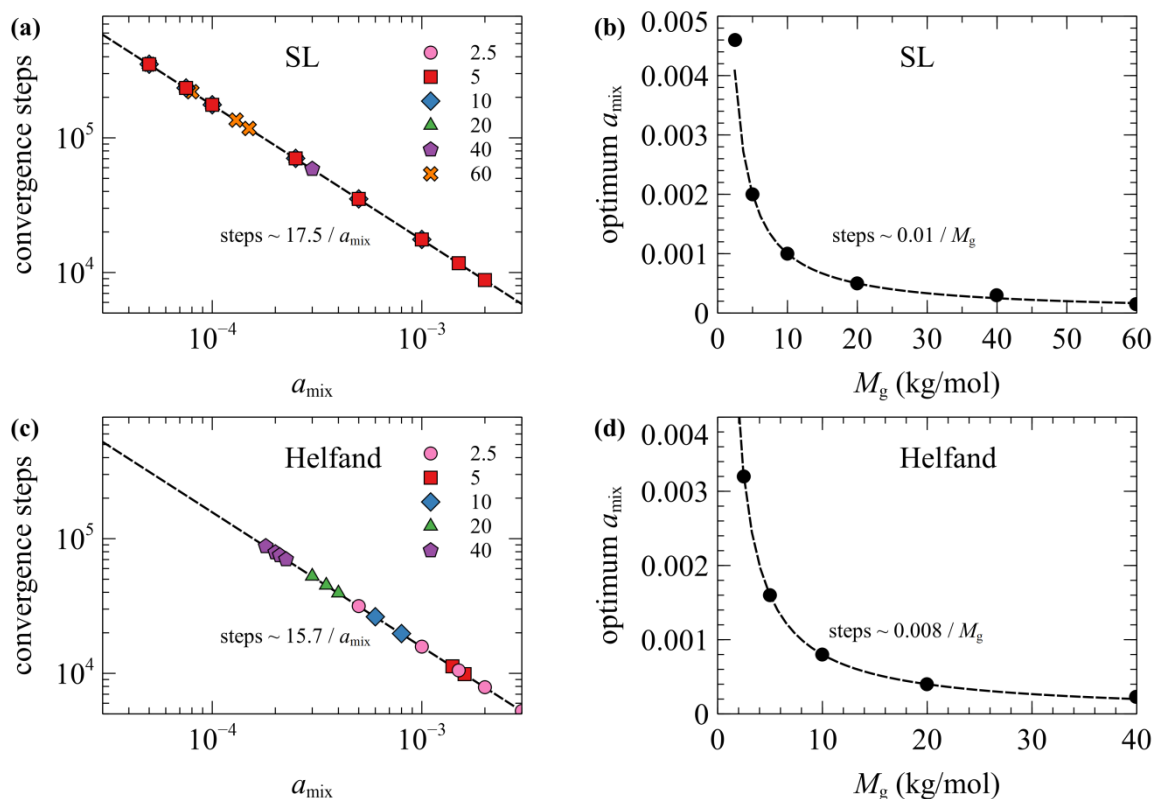


Figure I.1 (a, c) Number of steps to achieve field convergence ($\Delta w_{\text{ifc}}^{\text{max}} \leq 10^{-5} k_B T$) for various chain molecular weights. (b, d) Optimal field mixing fraction, a_{mix} , versus chain molar mass, M_g . In (a,b), the *Sanchez-Lacombe* EoS was used in conjunction with the square gradient theory term, while in (c,d) the *Helfand* free energy density was used. In all cases, the molecular weight of matrix chains is equal to that of grafted chains, $M_g = M_m$. The radius of the particle is equal to $R_S = 8$ nm and the grafting density is equal to $\sigma_g = 0.8$ nm $^{-2}$.

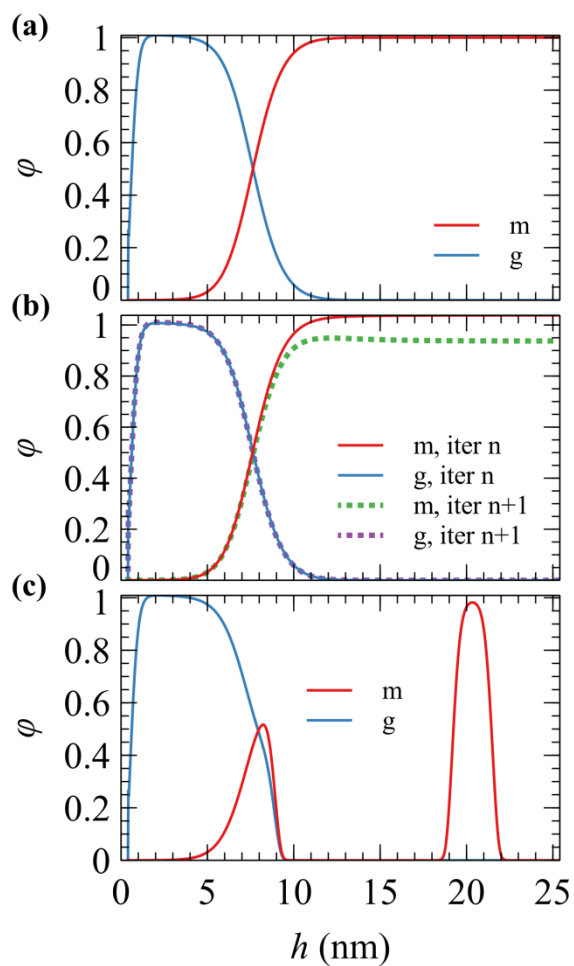


Figure I.2 Reduced radial density profiles for a system with chain molecular weight $M_g = M_m = 5$ kg/mol, grafting density $\sigma_g = 0.8$ nm⁻² and particle radius $R_S = 8$ nm. The field mixing fraction, a_{mix} , for each case was set to **(a)** $2 \cdot 10^{-3}$, **(b)** $2.5 \cdot 10^{-3}$ and **(c)** $5 \cdot 10^{-3}$; the corresponding maximum field errors are $\Delta w_{\text{ifc}}^{\text{max}} = 10^{-6}$, 0.42 and 0.6 $k_B T$.

Appendix J Instructions for compiling RuSseL3D and its dependencies

GCC-5.1.0

Before performing the steps shown below, it is highly recommended to execute the following command:

```
$unset LIBRARY_PATH CPATH C_INCLUDE_PATH PKG_CONFIG_PATH
CPLUS_INCLUDE_PATH INCLUDE LD_LIBRARY_PATH
```

After downloading `gcc-5.1.0.tar.gz` from <https://ftp.gnu.org/gnu/gcc/>, you can follow the instructions presented below:

- `$tar xzf gcc-5.1.0.tar.gz`
- `$cd gcc-5.1.0`
- `./contrib/download_prerequisites`
- `$cd ../`
- `$mkdir objdir`
- `$cd objdir`
- `$pwd/./gcc-5.1.0/configure --prefix=$HOME/GCC-5.1.0 --disable-multilib`
- `$make -j 6`
- `$make install -j 6`
- Go to home (~) directory and open the `.bashrc` (hidden) file:

```
$vi .bashrc
```

and add the following snippets:

```
alias gfortran=/pathToGCC/bin/gfortran
alias gcc=/pathToGCC/bin/gcc
alias g++=/pathToGCC/bin/g++
export LD_LIBRARY_PATH=/pathToGCC/lib64
```

In order for the changes of the `.bashrc` file to be activated, you must issue the following command (obviously while in the home directory):

```
$source .bashrc
```

OPENMPI-4.0.5

We need to connect `openmpi` wrapper compilers with the `gcc` compilers that we have already installed. Before doing so, the `openmpi` requires for some reason that all `*.la` static libraries are removed from `gcc/lib` directory (at least that was the case when I tried to install it myself).

```
$cd pathToGCC/lib
```

```
$rm *.la
```

Be careful not to remove the `*.a` files as well! Otherwise the `gcc` compilers must be recompiled to retrieve those static libraries.

Download `openmpi-5.2.1.tar.gz` using the link <https://www.openmpi.org/software/ompi/v4.0/> and then issue the following:

- `$tar xzf openmpi-4.0.5.tar.gz`
- `./configure -prefix=pathToOpenmpi/openmpi --disable-mca-dso CC=pathToGCC/bin/gcc CXX=pathToGCC/bin/g++ FC=pathToGCC/bin/gfortran`
- `$make -j 6 all install`

Appendices

- Go to home (~) directory and open the `.bashrc` (hidden) file:
`$vi .bashrc`
and add the following snippets:
`export LD_LIBRARY_PATH=/pathToOpenmpi/lib`
`export OPAL_PREFIX=/pathToOpenmpi`
`alias mpicc=/pathToOpenmpi/bin/mpicc`
`alias mpifort=/pathToOpenmpi/bin/mpifort`
`alias mpirun=/pathToOpenmpi/bin/mpirun -mca btl vader,self`
In order for the changes of the `.bashrc` file to be activated, you must issue the following command (obviously while in the home directory ☺):
`$source .bashrc`

- When running the application with `mpirun`, you might deal with a message saying that the library `libmpi.so.1` was not found or does not exist. You can bypass this problem by performing the following:
 - `$cd pathToOpenmpi/lib`
 - `$ln -s libmpi.so limpi.so.1`

Most likely the application will run without issues this time.

MAKE SURE THAT OPENMPI HAS BEEN COMPILED WITH THE NON-DEFAULT GNU COMPILER!

OPENBLAS-0.3.7

Download `openblas-0.3.7.tar.gz` from <https://www.openblas.net/> and then issue the following:

- `$tar xzf openblas-0.3.7.tar.gz`
- `$make -j 6 FC=/pathToGCC/bin/gfortran CC=/pathToGCC/bin/gcc PREFIX=/pathToInstall`
- `$make -j 6 FC=/pathToGCC/bin/gfortran CC=/pathToGCC/bin/gcc PREFIX=/pathToInstall install`

- Go to home (~) directory and open the `.bashrc` (hidden) file:
`$vi .bashrc`
and add the following snippets:
`export LD_LIBRARY_PATH=/pathToOpenblas/lib`

MAKE SURE THAT OPENBLAS HAS BEEN COMPILED WITH THE NON-DEFAULT GNU COMPILER!

PARMETIS-4.0.2

Download `parmetis-4.0.2.tar.gz` using the link <http://glaros.dtc.umn.edu/gkhome/metis/parmetis/download> and then issue the following:

- `$tar xzf parmetis-4.0.2.tar.gz`
- `$mkdir parmetis`
- `$mkdir metis`
- `$cd parmetis-4.0.2/`
- `$make -j 6 config cc=/pathToOpenmpi/bin/mpicc cxx=/pathToOpenmpi/bin/mpicxx prefix=~/.parmetis/parmetis shared=1`
- `$make -j 6 install`
- `$cd ../parmetis-4.0.2/metis`

- `$make -j 6 config cc=/pathToOpenmpi/bin/mpicc cxx=/pathToOpenmpi/bin/mpicxx prefix=~/.pathToMetis/metis shared=1`
 - `$make -j 6 install`
 - `$cp metis/include/metis.h parmetis/include`
 - `$vi parmetis/include/parmetis.h`
`replace: #include <metis.h> with: #include "metis.h"`
`replace: #include <mpi.h> with: #include /pathToOpenmpi/include/mpi.h`
 - Go to home (~) directory and open the `.bashrc` (hidden) file:
`$vi .bashrc`
 and append the following library paths in `LD_LIBRARY_PATH` variable:
`export LD_LIBRARY_PATH=...:/pathToParmetis/lib`
`export LD_LIBRARY_PATH=...:/pathToMetis/lib`
 In order for the changes of the `.bashrc` file to be activated, you must issue the following command (obviously while in the home directory):
`$source .bashrc`
 - Create a file named `test.cpp` in the `pathToParmetis` directory:
`$vi test.cpp`
 And copy-paste the following code snippet:

```
-----
#include <iostream>
#include "metis/include/metis.h"
#include "parmetis/include/parmetis.h"

int main(){
    std::cout << "Test!" << std::endl;
    return 0;
}
-----
```
 - `$mpic++ test.cpp`
 - `$mpirun a.out`
 If you get "Test!" on your screen, then everything is ok! (probably)
- MAKE SURE THAT PARMETIS HAS BEEN COMPILED WITH THE NON-DEFAULT MPI COMPILER!*

LAPACK-3.9.0

Download `lapack-3.9.0.tar.gz` from <http://www.netlib.org/lapack/> and then issue the following:

- `$tar xzf lapack-3.9.0.tar.gz`
 - `$cp make.inc.example make.inc`
 - `$vi make.inc`
`Set gcc and gfortran compiler paths.`
`In the end of the file, link with openblas.`
 - `make -j 6`
- FOR THE SERIAL MUMPS COMPILATION, LAPACK DOES NOT NEED TO BE INSTALLED BECAUSE OPENBLAS CONTAINS ITS OWN SERIAL LAPACK LIBRARY.*

Appendices

SCALAPACK-2.0.2

Download `scalapack-2.0.2.tar.gz` from <http://www.netlib.org/scalapack/> and then issue the following:

- `$tar xzf scalapack-2.0.2.tar.gz`
- `$cp SLmake.inc.example SLmake.inc`
- `$vi SLmake.inc`
 - Set `FCFLAGS`, `FFFLAGS` compiler/cpu optimization variables:

```
FC=/pathToOpenmpi/bin/mpifort
CC=/pathToOpenmpi/bin/mpicc
FCFLAGS=-O3 -msse2
CCFLAGS=-O3 -msse2
BLASLIB=-L/pathToOpenblas -lopenblas
LAPACKLIB=-L/pathToOpenblas -lopenblas
(openblas library contains both lapack and blas)
```
- `make -j 6`
- Go to home (`~`) directory and open the `.bashrc` (hidden) file:

```
$vi .bashrc
```

and add the following snippets:

```
export LD_LIBRARY_PATH=/pathToScalapack
```

MAKE SURE THAT SCALAPACK HAS BEEN COMPILED WITH THE NON-DEFAULT MPI COMPILER!

MUMPS-5.2.1

Download `mumps-5.2.1.tar.gz` using the link <http://mumps.enseeiht.fr/index.php?page=dwnld> (you will actually have to send a request and then receive the source code via email) and then issue the following:

- `$tar xzf mumps-5.2.1.tar.gz`
- `$vi pathToMumps/Makefile.inc`
 - If the serial version of `mumps` is to be compiled:

```
CC=pathToGCC/bin/gcc
FC=pathToGCC/bin/gfortran
FL=pathToGCC/bin/gfortran
LAPACK=-L/pathToScalapack/ -llapack
```
 - If the parallel version of `mumps` is to be compiled:

```
CC=pathToOpenmpi/bin/mpicc
FC=pathToOpenmpi/bin/mpifort
FL=pathToOpenmpi/bin/mpifort
LAPACK=-L/pathToScalapack/ -lscalapack
SCALAP=-L/pathToScalapack/ -lscalapack
```
 - ```
OPTF=-O3 -msse2 (or fma, avx: depends on compiler and cpu)
OPTL=-O3 -msse2 (or fma, avx: depends on compiler and cpu)
OPTC=-O3 -msse2 (or fma, avx: depends on compiler and cpu)
```
- `$make -j 6`

## REFERENCES

- (1) Fredrickson, G. H. *The Equilibrium Theory of Inhomogeneous Polymers*; International Series of Monographs on Physics, Oxford University Press: Oxford, UK, 2006.
- (2) Lakkas, A. T.; Sgouros, A. P.; Theodorou, D. N. Self-Consistent Field Theory Coupled with Square Gradient Theory of Free Surfaces of Molten Polymers and Compared to Atomistic Simulations and Experiment. *Macromolecules* **2019**, *52*, 5337–5356.
- (3) Theodorou, D. N. Polymers at Surfaces and Interfaces. *Comput. Simulations Surfaces Interfaces* **2003**, 329–419.
- (4) Müller M; Schmid F. Incorporating Fluctuations and Dynamics in Self-Consistent Field Theories for Polymer Blends. *Adv. Polym. Sci.* **2005**, *185*, 1–58.
- (5) Schmid, F. Self-Consistent-Field Theories for Complex Fluids. *J. Phys Condens. Matter* **1998**, *10*, 8105–8138.
- (6) Allen, M. P.; Tildesley, D. J. *Computer Simulation of Liquids*; Clarendon Press: New York, 1989.
- (7) Vogiatzis, G. G.; Theodorou, D. N. *Multiscale Molecular Simulations of Polymer-Matrix Nanocomposites: Or What Molecular Simulations Have Taught Us About the Fascinating Nanoworld*; Springer Netherlands, 2017; Vol. 25.
- (8) Fredrickson, G. H.; Ganesan, V.; Drolet, F. Field-Theoretical Computer Simulation Methods for Polymer and Complex Fluids. *Macromolecules* **2002**, *35*, 16–39.
- (9) Guerrini, L.; Alvarez-Puebla, R. A.; Pazos-Perez, N. Surface Modifications of Nanoparticles for Stability in Biological Fluids. *Materials (Basel)*. **2018**, *11*, 1–28.
- (10) Klushin, L.; Skvortsov, A.; Qi, S.; Kreer, T.; Schmid, F. Polydispersity Effects on Interpenetration in Compressed Brushes. *Macromolecules* **2019**, *52*, 1810–1820.
- (11) Ivanova, A. S.; Polotsky, A. A.; Skvortsov, A. M.; Klushin, L. I.; Schmid, F. Adsorption-Active Polydisperse Brush with Tunable Molecular Mass Distribution. *J. Chem. Phys.* **2022**, *156*, 44902.
- (12) Ivanova, A. S.; Polotsky, A. A.; Skvortsov, A. M.; Klushin, L. I.; Schmid, F. Compression and Interpenetration of Adsorption-Active Brushes. *J. Chem. Phys.* **2023**, *158*, 24902.
- (13) Savin, D. A.; Pyun, J.; Patterson, G. D.; Kowalewski, T.; Matyjaszewski, K. Synthesis and Characterization of Silica-Graft-Polystyrene Hybrid Nanoparticles: Effect of Constraint on the Glass-Transition Temperature of Spherical Polymer Brushes. *J. Polym. Sci. Part B Polym. Phys.* **2002**, *40*, 2667–2676.
- (14) Zhao, D.; Ge, S.; Senses, E.; Akcora, P.; Jestin, J.; Kumar, S. K. Role of Filler Shape and Connectivity on the Viscoelastic Behavior in Polymer Nanocomposites. *Macromolecules* **2015**, *48*, 5433–5438.
- (15) Moll, J. F.; Akcora, P.; Rungta, A.; Gong, S.; Colby, R. H.; Benicewicz, B. C.; Kumar, S. K. Mechanical Reinforcement in Polymer Melts Filled with Polymer Grafted Nanoparticles. *Macromolecules* **2011**, *44*, 7473–7477.
- (16) Giovino, M.; Pribyl, J.; Benicewicz, B.; Kumar, S.; Schadler, L. Linear Rheology of Polymer Nanocomposites with Polymer-Grafted Nanoparticles. *Polymer (Guildf)*. **2017**, *131*, 104–110.

## References

---

- (17) Hamaker, H. C. The London—van Der Waals Attraction between Spherical Particles. *Physica* **1937**, *4*, 1058–1072.
- (18) Green, P. F. The Structure of Chain End-Grafted Nanoparticle/Homopolymer Nanocomposites. *Soft Matter* **2011**, *7*, 7914–7926.
- (19) Hore, M. J. A. Polymers on Nanoparticles: Structure & Dynamics. *Soft Matter* **2019**, *15*, 1120–1134.
- (20) Frischknecht, A. L.; Hore, M. J. A.; Ford, J.; Composto, R. J. Dispersion of Polymer-Grafted Nanorods in Homopolymer Films: Theory and Experiment. *Macromolecules* **2013**, *46*, 2856–2869.
- (21) Trombly, D. M.; Ganesan, V. Curvature Effects upon Interactions of Polymer-Grafted Nanoparticles in Chemically Identical Polymer Matrices. *J. Chem. Phys.* **2010**, *133*, 154904.
- (22) Sunday, D.; Ilavsky, J.; Green, D. L. A Phase Diagram for Polymer-Grafted Nanoparticles in Homopolymer Matrices. *Macromolecules* **2012**, *45*, 4007–4011.
- (23) Voyiatzis, G. G.; Theodorou, D. N. Structure of Polymer Layers Grafted to Nanoparticles in Silica-Polystyrene Nanocomposites. *Macromolecules* **2013**, *46*, 4670–4683.
- (24) Lakkas, A. T.; Sgouros, A. P.; Revelas, C. J.; Theodorou, D. N. Structure and Thermodynamics of Grafted Silica/Polystyrene Dilute Nanocomposites Investigated through Self-Consistent Field Theory. *Soft Matter* **2021**, *17*, 4077–4097.
- (25) Xu, J.; Zhang, H.; Yang, Y. Morphology and Interactions of Polymer Brush-Coated Spheres. *J. Polym. Sci.* **2006**, *44*, 2811–2820.
- (26) Hasegawa, R.; Aoki, Y.; Doi, M. Optimum Graft Density for Dispersing Particles in Polymer Melts. *Macromolecules* **1996**, *29*, 6656–6662.
- (27) Ferreira, P. G.; Ajdari, A.; Leibler, L. Scaling Law for Entropic Effects at Interfaces between Grafted Layers and Polymer Melts. *Macromolecules* **1998**, *31*, 3994–4003.
- (28) Sgouros, A. P.; Revelas, C. J.; Lakkas, A. T.; Theodorou, D. N. Potential of Mean Force between Bare or Grafted Silica/Polystyrene Surfaces from Self-Consistent Field Theory. *Polymers (Basel)*. **2021**, *13*, 1197.
- (29) Green, D. L.; Mewis, J. Connecting the Wetting and Rheological Behaviors of Poly(Dimethylsiloxane)- Grafted Silica Spheres in Poly(Dimethylsiloxane) Melts. *Langmuir* **2006**, *22*, 9546–9553.
- (30) Kumar, S. K.; Jouault, N.; Benicewicz, B.; Neely, T. Nanocomposites with Polymer Grafted Nanoparticles. *Macromolecules* **2013**, *46*, 3199–3214.
- (31) Sunday, D. F.; Green, D. L. Thermal and Rheological Behavior of Polymer Grafted Nanoparticles. *Macromolecules* **2015**, *48*, 8651–8659.
- (32) Drolet, F.; Fredrickson, G. H. Optimizing Chain Bridging in Complex Block Copolymers. *Macromolecules* **2001**, *34*, 5317–5324.
- (33) Arora, A.; Qin, J.; Morse, D. C.; Delaney, K. T.; Fredrickson, G. H.; Bates, F. S.; Dorfman, K. D. Broadly Accessible Self-Consistent Field Theory for Block Polymer Materials Discovery. *Macromolecules* **2016**, *49*, 4675–4690.
- (34) Matsen, M. W.; Schick, M. Stable and Unstable Phases of a Diblock Copolymer Melt. *Phys. Rev. Lett.* **1994**, *72*, 2660–2663.
- (35) Ackerman, D. M.; Delaney, K.; Fredrickson, G. H.; Ganapathysubramanian, B. A Finite Element Approach to Self-Consistent Field Theory Calculations of Multiblock Polymers. *J. Comput. Phys.* **2017**, *331*, 280–296.
- (36) Ndro, T. V. M.; Voyiatzis, E.; Ghanbari, A.; Theodorou, D. N.; Böhm, M. C.; Müller-Plathe, F. Interface of Grafted and Ungrafted Silica Nanoparticles with a Polystyrene Matrix: Atomistic Molecular Dynamics Simulations. *Macromolecules* **2011**, *44*, 2316–2327.
- (37) Meng, D.; Kumar, S. K.; Lane, J. M.; Grest, G. S. Effective Interactions between Grafted Nanoparticles in a Polymer Matrix. *Soft Matter* **2012**, *8*, 5002–5010.
- (38) Kalb, J.; Dukes, D.; Kumar, S. K.; Hoy, R. S.; Grest, G. S. End Grafted Polymer Nanoparticles in a Polymeric Matrix: Effect of Coverage and Curvature. *Soft Matter* **2011**, *7*, 1418–1425.
- (39) Ethier, J. G.; Hall, L. M. Modeling Individual and Pairs of Adsorbed Polymer-Grafted Nanoparticles: Structure and Entanglements. *Soft Matter* **2018**, *14*, 643–652.
- (40) Müller, M. Phase Diagram of a Mixed Polymer Brush. *Phys. Rev. E - Stat. Physics, Plasmas,*



- Fluids, Relat. Interdiscip. Top.* **2002**, *65*, 030802.
- (41) Chantawansri, T. L.; Hur, S. M.; Garca-Cervera, C. J.; Cenicerros, H. D.; Fredrickson, G. H. Spectral Collocation Methods for Polymer Brushes. *J. Chem. Phys.* **2011**, *134*, 244905.
- (42) Abbas, Z. M.; Tawfilas, M.; Khani, M. M.; Golian, K.; Marsh, Z. M.; Jhalaria, M.; Simonutti, R.; Stefik, M.; Kumar, S. K.; Benicewicz, B. C. Reinforcement of Polychloroprene by Grafted Silica Nanoparticles. *Polymer (Guildf)*. **2019**, *171*, 96–105.
- (43) Askar, S.; Li, L.; Torkelson, J. M. Polystyrene-Grafted Silica Nanoparticles: Investigating the Molecular Weight Dependence of Glass Transition and Fragility Behavior. *Macromolecules* **2017**, *50*, 1589–1598.
- (44) Giovino, M.; Buenning, E.; Jimenez, A.; Kumar, S. K.; Schadler, L. Polymer Grafted Nanoparticle Viscosity Modifiers. *Macromol. Chem. Phys.* **2019**, *220*, 1–7.
- (45) Bornani, K.; Rahman, M. A.; Benicewicz, B.; Kumar, S.; Schadler, L. Using Nanofiller Assemblies to Control the Crystallization Kinetics of High-Density Polyethylene. *Macromolecules* **2021**, *54*, 5673–5682.
- (46) Jiao, Y.; Hsiao, M.-S.; Vaia, R. A.; Tibbits, A.; Drummy, L. F.; Gillman, A.; Buskohl, P. Deformation Behavior of Polystyrene-Grafted Nanoparticle Assemblies with Low Grafting Density. *Macromolecules* **2018**, *51*, 7257–7265.
- (47) Adhikari, S.; Nikoubashman, A.; Leibler, L.; Rubinstein, M.; Midya, J.; Kumar, S. K. Gas Transport in Interacting Planar Brushes. *ACS Polym. Au* **2021**, *1*, 39–46.
- (48) Bilchak, C. R.; Jhalaria, M.; Huang, Y.; Abbas, Z.; Midya, J.; Benedetti, F. M.; Parisi, D.; Egger, W.; Dickmann, M.; Minelli, M.; Doghieri, F.; Nikoubashman, A.; Durning, C. J.; Vlassopoulos, D.; Jestin, J.; Smith, Z. P.; Benicewicz, B. C.; Rubinstein, M.; Leibler, L.; Kumar, S. K. Tuning Selectivities in Gas Separation Membranes Based on Polymer-Grafted Nanoparticles. *ACS Nano* **2020**, *14*, 17174–17183.
- (49) Jeong, S. P.; Kumar, R.; Genix, A. C.; Popov, I.; Li, C.; Mahurin, S. M.; Hu, X.; Bras, W.; Popovs, I.; Sokolov, A. P.; Bocharova, V. Improving Gas Selectivity in Membranes Using Polymer-Grafted Silica Nanoparticles. *ACS Appl. Nano Mater.* **2021**, *4*, 5895–5903.
- (50) Midya, J.; Rubinstein, M.; Kumar, S. K.; Nikoubashman, A. Structure of Polymer-Grafted Nanoparticle Melts. *ACS Nano* **2020**, *14*, 15505–15516.
- (51) Sorkin, V.; Pei, Q. X.; Liu, P.; Thitsartarn, W.; He, C. B.; Zhang, Y. W. Atomistic-Scale Analysis of the Deformation and Failure of Polypropylene Composites Reinforced by Functionalized Silica Nanoparticles. *Sci. Rep.* **2021**, *11*, 1–14.
- (52) Yavitt, B. M.; Salatto, D.; Zhou, Y.; Huang, Z.; Endoh, M.; Wiegart, L.; Bocharova, V.; Ribbe, A. E.; Sokolov, A. P.; Schweizer, K. S.; Koga, T. Collective Nanoparticle Dynamics Associated with Bridging Network Formation in Model Polymer Nanocomposites. *ACS Nano* **2021**, *15*, 11501–11513.
- (53) Senses, E.; Darvishi, S.; Tyagi, M. S.; Tyagi, M. S.; Faraone, A. Entangled Polymer Dynamics in Attractive Nanocomposite Melts. *Macromolecules* **2020**, *53*, 4982–4989.
- (54) Moghimikheirabadi, A.; Kröger, M.; Karatrantos, A. V. Insights from Modeling into Structure, Entanglements, and Dynamics in Attractive Polymer Nanocomposites. *Soft Matter* **2021**, *17*, 6362–6373.
- (55) Medidhi, K. R.; Padmanabhan, V. Viscosity of Polyelectrolyte-Grafted Nanoparticle Solutions. *Soft Matter* **2021**, *17*, 3455–3462.
- (56) Liu, A. Y.; Emamy, H.; Douglas, J. F.; Starr, F. W. Effects of Chain Length on the Structure and Dynamics of Semidilute Nanoparticle-Polymer Composites. *Macromolecules* **2021**, *54*, 3041–3051.
- (57) Miller, C. A.; Hore, M. J. A. Simulation of the Coronal Dynamics of Polymer-Grafted Nanoparticles. *ACS Polym. Au* **2021**, No. 2.
- (58) Lin, E. Y.; Frischknecht, A. L.; Riggelman, R. A. Chain and Segmental Dynamics in Polymer-Nanoparticle Composites with High Nanoparticle Loading. *Macromolecules* **2021**, *54*, 5335–5343.
- (59) Bailey, E. J.; Winey, K. I. Dynamics of Polymer Segments, Polymer Chains, and Nanoparticles in Polymer Nanocomposite Melts: A Review. *Prog. Polym. Sci.* **2020**, *105*, 101242.
- (60) Flory, P. J. *In Principles of Polymer Chemistry*; Press, C. U., Ed.; Ithaca NY, 1953.

## References

---

- (61) Scheutjens, J. M. H. M.; Fleer, G. J. Statistical Theory of the Adsorption of Interacting Chain Molecules. 1. Partition Function, Segment Density Distribution, and Adsorption Isotherms. *J. Phys. Chem.* **1979**, *83*, 1619–1635.
- (62) Scheutjens, J. M. H. M.; Fleer, G. J. Statistical Theory of the Adsorption of Interacting Chain Molecules. 2. Train, Loop, and Tail Size Distribution. *J. Phys. Chem.* **1980**, *84*, 178–190.
- (63) Theodorou, D. N. Structure and Thermodynamics of Bulk Homopolymer/Solid Interfaces: A Site Lattice Model Approach. *Macromolecules* **1988**, *21*, 1400–1410.
- (64) Theodorou, D. N. Lattice Models for Bulk Polymers at Interfaces. *Macromolecules* **1988**, *21*, 1391–1400.
- (65) Helfand, E.; Tagami, Y. Theory of the Interface between Immiscible Polymers. II. *J. Chem. Phys.* **1972**, *56*, 3592–3601.
- (66) Daoulas, K. C.; Theodorou, D. N.; Harmandaris, V. A.; Karayiannis, N. C.; Mavrantzas, V. G. Self-Consistent-Field Study of Compressible Semiflexible Melts Adsorbed on a Solid Substrate and Comparison with Atomistic Simulations. *Macromolecules* **2005**, *38*, 7134–7149.
- (67) Revelas, C. J.; Sgouros, A. P.; Lakkas, A. T.; Theodorou, D. N. A Three-Dimensional Finite Element Methodology for Addressing Heterogeneous Polymer Systems with Simulations Based on Self-Consistent Field Theory. In *International Conference of Computational Methods In Science and Engineering 2020 (ICCMSE 2020)*; AIP Conference Proceedings, 2020; p 130002.
- (68) Schwarz, K.; Rieger, H. Efficient Kinetic Monte Carlo Method for Reaction-Diffusion Problems with Spatially Varying Annihilation Rates. *J. Comput. Phys.* **2013**, *237*, 396–410.
- (69) Versypt, A. N. F.; Arendt, P. D.; Pack, D. W.; Braatz, R. D. Derivation of an Analytical Solution to a Reaction-Diffusion Model for Autocatalytic Degradation and Erosion in Polymer Microspheres. *PLoS One* **2015**, *10*, 1–14.
- (70) Sanchez, I. C.; Lacombe, R. H. Statistical Thermodynamics of Polymer Solutions. *Macromolecules* **1978**, *11*, 1145–1156.
- (71) Sanchez, I. C.; Lacombe, R. H. An Elementary Molecular Theory of Classical Fluids. Pure Fluids. *J. Phys. Chem.* **1976**, *80*, 2352–2362.
- (72) Sgouros, A. P.; Vogiatzis, G. G.; Kritikos, G.; Boziki, A.; Nikolakopoulou, A.; Liveris, D.; Theodorou, D. N. Molecular Simulations of Free and Graphite Capped Polyethylene Films: Estimation of the Interfacial Free Energies. *Macromolecules* **2017**, *50*, 8827–8844.
- (73) Poser, C. I.; Sanchez, I. C. Surface Tension Theory of Pure Liquids and Polymer Melts. *J. Colloid Interface Sci.* **1979**, *69*, 539–548.
- (74) Rolo, L. I.; Caço, A. I.; Queimada, A. J.; Marrucho, I. M.; Coutinho, J. A. P. Surface Tension of Heptane, Decane, Hexadecane, Eicosane, and Some of Their Binary Mixtures. *J. Chem. Eng. Data* **2002**, *47*, 1442–1445.
- (75) Wang, S.; Jiang, L. Definition of Superhydrophobic States. *Adv. Mater.* **2007**, *19*, 3423–3424.
- (76) Revelas, C. J.; Sgouros, A. P.; Lakkas, A. T.; Theodorou, D. N. RuSseL: A Self-Consistent Field Theory Code for Inhomogeneous Polymer Interphases. *Computation* **2021**, *9*, 57.
- (77) Everaers, R.; Ejtehadi, M. R. Interaction Potentials for Soft and Hard Ellipsoids. *Phys. Rev. E - Stat. Physics, Plasmas, Fluids, Relat. Interdiscip. Top.* **2003**, *67*, 8.
- (78) Theodorou, D. N.; Vogiatzis, G. G.; Kritikos, G. Self-Consistent-Field Study of Adsorption and Desorption Kinetics of Polyethylene Melts on Graphite and Comparison with Atomistic Simulations. *Macromolecules* **2014**, *47*, 6964–6981.
- (79) Mansfield, K. F.; Theodorou, D. N. Atomistic Simulation of a Glassy Polymer/Graphite Interface. *Macromolecules* **1991**, *24*, 4295–4309.
- (80) Hong, K. M.; Noolandi, J. Conformational Entropy Effects in a Compressible Lattice Fluid Theory of Polymers. *Macromolecules* **1981**, *14*, 1229–1234.
- (81) Mortezaei, M.; Famili, M. H. N.; Kokabi, M. The Role of Interfacial Interactions on the Glass-Transition and Viscoelastic Properties of Silica/Polystyrene Nanocomposite. *Compos. Sci. Technol.* **2011**, *71*, 1039–1045.
- (82) Rosenholm, J. B. Wetting of Surfaces and Interfaces: A Conceptual Equilibrium Thermodynamic Approach. In *Colloid Stability - The Role of Surface Forces - Part II*; Tadros, T. F., Ed.; Wiley-VCH Verlag GmbH & Co. KGaA: Weinheim, 2007; pp 1–83.
- (83) Drolet, F.; Fredrickson, G. H. Combinatorial Screening of Complex Block Copolymer Assembly

- with Self-Consistent Field Theory. *Phys. Rev. Lett.* **1999**, *83*, 4317–4320.
- (84) Press, W. H.; Teukolsky, S. A.; Vetterling, W. T.; Flannery, B. P. *Numerical Recipes in C - The Art of Scientific Computing*; New York, 1992.
- (85) Higham, N. J. *Accuracy and Stability of Numerical Algorithms*, 2nd ed.; Society for Industrial and Applied Mathematics: USA, 2002.
- (86) Datta, B. N. *Numerical Linear Algebra and Applications*, 2nd ed.; Society for Industrial and Applied Mathematics Philadelphia, PA, USA, 2010.
- (87) Rasmussen, K.; Kalosakas, G. Improved Numerical Algorithm for Exploring Block Copolymer Mesophases. *J. Polym. Sci. Part B Polym. Phys.* **2002**, *40*, 1777–1783.
- (88) Kim, J. U.; Matsen, M. W. Finite-Stretching Corrections to the Milner-Witten-Cates Theory for Polymer Brushes. *Eur. Phys. J. E* **2007**, *23*, 135–144.
- (89) Vigil, D. L.; García-Cervera, C. J.; Delaney, K. T.; Fredrickson, G. H. Linear Scaling Self-Consistent Field Theory with Spectral Contour Accuracy. *ACS Macro Lett.* **2019**, *8*, 1402–1406.
- (90) Ouaknin, G.; Laachi, N.; Delaney, K.; Fredrickson, G. H.; Gibou, F. Self-Consistent Field Theory Simulations of Polymers on Arbitrary Domains. *J. Comput. Phys.* **2016**, *327*, 168–185.
- (91) Hutton, D. V. *Fundamentals of Finite Element Analysis*; McGraw Hill, 2004.
- (92) Smith, I. M., Griffiths, D. V., Margetts, L. *Programming the Finite Element Method*, Fifth.; Wiley, 2014.
- (93) Geuzaine, C., Remacle, J. Gmsh: A 3-D Finite Element Mesh Generator with Built-in Pre- and Post-Processing Facilities. *Int. J. Numer. Methods Eng.* **2009**, *79*, 1309–1311.
- (94) Lin, H.; Duan, Y. Y.; Min, Q. Gradient Theory Modeling of Surface Tension for Pure Fluids and Binary Mixtures. *Fluid Phase Equilib.* **2007**, *254*, 75–90.
- (95) Amestoy, P. R.; Duff, I. S.; L'Excellent, J. Y.; Koster, J. A Fully Asynchronous Multifrontal Solver Using Distributed Dynamic Scheduling. *SIAM J. Matrix Anal. Appl.* **2001**, *23*, 15–41.
- (96) Amestoy, P. R.; Buttari, A.; L'Excellent, J. Y.; Mary, T. Performance and Scalability of the Block Low-Rank Multifrontal Factorization on Multicore Architectures. *ACM Trans. Math. Softw.* **2019**, *45*, 1–26.
- (97) Wu, D. T.; Fredrickson, G. H.; Carton, J. -P; Ajdari, A.; Leibler, L. Distribution of Chain Ends at the Surface of a Polymer Melt: Compensation Effects and Surface Tension. *J. Polym. Sci. Part B Polym. Phys.* **1995**, *33*, 2373–2389.
- (98) Daoulas, K. C.; Harmandaris, V. A.; Mavrantzas, V. G. Detailed Atomistic Simulation of a Polymer/Solid Interface: Structure, Density and Conformation of a Thin Film of Polyethylene Melt Adsorbed on Graphite. *Macromolecules* **2005**, *38*, 5780–5795.
- (99) Sgouros, A. P.; Lakkas, A. T.; Megariotis, G.; Theodorou, D. N. Mesoscopic Simulations of Free Surfaces of Molten Polyethylene: Brownian Dynamics/Kinetic Monte Carlo Coupled with Square Gradient Theory and Compared to Atomistic Calculations and Experiment. *Macromolecules* **2018**, *51*, 9798–9815.
- (100) Matsen, M. W.; Griffiths, G. H. Melt Brushes of Diblock Copolymer. *Eur. Phys. J. E* **2009**, *29*, 219–227.
- (101) Vigil, D. L.; Delaney, K. T.; Fredrickson, G. H. Quantitative Comparison of Field-Update Algorithms for Polymer SCFT and FTS. *Macromolecules* **2021**, *54*, 9804–9814.
- (102) Raju, M. P. Parallelization of Finite Element Navier-Stokes Codes Using MUMPS Solver. *Innov. Adv. Comput. Sci. Eng.* **2010**, *4*, 515–518.
- (103) Deserno, M. How to Generate Equidistributed Points on the Surface of a Sphere. **2004**, 55128.
- (104) Cahn, J. W.; Hilliard, J. E. Free Energy of a Nonuniform System. I. Interfacial Free Energy. *J. Chem. Phys.* **1958**, *28*, 258–267.
- (105) Mathioudakis, I. G.; Vogiatzis, G. G.; Tzoumanekas, C.; Theodorou, D. N. Multiscale Simulations of PS–SiO<sub>2</sub> Nanocomposites: From Melt to Glassy State. *Soft Matter* **2016**, *12*, 7585–7605.
- (106) Träskelin, P.; Kuhl, T. L.; Faller, R. Molecular Dynamics Simulations of Polystyrene Brushes in Dry Conditions and in Toluene Solution. *Phys. Chem. Chem. Phys.* **2009**, *11*, 11324–11332.
- (107) Gharib-Zahedi, M. R.; Tafazzoli, M.; Böhm, M. C.; Alaghemandi, M. Interfacial Thermal Transport and Structural Preferences in Carbon Nanotube-Polyamide-6,6 Nanocomposites: How Important Are Chemical Functionalization Effects? *Phys. Chem. Chem. Phys.* **2015**, *17*, 14502–

## References

---

- 14512.
- (108) Theodorou, D. N.; Suter, U. W. Detailed Molecular Structure of a Vinyl Polymer Glass. *Macromolecules* **1985**, *18*, 1467–1478.
- (109) Rowlinson, J. S. A Drop of Liquid. *J. Phys. Condens. Matter* **1994**, *6*, A1–A8.
- (110) Sodt, A. J.; Pastor, R. W. The Tension of a Curved Surface from Simulation. *J. Chem. Phys.* **2012**, *137*, 234101.
- (111) Thompson, S. M.; Gubbins, K. E.; Walton, J. P. R. B.; Chantry, R. A. R.; Rowlinson, J. S. A Molecular Dynamics Study of Liquid Drops. *J. Chem. Phys.* **1984**, *81*, 530–542.
- (112) Nijmeijer, M. J. P. P.; Bruin, C.; Van Woerkom, A. B.; Bakker, A. F.; van Leeuwen, J. M. J. J. Molecular Dynamics of the Surface Tension of a Drop. *J. Chem. Phys.* **1992**, *96*, 565–576.
- (113) Cao, Z.; Stevens, M. J.; Dobrynin, A. V. Adhesion and Wetting of Nanoparticles on Soft Surfaces. *Macromolecules* **2014**, *47*, 3203–3209.
- (114) Carrillo, J.-M. Y.; Raphael, E.; Dobrynin, A. V. Adhesion of Nanoparticles. *Langmuir* **2010**, *26*, 12973–12979.
- (115) Bruil, H. G.; van Aartsen, J. J. The Determination of Contact Angles of Aqueous Surfactant Solutions on Powders. *Colloid Polym. Sci.* **1974**, *252*, 32–38.
- (116) Kirchberg, S.; Abdin, Y.; Ziegmann, G. Influence of Particle Shape and Size on the Wetting Behavior of Soft Magnetic Micropowders. *Powder Technol.* **2011**, *207*, 311–317.
- (117) Smith, G. D.; Bedrov, D. Dispersing Nanoparticles in a Polymer Matrix: Are Long, Dense Polymer Tethers Really Necessary? *Langmuir* **2009**, *25*, 11239–11243.
- (118) Martin, T. B.; Dodd, P. M.; Jayaraman, A. Polydispersity for Tuning the Potential of Mean Force between Polymer Grafted Nanoparticles in a Polymer Matrix. *Phys. Rev. Lett.* **2013**, *110*, 018301.
- (119) Jayaraman, A.; Nair, N. Integrating PRISM Theory and Monte Carlo Simulation to Study Polymer-Functionalised Particles and Polymer Nanocomposites. *Mol. Simul.* **2012**, *38*, 751–761.
- (120) Barnett, J. W.; Kumar, S. K. Modeling Gas Transport in Polymer-Grafted Nanoparticle Membranes. *Soft Matter* **2019**, *15*, 424–432.
- (121) Chakrabarti, A.; Nelson, P.; Toral, R. Structure of Polymer Chains End-Grafted on an Interacting Surface. *Physical Review A*. 1992, pp 4930–4934.
- (122) Lafitte, T.; Kumar, S. K.; Panagiotopoulos, A. Z. Self-Assembly of Polymer-Grafted Nanoparticles in Thin Films. *Soft Matter* **2014**, *10*, 786–794.
- (123) Ibergay, C.; Malfreyt, P.; Tildesley, D. J. Electrostatic Interactions in Dissipative Particle Dynamics: Toward a Mesoscale Modeling of the Polyelectrolyte Brushes. *J. Chem. Theory Comput.* **2009**, *5*, 3245–3259.
- (124) de Gennes, P. G. Polymers at an Interface; a Simplified View. *Adv. Colloid Interface Sci.* **1987**, *27*, 189–209.
- (125) Milner, S. T.; Witten, T. A.; Cates, M. E. Theory of the Grafted Polymer Brush. *Macromolecules* **1988**, *21*, 2610–2619.
- (126) de Gennes, P. G. Conformations of Polymers Attached to an Interface. *Macromolecules* **1980**, *13*, 1069–1075.
- (127) Alexander, S. Adsorption of Chain Molecules with a Polar Head - A Scaling Description. *Le J. Phys.* **1977**, *38*, 983–987.
- (128) Ganesan, V.; Jayaraman, A. Theory and Simulation Studies of Effective Interactions, Phase Behavior and Morphology in Polymer Nanocomposites. *Soft Matter* **2014**, *10*, 13–38.
- (129) Lettow, J. H.; Yang, H.; Nealey, P. F.; Rowan, S. J. Effect of Graft Molecular Weight and Density on the Mechanical Properties of Polystyrene-Grafted Cellulose Nanocrystal Films. *Macromolecules* **2021**, *54*, 10594–10604.
- (130) Wijmans, C. M.; Zhulina, E. B. Polymer Brushes at Curved Surfaces. *Macromolecules* **1993**, *26*, 7214–7224.
- (131) Daoud, M.; Cotton, J. P. Star Shaped Polymers: A Model for the Conformation and Its Concentration Dependence. *J. Phys. Paris* **1982**, *43*, 531–538.
- (132) Gennes, P. De. *Pierre-Giles De Gennes - Scaling Concepts in Polymer Physics (1979, Cornell University Press) - Libgen.Lc.Pdf*, Cornell University Press: UK, 1979.
- (133) Candau, F.; Rempp, P.; Benoit, H. A New Theoretical Approach to the Problem of Solution Behavior of Branched Polymers. *Macromolecules* **1972**, *5*, 627–635.

- (134) Meyer, M. The Microscopic Structure of Polymer Grafted Nanoparticles, Westfälische Wilhelms-Universität Münster, 2012.
- (135) Lenart, W. R.; Hore, M. J. A. Structure–Property Relationships of Polymer-Grafted Nanospheres for Designing Advanced Nanocomposites. *Nano-Structures and Nano-Objects* **2018**, *16*, 428–440.
- (136) Sgouros, A. P.; Revelas, C. J.; Lakkas, A. T.; Theodorou, D. N. Solvation Free Energy of Dilute Grafted (Nano)Particles in Polymer Melts via the Self-Consistent Field Theory. *J. Phys. Chem. B* **2022**, *126*, 7454–7474.
- (137) Akcora, P.; Liu, H.; Kumar, S. K.; Moll, J.; Li, Y.; Benicewicz, B. C.; Schadler, L. S.; Acehan, D.; Panagiotopoulos, A. Z.; Pryamitsyn, V.; Ganesan, V.; Ilavsky, J.; Thiyagarajan, P.; Colby, R. H.; Douglas, J. F. Anisotropic Self-Assembly of Spherical Polymer-Grafted Nanoparticles. *Nat. Mater.* **2009**, *8*, 354–359.
- (138) Chevigny, C.; Dalmas, F.; Di Cola, E.; Gignes, D.; Bertin, D.; Boué, F.; Jestin, J. Polymer-Grafted-Nanoparticles Nanocomposites: Dispersion, Grafted Chain Conformation, and Rheological Behavior. *Macromolecules* **2011**, *44*, 122–133.
- (139) Seddon, A. M.; Casey, D.; Law, R. V.; Gee, A.; Templer, R. H.; Ces, O. Drug Interactions with Lipid Membranes. *Chem. Soc. Rev.* **2009**, *38*, 2509–2519.
- (140) Endo, S.; Escher, B. I.; Goss, K.-U. Capacities of Membrane Lipids to Accumulate Neutral Organic Chemicals. *Environ. Sci. & Technol.* **2011**, *45*, 5912–5921.
- (141) Lipinski, C. A.; Lombardo, F.; Dominy, B. W.; Feeney, P. J. Experimental and Computational Approaches to Estimate Solubility and Permeability in Drug Discovery and Development Settings. *Adv. Drug Deliv. Rev.* **2001**, *46*, 3–26.
- (142) Lipinski, C. A. Lead- and Drug-like Compounds: The Rule-of-Five Revolution. *Drug Discov. Today. Technol.* **2004**, *1*, 337–341.
- (143) Colby, A. H.; Liu, R.; Schulz, M. D.; Padera, R. F.; Colson, Y. L.; Grinstaff, M. W. Two-Step Delivery: Exploiting the Partition Coefficient Concept to Increase Intratumoral Paclitaxel Concentrations In Vivo Using Responsive Nanoparticles. *Sci. Rep.* **2016**, *6*, 18720.
- (144) Praetorius, A.; Tufenkji, N.; Goss, K. U.; Scheringer, M.; Von Der Kammer, F.; Elimelech, M. The Road to Nowhere: Equilibrium Partition Coefficients for Nanoparticles. *Environ. Sci. Nano* **2014**, *1*, 317–323.
- (145) Schönsee, C. D.; Bucheli, T. D. Experimental Determination of Octanol–Water Partition Coefficients of Selected Natural Toxins. *J. Chem. Eng. Data* **2020**, *65*, 1946–1953.
- (146) Yang, L.; Peng, C.; Liu, H. Prediction of Solvation Free Energy and Partition Coefficient of Polychlorinated Biphenyls Using Thermodynamic Integration. *Chem. Phys. Lett.* **2020**, *754*, 137708.
- (147) Hansch, C.; Fujita, T. P- $\sigma$ - $\pi$  Analysis. A Method for the Correlation of Biological Activity and Chemical Structure. *J. Am. Chem. Soc.* **1964**, *86*, 1616–1626.
- (148) Garrido, N. M.; Queimada, A. J.; Jorge, M.; Macedo, E. A.; Economou, I. G. 1-Octanol/Water Partition Coefficients of n-Alkanes from Molecular Simulations of Absolute Solvation Free Energies. *J. Chem. Theory Comput.* **2009**, *5*, 2436–2446.
- (149) Soria, V.; Campos, A.; Figueruelo, J. E.; Gómez, C.; Porcar, I.; Garcia, R. Modeling of Stationary Phase in Size Exclusion Chromatography with Binary Eluents. *ACS Symp. Ser.* **1996**, *635*, 103–126.
- (150) García, R.; Celda, B.; Soria, V.; Tejero, R.; Campos, A. Non-Exclusion Phenomena in Size Exclusion Chromatography with Inorganic Porous Packing: A Thermodynamic Treatment. *Polymer (Guildf)*. **1990**, *31*, 1694–1702.
- (151) Fischer, F. C.; Cirpka, O. A.; Goss, K.-U.; Henneberger, L.; Escher, B. I. Application of Experimental Polystyrene Partition Constants and Diffusion Coefficients to Predict the Sorption of Neutral Organic Chemicals to Multiwell Plates in in Vivo and in Vitro Bioassays. *Environ. Sci. Technol.* **2018**, *52*, 13511–13522.
- (152) Torrens, F.; Soria, V. Stationary-Mobile Phase Distribution Coefficient for Polystyrene Standards. *Sep. Sci. Technol.* **2002**, *37*, 1653–1665.
- (153) Ben-Naim, A. *Solvation Thermodynamics*; Springer Boston MA, 1987.
- (154) Graziano, G. Solvation Thermodynamics in a van Der Waals Liquid. *Thermochim. Acta* **2003**, *399*, 181–187.

## References

---

- (155) Forouzangohar, M.; Kookana, R. S. Sorption of Nano-C60 Clusters in Soil: Hydrophilic or Hydrophobic Interactions? *J. Environ. Monit.* **2011**, *13*, 1190–1194.
- (156) Tufenkji, N. Modeling Microbial Transport in Porous Media: Traditional Approaches and Recent Developments. *Adv. Water Resour.* **2007**, *30*, 1455–1469.
- (157) Hristovski, K. D.; Westerhoff, P. K.; Posner, J. D. Octanol-Water Distribution of Engineered Nanomaterials. *J. Environ. Sci. Heal. Part A* **2011**, *46*, 636–647.
- (158) Cornelis, G.; Kirby, J. K.; Beak, D.; Chittleborough, D.; McLaughlin, M. J. A Method for Determination of Retention of Silver and Cerium Oxide Manufactured Nanoparticles in Soils. *Environ. Chem.* **2010**, *7*, 298–308.
- (159) Jang, M.-H.; Hwang, Y. S.; Lee, S.-K.; Lee, Y.-J. Determination of Phase Distributions for Multi-Walled Carbon Nanotubes Between Water and Soils: Limitation of Correlations with K<sub>ow</sub>. *Fullerenes, Nanotub. Carbon Nanostructures* **2013**, *21*, 916–929.
- (160) Ginzburg, V. V.; Weinhold, J. D.; Jog, P. K.; Srivastava, R. Thermodynamics of Polymer–Clay Nanocomposites Revisited: Compressible Self-Consistent Field Theory Modeling of Melt-Intercalated Organoclays. *Macromolecules* **2009**, *42*, 9089–9095.
- (161) Kim, Y.; Park, C. B.; Chen, P.; Thompson, R. B. Maximal Cell Density Predictions for Compressible Polymer Foams. *Polymer (Guildf)*. **2013**, *54*, 841–845.
- (162) Kim, J. U.; Matsen, M. W. Repulsion Exerted on a Spherical Particle by a Polymer Brush. *Macromolecules* **2008**, *41*, 246–252.
- (163) Matsen, M. W.; Gardiner, J. M. Autophobic Dewetting of Homopolymer on a Brush and Entropic Attraction between Opposing Brushes in a Homopolymer Matrix. *J. Chem. Phys.* **2001**, *115*, 2794–2804.
- (164) Binder, K.; Milchev, A. Polymer Brushes on Flat and Curved Surfaces: How Computer Simulations Can Help to Test Theories and to Interpret Experiments. *J. Polym. Sci. Part B Polym. Phys.* **2012**, *50*, 1515–1555.
- (165) Hansoge, N. K.; Gupta, A.; White, H.; Giuntoli, A.; Keten, S. Universal Relation for Effective Interaction between Polymer-Grafted Nanoparticles. *Macromolecules* **2021**, *54*, 3052–3064.
- (166) Lum, K.; Chandler, D.; Weeks, J. D. Hydrophobicity at Small and Large Length Scales. *J. Phys. Chem. B* **1999**, *103*, 4570–4577.
- (167) Aubouy, M.; Fredrickson, G. H.; Pincus, P.; Raphael, E. End-Tethered Chains in Polymeric Matrices. *Macromolecules* **1995**, *28*, 2979–2981.
- (168) Zhao, B.; Brittain, W. J. Polymer Brushes: Surface-Immobilized Macromolecules. *Prog. Polym. Sci.* **2000**, *25*, 677–710.
- (169) Morozova, T. I.; Lee, V. E.; Bizmark, N.; Datta, S. S.; Prud'homme, R. K.; Nikoubashman, A.; Priestley, R. D. In Silico Design Enables the Rapid Production of Surface-Active Colloidal Amphiphiles. *ACS Cent. Sci.* **2020**, *6*, 166–173.
- (170) Chremos, A.; Jeong, C.; Douglas, J. F. Influence of Polymer Architectures on Diffusion in Unentangled Polymer Melts. *Soft Matter* **2017**, *13*, 5778–5784.
- (171) Liu, S.; Lu, Y.-J.; Kappes, M. M.; Ibers, J. A. The Structure of the C60 Molecule: X-Ray Crystal Structure Determination of a Twin at 110 K. *Science (80-. )*. **1991**, *254*, 408–410.
- (172) Mishra, J.; Tiwari, S. K.; Abolhasani, M. M.; Azimi, S.; Nayak, G. C. 2 - Fundamental of Polymer Blends and Its Thermodynamics. In *Woodhead Publishing Series in Composites Science and Engineering*; Mishra, R. K., Thomas, S., Kalarikkal, N. B. T.-M. and N. F. C. (MFCs and Nfc. from P. B., Eds.; Woodhead Publishing, 2017; pp 27–55.
- (173) Gooch, J. W. Flory-Huggins Theory BT - Encyclopedic Dictionary of Polymers; Gooch, J. W., Ed.; Springer New York: New York, NY, 2011; p 315.
- (174) Maguire, S. M.; Boyle, M. J.; Bilchak, C. R.; Demaree, J. D.; Keller, A. W.; Krook, N. M.; Ohno, K.; Kagan, C. R.; Murray, C. B.; Rannou, P.; Composto, R. J. Grafted Nanoparticle Surface Wetting during Phase Separation in Polymer Nanocomposite Films. *ACS Appl. Mater. Interfaces* **2021**, *13*, 37628–37637.
- (175) Panayiotou, C. Interfacial Tension and Interfacial Profiles of Fluids and Their Mixtures. *Langmuir* **2002**, *18*, 8841–8853.
- (176) Sahimi, M.; Davis, H. T.; Scriven, L. E. Thermodynamic Modeling of Phase and Tension Behavior of CO<sub>2</sub>/Hydrocarbon Systems. *Soc. Pet. Eng. J.* **1985**, *25*, 235–254.

- (177) Sahimi, M.; Taylor, B. N. Surface Tension of Binary Liquid–Vapor Mixtures: A Comparison of Mean-field and Scaling Theories. *J. Chem. Phys.* **1991**, *95*, 6749–6761.
- (178) Gupta, M. K.; Robinson Robert L., J. Application of Gradient Theory of Inhomogeneous Fluid to Prediction of Low Interfacial Tensions in CO<sub>2</sub>/Hydrocarbon Systems. *SPE Reserv. Eng.* **1987**, *2*, 528–530.
- (179) Cornelisse, P. M. W.; Wijtkamp, M.; Peters, C. J.; de Swaan Arons, J. Interfacial Tensions of Fluid Mixtures with Polar and Associating Components. *Fluid Phase Equilib.* **1998**, *150–151*, 633–640.
- (180) Garrido, J.; Quinteros-Lama, H.; Piñeiro, M.; Mejia, A.; Segura, H. On the Phase and Interface Behavior along the Three-Phase Line of Ternary Lennard-Jones Mixtures: A Collaborative Approach Based on Square Gradient Theory and Molecular Dynamics Simulations. *J. Chem. Phys.* **2014**, *141*, 14503.
- (181) Lafitte, T.; Mendiboure, B.; Piñeiro, M. M.; Bessières, D.; Miqueu, C. Interfacial Properties of Water/CO<sub>2</sub>: A Comprehensive Description through a Gradient Theory–SAFT-VR Mie Approach. *J. Phys. Chem. B* **2010**, *114*, 11110–11116.
- (182) Miqueu, C.; Míguez, J. M.; Piñeiro, M. M.; Lafitte, T.; Mendiboure, B. Simultaneous Application of the Gradient Theory and Monte Carlo Molecular Simulation for the Investigation of Methane/Water Interfacial Properties. *J. Phys. Chem. B* **2011**, *115*, 9618–9625.
- (183) Chow, Y. T. F.; Eriksen, D. K.; Galindo, A.; Haslam, A. J.; Jackson, G.; Maitland, G. C.; Trusler, J. P. M. Interfacial Tensions of Systems Comprising Water, Carbon Dioxide and Diluent Gases at High Pressures: Experimental Measurements and Modelling with SAFT-VR Mie and Square-Gradient Theory. *Fluid Phase Equilib.* **2016**, *407*, 159–176.
- (184) Sgouros, A. P.; Knippenberg, S.; Guillaume, M.; Theodorou, D. N. Multiscale Simulations of Polyzwitterions in Aqueous Bulk Solutions and Brush Array Configurations. *Soft Matter* **2021**, *17*, 10873–10890.
- (185) Kwon, N. K.; Kim, H.; Shin, T. J.; Saalwächter, K.; Park, J.; Kim, S. Y. Control of Particle Dispersion with Autophobic Dewetting in Polymer Nanocomposites. *Macromolecules* **2020**, *53*, 4836–4844.
- (186) Kumar, S. K.; Benicewicz, B. C.; Vaia, R. A.; Winey, K. I. 50th Anniversary Perspective: Are Polymer Nanocomposites Practical for Applications? *Macromolecules* **2017**, *50*, 714–731.
- (187) Deng, S.; Zhang, L.; Zhou, X.; Fan, C.; Lin, Q.; Lin, J. Exploring Microstructures and Interphase Properties of Surface- Grafted Diblock Copolymers in a Homopolymer Melt by Self-Consistent Field Theory Simulations. *J. Macromol. Sci. Part B Phys.* **2015**, *54*, 348–364.
- (188) Hur, S. M.; Frischknecht, A. L.; Huber, D. L.; Fredrickson, G. H. Self-Consistent Field Simulations of Self- and Directed-Assembly in a Mixed Polymer Brush. *Soft Matter* **2011**, *7*, 8776–8788.
- (189) Patel, N.; Egorov, S. A. Interactions between Colloidal Particles in Polymer Solutions: A Density Functional Theory Study. *J. Chem. Phys.* **2004**, *121*, 4987–4997.
- (190) Striolo, A.; Egorov, S. A. Steric Stabilization of Spherical Colloidal Particles: Implicit and Explicit Solvent. *J. Chem. Phys.* **2007**, *126*, 014902.
- (191) Egorov, S. A. Interactions between Polymer Brushes in Solvents of Variable Quality: A Density Functional Theory Study. *J. Chem. Phys.* **2008**, *129*, 064901.
- (192) Lo Verso, F.; Egorov, S. A.; Milchev, A.; Binder, K. Spherical Polymer Brushes under Good Solvent Conditions: Molecular Dynamics Results Compared to Density Functional Theory. *J. Chem. Phys.* **2010**, *133*, 184901.
- (193) Frischknecht, A. L.; Yethiraj, A. Two- and Three-Body Interactions among Nanoparticles in a Polymer Melt. *J. Chem. Phys.* **2011**, *134*, 174901.
- (194) Karatrantos, A.; Clarke, N.; Composto, R. J.; Winey, K. I. Polymer Conformations in Polymer Nanocomposites Containing Spherical Nanoparticles. *Soft Matter* **2015**, *11*, 382–388.
- (195) Martin, T. B.; Mongcopa, K. I. S.; Ashkar, R.; Butler, P.; Krishnamoorti, R.; Jayaraman, A. Wetting-Dewetting and Dispersion-Aggregation Transitions Are Distinct for Polymer Grafted Nanoparticles in Chemically Dissimilar Polymer Matrix. *J. Am. Chem. Soc.* **2015**, *137*, 10624–10631.
- (196) Shen, J.; Liu, J.; Li, H.; Gao, Y.; Li, X.; Wu, Y.; Zhang, L. Molecular Dynamics Simulations of

## References

---

- the Structural, Mechanical and Visco-Elastic Properties of Polymer Nanocomposites Filled with Grafted Nanoparticles. *Phys. Chem. Chem. Phys.* **2015**, *17*, 7196–7207.
- (197) Smith, G. D.; Bedrov, D.; Li, L.; Bytner, O. A Molecular Dynamics Simulation Study of the Viscoelastic Properties of Polymer Nanocomposites. *J. Chem. Phys.* **2002**, *117*, 9478–9490.
- (198) Bore, S. L.; Kolli, H. B.; De Nicola, A.; Byshkin, M.; Kawakatsu, T.; Milano, G.; Cascella, M. Hybrid Particle-Field Molecular Dynamics under Constant Pressure. *J. Chem. Phys.* **2020**, *152*.
- (199) Munaò, G.; Correa, A.; Pizzirusso, A.; Milano, G. On the Calculation of the Potential of Mean Force between Atomistic Nanoparticles. *Eur. Phys. J. E* **2018**, *41*.
- (200) Baran; Sokołowski, S. Effective Interactions between a Pair of Particles Modified with Tethered Chains. *J. Chem. Phys.* **2017**, *147*, 044903.
- (201) Posel, Z.; Posocco, P.; Lísal, M.; Fermeglia, M.; Pricl, S. Highly Grafted Polystyrene/Polyvinylpyridine Polymer Gold Nanoparticles in a Good Solvent: Effects of Chain Length and Composition. *Soft Matter* **2016**, *12*, 3600–3611.
- (202) Gautham, S. M. B.; Patra, T. K. Deep Learning Potential of Mean Force between Polymer Grafted Nanoparticles. *Soft Matter* **2022**, *18*, 7909–7916.
- (203) Xuan, Y.; Delaney, K. T.; Ceniceros, H. D.; Fredrickson, G. H. Deep Learning and Self-Consistent Field Theory: A Path towards Accelerating Polymer Phase Discovery. *J. Comput. Phys.* **2021**, *443*, 110519.
- (204) Harton, S. E.; Kumar, S. K. Mean-Field Theoretical Analysis of Brush-Coated Nanoparticle Dispersion in Polymer Matrices. *J. Polym. Sci.* **2008**, *46*, 351–358.
- (205) Verso, F. Lo; Yelash, L.; Egorov, S. A.; Binder, K. Interactions between Polymer Brush-Coated Spherical Nanoparticles: The Good Solvent Case. *J. Chem. Phys.* **2011**, *135*, 214902.
- (206) Munaò, G.; Pizzirusso, A.; Kalogirou, A.; De Nicola, A.; Kawakatsu, T.; Müller-Plathe, F.; Milano, G. Molecular Structure and Multi-Body Potential of Mean Force in Silica-Polystyrene Nanocomposites. *Nanoscale* **2018**, *10*, 21656–21670.
- (207) Tong, C. Numerical Self-Consistent Field Theory Study of the Response of Strong Polyelectrolyte Brushes to External Electric Fields. *J. Chem. Phys.* **2015**, *143*, 054903.
- (208) Daoulas, K. C.; Müller, M. Exploring Thermodynamic Stability of the Stalk Fusion-Intermediate with Three-Dimensional Self-Consistent Field Theory Calculations. *Soft Matter* **2013**, *9*, 4097–4102.
- (209) Iacovella, C. R.; Keys, A. S.; Horsch, M. A.; Glotzer, S. C. Icosahedral Packing of Polymer-Tethered Nanospheres and Stabilization of the Gyroid Phase. *Phys. Rev. E* **2007**, *75*, 40801.
- (210) Phillips, C. L.; Iacovella, C. R.; Glotzer, S. C. Stability of the Double Gyroid Phase to Nanoparticle Polydispersity in Polymer-Tethered Nanosphere Systems. *Soft Matter* **2010**, *6*, 1693–1703.
- (211) Roan, J. R. Soft Nanopolyhedra as a Route to Multivalent Nanoparticles. *Phys. Rev. Lett.* **2006**, *96*, 1–4.
- (212) Frischknecht, A. L. Forces between Nanorods with End-Adsorbed Chains in a Homopolymer Melt. *J. Chem. Phys.* **2008**, *128*, 224902.
- (213) Koski, J. P.; Frischknecht, A. L. Fluctuation Effects on the Brush Structure of Mixed Brush Nanoparticles in Solution. *ACS Nano* **2018**, *12*, 1664–1672.
- (214) Koski, J.; Chao, H.; Riggelman, R. A. Predicting the Structure and Interfacial Activity of Diblock Brush, Mixed Brush, and Janus-Grafted Nanoparticles. *Chem. Commun.* **2015**, *51*, 5440–5443.
- (215) Rungta, A.; Natarajan, B.; Neely, T.; Dukes, D.; Schadler, L. S.; Benicewicz, B. C. Grafting Bimodal Polymer Brushes on Nanoparticles Using Controlled Radical Polymerization. *Macromolecules* **2012**, *45*, 9303–9311.
- (216) Ahrens; James; Geveci; Berk; Law; Charles. *ParaView: An End-User Tool for Large Data Visualization*; Visualization Handbook, Elsevier, 2005.
- (217) Ayachit; Utkarsh. *The Paraview Guide: A Parallel Visualization Application*; Kitware, 2015.
- (218) Gaines, G. L. Surface and Interfacial Tension of Polymer Liquids –a Review. *Polym. Eng. Sci.* **1972**, *12*, 1–11.
- (219) Hore, M. J. A.; Korley, L. T. J.; Kumar, S. K. Polymer-Grafted Nanoparticles. *J. Appl. Phys.* **2020**, *128*, 030401.
- (220) Liu, P.; Su, Z. Preparation of Polystyrene Grafted Silica Nanoparticles by Two-Steps UV Induced



- Reaction. *J. Photochem. Photobiol. A Chem.* **2004**, *167*, 237–240.
- (221) Liu, C. H.; Pan, C. Y. Grafting Polystyrene onto Silica Nanoparticles via RAFT Polymerization. *Polymer (Guildf)*. **2007**, *48*, 3679–3685.
- (222) Tumnantong, D.; Rempel, G. L.; Prasassarakich, P. Synthesis of Polystyrene-Silica Nanoparticles via RAFT Emulsifier-Free Emulsion Polymerization. *Eur. Polym. J.* **2016**, *80*, 145–157.
- (223) Pépin, M. P.; Whitmore, M. D. Monte Carlo and Numerical Self-Consistent Field Study of Systems with End-Grafted and Free Polymers in Good Solvent. *J. Chem. Phys.* **2001**, *114*, 8181–8195.
- (224) Nodoro, T. V. M.; Böhm, M. C.; Müller-Plathe, F. Interface and Interphase Dynamics of Polystyrene Chains near Grafted and Ungrafted Silica Nanoparticles. *Macromolecules* **2012**, *45*, 171–179.
- (225) Roan, J. R.; Kawakatsu, T. Self-Consistent-Field Theory for Interacting Polymeric Assemblies. II. Steric Stabilization of Colloidal Particles. *J. Chem. Phys.* **2002**, *116*, 7295–7310.
- (226) Jhalaria, M.; Buenning, E.; Huang, Y.; Tyagi, M.; Zorn, R.; Zamponi, M.; García-Sakai, V.; Jestin, J.; Benicewicz, B. C.; Kumar, S. K. Accelerated Local Dynamics in Matrix-Free Polymer Grafted Nanoparticles. *Phys. Rev. Lett.* **2019**, *123*, 158003.
- (227) Grabowski, C. A.; Koerner, H.; Meth, J. S.; Dang, A.; Hui, C. M.; Matyjaszewski, K.; Bockstaller, M. R.; Durstock, M. F.; Vaia, R. A. Performance of Dielectric Nanocomposites: Matrix-Free, Hairy Nanoparticle Assemblies and Amorphous Polymer-Nanoparticle Blends. *ACS Appl. Mater. Interfaces* **2014**, *6*, 21500–21509.
- (228) Wei, Y.; Xu, Y.; Faraone, A.; Hore, M. J. A. Local Structure and Relaxation Dynamics in the Brush of Polymer-Grafted Silica Nanoparticles. *ACS Macro Lett.* **2018**, *7*, 699–704.
- (229) Bilchak, C. R.; Buenning, E.; Asai, M.; Zhang, K.; Durning, C. J.; Kumar, S. K.; Huang, Y.; Benicewicz, B. C.; Gidley, D. W.; Cheng, S.; Sokolov, A. P.; Minelli, M.; Doghieri, F. Polymer-Grafted Nanoparticle Membranes with Controllable Free Volume. *Macromolecules* **2017**, *50*, 7111–7120.
- (230) Lee, P. W.; Isarov, S. A.; Wallat, J. D.; Molugu, S. K.; Shukla, S.; Sun, J. E. P.; Zhang, J.; Zheng, Y.; Lucius Dougherty, M.; Konkolewicz, D.; Stewart, P. L.; Steinmetz, N. F.; Hore, M. J. A.; Pokorski, J. K. Polymer Structure and Conformation Alter the Antigenicity of Virus-like Particle-Polymer Conjugates. *J. Am. Chem. Soc.* **2017**, *139*, 3312–3315.
- (231) Shah, I. U.; Jadhav, S. A.; Belekar, V. M.; Patil, P. S. Smart Polymer Grafted Silica Based Drug Delivery Systems. *Polym. Adv. Technol.* **2023**, *34*, 24–43.
- (232) Aubouy, M.; Fredrickson, G. H.; Pincus, P.; Raphael, E. End-Tethered Chains. *Macromolecules* **1995**, *28*, 2979–2981.
- (233) Theodorou, D. N. Variable-Density Model of Polymer Melt/Solid Interfaces: Structure, Adhesion Tension, and Surface Forces. *Macromolecules* **1989**, *22*, 4589–4597.
- (234) Allegra, G.; Raos, G.; Vacatello, M. Theories and Simulations of Polymer-Based Nanocomposites: From Chain Statistics to Reinforcement. *Prog. Polym. Sci.* **2008**, *33*, 683–731.
- (235) Balazs, A. C.; Emrick, T.; Russell, T. P. Nanoparticle Polymer Composites: Where Two Small Worlds Meet. *Science (80-. )*. **2006**, *314*, 1107–1110.
- (236) Rahimi, M.; Iriarte-Carretero, I.; Ghanbari, A.; Böhm, M. C.; Müller-Plathe, F. Mechanical Behavior and Interphase Structure in a Silica-Polystyrene Nanocomposite under Uniaxial Deformation. *Nanotechnology* **2012**, *23*, 305702.
- (237) Jancar, J.; Douglas, J. F.; Starr, F. W.; Kumar, S. K.; Cassagnau, P.; Lesser, A. J.; Sternstein, S. S.; Buehler, M. J. Current Issues in Research on Structure-Property Relationships in Polymer Nanocomposites. *Polymer (Guildf)*. **2010**, *51*, 3321–3343.
- (238) Choi, J.; Dong, H.; Matyjaszewski, K.; Bockstaller, M. R. Flexible Particle Array Structures by Controlling Polymer Graft Architecture. *J. Am. Chem. Soc.* **2010**, *132*, 12537–12539.
- (239) Dukes, D.; Li, Y.; Lewis, S.; Benicewicz, B.; Schadler, L.; Kumar, S. K. Conformational Transitions of Spherical Polymer Brushes: Synthesis, Characterization, and Theory. *Macromolecules* **2010**, *43*, 1564–1570.
- (240) Ghanbari, A.; Rahimi, M.; Dehghany, J. Influence of Surface Grafted Polymers on the Polymer Dynamics in a Silica-Polystyrene Nanocomposite: A Coarse-Grained Molecular Dynamics Investigation. *J. Phys. Chem. C* **2013**, *117*, 25069–25076.

## References

---

(241) Doi, M., Edwards, S. F. *The Theory of Polymer Dynamics*; Clarendon Press, 1986.

## CURRICULUM VITAE

### Constantinos J. Revelas, M.Sc.

Date of Birth: 27 July 1993, Cholongos, Attica

Address: Karaoli Dimitriou 87, Piraeus

#### Search/Contact Me

---

- *Email:* cjrevelas@gmail.com
- *Google (Scholar):* Constantinos J. Revelas
- *Scopus Author Id:* 57222727857
- *OrcID:* 0000-0002-7114-5464
- *Web of Science ResearcherID:* GOV-5909-2022
- *Github:* Constantinos J. Revelas
- *Skype:* Constantinos J. Revelas
- *Zoom:* Constantinos J. Revelas
- *ResearchGate:* Constantinos J. Revelas
- *LinkedIn:* Constantinos J. Revelas

#### Current Research Status

---

- PhD Candidate, National Technical University of Athens June 2018 - April 2023  
*Department:* Chemical Engineering  
*Scientific area:* Computational Materials Science  
*Advisor:* Prof. D. N. Theodorou, School of Chemical Engineering

#### Education

---

- National Technical University of Athens, Department of Chemical Engineering: Master of Engineering (ECTS: 300) October 2012 - July 2017  
Diploma Grade: 9.54  
Thesis title: “*Catalytic hydrodeoxygenation of phenolic molecules*”  
Thesis supervisor: Prof. N. G. Papayannakos
- Lycée Léonin (Néa Smyrni) Graduation Year: 2011  
Certificate Grade: 19.00/20.00

#### Foreign Languages

---

- English (FCE)
- French (C1)

#### Awards

---

- Thomaidis award (2019):  
Highest score concerning the courses of 9<sup>th</sup> semester
- Award from the Technical Chamber of Greece (2018):  
Award for graduating with the second highest score from the Chemical Engineering school of the National Technical University of Athens
- Limmat Stiftung award from the “Swiss Federal Department for Internal Affairs” (2018):  
Award for graduating with the second highest score from the Chemical Engineering school of the National Technical University of Athens
- Thomaidis award (2017):  
Highest score concerning the courses of 7<sup>th</sup> and 8<sup>th</sup> semester
- Award of “SARAFI’S” foundation (2017):  
Highest score concerning the courses of 7<sup>th</sup> and 8<sup>th</sup> semester

## Publications

---

- **C. J. Revelas**, A. P. Sgouros, A. T. Lakkas, D. N. Theodorou, “Addressing Nanocomposite Systems via 3D-SCFT: Assessment of the Smearing Approximation and Irregular Grafting Distributions”, *Macromolecules*, 2023, 56, 1731-1746, DOI: [10.1021/acs.macromol.2c02474](https://doi.org/10.1021/acs.macromol.2c02474)
- A. P. Sgouros, **C. J. Revelas**, A. T. Lakkas, D. N. Theodorou, “Solvation Free Energy of Dilute Grafted (Nano)Particles in Polymer Melts via the Self-Consistent Field Theory”, *The Journal of Physical Chemistry B*, 2022, 126, 7454-7474, DOI: [10.1021/acs.jpccb.2c05306](https://doi.org/10.1021/acs.jpccb.2c05306)
- **C. J. Revelas**, A. P. Sgouros, A. T. Lakkas, D. N. Theodorou, “RuSseL: A Self-Consistent Field Theory Code for Inhomogeneous Polymer Interphases”, *Computation*, 2021, 9, 57, DOI: [10.3390/computation9050057](https://doi.org/10.3390/computation9050057)
- A. P. Sgouros, **C. J. Revelas**, A. T. Lakkas, D. N. Theodorou, “Potential of Mean Force between Bare or Grafted Silica/Polystyrene Surfaces from Self-Consistent Field Theory”, *Polymers*, 2021, 13, 1197, DOI: [10.3390/polym13081197](https://doi.org/10.3390/polym13081197)
- A. T. Lakkas, A. P. Sgouros, **C. J. Revelas**, D. N. Theodorou, “Structure and Thermodynamics of Grafted Silica/Polystyrene Nanocomposites Investigated Through Self-Consistent Field Theory”, *Soft Matter*, 2021, 17, 4077-4094, DOI: [10.1039/d1sm00078k](https://doi.org/10.1039/d1sm00078k)
- **C. J. Revelas**, A. P. Sgouros, A. T. Lakkas, D. N. Theodorou, “A Three-Dimensional Finite Element Methodology for Addressing Heterogeneous Polymer Systems with Simulations Based on Self-Consistent Field Theory”, *International Conference of Computational Methods in Science and Engineering 2020 (ICCMSE 2020)*, 2021, DOI: [10.1063/5.0047729](https://doi.org/10.1063/5.0047729)
- Ch. C. Templis, **C. J. Revelas**, A. A. Papastilianou, N. G. Papayannakos, “Phenol Hydrodeoxygenation Over a Reduced and Sulfided NiMo/ $\gamma$ -Al<sub>2</sub>O<sub>3</sub> Catalyst”, *Industrial and Engineering Chemistry Research*, 2019, 58, 6278-6287, DOI: [10.1021/acs.iecr.8b06465](https://doi.org/10.1021/acs.iecr.8b06465)

## Conference Presentations

---

- **C. J. Revelas**, A. P. Sgouros, D. N. Theodorou, “Multiscale Modeling of Polymer-Nanoparticle Systems”, *Centre Européen de Calcul Atomique et Moléculaire (CECAM)*, Mixed-gen Season 2 – Session 1, Multiscale Simulations of complex materials, 2021
- **C. J. Revelas**, A. P. Sgouros, A. T. Lakkas, D. N. Theodorou, “A Three-Dimensional Finite Element Methodology for Addressing Heterogeneous Polymer Systems with Simulations Based on Self-Consistent Field Theory”, *International Conference of Computational Methods in Science and Engineering 2020 (ICCMSE)*, 2020

## Reviews

---

- 2 manuscript reviews for *Soft Matter*, Royal Society of Chemistry

## Research Projects

---

- “Multiscale Simulations of Polymers at Interfaces” (MuSiPolI), Hellenic Foundation for Research and Innovation (HFRI), Athens, Greece, 23 December 2019 – 22 December 2022
- “Molecular Simulations of Complex Polymer Systems” (MuSiCompS), Limmat Foundation, Zurich, Switzerland, 01 July 2019 - 31 January 2020

## Fellowships

---

- Fellowship offered to PhD students by the “Special Account for Research Funding” of the National Technical University of Athens, 24 May 2019 - 23 May 2023

## Additional Information

---

- Member of the Technical Chamber of Greece (Member number: 145446)
- C/C++/C++20, Fortran 90/95/2003, Python 3, Matlab, Bash shell scripting
- MPI protocol, Git version control, Linux systems administration, Basic knowledge of CUDA